Analysis of particle suspension and mixing in biological systems: an application of tomography

A thesis submitted to the University of Cape Town
in fulfilment of the requirements for the degree of
Doctor of Philosophy

by

Ryan Stevenson
BSc. (Chem. Eng)

Department of Chemical Engineering
University of Cape Town
September 2006

Abstract

The presence of solids in biological systems is found in many industrial applications including bead mills, minerals bioprocessing, soil bioremediation and immobilised biocatalysts. In these systems, the particulate phase is a nutrient, an agent for cell disruption or a surface for attachment. In systems where the solid particle is a nutrient or surface for attachment, mass transfer effects become significant. Alternatively, the solid particle is used as a mechanism to disrupt the cell, whereupon the frequency of solid-cell-solid collisions becomes important. In systems where cell disruption is not sought, it is important to understand the relative momentum, heat and mass transfer in order to control and prevent cell damage, while maintaining optimum operating conditions.

These processes are typically carried out in a slurry bioreactor. The slurry bioreactor is typically a mixing system containing a microbial phase and an abiotic particulate phase suspended in a liquid phase through which a gaseous phase may be distributed. This study presents an investigation into the distribution of phases in this reactor while varying key operating parameters. This information on phase distribution was predominantly obtained through application of tomographic technologies. Particles of quartzite, glass ballotini and nylon modelled the solid phase while the microbial phase was modelled with Bakers' yeast.

The key objective was to increase understanding of mixing and suspension in the slurry bioreactor environment. This knowledge is required to aid reactor design and to provide information on the effect of the main operating parameters on slurry bioreactor performance. It was also desired to relate this knowledge to previous work on microbial cell disruption on a similar scaled vessel by Scholtz-Brown (1998). A further objective was to increase understanding of the application of tomography to multiphase environments, while examining the development of this technology throughout this study.

The available technology consisted of electrical resistance tomography (ERT) and magnetic resonance imaging (MRI). The initial ERT system was applied to simple phantoms and to a swirling solid-liquid suspension in an industrial pipeline. Here, ERT resulted in clear visualisation of the swirling flow of particulates (sand 710 – 1180 μm and 2 x 3 mm plastic beads). The 3D images, created from interpolating 2D tomograms, further enhanced the visualisation of bulk particle flow behaviour. This successful application of ERT to a dynamic solid-liquid environment allowed more complex investigations to proceed.

ERT, with updated reconstruction software, was applied to a 220 mm diameter slurry reactor of 8.36 litres. Three size fractions of silica (106 – 212, 425 – 600 and 600 – 850 μm) at solids loadings of 5 to 20 % by volume were suspended at agitation rates of 236 to 547 rpm by Rushton and pitched blade impellers. The reactor volume from the impeller zone to the vessel wall was examined. The effect of agitation rate, solids loading, particle size and impeller type on suspension was clearly observed in axial and radial concentration profiles. Finer particles produced a more consistent suspension, while the Rushton impeller resulted in increased suspension over the pitched blade impeller at the same agitation rate. Particle homogeneity was examined through creating an expression based on weighted standard deviations of these profiles. This allowed a holistic description of particle distribution based on operating conditions. This concept aids comparison to other mixing systems.

At conditions of incomplete suspension, particle diameter was directly related to the shape of the axial concentration profile. This was related to previous work of Barresi and Baldi (1987a) who used a Peclet number to describe the quality of particle distribution. At increasing solid loadings with all size fractions, particle-particle interaction was observed at both upper and lower agitation rates. This effect was observed to be maximum in the 15 to 20 % vol. range. It was postulated that further solids addition would lead to suspension inefficiency. Physical methods of validation, namely sample withdrawal and conductivity probing, showed agreement with ERT in general.

Improved ERT hardware and software was applied to a smaller scale 50 mm reactor agitated by a Rushton impeller. Silica (600 – 850 μm) was agitated at the same tip speeds as the 220 mm reactor. Greater homogeneity was observed in the axial concentration profiles of the smaller vessel. This was postulated due to the higher power per unit volume. This indicates that scaling up based upon tip speed would result in decreased particle suspension. Through examining local solids concentration, perfect homogeneity was not attainable with increasing agitation rate. Optimal homogeneity was achieved at a lower power per unit volume in the 220 mm tank than the 50 mm vessel. This was postulated due to the larger scale eddies present in this vessel. Reconstructions in the 50 and 220 mm vessel had reproducibilities of 5 and 10 % respectively. This higher reproducibility for the smaller vessel was postulated due to the higher density of elements mapping this reactor's domain.

MRI was successfully applied to an identical 50 mm stirred tank reactor with a Rushton impeller. High resolution axial and radial concentration profiles were

generated using 1D and 3D MRI techniques on a suspension of borosilicate ballotini (50 and 100 μm, S.G = 2.20) and polyamide nylon particles (500 μm, S.G = 1.13). This allowed analysis of the effect of particle size, density and concentration on suspension. The lighter nylon particles showed a high degree of homogeneity. A linear relationship between agitation rate and unsuspended particles was observed for the 50 μm ballotini up to 480 rpm. In general, good suspension was achieved at sub critical suspension speeds based upon the Zwietering (1958) correlation. Such information is valuable for operating at incomplete solids suspension in the slurry bioreactor where solid-cell-solid collisions cause cell disruption. 2D radial slices depicted a clear view of incomplete suspension at the vessel bottom for a 10 % vol. suspension of the 50 μm particles. A swirl deposit of solids was observed originating from the baffles. It was deduced a uniform expansion of the unsuspended particle bed does not occur with increasing agitation rate. Complementary ERT experiments were performed, finding general agreement with radial concentration profiles. The more accurate 1D MRI was found to have better agreement with ERT than 3D MRI when comparing axial profiles. This supported the accuracy of the improved ERT hardware and software.

A qualitative ERT examination of air distribution in a 610 mm diameter vessel observed gas phase distribution altering with agitation rate. Further analysis in the 220 mm vessel quantified gas hold-up and surface aeration. At higher agitation rates the amount of entrained air was observed to be significant. However, this was concluded to contribute minimally to the oxygen mass transfer coefficient, based upon literature studies. ERT and MRI successfully detected a microbial phase and unexpectedly found axial concentration gradients of yeast. These gradients were further affected by agitation rate indicating particle-like behaviour of yeast. Similar gradient trends were observed in the nylon axial concentration profiles. These gradients influence heat, mass and momentum transfer in the slurry bioreactor. A slurry bioreactor was further simulated as yeast-nylon particle suspension, whereby decreased homogeneity was observed relative to nylon only suspensions. This was due to the increased viscosity of the microbial phase.

Hypothetical cell disruption was calculated based on the particle distribution information in the 220 mm reactor obtained from ERT. The model from Scholtz-Brown (1998) was applied to postulate where the dominant location of cell disruption occurs in the slurry bioreactor. In considering the design of large scale processes it was recommended that scale-up be based upon the desired axial solids concentration profile. The implications of knowledge obtained on solid, gaseous and microbial phase distribution from ERT and MRI was further related to heat, mass and momentum transfer literature concerning the slurry bioreactor.

Acknowledgments

Excluding sustained effort, this dissertation only exists through the interaction and support I have received from a fair number of people after its original conception:

My supervisor, Prof. Sue Harrison, for her optimism and keen mind, ready for scientific discussion and encouragement, while allowing the freedom to explore new territory. I enjoyed our "off-topic" philosophical conversations. I am particularly grateful for varied international opportunities, including research at the Universities of Manchester and Cambridge, and presentations at the 5th European Symposium of Biochemical Engineering Science in Stuttgart and the 7th World Congress of Chemical Engineering in Glasgow.

Research at the University of Manchester was only possible through the collaboration and support of Prof. Jan Cilliers. The eccentric Dr. Stephen Neethling was extremely accommodating and helpful, especially with Matlab, and as a flatmate. I am thankful for the close friendship and good humour of the Froth and Foam Research Group based at Manchester. Mike Cooke must be noted for providing much assistance with setting up the large scale reactor.

Dr. Mike Johns of Cambridge provided excellent collaboration and support, along with the mad scientists, Drs. Andrew Sederman and Mick Mantle. I have fond memories of my time there. I am also grateful for the friendship of the Magnetic Resonance Research Group at Cavendish Labs headed by Prof. Lynn Gladden.

Prof. Nick Miles of the School of Chemical, Environmental and Mining Engineering at the University of Nottingham needs to be thanked for his collaboration with the initial tomography trials.

Bill Randall, co-creator of the ERT system, was always available for discussion and assistance, while having one hand poking a circuit board. Stimulating electric field discussions were held with co-creator Andrew Wilkinson. Tim Long, programmer extraordinaire, provided much of his time in helping with tailored image reconstruction software. Granville de la Cruz must be thanked for his magnificent soldering and sharp wit.

Peter Dobias and David Bramble provided highly skilled workmanship, as shown in the varied equipment produced for this study. Martin Williams was always ready to lend a hand.

The Bioprocessing Group at UCT, many of you have provided assistance and friendship over the years. My other friends, too many to mention here, have kept me sane and motivated during this period. Special mention must go to Bala for his close friendship and thesis support, along with many hilarious moments. I also thank my friend Mike for his continued support and humour during this time.

Craig, my brother, thanks for the quick dinners and chats during "rush hour". And lastly, my parents, for their constant, multivariable support over the years. This thesis is dedicated to them.

Table of Contents

Abstract....i
Acknowledgements....iv
List of Figures....x
List of Tables....xviii
Nomenclature....xx
Glossary....xxiii

Chapter 1: Introduction
1.1 Background....1-1
1.2 Thesis Objectives....1-2
1.3 Thesis Outline....1-3

Chapter 2: Literature Review
2.1 Introduction....2-1
2.2 Heat Transfer in Stirred Tank Reactors....2-2
2.2.1 The Effect of Agitation on Heat Transfer....2-2
2.2.2 Heat Transfer in Non-Newtonian Liquids....2-3
2.2.3 Heat Transfer in Bioreactors....2-3
2.2.4 Heat Transfer in Aerated Systems....2-5
2.2.5 Heat Transfer in Three-Phase Fluidised beds....2-6
2.2.6 Conclusions....2-6
2.3 Mass Transfer in Stirred Tank Reactors....2-7
2.3.1 Gas-Liquid Mass Transfer....2-7
2.3.1.1 The Volumetric Mass Transfer Coefficient....2-7
2.3.1.2 Bubble Size....2-8
2.3.1.3 Gas Distribution and Hold-up....2-10
2.3.1.4 Gas-Liquid Transfer in Non – Newtonian Liquids and Microbial Cultures....2-10
2.3.1.5 Gas-Liquid Mass Transfer in Three-Phase Stirred Tanks....2-11
2.3.2 Conclusions....2-15
2.4 Parameters Affecting Suspension and Mixing in Stirred Tanks....2-16
2.4.1 Conclusions....2-20
2.5 Challenges Affecting Growth of Microorganisms in Stirred Tank Slurry Bioreactors....2-20
2.5.1 The Influence of Particulates on Slurry Bioreactor Performance....2-20
2.5.2 The Influence of Particle Size on Slurry Bioreactor Performance....2-21
2.5.3 The Influence of Agitation Rate on Slurry Bioreactor Performance....2-22
2.5.4 Gas-Liquid Mass Transfer Effects on Slurry Bioreactor Performance....2-22
2.5.5 Solid-Solid Particle Interaction in Stirred Tank Reactors....2-23
2.5.6 Conclusions....2-23
2.6 Quantifying Mixing and Suspension – Direct Methods....2-23
2.6.1 Sample Withdrawal in Slurry Reactors....2-23
2.6.1.1 Experimental Determination of Concentration Profiles by Sample Withdrawal....2-23
2.6.1.2 Quantifying Solid Suspension using Sample Withdrawal....2-26
2.6.2 Examining Suspension in Stirred Tanks Visually....2-28
2.6.2.1 Experimental Approach to Visual Determination of N_{js}....2-28
2.6.2.2 Quantifying Suspension through Visual Observation....2-30

2.6.3 Conclusions 2-31
2.7 Quantifying Mixing and Suspension – Indirect Methods 2-31
2.7.1 Determining Solids Distribution using Indirect Optical Techniques 2-31
2.7.1.1 Experimental Approach Using Optical Techniques 2-31
2.7.1.2 Quantifying Suspension Using Optical Methods 2-32
2.7.2 Conductivity Probing of the Slurry Reactor 2-34
2.7.2.1 Experimental Approach to Conductivity Probing 2-34
2.7.2.2 Quantifying Suspension Using Conductivity Probing 2-35
2.7.3 The Development of Suspension Models 2-36
2.7.4 Conclusions 2-40
2.8 Indirect Tomographic Methods Quantifying Suspension 2-40
2.8.1 Electrical Resistance Tomography 2-40
2.8.1.1 Introduction 2-40
2.8.1.2 Measurement Principle and Data Processing 2-41
2.8.1.3 Domain Discretisation 2-43
2.8.1.4 Reconstruction Algorithms 2-45
2.7.4.4.1 Linear Back Projection Algorithm 2-45
2.7.4.4.2 Newton-Raphson Algorithm 2-47
2.8.1.5 Calibration 2-48
2.8.1.6 ERT and Process Applications 2-49
2.8.1.7 ERT and Characterising Multiphase Systems 2-50
2.8.1.8 ERT and Solid-Liquid Mixing Models 2-52
2.8.1.9 Velocity Measurement from ERT 2-55
2.8.1.10 Three-Dimensional ERT 2-55
2.8.1.11 Limitations of ERT Measurement 2-56
2.8.1.12 Conclusions 2-57
2.8.2 Nuclear Magnetic Resonance Imaging 2-57
2.8.2.1 Introduction 2-57
2.8.2.2 Imaging with Magnetic Resonance 2-58
2.8.2.3 Spin-Lattice Relaxation 2-58
2.8.2.4 Spin-Spin Relaxation 2-59
2.8.2.5 Contrast Effects 2-59
2.8.2.6 The Limitations of NMR 2-60
2.8.2.7 Nuclear magnetic Resonance and Chemical Engineering 2-60
2.8.2.8 Determining Velocity Components with MRI in Single Phase Systems 2-61
2.8.2.9 MRI and Solid-Liquid Systems 2-62
2.8.2.10 Conclusions 2-63
2.9 Summary of Mixing and Suspension Knowledge for Stirred Tanks 2-63
2.9.1 Axial concentration profiles 2-63
2.9.2 Radial concentration profiles 2-64
2.9.3 Particle Suspension and Homogeneity 2-64
2.9.4 Summary of Methodologies Quantifying Suspension 2-65
2.10 Review Conclusions 2-66

Chapter 3: Materials and Methods
3.1 The ERT- Stirred Tank Reactor System 3-1
3.1.1 The Perspex Tank 3-2
3.1.2 Electrode Design 3-4
3.1.3 Impeller Design 3-6
3.1.4 Sparger Design 3-8
3.1.5 The Particulate Phases in the 220 mm ID Stirred Tank 3-8

3.1.6 The Fluid Phase in the 220 mm ID Stirred Tank 3-9
3.1.7 ERT Calibration Procedure 3-10
3.1.8 ERT Experimental Procedure 3-10
3.1.9 Conductivity Measurements 3-10
3.1.10 Pipette Sampling of the Stirred Tank 3-11
3.2 The Swirling Flow System 3-11
3.2.1 The Perspex Pipe and Electrodes 3-11
3.2.2 Swirl Inducement 3-13
3.2.3 The Liquid Phase in the Pipeline 3-14
3.2.4 The Solid Phase in the Pipeline 3-14
3.2.5 ERT Calibration Procedure 3-14
3.2.6 ERT Experimental Procedure 3-15
3.3 The MRI Miniature Stirred Tank Reactor 3-15
3.3.1 Geometry of Mini-STR 3-15
3.3.2 The Magnet and Probe 3-18
3.3.3 The Liquid and Solid Phases in the Mini-STR 3-18
3.3.4 MRI Calibration Procedure 3-19
3.3.5 MRI Experimental Procedure 3-20
3.4 The Miniature ERT-Stirred Tank Reactor 3-20
3.4.1 The Liquid and Solid Phases in the ERT Mini-STR 3-22
3.4.2 ERT Calibration Procedure 3-22
3.4.3 ERT Experimental Procedure 3-22
3.5 The Pilot-Scale Stirred Tank System 3-22
3.6 Experimental Overview 3-24

Chapter 4: ERT Hardware and Software

4.1 Introduction 4-1
4.2 ERT Hardware System I 4-1
4.2.1 The Measurement Principle 4-1
4.2.2 Measurement System 4-2
4.2.3 Calibration 4-3
4.3 Reconstruction Code I 4-5
4.4 Reconstruction Code II 4-6
4.5 Reconstruction Code III 4-7
4.5.1 Calibration and Algorithm 4-9
4.5.2 Data Extraction 4-9
4.6 ERT Hardware System II 4-9
4.7 Reconstruction Code IV 4-10
4.8 ERT Hardware System III 4-11
4.9 Reconstruction Code V 4-12
4.9.1 The Algorithm 4-13
4.9.2 Meshes 4-13
4.9.3 Calibration 4-14
4.9.4 Data Extraction 4-14
4.10 Summary of ERT Systems Used in Experimentation 4-14

Chapter 5: ERT as an Applicable Technology

5.1 Introduction 5-1
5.2 Examination of Phantoms 5-1
5.2.1 2D Slices of a Phantom in the 220 mm ID Tank 5-1
5.2.2 3D Interpolated Images 5-3
5.2.3 3D Examinations of Phantoms with EIDORS 5-4

5.2.4 Conclusions 5-5
5.3 Examining Flowing Solid-Liquid Systems with ERT 5-6
5.3.1 Introduction 5-6
5.3.2 Swirling Flow: Bead-Water System 5-7
5.3.2.1 2 % Bead Concentration 5-7
5.3.2.2 3 % Bead Concentration 5-9
5.3.2.3 4 % Bead Concentration 5-12
5.3.3 Swirling Flow: Sand-Water System 5-13
5.3.4 Discussion: Swirling Beads and Sand 5-14
5.4 Conclusions 5-18

Chapter 6: Quartzite Suspension and Reactor Homogeneity
6.1 Introduction 6-1
6.2 Quartzite Suspension in the 220 mm ID Perspex Tank 6-2
6.2.1 Conversion of ERT Data to Concentration Profiles 6-2
6.2.2 Radial Concentration Profiles for the Rushton Impeller 6-4
6.2.3 Radial Concentration Profiles for the Pitched Blade Impeller 6-10
6.2.4 Axial Concentration Profiles 6-17
6.2.5 Analysing Reactor Homogeneity 6-21
6.2.6 The Effect of Particle Diameter on Homogeneity 6-27
6.2.7 The Effect of Solids Loading upon Solids Hold-up 6-30
6.3 The Physical Validation of ERT 6-33
6.3.1 Direct Sample Withdrawal and Gravimetric Analysis 6-33
6.3.1.1 Pipette Sampling of the 220 mm ID Tank 6-33
6.3.1.2 Error Analysis of Pipette Sampling 6-35
6.3.2 Determination of the Concentration Profile through Conductivity Measurement 6-36
6.3.2.1 Conductivity Probing of the 220 mm ID Tank 6-36
6.3.2.2 Conductivity Probe Error Analysis 6-38
6.3.3 General Error Associated with ERT 6-38
6.4 Conclusions 6-38

Chapter 7: Developments in ERT and the Effect of Reactor Scale
7.1 Introduction 7-1
7.2 Detecting Physical Phantoms 7-1
7.3 Comparison of Latest ERT system with Initial System 7-2
7.4 Quartzite Suspension in the 50 mm ID Perspex Tank 7-3
7.4.1 Characterisation of the 50 mm ID Stirred Tank System 7-3
7.4.2 Radial Concentration Profiles for the 50 mm ID Tank 7-6
7.4.3 Axial Concentration Profiles for the 50 mm ID Tank 7-10
7.5 Error between Reconstructed Frames 7-12
7.6 Error between ERT Experiments 7-13
7.7 Conclusions 7-14

Chapter 8: Magnetic Resonance Imaging of the Slurry Reactor
8.1 Introduction 8-1
8.2 Conversion of MRI Data into Concentration Profiles 8-1
8.3 1D Examination of Particle Suspension 8-2
8.3.1 Suspension of Ballotini 8-3
8.3.1.1 Examination of the Effect of Particle Size and Solids Loading 8-3
8.3.1.2 Examining Incomplete Suspension 8-8
8.3.2 500 μm Nylon Suspensions 8-10

8.3.2.1 Examining Solids Loading 8-10
8.4 3D Examination of Particle Suspension 8-12
8.4.1 The 3D Experiment 8-12
8.4.2 Radial Concentration Profiles of Ballotini 8-12
8.4.3 2D Radial Slices of Incomplete Suspension 8-17
8.4.4 Radial Concentration Profiles of 500 μm Nylon particles 8-19
8.5 Errors Associated with MRI Experiments 8-22
8.5.1 Error while Maintaining Tuning 8-22
8.5.2 Uncertainty between Experiments after Re-tuning 8-23
8.5.3 Resolution 8-24
8.6 Comparisons of MRI with ERT Experiments 8-24
8.6.1 Radial Concentration Profiles Determined by ERT and MRI 8-24
8.6.2 Axial Concentration Profiles of ERT and MRI 8-28
8.7 Conclusions 8-29

Chapter 9: The Distribution of Air and Microorganisms in Stirred Tanks
9.1 Introduction 9-1
9.2 The Examination of a Gaseous Phase in Stirred Tanks 9-2
9.2.1 Detection of Air in the Pilot Scale Tank 9-2
9.2.2 Examining Hold-up in the 220 mm ID Tank 9-5
9.2.3 Surface Aeration in the 220 mm ID Tank 9-8
9.3 The Examination of Microorganisms in Stirred Tanks 9-12
9.3.1 ERT Detection of Yeast in the 220 mm ID Vessel 9-12
9.3.2 ERT and 1D MRI Yeast Detection with the 50 mm ID Vessel 9-13
9.3.3 Examination of Nylon-Yeast Mixtures with ERT and 1D MRI in the 50 mm ID Vessel 9-17
9.4 Conclusions 9-19

Chapter 10: The Slurry Bioreactor
10.1 Introduction 10-1
10.2 The Effect of Hydrodynamic Forces on the Microbial Phase 10-2
10.2.1 The Effect of Fluctuating Velocity Components 10-2
10.2.2 The Effect of Time-Averaged Velocity Components 10-3
10.3 Solid-Cell Interactions in the Slurry Bioreactor 10-4
10.3.1 Modelling of Cell Disruption 10-4
10.3.2 Localised Cell Disruption in the Slurry Bioreactor 10-5
10.3.2.1 Hypothetical Cell Disruption in the 220 mm Reactor 10-5
10.3.2.2 Hypothetical Cell Disruption in the 50 mm Reactor 10-7
10.3.2.3 The Influence of Local Cell Concentration on Cell Disruption 10-7
10.4 Heat Transfer in the Slurry Bioreactor 10-8
10.5 The Oxygen Mass Transfer Coefficient in the Slurry Bioreactor 10-9
10.6 The Microbial Phase in the Slurry Bioreactor 10-10
10.7 Conclusions 10-11

Chapter 11: Conclusions and Recommendations
11.1 Summary and Conclusions of the Study 11-1
11.2 Contribution to Knowledge 11-4
11.3 Recommendations 11-5

References R1-R13

Appendices A1-A33

List of Figures

Chapter 2: Literature Review

Figure 2.1: Overall effect of solid concentration on k_La at u_{sg} = 0.34 $cm.s^{-1}$ (a) and 1.36 $cm.s^{-1}$ (b) (van Weerts *et al.*, 1995). 2-12

Figure 2.2: Volumetric mass transfer coefficient k_La as a function of the air flow rate at a solids fraction of 10 vol. % and impeller speed of 500 rpm 2-13

Figure 2.3: Influence of the withdrawal velocity and the edge of the withdrawal tube on the axial concentration profiles..... 2-25

Figure 2.4: Mean axial solids concentration for particle sizes 89, 240 and 385 μm at N_{js}. (Baldi *et al.*, 1981)..... 2-26

Figure 2.5: Radial and axial concentration profiles through direct wall sampling (Barresi and Baldi, 1987a)..... 2-28

Figure 2.6: Solid suspension stages from Bujalski *et al.* (1999). The solid line represents the static solids at the bottom, while the dotted line represents the solid-liquid interface. 2-30

Figure 2.7: Relating the dimensionless solid concentration ratio to the dimensionless height for different impeller speeds..... 2-33

Figure 2.8: Relating the dimensionless solid concentration ratio to the dimensionless height for different impeller speeds..... 2-33

Figure 2.9: Relating the dimensionless solid concentration ratio to the dimensionless height for different impeller speeds..... 2-34

Figure 2.10: Axial concentration profiles obtained from conductivity probe measurements. 425 - 500 μm particle size fraction (a), 600 - 710 μm (b). 2-36

Figure 2.11: Electrical resistance tomography system 2-42

Figure 2.12: Flow chart depicting the typical iterative data processing procedure in electrical resistance tomography (Naidoo, 2002). 2-44

Figure 2.13: The effect of increasing the number elements of the domain mesh on the accuracy of the solution..... 2-45

Figure 2.14: Axial concentration profile of 3.5 wt. % beads (Mann *et al.*, 2001). 2-52

Figure 2.15: Variation of the relative standard deviation with agitation rate 2-53

Figure 2.16: The effect of impeller type on axial concentration for a pitched-blade impeller (a), and an A310 (b) for 150-210 μm quartzite in water. Geometry: C = T/3, D =T/2, B = T/12, H = T = 305 mm. (Williams *et al.*, 1996) 2-54

Chapter 3: Materials and Methods

Figure 3.1: The ERT-stirred tank apparatus depicting drill press, shaft, impeller, sparger, switch boxes, tomography hardware and a PC. 3-2

Figure 3.2: Design of the Perspex stirred tank reactor including positioning of electrode layers..... 3-3

Figure 3.3: Design of high density polypropylene base showing position of O-ring used as a seal with the Perspex cylinder..... 3-4

Figure 3.4: A photograph of the Perspex tank reactor showing 4 layers of electrodes. 3-4

Figure 3.5: The components of the electrode system 3-5

Figure 3.6: Layout and design of the copper electrodes. Electrodes are 1 mm thick..... 3-5

Figure 3.7: Close-up image of the electrodes: the black neoprene rubber is visible against the wall of the tank. 3-6

Figure 3.8: The six-bladed Rushton turbine..... 3-6

Figure 3.9: The six-bladed pitched-blade turbine (pumping downwards at 45°)..... 3-7

Figure 3.10: The pitched-blade (pumping-downwards) and Rushton turbine impellers 3-7
Figure 3.11: Design of pipe sparger used in aeration experiments (a); and the photo thereof (b). 3-8
Figure 3.12: Three sieved size distributions examined by Malvern Mastersizer: 106 – 212 μm (a); 425 – 600 μm (b); 600 – 850 μm (c). 3-9
Figure 3.13: Perspex pipe section with 4 layers of 16 electrodes 3-12
Figure 3.14: (a) The University of Nottingham Perspex pipe system with associated ERT apparatus; and (b) close-up of the contoured copper electrodes. 3-12
Figure 3.14: Swirly-flow boiler tubing connected to the Perspex pipe. White plastic beads simulated slurry conditions. 3-13
Figure 3.15: Perspex pipe section wired up to the ERT hardware monitoring swirling plastic beads 3-13
Figure 3.16: Quartzite size distribution for the pipeline. 3-14
Figure 3.17: Design and photo of the mini-STR for magnetic resonance imaging 3-16
Figure 3.18: The impeller and shaft were constructed out of a single piece of PEEK and designed to be geometrically similar to the Rushton turbine used in the 220 mm ID Perspex tank. ... 3-17
Figure 3.19: The Bruker 200 MHz magnet 3-18
Figure 3.20: Malvern size distributions of 100 μm borosilicate ballotini (a), 50 μm borosilicate ballotini (b), and 600 μm nylon particles (c). 3-19
Figure 3.21: Electrode configuration for the mini-STR 3-21
Figure 3.22: Photo of the mini-ERT STR with 4 layers of 16 stainless steel electrodes connected via shielded wire and driven by a drill press. 3-21
Figure 3.23: Pilot-scale 252 litre, 2-foot diameter stirred tank with dished bottom 3-23
Figure 3.24: The Perspex pilot-scale vessel with 8 layers of 16 stainless steel electrodes 3-23
Figure 3.25: The gas-foil impeller, D = 304.8 mm 3-24

Chapter 4: ERT Hardware and Software

Figure 4.1: The current drive system to the pair of electrodes on the tank and the voltage recorded by a differential amplifier 4-2
Figure 4.2: Hypothesised symmetry of current injection and voltage measurement for the method of twin-scaling calibration applied to an eight electrode system (Naidoo, 2002). 4-3
Figure 4.3: 182 raw un-scaled voltages from measurement sequence 4-4
Figure 4.4: 104 empirically – scaled voltages from measurement sequence. 4-4
Figure 4.5: 2D FEM mesh containing 357 nodes and 616 triangular elements. There is a greater density of elements at the perimeter to account for larger voltage gradients 4-5
Figure 4.6: Reconstruction of a plastic rod in tank filled with water 4-6
Figure 4.7: 2 x 8 electrode layer 3D EIDORS mesh with 92 elements (Polydorides, 2002). 4-7
Figure 4.8: Matlab™ Reconstruction Code III showing functions available through submenus. 4-8
Figure 4.9: 12 ring, 712 element FEM mesh with a higher density of elements near the boundary to compensate for higher voltage gradients 4-8
Figure 4.10: LBP reconstructed tomograms for the 8 x 16 electrode layer tank as detailed in Section 3.5 4-11
Figure 4.11: Screenshot of Reconstruction Code V showing raw and calibrated voltages with 3D visualisation of the conductivity distribution 4-12
Figure 4.12: Stack of layer tomograms from a glass rod placed in an 8 electrode layer tank at an angle. 4-13
Figure 4.13: 934 element baffled irregular mesh (a) and the 788 element irregular mesh (excluding impeller zone) created with *Mesh Creator* (b). 4-14

Chapter 5: ERT as an Applicable Technology

Figure 5.1: Tomograms of the phantom (measuring cylinder) in the 220 mm ID tank with Layer 1 closest to the tank bottom. 5-2
Figure 5.2: The plastic measuring cylinder orientated near the vessel wall in the 220 mm ID tank. 5-2
Figure 5.3: Comparison of axial behaviour of field lines originating from the middle of the tank (L2) and near the liquid surface (L4) showing $d_1 < d_2$. 5-3
Figure 5.4: 3D interpolated image of the phantom from 2-D slices from L1-4 5-3
Figure 5.5: 2D slices of a 3D conductivity distribution while examining a submerged phantom using Reconstruction Code II. 5-5
Figure 5.6: 2 % bead concentration at 0.5 $m.s^{-1}$ resulting in slug formation. 5-7
Figure 5.7: 2 % bead concentration at 1.0 $m.s^{-1}$ where angular components are visible at L1, but dissipate towards L4 resulting in deposition at the pipe bottom 5-8
Figure 5.8: 2 % bead concentration at 2.0 $m.s^{-1}$. Beads appear spread out on the pipe wall due to the higher velocity 5-8
Figure 5.9: Tomograms for 2 % bead concentration at 1.0 $m.s^{-1}$ (a) and 2.0 $m.s^{-1}$ (b). 5-8
Figure 5.10: 3 % bead concentration at 1.0 $m.s^{-1}$ (a); 1.5 $m.s^{-1}$ (b); 2.0 $m.s^{-1}$ (c) 5-10
Figure 5.11: 3D surface generated with Matlab™ from the tomograms in Figure 5.10 (b) showing the bulk flow of beads swirling for 3 % bead concentration at 1.5 $m.s^{-1}$. 5-11
Figure 5.12: 4 % bead concentration at 1.5 $m.s^{-1}$ (a) and 2.0 $m.s^{-1}$ (b) 5-12
Figure 5.13: 3D surface generated with Matlab™ from the tomograms in Figure 5.12 (b) showing the bulk flow of beads swirling for 4 % bead concentration at 2.0 $m.s^{-1}$ 5-13
Figure 5.14: 1 mm sand leaving the swirtly-flow boiler tubing under opaque conditions. 5-14
Figure 5.15: Tomgrams for sand at 2 % concentration at 2 $m.s^{-1}$ and the picture of the conditions at electrode layers 1 and 4. 5-14
Figure 5.16: The fraction of the tomogram which is greater than the relative non-conductivity of 0.6 (this represents bright yellow to red and the bulk flow of beads) for the successive electrode layers along the pipe. 5-17

Chapter 6: Quartzite Suspension and Reactor Homogeneity

Figure 6.1: The 712 FEM mesh and the relative position of the baffles and impeller 6-2
Figure 6.2: Examining resistance data to remove the presence of peaks associated with the 4 non-conducting baffles (a); Matlab™ software (Reconstruction Code III) showing 3D map of conductivity in the lowest plane of electrodes and the Newton-Raphson reconstructed image (1 iteration). The 4 baffles are visible on the outside of the tank wall and the impeller in the centre (in white) (b) 6-3
Figure 6.3: Radial concentration profiles for Rushton impeller at 236 rpm 5 % vol., 106-212 μm (a); 425-600 μm (b); 600-850 μm (c) 6-7
Figure 6.4: Radial concentration profiles for Rushton impeller at 236 rpm 15 % vol., 106-212 μm (a); 425-600 μm (b); 600-850 μm (c). 6-7
Figure 6.5: Radial concentration profiles for Rushton impeller at 547 rpm 5 % vol., 106-212 μm (a); 425-600 μm (b); 600-850 μm (c) 6-8
Figure 6.6: Radial concentration profiles for Rushton impeller at 547 rpm 15 % vol., 106-212 μm (a); 425-600 μm (b); 600-850 μm (c). 6-8
Figure 6.7: The effect of solids loading on radial concentration profiles for the Rushton impeller at 353 rpm for the 425 – 600 μm fraction. L1 (a), L2 (b), L3 (c) and L4 (d). 6-9
Figure 6.8: The effect of agitation rate on radial concentration profiles for the Rushton impeller at 15 % loading for the 425 – 600 μm fraction. L1 (a), L2 (b), L3 (c) and L4 (d). 6-9

Figure 6.9: Radial concentration profiles for pitched blade impeller at 236 rpm 5 % vol., 106-212 μm (a); 425-600 μm (b); 600-850 μm (c). 16-2
Figure 6.10: Radial concentration profiles for pitched blade impeller at 236 rpm 15 % vol., 106-212 μm (a); 425-600 μm (b); 600-850 μm (c). 6-12
Figure 6.11: Radial concentration profiles for pitched blade impeller at 547 rpm 5 % vol., 106-212 μm (a); 425-600 μm (b); 600-850 μm (c). 6-13
Figure 6.12: Radial concentration profiles for pitched blade impeller at 547 rpm 15 % vol., 106-212 μm (a); 425-600 μm (b); 600-850 μm (c). 6-13
Figure 6.13: The effect of agitation rate on radial concentration profiles for the pitched blade impeller impeller at 15 % loading for the 425 – 600 μm fraction. L1 (a), L2 (b), L3 (c) and L4 (d). 6-14
Figure 6.14: The effect of impeller type on particle suspension at the same agitation rate. 6-14
Figure 6.15: Radial concentration profiles for the pitched-blade impeller 20 % vol. at 236 rpm: 106-212 μm (a); 425-600 μm (b); 600-850 μm (c) 6-15
Figure 6.16: Radial concentration profiles for the pitched-blade impeller 20 % vol. at 547 rpm: 106-212 μm (a); 425-600 μm (b); 600-850 μm (c) 6-15
Figure 6.17: Radial concentration profiles for the Rushton impeller 20 % vol. at 236 rpm: 106-212 μm (a); 425-600 μm (b); 600-850 μm (c). 6-16
Figure 6.18: Radial concentration profiles for the Rushton impeller 20 % vol. at 547 rpm: 106-212 μm (a); 425-600 μm (b); 600-850 μm (c). 6-16
Figure 6.19: Axial concentration profiles for Rushton impeller for 5 % volume fraction at 236 rpm (a) and 547 rpm (b). 6-17
Figure 6.20: Axial concentration profiles for Rushton impeller for 15 % volume fraction at 236 rpm (a) and 547 rpm (b). 6-17
Figure 6.21: Axial concentration profiles for pitched blade impeller for 5 % volume fraction at 236 rpm (a) and 547 rpm (b). 6-18
Figure 6.22: Axial concentration profiles for pitched blade impeller for 15 % volume fraction at 236 rpm (a) and 547 rpm (b). 6-18
Figure 6.23: Axial concentration profiles for different agitation rates for the 106-212 μm fraction for 15 % solids concentration with the Rushton impeller (a) and the pitched blade impeller (b). 6-20
Figure 6.24: Axial concentration profiles for different agitation rates for the 425-600 μm fraction for 15 % solids concentration with the Rushton impeller (a) and the pitched blade impeller (b). 6-20
Figure 6.25: Axial concentration profiles for different agitation rates for the 600-850 μm fraction for 15 % solids concentration with the Rushton impeller (a) and the pitched blade impeller (b). 6-20
Figure 6.26: The effect of solids loading on normalised axial concentration at 353 rpm for the 425 – 600 μm fraction. 6-21
Figure 6.27: The effect of particle size, solids loading and agitation rate on the overall reactor homogeneity using the Rushton impeller. 6-24
Figure 6.28: The effect of particle size, solids loading and agitation rate on the overall reactor homogeneity using the pitched blade impeller. 6-25
Figure 6.29: The effect of agitation rate on reactor homogeneity for 5 and 15 vol. % suspensions of 425 – 600 μm quartzite using Rushton (a), and pitched blade impellers (b). 6-26
Figure 6.30: The effect of solids loading on reactor homogeneity at constant agitation rate of 353 rpm for 425 – 600 mm quartzite fraction 6-27

Figure 6.31: Exponential fitting of the axial concentration data for the 5 % solids loading (a) and the 15 % solids loading using a Rushton impeller at 236 rpm, and 20 % solids loading (c) at 304 rpm using the pitched blade impeller. Each layer concentration was normalised with respect to L4 fraction to aid visual display. 6-29
Figure 6.32: The linear relationship between the mean particle diameter and the exponent of the concentration profile (when applying exponential fitting to the axial profile). 6-29
Figure 6.33: The relationship between solids loading and solids hold-up at 236 rpm for the Rushton impeller. 106-212 μm (a); 425-600 μm (b); 600-850 μm (c). *C* is the volume fraction..... 6-32
Figure 6.34: The relationship between solids loading and solids hold-up at 547 rpm for the Rushton impeller. 106-212 μm (a); 425-600 μm (b); 600-850 μm (c). *C* is the volume fraction..... 6-32
Figure 6.35: The examination of particle-particle interaction at increasing solid loading for the Rushton impeller at 236 rpm (a), and 547 rpm (b)..... 6-33
Figure 6.36: 15 % volume concentration of the 600-850 μm fraction representing sample values (L4 and L3) and ERT values (L1-L4). 236 rpm (a); 353 rpm (b); 460 rpm (c). 6-34
Figure 6.37: 5 % volume concentration of the 106-212 μm fraction representing sample values (L4 and L3) and ERT values (L1-L4). 236 rpm (a); 353 rpm (b)..... 6-35
Figure 6.38: 5 % volume concentration of the 106-212 μm fraction representing conductivity probe values (L4 and L3) and ERT values (L1-L4). 236 rpm (a); 353 rpm (b)..... 6-37
Figure 6.39: 10 % volume concentration of the 425-600 μm fraction representing conductivity probe values (L4 and L3) and ERT values (L1-L4). 236 rpm (a); 353 rpm (b)..... 6-37

Chapter 7: Developments in ERT and the Effect of Reactor Scale

Figure 7.1: Conducting and non-conducting cylinders in a 20 cm ID, 8-layered tank of the University of Manchester (a), and the online image from Reconstruction Code V (b)..... 7-1
Figure 7.2: Comparison of the calculated conductivity profile with the actual object..... 7-2
Figure 7.3: Comparison of Reconstruction Code V and ERT Hardware III (a), with Reconstruction Code III and ERT Hardware I (b) at 15 % solids concentration with the 600 – 850 μm quartzite fraction at 547 rpm. 7-3
Figure 7.4: Radial concentration profiles for 5 % volume fraction for the 50 mm tank. Rushton impeller, 600-850 μm. 7-6
Figure 7.5: Radial concentration profiles for 5 % volume fraction for the 50 mm tank. Rushton impeller, 600 - 850 μm..... 7-7
Figure 7.6: Radial concentration profiles for 5 % volume fraction for the 220 mm tank. Rushton impeller, 600 - 850 μm..... 7-7
Figure 7.7: Radial concentration profiles for 15 % volume fraction for the 50 mm tank. Rushton impeller, 600 - 850 μm..... 7-8
Figure 7.8: Radial concentration profiles for 15 % volume fraction for the 220 mm tank. Rushton impeller, 600 - 850 μm..... 7-8
Figure 7.9: The effect of specific power (a) and impeller tip speed (b) on the mixing index for a 15 % suspension of 600 – 850 μm quartzite in the 50 and 220 mm tanks. 7-9
Figure 7.10: Reynolds numbers in the 50 and 220 mm tanks at the same P/V (a), and the same tip speed (b). 7-9
Figure 7.11: Examining the effect of increasing P/V on local particle concentration (L1)..... 7-10
Figure 7.12: Axial concentration profiles for 5 % volume fraction for the 50 mm tank (a-c) and the 220 mm tank (d-f). Rushton impeller, 600-850 μm. 7-11
Figure 7.13: Axial concentration profiles for 15 % volume fraction for the 50 mm tank (a-c) and the 220 mm tank (d-f). Rushton impeller, 600-850 μm. 7-12

Figure 7.14: The effect of impeller tip speed on $MI_{r(L1-L3)}$ for 5 (a) and 15 % (b) suspensions of 600 – 850 μm quartzite in the 50 and 220 mm reactors 7-12
Figure 7.15: The standard deviation with respect to the radial position of the element from reconstructing the 934 element mesh for 119 frames of data. Operating conditions: 15 % volume concentration of the 600-850 μm at 304 rpm. Layers 1 to 4 are presented (a-d)..... 7-13
Figure 7.16: Reproducibility of ERT experiments. 15 % quartzite (600-850 μm) at 353 rpm in the 220 mm tank (a) and at 1338 rpm in the 50 mm tank (b)..... 7-14

Chapter 8: Magnetic Resonance Imaging of the Slurry Reactor

Figure 8.1: Proton signal intensity related to the height of observation within the probe using the 50 mm tank containing water only 8-2
Figure 8.2: Axial concentration profiles generated by MRI for 5 % suspension of 100 μm ballotini for agitation rates 306, 366, 426 and 480 rpm 8-3
Figure 8.3: Axial concentration profiles generated by MRI for 5 % suspension of 50 μm ballotini (a) and 10 % suspension of 50 μm ballotini (b). The Rushton impeller is located at z/Z = 0.33 to 0.43..... 8-4
Figure 8.4: The fraction of ballotini (5 % suspension of 100 μm; 5 and 10 % suspension of 50 μm) remaining on the tank bottom with respect to the ratio of the agitation rate to the Zwietering critical suspension speed. 8-9
Figure 8.5: The fraction of solids (5 % suspension of 100 μm; 5 and 10 % suspension of 50 μm) above the impeller with respect to the ratio of the agitation rate to the Zwietering critical suspension speed. 8-9
Figure 8.6: Axial concentration profiles of the 500 μm nylon particles at volume concentrations of 5 % (a), 10 % (b), 15 % (c) and 20 % (d). 8-11
Figure 8.7: The fraction of nylon particles above the Rushton impeller at 186 rpm for 5 – 20 % solids concentration. The agitation rate (186 rpm) is further represented as a fraction of N_{js} with respect to each solid concentration (secondary y-axis). 8-11
Figure 8.8: Axial concentration profile obtained from 3D data for 5 % suspension of 50 μm ballotini at 480 rpm with Rushton impeller. Above approximately 40 mm (z/Z = 0.80) in height r.f. decay at the top of the probe is apparent..... 8-12
Figure 8.9: Radial concentration profiles for the bottom of the reactor at heights of 1.6 (z/Z = 0.03), 3.1 (z/Z = 0.06) and 4.7 mm (z/Z = 0.05) for the 5 % suspension of 50 μm ballotini agitated by 8-13
Figure 8.10: Radial concentration profiles for the Rushton impeller region and below at heights of 6.3 (z/Z = 0.13), 10.9 (z/Z = 0.22), 15.6 (z/Z = 0.31) and 21.9 mm (z/Z = 0.44) for the 5 % suspension of 50 μm ballotini at 480 rpm..... 8-13
Figure 8.11: Radial concentration profiles above the Rushton impeller at heights of 26.6 (z/Z = 0.53), 31.3 (z/Z = 0.63) and 35.9 mm (z/Z = 0.72) for the 5 % suspension of 50 μm ballotini at 480 rpm..... 8-14
Figure 8.12: Axial concentration profile obtained from 3D data for 10 % suspension of 50 μm ballotini at 480 rpm with Rushton impeller. 8-15
Figure 8.13: Radial concentration profiles for the bottom of the reactor at heights of 0.9 (z/Z = 0.02), 1.8 (z/Z = 0.04), 2.7 (z/Z = 0.05) and 4.5 mm (z/Z = 0.09) for the 10 % suspension of 50 μm ballotini using a Rushton impeller at 480 rpm. 8-15
Figure 8.14: Radial concentration profiles for below the Rushton impeller at heights of 10.7 (z/Z = 0.21), 13.4 (z/Z = 0.27), 15.2 (z/Z =0.30) and 17.0 mm (z/Z = 0.34) for the 10 % suspension of 50 μm ballotini at 480 rpm. 8-16

Figure 8.15: Radial concentration profiles above the Rushton impeller at heights of 25.9 (z/Z = 0.52), 31.3 (z/Z = 0.63) and 38.4 mm (z/Z = 0.77) for the 10 % suspension of 50 μm ballotini at 480 rpm. 8-17
Figure 8.16: 2D slices at the tank bottom for the 10 % v/v 50 μm ballotini particles on agitation with Rushton impeller at 480 rpm 8-18
Figure 8.17: The average concentration in the x-direction with respect to the radius of the tank for the 10 % suspension of 50 μm concentration for the heights of 0.9, 1.9, 2.8 and 3.7 mm. z/Z = 0.02 to 0.07 8-18
Figure 8.18: 2D slices at the impeller zone for the 10 % v/v suspension of 50 μm ballotini particles agitated by the Rushton impeller at 480 rpm 8-19
Figure 8.19: Axial concentration of 10 % suspension of 500 μm nylon with Rushton impeller obtained from 3D data. Data was useable up to a height of 40 mm (z/Z = 0.8) and an average volume fraction of 0.11 was calculated for this profile. 8-20
Figure 8.20: Radial concentration profiles for the bottom of the reactor at heights of 0.0, 0.9, 1.8 and 2.6 mm for the 10 % suspension of 500 μm polyamide nylon agitated by Rushton impeller at 480 rpm. z/Z = 0 to 0.05. 8-20
Figure 8.21: Radial concentration profiles below the Rushton impeller at heights of 6.1 (z/Z = 0.12), 10.5 (z/Z = 0.21), 14.0 (z/Z = 0.28) and 16.7 mm (z/Z = 0.33) for the 10 % suspension of 500 μm polyamide nylon at 480 rpm. 8-21
Figure 8.22: Radial concentration profiles above the Rushton impeller at heights of 21.1 (z/Z = 0.42), 26.3 (z/Z = 0.53), 31.6 (z/Z = 0.63) and 38.6 mm (z/Z = 0.77) for the 10 % suspension of 500 μm polyamide nylon at 480 rpm. 8-21
Figure 8.22: Uncertainty with respect to agitation rate and reactor height for 1D scans of the 5 % suspension of 100 μm ballotini. 8-22
Figure 8.23: Uncertainty with respect to signal intensity across the reactor for water at zero agitation. 8-23
Figure 8.24: Uncertainty with respect to reactor height between re-tuned experiments for the 10 % suspension of 50 μm ballotini agitated by Rushton impeller at 480 rpm. 8-23
Figure 8.25: Comparison of average radial ERT profiles and location specific MRI profiles at the same heights (L1 – L4). 5 % suspension of 50 μm ballotini agitated by Rushton impeller at 480 rpm. 8-25
Figure 8.26: A comparison of the average radial profile for the whole reactor for both tomographies. 5 % suspension of 50 μm ballotini at 480 rpm. 8-25
Figure 8.27: Comparison of average radial ERT profiles and location specific MRI profiles at the same heights (L1 – L4). 10 % suspension of 50 μm ballotini agitated at 480 rpm. 8-26
Figure 8.28: A comparison of the average radial profile for the whole reactor for both tomographies. 10 % suspension of 50 μm ballotini agitated by Rushton impeller at 480 rpm. 8-26
Figure 8.29: Comparison of average radial ERT profiles and location specific MRI profiles at the same heights (L1 – L4). 10 % suspension of 500 μm nylon particles at 480 rpm. 8-27
Figure 8.30: A comparison of the average radial profile for the whole reactor for both tomographies. 10 % suspension of 500 μm nylon particles at 480 rpm. 8-27
Figure 8.31: Axial concentration profile comparison of tomographies: 8-29

Chapter 9: The Distribution of Air and Microorganisms in Stirred Tanks

Figure 9.1: Air sparged at 0.5 vvm into the 8 electrode layer, 2.3 m3 tank fitted with a gasfoil impeller and operated at increasing agitation rates of 100 rpm (a), 200 rpm (b), 300 rpm (c), 450 rpm (d)..... 9-3
Figure 9.2: Tomograms stacked for x and y positions midway in the vessel (x = y = 10; grid = 20 x 20 pixels) with increasing agitation rate from left to right, 100 – 450 rpm. 9-4
Figure 9.3: The general increase in resistance (presence of air) in the electrode layer with increasing agitation rate..... 9-4
Figure 9.4: The volume fraction of air in the reactor at 0.5 vvm at increasing agitation rates using the Rushton impeller for r/R = 0.55 to 1.00..... 9-6
Figure 9.5: The volume fraction of air in the reactor at 1.0 vvm at increasing agitation rates using the Rushton impeller for r/R = 0.55 to 1.00..... 9-6
Figure 9.6: The relationship between the observed volume fraction of air and that estimated by ERT. 9-7
Figure 9.7: The volume fraction of air entrained for electrode layers L1 - L3 at agitation rates of 304 - 547 rpm with Rushton impeller..... 9-10
Figure 9.8: The average amount of entrained air for L1 – L3 with respect to agitation rate. Rushton impeller, data: r/R = 0.55 to 1.00..... 9-10
Figure 9.9: Micrograph of budding *Saccharomyces cerevisiae.* (a) Scanning electron micrograph at 14400x magnification (Scholtz-Brown, 1998). 9-12
Figure 9.10: Radial concentration profile of 5 % yeast at 236 rpm in the 220 mm ID tank using the Rushton impeller 9-13
Figure 9.11: Axial concentration profile of 5 % yeast at 236 rpm in the 220 mm ID tank using the Rushton impeller. (r/R = 0.55 to 1.00) 9-13
Figure 9.12: ERT radial concentration profiles for 5 and 11 vol. % yeast agitated at 480 rpm with the Rushton impeller in the 50 mm reactor..... 9-14
Figure 9.13: Axial concentration profiles for 5 % yeast at 186 – 480 rpm produced from MRI data (a); ERT axial concentration profile for 5 % yeast at 480 rpm, data from r/R = 0.55 – 1.00 (b); Axial concentration profiles for 11 % yeast at 186 – 480 rpm produced from MRI data (c); ERT axial concentration profile for 11 % yeast at 480 rpm, data from r/R = 0.55 – 1.00 (d)..... 9-15
Figure 9.14: Normalised average concentration for the agitation rate range of 186 to 480 rpm for the 5 and 11 % yeast concentrations. 9-16
Figure 9.15: Radial profiles of suspensions of 10 % nylon particles with 5 % yeast generated by ERT (a) and MRI (b), and radial profiles of 10 % nylon suspension from ERT (c) in the 50 mm ID vessel agitated at 480 rpm with Rushton turbine. 9-18
Figure 9.16: MRI 1D axial concentration profiles for 10 % nylon particles and 5 % yeast (a) and 10 % nylon particles (b) agitated at 186 – 460 rpm with Rushton turbine. 9-18
Figure 9.17: 5 % yeast, 10 % nylon and their combination agitated at 480 rpm (a); 15 % nylon agitated at 186 to 480 rpm (b)..... 9-19

Chapter 10: The Slurry Bioreactor

Figure 10.1: Soluble protein released as a function of time for a 5 % solids loading of 600 – 850 μm quartzite agitated at 749 rpm with the Rushton impeller. 10-4
Figure 10.2: The local cell disruption rate constant for the 5 % volume fraction agitated at 236 to 547 rpm (assuming ERT accounts for suspended solids) (a), and the local disruption rate constant for 5 to 20 % volume fraction agitated at 547 rpm (b). 10-6

List of Tables

Chapter 2: Literature Review

Table 2.1: The effect of increasing aeration rate on the heat transfer coefficient (Gogate *et al.*, 2000).....2-5
Table 2.2: The effect of pyrite and silica addition on oxygen transfer in a stirred tank reactor.....2-13
Table 2.3: Parameters affecting suspension and mixing in stirred tanks.....2-17
Table 2.4: Suspension models reported in literature.....2-38
Table 2.5: Comparison of measured flow variables with those obtained from ERT (Lucas *et al.*, 1999).....2-55
Table 2.6: Summary of methodologies capable of quantifying solids suspension.....2-65

Chapter 3: Materials and Methods

Table 3.1: Dimensions of the tanks reactor.....3-3
Table 3.2: Particle statistics for the three size distributions determined by the Malvern Mastersizer.....3-9
Table 3.3: Particle statistics for sand tested in pipeline.....3-14
Table 3.4: Dimensions of the mini-STR.....3-17
Table 3.5: Particle information for solids tested with MRI.....3-19
Table 3.6: Overview of experimental approach and objectives.....3-25

Chapter 4: ERT Hardware and Software

Table 4.1: Summary of ERT hardware and software used in this study.....4-15

Chapter 5: ERT as an Applicable Technology

Table 5.1: Review of initial ERT systems.....5-6
Table 5.2: Reynolds numbers for the flow conditions.....5-15

Chapter 6: Quartzite Suspension and Reactor Homogeneity

Table 6.1: Sample Data for the 5 % v/v 600 – 850 μm quartzite fraction at 236 and 304 rpm.....6-3
Table 6.2: Two dimensional mixing indices and the overall mixing index for the specific reactor condition.....6-24
Table 6.3: The effect of agitation rate on mixing indices for the 425 – 600 μm fraction.....6-25
Table 6.4: The effect of solids loading on mixing indices for the 425 – 600 μm fraction agitated at 353 rpm.....6-26
Table 6.5: Relative $\overline{MI}_r$ values for 5 and 15 % solids loading.....6-30
Table 6.6: Data of gradients and linear fitting of log(C) from Figures 6.26 and 6.27.....6-31
Table 6.7: Standard deviations as a percentage of the mean for the sample data collected at 5 % solids loading (106-212 μm).....6-36

Table 6.8: Standard deviations as a percentage of the mean for the sample data collected at 15 % solids loading (600-850 μm).....6-36
Table 6.9: Standard deviations and overall deviation (% of mean) of 4 samples taken at 304 rpm for L3 at r/R = 0.73 for 5 % solids concentration (106-212 μm).....6-36
Table 6.10: Standard deviation of conductivity measurement as a percentage of the mean for the 5 % solids concentration (106-212 μm).....6-38
Table 6.11: Standard deviation of conductivity measurement as a percentage of the mean for the 10 % solids concentration (425-600 μm).....6-38

Chapter 7: Developments in ERT and the Effect of Reactor Scale

Table 7.1: A comparison of Reynolds numbers, tip speeds and approximate power per unit volume for the 220 mm and 50 mm tanks.....7-5
Table 7.2.: Approximate Kolmogorov eddy sizes for the 220 and 50 mm tanks.....7-5
Table 7.3.: Critical suspension speeds for the 600- 850 μm fraction for the 220 and 50 mm tanks.....7-5

Chapter 8: Magnetic Resonance Imaging of the Slurry Reactor

Table 8.1: Observation of a peak solids concentration at the height of the impeller.....8-6

Chapter 9: The Distribution of Air and Microorganisms in Stirred Tanks

Table 9.1: Reynolds numbers and tip speeds for the 0.68 m and 0.22 m diameter tanks.....9-7
Table 9.2: Volume fraction of air detected from surface aeration related to that during sparging (L1 – L3).....9-11

Chapter 10: The Slurry Bioreactor

Table 10.1: Time-averaged velocity effects in a liquid phase CSTR based on similar tip speed of the 220 mm vessel (236 – 547 rpm).....10-3

Nomenclature

a	the shear stress ratio, τ_0/τ, Equation 2.3
a	the interfacial area (m^2) in the oxygen mass transfer coefficient
Ar	Archimedes number, $g\Delta\rho d_p^3/\nu^2\rho_L$
B	baffle width (m)
B	magnetic field
C	impeller clearance (m)
C_0	initial concentration (wt. %)
Q_g	volumetric gas flow rate, $m^3.s^{-1}$
c_p	heat capacity ($J.kg^{-1}.K^{-1}$)
D	impeller diameter (m)
d	pipe diameter (m)
d_{32}	Sauter bubble diameter (m)
d_{50}	mean particle diameter (μm)
d_{90}	contains 90 % of size distribution (μm)
d_p	particle diameter (μm)
Fr	Froude number, u_{sg}^2/D_cg
g	gravitational constant ($m.s^{-2}$)
h	Planck constant, 6.67 x 10^{-34} $J.s^{-1}$,Equation 2.16
h	heat transfer coefficient ($W.m^{-2}.K^{-1}$)
H	tank height (m)
H_1	height of tank (220 mm tank) (mm)
H_2	height of working volume (220 mm tank) (mm)
H_u	diameter of disc of Rushton and pitched blade turbines (mm)
k	first order cell disruption rate constant (s^{-1})
K	Stokes number, $\rho d^2u_s/18\mu(\phi/2)$
K	the consistency index ($N.S^n.m^{-2}$), Equation 2.2
k	thermal conductivity ($W.m^{-1}.K^{-1}$)
k_La	oxygen mass transfer coefficient (s^{-1})
L	characteristic length (m)
L_i	length of impeller blade (mm)
MI	overall mixing index
MI_r	mixing index in the vertical reactor plane
MI_z	mixing index in the horizontal reactor plane
M_Y	transverse nuclear magnetisation
n	flow index, Equation 2.2
N	impeller agitation rate (s^{-1})

N_{js}	critical impeller speed (rpm)
N_P	impeller power number, $P/\rho N^3D^5$
Nu	Nusselt number, hL/k
P	power (W)
Pr	Prandtl number, $\mu c_p/k$
Q	gas flow rate ($m^3.hr^{-1}$)
r	radial coordinate (m)
R	radius of reactor (m)
R	soluble protein released at time t (mg protein/g cell), Equation 10.5
Re	Reynolds number, $du\rho/\mu$
Re_i	impeller Reynolds number, ND^2/ν
s_1	constant based on tank geometry, Equation 2.6
S	element sensitivity in LBP algorithm
T	tank diameter (m)
T_1	spin-lattice relaxation time (s)
T_2	spin-spin relaxation time (s)
u_s	fluid superficial velocity ($m.s^{-1}$)
u_{sg}	gas superficial velocity ($m.s^{-1}$)
V	volume (m^3)
$V_{i,j}$	voltage between two equipotential lines in LBP algorithm
w_r	mixing index weighting for radial distance of MI_z
w_z	mixing index weighting for vertical distance of MI_r
W	height of impeller blade (mm)
X	mass of solids per mass of liquids as a percent
Z	liquid height (m)
z	vertical coordinate (m)

Greek Symbols

α	local solids volume fraction
ε	the turbulent power dissipation per mass of liquid, ($W.kg^{-1}$)
ΔE	energy difference between orientations of molecule (J)
ϕ	gas hold-up, or tube diameter (m)
$\Phi(\rho)$	objective error function in Newton-Raphson algorithm
Φ	bulk solids volume fraction, Equation 10.6
γ	shear rate (s^{-1})
η	Kolmogorov eddy length (m), Equation 7.1
μ	fluid dynamic viscosity (Pa.s)
ν	kinematic viscosity ($m^2.s^{-1}$)
ρ	resistance, (ohms), Equation 2.7

ρ	density ($kg.m^{-3}$)
$\Delta\rho$	density difference between solid and liquid phases ($kg.m^{-3}$)
σ	conductivity (1/ohms)
σ^2	variance, Equation 2.14
τ	shear stress (Pa)
ω_0	frequency of radiation field, s^{-1}
Ψ	Power number, N_P

Subscripts

0	initial
1-4	electrode layers of reactor
B	based on plastic viscosity
b	bubble
b	bulk
c	coil side (heat transfer coefficient)
cr	critical
i	jacket side (heat transfer coefficient)
l	liquid
m	measured
p	particle
s	solid
sl	slurry
w	water

Superscripts

T	transpose
k	k^{th} element
max	maximum
min	minimum

Glossary

Bead Mill	An industrial cell disruption device through which cells are mixed in a chamber with a high volume fraction of solids at high rotational speeds.
Cell Damage	The altered response of cells on exposure to stress. This can result in a change in cell morphology, their ability to grow and reproduce and the metabolic pathway.
Critical Suspension Speed	The agitation rate at which solids do not remain on the vessel base for more than 2 seconds in accordance with the definition of Zwietering (1958).
Frame Rate	The rate at which the ERT hardware and software is able to record a full injection – measurement sequence.
Multiplexer	Switching device enabling specific current injection and voltage measurement from the electrode system.
Slurry Bioreactor	Agitated reactor system containing solid particles and microorganisms, often sparged with air or carbon dioxide. An additional organic liquid phase may be present.
Voxel	Volume element of pixels

Abbreviations

AC	Alternating current
ADC	Analogue to Digital Converter
CFD	Computational Fluid Dynamics
DC	Direct current
ECT	Electrical Capacitance Tomography
EIDORS	Electrical Impedance and Diffuse Optical Reconstruction Software
EIT	Electrical Impedance Tomography
ERT	Electrical Resistance Tomography
FEM	Finite Element Modelling
LDA	Laser Doppler Anemometry
MRI	Magnetic Resonance Imaging
PC	personal computer
PEEK	polyethylene-ethylene-ketone
PIV	Particle Image Velocimetry
PVC	polyvinyl chloride
RC	Resistor-capacitor
r.f.	radio frequency
v/v	volume per volume
vvm	litres air, per litres reactor volume, per minute

Chapter 1

Introduction

1.1 Background

On examining the industrial needs for research into mixing sixteen years ago, Smith (1990) emphasised the need for knowledge generated in the areas of blending, scale-up, high solids content systems, heat transfer and improved computational modelling. He reported solid-liquid mixing to be involved in 80 % of industrial chemical process operations. Despite the advances in knowledge and computational power, these research needs persist today due to the complexity of multi-variable interactions in turbulent multiphase systems. Moreover, applications in biotechnology have expanded rapidly and increased understanding of mixing in these systems is currently sought.

Solids in biosystems is one such application. These systems have broad use in industry and include bead mills for cell disruption, minerals bioprocessing, soil bioremediation and immobilised biocatalyst systems. These processes are often performed in a slurry bioreactor. The slurry bioreactor is a mixing system containing a microbial phase and an abiotic particulate phase suspended in a gaseous or organic liquid phase or both. In these systems, solid particles may provide a nutrient source, a surface for attachment, or a means to disrupt the cell envelope. In the slurry bioreactor, mixing is complex and the distribution of phases is largely unknown. In optimising cell growth there is a conflict between providing adequate nutrient transfer and hydrodynamic mixing, and the resulting damage to the cell envelope. Thus information concerning the distribution of phases would aid understanding of heat and mass transfer, the solid – cell interactions and microbial growth, reactor design and scale-up, and the optimum operating conditions.

In the mid to late 1990's the development and application of a new measurement technology, electrical resistance tomography (ERT), led to a non-invasive and rapid means to acquire information on the state of a process. This technology allows the direct characterisation of multiphase systems without theoretical models and computational fluid dynamics. Additionally, the application of magnetic resonance imaging (MRI) has extended from its clinical roots to the area of chemical engineering science. These tomographic technologies have been applied to mixing systems in this study, with particular focus on the slurry bioreactor.

It was desired to characterise phase distribution with these technologies while varying the reactor operating environment. In this way, understanding would be

increased beyond the traditional approach of solely examining the point of complete suspension of the solid phase. Further analysis of gaseous and microbial phases would lead to increased knowledge of the slurry bioreactor. This information would aid design and operation of these units while providing data for the validation of theoretical models.

Tomography has the potential to provide this information. The ongoing development of technology has resulted in the available ERT system improving continuously during this study. Thus the improvement of this technology cannot be separated from the content, and so forms a part of the analysis. The ERT system was first evaluated according to its ability to characterise simple solid objects before moving to a dynamic solid-liquid system in an industrial pipeline. These initial applications provided the background to investigate the slurry bioreactor.

The effect of completely and incompletely suspended particulates on cell disruption was previously examined and modelled by Scholtz-Brown (1998). Therefore this work forms an extension of her study, whereby mixing and the distribution of phases is examined in geometrically scaled vessels and finally related to cell disruption. This work has further application to bioleaching, where the distribution of the solid phase affects the nutrient uptake of the microbial phase. The slurry bioreactor is simplified through examination of quartzite as a model particle in a saline solution, while *Saccharomyces cerevisiae*, or Bakers' yeast, is treated as the model microorganism in a liquid phase. Further particulates in the form of ballotini and nylon are examined regarding the nature of their suspension. The introduction of air into the reactor, via sparging apparatus or surface aeration, is further studied as a phase of interest. Radial and axial flow patterns are generated in this reactor through using a Rushton and pitched-blade impeller respectively.

1.2 Thesis Objectives

Tomography, in the form of ERT and MRI, provides a new means of process visualisation, providing information on multiphase environments. Thus, a primary objective of this study was to examine particle suspension in a stirred tank to examine the homogeneity of a particle concentration in axial and radial directions as a function of key parameters. This homogeneity would then need to be quantified to allow comparison to different operating conditions. Consequently, this would transcend the concept of the critical suspension speed as the only means to characterise particle suspension. This tomographic examination would form a key component of the simulation of a slurry bioreactor.

As ERT cannot be excluded from this study, it was an objective to examine developing ERT hardware and software capability in the form of quantity and quality of information, and the validation of this information through direct physical means. It was further desired to apply tomography to microbial environments to firstly determine if detection was possible, and secondly to examine the possibility of cellular gradients in the reactor. A further phase of influence in the slurry bioreactor is the gaseous phase. The study aimed to detect and quantify the gaseous distribution, while further attempting the examination of surface aeration in the reactor.

MRI and ERT are complementary tomographies, providing information at different spatial scales and time frames. An additional objective of this study was the comparison of these tomographies on application to the same operating conditions and reactor. The application of ERT to different vessels of scale would potentially provide information on particle distribution relating to different hydrodynamic environments, thus forming another objective. Finally, it was an objective to relate potential particle distribution information to the previous study of microbial cell disruption in a smaller scale vessel. With the meeting of these objectives, increased understanding should thus result concerning the slurry bioreactor and the application of ERT.

1.3 Thesis Outline

- Key physical parameters affecting the slurry bioreactor environment are reviewed in Chapter 2. Literature on particle suspension and methods of concentration measurement follow, including theoretical models. Lastly, a review of tomography theory and application provides a suitable background for this study.

- Chapter 3 details the reactors and pipeline used in ERT and MRI experiments, including internal components and composition of phases. Apparatus used for validating ERT is further described.

- The ERT hardware and software are specifically detailed in Chapter 4 to provide a background to the technology, as well as fulfilling a key objective of analysing ERT capability.

- The examination of ERT as a tool to characterise solid-liquid systems is evaluated on application to physical phantoms and a swirling pipeline suspension. Chapter 5 thereby sets the scene for analysing the more complex stirred tank environment.

- Chapter 6 is a key section and details the results and discussion of particle suspension and homogeneity in the 220 mm stirred tank reactor. Physical validation of ERT data through sample withdrawal and conductivity probing is further described.

- Chapter 7 examines the newer ERT system developed concomitantly with this study and its application to the smaller 50 mm reactor, including scale effects relative to the 220 mm reactor. Errors associated with ERT experiments are investigated.

- MRI and ERT investigations of ballotini and nylon suspension in the 50 mm reactor are described in Chapter 8. The comparison between the technologies is detailed. Further suspension analysis is performed using the high resolution information of MRI.

- A gaseous phase in the 220 mm reactor and in an industrial scaled vessel is analysed using ERT in Chapter 9. MRI and ERT are further applied to examine microbial phase distribution and the simulation of a slurry bioreactor as a solid-cell system in the 50 and 220 mm vessels.

- Chapter 10 relates ERT and MRI information to a previous cell disruption model and to the slurry bioreactor in general. This is followed by the thesis conclusions in Chapter 11, the references and lastly the appendices.

Chapter 2

Literature Review

2.1 Introduction

This study of mixing in a slurry bioreactor requires the examination of a number of disciplines. These include fundamental chemical engineering in the form of transport phenomena and macroscale operations of mixing and suspension, bioprocess engineering in the form of microbial growth and stress, and measurement technology which allows examination of the reactor environment.

Heat, momentum and mass transfer dictate growth for microbial populations in slurry bioreactors. These phenomena are thus discussed with reference to this environment. Momentum and mass transfer effects are further detailed through providing knowledge of suspension and mixing. This provides a context for evaluating information obtained on solid and gas phase distribution in stirred tank reactors. Parameters which affect mixing in this environment are further investigated.

The methods of obtaining mixing and suspension information are reviewed. This is necessary to evaluate past and current measurement technology and theories, and to examine what is viable and preferred in this study. The dominant measurement technologies proposed, electrical resistance tomography (ERT) and nuclear magnetic resonance (NMR), are reviewed.

Heat and mass transfer provide the platform for examining suspension and mixing in Sections 2.2 and 2.3. Parameters affecting mixing in stirred tanks are covered in Section 2.4. Mass and momentum transfer effects in the slurry bioreactor are further analysed in Section 2.5 with a review of the challenges of cell growth in this environment. Direct methods of examining suspension, namely sampling and optical techniques are introduced in Section 2.6, while indirect methods, namely further optical methods, conductivity probing, and suspension theories follow in Section 2.7. The indirect tomographic methods of ERT and NMR are reviewed in detail in Section 2.8. A summary of current knowledge of suspension and particle distribution in stirred tanks is presented in Section 2.9. Final chapter conclusions complete this review in Section 2.10.

It must be noted apart from the analogies of heat and mass transfer when performing dimensional analysis, interrelationships exist in the slurry bioreactor. In the study of mixing and suspension of particles in stirred tanks, particle distribution is governed by

operating conditions in two and three-phase systems. Thus the unique spatial location of particles directly affects the heat and mass transfer coefficients and the frequency with which cells contact particles. This can have further implications if the solid phase is a nutrient source.

2.2 Heat Transfer in Stirred Tank Reactors

Temperature optima within bioreactors are narrow and frequently require control using a low heat load. Heat transfer depends on the flow system within the tank generated by the impeller, the liquid or slurry medium, as well as the geometry and location of the heat transfer apparatus, as discussed below.

2.2.1 The Effect of Agitation on Heat Transfer

Heat transfer in a process vessel can be improved by mechanical agitation (Oldshue, 1983). Oldshue (1983) divided heat transfer systems into two categories: open impellers that operate at some distance from the vessel wall, and impellers which operate at close radial clearances to the vessel wall, normally less than 5 % of the vessel inside diameter. Close-clearance impellers (e.g. anchor and helical impellers) are used in highly viscous liquids where homogenous mixing is necessary to control the heat of reaction. In slurry bioreactors, the former are typical where shear stress is minimised and mixing is preferred with the use of smaller impellers and baffles.

Agitation is a necessary condition to induce forced convection to ensure adequate heat transfer. Sizing an agitator to maintain a specific heat transfer coefficient may be impractical (Oldshue, 1983). Oldshue (1983) used a general correlation from helical coil heat transfer, and combined it with the power number relation ($N_p = P/N^3D^5$) to relate the heat transfer coefficient directly to the power input for comparison of a given impeller type. It was shown that at constant impeller diameter,

$$h = P^{0.22} \tag{2.1}$$

where h is the heat transfer coefficient, $W.m^{-2}.K^{-1}$

To double the heat transfer coefficient the power input must be increased by a factor of 23, depending on the geometry of the mixer. Therefore, on forced convection through agitation, increasing the degree of mixing does not economically provide a significant change in the heat transfer coefficient. Increasing agitation also increases shear on microorganisms. Hence, change in factors other than mixing parameters is preferable to increase heat transfer.

Further, the heat transfer coefficient is not constant throughout the vessel. Askew and Beckman (1965), Akse *et al.*, (1967), Bourne *et al.,* (1984), Kupčik (1965) and Man *et al.* (1984), as cited by Wichterle (1994), found that the index of the Reynolds exponent in the typical correlation involving Nusselt, Prandtl and Reynolds numbers, was found to vary on the surface of the wall. Different values of this exponent were found for different boundary conditions and for non-Newtonian fluids. This means that there may be a more complex structure of the distribution of heat transfer coefficients on the wall of the tank.

2.2.2 Heat Transfer in Non-Newtonian Liquids

Dense fermentation broths often exhibit non-Newtonian flow characteristics, thus heat transfer is examined in these fluids prior to focusing on bioreactors. In non-Newtonian liquids, the extra parameter of the simplexes of rheological similarity affects the Nusselt number. In the case of the simplest non-Newtonian liquids it can be represented by a single value of the flow index *n* related to the rheological model (Wichterle, 1994):

$$\tau = K\gamma^n \qquad (2.2)$$

where τ is the shear stress
γ is the shear rate
K is the consistency coefficient
n is the flow index

Wichterle *et al.* (1985) found that for highly pseudo-plastic liquids exhibiting low *n*, there are immobile zones exist at the walls below a certain critical Reynolds number. At a higher N_{Re} a limited zone appeared where the shear rate was approximately constant. Heat transfer in non-Newtonian liquids can be greatly intensified by using impellers with a larger D/T ratio, thereby increasing impeller tip speed and shear rate (Hagedorn and Salamon, 1967; Wichterle *et al.*, 1985).

2.2.3 Heat Transfer in Bioreactors

Efficient heat transfer in bioreactor media is a basic requirement for successful bioreactor control. The media is usually complex; several phases occur, and some parameters are time dependent making modelling difficult. In large scale bioreactors, heat transfer becomes critical as microbial concentration increases (Kawase and Moo-Young, 1989). A high degree of turbulence is thus required to provide the necessary heat transfer; this may also lead to shear damage to organisms.

Kawase and Moo-Young (1989) highlighted two approaches to modelling transport processes as a function of viscosity in dense slurry systems:

(i) shear-dependent viscosity: the slurry is treated as a pseudo-homogenous liquid exhibiting a yield stress

(ii) volume fraction-dependent viscosity: the viscosity of the slurry is given as a volume fraction of the solids.

Using the volume fraction-dependent approach, Kung and Harriott (1987), as cited by Kawase and Moo-Young (1989), measured heat transfer coefficients for suspensions in a jacketed tank and found that the heat transfer coefficient decreased gradually with increased solid concentration. Similarly, Kawase and Moo-Young (1989) developed a theoretical model that showed an increase in yield stress causes a decrease in heat transfer coefficient. These authors found at a fairly high degree of turbulence the influence of yield stress is insignificant and the decrease in heat transfer coefficient was mainly attributed to the increase in plastic viscosity. This correlation was based on the shear-dependent viscosity approach whereby the authors approximated the microbial culture by the Bingham plastic model in a jacketed tank,

$$Nu_c = 0.138(1-a)^{0.516}\,\mathrm{Pr}_B^{1/3}\,\mathrm{Re}_B^{3/4}\,Fr^{-1/4} \qquad (2.3)$$

where Fr = Froude number, u_{sg}^2/D_cg

u_{sg} = superficial gas velocity

D_c = column diameter

a = shear stress ratio, τ_0/τ

subscripts

B = based on plastic viscosity

This correlation was found to have reasonable agreement with those obtained from predicted and experimental values of the heat transfer coefficient in stirred tanks and bubble columns. These authors thus suggest that heat transfer correlations developed for homogenous Newtonian fluids are capable of representing heat transfer for dense suspensions if a plastic viscosity or a viscosity of suspension is used in place of a Newtonian viscosity. They hypothesise that owing to the small density difference between the microbial cells and media, as well as the small energy requirement for their suspension, a homogenous suspension may be realised in many bioreactors.

Radež *et al.* (1991) examined heat transfer in filamentous cultures of *Streptomyces* for the production of the antibiotics oxytetracycline and salinomycin. The viscosity of the culture was dependent on biomass concentration and the morphology of the

filamentous form of the microorganism. Viscosity thus increased with increasing biomass concentration but decreased when fragmentation of mycelia occurred.

2.2.4 Heat Transfer in Aerated Systems

The effect of air flow rate on heat transfer in aerated stirred vessels has been found to differ amongst various workers. Radež *et al.* (1991) concluded that as the flow of air increases, sparging of air to the turbine first causes a decrease in the heat transfer coefficient, followed by a relative independence of air flow in the range typical of bioreactors. At gas flows where flooding of the impeller occurs, a slight increase in the heat transfer coefficient was found. Gogate *et al.* (2000) compared the findings of several researchers with respect to aeration and heat transfer in Table 2.1. They suggest disparity between the results reported in Table 2.1 is due to the different conditions applied, the type of sparger and the variation in operating conditions (u_{sg} and N). Desplanches *et al.* (1988) also showed that the effect of aeration on heat transfer is a function of u_{sg} and N.

Table 2.1: The effect of increasing aeration rate on the heat transfer coefficient (Gogate *et al.*, 2000)

Effect of aeration on heat transfer coefficient	Reference
h_j, h_c increases	Rao and Murthy (1973)
h_c increases at low N, constant at high N	Pollard and Topiwala (1976)
h_c constant ($u_{sg} \leq 0.02$ m.s^{-1})	Edney and Edwards (1976)
h_j increases ($u_{sg} \leq 0.05$ m.s^{-1})	Steiff and Weinspach (1978)
h_c increases for N> critical speed, h_c decreases for N < critical speed	De Maerteleire (1978)

* u_{sg} is the gas velocity, h_c is the heat transfer coefficient on the coil side, while h_j is for the jacket side.

Although bubble columns have no moving parts, the analysis of heat transfer in a gaseous biological environment provides insight relevant to the aerated stirred tank environment. High heat transfer rates are one of the main characteristics for the wide applications of bubble column reactors (Lin and Wang, 2001). It is commonly accepted that the heat transfer coefficient increases with gas and liquid velocities, the diameter of the column, and the thermal conductivity and heat capacity of the liquid, but decreases with increasing liquid viscosity (Lewis *et al.* 1982, Magiliotou *et al.* 1988, Kim and Laurent 1991, as cited by Lin and Wang 2001). Baker *et al.* (1978) reported that, at low gas velocity, the increase in the heat transfer coefficient with increasing gas velocity was marked, but the magnitude of the dependence decreased at higher gas flow rates. Hydrodynamics had a significant influence on heat transfer in bubble column systems. Similarly as with forced convection using an impeller, the increase in gas velocity increases turbulence and thus heat transfer.

Prakash *et al.* (2001) investigated the hydrodynamics and local heat transfer in a bubble column using a yeast suspension. A maximum in the gas hold-up was observed at a specific superficial gas velocity, beyond which fast rising large bubbles induce turbulent flow and decrease the gas hold-up in the region. A decrease in bubble rise velocity was observed with increasing yeast concentration. In other studies (Li and Prakash 2000a, Krishna *et al.* 1997, cited by Prakash *et al.* 2001), an increase in the rise velocities of small-bubbles was observed with the addition of solids in a liquid. This was attributed to an increase in apparent slurry viscosity. However, the change in apparent slurry viscosity was suggested to be very small. Prakash *et al.* (2001) further noted that heat transfer coefficients obtained in air-water and air-water-glass bead systems were similar. However, in the air-water-yeast system the heat transfer coefficients were higher in the central region of the column, but lower at the wall. This increase in the centre region was attributed to the large bubbles that pass through the centre of the column.

2.2.5 Heat Transfer in Three-Phase Fluidised beds

Heat transfer literature is lacking for three-phase stirred tank reactors, thus the three-phase fluidised bed environment may provide some insight into heat transfer mechanisms in a slurry stirred tank bioreactor. Kim and Kang (1997) noted that h increased with gas velocity, and attributed this to the turbulence generated by gas injection. The h value exhibited a maximum with increasing liquid velocity, and this maximum was dependent upon the properties of the liquid and the solid particles. The heat transfer coefficient increased with larger and denser particles, but decreased as the liquid viscosity increased. Chiu and Ziegler (1983) reported that the type and shape of particles do not influence the heat transfer coefficient in three-phase fluidised beds greatly. However, Kang et al. (1985), cited by Kim and Kang (1997), reported that the heat transfer coefficient decreased for particles larger than 5 mm, owing to the energy dissipation between the phases.

2.2.6 Conclusions

While the heat transfer coefficient in stirred tanks increases with agitation rate, increasing the degree of mixing is not an economical way to provide significant change in h under forced convection. Further, increasing h through increased power input increases shear exerted on microorganisms. Non-Newtonian fluids, typical of biological suspensions, result in immobile zones near the vessel wall causing a decrease in heat transfer. This can be improved with stirrer geometric ratios (D/T), although the stirrer type has little influence on the heat transfer coefficient. Increasing the fluid yield stress decreases h, while at increased turbulence the plastic viscosity of the fluid has a greater influence on heat transfer. A change in cell morphology and

biomass concentration in the bioreactor alters the viscosity leading to a change in the heat transfer coefficient.

There is no clear understanding of the effect of introducing air from a sparger on the heat transfer coefficient combined with agitation. At low agitation rates a decrease in *h* has been observed although beyond a critical agitation rate an increase in *h* has been reported (De Maerteleire, 1978). As the aeration rate continues to rise an independence of the heat transfer coefficient has been found (Pollard and Topiwala, 1976). It is generally thought that increasing aeration leads to an increase in turbulence and thus heat transfer. At high aeration rates in bubble columns an increase in the heat transfer coefficient has been observed, while larger bubbles appear to result in a higher heat transfer. In three-phase fluidised beds, heat transfer increases with increasing particle size for non-viscous solutions, however, there is a lack of agreement in the literature.

2.3 Mass Transfer in Stirred Tank Reactors

In addition to promoting more uniform mixtures of components and heat transfer, an important role of agitation is transfer of materials to or from surfaces of particles or between phases (Uhl and Gray, 1966). The transport of oxygen and nutrients to the cell are critical for microbial metabolism, thus gas-liquid and solid-liquid mass transfer are discussed with reference to stirred tanks.

2.3.1 Gas-Liquid Mass Transfer

The rate of oxygen transfer in biological systems is of particular importance in maintaining adequate conditions for cell growth, where it is often a limiting factor. Consideration of the volumetric mass transfer coefficient k_La, the size of bubbles, the gas distribution in the tank, the degree of gas hold-up and the effect of the geometric arrangement provide a greater understanding of gas-liquid mass transfer.

2.3.1.1 The Volumetric Mass Transfer Coefficient

Garcia-Ochoa and Gomez (2004) stated that the most important characteristics affecting the mass transfer between the gas-liquid phases are the energy dissipated by turbulence, the gas hold-up and the size of the bubbles or their distribution within the volume being mixed. These variables are a function of operating conditions, physical properties of the solution and gas phase, and the geometry of the vessel. The effects of these variables on k_La have typically been taken into account by means of empirical correlations using dimension or dimensionless groups. There are

a high number of correlations available in this regard, but there is often disagreement in the results using different equations (Gogate *et al.* 2000).

2.3.1.2 Bubble Size

Through a more detailed analysis of bubble sizes, the mass transfer coefficient k_L, and the interfacial area, *a*, can be separated to allow better understanding. Alves *et al.* (2002) found that the average bubble size increases rapidly in the turbine discharge stream to reach a bulk value which is roughly constant for the rest of the tank. Barigou and Greaves (1992) noted that in a stirred tank filled with tap water, most of the coalescence has occurred when the discharge stream reaches the wall, although a small amount of coalescence still occurs upwards and downwards close to the tank wall. Nagata (1975) reported that a larger portion of gas absorption takes place when the bubbles divide and new surfaces develop, while a smaller contribution to absorption takes place during its rising in the liquid thereafter. Thus an increase in liquid depth is of limited advantage, although multistage impellers are effective. Alves *et al.* (2002) noted regions of exception to the bulk bubble size using a double Rushton turbine, namely:

(i) below the bottom turbine and in a small region above it, only small bubbles with low buoyancy follow the downward liquid circulation stream, particularly at low turbine speeds. This led to lower average bubble sizes and lower gas hold-ups;
(ii) near the wall, just below the turbine discharge streams the upcoming bubbles from the lower part of the tank meet those in the down-coming stream of the upper turbine, promoting coalescence;
(iii) near the surface, at the centre of the tank, larger bubbles were observed most likely due to surface entrainment.

Surfactants and electrolytes did not alter the process of bubble formation significantly, but rather the subsequent coalescence process (Alves *et al.*, 2002). Bubble sizes in electrolyte solutions are smaller and more sensitive to power input than in water. Surfactant addition results in a further decrease in bubble size. Alves *et al.* (2004) found that the volumetric mass transfer coefficient for a salt solution is significantly higher in the bottom half of the tank, despite a lower specific transfer area in that region. They explained this phenomenon through the film coefficient being much higher here, as the fraction of cleaner bubbles (i.e. not contaminated by salt) is much larger lower in the reactor. Barigou and Greaves (1992) found that following ionic solution addition (0.15M NaCl), finer and more uniform dispersions of bubbles were produced. Pandit and Joshi (1983) reported increased mixing time in the presence of electrolytes. They suggested that the decrease in bubble size causes an increase in the gas-phase hold-up, a decrease in terminal rise velocity and an

increase in liquid viscosity, which leads to a decrease in the liquid circulation velocity and an increase in the mixing time.

Barigou and Greaves (1992) used a computerised capillary suction probe to determine the bubble-size distributions in a mechanically agitated vessel. Variation of bubble size was found to deviate considerably from the standard normal distribution from one region of the vessel to another. These authors examined four regions:

(i) The impeller region, where the smallest bubble size was found. At other positions in the same plane bubble size was much larger, indicating high rates of bubble coalescence occur in the impeller discharge stream, in accordance with the findings of Alves *et al.* (2002). No systematic trend was found with the effect of stirrer speed on local bubble size in this region. At high air flow rates, the effect of agitation rate on bubble size was negligible. At constant agitation rate the effect of increasing the air rate led to an increase in bubble size. This was hypothesised to result from reduced turbulence due to the reduction in mechanical power dissipation through the growth of gas cavities behind the turbine blades, and due to bubble density increasing owing to greater gas hold-up, leading to higher rates of bubble collision and coalescence.

(ii) In the region below the impeller, the central zone was void of bubbles at low agitation speeds. As the speed increases the lower circulation loop enlarges causing more gas to be dispersed in this region, with the bubble size being quite large compared to that in the impeller region. Consequently, the principal factor in this region is coalescence.

(iii) In the bulk region, the effect of agitator speed on the overall Sauter diameter d_{32},

$$d_{32} = \frac{\sum_{i=1}^{i=n_b} d_i^3}{\sum_{i=1}^{i=n_b} d_i^2} \tag{2.4}$$

where d is the bubble diameter, and n_b is the sample size, was found to be insignificant. Thus it appears that increased turbulence is balanced by an increase in bubble coalescence due to the rise in gas hold-up.

(iv) In the vertical baffle plane, a finer dispersion of bubbles was found. This difference relative to the bulk size was more significant above and below the plane of the impeller. Barigou and Greaves (1992) calculated that the global interfacial area was 11 to 30 % higher than that in the plane between baffles. On the leeward side of the baffle, the bubble size is greater with more coalescence occurring, although the bubble density is lower.

2.3.1.3 Gas Distribution and Hold-up

Calderbank (1958) determined two maxima of interfacial area in the vicinity of the impeller and the middle height between the impeller and the free surface using a light transmission technique. In addition to distribution, the concept of gas hold-up is useful in gas-phase mass transfer analysis. The gas hold-up is quantified by the expansion in the working volume of the stirred tank to accommodate the presence of the gas phase. This concept allows calculation of the gas-liquid interfacial area. This specific area is strongly dependent on the physico-chemical properties of the system and geometrical parameters of the contactor (Garcia-Ochoa and Gomez, 2004). With sodium chloride addition (0.15M), Barigou and Greaves (1992) found a 70 % increase in the total hold-up. The reduction in bubble size due to the ionic addition resulted in the increase in hold-up, together causing large increases in interfacial area (Barigou, 1987; as cited by Barigou and Greaves, 1992). Pandit and Joshi (1983) changed surface tension through the addition of butanol (0.1 %) and observed a 100 % increase in the hold-up. Arjunwadkar *et al.* (1998) formed a non-coalescing system by addition of 5 % Na_2SO_4. This gave an increase of almost 25 % in the mass transfer rate over the coalescing system of air and water. The increase in k_La was about the same as the increase in the fractional hold-up, indicating the interfacial area is responsible for the observed increase in the overall mass transfer coefficient.

Veera *et al.* (2001) reported that most correlations for the estimation of gas hold-up predict the average or overall hold-up. These correlations are typically developed only for air-water systems, limiting their predictive ability in industrial systems. These authors argue that in order to design reactors on a rational basis, the local values of the fractional gas hold-up and the effect of operating conditions need to be known. With this information, the local rates of heat and mass transfer can be predicted, and the overall performance can be estimated. Gamma ray tomography was used to obtain local gas hold-up by these authors with signal data being reconstructed according to the trajectory of a curtate cycloid. Hold-up was determined at varying reactor height, indicating higher gas fraction near the impeller tip and a maximum in the radial profile of gas fraction at a dimensionless radius of 0.57. Fischer *et al.* (1992) measured the bubble size distribution and interfacial area in an aerated stirred tank reactor with a Rushton turbine using a pulsed ultrasound Doppler technique and also reported high gas fraction near the impeller zone.

2.3.1.4 Gas-Liquid Transfer in Non – Newtonian Liquids and Microbial Cultures

The presence of organic macromolecules and microorganisms often cause non-Newtonian behaviour of the suspension. An increase in viscosity e.g. through the

presence of microorganisms, reduces the mass transfer coefficient (Oldshue, 1983). Non-Newtonian fluid effects are often tested through the addition of carboxy methyl cellulose (CMC).

Pandit and Joshi (1983) noted that the consistency index *k* ($Pa.sec^n$) increased with the addition of CMC, and an increase in mixing time was observed with this increase in *k*. Arjunwadkar *et al.* (1998) noted with multiple impellers that the optimal disc turbine-pitched blade impeller combination was equally valid for viscous liquids. These authors noted a 30 % decrease in gas hold-up compared to the air-water system, using a 0.7 % by weight CMC solution. This behaviour was attributed to the increase in the formation of larger bubbles, due to the promotion of coalescence. These pass through the liquid with high rise velocities reducing the gas hold-up. Although it must be noted that a certain fraction of fine bubbles with a long residence time was observed. Muller and Davidson (1992), as cited by Arjunwadkar *et al.* (1998), estimated the contribution of these small bubbles towards the overall mass transfer process in the range of 20 to 60 %.

Galaction *et al.* (2004) examined aeration in stirred tanks containing cultures of bacteria, yeast and fungus. The oxygen mass transfer rate for biomass suspensions was lower than biomass-free broths of the same apparent viscosity. The influence of cells was found to reduce oxygen solubility and create a blocking effect on air bubbles due to their adsorption to the bubble surface.

2.3.1.5 Gas-Liquid Mass Transfer in Three-Phase Stirred Tanks

Oxygen transfer in slurry biosystems is critical for maintaining adequate microbial growth. The oxygen transfer coefficient is further affected by the presence of solids (Derksen *et al.*, 2000; Mills *et al.*, 1987; Oguz *et al.,* 1987; Van Weert *et al.,* 1995). Oxygen transfer from air sparged in agitated slurries represents an important unit operation in the minerals processing industry e.g. gold leaching, iron precipitation, base metal leaching and bio-oxidation. However, little engineering information is available on the effect of mineral solids on such oxygen transfer (Van Weert *et al.,* 1995). More common in the literature is the study of the effect of solids on oxygen transfer using glass beads and low weight fractions. They provide limited representation of industrial systems (e.g. in gold recovery) where particles are rarely spherical and larger weight fractions of pyrite or arsenopyrite require oxidation.

The bio-oxidation reactions for pyrite and arsenopyrite are as follows (Van Weert *et al.,* 1995):

$$4\ FeS_2 + 15O_2 + 2H_2O \rightarrow 2Fe_2(SO_4)_3 + 2H_2SO_4$$

$2FeAsS + 7O_2 + 2H_2O \rightarrow 2FeAsO_4 + 2H_2SO_4$

As can be seen from these reactions, considerable amounts of oxygen are needed.

Mills *et al.* (1987) performed experiments in a baffled cylindrical glass vessel to determine the relationship between solids fraction, power input and superficial gas velocity with respect to k_La. Glass beads (mean diameter 66 μm) were suspended in concentrations of up to 40 % by volume. As the solids concentration was increased, a considerable reduction in k_La resulted. This study did not consider variations in viscosity at the same percent of solids as well as solid properties such as density, shape factor and size.

Van Weert *et al.* (1995) examined the effect of solids on k_La using quartzite with a nominal diameter of 66 μm at speeds twice that required for just suspension in an ungassed medium, to ensure complete suspension of the particles. Volume fractions of 10 to 40 % were tested with the volumetric mass transfer coefficient showing a decrease of 55 to 65 % for the 40 % volume fraction compared to that of a medium containing no solids (Figures 2.1). Thus areas of high solids concentration in a stirred tank may be expected to have a poorer mass transfer of oxygen. No apparent effect was found on k_La at quartzite concentrations less than 10 % by volume (data not shown).

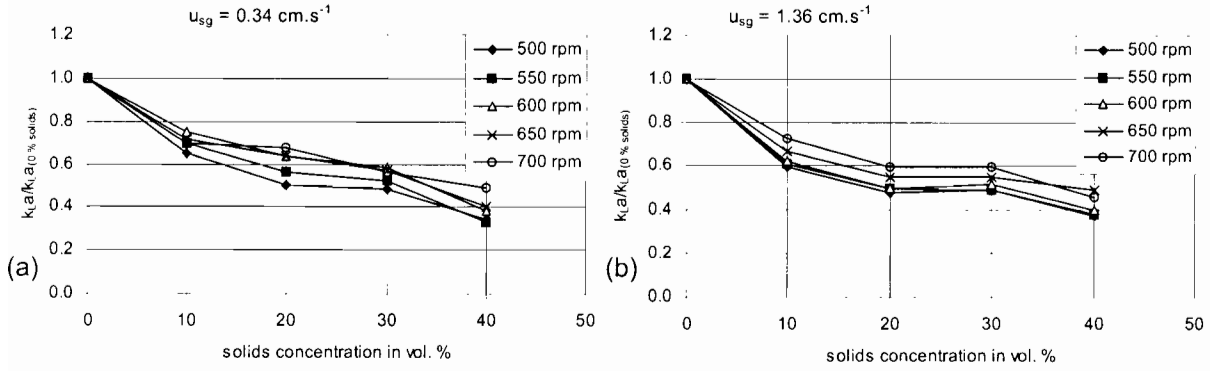


Figure 2.1: Overall effect of solid concentration on k_La at u_{sg} = 0.34 cm.s^{-1} (a) and 1.36 cm.s^{-1} (b) (van Weerts *et al.*, 1995).

Derksen *et al.* (2000) extended this investigation to the effect of particle type on k_La, while measuring gas hold-up, power input and local bubble sizes. Using a 67 litre agitated tank (Rushton turbine and a Lightnin A315), these researchers compared the effects of quartzite (d_{50} = 13 μm) and pyrite (d_{50} = 14 μm) on oxygen transfer. Necessary precautions were taken to prevent the concomitant oxidation of the pyrite. The dynamic method of k_La measurement was employed (van Weert *et al.*, 1995; Mills *et al.*, 1987) whereby the slurry is first deoxygenated by nitrogen, then quickly switched over to air and the response measured. Bubble sizes were measured by means of a 1 mm diameter capillary tube coupled to an optical system.

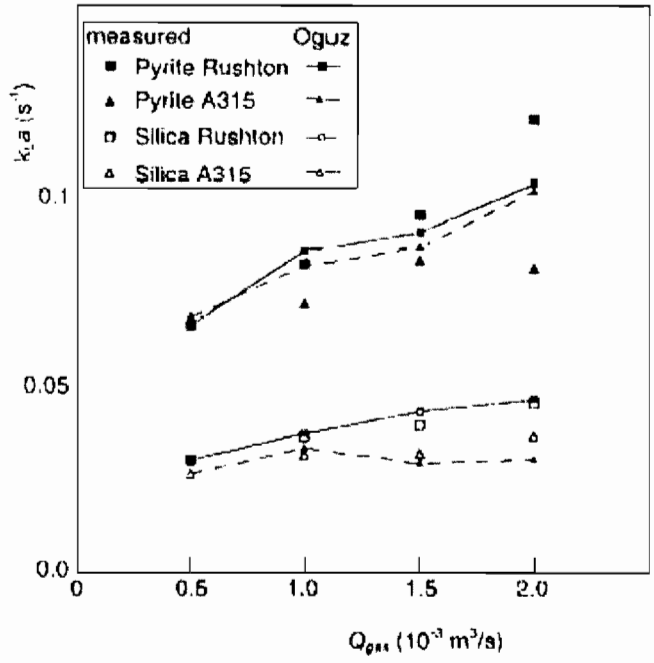


Figure 2.2: Volumetric mass transfer coefficient k_La as a function of the air flow rate at a solids fraction of 10 vol. % and impeller speed of 500 rpm. The points represent the experimental measurements, while the lines represent values based on the correlation from Oguz *et al.* (1987), $k_La \propto P^{0.75}Q_g^{0.5}$. (Derksen *et al.*, 2000)

From Figure 2.2, it is seen that the mass transfer coefficients in the pyrite slurries were much higher than in the quartzite slurries. The relation between solids volume fraction and k_La was found to be approximately linear, while impeller speed and k_La were positively correlated i.e. the higher the impeller speed, the more k_La increased. The findings of Derksen *et al.* (2000) are summarised in Table 2.2.

Table 2.2: The effect of pyrite and silica addition on oxygen transfer in a stirred tank reactor using d_{50} of 13 to 14 μm

Parameter	Pyrite Addition	Silica Addition
k_La	increased by 50 % for 12.7 % vol. slurry compared to no-solids case	decreased by 40 % for 15 % vol. slurry compared to no-solids case
impeller type	Rushton produced higher k_La, but A315 used half the power at same rpm	
bubble size	no significant difference between solid types, largest bubbles observed for low vol. frac. solids	
hold-up	constant for both impellers with increasing concentration	decreased by 25 % for 15 %. vol solids
interfacial area, *a*	increased	not significantly affected
conclusion	the higher interfacial area increased k_La	decreased k_L due to possible hydrophobic effect at gas-liquid interface

This investigation was continued by Zuidevaart *et al.* (2000) to understand the influence of pyrite particles. The effect of mineral density, oxygen demand due to homogenous reactions and ionic strength were examined. The ionic strength was only found to be significantly greater for pyrite than quartzite particles. This suggested that pyrite oxidation occurred, leading to the presence of dissolved ferrous, ferric and sulphate ions. An increased ionic strength reduced bubble coalescence and bubble size leading to greater hold-up. For a 15 % vol. slurry of pyrite particles, the increased ionic strength accounted for 60 % of the k_La enhancement. Factors causing the remaining 40 % of the enhancement were not identified.

Further studies of k_La in slurry reactors have been reported using carbon particles. Kralj and Sinčić (1983) examined the effect of 0.00, 0.25 and 0.5 wt % active carbon particles in a solution of 3 % 2-hydroxybenzyl-alcohol in 10 % aqueous NaOH in a round bottom stirred tank using a Rushton turbine. At low superficial gas velocities lower hold-up values were obtained compared to the two-phase system, while at higher superficial gas velocities the presence of particles increased hold-up.

Alpher *et al.* (1980) and Alpher and Ozturk (1986) suggested that the initial two-film model of Whitman (1923) and the later penetration model (Higbie, 1935; Danckwerts 1951) which describes non-stationary mass transfer, could not describe the observed mass transfer phenomena in three-phase systems with small particles. Demmink *et al.* (1998) observed enhancements in the absorption rate of acetylene into aqueous solutions of iron chelates, caused by the presence of fine sulphur particles. The enhancement was modelled according to Danckwerts' surface renewal theory, although quantitative agreement was lacking when applied to carbon particle systems.

Alpher *et al.* (1980) thus introduced the concept of mass transfer enhancement due to the presence of small particles in a three-phase system. These particles are postulated to absorb an additional amount of gas at or near the gas-liquid interface within the boundary layer, after which the gas desorbs from the particles in the liquid bulk phase (Kluytmans *et al.*, 2003). This effect has been described as the "shuttle" or "grazing" effect. The exact cause of this effect remains unknown (Beenackers and van Swaaij, 1993; as cited by Kluytmans *et al.*, 2003).

Kluytmans *et al.* (2003) undertook a significant investigation of the effect of carbon particles and electrolyte on mass transfer in a stirred tank system and in a 2D slurry bubble column. In the bubble column, gas hold-up was measured using four pressure sensors with a float on top of the column in a geometry consisting of two parallel Perspex plates (200 cm x 30 cm x 1.5 cm apart). Experiments with a known gas-liquid interfacial area a_{gl} in a flat-surface stirred tank (T = 0.25 m, V = 4.8 l) were

performed so that k_l could be determined separately. Mass transfer was determined by pressure measurement after initial degassing (N_2). Further, a reactor (T = 0.15 m, V = 1.5 l) with a gas inducing impeller was tested to study the combined effect of stirring and sparging. These vessels were tested with carbon particles (mean size 30 μm, concentration 0.1 to 20 g.l^{-1}) and electrolyte.

In the bubble column, k_La increased with increasing gas rate and gas hold-up. No dependency was found between the mass transfer coefficient and carbon particle concentration (within the measurement error of ±10 %). Image analysis of bubble sizes showed the specific gas-liquid interfacial area, *a,* was not dependent on carbon particle concentration and thus the shuttle or grazing effect was unlikely to be the dominant transfer mechanism.

In the stirred tank with the flat gas-liquid interface, experiments with carbon slurries resulted in a higher value of k_l compared to distilled water and electrolyte solutions. The combined experiment of carbon particles and electrolyte showed an increase in k_l only at higher stirring speeds (>400 rpm). Hence, although carbon particles were beneficial to mass transfer, no dependency of the mass transfer coefficient on carbon particle concentration was found. Thus shuttle effects seemed unlikely, and a hydrodynamic effect was suggested whereby the particles enforce the level of turbulence at the gas-liquid interface resulting in a thinner effective boundary layer thereby increasing mass transfer. At higher speeds, the shear stress at the gas-liquid interface increased thus leading to a decreased effect of the carbon particles.

With the gas-inducing impeller system, k_La increased with increasing carbon particle concentration, particularly in the carbon - electrolyte combination where mass transfer increased by 200 - 300 %. The rate of increase in mass transfer decreased with increasing speed, and at speeds above 1000 rpm the effect was negligible. In this reactor it was concluded that the increase in mass transfer upon addition of particles could be ascribed to the increase in gas-liquid interfacial area.

2.3.2 Conclusions

The size distribution of bubbles in an aerated stirred tank is not uniform. The greatest differences occur in the impeller plane where small bubbles from the impeller coalesce on approaching the wall. Bubble sizes are smaller in electrolyte solutions, increasing both hold-up and interfacial area. It has been postulated that the gas hold-up as local gas fraction in the tank needs to be known to allow full quantification of heat and mass transfer to facilitate vessel design. With non-Newtonian fluids, typical of slurry bioreactors, an increase in viscosity results in a decrease in hold-up, while coalescence is promoted leading to larger bubble sizes.

In three-phase stirred tanks in general, increasing the solid fraction results in a decrease in k_La. However, this has been found to be particle type dependent, with an increase in k_La observed for pyrite loading and a decrease in k_La for silica loading (13-14 μm particles). This difference has been suggested to relate to the higher ionic strength of pyrite slurries and the possible hydrophobic nature of silica at the gas-liquid interface. With increasing aeration and agitation rate, an increase in k_La was found with both particle types. Investigations with carbon particle slurries (30 μm) showed an increase in k_L with increasing particle concentration, although no dependency of the mass transfer coefficient on carbon particle concentration was found. A hydrodynamic effect was postulated to explain this phenomenon whereby the particles enforce turbulence, with this effect becoming less dominant at higher agitation rates. An increase in gas-liquid interfacial area through hydrodynamic effects was ascribed to the increase in mass transfer upon particle addition. This particle behaviour will aid understanding in aerated slurry bioreactors.

2.4 Parameters Affecting Suspension and Mixing in Stirred Tanks

The parameters affecting mass transfer operations in stirred tanks are summarised in Table 2.3. There is a specific focus on particle suspension and the introduction of a gaseous phase. The critical suspension speed (N_{js}) is described as the point where no solids rest on the base of the vessel for more than 1 to 2 seconds, in accordance with Zwietering (1958).

The dominant factors influencing particle homogeneity in stirred tanks are particle size and density, agitation rate and tank geometry. Increasing particle concentration increases the required agitation rate for complete suspension, thereby decreasing absolute homogeneity. The introduction of a gaseous phase decreases the power transferred from the impeller, thereby leading to a decrease in particle suspension. These factors are expanded upon in Table 2.3.

Table 2.3: Parameters affecting suspension and mixing in stirred tanks

Parameter	Effect/Comment	Reference
Particle size and density	An increase in particle size or density (ρ_s) increases the terminal settling velocity, thereby increasing N_{js}. At constant agitation rate, these effects decrease particle homogeneity in the reactor. Larger particles have increased drag forces, while smaller particles can lead to a change in the bulk viscosity. Increased particle concentrations can lead to particle-particle interaction leading to hindered settling[1].	Zwietering (1958) Nienow (1968) [1]Shamlou and Koutsakos (1989)
Fluid density	The density difference between fluid and solid particle is directly proportional to N_{js}.	Zwietering (1958) Nienow (1968) Rieger and Ditl (1994)
Viscosity	N_{js} has been correlated to slurry viscosity, especially at high solids concentrations[1]. In the turbulent regime, N_{js} does not depend upon liquid viscosity[2]. In the transitional regime ($Re < 10^4$), an increase in viscosity increases N_{js}[3]. This last result is contrary to theoretical suggestions that suspension was only linked to viscosity through its impact on the particle drag coefficient, which implies a reduction in N_{js} with increasing viscosity[4].	Zwietering (1958) [1]Oldshue (1983) [2]Rieger and Ditl (1994) [3]Ibrahim and Nienow (1999) [4]Shamlou (1993)
Agitation rate	Increasing agitation rate increases particle suspension, although at very high agitation rates particle homogeneity can be decreased.	Shamlou and Koutsakos (1989) Williams *et al.* (1996)
Impeller type and diameter	Down-pumping axial impellers are the most efficient for solid suspension. Radial and up-pumping impellers require much higher energy dissipation rates to achieve equivalent homogeneity[1]. Radial impellers achieve increased particle suspension relative to axial impellers at the same agitation rate[2]. An inverted cone of solids can form under pitched blade impellers that inhibits complete suspension[3]. It has been concluded the larger the impeller for suspension, the lower the speed and power input required[4,5]. Conversely, it has been reported there is no conclusive unanimity on the effect of impeller diameter on critical suspension speeds, although for a given system, N_{js} will decrease with increasing impeller size[3].	[1]Nienow (1997) [2]Scholtz-Brown (1998) [3]Sharma and Shaikh (2003) [4]Nienow and Miles (1978) [5]Oldshue (1983)

Table 2.3: Parameters affecting suspension and mixing in stirred tanks continued

Parameter	Effect/Comment	Reference
Impeller clearance	Decreasing impeller clearance decreases N_{js} for propellers, paddles, vaned disc turbines, and not for six bladed fan disc turbines[1]. However, later studies on the disc turbine showed N_{js} decreased with decreasing clearance[2,3]. Clearance effects have been determined separately, with flow patterns scouring vessel corners at low clearances(C/H < 1/6), and splitting into two at higher clearances (C/H > 1/3). A low clearance increased particle homogeneity[4]. Suspension data have been correlated using equal power per unit volume assuming equally efficient geometries[5,6], supported by assumptions of isotropic turbulence[7]. Further, the terminal velocity-slip velocity theory suggests that the mass transfer coefficient for different geometries is constant at complete suspension[7,8]. However, the rate of change in this coefficient can vary after suspension, affected by the particular hydrodynamics[9]. The effect of impeller clearance on N_{js} has been further modelled[10,11,12], with some anomalies reported[13]. Similar exponents for correlations of 'double eight' flow have been found applicable for decreased clearance correlations, indicating dependence on particle diameter, viscosity, density and solids loading is not substantially affected[12]. More recently, three zones of N_{js} dependence affected by clearance have been found and modelled for pitched blade impellers[14].	[1]Zwietering (1958) [2]Harriot (1962) [3]Barker and Treybal (1960) [4]Nienow (1968) [5]Brian *et al.* (1969) [6]Calderbank and Moo-Young (1961) [7]Nienow (1975) [8]Nienow (1969) [9]Nienow and Miles (1978) [10]Conti *et al.* (1981) [11]Gray (1987) [12]Armenante and Nagamine (1998) [13]Chudacek (1985) [14]Sharma and Shaikh (2003)
Sparging apparatus	Traditionally, a circular sparge ring is present in aerated stirred tanks[1]. However, pipe spargers result in a greater reduction in power consumption in three-phase systems. Power consumption can be further reduced by decreasing the distance between the sparger and impeller[2,3]. A minimum sparger diameter ($D_{sparger}$ = 0.26 m; T = 0.45 m) has been found with pitched blade turbines where N_{js} is independent of gas flow at low aeration rates[4].It has further been shown that the presence of a sparger increases N_{js} even without gas flow, through changing the tank hydrodynamics[3]. Ring spargers result in more symmetric liquid flow leaving the impeller than pipe spargers, while concentric ring spargers increase N_{js} more than any other sparger designs[3].	[1]Perry *et al.* (1998) [2]Frijlink *et al.* (1984) [3]Rewatkar *et al.* (1991) [4]Breucker *et al.* (1988)

Table 2.3: Parameters affecting suspension and mixing in stirred tanks continued

Parameter	Effect/Comment	Reference
Introducing a gaseous phase	There is a wide lack of information on the complex interactions among solid particles, gas bubbles and the liquid phase at the various agitated regimes[1-3]. Three-phase systems are far from academic[2], and over 100 industrial processes have been reported[4]. This lack of data causes severe uncertainties in the design and development of these systems. The presence of gas affects N_{js}[2,3,5-7], and the presence of solids modifies the minimum speed required for complete dispersion of gas in the vessel[2].In different systems, the limiting factor governing power requirements can be either gas dispersion or solids suspension[5]. Higher agitation rates are necessary for complete suspension for increasing aeration rates. Further, N_{js} becomes increasingly dependent on superficial gas velocity with increasing solids loading[3]. More recently, pressure measurements at the tank bottom have quantified suspension in three-phase systems through accounting for the increased pressure due to particle lift-off[1].	[1]Micale *et al.* (2000) [2]Frijlink *et al.* (1990) [3]Rewatkar *et al.* (1991) [4]Shah (1979) [5]Chapman *et al.* (1981) [6]Chapman *et al.* (1983) [7]Nienow *et al.* (1986)

2.4.1 Conclusions

Physical and physico-chemical factors influencing particle suspension in the stirred tank environment have been reviewed. While this summary defines the effect of the parameters, it clearly shows the need for new technology to elucidate their interaction and to extract detailed information from the stirred tank environment. These factors provide the basis for evaluating the change in suspension quality when implementing the two tomographic techniques.

2.5 Challenges Affecting Growth of Microorganisms in Stirred Tank Slurry Bioreactors

In aerobic, metabolically active biological systems, good mixing and energy dissipation are required to ensure homogeneity and sufficient gas-liquid mass transfer and heat transfer. However, excessive agitation can result in microbial cell damage owing to fluid mechanical forces (Toma *et al.*, 1991; Lilly *et al.,* 1992; Scholtz-Brown, 1998). Interactions between microbial cells and solid particles (Croughan et al., 1988; Scholtz-Brown *et al.,* 1997) and bubble rupture at the gas liquid interface (Kunas and Papoutsakis, 1990; Michaels *et al.,* 1996; Scholtz-Brown, 1998) have also been shown to be damaging to the cells. It has been found that hydrodynamic stress can lead to changes in the microbial metabolic rate, morphology and metabolic pathway (Kunas and Papoutsakis, 1990; Smith *et al.,* 1990; Toma *et al.*, 1991; Scholtz-Brown, 1998; Potgieter, 2002). These effects result in reduced microbial productivity and may result in cell disruption. This is particularly noted in cell systems lacking structural strength in their cell wall and in metabolically active microbial systems in slurry bioreactors (Nemati *et al.*, 2000; Lamaignere, 2002; Sissing and Harrison, 2003; Harrison *et al.,* 2003a). Thus, a compromise is required between intensive agitation promoting mass and energy transport and the extent of cell damage and growth inhibition in the biological system, particularly the slurry bioreactor.

This study is concerned with particle distribution and mixing in slurry bioreactors. To deduce the resulting effects on microorganisms and hence the performance of the slurry bioreactor according to the conclusions of this study, it is necessary to examine solids loading, agitation rate and gas-liquid mass transfer effects on the microorganisms in greater depth through review of previous research.

2.5.1 The Influence of Particulates on Slurry Bioreactor Performance

Scholtz *et al.* (1997) examined the increase in cell disruption of a stationary phase yeast, *Saccharomyces cerevisiae*, across the range of quartzite loading of 5 to 40 %

(v/v). Disruption in excess of 90 % was found in this range. The extent of disruption was independent of the solids loading. The disruption rate was related to both the power input per unit volume and the amount of solids present. Lamaignere (2002) extended this study to a growing system using the range of 0 to 5 % quartzite. She found a decrease in growth at 1.5 and 2 % solids loading, while at 5 % (v/v) growth ceased.

The influence of solids loading (5, 10 and 20 % (v/v)) on acidophilic iron and sulphur oxidising mesophiles was studied and found to increase the lag phase, while at 20 % concentration the cells appeared not to reach the exponential growth phase (Harrison *et al.*, 2003b). Acidophilic thermophilic microorganisms, primarily *Sulfolobus metallicus*, have been studied in the range of 3 to 18 % (w/v) using pyrite fractions of 53 to 75 μm in a one litre stirred tank at an agitation rate of 500 to 550 rpm (Nemati and Harrison, 2000). From 3 to 9 % loading, little effect was observed. At 12 to 15 % solids, the leach rate was impaired, while at 18 % the system failed and cell death was observed. These studies were extended by maintaining constant physicochemical conditions through addition of inert quartzite to a base of 3 % (w/v) pyrite (Harrison *et al.*, 2003b; Sissing and Harrison, 2003) or 3 % (w/v) chalcopyrite (Harrison *et* al., 2003b; Raja, 2005), and a similar trend of decreased solubilisation of iron and copper was observed based on reduced microbial growth and overall metabolic activity.

2.5.2 The Influence of Particle Size on Slurry Bioreactor Performance

Particle size can influence the slurry properties e.g. viscosity, while the nature of the interaction with the microbe is affected in terms of frequency of collision, momentum transfer and the average path length of collision. Harrison *et al.* (2003b) found that increasing particle size in a system with *S. cerevisiae* led to an increase in the disruption rate of the cells, and this was similarly correlated to the fraction of protein release. Below a particle size of 300 μm, the disruption rate constant is less than 20 % of the maximum observed at greater particle diameters of 700 to 1000 μm. Increasing the particle size above 700 μm showed no further effect on the disruption rate.

Nemati *et al.* (2000) conducted pyrite leaching in the presence of *Sulfolobus metallicus* and examined the effect of particle size on microbial growth and leaching performance. Leaching rate was found to increase with decreasing particle size across a range of 37 to 150 μm, which is in accord with the effect of increased interfacial area. At mean particle diameters less than 25 μm, it was found that leaching performance and the specific growth rate were reduced, suggesting the influence of the changing physicochemical properties of the slurry. Further studies,

reported by Harrison *et al.* (2003b), illustrated both a reduction in microbial growth and leach performance as the mineral fraction was reduced to a diameter of 15 μm and less.

2.5.3 The Influence of Agitation Rate on Slurry Bioreactor Performance

Harrison *et al.* (2003b) investigated the effect of agitation rate in the slurry bioreactor on acidothiobacilli over the range 400 to 1100 rpm in a one litre tank reactor using a Rushton impeller. Agitation with the presence of quartzite resulted in an extended lag phase of 40 hours at rates of 400 and 770 rpm (impeller tip speeds of 1.1 and 2.2 $m.s^{-1}$), while agitation at 1090 rpm resulted in further extension of the lag phase. Similar studies were carried out using the acidophilic thermophile *Sulfolobus metallicus*, a key microorganism in thermophilic tank bioleaching of metal sulphides. These archae are characterised by a cell wall of reduced structural strength. A biological stress response in terms of reduced microbial growth and bioleaching was observed on increase of the agitation rate in the 1 litre laboratory reactor from 250 to 550 rpm, achieving complete suspension. At 760 rpm (tip speed of 2.3 $m.s^{-1}$), cell damage exceeded the cell growth rate and the system failed.

Further investigations with *S. cerevisiae* at tip speeds of 1.9 to 3.5 $m.s^{-1}$ showed the presence of an optimum tip speed of 2.3 $m.s^{-1}$, indicating the compromise between providing adequate mass transfer and minimising hydrodynamic stress. Studies on hydrodynamic stress in turbulent flow indicate that a key parameter of particle breakage is the ratio of the Kolmogorov microscale of turbulence (Kolmogorov, 1941) to the particle size (Illing, 1996). Eddies sizes less than the cell have insufficient energy to cause damage, while eddy sizes approaching the cell diameter impart the maximum hydrodynamic force.

2.5.4 Gas-Liquid Mass Transfer Effects on Slurry Bioreactor Performance

The effect of solids on k_La has been reviewed in Section 2.3.1.5. It has been further hypothesised that the observed decrease in microbial oxidation rates of minerals is due to oxygen and carbon-dioxide mass transfer limitation on increasing mineral concentration, rather than slurry concentration per se and initial specific surface area of particles (Boogerd *et al.,* 1989; Boon and Heijnen, 1998; Torma *et al.,* 1972). Boon and Heijnen (1998) suggest other factors may also cause a decrease of the microbial oxidation rate at higher pyrite concentrations e.g. nutrient limitation, low pH values, low concentration of microorganisms due to the inoculum, microbial shear, or inhibition by substances that leach from the mineral. Although shear can be significant (Kunas and Papoutsakis, 1990; Smith *et al.,* 1990; Toma *et al.*, 1991; Scholtz-Brown, 1998; Potgieter, 2002), Boon and Heijnen (1998) fail to mention the effect of mechanical stress through particle collision. The studies of Sissing and Harrison (2003), Harrison *et al.* (2003b) and Raja (2005) confirm the influence of the physical presence of the solid phase on microorganisms in the absence of increasing mass transfer requirements through use of an inert solid phase that does not partake in bioxidation.

2.5.5 Solid-Solid Particle Interaction in Stirred Tank Reactors

At high concentrations of solids it is necessary to consider the interaction between the particles themselves which results in particle abrasion (Nienow and Conti, 1978). Examples of these operations include the erosion of solid support particles used to immobilise enzymes (Regan *et al.*, 1974), the break-up of activated carbon and catalyst particles, and the abrasion of particles in bead mills. This study will be mainly focused on particle distribution in the stirred tank using quartzite, ballotini and nylon particles. Changes in morphology will be assumed negligible over the experiment duration.

2.5.6 Conclusions

Increased solids loading and shear stress (through increased agitation rate) affect the slurry bioreactor performance under general conditions. It is evident that a critical solids loading exists above which performance is impaired, while particle size further affects microbial growth in slurry systems. Furthermore, if particle concentration is variable in the stirred tank, this suggests that the particle-cell collision frequency and the availability of a nutrient source vary spatially in the reactor.

2.6 Quantifying Mixing and Suspension – Direct Methods

Direct methods are those in which the point of critical suspension i.e. when all particles are suspended, or degree of mixing can be immediately determined experimentally, without further correlation or translation. Traditionally the point of critical suspension has been achieved subjectively through human eyes, while the degree of mixing has been determined via grab sampling from ports in the stirred tank. Visual determination is non-invasive while sampling causes a disturbance in the vessel and is invasive.

2.6.1 Sample Withdrawal in Slurry Reactors

2.6.1.1 Experimental Determination of Concentration Profiles by Sample Withdrawal

Experimental validation in the form of grab sampling is often needed in determining solids concentration in stirred tanks when using indirect methods i.e. radiation, sound, CFD. It has been employed in the past as the principal method before the advances in instrumentation and sensing. This method is tedious and it is important that the withdrawal technique does not influence the reactor hydrodynamics.

Sampling continuously from reactor side ports has been reported (Baldi and Conti, 1978; Baldi *et al.*, 1981; Barresi and Baldi, 1987a; Nasr-El-Din *et al.*, 1984 Nasr-El-Din *et al.*, 1985; Nasr-El-Din, 1989; MacTaggart *et al.*, 1993). Nasr-el-din *et al.* (1985) focused solely on the errors arising from wall sampling in a two-dimensional model. They investigated particle momentum and drag, while examining sampling of 3 size fractions of sand (165, 325 and 720 μm) from a pipe wall. These authors found a higher withdrawal velocity increased sampling efficiency, while a smaller withdrawal aperture decreased the concentration ratio C/C_b, where C_b is the bulk concentration of particles. A projection added on to the side port changed the flow pattern and affected the variations of the size distribution with sampling velocity. On decreasing sampling velocity, the normal side port decreased the mean particle size while larger particles were sampled with the extended side port. These authors reported that side wall sampling causes serious errors in concentration and size distribution measurements. These errors are compounded as the sampling velocity decreases, while they decrease as the solids concentration increases.

Barresi and Baldi (1987a) used 10 side ports of 6 mm diameter (45° cut edge) placed radially, with openings 20 mm from tank wall (Rushton, 1965). Withdrawal tubes, as shown in Figure 2.3, were suitable for upward and radial flow, but less suitable for downward flow e.g. below the impeller using a radial disk turbine. Measurements were found to have a reproducibility of 10 %, while reporting that sample concentration is generally different from that in the vessel due to challenges of isokinetic operation. Consistency of the experimental data was examined by relating the integrated solids concentration distribution with the average solid concentration, with the former usually 10-20 % less than the known average concentration. Complete mass balancing to determine accuracy was not possible as the tank bottom was not sampled. The effect of withdrawal velocity and shape of the withdrawal tube is observed in the change in the axial concentration profile in Figure 2.3.

As an extension of the study of Nasr-El-Din *et al.* (1985), MacTaggart *et al.* (1993) focused on obtaining a representative sample from a mixing tank, as investigated by Nienow (1985). Sampling errors arise due to inertial differences between the fluid and particles of different size or density (Nasr-El-Din, 1987; Smith, 1990). The sample tube design (shape, diameter and tip angle) and sampling technique (withdrawal velocity and location in the vessel) were found to significantly affect the solids concentration and the particle size distribution of the sample withdrawn. Nasr-El-Din (1989) found that sampling errors can be caused by the difference in particle inertia relative to an equal volume of surrounding fluid, the flow structure ahead of the sampling point and particle bouncing. The particle inertia can be represented by the Stokes number:

$$K = \frac{\rho_p d_p^2 u_s}{18\mu_L(\phi/2)} \tag{2.5}$$

where d_p is the particle size, u_s is the local velocity, μ_L is the liquid viscosity, ρ_p is the particle density and ϕ is the inside diameter of the sample tube. Thus very small particles or particles of similar density to the fluid will have a low inertia relative to an equal volume of fluid. These particles will follow the fluid and enter the sample tube. Very coarse or dense particles with high inertia will not follow the fluid streamlines, but rather travel in straight lines resulting in sampling errors. However, representative samples can be withdrawn parallel to well developed flow when sampling at the isokinetic velocity with a properly designed sample tube (Nasr-El-Din *et al.*, 1984). Thus the most accurate sampling can be done in the impeller plane using a radial flow impeller (MacTaggart *et al.,* 1993).

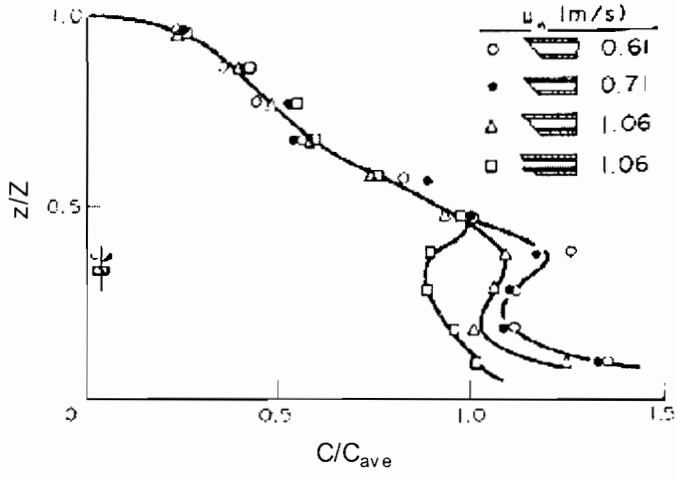


Figure 2.3: Influence of the withdrawal velocity and the edge of the withdrawal tube on the axial concentration profiles. Four pitched blade turbine: d_p = 208-250 μm, X = 1.51, N = N_{js} (Barresi and Baldi, 1987a)

MacTaggart *et al.* (1993) used a flat-bottomed plexiglass mixing tank with a Rushton six-bladed turbine (H = 0.292; H/T = 1; D/T = 1/3). In conclusion these authors found that the sample solids concentration could vary widely, mainly due to the sampling velocity, the shape and diameter of the sample tube, the degree of alignment with the flow, and the particle size and bulk solids concentration in the tank. MacTaggart *et al.* (1993) reported that it is very difficult to obtain a representative measure of the local solids concentration in a slurry mixing tank by sample withdrawal. The variation of sample solids concentration can be minimised as described above, mainly through using fine solids and a high withdrawal velocity. These authors state that to obtain a reliable measure of the local solids concentration in a slurry mixing tank it would be necessary to use another technique. In a follow up study, Nasr-El-Din *et al.* (1996) confirm these sampling errors through use of an invasive conductivity probe.

2.6.1.2 Quantifying Solid Suspension using Sample Withdrawal

Baldi *et al.* (1981) sampled from a stirred tank ($H = T = 0.175$ m; D/T = 0.27; 8 bladed Rushton) and related concentration profiles to the critical suspension speed, N_{js}. They found profiles for complete suspension did not depend on the concentration range tested (5-20 $kg.m^{-3}$). However, the gradients did increase with the diameter of the particle as shown in Figure 2.4. A ten-fold increase in power was necessary to achieve complete suspension of 240 μm particles compared to that of the 89 μm particles. It was concluded inadvisable to aim for a greater degree of homogeneity than that obtained at $N = N_{js}$. In their reactor, pseudohomogeneity was observed for the zone $z/Z = 0.25 - 0.55$ (dimensionless height) at conditions of suspension and with $N > N_{js}$. However, this homogenous zone was also observed for $N/N_{js} = 0.75$. The authors suggest that, as an energy saving of up to 50 % can be obtained on operating at $N = 0.8\ N_{js}$, there is a case for operating under incomplete suspension provided that the output criteria are achieved. Verification of the output criteria requires reliable measurement of concentration profiles.

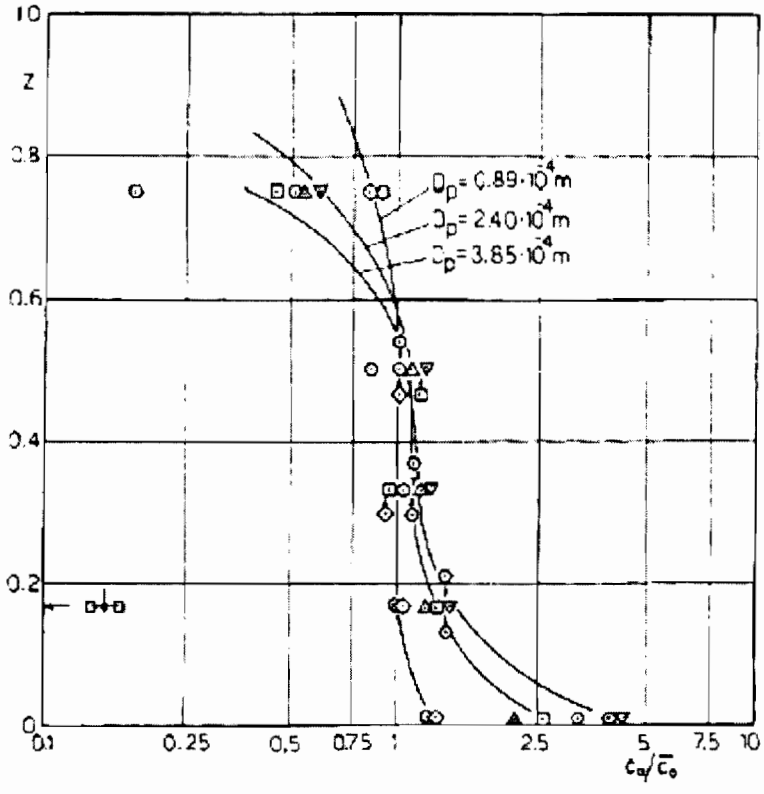


Figure 2.4: Mean axial solids concentration for particle sizes 89, 240 and 385 μm at N_{js}. (Baldi *et al.*, 1981)

Barresi and Baldi (1987a) examined particle distribution in a baffled vessel of 0.390 m diameter with a torispherical bottom ($r_k/L = 1/10$) using four types of stirrers: an A310 Lightnin axial propeller, a 45° pitched four-blade turbine, a disk turbine with six

flat blades inclined at 45° (mixed flow impellers), and a Rushton type radial turbine. All had dimensions of T/3 and a clearance of H/3, while axial impellers were pumping downwards. Monomodal glass beads (100-177 μm, 208-250 μm, 417-500 μm; ρ = 2600 kg.m^{-3}) were introduced at dilute concentrations of 0.50, 1.51 and 5.10 kg/100 kg.

Axial profiles were generated from side ports near the wall, and these authors state that the solids concentration usually increases towards the centre, especially in the lower parts of the vessel. Furthermore, the concentration near the bottom is very high but uncertain. These authors had some difficulty in determining complete suspension with the downward pumping pitched-blade turbine due to flow instability, as well as positive effects from the dished bottom when using the Rushton turbine. As found by Zwietering (1958), these authors found:

$$N_{js} \propto X^{0.13} \tag{2.7}$$

The influence of particle size was different to that of Zwietering (1958) and found to be dependent on stirrer geometry, in accordance with Conti and Baldi (1978) who noticed a change in the exponents of the N_{js} relationship with impeller geometry. This was suggested to be due to a different distribution of the local dissipated power per unit volume (Baldi *et al.*, 1978).

On analysing the concentration profiles, these authors noted gradients along the radius are generally slight for axial flow impellers, but increase if larger particles are tested. The disk turbines had strong concentration gradients in the zone below the impeller (C/C_{wall} = 1 to 2), as shown in Figure 2.5 (a). However, in the rest of the vessel a good radial homogeneity was observed. It must be noted that these studies were carried out using dilute concentrations of solids of 0.2 to 2.0 vol. % (X = 0.5 to 5.0). In Figure 2.5 (b), the effect of different stirrer geometries on the axial concentration profiles show the influence of turbulence intensity.

The suspension quality was improved when the power number increased and particle size was decreased. The concentration profiles at dilute concentrations (0.2 and 0.6 vol. %) were unaffected by the mean concentration relative to N/N_{js}, as reported by Baldi *et al.* (1981). It was observed near the tank bottom at the condition of complete suspension, C/C_{av} increased upon increasing the mean concentration to 2.0 vol. % (X = 5.10), as shown in Figure 2.5 (c).

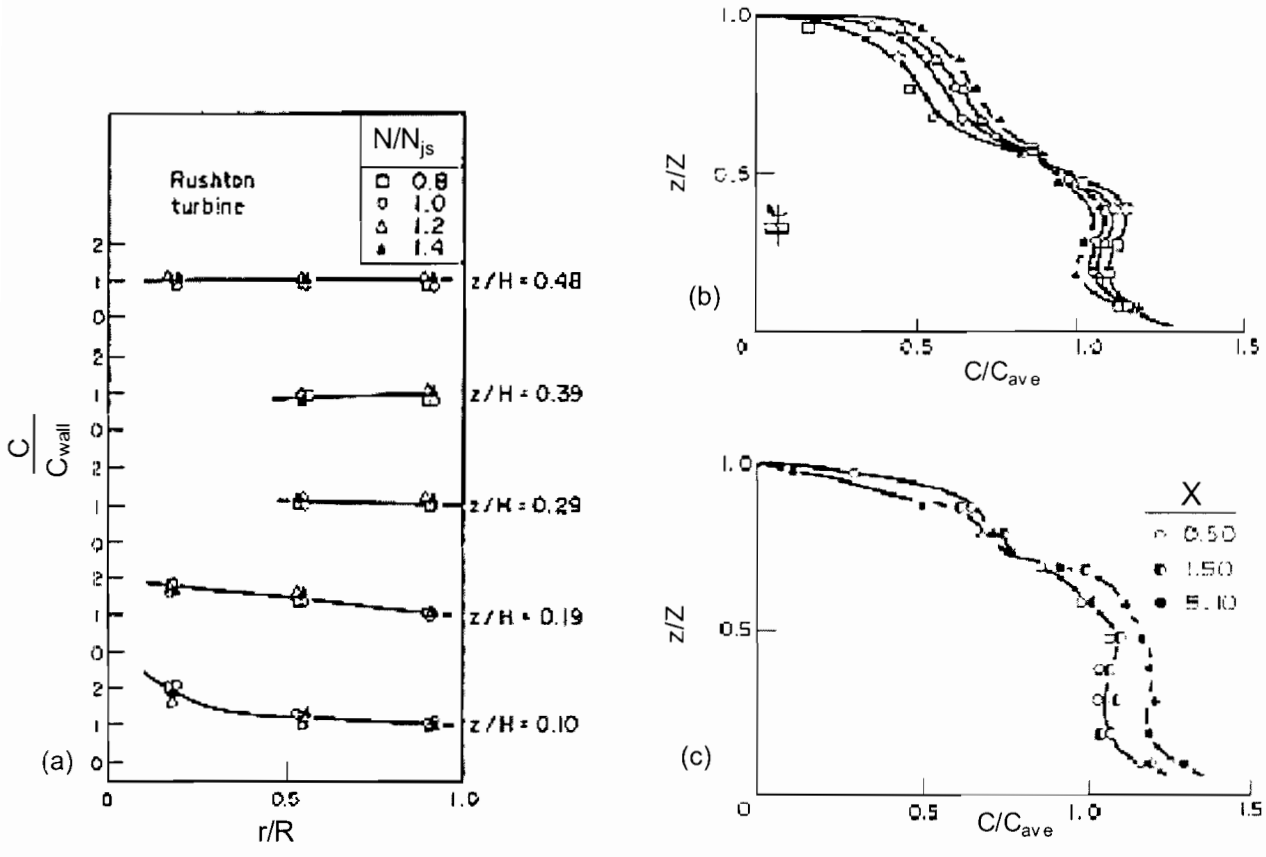


Figure 2.5: Radial and axial concentration profiles through direct wall sampling (Barresi and Baldi, 1987a). Rushton turbine; d_p = 100-177 *pm*, X = 1.51 (a). Axial concentration profiles at N_{js} for different types of impellers: (□) A 310 Lightnin; (○) four pitched blade turbine; (△) six pitched blade disk turbine; (▲) Rushton turbine. d_p = 100-177 *μm*, X = 0.50 (b). Axial concentration profile using six pitched blade disk turbine for X = 0.50 to 5.10 suspended at N_{js} (c).

2.6.2 Examining Suspension in Stirred Tanks Visually

2.6.2.1 Experimental Approach to Visual Determination of N_{js}

Zwietering (1958) developed the concept of quantifying suspension on the work Kneule (1956), who stressed the importance of the point at which all particles are just in suspension in his investigation of the solution of crystals. Zwietering (1958), in a set of pioneering experiments, took this concept further to include various stirrer geometries, particle sizes, weight fractions and speeds using sand and sodium chloride with low viscosity fluids to produce an empirical correlation for just suspension:

$$N_{js} = s_1 \nu^{0.1} \left(\frac{g\Delta\rho}{\rho_L} \right)^{0.45} d_p^{0.2} X^{0.13} D^{-0.85} \qquad (2.6)$$

where N_{js} = impeller speed at which complete suspension is achieved (s^{-1})
d_p = particle diameter (m)
g = acceleration due to gravity ($m.s^{-2}$)
s_1 = dimensionless constant
X = weight % of solids per liquid
ν = kinematic viscosity ($m^2.s^{-1}$)
ρ_L = bulk fluid density ($kg.m^{-3}$)
$\Delta\rho$ = difference in density of suspended solid and bulk fluid ($kg.m^{-3}$)
D = the diameter of the impeller (m)

Subjective observation was difficult as even at high stirrer speeds streaks of solid particles were visible at the bottom of the tank. At the border between incomplete and complete suspension, particles were observed which settled temporarily at the bottom and remained for a short time in a fixed position relative to each other. When such a small pile was at rest for longer than 1 or 2 seconds before being dispersed it was deemed incomplete suspension. When no such deposits remained on the bottom for more than one second, the suspension was considered complete. Using this method with the same observer, a reproducibility of 2 to 3 % was achieved. This method has been used in later studies: Nienow (1968), reproducibility 3-5 %; Armenante and Nagamine (1998), reproducibility 4 %. Although there is a subjective element, this observation method is simple and effective. Difficulties arise at higher solid concentrations (>10 % wt.; Bujalski *et al.*, 1999), or when using opaque broths where observation is limited. Bujalski *et al.* (1999) further stated it is extremely problematical at high solids loading to achieve experimental confirmation of the validity of any predictive equation.

A further method for determining critical suspension is to measure the height and radius of the unsuspended particles on the tank bottom (Havelkova, 1987; Rieger and Ditl, 1994). This was argued to be more objective in determining N_{js} although more labour intensive. Rieger *et al.* (1980) reported that this contact method was mainly used in analysing industrial-size vessels that are usually non-transparent. In this case, the height of the sedimented particle layer was measured by means of a rod, at the end of which was fixed a flat baffle perpendicular to it. A criticism of this method is the assumption of a uniform height of unsuspended solids which is often not realistic.

Another direct method is the use of a scintillation probe located under the bottom of the agitated vessel (Ditl and Rieger, 1984). With the decreasing height of the particle layer the frequency of impulses decreases and approaches a constant value as soon as the complete suspension speed is reached. The disadvantage of this method is that it only analyses one spot on the bottom of the vessel.

The suspension can often form a distinct interface with the clear liquid layer near the tank surface. This "cloud height" allows direct analysis of particle suspension. Einenkel and Mersmann (1977) determined the critical suspension speed when a sudden change occurred in the cloud height. Similarly, Zehner and Tebel (1984) defined the critical suspension speed as that at which the cloud height reached 90 % of the liquid height. Rieger and Ditl (1994) criticised this approach as they found in many systems the particle cloud reached the surface in the state of complete suspension and an interface could not be determined.

2.6.2.2 *Quantifying Suspension through Visual Observation*

Bujalski *et al.* (1999) examined cloud height for high solids concentration (> 10 % wt.), and determined five suspension stages as shown in Figure 2.6:

(i) at low speeds a small fraction of particles are lifted up and distributed throughout the vessel;
(ii) with increasing impeller speed, an interface appears between the suspended particles and a clear liquid layer in the upper part of the vessel;
(iii) the height of this interface is reduced with further increases in speed; while the volume of the static bed also decreases
(iv) upon further increases in agitation rate the height of the interface is increased finally; and
(v) there is no interface between the slurry and clear liquid

Critical suspension is typically achieved during stage (iv) (Bujalski *et al.*, 1999; Kraume, 1992). N_{js} was found to decrease with decreasing particle size and density, while the height of the suspended solids layer at the corresponding speed was reduced. This is contrary to the intuitive view that very fine and low density solids will reach the liquid surface easily once N_{js} is reached. Hicks *et al.* (1997) found that the most energy efficient way of enhancing the cloud height is through the use of dual impellers, though it approximately doubles the required power for N_{js}.

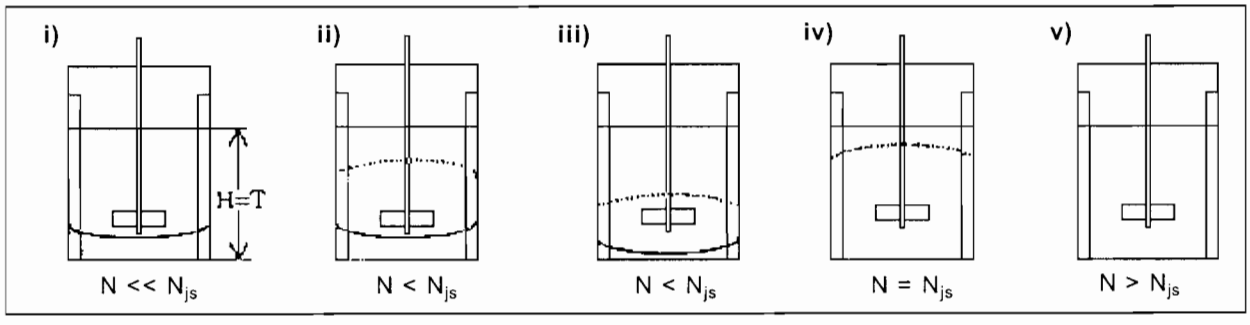


Figure 2.6: Solid suspension stages from Bujalski *et al.* (1999). The solid line represents the static solids at the bottom, while the dotted line represents the solid-liquid interface.

2.6.3 Conclusions

Sample withdrawal is not a reliable method for determining local solids concentration. However, sampling errors can be minimised to yield qualitative information and provide validation for indirect methods of slurry analysis. Radial and axial concentration profiles have been generated which provide comparative information for this study.

The visual method is still one of the simplest and most powerful techniques for determining the point of critical suspension. However, it has a subjective element with judgement becoming more uncertain with increasing particle concentration. Further, the presence of a solid-liquid interface or cloud height is not universal under all stirred tank operating conditions. Optical methods can only be applied in clear media, and thus for a slurry bioreactor these methods will not be applicable. Furthermore, determining the critical suspension speed yields little information about particle distribution throughout the vessel (Shamlou and Koutsakos, 1989).

2.7 Quantifying Mixing and Suspension – Indirect Methods

Indirect methods are those in which the measured variable can be related to solids concentration or N_{js}. With increasing development of measurement technology more objective methods are possible through the use of lasers, LEDs, conductivity probes and tomography. However, there is still a subjective element in the creation of criteria and the interpretation of the measured variable. Most of these methods are non-invasive, except for the use of endoscopes or conductivity probes within the stirred tank environment. In this section, optical methods and conductivity measurement are reviewed. Thereafter mixing and suspension models are investigated as an indirect analysis of particle distribution.

2.7.1 Determining Solids Distribution using Indirect Optical Techniques

2.7.1.1 Experimental Approach Using Optical Techniques

Kolar (1961) defined a homogenous suspension as one in which the mean particle concentration measured by a light intensity method was the same at one quarter and three quarters of the liquid height. Means were taken over three minutes, despite there being much fluctuation in the upper level. Nienow (1968) criticised this approach, as fulfilment of this criterion did not necessary mean that particles were evenly distributed. Nienow (1968) further observed periodic concentrated particle eddies that were flung into the upper regions of the vessel. These would influence the mean concentration measured by Kolar (1961).

Fajner *et al.* (1985) examined solids distribution of glass beads (d_p = 137 and 327 μm, solids concentration = 15 kg.m^{-3}) in a staged, multi-impeller stirred column. The mean solids concentration along the vertical axis was determined using a light-emitting diode (LED) with a miniature silicon photo-diode as the receiver. This transformed the incident radiation into a current. The light beam was approximately 4 mm in diameter and passed midway between the baffles. The signal was filtered to remove ambient light. Measurements were assumed to give a mean solids concentration in the horizontal section. Calibration was achieved by measuring the light intensity on a vessel of similar geometry which was stirred rapidly. Measurements at different heights in the vessels gave the same signal, indicating to these authors that homogeneity had been achieved, and calibration curves could be generated. An overall mass balance determined that the consistency of the measurements was satisfactory within 10 %. The deviations were attributed to the slight variation of the beads size distribution and a lack of perfect alignment and collimation of the optical equipment.

Shamlou and Koutsakos (1989) examined solids distribution (glass ballotini up to 6 wt %, d_p = 390, 530 and 780 μm) in a dish-bottomed vessel (T = 0.225 m, H/T = 3, pitched-blade impeller) using a 5 mW He-Ne laser transmitter with an expanded beam diameter of 9.0 mm. The intensity after passing through the suspension was measured by a photovoltaic receiver. Based on the linear response, voltage output was used directly as a measure of the light intensity. For the mono-sized particles with constant optical path length and low solids concentration, the relationship between transmitted light and concentration was found by using well-defined and near-homogeneous solutions (Shamlou and Koutsakos, 1986).

2.7.1.2 Quantifying Suspension Using Optical Methods

Similarly to Baldi *et al.* (1981), Fajner *et al.* (1985) found the dimensionless axial concentration profiles to be independent of the mean solids concentration. However, low concentrations were examined (0.6 % by volume).

Shamlou and Koutsakos (1989) examined particle distribution using the system described in Section 2.7.1.1. Results suggested in most cases the greatest variation in solids concentration was in the "core of the liquid" in the axial direction (Koutsakos, 1988). The "core of the liquid" referred to the bulk of the agitated fluid away from the walls, the region near the liquid surface and the discharge zone of the impeller. Two sample positions (A and B) were used with the laser transmitter: position A was located at 0.044T (10 mm from wall) and position B at 0.25T (56 mm from wall). Solids concentration ranged from 1 to 3 wt. %. Axial concentration profiles are shown in Figures 2.7 - 2.9.

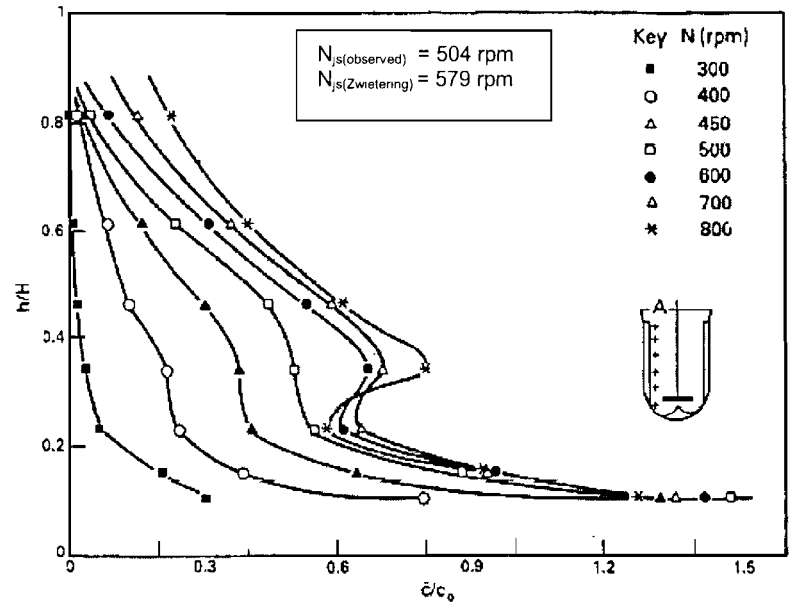


Figure 2.7: Relating the dimensionless solid concentration ratio to the dimensionless height for different impeller speeds (d_p = 390 μm, ρ_s = 2900 kg.m^{-3}, ρ_L = 1000 kg.m^{-3}, D = 10 cm, pitched blade, C = 13 cm, H = 65 cm, C_o= 1 wt %, sample position = 0.044T). (Shamlou and Koutsakos, 1989)

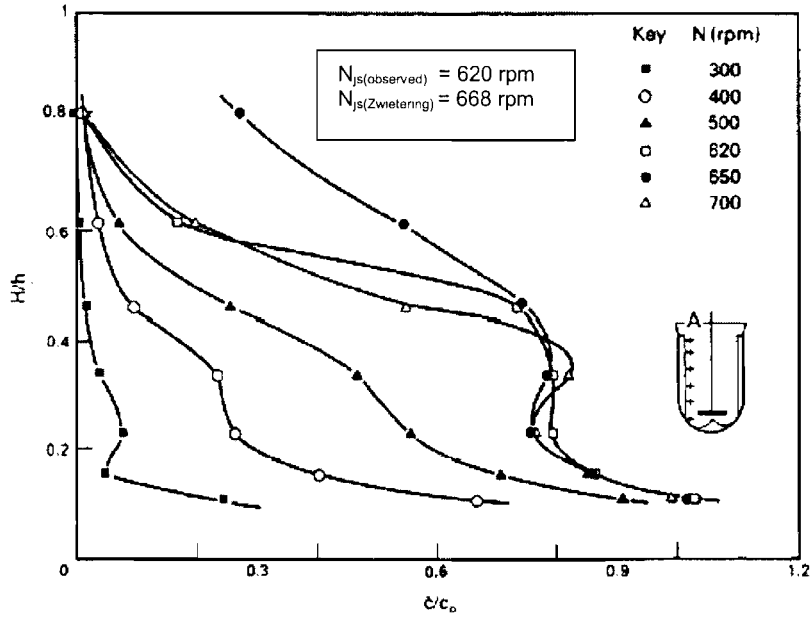


Figure 2.8: Relating the dimensionless solid concentration ratio to the dimensionless height for different impeller speeds (similar experimental conditions as Figure 2.7, except C_o = 3 wt %, sample position = 0.044T). (Shamlou and Koutsakos, 1989)

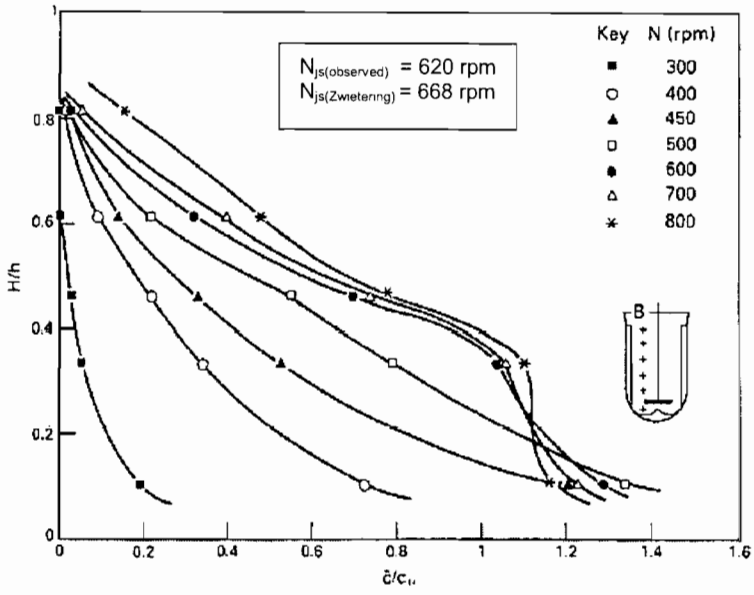


Figure 2.9: Relating the dimensionless solid concentration ratio to the dimensionless height for different impeller speeds (3 wt. %, similar experimental conditions as Figure 2.7 except sample point = 0.25T). (Shamlou and Koutsakos, 1989)

It is apparent that the profiles are smoother from the 0.25T sample position (comparing Figure 2.8 and 2.9), while a sharp increase in concentration is apparent above the impeller plane. Further observations were made by Shamlou and Koutsakos (1989) from their results:

(i) At low impeller speeds (< 200 rpm) most particles remain on the bottom of the vessel with limited motion (data not shown).

(ii) At higher speeds an intermediate zone is formed characterised by a relatively steep curve indicating a sharp increase in solids concentration with speed as particles are picked up from the base.

(iii) At each case a peak concentration occurs at a critical impeller speed which has been identified as the just-suspension speed (Shamlou and Koutsakos, 1986; Musil *et al.*, 1984; Bourne and Sharma, 1974; Machon *et al.*, 1982; Ohiaeri, 1981).

(iv) As the agitation rate increases further beyond the point of maximum concentration a third zone is formed where the local solids concentration remains constant or decreases slightly with an increase in speed.

2.7.2 Conductivity Probing of the Slurry Reactor

2.7.2.1 Experimental Approach to Conductivity Probing

McKee *et al.* (1995) measured conductivity in a stirred tank with a probe consisting of two epoxy resin arms separated by 10 mm. A platinum electrode (10 x 10 mm) was

mounted on each arm and readings were logged by computer. Four axial positions were investigated with the probe in a stirred tank which provided support for ERT conductivity data.

Nasr-El-Din *et al.* (1996) inserted a 610 mm x 4.8 mm diameter conductivity probe into a slurry reactor at 9 axial and 3 radial positions. The conductivity values were found to correspond accurately to solids volume fraction through application of an equation from Maxwell (1873), given as Equation 2.13 in Section 2.8.1.7.

In the study of Lucas *et al.* (1999), a 25 x 4 mm diameter conductivity probe was inserted into a slurry pipeline to provide reference measurements for ERT. This probe was designed through extensive finite element modelling to optimise the position of the field and sense electrodes. Equation 2.13 was similarly applied to calculate solids volume fraction.

2.7.2.2 Quantifying Suspension Using Conductivity Probing

McKee *et al.* (1995) examined three size fractions (150-210 μm, 425-500 μm and 600-710 μm) of quartzite at a concentration of 6.3 vol. % (15 wt. %) suspended by a pitch bladed impeller (4 x 45° blades, T/3) in a 21 litre tank using the probe described in Section 2.7.2.1. Axial concentration profiles were produced from the conductivity probe data through maintaining the intrusive probe at a single position at four heights up the reactor. As agitation speed increased from 180 to 415 rpm a higher concentration of particles was detected just above the impeller plane (Figure 2.10), similar to the data of Barresi and Baldi (1987a) shown in Figure 2.5.

Approaching the maximum of 428 rpm for the 425 – 500 μm fraction (Figure 2.10 (a)), a tendency towards axial homogeneity was reflected, however, for the 600-710 μm particles at 415 rpm the profiles remained non-uniform (Figure 2.10 (b)).

Nasr-El-Din *et al.* (1996) generated axial and radial concentration data through insertion of a conductivity probe (Section 2.7.2) into a stirred tank reactor (T = 0.292; H/T = 1.00; D/T = ⅓; C/T = 0.300; Rushton impeller). Solids concentration profiles were found to be dependent on particle size (82, 255 and 410 μm), solids loading and agitation rate. Varying radial profiles were observed, except when fine sand particles of 82 μm were used. In general, solids concentration above the impeller increased on approaching the vessel wall (r/R = 0.9). Below the impeller, radial concentrations were observed to be highest at r/R = 0.6 for 410 μm particles. A peak concentration was also observed in the impeller plane at r/R = 0.6 for these particles.

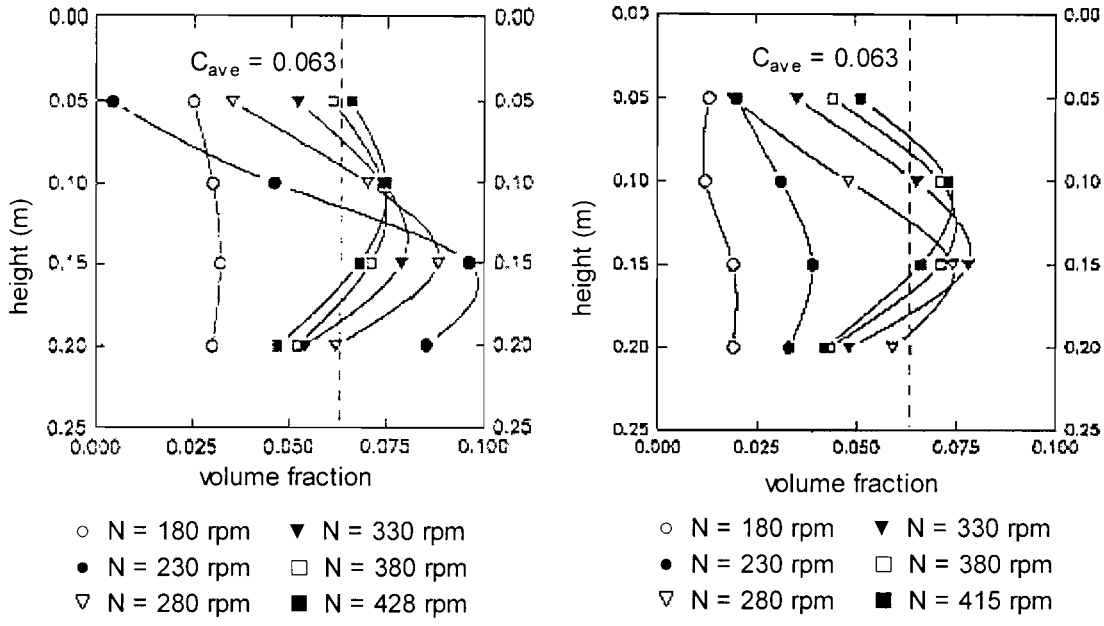


Figure 2.10: Axial concentration profiles obtained from conductivity probe measurements. 425 - 500 μm particle size fraction (a), 600 - 710 μm (b). C_m is the mean particle concentration (pitched blade T/3, C = T/3). (McKee *et al.*, 1995)

In the study of Lucas *et al.* (1999), conductivity probe data compared well with those obtained from the ERT results generated using an LBP reconstruction algorithm. The solids volume fractions estimated from the ERT agreed within 10 % of the measured values. The probe was further applied to a slurry velocity study combined with ERT and is detailed in Section 2.8.1.9.

2.7.3 The Development of Suspension Models

The literature on solids distribution over the height of the vessel is sparse, and successful modelling is limited to the case of low solids concentration (Bittorf and Kresta, 2003). Rewatkar *et al.* (1991) reported that suspension models can be classified into two general categories. In the first, a force or energy balance is established in the vicinity of the vessel bottom, while in the second the force or energy balance is established in the main body of the vessel. The first category is based on the lifting of particles from the bottom, while the criteria for the bulk region modelling are based on homogenisation of the solid suspension e.g. turbulent diffusion.

They noted the complexities in quantifying forces in the stirred environment when establishing a suitable model:

- the energy dissipation rate is inhomogeneous,

- the drag coefficient for a particle in a turbulent field is vastly different from the single-particle drag coefficient,
- the solid phase concentration profiles in the radial and axial directions have been incompletely understood, and
- information on velocity and turbulence structure as a function of impeller design, geometry, solid loading, and size is still lacking.

Suspension models are presented in Table 2.4.

Table 2.4: Suspension models reported in literature

No.	Model description	Reference
1	(axial flow impeller) The net force acting on suspending particles is zero i.e. a balance of gravity and the slurry head force with buoyancy and drag forces	Narayan *et al.* (1969)
2	(radial flow impeller) Turbulent eddies of the order of particle size are responsible for particle suspension. The energy balance is established between the kinetic energy imparted by eddies on the particle and the potential energy gained by the particle.	Baldi *et al.* (1978)
3	(axial flow impeller) At the condition of solid suspension the energy dissipated at the solid-liquid interface is assumed to equal a fraction of the energy supplied by the impeller. This fraction is estimated with a decay function.	Musil and Vlk (1978)
4	(axial flow impeller) Suspension is achieved when particle settling velocity equals the rise velocity in the bulk region.	Subbarao and Taneja (1979)
5	(staged column reactor) Modelled solid concentration profiles by means of a one-dimensional sedimentation-dispersion model with the particle settling velocity as a function of the free-settling velocity	Fajner *et al.* (1986)
6	Developed criteria based on the d_p/T ratio by relating it to the mean axial velocity and to the Froude number. The Froude number was defined on the basis of the vessel diameter.	Voit and Mersmann (1986)
7	(axial flow impeller) Suspension criteria depend upon the particle size of the Archimedes number (Ar). The suspension of fine particles ($Ar \leq 40$) immersed in a viscous sublayer occurs due to shear stress in the wall boundary layer of the vessel bottom. The shear force and buoyancy forces are equated to yield a relationship between Reynolds and Archimedes numbers. For larger particles ($Ar > 40$), the particle sedimentation velocity is assumed to be insignificant as compared to the fluid velocity. The liquid velocity is estimated from the impeller pumping capacity.	Molerus and Latzel (1987)
8	Extension of (2). The concept of a 'K' parameter, related to the Peclet number which incorporates the concepts of turbulent diffusion and anistropic turbulent motion. The standard deviation of the axial concentration profiles was related to this parameter to describe suspension quality.	Barresi and Baldi (1987a)

Table 2.4: Suspension models reported in literature continued

No.	Model description	Reference
9	(axial flow impeller) At the condition of complete suspension, the ratio of the characteristic velocity to the particle settling velocity is constant. The characteristic velocity of the liquid was based on actual shear rates in the boundary layer measured using electrodiffusion.	Wichterle (1988)
10	(three-phase) Established a sedimentation – dispersion model which includes the parameters of vessel and impeller diameter, sparger design, particle type and loading. LDA and mixing time were used to establish model parameters. Correlations for solid-liquid systems had a standard deviation ranging from 12-20 %.	Rewatkar *et al.* (1991)
11	Archimedes number is not a valid criterion defining any suspension regions in mixing vessels, thus (7) and (9) fail. In this model particle to vessel diameter ratio is also used and related to the Froude number, but new correlations are created for fine and large particles.	Rieger and Ditl (1994)
12	Mersmann *et al.* (1998) pursued a purely theoretical derivation of N_{js}. They considered a force and energy balance on the volume of a single particle and then extended to the entire volume using time-averaged velocities. A fluctuating velocity component was included. The model was tested against data of Zehner (1986), who determined N_{js} according to the 90 % layer criterion (previously criticised by Rieger and Ditl (1994)). Fair agreement was found with these data	Mersmann *et al.* (1998)
13	(two- and three-phase, radial impeller) Murugesan (2001) proposed a unified empirical correlation for the prediction of N_{js}. He followed a similar enquiry to Rieger and Dilt (1994), with a basis from Navier-Stokes equations and further dimensional analysis. He examined 1212 data points and found a RMS error of 7.3 % with a maximum deviation of ± 18.2 %.	Murugesan (2001)

2.7.4 Conclusions

Indirect optical techniques for the analysis of suspension quality are only applicable at low volume fractions of solids (< 3 wt. %). However, the axial profiles (Shamlou and Koutsakos, 1989) are of value for comparison with higher concentration experiments as in this study. The examination of cloud height has found agreement with the critical point of suspension when examining greater than 10 wt. % solids. However, the interface is not always clearly defined, as was experienced in this study. Moreover, even if the interface is easily distinguishable there is still a lack of information concerning the distribution of particles in the reactor.

Manual conductivity probing shows potential as an accurate means for determining local solids concentration. However, it is invasive, disrupting the tank flow and is fairly tedious.

Theoretical suspension models have progressed in accounting for the forces on a particle and the possible mechanisms of lift-off in a turbulent field, as well as the validation of models with experimental data. However, they are primarily concerned with N_{js}, which describes little about particle distribution within the vessel. Modeling or describing incomplete suspension has not been attempted. Most models have been criticized as geometry specific. More general models are typified by a standard deviation of the order of 20 %. Information on axial and radial concentration profiles has been described as lacking (Rewatkar *et al.*, 1991). The provision of reliable data on particle distribution would aid model development and validation, and the development of a more complete understanding of the dynamics of mixing in stirred tanks.

2.8 Indirect Tomographic Methods Quantifying Suspension

The indirect measurement technologies of electrical resistance tomography (ERT) and magnetic resonance imaging (MRI) are considered in depth with regard to historical development, the measurement principle and chemical engineering applications.

2.8.1 Electrical Resistance Tomography

2.8.1.1 Introduction

Tomography comes from the Greek word 'tomos' meaning slice, and 'graph' as in image. The mathematical concept of tomography was first suggested early in the 19th century. A hundred years later, Radon, an Austrian mathematician, extended the

ideas to objects of arbitrary shapes (Deans, 1983, as cited by York, 2001). In the first half of the 20th century several independent researchers e.g. Bocage, Ziedes des Plantes, Grossman and Watson, suggested methods for imaging a plane using x-rays. In 1979 Godfrey Hounsfield and Allen Cormack (originally from the University of Cape Town) were jointly awarded the Nobel Prize in Medicine for their work on computed x-ray tomography.

Resistance imaging can be traced back to the 1920's when geophysicists inserted an array of metallic electrodes into the ground and injected a current to obtain a map of the sub-surface strata. This led to a more precise delineation of oil-bearing rock (Dickin and Wang, 1996). In 1978 the first papers on impedance imaging were introduced by Henderson and Webster (Breckon, 1990; Brown, 2001). This method was seen as a cheaper and simpler system than x-ray tomography. Since the 1990's the technologies of personal computing and sensor design have improved and research into industrial applications of tomography has gained popularity. This is especially true of electrical impedance tomography (EIT), where three relatively low frequency measurement modalities can be exploited to determine distributions of conductivity (resistance), permittivity (capacitance) and permeability (inductance) (York, 2001).

Electrical resistance tomography (ERT) is an imaging technique whereby a conductivity distribution is determined from a conducting system by placing electrodes on the system boundaries followed by injection and removal of current via pairs of electrodes. The remaining pairs of electrodes i.e. those not involved in current injection, measure voltage differences around the system boundary. The complete set of voltage measurements are translated into a conductivity distribution via an appropriate algorithm. With the assignment of colour and implementation of threshold conductivities, the conductivity distribution can be examined visually allowing interpretation of the species within the system boundaries.

In this review, the mechanism of ERT is discussed (Section 2.8.1.2 – 2.8.1.3), followed by the processes of calibration and reconstruction (Section 2.8.1.4 – 2.8.1.5), and the application to chemical engineering and multiphase environments (2.8.1.6 -2.8.1.10).

2.8.1.2 Measurement Principle and Data Processing

ERT systems are comprised of sensors or rings of electrodes, amplification and multiplexing equipment, signal processing, communications and a PC hosting control and data processing often with reconstruction, analysis and display algorithms (York, 2001), as illustrated in Figure 2.11.

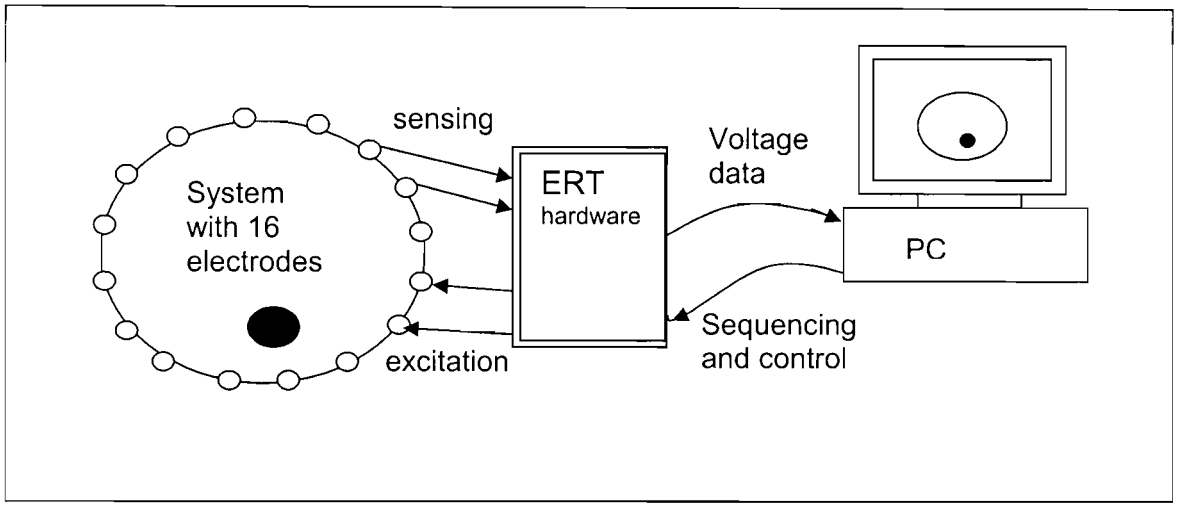


Figure 2.11: Electrical resistance tomography system

Electrodes are located in rings around the object, usually with 16 electrodes in chemical engineering applications (McKee *et al.*, 1995; Williams *et al.*, 1996; Mann *et al.*, 1997a; Ma *et al.*, 2001; Randall *et al.*, 2001). Typically, the electrodes are often copper or stainless steel, and can be intrusive in the vessel or, preferably, contoured to the system boundaries. Advances have been made in decreasing sensor size (Tapp and Williams, 2000; York, 2001). The variety in electrode configurations is increasing, potentially leading to more unique measurements in the system and thus more accurate image reconstruction. Wang *et al.* (1995) report from FEM results that the smaller the size of the electrode, the higher the sensitivity of the voltage measurement at the measurement electrodes and the higher the common voltage at the current – driven electrodes. A higher common voltage produces a poorer signal-to-noise ratio (Mann *et al.*, 1997a). Pairs of electrodes are usually excited with a sinusoidal current, typically in the order of tens of kilohertz (Dickin and Wang, 1996; Randall *et al.*, 2001; York, 2001). The differential voltages between the measuring electrode pairs are determined by analogue synchronous detection circuits or digital signal processing techniques. With sinusoidal current, care is needed to decrease noise associated with the 50 kHz main power supply. The impedance of the electrolytic cell or vessel has a capacitative and a resistive component, and thus alternating current (AC) measurement techniques have the potential to resolve both components. Direct current techniques have not generally been used due to electrolytic reactions occurring at the electrodes leading to a change in conductivity with time.

A common approach is to excite and detect current between pairs of adjacent electrodes; this increases sensitivity near the vessel walls but has poorer sensitivity in the centre of the system (York, 2001). Other strategies are possible e.g. to inject current between opposite electrodes or inject a specific spectrum of frequencies. Metal vessel walls can pose a problem due to current leakage but a system using a

common ground has been developed by Industrial Tomography Systems Ltd. (http://www.itoms.com). With all strategies a specific measuring sequence is needed to extract the maximum number of unique measurements. In summary, as illustrated in Figure 2.11, an injection-measurement strategy is implemented from the PC to the ERT hardware, where each pair of electrodes is excited while the remaining pairs record the potential difference. The complete voltage set is captured via multiplexers and relayed to the PC for reconstruction.

Measurement speed in ERT systems is usually reported as the time it takes to record a frame of data; where a frame contains all the voltage measurements from the specific measurement sequence. This is typically 104 data points obtained from the 16 electrodes (Barber *et al.*, 1983). Naturally for dynamic fluid systems faster measurement is required. Some speeds that have been reported are: Randall *et al.* (2001), 5 frames/s; Ma *et al.* (2001), 7 frames/s; Fangary *et al.* (1998), 10 frames/s; Mann *et al.* (1997a), 20 frames/s; Mann *et al.* (2001), 24 frames/s; Lucas *et al.* (1999), 100 frames/s; Wilkinson *et al.* (2005), 1000 frames/s. An impeller at 480 rpm is thus travelling at 8 $rev.s^{-1}$, thus with Wilkinson *et al.* (2005) system 125 frames would capture the conductivity variability from an impeller revolution accurately, although the actual blades cannot be distinguished in the tomogram.

2.8.1.3 Domain Discretisation

Prediction of the electrical field and consequently the boundary values of a system due to specific electrical excitation of materials in a system is referred to as the forward problem, and often realised through finite element modeling (York, 2001). The opposite process whereby the distribution of materials is determined from the boundary values is called the inverse problem and also particular to electrical resistance tomography. Data processing can be split into three distinct areas, namely the meshing of the domain, the forward solution and the inverse solution. It is important that the domain is imaged accurately since this is used in determining the unknown conductivities (Cheney *et al.*, 1990; Hua and Woo, 1990; Kolehmainen *et al.*, 1997; Molinari *et al.*, 2001a; Vauhkonen *et al.*, 2000). The forward and inverse solutions have a cyclic nature; this is best observed in the flow chart provided in Figure 2.12 (Naidoo, 2002).

Domain discretisation forms an integral part of the Finite Element Method (Naidoo, 2002). Two dimensional elements are usually triangular, or a quadrilateral or pentagon, while three dimensional elements are usually tetrahedral, quadrahedral or hexahedral. A mesh should exhibit the following geometric properties (Burnett, 1987; Cook *et al.*, 2002; George, 1991; Hua and Woo, 1990; Logan, 2002; Molinari *et al.*, 2001; Pepper and Heinrich, 1992; Rao, 1999; Zienkiewicz and Taylor, 2000):

i) Variation of the size between adjacent elements must be gradual if the size is not constant to avoid step changes in voltage.
ii) Areas with large changes in the field variable e.g. conductivity, must contain a higher density of elements to accurately model the changes.
iii) Obtuse angles in triangular elements must be avoided as they bias the field directionally.
iv) Discretisation of an irregular domain must be closely approximated by the boundary elements to improve accuracy of the solution.

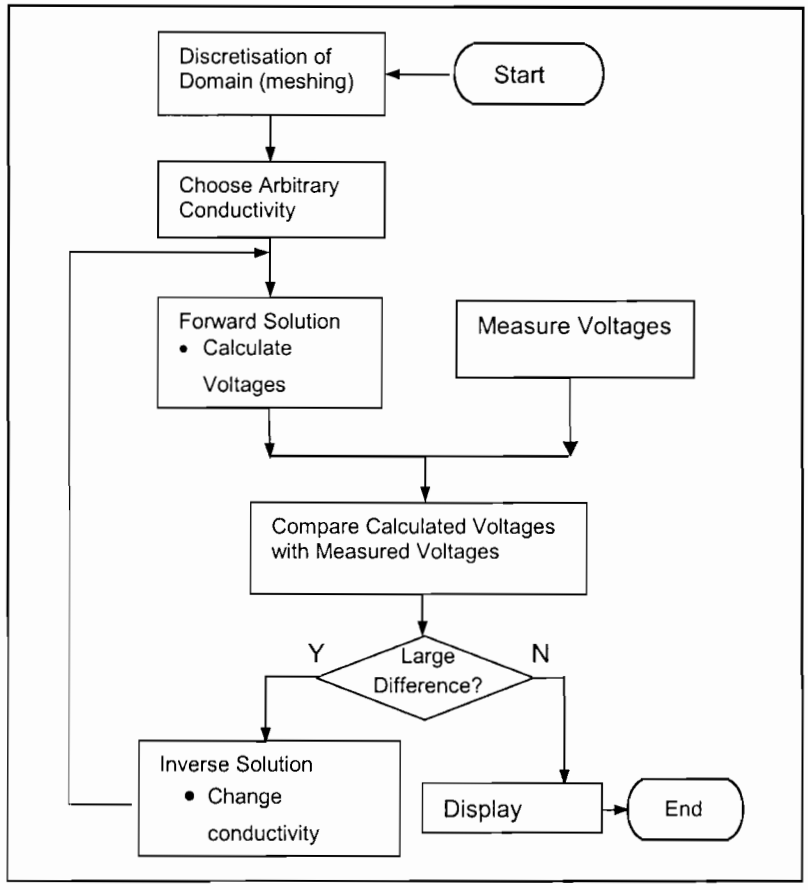


Figure 2.12: Flow chart depicting the typical iterative data processing procedure in electrical resistance tomography (Naidoo, 2002).

Furthermore, a mesh can be refined to improve the accuracy and decrease the error of the forward solution and to minimize the time required for the convergence of the solution. Naturally, use of large numbers of elements is recommended in modeling the domain to enhance the accuracy of the solution as shown in Figure 2.12.

However, the computational expense is increased exponentially (Molinari *et al.*, 2001a; Pepper and Heinrich, 1992) and a point is reached beyond which no further accuracy is gained (Figure 2.13). Indeed, divergence can result due to the increase

in numerical rounding errors with very large numbers of elements (Hua and Woo, 1990; Molinari *et al.*, 2001a; Rao, 1999).

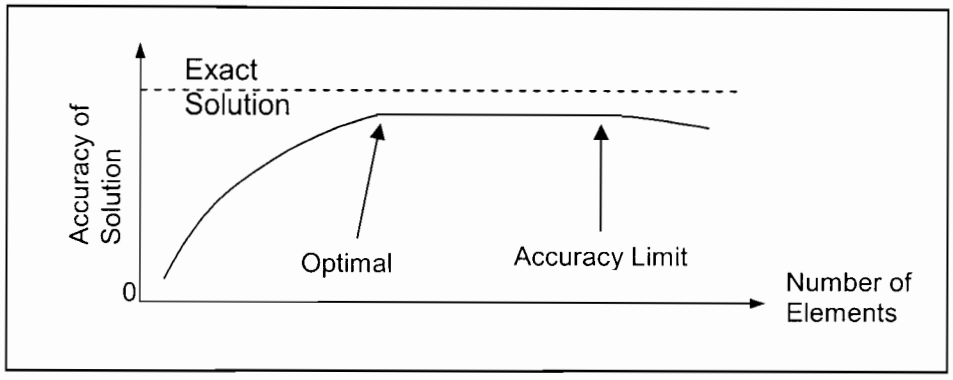


Figure 2.13: The effect of increasing the number elements of the domain mesh on the accuracy of the solution. An optimal point is shown where no further accuracy is achieved, and with further increase in elements accuracy can decrease as shown by 'Accuracy limit'. Adapted from Naidoo (2002).

2.8.1.4 Reconstruction Algorithms

Since the industrial relevance of tomography applications was recognised in the 1990's, a number of algorithms have been developed in the search for greater robustness, efficiency and speed. The Compensation Theorem, Double Constraint Method, Kalman Filter, Linear Back Projection, neural networks, Newton-Raphson algorithm and Perturbation Methods as well as statistical methods are some of the techniques which have been successfully implemented in ERT (Naidoo, 2002). Linear Back Projection and the Newton-Raphson method are reviewed as they are most commonly applied in chemical engineering environments (Fangary *et al.*, 1998; Lucas *et al.*, 1999; Ma *et al.*, 2001; Mann *et al.*, 1997a; Mann *et al.*, 2001; Randall *et al.*, 2001; Wilkinson *et al.*, 2005).

2.7.4.4.1 Linear Back Projection Algorithm

This method (Equation 2.7) is called linear back projection (LBP) since it back projects the potential difference between two equipotential lines on the surface to the resistivity value in the inside area between those two equipotential lines (Barber *et al.*, 1983).

$$\rho = \rho_0 \frac{(V_i - V_j)_{measured}}{(V_i - V_j)_{expected}} \tag{2.7}$$

where ρ is the resistance, V is the voltage and i and j are the two equipotential lines originating from the pair of excited electrodes.

This method averages the resistance over the entire image after all projection angles have been accounted. This averaged image is then filtered to reduce the inherent blurring in back projection (Hua and Woo, 1990). Breckon and Pidcock (1987) created a sensitivity matrix to enhance resolution and noted that the back projection between equipotential lines only uses the diagonal elements of the matrix. They thus suggested that that this method might be improved upon by utilising other sensitivity values since they are not negligible (Hua and Woo, 1990). Kotre (1989) followed up on these recommendations and developed a back projection algorithm that uses all sensitivity coefficients as weights. These sensitivities can be determined in the domain to form a pre-calculated element sensitivity matrix (Equation 2.8) (Randall *et al.*, 2001).

The sensitivity S_{ij}, for each element, k, is estimated as:

$$S_{ij}(k) = \frac{V_{ij}^{k} - V_{ij}^{\min}}{V_{ij}^{\max} - V_{ij}^{\min}} \tag{2.8}$$

where i and j are the excitation electrodes, V_{ij}^{min} and V_{ij}^{max} are the voltages calculated when all elements have the highest and lowest resistivity respectively, and V_{ij}^{k} is the voltage calculated when all elements have the lowest resistivity except the k^{th}, which has the highest resistivity (Randall *et al.*, 2001).

Combining Equations 2.7 and 2.8 allows the calculation of the relative resistivity for the k^{th} element in the imaginary domain, $\rho(k)$,

$$\rho(k) = \frac{\sum_{i=1}^{n-1}\sum_{j=i+1}^{n} \frac{V_{ij}^{m} - V_{ij}^{\min}}{V_{ij}^{\max} - V_{ij}^{\min}} S_{ij}(k)}{\sum_{i=1}^{n-1}\sum_{j=i+1}^{n} S_{ij}(k)} \tag{2.9}$$

where V_{ij}^{m} are the measured voltages. There is only one iteration as the reconstruction is performed rapidly in a single step using matrix-vector multiplication. Since the inverse of resistance is conductivity, the conductivity distribution in the plane can be realised. The object within the system boundaries can then be identified graphically through implementation of a colour conductivity scale, along with scale threshold manipulation.

LBP is favoured for its speed and simplicity, and is often used in clinical applications (Hua and Woo, 1990). It is used by some chemical engineering researchers (Mann *et al.,* 1995; Mann *et al.*, 2001; McKee *et al.*, 1995; Williams *et al.*, 1996; Wood and Jones, 2003) in multiphase environments, mostly spurred on by the commercial entity of Industrial Tomography Systems Ltd. Supporters of this algorithm commonly argue that less quantitative data are necessary for industrial applications, while reliability and the fast computation speed make it more attractive.

This algorithm is based on the assumptions that the object has a circular boundary with equally spaced electrodes and is two-dimensional (Hua and Woo, 1990). Furthermore, it assumes that the resistivity distribution to be reconstructed is close to the reference resistivity distribution. Images appear to be 'blocky' and are more qualitative in nature (as observed in Section 4.3). The application of this algorithm has been avoided in some studies (Binley *et al.*, 1996; Lucas *et al.*, 1999; Randall *et al.*, 2001; Wilkinson *et al.*, 2005) most likely due to the necessity of greater accuracy and discrimination required in multiphase studies. These include the monitoring of changes in slurry concentration to determine local velocity as well as the direct quantification of non-conducting species.

2.7.4.4.2 Newton-Raphson Algorithm

The reconstruction error can be directly obtained through comparison of the real resistivity distribution with the reconstructed one. However, since the real distribution is unknown, an indirect measure must be used. Thus the voltage responses of the assumed resistivity distribution can be related to those of the real distribution (Hua and Woo, 1990). This error that is desired to be minimised is called the objective function. Yorkey (1986) developed this algorithm where the objective function is the mean square difference between the measured and estimated voltage responses (Equation 2.10):

$$\Phi(\rho) = 0.5\,[f(\rho) - V_0]^T.[f(\rho) - V_0] \qquad (2.10)$$

where $\Phi(\rho)$ is the objective error function, $f(\rho)$ is the estimated boundary voltage from the resistivity distribution (ρ), V_0 is the measured boundary voltage and T is the transpose.

The resistivity distribution is optimised until the convergence criterion is reached, using:

$$\Delta\rho^k = -\,[f'(\rho^k)^T f'(\rho^k)]^{-1}[f'(\rho^k)]^T[f(\rho^k)-V_0] \qquad (2.11)$$

where $\rho^{k+1} = \rho^k + \Delta\rho^k$ (2.12)

Equations (2.11) and (2.12) form the basis of the Newton-Raphson algorithm. The performance of the Newton-Raphson method is well known for a quadratic function (Hua and Woo, 1990). However, in ERT the voltages are non-linear functions of the resistivity distributions instead of quadratic functions. Thus the search may result in a local minimum, depending on the initial guess of the resistivity distribution (Hua and Woo, 1990). This can be avoided through an appropriate guess, which could be supported through a conductivity probe measurement.

A Hessian matrix is formed by the product of the transposed Jacobian matrix and itself (the first expression on the right-hand side of Equation (2.11)). This matrix is often ill-conditioned and makes the inverse difficult to calculate, as well as being sensitive to measurement errors (Randall *et al.*, 2001). This ill-conditioning arises due to the non-linear behaviour of the resistivity distribution with respect to the measured boundary voltages e.g. changes in the centre elements produce minimal changes in the boundary elements. The Marquardt method (Marquardt, 1963) can be used to smooth a normalised Hessian matrix, and thus improve the conditioning. Another method of regularisation is adding a dampening factor to the solution to cancel out noisy errors; this is called Tikhonov regularisation (Polydorides and Lionheart, 2002).

Once there is sufficient agreement between the assumed and real resistivity distributions, the conductivity distribution can be calculated and graphically represented to facilitate object discrimination.

This algorithm has been used in multiphase environments with good effect e.g. porous media (Binley *et al.*, 1996), slurry flow in an inclined pipeline (Lucas *et al.*, 1999), foam studies (Cilliers e*t al.*, 2001) and further slurry conveyance studies (Wilkinson *et al.*, 2005).

The Newton-Raphson (N-R) algorithm requries more computation time than the LBP method, but it is more quantitative (Randall, 2001). Initially LBP was favoured for online visualisation. Through the advances in personal computing, online application and visualisation of the N-R algorithm is quite feasible (Wilkinson *et al.*, 2005).

2.8.1.5 Calibration

In any system there are geometric imperfections to be accounted for, as well as the requirement for a reference measurement set when altering the system. In modelling ERT the following imperfections can give rise to inaccuracy (Fransolet *et al.*, 2002; Kolehmainen *et al.*, 1997; Randall, 2005; Wilkinson, 2005):

i) Misalignment of electrode location relative to other electrodes
ii) Tolerances and gains from the electronic components
iii) Oxidising and fouling on the electrodes
iv) Temperature fluctuations within the system e.g. energy dissipation by the impeller

Calibration thus defines the reference measurement set and minimises errors through correction for imperfections. Calibration schemes in applications are not well published in ERT literature; however, for most systems an initial reference data set is subtracted from subsequent measurements. The most implemented scheme assumes that each electrode pair has a misaligned gain. Data are multiplied by a scalar factor to address this inaccuracy (Fransolet *et al.*, 2002). Ideally, electrodes should be modelled (Wilkinson, 2005) as separate units in the system. Some researchers have developed models for the contact impedance effects of the electrodes (Vauhkonen, 1997), although these are still lacking in a number of commercial applications.

Calibration procedures can be operated from the software on the PC, or be integrated into the ERT hardware through machine code. In both cases, multiple frames are collected to provide an average set of voltage measurements as the reference condition.

2.8.1.6 ERT and Process Applications

Mixing of multiphase systems of conducting and non-conducting phases are common to chemical engineering and process design. Thus ERT has been tested on a number of solid-fluid systems since the mid 1990's and has created a new area of exploration in the form of process visualisation and monitoring, enhanced design, validation of models and the determination of transport parameters. Early applications of electrical resistance tomography have been reviewed (Dickin and Wang, 1996; Beck *et al.*, 1998) and many were presented at the 1st World Congress on Industrial Process Tomography in 1999, as reported by York (2001). A brief review of some recent applications is provided, before focusing on the use of ERT in solid-liquid mixing and transport.

Binley *et al.* (1996) used ERT to analyse a dispersion system of a soil and dye core, allowing dispersion modelling. It was concluded that ERT was ideal for monitoring porous media flow problems. Slater *et al.* (2002) took this further with a 3D examination of solute transport (NaCl tracer) in a large tank of porous media (1.85 x 2.45 x 1.86 m). The ERT data was in agreement with the flow/transport modelling. Similarly Kemna *et al.* (2002) applied ERT to image and characterise subsurface solute transport in heterogenous unconfined aquifers, and found that ERT quantified

the variability of flow and transport parameters. Bolton *et al.* (2004) examined flow distribution in a fixed bed with ERT and CFD, and found the information from ERT suitable for CFD code confirmation. Cilliers *et al.* (2001) applied a DC – based ERT measurement system to a model system of non-conducting objects in a conducting liquid and to liquid foams of varying bubble size. The system resolved the position and size of the objects and identified coarse foam regions. Xie (2002) explored this further and related conductivity to foam structure and bubble size, with potential application to flotation processes in the minerals industry. Williams (2003) reported on the application of ERT to the minerals industry. He proposed how the future of mineral processing may be influenced by sensors and measurement technology with examples of ERT imaging of oil-water separation and swirling slurry flow in pipelines. Fransolet *et al.* (2005) explored the influence of fluid rheology on the gas flow pattern in a bubble column reactor using pressure probes and ERT. The results clearly showed that bubble size distributions were different in Newtonian and non-Newtonian fluids. Kaminoyama *et al.* (2005) applied ERT to visualise the dispersion states of liquid monomer and polymer droplets during suspension polymerisation and a method was found to maintain reaction rate stability. These processes illustrate the broad potential for ERT application. The specific application of ERT in characterising mixing processes to date is reviewed in Section 2.8.1.7.

2.8.1.7 ERT and Characterising Multiphase Systems

ERT has been successfully applied to multiphase environments achieving discrimination of slurries and gaseous slugs in pipelines, and visualisation of solid-liquid and gas-liquid mixing in stirred tanks. Furthermore, the potential online viewing of the state of a process is possible (Wilkinson *et al.*, 2005; Williams *et al.*, 1996).

Fangary *et al.* (1998) applied ERT to monitor the extent of solids deposited during slurry conveying in a horizontal pipe (5 mm monosize glass beads, ρ = 2950 kg.m^{-3} and 350 μm polydisperse angular sand, ρ = 2650 kg.m^{-3}, at 7 -14 wt. %, flow velocities up to 3.5 m.s^{-1}). A two-dimensional conductivity map was produced from a qualitative algorithm after excitation of 16 electrodes. These authors used Maxwell's (1892) equation (Equation 2.13) relating volume fraction to a non-conducting sphere to quantify the deposition. The ERT measured deposit height was found to be greater than the actual deposit height. This was suggested to relate to the packing factor of the deposit. Similarly Lucas *et al.* (1999) applied ERT to quantify inclined solid-liquid flows (4 mm spherical plastic beads, ρ = 1340.8 kg.m^{-3}, 16 vol. %) with application to the removal of cuttings in the oil industry. They also applied Maxwell's equation:

$$\alpha = \frac{2\sigma_w - 2\sigma_m}{\sigma_m + 2\sigma_w} \qquad (2.13)$$

where α is the local solids volume fraction, σ_m is the measured conductivity and σ_w is the conductivity of the continuous water, or pure liquid phase. Good agreement (within 10 %) was found between ERT and conductivity probe data as reported in Section 2.7.2.2.

More recently Ma *et al.* (2001) applied ERT to monitor gas-liquid flow in a horizontal pipeline (50 mm ID) and clearly characterised slug flow, along with developing a novel liquid-level detection system based on ERT.

Mann *et al.* (1997a) point out that process calculations of chemical reactions in stirred tanks often apply assumptions of perfect backmixing, leading to simplified evaluations of the reaction process e.g. components only change with time. However, when reaction rates are fast relative to internal mixing, spatial concentration gradients exist. These authors applied ERT to a 2.3 m^3 pilot scale stirred tank (8 levels of 16 electrodes, 1.5 m ID) using a qualitative LBP-based algorithm (400 spatial elements, resolution about 5 %) to image three case studies: a three-dimensional air-core vortex in an unbaffled tank, gas-liquid mixing with an impeller showing the effects of hold-up, and miscible fluids with a brine injection showing the dynamics of mixing in 3D after interpolating 2D images. In this manner internal mixing was monitored and phase discrimination was observed. Wang *et al.* (2000) used this experimental setup to distinguish gas-liquid mixing between water (1 cP) and a relatively viscous 0.05 % carbopol solution (100 cP) and to produce temporal mixing curves. Further brine injection was performed by Mann *et al.* (2001) using the same system to monitor dynamic unsteady mixing where it was suggested validation of CFD code was possible. Mixing behind baffles was found to be in the order of three times slower than the bulk fluid. These authors also examined solid-liquid mixing in the form of suspension and dynamic addition of solids (cylindrical polypropylene particles, 3.5 wt %). Average axial solids concentration profiles were produced which exhibited a diagonal shape (Figure 2.14) plotting dimensionless height as a function of concentration, and increased suspension was observed with increasing agitation rate.

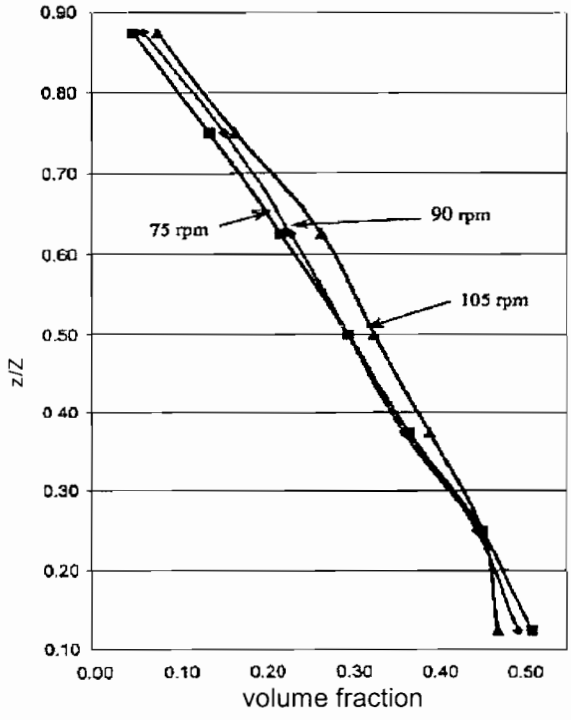


Figure 2.14: Axial concentration profile of 3.5 wt. % beads (Mann *et al.*, 2001).

2.8.1.8 ERT and Solid-Liquid Mixing Models

McKee *et al.* (1995) argue that the limited knowledge of the fundamentals involved in mixing processes is mainly related to the lack of reliable *in situ* measurement instrumentation. The need for tomographic technology to aid in the development of reliable scale-up correlations for slurry mixing processes is therefore required. These authors applied ERT, a conductivity probe and positron emission tomography (PET) to examine slurry mixing. Barresi and Baldi (1987a) proposed that the extent of homogeneity could be determined by plotting the standard deviation of the concentration profiles as a function of $(P_0^{1/3}ND/u_t)/X^{0.13}$, where P_0 is the power number, N is the impeller speed, u_t is the terminal settling velocity and X is the percentage mass ratio of solids to liquid. The term $P_0^{1/3}ND/u_t$ is analogous to a Peclet number, although also accounting for anisotropic turbulent motion. McKee *et al.* (1995) expanded this concept to determine the variance of the reconstructed tank conductivities, σ^2:

$$\sigma^2 = \frac{1}{(n-1)}\sum_{i=1}^{n}(C_{xz} - C_M)^2 \qquad (2.14)$$

where C_{xz} is the local solid concentration at x position and z height, C_M is the mean bulk concentration and n is the number of sampling positions. This variance is

related to radial uniformity in the mixing plane and thus each 2D image can be quantified and used for control decision making.

Equation (2.14) was extended into the form of a mixing index in the *z* plane:

$$MI_z = \frac{1}{C_M}\left(\frac{1}{(n-1)}\sum_{i=1}^{n}(C_{xz} - C_M)^2\right)^{1/2} \qquad (2.15)$$

This can also be interpreted as a relative standard deviation so when homogeneity increases, the mixing index tends towards zero. Data were initially obtained from conductivity probe measurements (Section 2.7.2.2) to produce the mixing index. The mixing index was plotted against agitation rate for the 425-500 μm fraction, showing its decrease with increasing speed, although at the critical impeller speed N_{js} (428 rpm) there was a slight increase in MI_z indicating a decrease in homogeneity. These data are shown in Figure 2.15. The authors reported that 380 rpm was the point of maximum homogeneity.

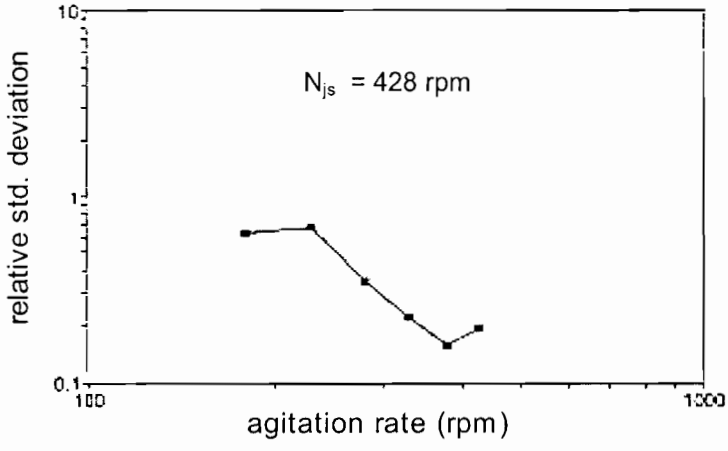


Figure 2.15: Variation of the relative standard deviation with agitation rate. 425 – 500 μm fraction, 15 % wt, pitched blade impeller (T/2) at clearance of T/4, T = H = 305 mm. (McKee *et al.*, 1995)

The ERT data from the experiments of McKee *et al.* (1995) were further reported by Williams *et al.* (1996). The data were reconstructed using a quantitative algorithm based on a FEM solution to the forward problem. A pitched blade and A310 impeller were used in the stirred tank described in Section 2.7.2.2. These authors noted that the metal impellers caused a discontinuity in the resistivity profile, appearing as a depressed zone. Thus for the lower two planes the outer 48 pixels from the finite element mesh were used to calculate the average resistivity in the xy plane. Williams *et al.* (1996) do not produce radial concentration gradients. They state that in many pilot-scale studies these are assumed to be insignificant, although noting this is questionable for polydisperse mixtures. This is also questionable for high solids concentrations.

Axial concentration profiles produced from the ERT data exhibited the same maximum in concentration in the plane above the impeller at higher agitation rates (Figure 2.16), similarly to the conductivity probe data (McKee *et al.*, 1995) in Section 2.7.2.2. The A310 exhibited poorer mixing ability, although being more energy efficient. It was also found that more power is required to achieve the same degree of homogeneity for the coarser fractions. At N_{js}, there was a greater homogeneity for the smaller fractions through examining mixing indices.

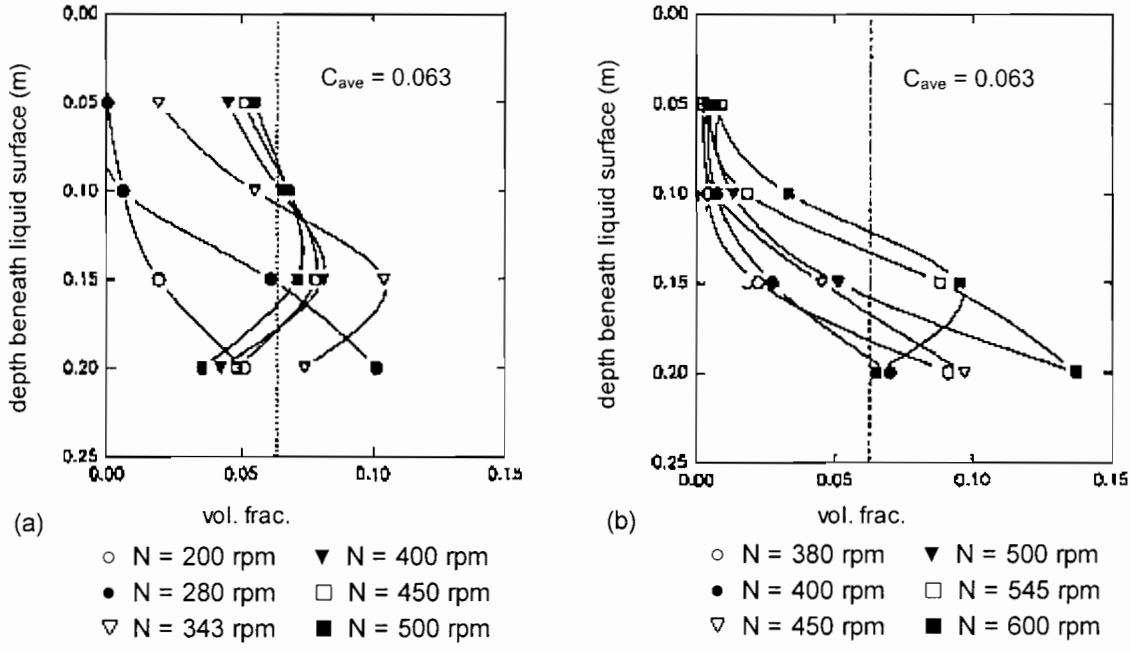


Figure 2.16: The effect of impeller type on axial concentration for a pitched-blade impeller (a), and an A310 (b) for 150-210 μm quartzite in water. Geometry: C = T/3, D =T/2, B = T/12, H = T = 305 mm. (Williams *et al.*, 1996)

Further analysis of mixing was performed with the ERT system by monitoring the upper plane of electrodes (5 cm below liquid surface) and altering the agitation rate with the 150-210 μm fraction. It was observed that operating at the highest agitation rate did not result in the highest particle concentration in this plane. Williams *et al.* (1996) suggested a change in fluid flow patterns occurred at the higher speed.

Further studies have also related ERT to fluid dynamics. Mann *et al.* (1997b) further developed the Network-of-Zones (NZ) model to provide estimates for empirical turbulence parameters. This model is comprised of 8000 zones describing the stirred tank and constitutes a simplified modelling basis without the need to resort to Navier-Stokes equations (Mann *et al.*, 1997b). It was anticipated that this model be used in unison with ERT to describe gas-liquid mixing. More recently, Zahradník *et al.* (2001) applied the NZ model to the analysis of mixing and mass transfer in industrial bioreactors.

2.8.1.9 Velocity Measurement from ERT

As mentioned in Section 2.7.2.2, Lucas *et al.* (1999) used a local conductivity probe in an inclined pipeline to calculate velocity of the fluid by cross correlating the outputs from two sensors on the probe. The probe position was altered within the pipeline cross section to produce a velocity profile. ERT measurements were conducted on two planes of 16 electrodes (50 mm apart) which were contoured with the pipe wall, and cross correlation between planes allowed the velocity determination. A comparison of the ERT and probe velocity profiles resulted in good qualitative agreement. Furthermore, the ERT-estimated average velocity agreed with the measured values within 8 % (Table 2.3).

Table 2.5: Comparison of measured flow variables with those obtained from ERT (Lucas *et al.*, 1999)

Flow variable	Measured value	ERT estimate
Volume fraction of solid	0.19	0.17
Slurry velocity ($m.s^{-1}$)	0.12	0.11
Flow rate ($m^3.h^{-1}$)	0.41	0.34

Bolton *et al.* (2004) introduced a high conductivity tracer into a packed bed (1 m high, 0.914 m ID, 3 and 10 mm alumina spheres) with 8 planes of 16 electrodes. The time was recorded at which high conductivity was detected in each plane allowing the calculation of velocity. Flow in this annular reactor had a radial and axial component, thus pixels were correlated within the plane for radial velocity determination and in adjacent planes for axial velocity determination. These results agreed qualitatively with those obtained using a CFD simulation, except for the lower two planes where velocity determination was hampered.

2.8.1.10 Three-Dimensional ERT

In most 3D graphical representations of vessels, 2D slices have been interpolated to create visualisation of volume e.g. Mann *et al.*, 1997a; Mann *et al.*, 2001; Bolton *et al.*, 2004. True 3D tomography involves 3D modelling of the forward problem and 3D data collection (Polydorides and Lionheart, 2002) i.e. interplanar current injection and voltage detection which results in more complex reconstruction algorithms. Furthermore, most 2D algorithms assume current travels only in the horizontal plane between electrodes, while in reality the electric field also bends in the axial direction. An endeavour has been made in the form of the Electrical Impedance and Diffuse Optical Reconstruction Software (EIDORS) project to develop freely available software to reconstruct electrical or optical material properties from boundary measurements (Polydorides and Lionheart, 2002). This software has 2D and 3D

Matlab™ functions available for application and compilation, although extensive testing has yet to be performed.

Mesh generation utilities are not included in the EIDORS toolkit, however, some mesh generators that are freely available (e.g. Netgen) allow export of meshes in a Matlab™ friendly format. In tank experiments containing rings of electrodes some fitting of the model is required for mesh refinement and estimation of the electrode contact impedances. This preserves the accuracy of the forward solution in matching the data (Polydorides and Lionheart, 2002). The global admittance or system matrix is largely computed via the **bld_master** function based on the technique of Vavasis (1996). The current pattern is modelled using the **set_3d_currents** function which generates current patterns based on opposite or adjacent pairs of electrodes, while **forward_solver** performs the main forward calculations using either the Cholesky method, LU decomposition or preconditioned conjugate gradients. Polydorides and Lionheart (2002) suggest that either a generalised inverse of the Jacobian Matrix can be inverted using the N-R algorithm, or a linearised form of the inverse problem can be created followed by a Tikhonov type regularisation to obtain a step solution within the N-R algorithm. EIDORS employs the latter, which is similar to the method proposed by Levenberg (1944) and Marquardt (1963). The inverse computations are performed by the **inv_sol** function which solves the non-linear inverse problem using the method from Molinari *et al.* (2001b). The regularisation matrices are provided by the **iso_f_smooth** and **iso_s_smooth** Gaussian functions, and visualisation of the solution in the *x*, *y* and *z* planes is possible through the **slicer_plot** function.

Polydorides and Lionheart (2002) set up a model of 8 electrodes per plane on a tank with two iron rods (30 x 35 mm) positioned close to the vessel wall. Due to hardware limitations only 104 measurements from horizontally adjacent electrode pairs were gathered. The spatial resolution of the tomograms was described as poor; with the shortage of an adequate set of measurements suggested to be responsible for the lack of resolution.

2.8.1.11 Limitations of ERT Measurement

Although temporal resolution is currently reported at 1000 data frames per second (Wilkinson *et al.*, 2005), spatial resolution is limited to approximately 5 % of the vessel diameter (Randall, 2005; Wilkinson, 2005). Disturbances in the electromagnetic field above and below the electrode affect local conductivity measurement (Randall, 2005). Modelling of the 3D field behaviour is therefore necessary, although many reported studies do not account for this in their software. Accurate calibration is limited in many studies through failure to model electrode impedance effects (Wilkinson, 2005). Characteristics and limitations of ERT hardware and software used in this study are reviewed in Chapter 4.

2.8.1.12 Conclusions

Electrical resistance tomography has the ability to image dynamic industrial processes and characterise flow properties in conducting systems. Considerable insight can be gained from applying ERT to stirred tank mixing processes, and it appears well suited for analysing mixing and suspension in slurry reactors. Although spatial resolution is limited to approximately 5 % of the vessel diameter, quantitative information can still be gained, and the excellent temporal resolution allows changes of state to be realistically imaged. ERT presents an opportunity to obtain axial and radial concentration gradients in the stirred tank, thus providing information beyond the concept of a critical suspension speed. Particle distribution in the stirred tank can thus be examined and related to fundamental heat and mass transfer processes, including the local effect on the microbial population. Further information can be potentially obtained from other phases of interest e.g. gaseous and microbial, which have proved difficult with conventional examination. There is also the potential to relate particle distribution to the flow pattern of a specific impeller type, while other affecting parameters e.g. particle size, solids loading and agitation rate can be analysed. Lastly, it is a valuable tool for model confirmation e.g. CFD codes, as well as potentially providing data for the creation of new models.

2.8.2 Nuclear Magnetic Resonance Imaging

2.8.2.1 Introduction

Felix Bloch (Stanford University) and Edward Purcell (Harvard University) first observed nuclear magnetic resonance (NMR) in the condensed phases of liquid and solids in 1946 and were awarded the Nobel Prize for Physics in 1952. Since this discovery the theory of magnetic resonance has been well documented (Callaghan, 1993). In its simplest form an NMR spectrophotometer consists of a magnet, a radiation source and a detector system, which measures the absorption of the radiation. The sample is placed in the magnetic field of the magnet. In order to achieve this absorption, the nuclei of the atoms must have a magnetic moment. In this case the nuclei behave like elementary, small magnets, although not every atomic nucleus has this property (Valk *et al.,* 1985). Magnetic resonance is nucleus and molecule specific with any nucleus of nonzero nucleur spin potentially applicable, but in most chemical engineering applications ^{1}H (referred to as "proton" observation), ^{13}C, ^{23}Na, ^{31}P, ^{19}F and ^{2}H are most commonly used (Gladden, 2003).

The nuclei of atoms with a magnetic moment can be regarded as a small top which spins around its axis. The charge of the nucleus also rotates thereby generating a rotating current which can be regarded as a small magnet. When the nuclei are placed in a strong magnetic field the elementary magnets align along the field

direction with only a number of discrete orientations possible. Protons only have two possible orientations, parallel and antiparallel (Valk *et al.,* 1985). The parallel position has the lowest potential energy. In a magnetic field, B_0, there is a constant energy difference between the parallel and the antiparallel orientations.

The radiation source induces transitions between these orientations and the frequency of this radiation field, ω_0, needs to correspond to the energy difference between orientations, ΔE. According to quantum mechanics:

$$\Delta E = h\,\omega_0 \qquad (2.16)$$

where h is the Planck constant, 6.67×10^{-34} J.s^{-1}.

This radiation can also be applied in specific pulse sequences where a great number of oscillations are possible.

2.8.2.2 Imaging with Magnetic Resonance

As mentioned earlier, by exposing the system to electromagnetic energy of appropriate frequency, a resonant absorption occurs between nuclear spin energy levels. By applying another magnetic field that varies linearly in space, the resonance frequency becomes dependent on spatial position, and with application of field gradients in one, two and three dimensions the corresponding images are obtainable typically with a 10 – 200 μm spatial resolution (Gladden, 2003). After the radio-frequency (r.f.) excitation, the return of the spin system to equilibrium is followed as a function of time. The data are directly Fourier-transformed to give the frequency spectrum or spatial domain image, with no algorithm for image reconstruction required. The rate at which spin systems return to thermal equilibrium following the r.f. excitations is characterised by its nuclear spin relaxation parameters – the spin-lattice relaxation (T_1) and the spin-spin relaxation (T_2) time constants (Gladden, 2003). With interpretation of the acquired image and setting up NMR experiments it is also important to consider contrasting effects, and this will be expanded upon in Section 2.8.2.3 – 5.

2.8.2.3 Spin-Lattice Relaxation

When the NMR sample in Earth's magnetic field is suddenly changed to the intense field B_0 of the spectrometer, typically 2-10 T (Gladden, 2003), the process of building up the appropriate Boltzmann population distribution can be quite slow. Initially, in the Earth's field, the population difference of nuclei between the upper and lower energy levels would be negligible. With the application of B_0, the nuclear spins are

'hot' (essentially equal populations) and they cool down by transferring some magnetic energy to their surroundings, a process called relaxation (Freeman, 1988). If the variation of the population difference was plotted as a function of time, there would be an exponential curve starting near zero and rising asymptotically towards the Bolzmann equilibrium condition. It would have a time constant T_1, the spin-lattice relaxation time, where 'lattice' is used as a general term for the nuclear environment.

With high resolution NMR, the delay ensuing between insertion of the sample and detection of the first free induction signal is seldom of concern. Spin-lattice relaxation is practiced in a more fundamental manner. The Boltzmann equilibrium nuclear magnetization is usually represented by M_0. Any deviation of the actual longitudinal magnetization, M_Z, away from M_0, is followed by an exponential recovery allowing T_1 to be defined phenomenologically as a longitudinal relaxation time (Freeman, 1988):

$$(M_z - M_0)_t = (M_z - M_0)_0 \exp(-t/T_1) \qquad (2.17)$$

2.8.2.4 Spin-Spin Relaxation

In initiating a NMR experiment all the spins are set to precess in phase at time zero through application of a radio-frequency pulse. This phase coherence is gradually lost with a time constant called the spin-spin relaxation time, T_2. In order to preserve this in practice, a perfectly stable spectrometer and a perfectly uniform magnetic field, B_0, would be necessary (Freeman, 1988). This relaxation time can thus be defined as the decay constant of transverse nuclear magnetisation, M_Y, neglecting instrumental aberrations.

It is important to distinguish between T_2 and the lifetime of the spins in a given excited energy state, T_1. In high resolution NMR of the liquid phase, often the same physical mechanisms determine both T_1 and T_2, so they are equal, although cases arise where T_2 is less than T_1. These cases can be defined by a phase memory time, accepting that certain interactions between spins may destroy their phase coherence faster that the spin-state lifetime (T_1).

2.8.2.5 Contrast Effects

There is great versatility in using NMR; as well as giving images of the concentration of nuclear spins, or molecular species, within any given image voxel, the relaxation characteristics of the sample and even the local transport properties can be spatially resolved (Gladden, 1995). However, it is important to remember that the same relaxation and transport effects can also influence the pixel intensities in a spin density image. If these effects are ignored, the image will no longer be quantitative and the image will contain "contrast".

Contrast effects may be chemical or physical in nature, with chemical contrasting allowing great resolution in the ability to focus upon a single molecular species in a multicomponent mixture due to the distinct molecular environment associated with each hydrogen atom (Gladden, 1995). Physical contrast parameters can arise if the timings in the r.f. pulse sequence are not absorbed by part of the spin population and thus the NMR technique becomes less quantitative. This could occur when the pulse sequence repetition rate is too fast, not allowing the system to get to equilibrium between successive pulse sequences and forming a T_1 contrast.

2.8.2.6 The Limitations of NMR

NMR is unable to study ferromagnetic materials and samples containing significant amounts of paramagnetic species (Gladden, 1995). Furthermore, temporal resolution can be limited with some species due to T_1 effects, although spatial resolution is generally excellent (40-100 μm). Studies are also limited in their size, as they need to fit within the r.f. probe which is inside the superconducting magnet. This is typically limited to 2.5 to 30 cm in diameter, although "inside out" experiments where the sample is outside of the magnet are possible. It is also an expensive piece of equipment with regard to initial investment and maintenance.

2.8.2.7 Nuclear magnetic Resonance and Chemical Engineering

Amundson (1988) identified nuclear magnetic resonance (NMR) spectroscopy as a potentially useful tool for studying catalytic structure and surface chemistry, noting the existence of magnetic resonance imaging, especially used in medical applications at that time. Many industrial and academic research laboratories now have NMR fully integrated in their research programmes and use MR spectroscopy, diffusion, dispersion, and flow velocity measurements directly in applications (Gladden, 2003). However Gladden (2003) notes that MR is still relatively underused in three distinct areas: characterising fluid flows; visualising structure-hydrodynamics relationships in process units; and the integrated use of MR with theoretical modelling and numerical simulation studies. Relating MRI to other tomographic technologies is also an area needing study, whereby information can analysed or combined to aid interpretation of physical processes.

Mantle and Sederman (2003) undertook a comprehensive review of MRI in chemical process and reaction engineering and state that nuclear MRI and spectroscopy is still the single most powerful tool available to physical scientists, medical practitioners, engineers, and biologists. Its frequency of use stems from its non-invasive nature, being a chemically specific, motion sensitive technique that allows the quantitative

structural, chemical and dynamical characterisation of many opaque systems (Mantle and Sederman, 2003).

Examples of such investigations include the study of granular flows while determining velocity and density measurements (Altobelli *et al.*, 1992), novel analysis of packed beds and characterising the fluid flow around the packing (Tallerek *et al.*, 1996; Sederman *et al.*, 1998; Johns *et al.*, 2000; Gladden *et al.*, 2003; Lim *et al.*, 2004) as well as the mixing of solids in gas-fluidised beds (Fennel *et al.*, 2005), examining turbulent complex flows in pipe structures (Elkins *et al.*, 2004; Sederman *et al.*, 2004), rheological characterisation of suspensions in pipes (McCarthy *et al.*, 1998), studying biofilms (Beuling, 1998) and metal deposition in bioreactors (Nott, 2001), flow in heat exchangers (Sun and Hall, 2001), and analysing the dissolving of particulate solids (Johns and Gladden, 2003). By way of these examples it is apparent that MRI is quite capable of examining mixing and transport phenomena in one and two phase environments.

2.8.2.8 Determining Velocity Components with MRI in Single Phase Systems

Obtaining the complete velocity components of a fluid in three dimensions has recently been achieved in single phase systems. Elkins *et al.* (2004) examined velocity vectors in heat transfer equipment using a 0.5 % Gadolinium solution and a good agreement was found with particle image velocimetry (PIV) with regards to magnitude and direction. Sederman *et al.* (2004) obtained velocity images in a cylindrical pipe with water at Reynolds numbers of up to 5000, showing quite clearly the onset of turbulence and orthogonal velocity components. Acceleration, or the convective derivative, was also determined, while the local velocity fluctuations were found to be small relative to the local velocities. This confirmed that data acquisition rates were rapid enough to capture real time images. Moser *et al.* (2003) examined flow in a partitioned pipe mixer and determined three-dimensional velocity components, clearly showing the velocity effect from the moving impeller, while Barnes *et al.* (2006) extruded polydimethylsiloxane (a soft solid) and a stiff biscuit dough (a paste) with a PEEK (polyethylene ethylene ketone) screw and determined radial and axial velocity profiles within the ram extruder.

Gladden (2003) reports that there is a range of velocities which are able to be measured, from ionic drift velocities of 10^{-3} mm.s^{-1} to pipe flows of about 1 m.s^{-1}. Furthermore, molecular diffusion coefficients greater than 10^{-14} m^2.s^{-1} can also be obtained.

2.8.2.9 MRI and Solid-Liquid Systems

MRI has a reasonably long history (10 -15 years) with the study of flowing particulate systems and is an ongoing area of research (Mantle and Sederman, 2003). One of the earliest MRI studies of particulate suspensions involved the exploitation of T_2 relaxation weighted imaging to investigate the casting process of an Al_2O_3 suspension in 30 wt. % water into a plaster of Paris mould (Hayashi *et al.*, 1988, as cited by Mantle and Sederman, 2003).

More recent experiments include Sommier *et al.* (2001) who used MRI to study the mixing process of free flowing sugar beads and poppy seeds in a 2.1 litre Turbula® mixer, with some beads doped in organic oil to increase sensitivity. A Turbula® mixer is a commercial device currently used in development laboratories. It operates by means of a three-dimensional tumbling motion which simulates manual shaking. The filled container was placed in a 56 mm diameter probe (Bruker mini 036) and imaged at 100 MHz with a Bruker DSX100 spectrometer using a 2.35 T superconducting magnet. The degree of mixing was examined through observing the disappearance of the sugar beads with increasing revolutions. Horizontal and vertical profiles of the mixer were produced which allowed analysis of the degree of segregation. Resolution was 938 μm, with acquisition times of 20 minutes for the beads and 5 minutes for the poppy seeds respectively. These experiments were performed using selective excitations and two-dimensional Fourier imaging (spin-warp) method, as reported by Callaghan (1991).

Lee *et al.* (2001) characterised the degree of mixing in a two phase (polyalkylene glycol of density 1.1 $g.cm^{-3}$ and polymethyl methacryalate (PMMA) spheres of 200 μm and similar density) batch system with MRI. The 875 ml mixing bowl was equipped with an 11 cm high, 8.5 cm wide paddle. Three particle loadings of 10, 20 and 30 % by weight were tested and related to the number of revolutions of the paddle through imaging, while standard deviations and the coefficient of variation showed the sequence of mixing. The MR spin echo images were obtained using a 0.6 T Oxford magnet at a proton frequency of 25.9 MHz. Resolution was 1 mm per voxel with a slice thickness of 2 mm. The number of revolutions was of interest in this study, rather than the impeller speed (6-7 rpm), as homogeneity with controlled agitation was the objective in this food science related study. Furthermore, it was found that the number of impeller revolutions required to achieve homogeneity was not a significant function of the particle loading.

Similarly Rao *et al.* (2002) also examined the number of revolutions in a two-phase mixture with MRI by examining batch sedimentation and viscous re-suspension in a Couette cell. PMMA particles of 794 μm diameter (denser than fluid) were suspended

in a 96 % glycerol solution, with the results agreeing qualitatively well with a numerical simulation and clearly showing particle and fluid rich regions.

The application of MRI to a baffled stirred tank reactor has not been reported, however, these mixing studies reviewed indicate potential in this regard.

2.8.2.10 Conclusions

Nuclear magnetic resonance imaging has gained considerable ground in the field of chemical engineering after its earlier origins in medical scanning. Mixing and transport phenomena on micro and macro scales can now be examined, and theoretical models which have remained untouched for lack of experiments are now open to investigation. Spatial resolution is excellent, although temporal resolution does not match the speed of ERT. MRI experiments have been conducted previously, analyzing mixing in two-phase systems, and show potential in this regard for the stirred tank environment. However, there is a constraint with the scale of the experiment. The potential high degree of resolution should provide valuable information concerning axial and radial particle distribution in a stirred tank, as well as potentially providing support for the data obtained from applying ERT.

2.9 Summary of Mixing and Suspension Knowledge for Stirred Tanks

It is useful at this point to summarise the status of knowledge and key aspects of mixing and suspension in multiphase stirred tank systems. This is provided through considering axial and radial concentration profiles, followed by suspension and homogeneity. Measurement technologies reviewed are summarised in Table 2.6.

2.9.1 Axial concentration profiles

- Higher particulate concentrations are observed at the tank bottom, with increasing agitation rate decreasing these concentrations.
- At higher agitation rates near N_{js}, a local peak in concentration is often observed in the impeller plane.
- Smaller particles are suspended higher in the tank and produce more consistent suspensions.
- Dilute concentrations of solids (< 2.0 vol. %) produce normalised axial concentration profiles that are independent of concentration.
- A rapid decrease in solids concentration can be present on approaching the liquid surface. This produces a clear interface where the cloud height is visible.
- Previous studies have been unable to determine accurately the solids concentration very close to the tank bottom.

- Axial profiles cannot be described by a simple dispersion model with a constant turbulent diffusion coefficient (Barresi and Baldi, 1987a). Macroscopic turbulence influences particle distribution.
- Sampling from the tank wall is not representative of particle concentration in that horizontal plane.
- Axial profiles have been produced from 10 data points (Barresi and Baldi, 1987a); 9 data points (Nasr-El-Din *et al.*, 1996); 7 data points (Mann *et al.*, 2001); 4 data points (McKee *et al.*, 1995; Williams *et al.*, 1996).

2.9.2 Radial concentration profiles

- Studies reporting radial concentration profiles are limited, especially for axial flow impellers.
- Studies often assume stirred tanks are radially homogenous (Williams *et al.*, 1996), or have been conducted at low solids concentrations which limit radial gradients (Barresi and Baldi, 1987a).
- From conductivity probing at three radial positions at solids volume fractions of 0.1 to 0.3, Nasr-El-Din *et al.* (1996) observed concentration increasing on approaching the tank wall above the Rushton turbine for quartzite particles greater than 82 μm. The 82 μm particles exhibited radial uniformity.
- Barresi and Baldi (1987a) observed solids concentration in the radial plane to be constant or slightly increasing above the Rushton impeller using sample withdrawal from three radial positions. Higher concentration gradients were observed below the impeller which decreased in concentration on approaching the tank wall.
- Radial concentration data is lacking for just above and below the impeller, as well as at the tank bottom.
- Radial concentration profiles have usually been produced from three radial positions (Barresi and Baldi, 1987a; Nasr-El-Din *et al.*, 1996).

2.9.3 Particle Suspension and Homogeneity

- Increasing agitation rate and impeller size or decreasing particle density and diameter, produce more homogenous mixtures.
- However, increasing the agitation rate high above N_{js} can lead to a decrease in homogeneity (Shamlou and Koutsakos, 1989). McKee *et al.* (1995) observed a slight decrease in overall homogeneity at N_{js} as defined by their mixing index.
- At incomplete suspension, particles are reported to form fillets at the tank corners and baffles. This can be eliminated with low clearance impellers. Detailed information is lacking concerning particle distribution near the tank bottom. The formation of a cone of solids can be present under the impeller zone for the pitched blade impeller.
- Concepts to describe particle homogeneity include the standard deviation of the concentration profile (Barresi and Baldi, 1987a) and mixing indices in the

horizontal plane (McKee *et al*, 1995), which can be averaged over the reactor height (Williams *et al.*, 1996).

- High degrees of homogeneity have been observed at mid height in vessels while operating with incomplete suspension (Baldi *et al.*, 1981).
- In the study of Shamlou and Koutsakos (1989), particle-particle effects appeared to influence suspension quality above 4 wt. % in concentration.
- Studies examining reactor scale effects upon axial and radial concentration profiles are lacking.

2.9.4 Summary of Methodologies Quantifying Suspension

Reviewed technologies which can quantify particle suspension are presented in Table 2.6.

Table 2.6: Summary of methodologies capable of quantifying solids suspension

Method	Advantages	Limitations	Reference
Visual	Simple and accurate, although element of subjectivity in determining N_{js}. Non-invasive	Can only be applied to low volume fractions of solids (<10 %) and clear suspension solutions.	Zwietering (1958) Nienow (1968)
Direct sampling	Not limited to opacity or solids concentration.	Affected by withdrawal velocity, sample tube geometry and relative position to the flow field. Tedious and invasive.	Barresi and Baldi (1987a) Nasr-El-Din *et al.* (1985,1996)
Optical (laser, LED)	Can be accurately calibrated allowing multiple sampling positions. Non-invasive	Limited to low solid concentrations (4 wt. %) due to opacity limitations.	Shamlou and Koutsakos (1989) Fajner *et al.* (1985)
Cloud height	Can determine N_{js} non-invasively without complicated equipment.	Often interface cannot be observed at N_{js}. Reliant on clear suspension media.	Einenkel and Mersmann (1977) Zehner and Tebel (1984) Bujalski *et al.* (1999)
Conductivity Probe	Conductivity can be related to volume fraction through the Maxwell relation, with accurate determination.	Invasive and tedious. Also disrupts flow field	Nasr-El-Din *et al.* (1996) McKee *et al.* (1995) Lucas *et al.* (1999)
ERT	Similar to conductivity probe, but non-invasive. Large amounts of information capture easily and quickly.	Need accurate calibration and reconstruction. Resolution limited to 5 % of vessel diameter	Mann *et al.* (1995,1997a,b, 2001) Williams *et al.* (1996) Cilliers *et al.* (2001) Wilkinson *et al.* (2006)
MRI	High resolution (up to 5 – 10 μm) No reconstruction necessary. Non-invasive. Can observe transport phenomena	No ferrous material. Limited to bore of magnet (often < 70 mm) Experiments can range from minutes to hours. Contrast effects	Gladden (1995, 2003) Johns *et al.* (2000) Mantle and Sederman (2003)

2.10 Review Conclusions

After initiating this review with a fundamental examination of transport phenomena relating to the slurry bioreactor, suspension knowledge was detailed showing methods of concentration determination and the related quality of information. As the slurry bioreactor is comprised of several phases, it is clear from this review that further knowledge of the distribution and interaction of these phases would aid understanding. From the literature, it is apparent further knowledge is desired on the distribution of:

The Inert Solid Phase: Greater detail of this phase distribution, ideally in two dimensions, would allow suspension to be examined as a function of operating parameters, including reactor scale. This would further allow analysis of particle homogeneity for the whole reactor. Knowledge of particle distribution at incomplete suspension, especially at the tank bottom, would aid slurry bioreactor studies. This would provide information relating to cell disruption and mineral bioleaching. This suspension knowledge would also aid model development and confirmation of CFD studies.

The Gaseous Phase: Examination of gas phase distribution in the stirred tank would promote hypotheses regarding the oxygen mass transfer coefficient and the resulting uptake by the microbial phase. Quantifying surface aeration would also contribute to understanding of stirred tank behaviour.

The Microbial Phase: The effect of a biomass concentration on solids suspension is lacking in the literature. Further, it has always been assumed the microbial phase is homogenous in a stirred tank. This requires investigation.

The reviewed tomographic technologies of MRI and ERT appear capable of obtaining this information.

Chapter 3

Materials and Methods

This chapter details the ERT and MRI apparatus used in all experimentation. Various sizes of vessels, types and amounts of solids, impeller geometries, agitation and aeration rates, and tomographies were investigated to obtain information on the dynamics of mixing and the capability of the tomographic technology. Investigations started from simple geometries and phantoms in vessels and were extended through to agitated multiphase systems.

Qualitative ERT investigations were performed on a swirling-flow pipeline at the University of Nottingham. This allowed examination of the capability of the ERT equipment in a solid-liquid environment before investigating the more complex stirred tank system. The 220 mm ID stirred tank system was the main vessel for investigating suspension and mixing of particles with ERT. Aeration experiments were mostly confined to this vessel. ERT experiments were conducted on a miniature stirred tank (50 mm ID) which was geometrically similar to the 220 mm ID tank. This provided opportunities to investigate scale effects. Comparative experiments were performed using MRI on an identically sized vessel at the University of Cambridge. This allowed the comparison of tomographic technologies. Further ERT aeration experiments were performed on a pilot-scale vessel at the University of Manchester. Information regarding the calibration procedure, conductivity probe measurements and the sample withdrawal technique is included. Details of the ERT hardware and software systems used in this study will be discussed in Chapter 4.

3.1 The ERT- Stirred Tank Reactor System

An 8.36 litre Perspex tank for suspension of solid and liquid phases was agitated by two types of impellers driven by a drill press (Figure 3.1). Addition of air through a sparger was enabled. Solid suspension was monitored using four layers of electrodes wired to switch boxes enabling switching between layers for both current injection and detection. A master switch allowed the option of 2D or 3D measurement. The switch box was wired to the ERT hardware system which was connected to a PC. The components of this system are detailed, except for the ERT hardware and software which are described in Chapter 4.

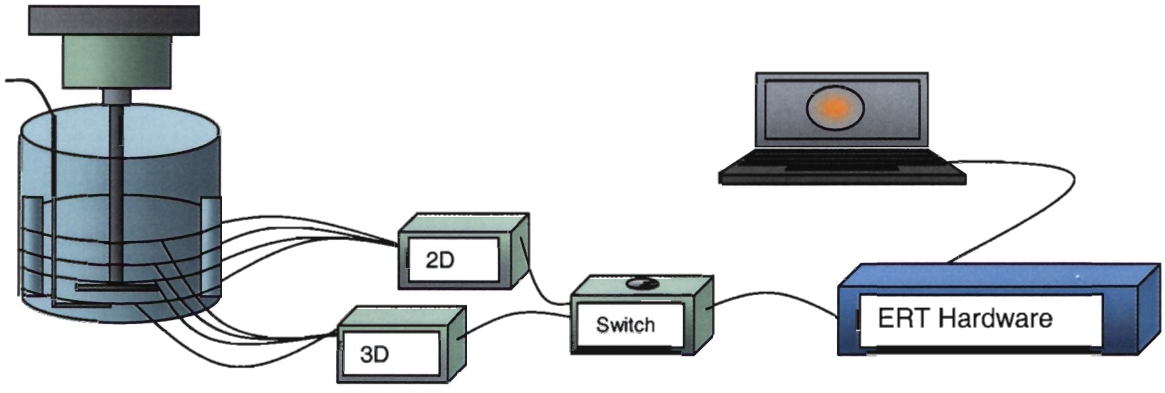


Figure 3.1: The ERT-stirred tank apparatus depicting drill press, shaft, impeller, sparger, switch box, tomography hardware and a PC.

3.1.1 The Perspex Tank

The stirred tank geometry was constructed to relate to provide a scaled-up version of the reactor used by Scholtz-Brown (1998) to quantify microbial cell damage in a slurry reactor in the research unit. This previous research was also conducted in the Bioprocessing Engineering Research Group at the University of Cape Town. The height was increased to allow for the study of different H/T ratios. However, all data collected in this study were obtained using a working volume of 8.36 litres based on equal height and tank diameter.

The material of construction of the cylinder and baffles is Perspex (5 mm wall thickness). The base is constructed from high density polypropylene and fitted to the Perspex cylinder by means of a rubber O-ring, which allowed removal for maintenance and cleaning. Four layers of 16 electrodes are positioned up the side of the tank. .The design of the reactor and the electrode spacing are shown in Figure 3.2. The base is illustrated in Figure 3.3 and the actual tank can be observed in Figure 3.4. The dimensions of the reactor are specified in Table 3.1.

Table 3.1: Dimensions of the tank reactor

Symbol	Description	Dimension (mm)
H_1	Height for operating volume	220
H_2	Height of tank	520
D	Impeller diameter	110
T	Tank diameter	220
C	Impeller clearance	73
B	Baffle width	22
H_1/T	1.00	~
B/T	0.10	~
C/T	0.33	~

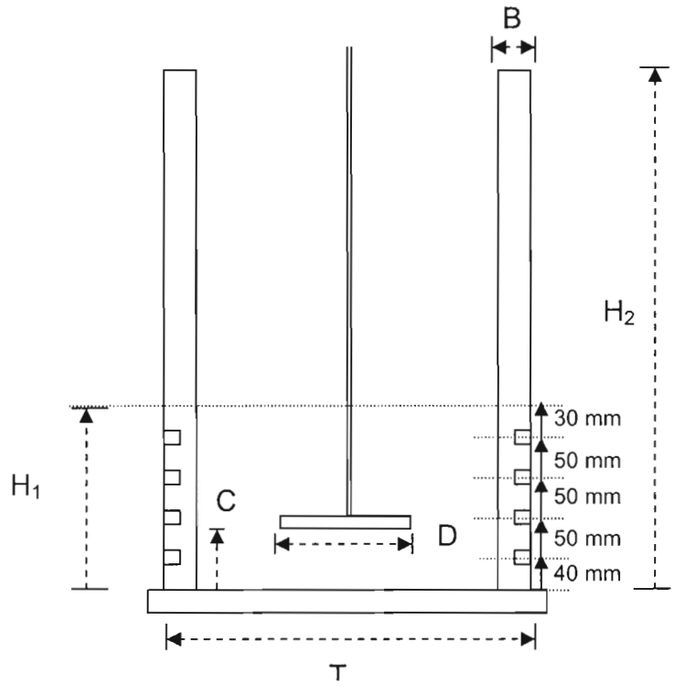


Figure 3.2: Design of the Perspex stirred tank reactor including positioning of electrode layers.

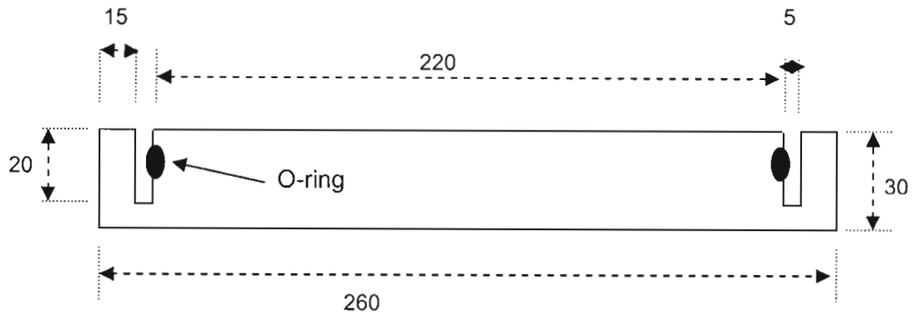


Figure 3.3: Design of high density polypropylene base showing position of O-ring used as a seal with the Perspex cylinder. Measurements in mm.

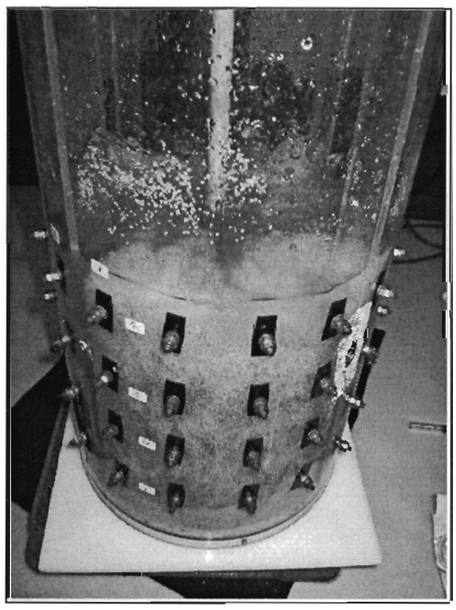


Figure 3.4: A photograph of quartzite suspension in the Perspex tank reactor showing 4 layers of electrodes.

3.1.2 Electrode Design

The electrodes are comprised of copper which is highly conductive. These are welded to brass screws. On the back of the copper electrodes is a layer of neoprene rubber to prevent fluid from leaking from the tank. The electrodes are situated on the inside of the tank, with a nut fastened from the outside securing their position (Figure 3.5). Electrodes were designed to be elongated to account for the electric field bending in 3D as well as to decrease the common voltage at the current driven electrodes (Wang *et al.*, 1995). Each electrode is connected to an unshielded wire,

sandwiched between washers and fastened with another nut (Figure 3.5). Thus each layer has 16 wires which connect to a multiplexor in the hardware system.

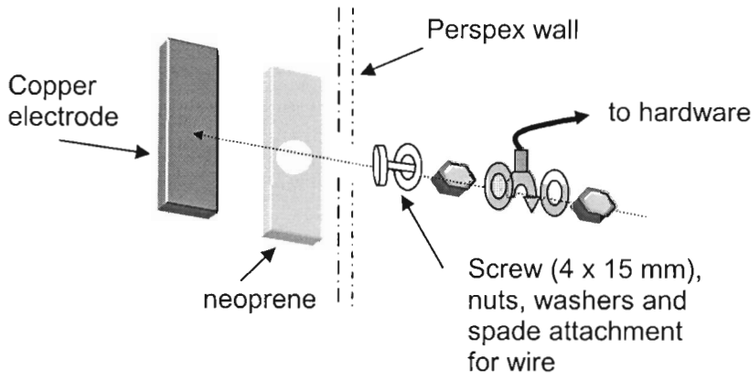


Figure 3.5: The components of the electrode system

A consistent electrode layout is vital for accurate reconstructions. This is illustrated in Figure 3.6. Minor geometrical irregularities can be normalised in the calibration process. A close-up image of the electrodes can be seen in Figure 3.7. Rectangular-shaped electrodes appear to yield better results with 2D reconstruction algorithms (Randall, 2005) or more specifically, with reconstruction software that does not model electrode geometry and impedance effects.

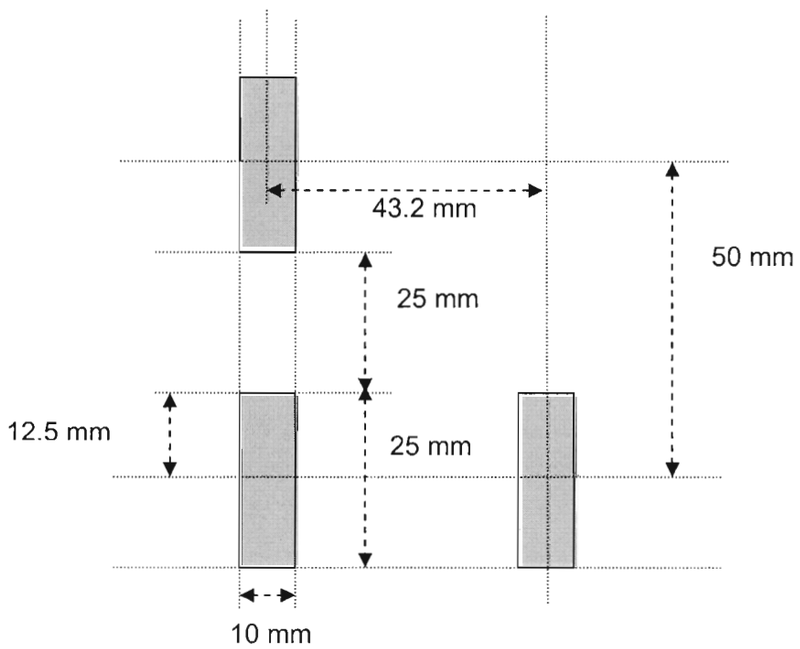


Figure 3.6: Layout and design of the copper electrodes. Electrodes are 1 mm thick.

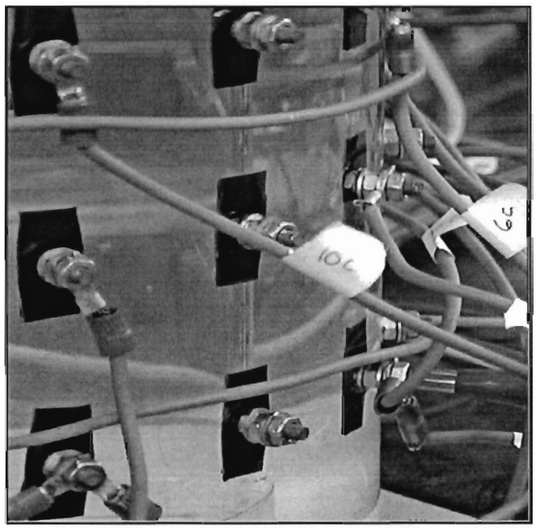


Figure 3.7: Close-up image of the electrodes: the black neoprene rubber is visible against the wall of the tank.

3.1.3 Impeller Design

The design of the Rushton and pitched-blade impellers was based on that previously used by Scholtz-Brown (1998). These impellers were scaled-up, maintaining the standard geometric ratios. Their designs are detailed in Figures 3.8 and 3.9.

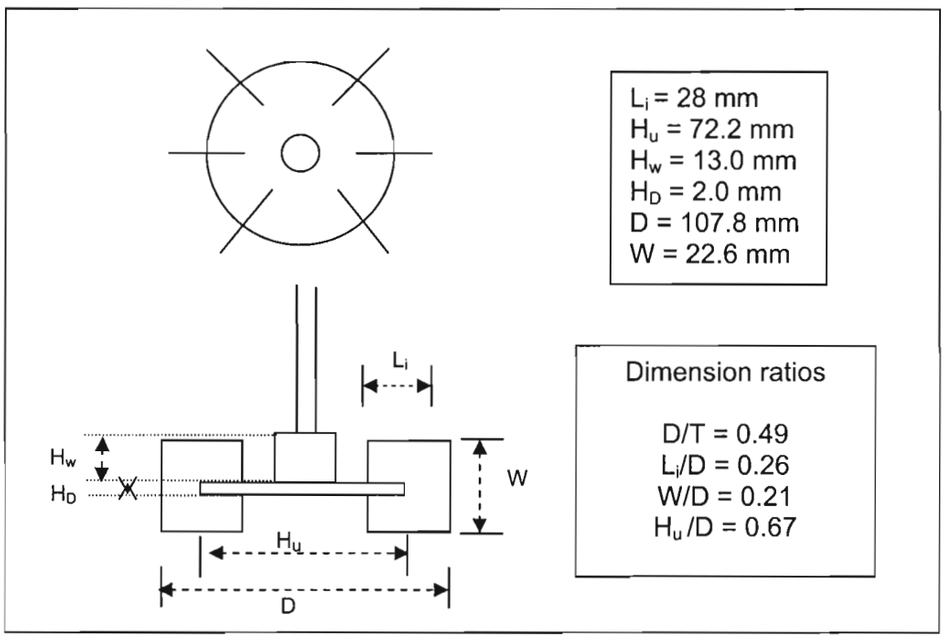


Figure 3.8: The six-bladed Rushton turbine

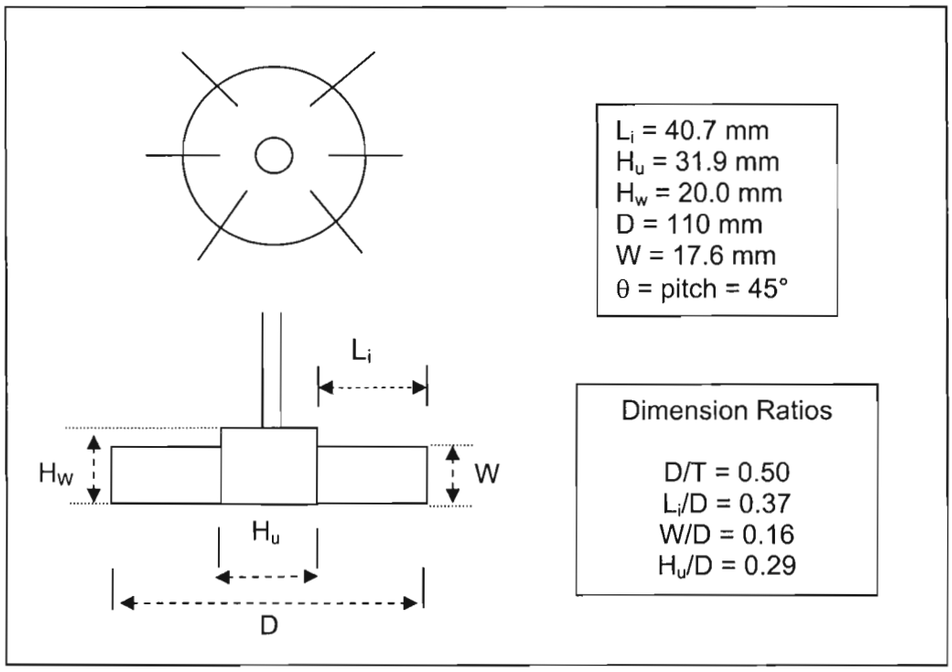


Figure 3.9: The six-bladed pitched-blade turbine (pumping downwards at 45°)

These impellers (Figure 3.10) were coated with black enamel paint and Loctite®, a rubberised paint. This was to ensure that they would be non-conducting in the stirred tank system and thus contribute similarly to the conductivity distribution as the non-conducting Perspex baffles.

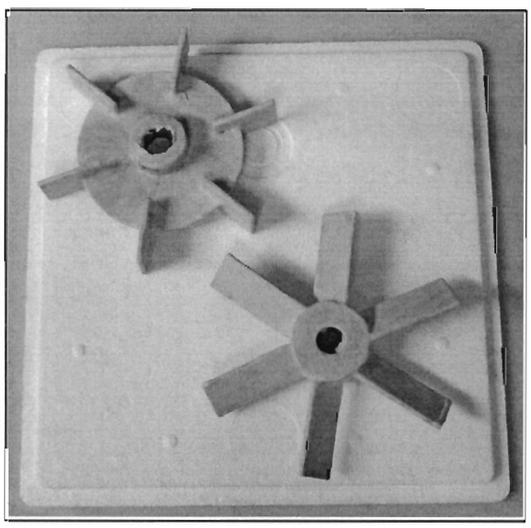


Figure 3.10: The pitched-blade (pumping-downwards) and Rushton turbine impellers

3.1.4 Sparger Design

The sparger tubing was stainless steel (1 mm wall thickness) and was coated with Loctite®. The sparger design is illustrated in Figure 3.11(a). A pipe sparger design was chosen as there is a greater reduction in power consumption compared to a ring sparger (Frijlink *et al.*, 1984). Further, it was the least obtrusive when considering ERT application and calibration.

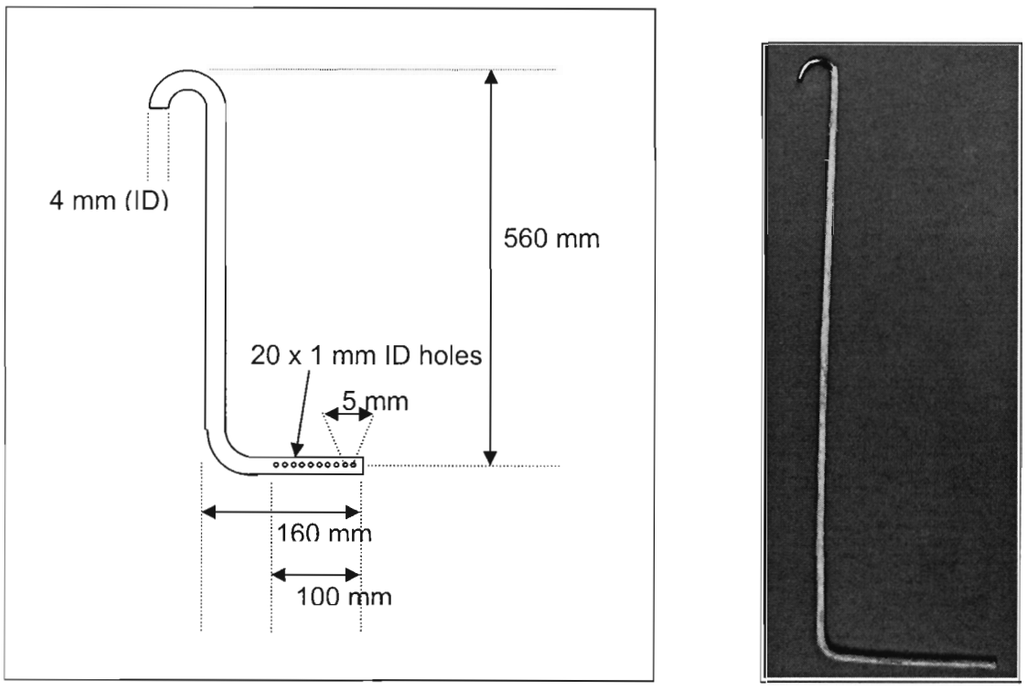


Figure 3.11: Design of pipe sparger used in aeration experiments (a); and the photo thereof (b).

3.1.5 The Particulate Phases in the 220 mm ID Stirred Tank

Particulate quartzite was obtained from Consol Glass (Cape Town) and prepared into three size distributions by dry sieving: 106-212 μm, 425-600 μm and 600-850 μm, ρ = 2650 kg.m^{-3}. The particle size distributions, measured by the Malvern Mastersizer, are given in Figure 3.12. The sizes determined by the Malvern Mastersizer appear larger than the sieve sizes due to the measurement of particle volume through laser light scattering rather than measurement of minimum particle diameter. Size fraction information is in Table 3.2. These particles were washed over a two week period to remove fines in a stirred tank environment, followed by a concentrated nitric acid wash to bleach particles and remove fines and metal content. After further washing to remove traces of acid, the particles were calcined at 550 °C for 20 hours. This preparation preceded the particle size measurement.

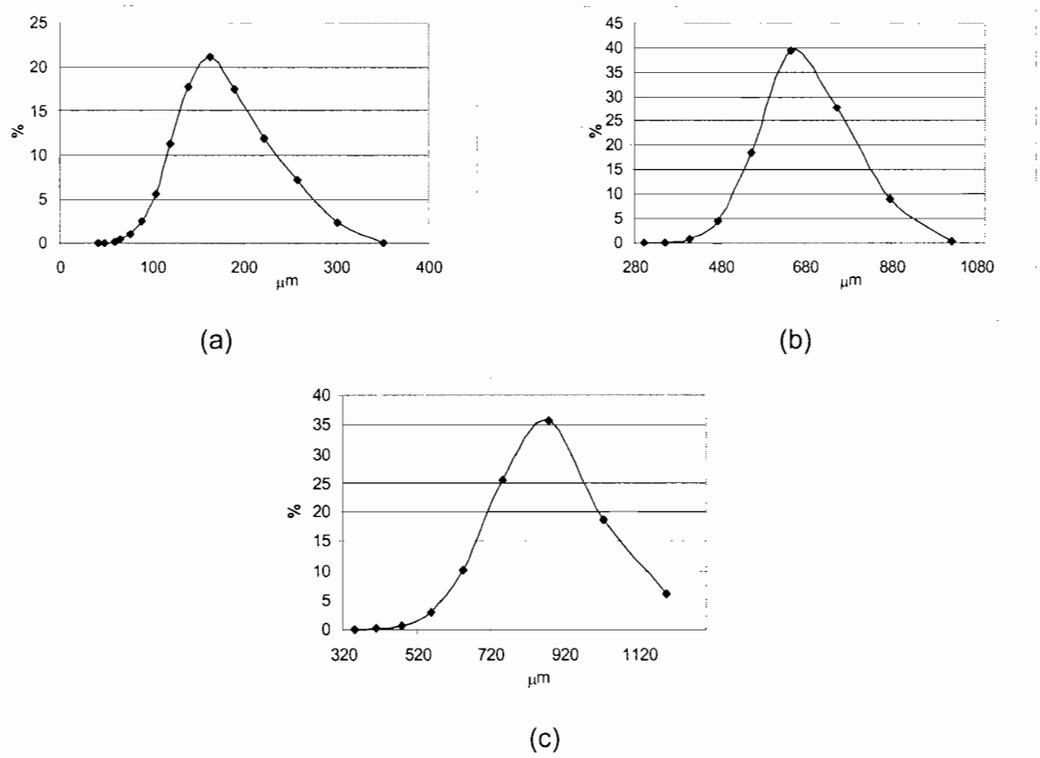


Figure 3.12: Three sieved size distributions examined by Malvern Mastersizer: 106 – 212 μm (a); 425 – 600 μm (b); 600 – 850 μm (c).

Table 3.2: Particle statistics for the three size distributions determined by the Malvern Mastersizer

Size distribution (μm)	Mean	Mode	d_{50}	d_{90}
106-212	168	164	153	222
425-600	671	647	617	754
600-850	857	754	790	993

Baker's yeast, *Saccharomyces cerevisiae*, was also tested as a model microorganism in the stirred tank. This yeast has a mean size of approximately 5 μm and a density of 1050 $kg.m^{-3}$ (while wet).

3.1.6 The Fluid Phase in the 220 mm ID Stirred Tank

Saline solution containing 100 $mg.l^{-1}$ NaCl at room temperature (20 °C) provided the liquid medium. This enhanced the conductivity to the range 300-400 $\mu S.cm^{-1}$. Air was introduced from the sparger at 0.5 and 1.0 vvm as specified.

3.1.7 ERT Calibration Procedure

Calibration was carried out in the presence of the baffles, shaft and impeller (at 236 or 304 rpm), but absence of solids. Thirty frames of data were recorded using the first ERT system (ERT Hardware I, Section 4.2) during this calibration and were averaged prior to reconstruction. One hundred frames of data were captured for calibration using the faster ERT Hardware III (Section 4.8).

3.1.8 ERT Experimental Procedure

With the equipment setup as depicted in Figure 3.1 calibration was initiated prior to changing the conditions in the stirred tank. Four concentrations of quartzite (5, 10, 15 and 20 vol. %) of the three size fractions (106 – 212 μm, 425 – 600 μm and 600 – 850 μm) with the Rushton and pitched-blade impeller were agitated at 236, 304, 353, 460 and 547 rpm in the stirred tank. After observing steady state with each condition, thirty frames of data were captured with ERT Hardware I from each layer. With this system, multiple layer multiplexing was not possible, thus each electrode layer was excited separately before switching manually to the next electrode layer. The boundary voltage data was recorded as a .txt file which could then be transformed into an .acm file for Reconstruction Codes I and III. Occasionally when high concentrations of solids were present in the tank at low agitation rates negative voltages would be recorded for the lower electrode layers. This was due to the voltage required for the higher resistance being beyond the ERT hardware limits. In these cases experiments were repeated until a useable data set was obtained.

Aeration experiments (sparging and surface aeration) were examined in the 220 mm ID tank with Reconstruction Code V and ERT Hardware III (Section 4.8 and 4.9). After calibration (100 frames) in the presence of the sparger the air flow rate was set to either 0.5 or 1.0 vvm. One hundred frames were captured with the data being automatically saved as a .tom file using Reconstruction Code V. The agitation rate was then increased for each experiment in the range of 236 – 547 rpm. This code allowed the capture of data for all four layers in one experiment through the multiplexors. The surface aeration experiments were similarly initiated although without the presence of the sparger.

3.1.9 Conductivity Measurements

Conductivity measurements were obtained using a Metrohm® 712 Conductometer with a Metrohm® 6.0908.110 glass/platinum probe. This was initially calibrated with a Metrohm® 6.2301.060 standard solution containing 0.1 M KCl at 20 °C. The probe was inserted into the stirred tank at the upper two electrode layer heights while

recording data from three radial positions. A 20 mm gap was maintained between the tank wall and the probe (Barresi and Baldi, 1987a).

3.1.10 Pipette Sampling of the Stirred Tank

Pipette sampling was performed to provide qualitative validation of the ERT data at the upper two electrode layers and at the same three radial positions as the conductivity measurements. Pipette sampling was not practical in the impeller zone or near the tank bottom. A 5 ml pipette tip (Eppendorf) was cut 10 mm from the end to facilitate particle extraction and prevent quartzite grains blocking the orifice. The withdrawal speed was more than double the terminal velocity of the largest particle used in this study (MacTaggart *et al.*, 1993). Sampling was performed on a 5 % volume fraction of the 106-212 μm quartzite and a 15 % vol. sample of the 600-850 μm quartzite in the stirred tank. Through knowledge of the slurry volume of the pipette, the fluid and particle density, the volume fraction of quartzite in the sample vial could be calculated directly without resorting to drying procedures (Equation 3.1).

$$\begin{aligned} &let\ V = \text{Volume of slurry in vial} \\ &\alpha = \text{volume fraction of sand} \\ &\text{M} = \text{total mass of sand and water, then} \end{aligned}$$

$$\alpha.V.\rho_{sand} + (1-\alpha)V.\rho_{water} = M$$

$$\text{rearranging}: \ \alpha = \frac{M - V.\rho_{water}}{(\rho_{sand} - \rho_{water})V} \qquad (3.1)$$

3.2 The Swirling Flow System

This system is comprised of a Perspex pipe section fitted with electrodes, swirly-flow boiler tubing and the associated solid and fluid phases.

3.2.1 The Perspex Pipe and Electrodes

A qualitative examination of swirling flow in a pipeline using ERT was conducted at the School of Chemical, Environmental and Mining Engineering at the University of Nottingham. A 50 mm diameter Perspex pipe of 1 m was constructed to fit into an existing pipeline (Wood and Jones, 2003). Four layers of 16 copper electrodes were designed and glued into the pipe section such that they were embedded in line with the inner pipe wall. A brass bolt was welded to the copper electrode and a wired spade was connected to the hardware system and fastened with a nut. The wires

were unshielded. The spacing of the electrodes is clearly shown in Figure 3.13 while the connection of the electrodes is shown in Figure 3.14 (b).

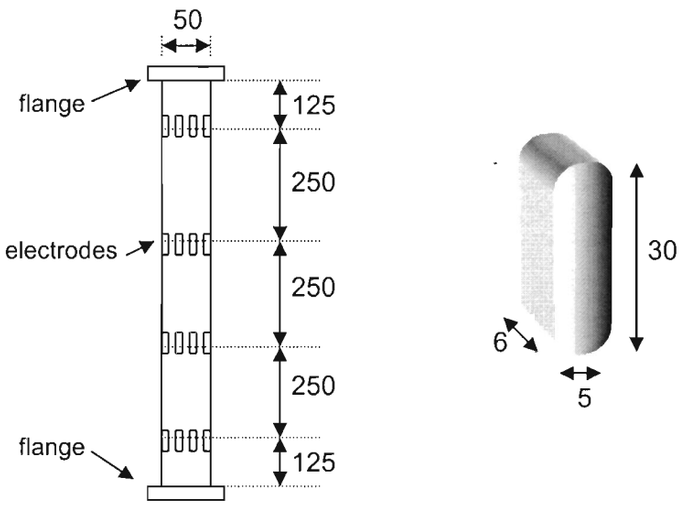
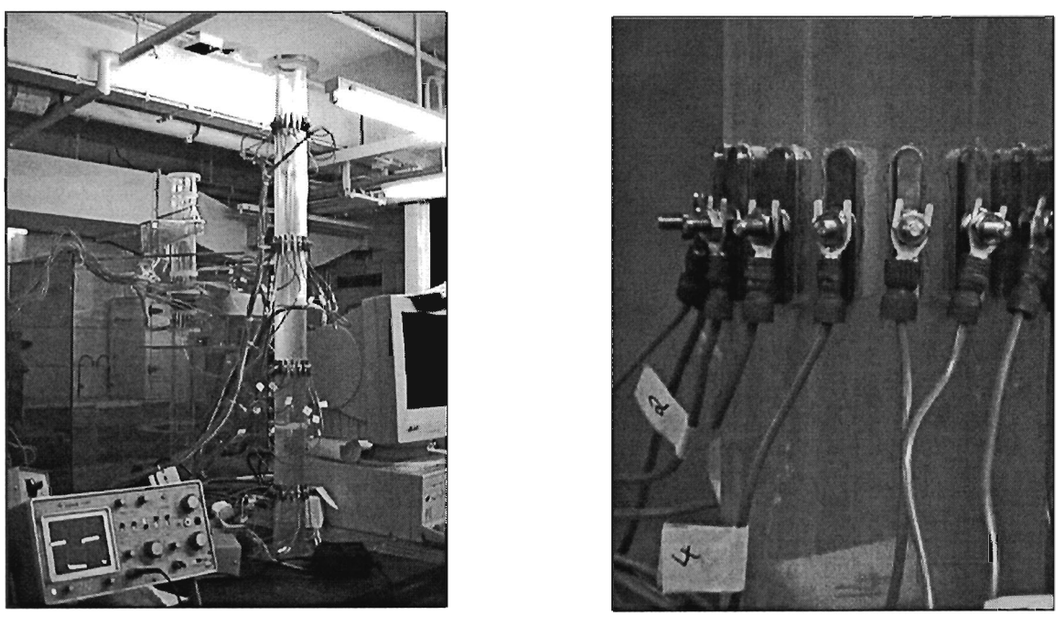


Figure 3.13: Perspex pipe section with 4 layers of 16 electrodes. The electrode is detailed on the right and was designed to be flush with the inner pipe wall. All measurements are in mm.



(a) (b)

Figure 3.14: (a) The University of Nottingham Perspex pipe system with associated ERT apparatus; and (b) close-up of the contoured copper electrodes.

3.2.2 Swirl Inducement

A 1 m section of stainless steel swirly-flow boiler tubing (Figure 3.14) of pitch/diameter ratio of 8 (Wood *et al.*, 2001), preceded the 1 m section of Perspex pipe with electrodes (Figure 3.15) by approximately 2 m. These were connected via flanges. The 2 m interlude provided sufficient distance to enable observation of the bulk particle movement down the side of the pipe wall where the electrodes were fitted.

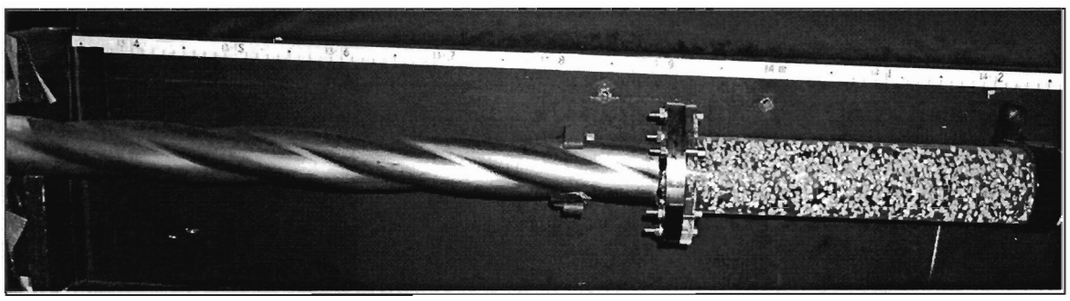


Figure 3.14: Swirly-flow boiler tubing connected to the Perspex pipe. White plastic beads simulated slurry conditions.

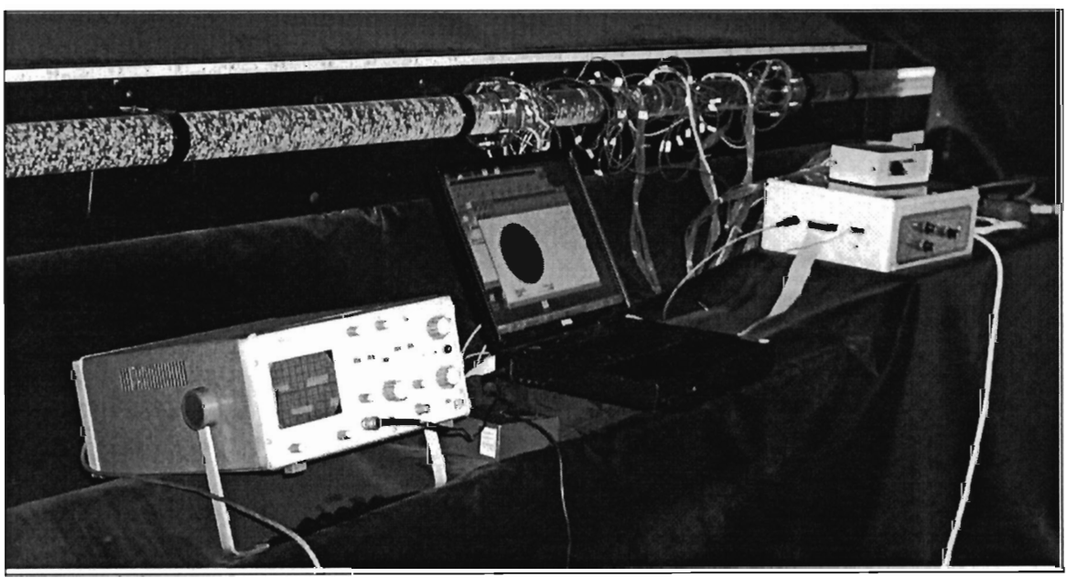


Figure 3.15: Perspex pipe section wired up to the ERT hardware monitoring swirling plastic beads. The oscilloscope monitored the amplitude of the square wave in the measurement system (see Section 4.2).

3.2.3 The Liquid Phase in the Pipeline

Tap water at room temperature (16 °C) in which 50 mg.l^{-1} NaCl was dissolved formed the liquid phase. The working volume of the pipeline is 202 litres and was powered by a centrifugal slurry pump with superficial velocities ranging from 0.5 to 2.5 m.s^{-1}.

3.2.4 The Solid Phase in the Pipeline

Cylindrical non-conductive plastic beads (2 x 3 mm, ρ = 1460 kg.m^{-3}) provided the simulant for slurry at 2, 3 and 4 % by mass. These have a similar density to coal particles (ρ = 1450 kg.m^{-3}). Quartzite (710-1180 μm, ρ = 2650 kg.m^{-3}) at 2 % by mass was also tested. Properties of the quartzite distribution are given in Figure 3.16 and Table 3.3.

Table 3.3: Particle statistics for quartzite tested in pipeline.

Size distribution (μm)	Mean	Mode	d_{50}	d_{90}
710 -1180	978	1000	895	1100

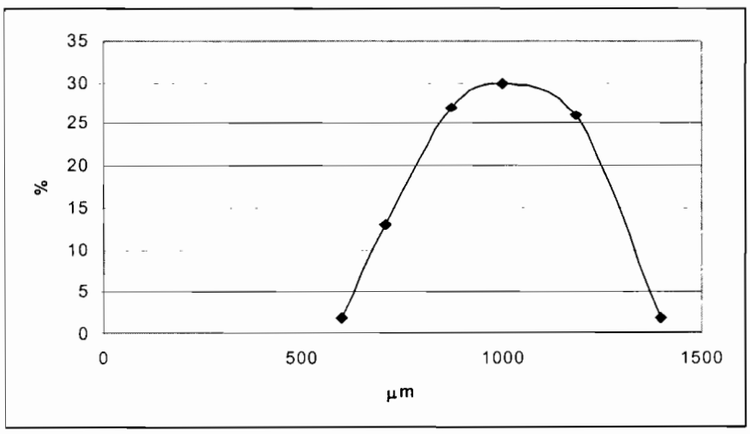


Figure 3.16: Quartzite size distribution for the pipeline.

3.2.5 ERT Calibration Procedure

After adding salt to the liquid, the solution was recirculated through the pipeline for 5 minutes to ensure complete solution. At a flow rate of 1 m.s^{-1} and with no presence of solids, calibration was initiated. Thirty frames of data were recorded using ERT Hardware I (Section 4.2) during this calibration and were averaged prior to reconstruction. Layers were examined sequentially with approximately 30 seconds between data capturing. Flow was at steady state.

3.2.6 ERT Experimental Procedure

After calibration the two types of solids (quartzite and plastic beads) were introduced into the pipeline at 2, 3 and 4 wt. % and superficial velocities of 1.5 to 2.5 $m.s^{-1}$. Circulation was allowed for 10 minutes to ensure even distribution of particles in the pipeline. Starting from electrode layer 1 which was closest to the boiler tubing, 30 frames of data were captured using ERT Hardware I. After data was recorded the following electrode layers were excited in turn manually with approximately 30 second intervals between layers. Steady state was assumed and was visually apparent thus time between switching layers was not a factor in image reconstruction.

3.3 The MRI Miniature Stirred Tank Reactor

It was desired to compare ERT with another tomographic technology to investigate the similarity and validity of results as well as the potential to provide further information on mixing and suspension. Thus higher resolution MRI was considered at the University of Cambridge at the Magnetic Resonance Research Centre (MRRC).

3.3.1 Geometry of Mini-STR

MRI has size limitations owing to magnet dimensions and thus a mini-STR was designed (Figure 3.17) to fit inside a 60 mm probe within the bore of a magnet. This design was a scaled-down version of the larger Perspex tank. Geometric ratios were maintained (Table 3.4). This further provided potential information to examine the effects of scale. The reactor walls and baffles were constructed out of Perspex, the top and bottom sections out of Teflon, and the six-bladed Rushton impeller and shaft out of polyethylene-ethylene-ketone (PEEK) (Figure 3.18), a hard, high density thermoplastic. These components were used to avoid the presence of ferro-magnetic materials which influence the magnetic resonance. The impeller was powered by a stepper motor (Figure 3.19(b)) at speeds of 186 - 480 rpm while located inside the magnet.

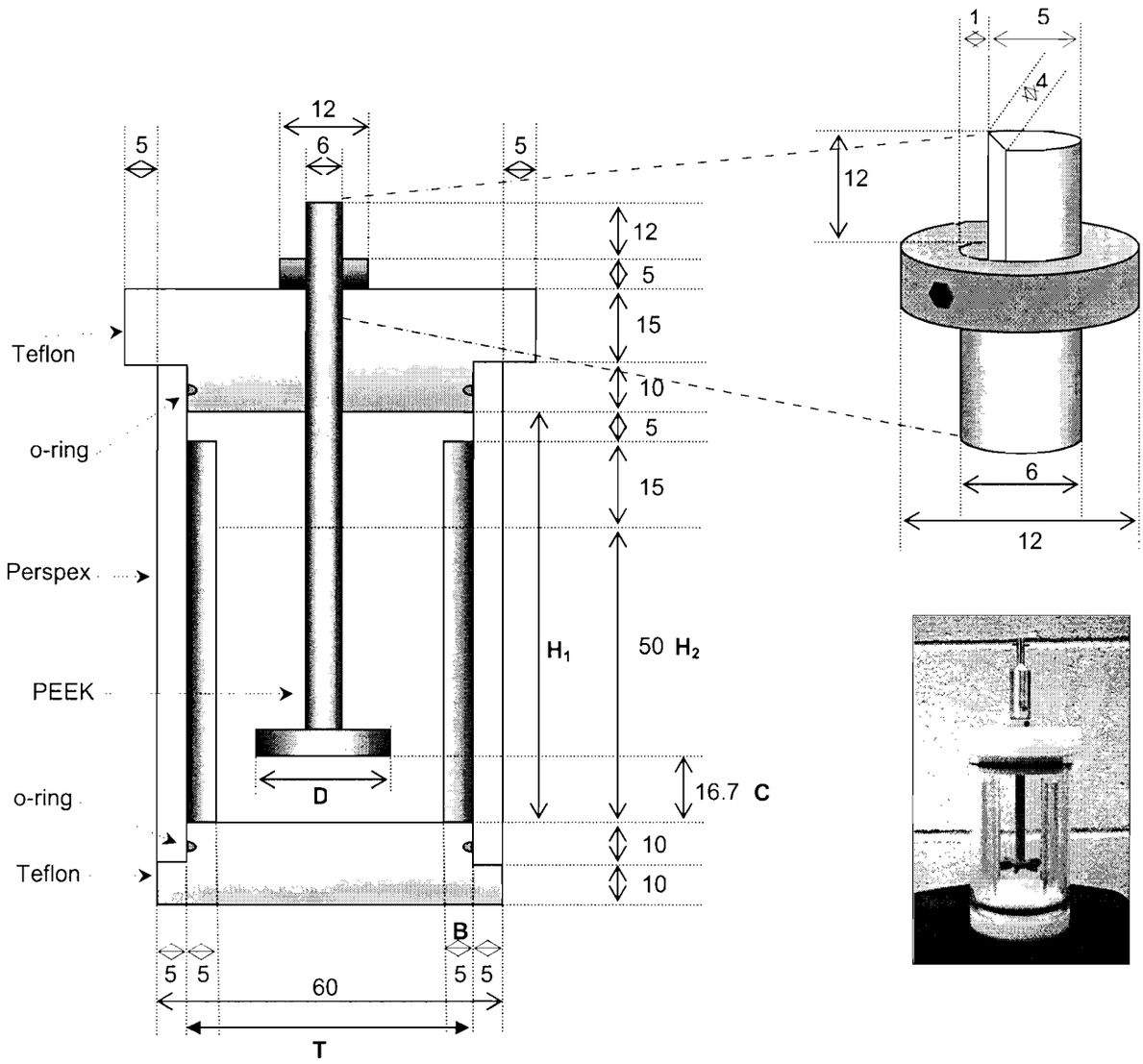


Figure 3.17: Design and photo of the mini-STR for magnetic resonance imaging. The expanded view is of the PEEK shaft and ringlet used to maintain specific shaft height by means of a grub screw. The shaft was cut away at the top to facilitate attachment to the stepper motor. The Teflon top and bottom sections were sealed with o-rings. All measurements are in mm.

Table 3.4: Dimensions of the mini-STR

Symbol	Description	Dimension (mm)
B	Baffle width	5
H_2	Height for operating volume	50
H_1	Height of tank	70
C	Impeller clearance	16.7
D	Impeller diameter	25
T	Tank diameter	50
H/T	1.00	~
B/T	0.10	~
C/T	0.38	~
D/T	0.5	~

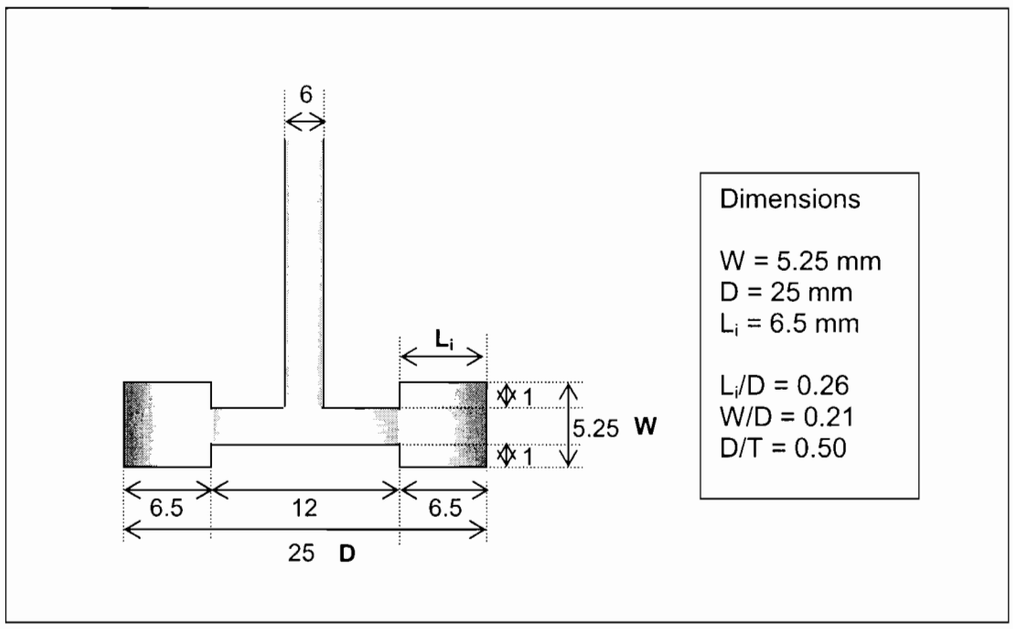
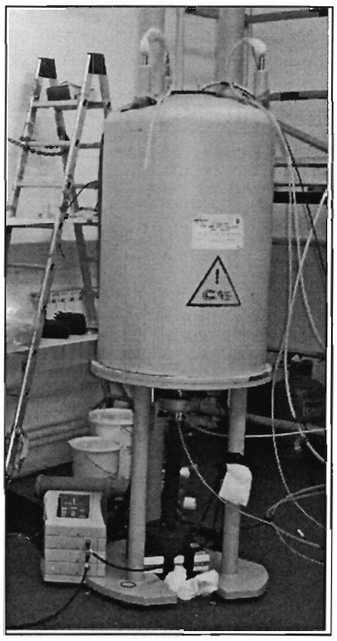


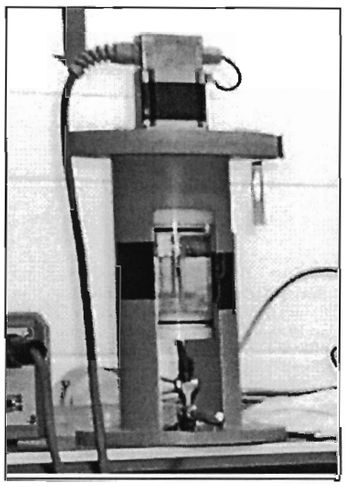
Figure 3.18: The impeller and shaft were constructed out of a single piece of PEEK and designed to be geometrically similar to the Rushton turbine used in the 220 mm ID Perspex tank.

3.3.2 The Magnet and Probe

The MRI apparatus was a Bruker Spectospin DMX 200, 4.7 Tesla superconducting magnet with a 64 mm r.f. probe. The magnet was kept cool by liquid helium and a further external jacket of liquid nitrogen to decrease the liquid helium evaporation rate.



(a)



(b)

Figure 3.19: The Bruker 200 MHz magnet (a). A 60 mm probe was fitted from underneath with the mini-STR inside, while the stepper motor (b) was attached to the top of the magnet and a long connecting shaft was connected to the shaft of the mini-STR. In (b) initial visual suspension tests were performed as evidenced by the mini-STR connected to the stepper motor.

3.3.3 The Liquid and Solid Phases in the Mini-STR

Tap water was used at room temperature (20 °C) due to its natural abundance of protons. Borosilicate ballotini of sizes 100 μm and 50 μm (S.G. 2.20), Baker's yeast, and 600 μm nylon particles (S.G 1.13) were used as suspended phases in the mini-reactor. The particle size distributions were measured by laser light scattering using the Malvern Mastersizer. These are presented in Figure 3.20 and particle information in Table 3.5. The ballotini have a higher degree of sphericity than the silica although being less dense.

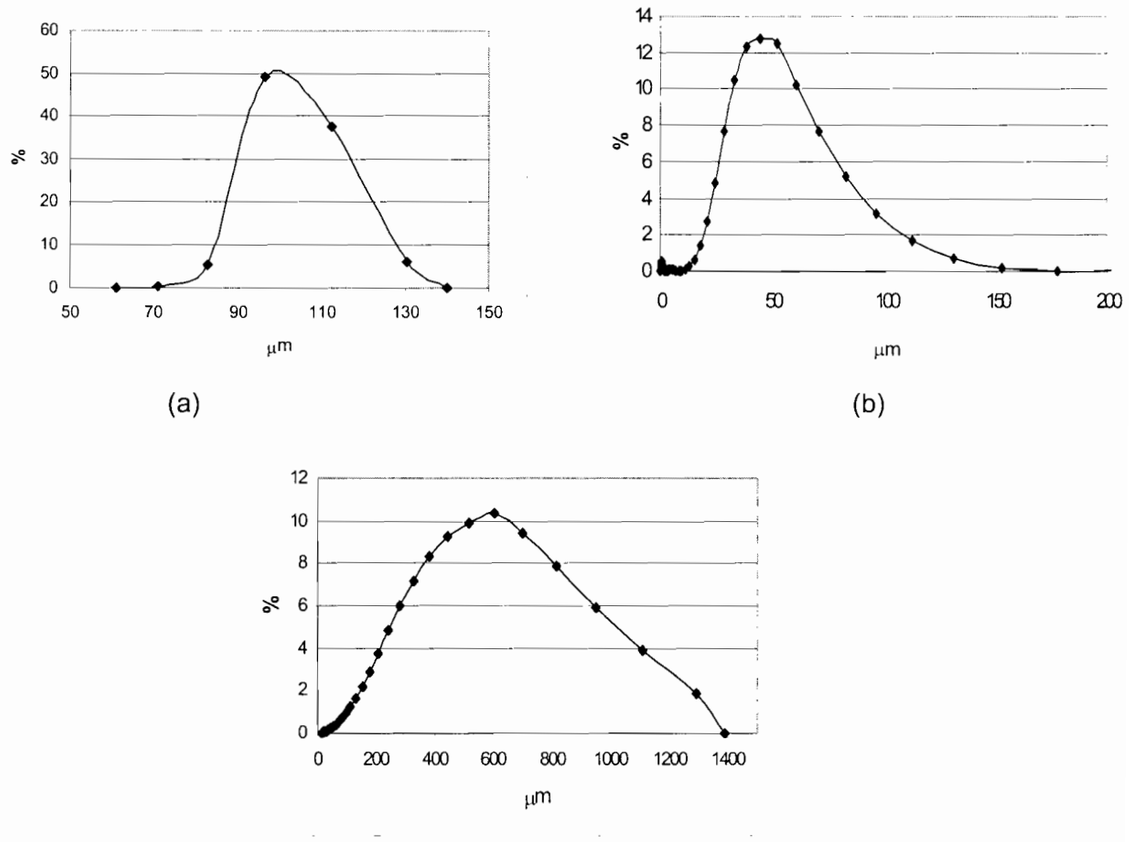


Figure 3.20: Malvern size distributions of 100 μm borosilicate ballotini (a), 50 μm borosilicate ballotini (b), and 600 μm nylon particles (c).

Table 3.5: Particle information for solids tested with MRI

Particle	Size distribution (μm)	Mean	Mode	d_{50}	d_{90}
100 μm ballotini	70-140	102	96	95	111
50 μm ballotini	13-152	54	56	44	82
600 μm nylon	0-1400	513	602	409	789

3.3.4 MRI Calibration Procedure

After insertion of the mini-STR into the 64 mm r.f. probe, the probe was inserted into the magnet and tuned to 199.7 MHz (proton frequency). The desired agitation rate was set on the stepper motor. Single point excitation had a heating effect on the probe, thus it was excited with single pulses for approximately 25 minutes until

attaining a steady temperature (± 28 °C). Thereafter experiments were conducted using single point imaging techniques (1D and 3D). Every time the STR was removed for a change of solid phase or solids concentration, the probe was retuned and reheated via pulses until reaching an equilibrium temperature. Each data set was Fourier transformed and divided by the signal values obtained from a sample containing tapwater only and agitated at 480 rpm representing the reference condition.

3.3.5 MRI Experimental Procedure

Following the tuning and reheating of the probe after the introduction of the different types of solids, 1D single point imaging proceeded in triplicate. 1D Experiments consisted of 50 μm and 100 μm ballotini (5 and 10 % by volume) and 600 μm nylon particles (5, 10, 15 and 20 % vol.) agitated at 186, 306, 366, 426 and 480 rpm. Bakers' yeast at wet volume concentrations of 5 and 11 % was agitated at the same speed. Nylon particles (10 and 20 % vol.) were further combined with 5 % vol. yeast for the 1D imaging.

3D experiments were approximately 12 hours in duration with 50 μm ballotini (5 and 10 vol. %), 5 vol. % yeast, 10 vol. % nylon in the presence of 5 vol. % yeast, 20 vol. % nylon in the presence of 5 vol. % yeast being imaged at 480 rpm. It was important to maintain the exact liquid level and reactor position as that recorded for the reference condition through 1D and 3D imaging.

3.4 The Miniature ERT-Stirred Tank Reactor

A small-scale Perspex STR was constructed identical to the tank designed for the MRI experiments (Figure 3.17), except for four layers of sixteen stainless steel electrodes which were added to the inside of the tank wall. The vessel geometry with superimposed electrode spacing is detailed in Figure 3.21 and the final tank is illustrated in Figure 3.22. The same PEEK impeller system described in Section 3.3.1 was used for these experiments. Thus only the design of the electrode system is given below.

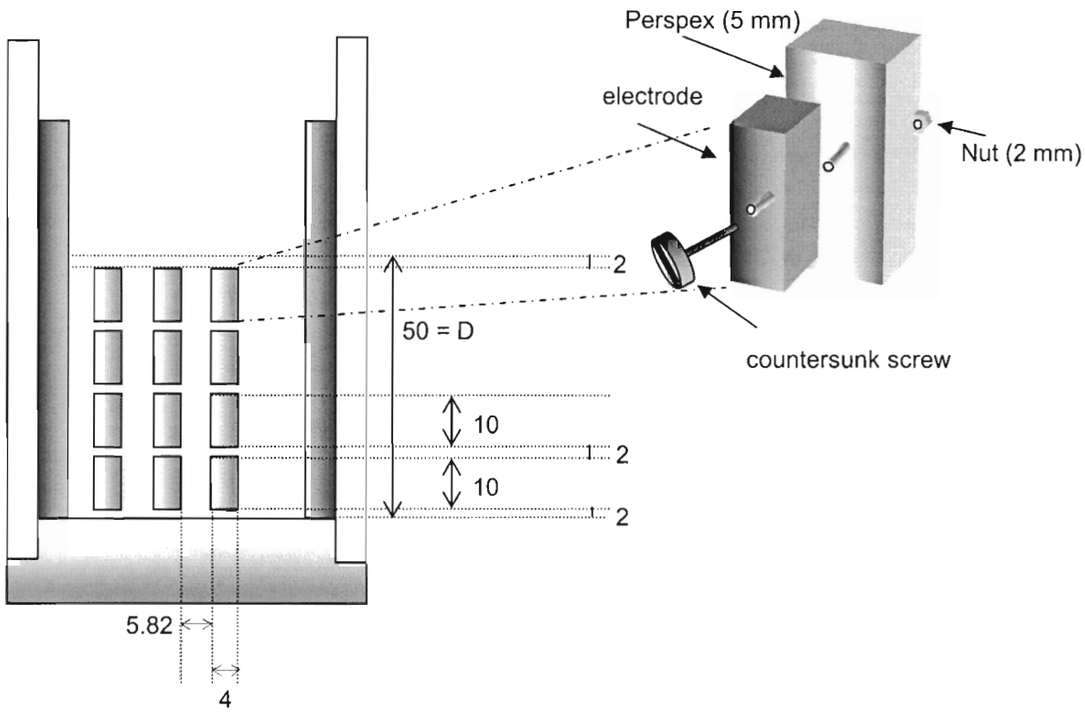


Figure 3.21: Electrode configuration for the mini-STR. The expanded view details the electrode attachment: a stainless steel countersunk screw (20 x 2 mm) secured the 1 mm thick stainless steel electrode through the Perspex and was fastened with a nut. Glue provided extra support. Shielded wire was then connected to the screw on the outside via spade connectors.

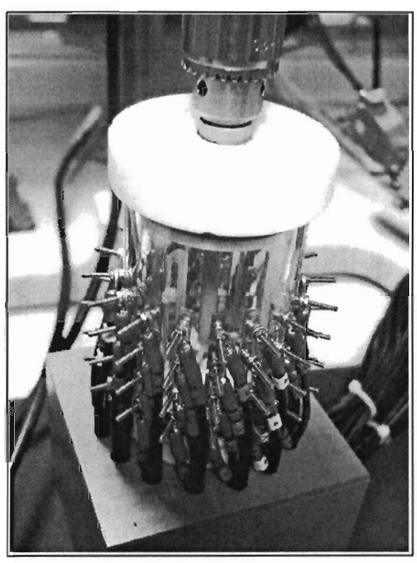


Figure 3.22: Photo of the mini-ERT STR with 4 layers of 16 stainless steel electrodes connected via shielded wire and driven by a drill press.

3.4.1 The Liquid and Solid Phases in the ERT Mini-STR

Saline tap water (100 mg.l^{-1} NaCl) was the reactor fluid. The particles suspended in this tank were the same as those used in the MRI system. In addition, the 600-850 μm quartzite fraction (from the 220 mm tank) was also examined. The system was agitated in the range of 200 to 2024 rpm by the drill press in order to reproduce the same tip speed as the impeller in the 220 mm ID tank.

3.4.2 ERT Calibration Procedure

Using only saline tapwater in the tank, 50 frames of data were obtained using ERT Software V and ERT Hardware III (Section 4.8 and 4.9). The impeller was agitated during the calibration at 200 rpm. The slurry was earthed to the hardware (System III) to maintain a common ground. This ground connection was found to improve the quality of the image with the new hardware through decreasing signal noise.

3.4.3 ERT Experimental Procedure

The same solids and concentrations examined in the MRI experiments were repeated in the mini-CSTR using ERT Hardware III and Reconstruction Code V. After calibration, 100 frames were captured at agitation rates of 200, 306, 366, 426 and 480 rpm and the higher rates of 1038, 1338, 1553 and 2024 rpm for the 600 – 850 μm quartzite to match the tip speeds of the impeller in the 220 mm ID vessel.

3.5 The Pilot-Scale Stirred Tank System

A 0.61 m diameter pilot-scale stirred tank with 8 layers of 16 electrodes was available for qualitative experimentation at the Department of Chemical Engineering, UMIST (now University of Manchester). The tank had a torospherical bottom and was in a water-filled rectangular housing to facilitate visual observation through decreased refraction. This has a similar geometry to the 220 mm and 50 mm ID tanks, apart from the torospherical bottom. The design is shown in Figure 3.23 and the photo and electrode layout is illustrated in Figure 3.24. A removable PVC rack consisting of 8 layers of 16 electrodes was inserted into the tank. The design of this sensor system is detailed by Mann *et al.* (1997).

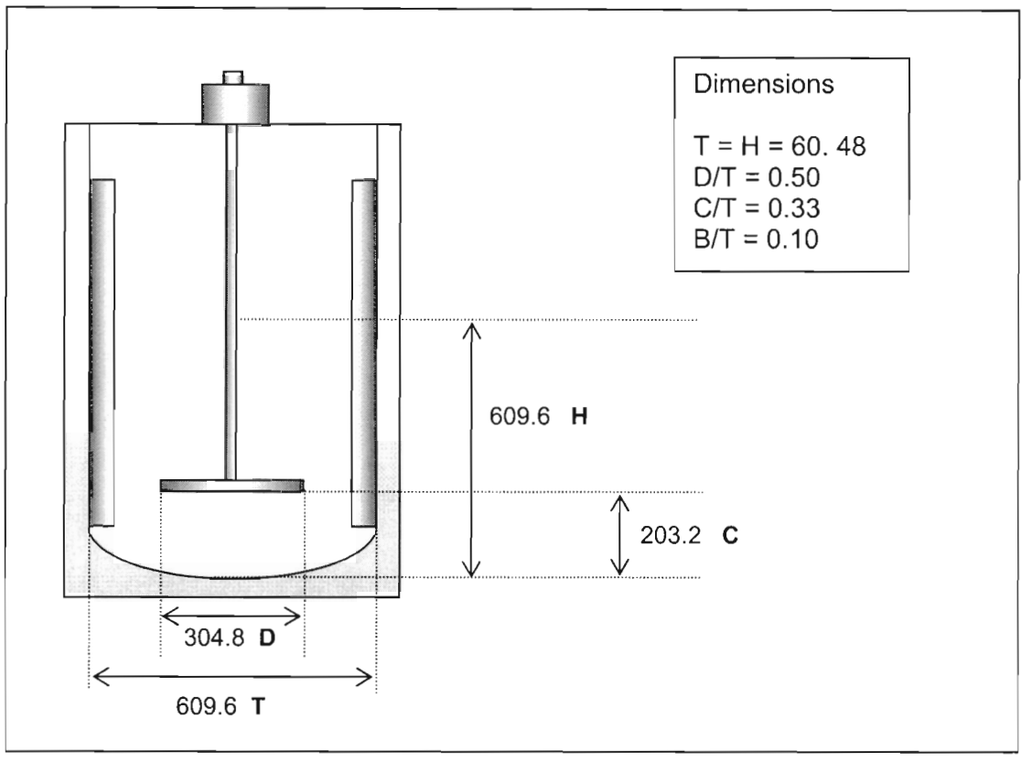
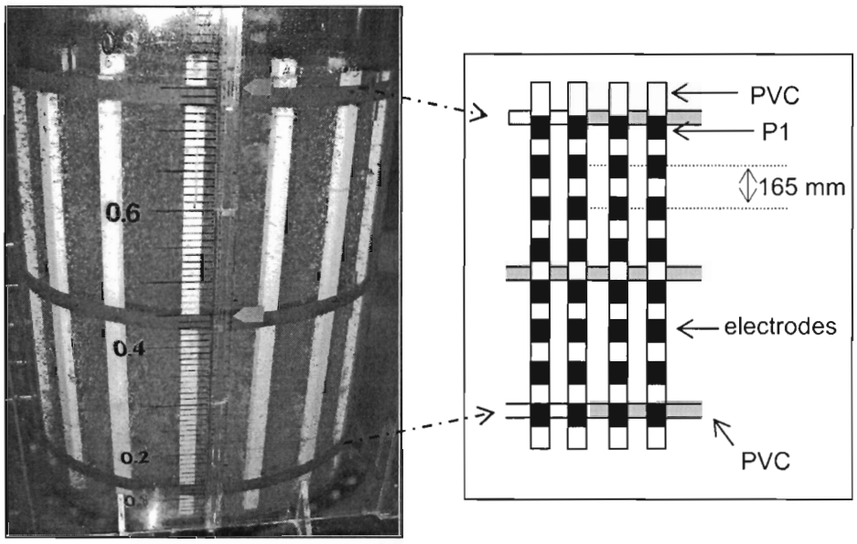


Figure 3.23: Pilot-scale 252 litre, 610 mm diameter stirred tank with dished bottom. All measurements are in mm.



Plane	z/Z
P1	0.88
P2	0.77
P3	0.66
P4	0.55
P5	0.44
P6	0.33
P7	0.22
P8	0.11

Figure 3.24: The Perspex pilot-scale vessel with 8 layers of 16 stainless steel electrodes. The right hand diagram describes how the electrodes were attached to a plastic rack which could be placed within the vessel. The lower five layers were submerged at H = D. Dimensionless heights of the electrode layers are given (P1 at top of reactor).

A gas-foil radial impeller was used (D = T/2) and was agitated from 100 to 450 rpm (Figure 3.25). This impeller has been found to be more efficient in gas dispersion than Rushton turbines (Cooke, 2004).

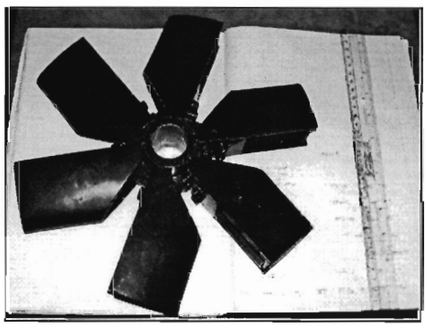


Figure 3.25: The gas-foil impeller, D = 304.8 mm

Saline tapwater (100 $mg.l^{-1}$ NaCl) was used while air at 0.5 and 1.0 vvm was tested. While the impeller was spinning at 150 rpm and with the fluid grounded to the tomography system (ERT Hardware II and III), 50 frames were recorded. After calibration, air was introduced at 0.5 and 1.0 vvm at agitation rates of 100, 150, 200, 250, 300, 400 and 450 rpm using the gas-foil impeller. One hundred frames of data were captured for each condition.

3.6 Experimental Overview

An overview of the experimental approach and use of equipment in this study is given in Table 3.6. The ERT hardware and software systems, as numbered in the table, are defined in Chapter 4

Table 3.6: Overview of experimental approach and objectives

Fluid system	Technology	Phase of interest	Variables examined	Experimental Objective	Chap.
220 mm tank Industrial pipeline	ERT Hardware I Software I and II	Solid plastic objects (phantoms) Plastic beads (2 x 3 mm, ρ = 1460 kg.m^{-3}) Quartzite (710 -1180 μm, ρ = 2650 kg.m^{-3})	Superficial velocity Solids loading Particle size	1. Examine potential and capabilities of initial ERT system 2. Resolve swirling flow	5
220 mm tank, Rushton and pitched blade impellers	ERT Hardware I Software III	Quartzite (106 -212, 425-600 and 600-850 μm, ρ = 2650 kg.m^{-3})	Impeller type Particle size Agitation rate Solids loading	Examine particle suspension in stirred tank as a function of parameters and characterise homogeneity	6
220 mm tank	Pipette and conductivity probe	Quartzite (106-212, 425-600 μm, ρ = 2650 kg.m^{-3})	Particle size	Examine validity of ERT data through physical means	6
220 mm tank 50 mm tank Rushton impeller	ERT Hardware III Software V	Quartzite (600-850 μm, ρ = 2650 kg.m^{-3})	Vessel size Impeller tip speed	1. Examine capability of new ERT system 2. Examine effects of scale on particle suspension	7
MRI 50 mm tank ERT 50 mm tank	MRI ERT Hardware III Software V	Borosilicate ballotini (100 μm and 50 μm, ρ = 2200 kg.m^{-3}), nylon particles (600 μm, ρ = 1130 kg.m^{-3})	Agitation rate Particle size Particle density Solids loading Imaging technology	1. Examine potential of MRI 2. Examine particle distribution as a function of parameters at high spatial resolution 3. Compare tomographies	8
610 mm tank 220 mm tank, sparger, Rushton, gasfoil impeller	ERT Hardware II and Software IV ERT Hardware III and Software V	Air (submerged and surface aeration)	Agitation rate Aeration rate Vessel size	Examine aeration (surface and submerged) and quantify hold-up	9
MRI 50 mm tank ERT 50 mm tank Rushton impeller	ERT Hardware III and Software V MRI	Bakers' yeast (5 μm, 1050 kg.m^{-3}) nylon particles (600 μm, ρ = 1130 kg.m^{-3})	Agitation rate Solids loading Imaging technology	1. To detect and explore behaviour of a microbial phase 2. Simulate a slurry bioreactor	9

Chapter 4

ERT Hardware and Software

4.1 Introduction

Since this study was initiated in 2002, the ERT hardware and software available has been developing continuously. This advancement in capability will thus form part of this study to provide knowledge of the state of the art and a basis for evaluating the results of the reconstructed solid objects, swirling flow and solids suspension in the 220 mm and 50 mm tanks.

Three ERT hardware systems and five reconstruction programmes were used in this study and will be examined according to measurement principle and the main features of the electronic design, the calibration method and reconstruction algorithm, the finite element method and calibration processes. Analysis will commence with the earliest system.

4.2 ERT Hardware System I

As the potential of ERT in the process industries became increasingly apparent, a need arose to create an ERT instrument that was simpler than the conventional high frequency (typically 50 kHz) sinusoidal current systems at that time. ERT Hardware I was developed in 2001 at UCT by Bill Randall (Dept. of Chem. Eng.) and Andrew Wilkinson (Dept. of Elec. Eng.) to meet this need. The key features of this system are the application of direct current for electrode excitation, multiplexing and the differential amplifiers (Cilliers *et al.*, 2001). Reconstruction Codes I – III were employed with this system and are discussed in Section 4.3 – 4.5.

4.2.1 The Measurement Principle

This system operates on a bi-directional current pulse technique in which current to the injection pair of electrodes is kept constant during the positive and negative half cycles (Figure 4.1(b)). This system is current driven and thus independent of electrode impedance effects. The resulting potential difference between the pairs of pickup electrodes which is measured by a differential amplifier, is also constant during each half cycle (Figure 4.1(c)). Electrode polarisation is minimised through the use of the bi-directional current. Readings are taken during the two half cycles and subtracted to give a single data point. These measurements are taken over a short

time frame (< 1 ms), thus low frequency noise usually present in direct current (DC) systems is cancelled in the subtraction (Cilliers *et al.*, 2001; Randall *et al.*, 2001). A similar design was developed by Boone and Holder (1995) for medical applications although difficulties were experienced with the high electrode to skin impedance. This impedance is not present in aqueous solutions. With regard to the pickup electrodes, negligible current flows between the ions in solution and the electrodes and therefore no current-induced electrochemical reactions are present that could give rise to a transient voltage (Randall *et al.*, 2001).

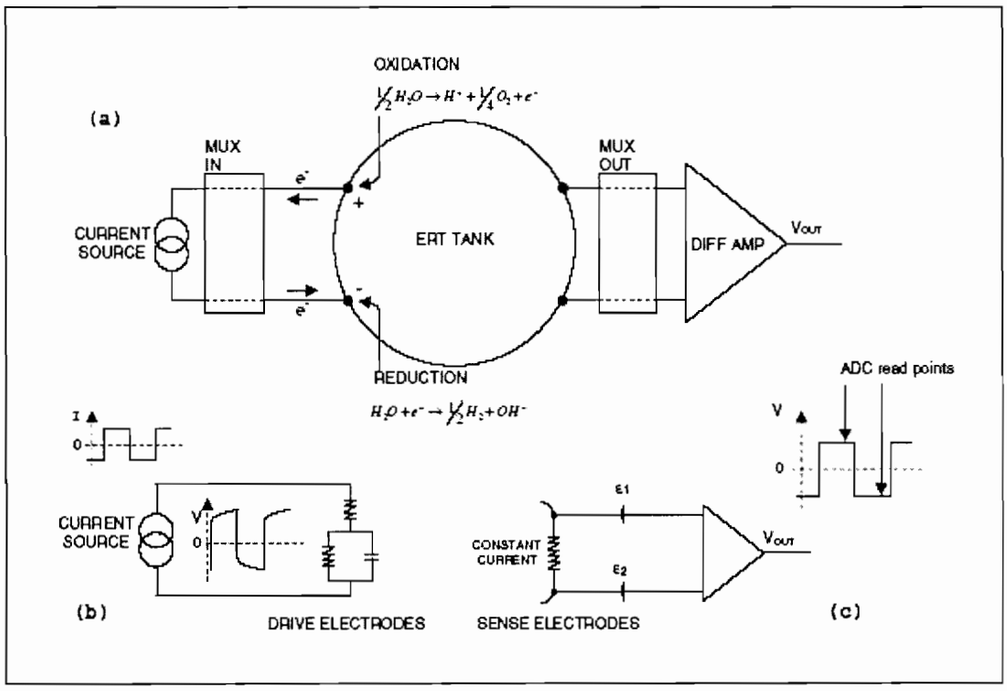


Figure 4.1: The current drive system to the pair of electrodes on the tank and the voltage recorded by a differential amplifier. Electrochemical reactions are shown at the drive pair but electrode polarisation is avoided with the bi-directional pulse (a). The current drive system to a pair of electrodes is represented in (b) with the impedance between the drive electrode pair modelled as a resistor-capacitor (RC) network. The constant current (conductivity of solution modelled as a resistor) and voltage out along with a depiction of the two Analogue to Digital Converter (ADC) read points on the square wave form is shown in (c). (Cilliers et al., 2001)

4.2.2 Measurement System

This ERT system consists of 16 electrodes, a multiplexing system (4 x 16 way devices), a bi-directional current source, a clock generator and a single differential amplifier. The electrodes were connected to the multiplexors by unshielded insulated copper wires, as it was assumed that electrical screening was not necessary at the

low frequencies tested (3 kHz). Using this system, a current is applied through the multiplexors to the necessary electrodes i.e. the excitation pair of electrodes in the measuring sequence. The multiplexor is then used to capture the voltage difference on the remaining pairs of electrodes where the signals are buffered and read by the ADC. A specific measurement sequence (Barber *et al.*, 1983) is used to acquire a single frame (104 unique readings) through electrode excitation (Table A1, Appendix A). The sequence was subsequently expanded to provide 182 measurements, although still only containing 104 unique measurements, with the extra readings being averaged to provide greater accuracy. The maximum acquisition rate was approximately 50 frames per second.

4.2.3 Calibration

With ERT Hardware I, calibration was implemented from the hardware side prior to data capture. Thus calibration code was written in machine code located on an embedded processor in the hardware and operated through initiating an executable file from DOS on a PC. A method of empirical scaling was applied to voltage measurements and is discussed with reference to Figure 4.2.

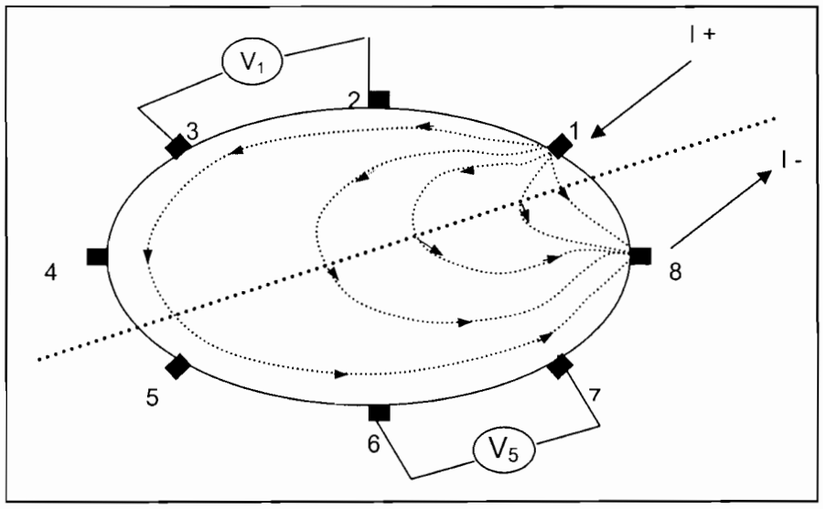


Figure 4.2: Hypothesised symmetry of current injection and voltage measurement for the method of empirical calibration applied to an eight electrode system (Naidoo, 2002).

If current is injected through electrodes 1 and 8 then the readings at V_1 and V_5 should be identical. Similarly if V_2 is measured between electrodes 3 and 4 it would be identical to V_4 (measured between electrodes 5 and 6). Averages are then taken for the voltages of the measurement sequence which correspond symmetrically (e.g. V_1 and V_5). This average is then divided by each voltage value to create a scaling factor. Each scaling factor is then multiplied by the original voltage value to produce a new

set of scaled voltages. For example, a raw set of 182 voltages (Figure 4.3) from a 16 electrode system can thus be normalized (Figure 4.4) and redundant measurements are averaged further to produce 104 calibrated data points prior to the experiment. These empirically – scaled measurements were then reconstructed using *Tomoview*, (Reconstruction Code I) which was developed at UMIST.

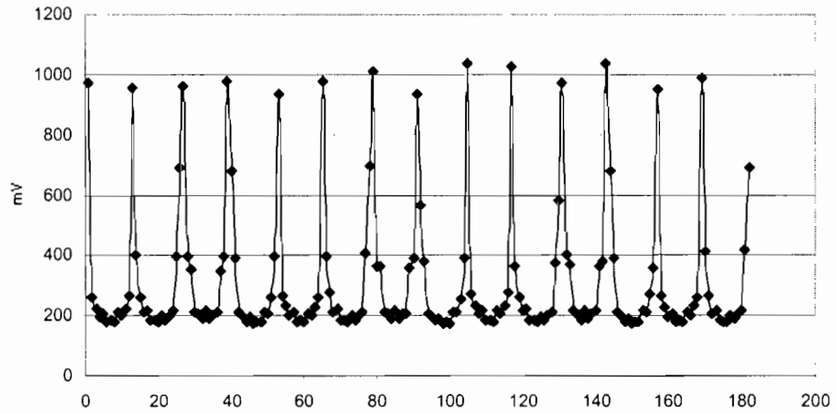


Figure 4.3: 182 raw un-scaled voltages from measurement sequence.

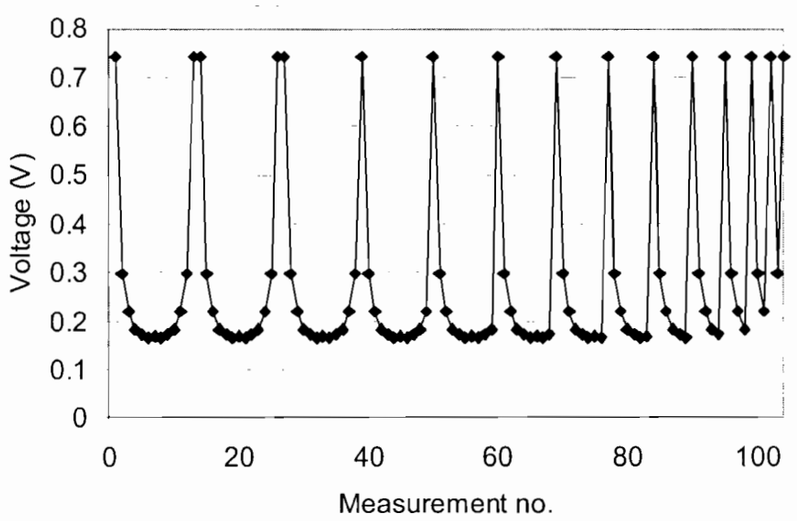


Figure 4.4: 104 empirically – scaled voltages from measurement sequence.

4.3 Reconstruction Code I

Tomoview, referred to as Reconstruction Code I in this study, was developed by Xie (2002) at UMIST (now the University of Manchester) in order to quantify the coalescence of flowing foams. This code contains two separate reconstruction numerical methods, the Newton-Raphson and Linear Back Projection (LBP) algorithms, and is written in C++. The LBP algorithm was programmed using the principal equation (Equation 2.9) with the sensitivity matrix, while the Newton-Raphson algorithm was based on Equations 2.11 and 2.12, but also included the Marquardt method (Marquardt, 1963) to improve the conditioning of the Hessian matrix and thereby increase accuracy. Conditioning further causes the update of Equation 2.11 to be sensitive to error measurement and thus smoothing is often required. The main feature of the Marquardt method is the use of a smoothing factor β which is effectively a regularisation of the matrix $f'(\rho^k)^T f'(\rho^k)$ (Huan and Woo, 1990). Equation 2.11 thus becomes:

$$\Delta\rho^k = -\{[f'(\rho^k)^T f'(\rho^k)] + \beta I\}^{-1}\{[f'(\rho^k)]^T[f(\rho^k)-V_0]\} \tag{4.1}$$

where I is the identity matrix and the initial value of β is often chosen as 0.001 (Xie, 2002).

A finite element mesh of 357 nodes and 616 triangular elements was created (Figure 4.5) for this endeavour. A comparison by Xie (2002) can be observed in Figure 4.6 where a non-conducting rod was moved around the inside of a 16 electrode vessel. It is clearly seen that the resolution of the object is greatly enhanced on application of the more quantitative Newton-Raphson algorithm, as illustrated in the lower row of tomograms.

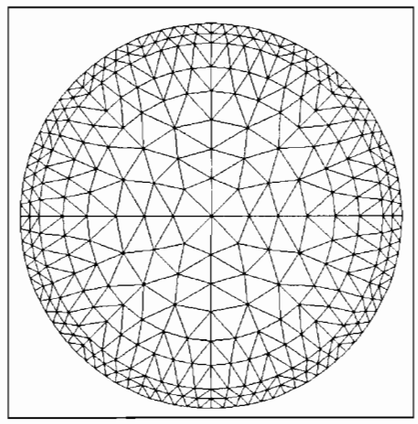


Figure 4.5: 2D FEM mesh containing 357 nodes and 616 triangular elements. There is a greater density of elements at the perimeter to account for larger voltage gradients.

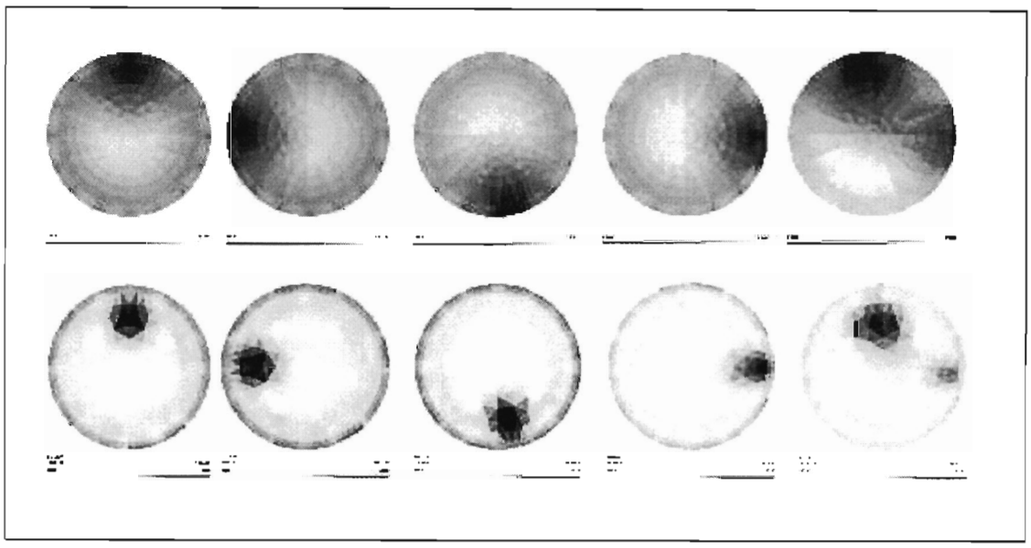


Figure 4.6: Reconstruction of a plastic rod in tank filled with water showing the implementation of the qualitative LBP algorithm (top row) and the modified Newton-Raphson algorithm (lower row). The far right tomograms were reconstructed after two plastic rods were placed in the tank (Xie, 2002).

Considering the LBP algorithm showed limited resolution for simple objects the N-R algorithm from this code was solely applied in experimentation. This N-R code did not include any filtering functions, although the relative conductivity range could be manipulated manually to improve the visual display. However, the Marquardt smoothing factor, β, was updated on applying each iteration. Convergence was attained when the mean squared difference between the estimated and measured voltage, $\Phi(\rho)$, was less than 0.001.

4.4 Reconstruction Code II

The open source EIDORS code was investigated in 2002 to implement 3D tomography to enable truer representation of objects compared to 2D interpolation. This code is comprised of a number of Matlab™ functions that can be compiled to cater for specific inverse problems (Section 2.7.5.10). A 2 x 8 electrode layer model (Figure 4.7) was used for this endeavour which allowed interplanar injections, although this decreased the 2D resolution due to the decrease in the number of unique measurements in an electrode layer. The Matlab™ code employing a number of EIDORS functions (Polydorides and Lionheart, 2002) to generate 2D object slices from 3D measurements is in Appendix B.

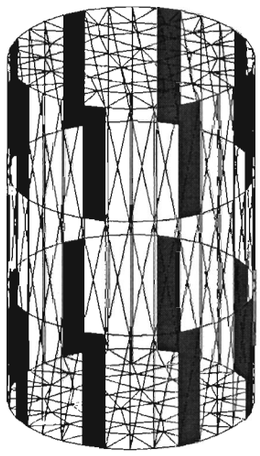


Figure 4.7: 2 x 8 electrode layer 3D EIDORS mesh with 92 elements (Polydorides, 2002).

This code relies heavily on a Tikhonov factor which smoothes the solution. This factor needs to be subjectively updated depending upon the quality of the image. Reconstruction time was in the order of 6 minutes on a 600 MHz processor due to the increased computation of the more complex Jacobian Matrix. The derivation of this matrix is detailed by Polydorides and Lionheart (2002) and includes the complete electrode model which accounts for electrode impedance.

4.5 Reconstruction Code III

This was the main code employed to investigate particle suspension in the 220 mm ID Perspex tank. It is written in Matlab™ as part of the M.Sc. dissertation of Naidoo (2002) from the Department of Electrical Engineering at the University of Cape Town. This code was designed incorporating a number of functions and visual aids, including *Tomoview* being assimilated into the Matlab™ menu (Figure 4.8).

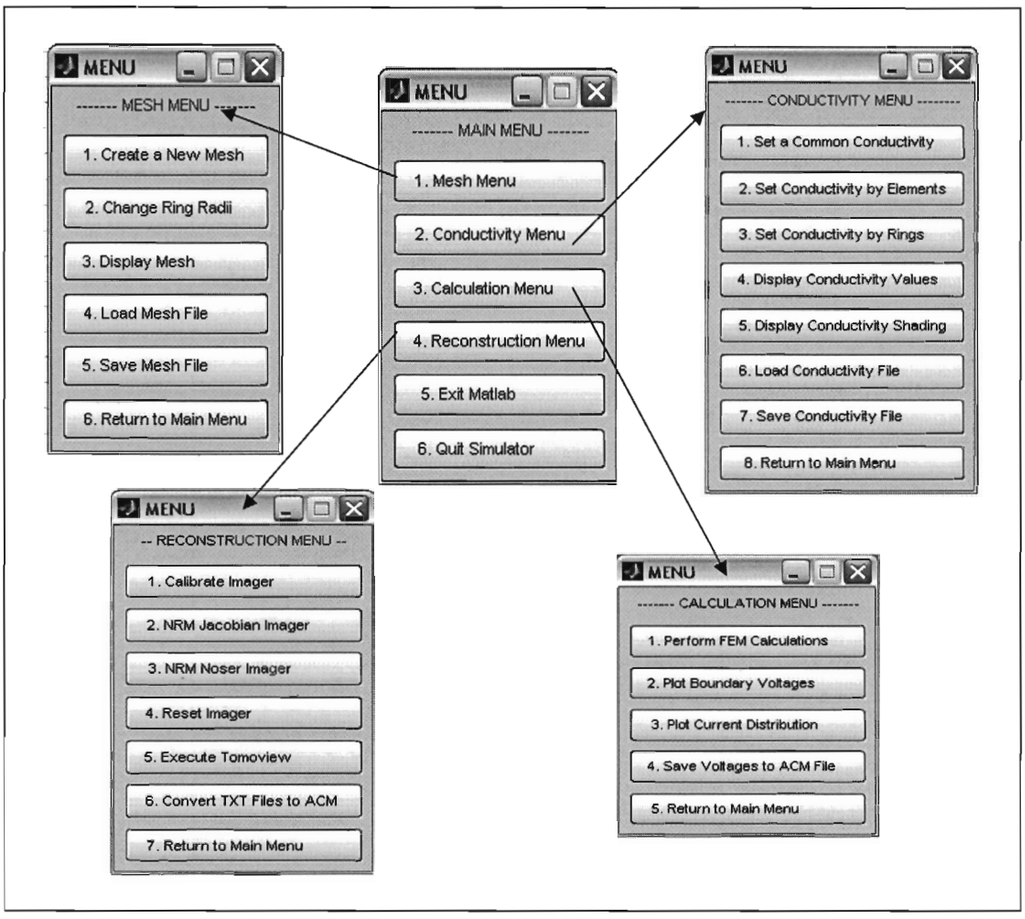


Figure 4.8: Matlab™ Reconstruction Code III showing functions available through submenus.

As seen in the 'Mesh Menu', a FEM mesh could be tailor made according to the number of elements and desire for a concentration of elements in a specific area. A 12-ring, 712 element mesh was created for the stirred tank investigation.

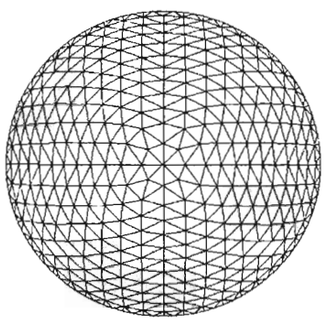


Figure 4.9: 12 ring, 712 element FEM mesh with a higher density of elements near the boundary to compensate for larger voltage gradients.

4.5.1 Calibration and Algorithm

With this code the calibration scheme was incorporated into the reconstruction software. Boundary voltages were produced from the forward solution and were found to be periodically dissimilar due to the FEM grid not being completely symmetrical to the electrodes. Thus these voltages were paired with the voltages of a homogenous tank (or reference condition) and scaling factors were found which matched the two data sets. These factors were recorded in a file and were used to multiply all subsequent data sets of the experiment prior to reconstruction.

A choice of algorithm was available with the modified Newton-Raphson or NOSER reconstruction methods. Newton's One-Step Error Reconstructor (NOSER) was proposed by Simske (1987) and presented in Cheney *et al.* (1990) in order to reduce the computation time. This speeding up is achieved through precomputation of the Jacobian Matrix. This reduces accuracy with successive iterations but concurrently reduces the solution time, thus being more attractive for online imaging. The modified Newton-Raphson algorithm was applied to the data from the stirred tank, and this algorithm included regularisation of the Hessian Matrix through the construction of a Smoothness Matrix (Pinheiro *et al.*, 1997) and application of a Tikhonov factor. This matrix aids the regularisation through weighting of neighbouring elements in the mesh.

4.5.2 Data Extraction

In the 'Conductivity Menu', the common conductivity of the clear fluid could be set, or the conductivity in the mesh by element or ring could be altered to examine numerical phantom effects. A function enabling the display of the 3D conductivity distribution in the plane was useful when preparing the optimum conditions prior to experiment. This helped to judge the relative differences in conductivities in the conducting medium e.g. distribution of quartzite. 'Display Conductivity Values' resulted in the reconstructed conductivities output. These values were recorded in a .txt file then exported to Excel© for analysis. Thirty frames of data were recorded per electrode layer for each experimental condition and averaged prior to reconstruction. Post-reconstruction, the data for each ring was averaged thereby creating 12 conductivity data points for the radial plane. Data representing the baffle area was eliminated prior to averaging.

4.6 ERT Hardware System II

A brief opportunity arose to test a commercial ERT system, ITS2000 (www.itoms.com), while performing qualitative experiments at the Department of

Chemical Engineering, UMIST. The key features of the original system (Mann *et al.*, 1997) were:

I. A sine wave generator used in conjunction with a voltage controlled current source and a multiplexer which injects alternating current into the electrode pairs.
II. Resulting voltages were multiplexed into a differential amplifier followed by a programmable gain amplifier.
III. The amplifier output was fed into a phase sensitive demodulator-low pass filter to provide voltage for digitisation by a 12 bit ADC.
IV. Data from the ADC was fed via a microcontroller to the host computer.

This system was since improved (Lucas *et al.*, 1999) as follows:

I. Demodulation was performed in software thus overcoming the settling time of the low pass filters used in the hardware.
II. Data was transferred to the host computer using an ISA bus, allowing data transfer rates of approximately 1 $MB.s^{-1}$.
III. A direct synthesis IC (AD7008) was used to generate the sine waveform, resulting in distortion as low as -55 dB.

This system resulted in an acquisition rate of 100 frames per second.

As observed, the alternating current injection introduces more complexity which results in higher cost and had slower acquisition rates than ERT Hardware III. This hardware was tested with software containing a qualitative algorithm, Reconstruction Code IV. At present, Leeds University have an AC system which is reported to operate at 1000 frames per second.

4.7 Reconstruction Code IV

This commercial ITS 2D code (www.itoms.com) employed the LBP algorithm described in Section 2.7.4.4.1 based on Equations 2.7 and 2.8. User-friendly options were available with data visualisation as stacks of images, while electrode layers could be visualised together. Further processing of images is applied to remove blurring from the backprojection process using a spatial frequency filtering operation. Tomograms consist of a 20 x 20 grid of pixels as shown in Figure 4.10.

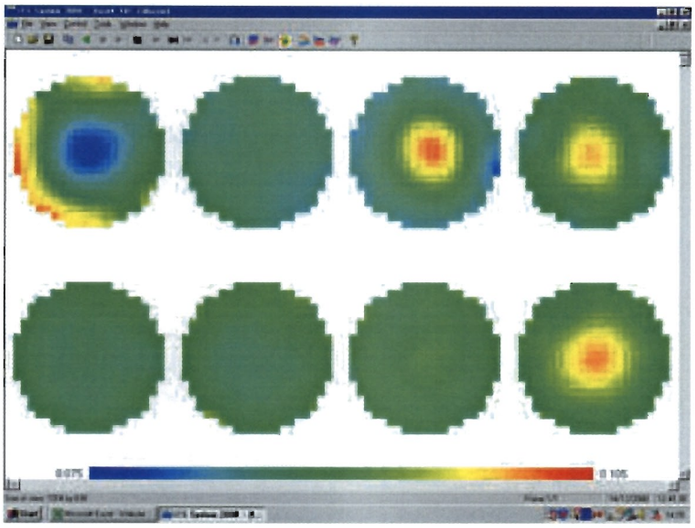


Figure 4.10: LBP reconstructed tomograms for the 8 x 16 electrode layer tank as detailed in Section 3.5.

4.8 ERT Hardware System III

This system is the latest implementation of a current pulse technique from the University of Cape Town characterised by a data acquisition speed of 1000 frames per second (Wilkinson *et al.*, 2005). This high speed was necessitated by the examination of transient phenomena in fluid systems, while a prime design criterion was the use of low cost and readily available components. The system is based on ERT System I, however certain modifications were introduced to increase the speed:

I. Multiple input amplifiers were installed so that all voltage differences between the sense electrodes could be measured during a single current injection (bipolar). Through this implementation the number of current pulse injections was reduced from 104 to 14.
II. The voltage sensing amplifiers were followed by high-speed sample and holds which were strobed simultaneously at the positive and negative current half cycles.
III. Timing was improved by the ADC on the PC card being intitiated by a hardware trigger generated by a microcontroller at the maximum rate of the Eagle PCI703 card (400 kilo-samples/second), while timing was not affected by the operating system (Windows) response.

4.9 *Reconstruction Code V*

This C++ code is currently being developed (Long, 2006), but it was available for testing in various beta versions which included the main reconstruction functions (Figure 4.11). The primary objectives of this code are to enable simultaneous layer reconstruction and display (Figure 4.12), while allowing online measurement. Multiple user functions have been included to aid visualisation e.g. 3D conductivity distribution in the plane, display of raw voltages, display of calibrated voltages, noise display, ability to record an online process and convert into an .avi file, the selection of electrode layers or individual electrodes. C++ was preferred over Matlab™ due to its increase in speed and for the real time front end (Wilkinson, 2005).

An offline version was also created for more rigorous reconstruction. This was mainly used for the data from the 50 mm ID stirred tank. This program allowed choice of a Tikhonov factor (normally set at 0.0001) and precomputation of the Jacobian Matrix, while tailor-made meshes could be loaded.

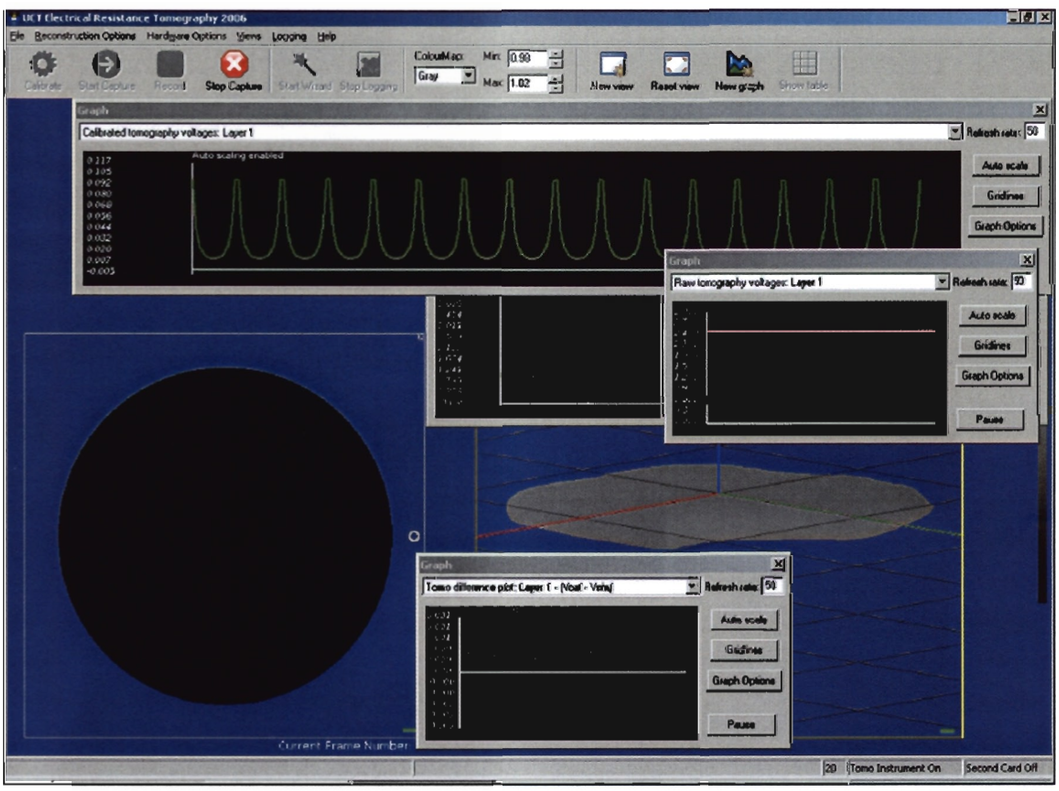


Figure 4.11: Screenshot of Reconstruction Code V showing raw and calibrated voltages with 3D visualisation of the conductivity distribution. Multiple layer (8) viewing is possible as well as online reconstruction.

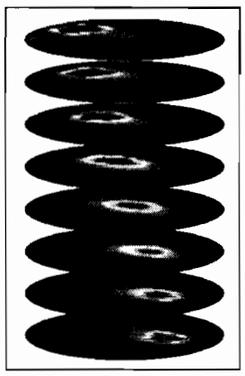


Figure 4.12: Stack of layer tomograms from a glass fibre rod of 20 mm diameter placed in an 8 electrode layer tank (T = 200 mm) at an angle.

4.9.1 The Algorithm

The algorithm was the same as Reconstruction Code III; however the regularisation was implemented slightly differently. An average radius of the surrounding element midpoints was calculated and a matrix was generated which gave increased weighting to the smaller or nearer elements. This matrix was then multiplied by the chosen Tikhonov factor to introduce a relaxation term in the algorithm. In the case of irregular meshes (Figure 4.13), smaller elements are present at the perimeter and near the baffles, thus more regularisation would occur in these regions.

4.9.2 Meshes

In order to improve the FEM solution the mesh should model the actual geometry as closely as possible. With Reconstruction Code III the mesh consisted of concentric rings and thus the effects of the baffles and impeller were ignored. Using a freeware program, *Mesh Creator*, different mesh geometries were investigated. The mesh most commonly used was that created to model the baffles while incorporating the impeller (Figure 4.13(a)), although reconstructions were investigated with the impeller excluded (Figure 4.13 (b)). Again, a higher density of elements was ensured near the perimeter. Regular meshes (i.e. exhibiting radial symmetry) tend to be more accurate in reconstructions, but this was not possible with this design and the program used.

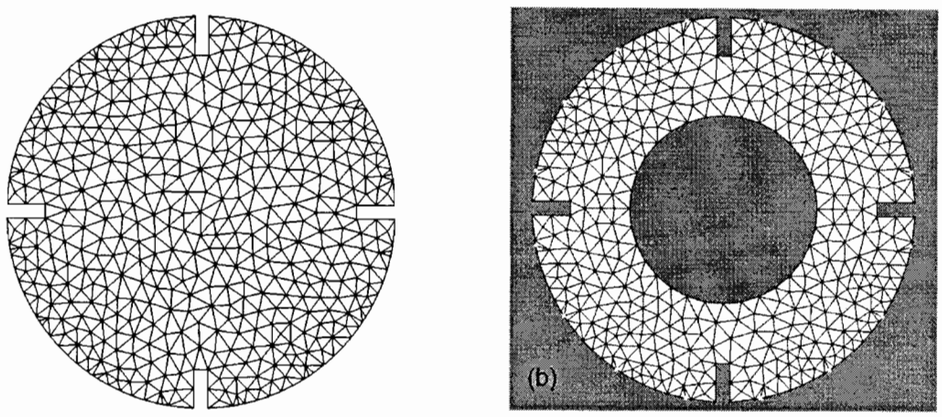


Figure 4.13: 934 element baffled irregular mesh (a) and the 788 element irregular mesh (excluding impeller zone) created with *Mesh Creator* (b).

4.9.3 Calibration

The empirical calibration method (Section 4.2.3) was found to have limited accuracy and an improved method was established. This method measures the DC offsets by injecting zero current. A gain correction factor is then computed for each measurement by comparing the measured voltage with that predicted by the finite element method (Wilkinson, 2005).

4.9.4 Data Extraction

One hundred data frames were recorded for each experiment. Each recorded frame was an average of 25 frames, thus data from 2500 frames were effectively captured. Each frame contained 208 measurements i.e. the full matrix depicted in Appendix A, and redundant measurements were averaged for greater accuracy. The .tom data file containing 100 frames was first averaged prior to reconstruction using the Matlab™ code in Appendix C. The output post-reconstruction was in .csv file format, however, there were too many columns to allow visualization in Excel so the data was transposed using the code in Appendix D. Since the mesh was irregular, twelve radial divisions were created so that conductivities could be averaged in these sections while still maintaining a degree of similarity with the mesh used in Reconstruction Code III for the 220 mm ID stirred tank.

4.10 Summary of ERT Systems Used in Experimentation

The hardware and software examined in this chapter are referred to throughout this study and have been summarised for ease of reference in Table 4.1. A further system has been recently developed at the University of Cape Town and is reported by Wilkinson *et al.* (2006). This system was not used in this study.

Table 4.1: Summary of ERT hardware and software used in this study

ERT System	Principal Features	Reference
Hardware I	Bi-directional direct current pulses, ADC read points on square wave, calibration written in machine code, 50 frames/s, developed at UCT	Cilliers *et al.* (2001), Randall *et al.* (2001),
Hardware II	Sine-wave generator, voltage controlled current, phase sensitive demodulator-low pass filter, 12-bit ADC, relatively expensive, 100 frames/s, developed at UMIST (University of Manchester)	Mann *et al.* (1997), Lucas *et al.* (1999)
Hardware III	Upgrade of Hardware I, multiple input amplifiers, high speed sample and holds, 8 multiplexers, timing through hardware trigger from microcontroller, 1000 frames/s, developed at UCT	Wilkinson *et al.* (2005)
Reconstruction Code I	*Tomoview*, separate 2D LBP and N-R algorithms, with N-R algorithm improved with Marquardt smoothing, 616 element mesh, manual conductivity threshold manipulation to aid visual display, developed at UMIST	Cilliers *et al.* (2001), Randall *et al.* (2001), Xie (2002)
Reconstruction Code II	EIDORS, open source 3D code, toolkit of Matlab™ functions, modeling of current patterns, Tikhonov regularization, visualization of 2D slices from solution matrix, 2 x 8 electrode 92 element mesh, developed at UMIST	Polydorides and Lionheart (2002)
Reconstruction Code III	2D Matlab™ code, incorporation of *Tomoview*, tailor-made concentric regular meshes, twin-scale calibration in software, modified N-R through construction of smoothing matrix, 2D and 3D visualisation of conductivity distribution, developed at UCT	Naidoo (2002), Wilkinson *et al.* (2005)
Reconstruction Code IV	2D LBP based code with spatial filtering, calibration in software, tomogram image stacking, multiple tomogram display, 20 x 20 pixel grid, commercial code, ITS (Pty) Ltd	www.itoms.com Mann *et al.* (1997)
Reconstruction Code V	2D code in C++, online capability and multiple layer (8) viewing, gain corrected calibration, 3D viewing of conductivity distribution, variable offline reconstruction, video capture, line stacking of conductivity gradient, tailor-made irregular mesh compatibility, precomputation of Jacobian Matrix to increase speed, developed at UCT	Long (2006)

Chapter 5

ERT as an Applicable Technology

5.1 Introduction

On commencing this study, limited solid-liquid applications had been examined with the newly created ERT system (ERT Hardware I), and thus the capabilities remained largely unknown. It was decided to examine increasing levels of complexity before examining the stirred tank system with irregular distribution of solids and complex geometry. Simple phantoms, therefore, were initially explored followed by the analysis of a more complex solid-liquid swirling flow pipeline to validate the applicability of the ERT hardware as an analysis tool.

5.2 Examination of Phantoms

Objects of known geometry and attenuation properties are classically used to validate and to test the potentialities (e.g. resolution, sensitivity) of a tomographic technique (Fransolet *et al.*, 2002). These objects can be real or simulated numerically, and are called 'physical' or 'numerical' phantoms. In this study static physical phantoms were investigated.

5.2.1 2D Slices of a Phantom in the 220 mm ID Tank

ERT Hardware System I was connected to the Perspex tank described in Section 3.1. Saline solution (20 °C, NaCl = 50 $mg.l^{-1}$) filled the tank to provide an aspect ratio of 1 (H = D). Calibration was performed using the empirical calibration method incorporated into the hardware (Section 4.2.3). A plastic non-conducting cylinder was placed near the perimeter inside the tank and data was captured for the four electrode layers. The data was reconstructed with four iterations of the Newton-Raphson algorithm, included in the *Tomoview* program (Reconstruction Code I). This data is displayed in Figure 5.1 using Matlab™ code in Appendix E. As observed in these tomograms, the reconstruction is more representative for Layers 1 and 4 compared to the actual object (Figure 5.2). This is most likely due to the inhibition of the electric field lines in the axial direction by the physical boundary of the bottom of the tank (L1) and the liquid surface (L4). This inhibition relates to the assumption of the 2D algorithm employed in the *Tomoview* software. The reduced representation in layers 2 and 3 is postulated to result from the greater magnitude of axial bending of

the electric field lines leading to a lower concentration of horizontally orientated field lines (Figure 5.3).

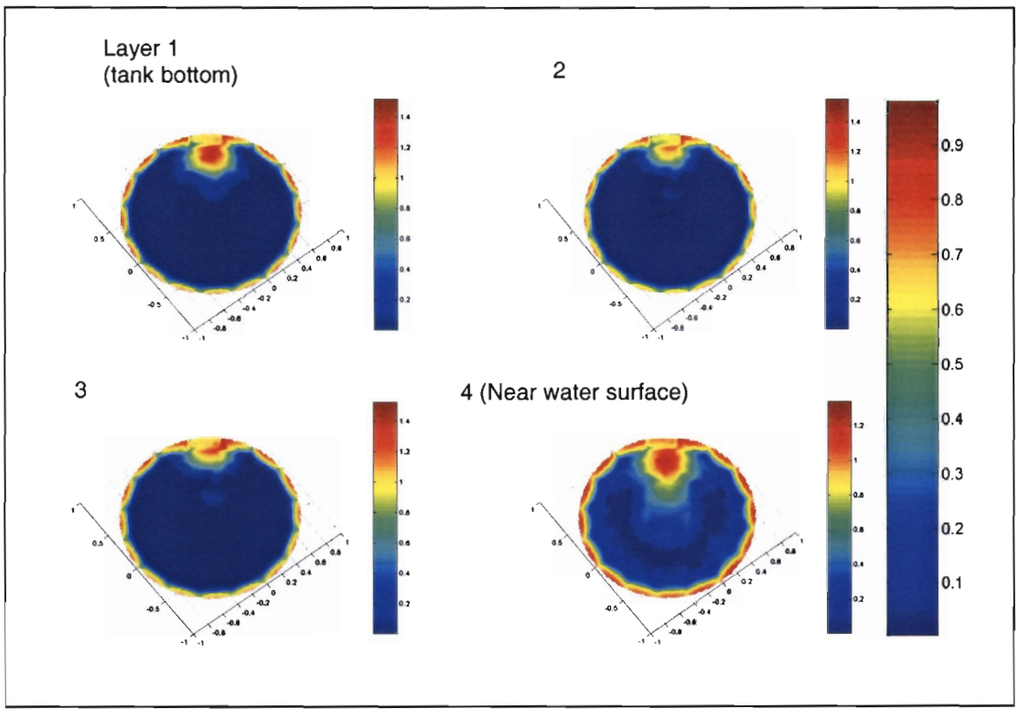


Figure 5.1: Tomograms of the phantom (measuring cylinder) in the 220 mm ID tank with Layer 1 closest to the tank bottom.

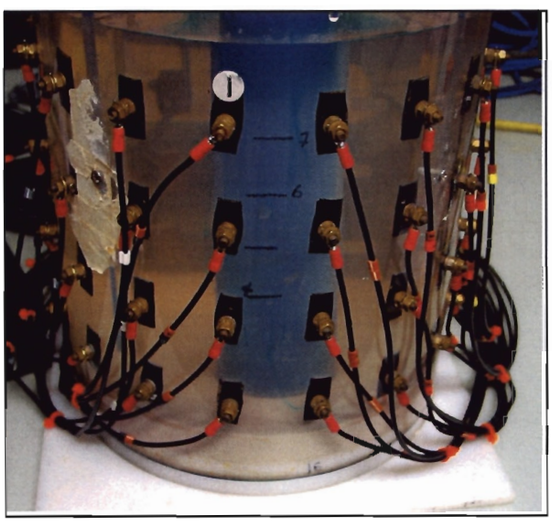


Figure 5.2: The plastic measuring cylinder orientated near the vessel wall in the 220 mm ID tank.

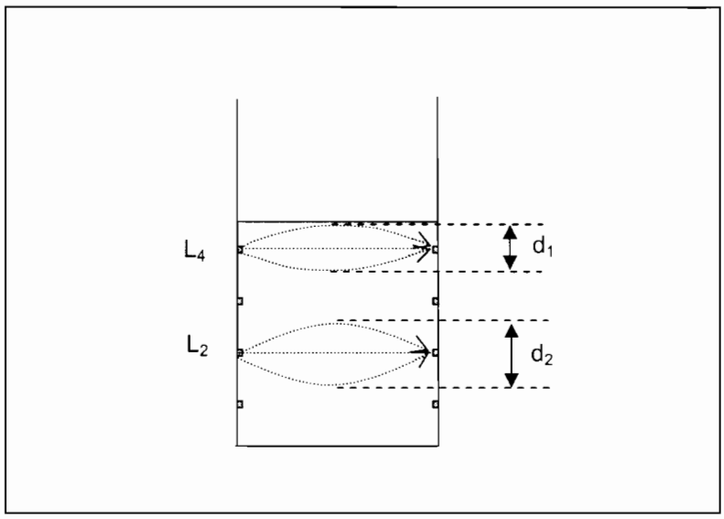


Figure 5.3: Comparison of axial behaviour of field lines originating from the middle of the tank (L2) and near the liquid surface (L4) showing $d_1 < d_2$.

5.2.2 3D Interpolated Images

Combining the 2D slices obtained from the phantom examination and interpolating between electrode layers at a relative threshold conductivity of 0.6 led to the creation of a 3D surface. This was performed using the Matlab™ code given in Appendix E.

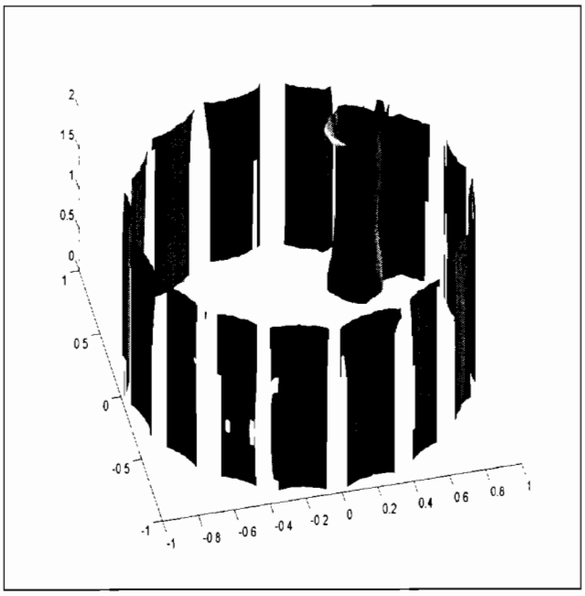


Figure 5.4: 3D interpolated image of the phantom from 2D slices from L1-4

In Figure 5.4 the 3D image of the phantom is clearly observed. The non-conducting Perspex of the tank wall between the electrodes has approximately the same relative conductivity as the plastic phantom. Thus, at the threshold conductivity of 0.6 these areas are also represented. This image was produced with ERT Hardware I and Reconstruction Code I with the interpolation performed with Matlab™ (Appendix E). These perimeter anomalies have been minimised with the latest code (Reconstruction Code V) combined with more accurate calibration and measurement (ERT Hardware III). This can be observed in Figure 4.12 where the stack of images of the rod has clearly a different relative conductivity and there are minimal aberrations near the vessel wall. This later technology thus provides greater accuracy in object definition.

5.2.3 3D Examinations of Phantoms with EIDORS

Pure 3D tomography of phantoms was investigated using Reconstruction Code II while employing the 8 electrode, 2 layer model with interplanar injections. ERT Hardware I was used with the wiring altered to conform to the model in Figure 4.7. A calibration set of measurements was recorded prior to inserting the same plastic phantom in the saline tank, followed by the usual injection sequence (Barber *et al.*, 1983). The data was loaded into the **slicer_plot** program (Appendix B) which employs a range of EIDORS Matlab™ function files. 2D slices were taken at increasing heights of the calculated conductivity distribution and the resulting phantom is shown in red. Although 2D slices are represented, they are calculated from interplanar injections and thus no interpolation is used to represent the different heights in the 220 mm ID tank. The phantom was submerged and thus there is a weaker depiction of non-conduction at the top of the tank (slice no. 6, Figure 5.5). However, resolution is poor with 8 electrodes per layer and further inaccuracy could result from the measuring sequence not being optimised for the model (Polydorides, 2002).

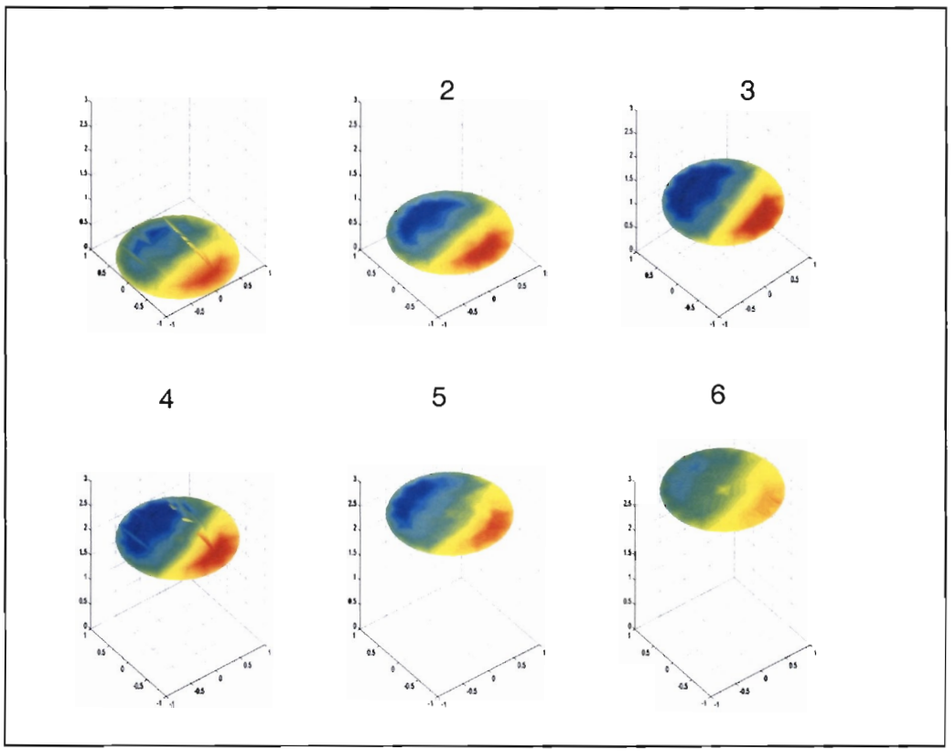


Figure 5.5: 2D slices of a 3D conductivity distribution while examining a submerged phantom using Reconstruction Code II. Slices are numbered and represent increasing height in the tank.

5.2.4 Conclusions

With Reconstruction Code I and further processing with Matlab™, phantoms were clearly identified and more complex visualisation was achieved through the interpolation of 2D tomograms into a pseudo-3D image. A weakness was observed in reconstructing the middle layers of electrodes due to the assumptions of the 2D algorithm. 3D tomography was investigated with Reconstruction Code II and the program in Appendix B; detection of the phantom was achieved although it was lacking in resolution relative to the 2D algorithm of Reconstruction Code I. Thus no further experiments continued with 3D tomography or Reconstruction Code II. A review of the initial ERT systems tested is presented in Table 5.1.

Table 5.1: Review of initial ERT systems

ERT Hardware I Combination	Detail	Limitation
Reconstruction Code I	-Measurement over 4 separate layers (4 x 16 electrodes) -N-R algorithm applied	-Non-conductivity effects from vessel wall e.g. Perspex detected. -Conductivity effects from vessel height (2D algorithm assumptions) -Basic calibration, part of ERT Hardware I
Reconstruction Code II	-Measurement over 2 combined layers (2 x 8 electrodes) -3D reconstruction through EIDORS	-Limited resolution -Long computation time -Basic calibration, part of ERT Hardware I

5.3 Examining Flowing Solid-Liquid Systems with ERT

5.3.1 Introduction

Applying the best available ERT system at that time, ERT Hardware I and Reconstruction Code I, the phenomenon of swirling flow was investigated at the School of Chemical, Environmental and Mining Engineering at the University of Nottingham in 2002. The apparatus and solid-liquid environment are described in Section 3.2. The study of this simpler solid-liquid system was ideal prior to the examination of the stirred tank in order to examine the measurement potential of ERT. However, the study of swirling flow is of interest in its own right due to the suspension of particles at lower pumping power, improved particle mixing and the reduced erosion of pipeline bends due to slurry attrition. Swirly-flo boiler tubing (Wood *et al.*, 2001) induces the swirling motion which leads to greater dispersion of particles within the pipe thereby leading to reduced erosion of the pipe wall.

Previous attempts to monitor the swirling flow with LDA technology had achieved limited success. With denser slurries LDA was hindered due to the opacity and thus the structure of the swirling flow remained unexamined. ERT therefore provided the potential ability for non-invasive visualisation of the swirling flow structure. ERT had been previously applied to pipelines as reviewed in Section 2.7.5.5 (Fangary *et al.*, 1998; Lucas *et al.*, 1999; Ma *et al.*, 2001), while more recently Wood and Jones (2003) examined swirling flow with ERT although only two dimensional visualisation of flow structure was presented. Furthermore, these authors did not examine fine particles in the pipeline.

The system was initially calibrated. Thereafter data were recorded sequentially from each layer using ERT Hardware I. This was achieved through manual switching between electrode layers. Images were produced with Matlab™ after using

Reconstruction Code I followed by further implementation of the code in Appendix E. Images are generally examined qualitatively to ascertain the ability of the ERT system, however, quantitative analysis is performed regarding particle bulk flow and particle deposition along the pipe section. Two solid-liquid components were examined in the pipeline: plastic beads (S.G. = 1.46) and quartzite (S.G. = 2.65) within saline solution (100 $mg.l^{-1}$ NaCl).

5.3.2 Swirling Flow: Bead-Water System

Beads at concentrations of 2, 3 and 4 mass % were introduced into the pipeline and circulated at superficial velocities ranging from 0.5 to 2.5 $m.s^{-1}$. These concentrations are considered on the lower end in slurry conveyance, however, optimal definition of the flow structure was desired with ERT before attempting higher concentrations of solids. Details of the solid and liquid phases are presented in Sections 3.2.3 and 3.2.4.

5.3.2.1 2 % Bead Concentration

At a fluid velocity of 0.5 $m.s^{-1}$, slugs of beads followed by regions of clear fluid developed as illustrated in Figure 5.6. Hence a dynamic situation ensued where particle concentration was dependent upon time. This was not ideal for ERT Hardware I as layers could not be activated simultaneously. Furthermore, the high density of beads lying on top of the electrodes (e.g. Layer 4 in Figure 5.6) led to an increasingly high voltage requirement which could result in erroneous data due to the voltage limits of ERT Hardware I (2047 mV). The velocity was thus increased to 1.0 $m.s^{-1}$ whereupon the first signs of an angular velocity component were visible with settling of beads occurring further along the pipeline (Figure 5.7). Furthermore, at this speed there were no presence of slugs or time dependent motion. The velocity was then doubled to 2 $m.s^{-1}$, shown in Figure 5.8. The swirling motion predominated with minimal settling occurring by the fourth layer of electrodes. Data was recorded for these conditions and reconstructed to produce the set of tomograms corresponding to the four electrode layers in Figure 5.9 (a) and (b).

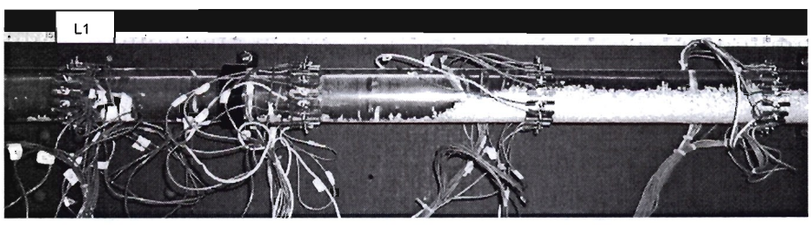


Figure 5.6: 2 % bead concentration at 0.5 $m.s^{-1}$ resulting in slug formation. L1 is on the left and nearest to the boiler tubing which induces the swirling flow. This flow condition was undesirable for ERT application with ERT Hardware I.

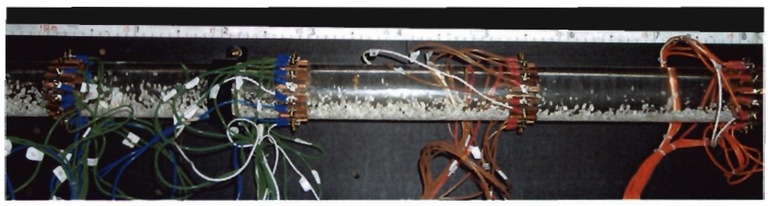


Figure 5.7: 2 % bead concentration at 1.0 m.s^{-1} where angular components are visible at L1, but dissipate towards L4 resulting in deposition at the pipe bottom.

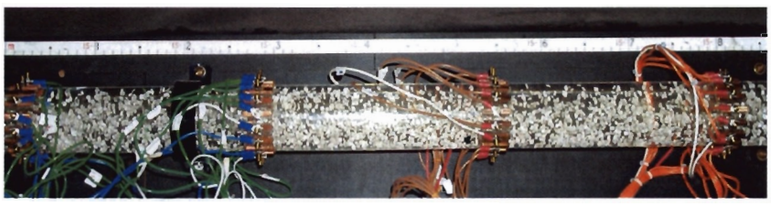


Figure 5.8: 2 % bead concentration at 2.0 m.s^{-1}. Beads appear spread out on the pipe wall due to the higher velocity.

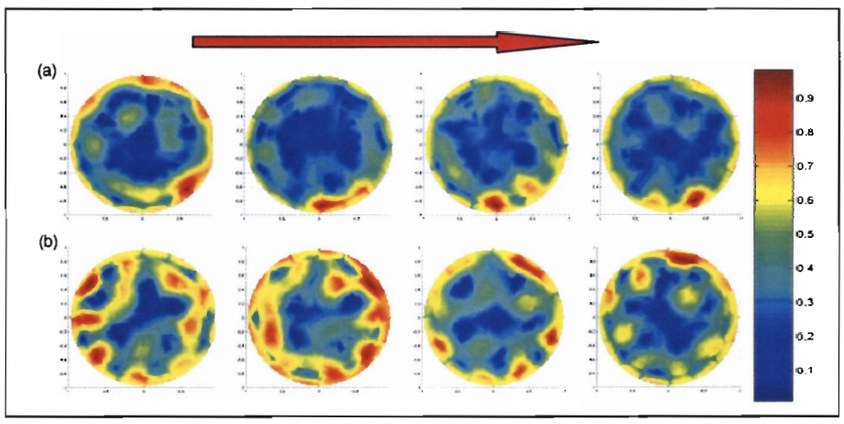


Figure 5.9: Tomograms for 2 % bead concentration at 1.0 m.s^{-1} (a) and 2.0 m.s^{-1} (b). Flow travels from left to right (arrow) with L1 on the left. The colour bar represents relative conductivity with red represented as non-conducting, or the greater presence of beads.

The tomograms shown from left to right in Figure 5.9 correspond to the planes of electrodes on the Perspex pipe, thus the first tomogram in the set of four is closest to the boiler tube in which swirling flow is established. In each tomogram, progression of colour from blue to red represents decreasing conductivity, thus red colours represent the presence of non-conductive elements in the plane and, thereby, the

position of the majority of the plastic beads. In Figure 5.9(a) the red portion representing areas of non-conduction i.e. higher bead density appears slightly at an angle on the pipewall in L1, before this bulk section moves to the bottom of the pipe (L4). This is in accordance with Figure 5.7. At the higher velocity of 2 $m.s^{-1}$ (Figure 5.9(b)), the tomograms have red and yellow areas indicating the greater presence of beads near the perimeter. This is similar to Figure 5.8 as the beads are well distributed around the perimeter and have not settled at the pipe bottom.

5.3.2.2 3 % Bead Concentration

The behaviour of a 3 % suspension at increasing velocity is presented in Figure 5.10. In Figure 5.10(a), the 3 % suspension of beads was at the lowest velocity studies of 1 $m.s^{-1}$. On examining the first tomogram, the beads are seen slightly up the side of the pipe wall and settle at the bottom of the pipe in the later tomograms at increasing distance from induction of swirling flow. In Figure 5.10(b), the beads can be seen to be suspended higher up on the pipe wall in the first tomogram, due to the increase in superficial velocity with respect to the conditions used in Figure 5.10(a). There is also a greater distribution of the beads around the perimeter due to an increase in centrifugal forces. This trend continues in Figure 5.10 (c). The movement of the higher bead concentration of 3 mass % appears to be more distinct in these tomograms (Figure 5.10) than the 2 % concentration tomograms (Figure 5.9). This difference in flow structure can be observed photographically when comparing Figure 5.8 with Figure 5.10. Thus a critical momentum of particles is needed before developing the swirling flow structure.

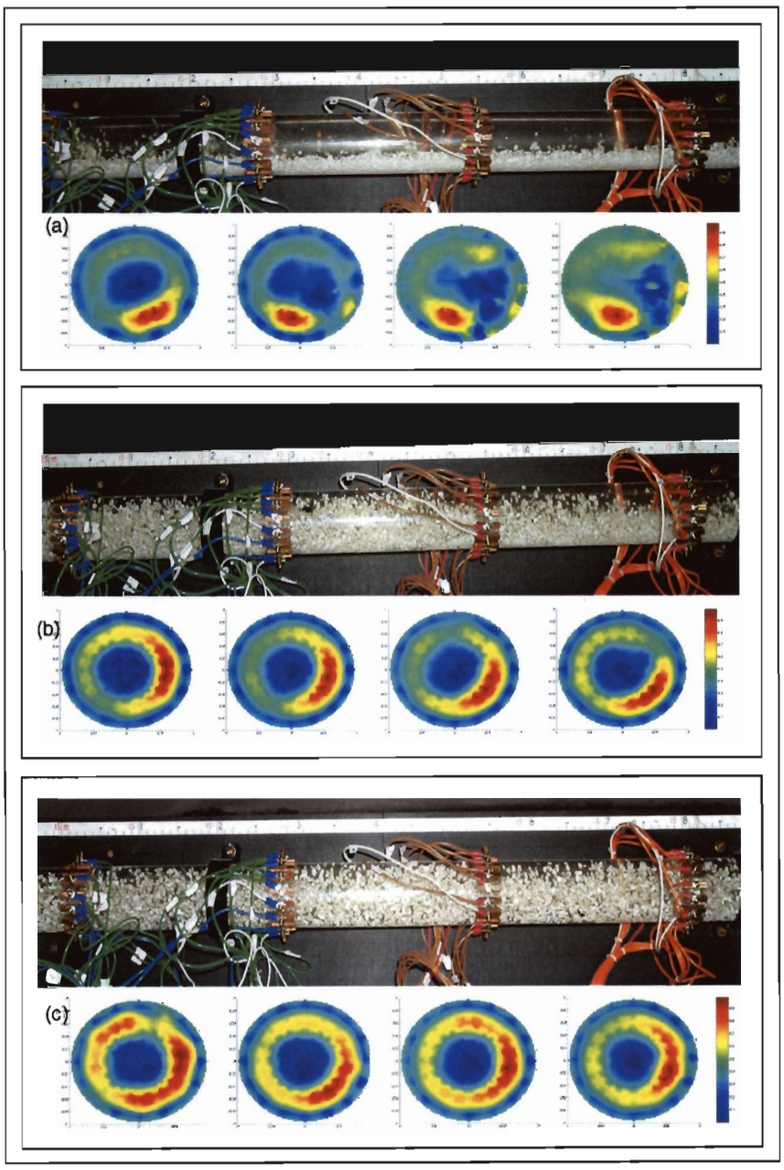


Figure 5.10: 3 % bead concentration at 1.0 m.s^{-1} (a); 1.5 m.s^{-1} (b); 2.0 m.s^{-1} (c)

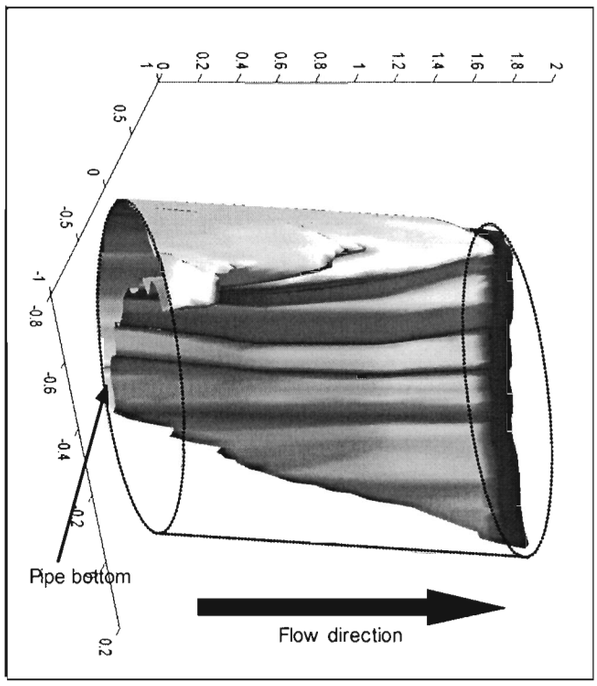


Figure 5.11: 3D surface generated with Matlab™ from the tomograms in Figure 5.10 (b) showing the bulk flow of beads swirling for 3 % bead concentration at 1.5 m.s^{-1}. The fluid is flowing as designated by the arrow.

Using the Matlab™ program in Appendix E the tomograms from Figure 5.10 (b) were interpolated to generate the 3D surface of the bulk flow of beads swirling illustrated in Figure 5.11. Such a clear representation of swirling flow had not been observed previously, nor could LDA technology allow such visualisation. Examining this flow structure shows the greater dispersion of particles compared to normal slurry conveyance, thereby supporting the decrease in pipewall erosion as observed by Wood *et al.* (2001). Furthermore, these authors modelled the pipe erosion and found the net effect of swirl flow to be beneficial. Such a visualisation as Figure 5.11 can therefore aid CFD modelling and increase understanding.

5.3.2.3 4 % Bead Concentration

Similar investigations proceeded with the 4 % concentration of beads relating tomograms to photographs (Figure 5.12) and the interpolation of Figure 5.12 (b) to represent the bulk flow of beads in 3D visualisation (Figure 5.13). The photograph in Figure 5.12 (a) appears well matched to the tomograms of the same conditions. Comparing the same superficial velocity, but different solids loading (Figure 5.12(a) and Figure 5.10 (b)) i.e. 4 % and 3 % at 1.5 $m.s^{-1}$, shows a greater conglomeration of beads at the higher mass loading. Thus to ensure the positive effects of swirling flow when increasing solids loading it is imperative to increase the superficial velocity. Although it must be noted that the velocity is still less than that required using regular pipes when conveying slurry (Wood *et al.*, 2001). Comparing the two 3D interpolations, Figures 5.11 and 5.13, the effect of the higher velocity is apparent with most of the bead bulk flow still on the side of the pipe wall at L4 in Figure 5.13.

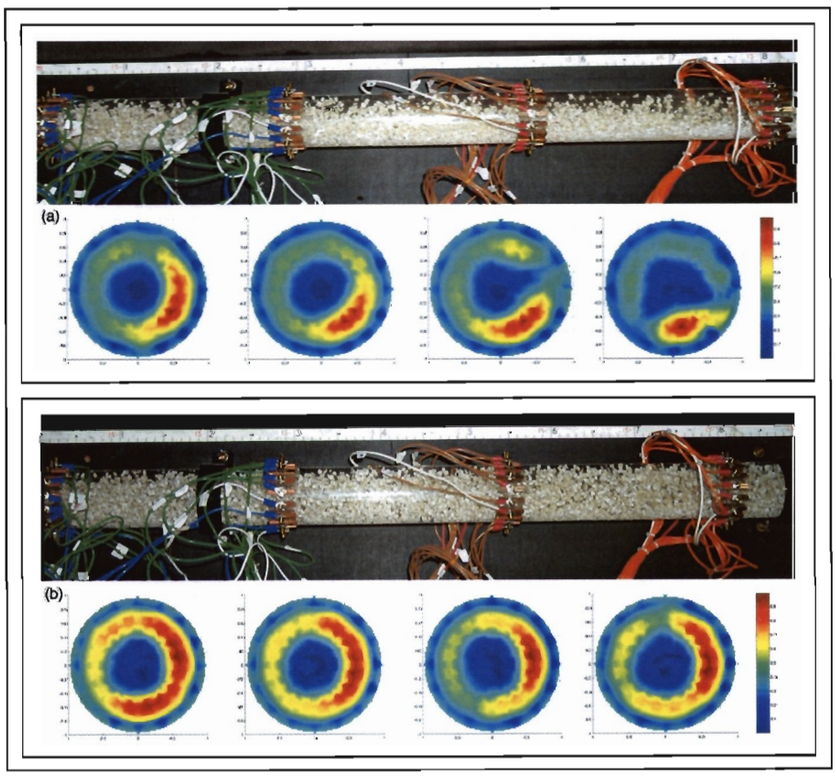


Figure 5.12: 4 % bead concentration at 1.5 $m.s^{-1}$ (a) and 2.0 $m.s^{-1}$ (b).

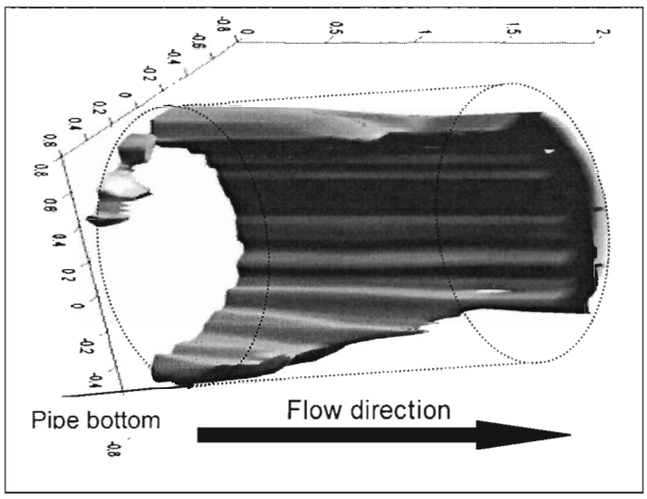


Figure 5.13: 3D surface generated with Matlab™ from the tomograms in Figure 5.12 (b) showing the bulk flow of beads swirling for 4 % bead concentration at 2.0 m.s^{-1}. The fluid is flowing as designated by the arrow.

5.3.3 Swirling Flow: Quartzite-Water System

In view of the plastic beads (2 x 3 mm) having been detected by ERT Hardware I the investigation continued to smaller particles, namely quartzite of approximately 1 mm diameter (size distribution given in Figure 3.16). This size and type of particle is more typical of slurry bioreactors than the plastic beads, and was thus of interest. At a concentration of 2 mass % and 2 m.s^{-1} the quartzite appeared opaque and homogenous near the outlet of the swirly flow boiler tubing (Figure 5.14), thus LDA techniques were not applicable (Miles, 2002).

Tomograms were obtained for the quartzite at 2 % concentration and at 2 m.s^{-1}. These are compared to the photographs at the first and last electrode layers in Figure 5.15. It is clear from the tomograms and pictures that deposition is occurring with distance along the pipeline as the swirling motion diminishes. In the last tomogram, L4, it appears that there is a clump of particles near the top of the pipe which does not seem realistic. This is possibly an artefact from the reconstruction process or a poor electrode connection.

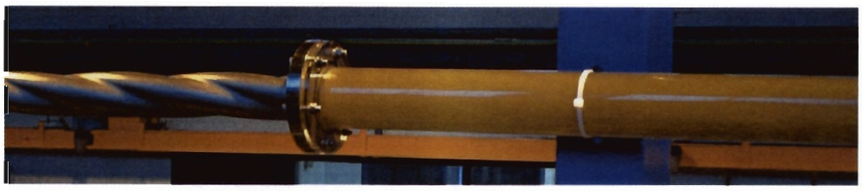


Figure 5.14: 1 mm quartzite leaving the swirtly-flow boiler tubing under opaque conditions.

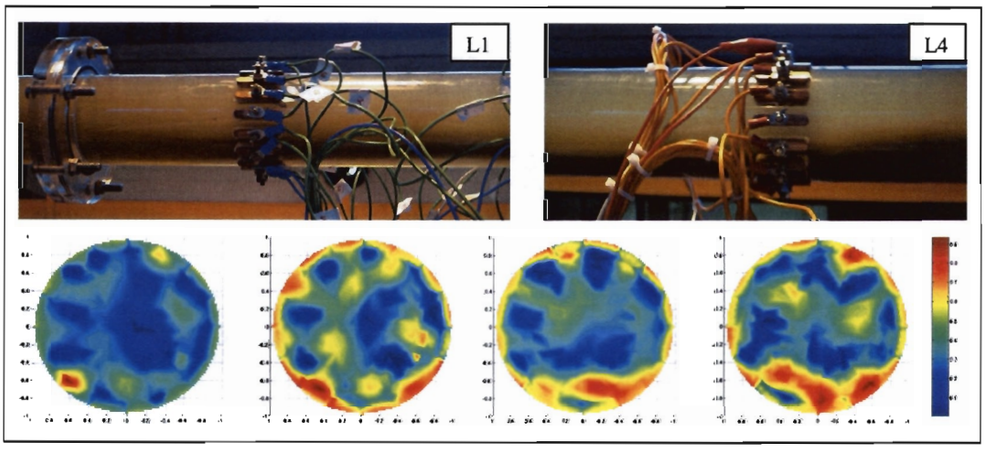


Figure 5.15: Tomgrams for quartzite at 2 % concentration at 2 m.s^{-1} and the picture of the conditions at electrode layers 1 and 4.

5.3.4 Discussion: Swirling Beads and Quartzite

Previously, Wood *et al.* (2003) examined slurry concentration profiles relating to swirling flow using a commercial ITS-P2000 ERT system (Lucas *et al.*, 1999). Current was induced by the excitation of adjacent electrodes using 10 kHz alternating current. Measurements were conducted over single plane and two-plane arrangements and were reconstructed using a sensitivity-coefficient back-projection algorithm. A profile was obtained indicating the presence of solids in the pipe at a slight angle off the pipe bottom, however, there was no visualisation of the swirling flow effects on the solids as the radial flow decreased with distance along the pipe. The back-projection algorithm is faster computationally and can be enhanced with element sensitivities; however, it is not as quantitative with regard to element resistivities as the Newton-Raphson algorithm employed in this study (Randall *et al.*, 2001).

Shook and Roco (1991), cited by Fangary *et al.* (1998), noted that solids suspension homogeneity in normal pipe flow varies significantly with solids concentration, particle

size, density distributions and velocity. This was quite evident from the range of tomograms produced in this study. Fangary *et al.* (1998) used ERT to examine the flow of polydisperse angular quartzite (d = 180 and 350 μm, ρ = 2650 $kg.m^{-3}$) and monosize glass beads (d = 5000 mm, ρ = 2950 $kg.m^{-3}$) in horizontal pipes up to velocities of 3.5 $m.s^{-1}$ and detected a static bed of particles. The solids level detected by ERT was consistently higher than the actual sediment height. This was attributed to the packing factor of the sediment as the conductivity reflects the available voidage. In this study of flow of a swirling suspension through a pipe, a static layer was not observed as swirling flow was induced. However the packing density of the settled particles is postulated to vary as deposition or agglomeration occurred along the pipeline. Fangary *et al.* (1998) also noticed that a minimum conductivity (2 mS) was required for adequate image reconstruction (backprojection method) by the addition of electrolyte. Adequate image reconstruction was ensured in this study through the addition of 50 $mg.l^{-1}$ sodium chloride (± 200 μS) which was sufficient for ERT Hardware I.

As observed in Figures 5.10 and 5.12 the solids phase appears to be slightly displaced from the pipe wall. This is either an artefact of the reconstruction process or behaviour associated with the fluid flow in the pipe. Ujhidy *et al.* (2003) report that limited results have been published on the velocity field in convoluted channels in terms of curvature and torsion of the helical movement. These authors found that secondary flow was induced in the channel between the tube wall and the surface of the helical element, thus potentially explaining the reduced particle density at the wall. Furthermore, Leighton and Acrivos (1986) reported on the phenomenon of viscous resuspension whereby a settled layer of negatively buoyant particles is entrained into the bulk fluid in the presence of a viscous shear flow. In this situation the downward gravitational flux of the particle is balanced with the shear-induced diffusion. Leighton and Acrivos (1986) observed shear-induced diffusion under laminar conditions and concluded that it would play a minor role under turbulent conditions.

In order to assess the presence of turbulent flow the Reynold's number for each flow condition was calculated (Table 5.2). The slurry density was obtained using Equation 5.1. The viscosity of the dilute suspension was estimated using Equation 5.2 (Einstein, 1906).

Table 5.2: Reynolds numbers for the flow conditions

wt. %	2		3	4
u_s ($m.s^{-1}$)	sand	beads		
1	5.07E+04	4.88E+04	4.82E+04	4.76E+04
1.5	7.61E+04	7.31E+05	7.23E+05	7.14E+05
2	1.01E+05			

Slurry density:

$$\textit{Solids loading as } wt\,\% = \frac{\rho_w(\rho_s - \rho_w)\times 100\%}{\rho_s(\rho_p - \rho_w)} \qquad (5.1)$$

where the density subscripts *w*, *s* and *p* refer to the water, slurry and particle respectively.

Viscosity of dilute suspensions (0-10 % solid fraction),

$$\mu = \mu_o(1 + 2.5\Phi) \qquad (5.2)$$

where μ_o is the fluid viscosity and Φ is the solid volume fraction.

Examining the calculated Reynolds numbers for the different flow conditions in the study presented here (Table 5.2), it is clear that the flow was turbulent. Typical turbulent flow in pipes is approximated in liquid phase systems at a Reynolds number of 2300. This turbulent flow, however, was not sufficient to result in the complete suspension of the beads beyond the swirly-flo boiler tubing and continual movement of the beads along the bottom of the pipe was observed.

Hence shear-induced diffusion is expected to be a minor effect at these conditions. The slight displacement off the wall is therefore postulated to be a characteristic of the reconstruction algorithm. This uniform anomaly has since been diminished in more recent work using Reconstruction Code III and Reconstruction Code V (Wilkinson *et al.*, 2005b). Although flow was turbulent, bead behaviour was steady along the bottom of the pipe and their position did not vary temporally. Only on inducing swirl did the beads achieve off-bottom suspension due to the angular momentum. This illustrates the benefit of incorporating such a system in areas requiring increased mixing or decreased erosion along a pipeline.

Analysis of the tomograms can yield particle deposition information related to time or distance, and hence the ability to optimise curvature design for the swirl-inducer within the constraint of limiting pressure drop. In Figure 5.16 the area fraction of pixels from the tomogram sets (3, 4 mass % beads; 2 mass % quartzite) that are greater than a relative non-conductivity of 0.6 (this is bright yellow to red, and represents bulk flow of particles) is shown with respect to electrode layer, which is related to distance or time from leaving the boiler tube.

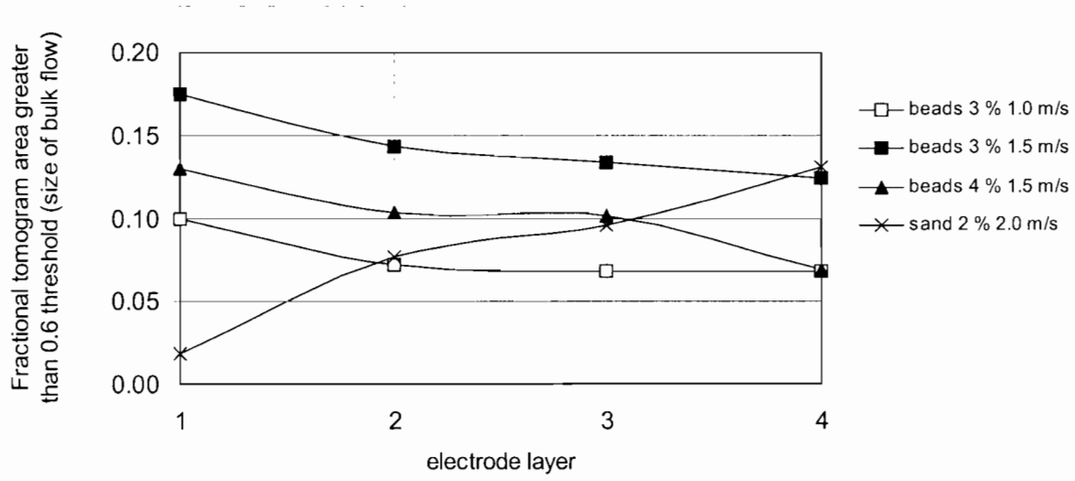


Figure 5.16: The fraction of the tomogram which is greater than the relative non-conductivity of 0.6 (this represents bright yellow to red and the bulk flow of beads and quartzite) for the successive electrode layers along the pipe.

Comparing the profiles for 3 % beads at velocities of 1.0 and 1.5 $m.s^{-1}$ the area of non-conductivity (>0.6), corresponding to bulk flow of suspended particles, increased with increasing velocity i.e. beads that were in the red region (concentrated) have dispersed (increase in bright yellow region). The 4 % beads at 1.5 $m.s^{-1}$ take up a greater area fraction than the 3 % beads at 1.0 $m.s^{-1}$ due to there being more mass, however, due to the increased weight of particles which inhibits angular momentum, the bulk area fraction is not as great as the 3 % bead suspension at a velocity of 1.5 $m.s^{-1}$. The bulk area fraction of the beads decreases along the pipeline as they become more concentrated at the bottom in accordance with the photographic record. In contrast, the bulk area fraction of quartzite increases along the pipeline. This is due to the suspended quartzite being well dispersed from the swirling flow and not sufficiently agglomerated to result in red and yellow regions in the tomograms. Thus this analysis of the ERT tomograms allows a non-invasive method to evaluate the deposition of fine particles in slurry conveyance systems, as well as the detection of the relative positions of groups of larger particles. With this system, ERT Hardware I and Reconstruction Code I, it is imperative that steady flow is achieved before this analysis proceeds due to the manual switching required between electrode layers.

This series of bead and quartzite experiments and ERT reconstructions were submitted for publication (Stevenson *et al.*, 2006).

5.4 Conclusions

The application of ERT in this study commenced with the detection of static physical phantoms. This was successfully achieved in 2D and interpolated 3D images with ERT Hardware I and Reconstruction Code I, followed by application of the Matlab™ code in Appendix E. Limitations were observed in the form of reconstruction artefacts near the perimeter of the vessel, most likely due to the reconstruction code applied. More accurate reconstructions were observed near the vessel top and bottom due to the assumptions of the 2D algorithm; this limitation will need to be heeded in the examination of stirred tanks.

Pure 3D tomography based on the EIDORS code (Reconstruction Code II) was found to yield poor resolution and thus abandoned. Following this, a suitable dynamic solid-liquid environment in the form of swirling pipeline suspensions was examined using ERT Hardware I and Reconstruction Code I. This investigation showed that the direct current ERT system using a switched bi-directional constant current source (ERT Hardware I) clearly allows the visualisation of solid suspension across pipe cross-sections, indicating the relative positions of the plastic beads or quartzite particles and bulk fluid. A series of these planar tomograms was converted into 3D images to allow a better understanding of the intensity and direction of the swirling flow. This clear representation of swirling flow had not been previously published. Moreover, the tomograms enabled the comparison of flow of the suspension at different superficial velocities and mass concentrations, and thus data can be captured which enables the analysis of the efficiency of the swirl induction as well as potential areas of pipeline erosion. Tracking and visualising particle deposition was also demonstrated to be possible with this system. Lastly, images can be retained to provide a visual database of key areas of attrition at specific conditions and thus aid the maintenance of pipeline systems.

Thus the ERT application to this dynamic solid-liquid environment was successful and the hypothesis that this ERT system can be used as an analysis tool has been validated. Furthermore, the imaging of fine particles in the pipeline, namely quartzite, allows further investigation of flowing fine particles in the stirred tank environment to proceed.

Chapter 6

Quartzite Suspension and Reactor Homogeneity

6.1 Introduction

One of the primary objectives of this study was to increase understanding of the distribution and mixing of particles in the slurry bioreactor. It was considered necessary, therefore, to transcend the description of a mixing system beyond the concept of a critical suspension speed, while increasing information available on suspension to facilitate modelling of phenomena dependent on solid-liquid interaction. Further, this knowledge would improve understanding of the hydrodynamics of the reactor and contribute to reactor design, particularly for large scale mineral bioprocessing. These processes typically contain two types of solid particles (the substrate or immobilisation matrix, and the microorganism), a liquid phase and a gas phase.

In this chapter, the investigation is simplified to a two-phase mixture with quartzite as the model particle. The effect of particle size and loading, impeller speed and type, and reactor scale are considered while applying ERT as the non-invasive monitoring technology. Three size fractions of quartzite particulates at concentrations of 5 to 20 % by volume across a range of speeds in the 220 mm ID tank were examined with ERT using both Rushton and pitched blade impellers. The UCT based ERT Hardware I was used in this study with Reconstruction Code III.

In Sections 6.2.2 and 6.2.3, the effect of the parameters of agitation rate, solids loading and particle size on suspension homogeneity are discussed with reference to the radial concentration profiles of the Rushton and pitched-blade impellers. These parameters are further examined with reference to the axial concentration profiles for both impellers in Section 6.2.4. Further analysis is applied to these profiles to quantify reactor homogeneity in Section 6.2.5, with attention given to particle size (Section 6.2.6) and solids loading (Section 6.2.7). The accuracy of ERT concentration profiles is determined through comparison with physical sampling and conductivity probing in Section 6.3.

6.2 Quartzite Suspension in the 220 mm ID Perspex Tank

The reactor system used is described in Section 3.1 including details of the solid-liquid environment and ERT calibration. The main set of experiments was performed with ERT Hardware I and Reconstruction Code III and thus the model for extracting information from this system will be detailed.

6.2.1 Conversion of ERT Data to Concentration Profiles

Conductivities were obtained for each element of the mesh (Figure 4.9 and 6.1 (a)), however, values associated with the position of the baffles and the impeller, which had been previously set to zero through calibration were eliminated. All four layer reconstructions were affected by the presence of the impeller in the center of the tank. Thus the annular zone from near the impeller to the vessel wall (70 – 110 mm) was focused upon for data extraction (Figure 6.1 (b)).

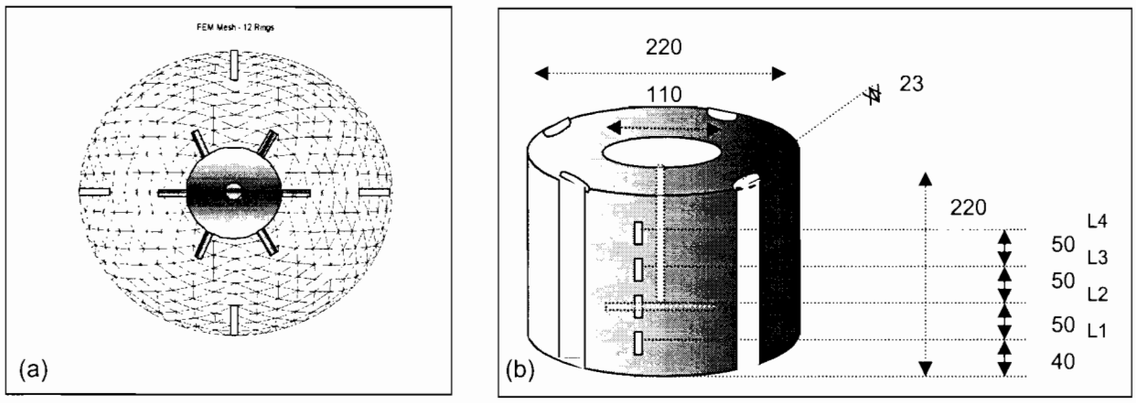


Figure 6.1: The 712 FEM mesh and the relative position of the baffles and impeller (a), and on the right the shaded region depicts the section of volume of the tank in which conductivity data was converted to suspension profiles (b). Measurements are in mm.

The higher resistance offered by the baffles can be observed by the four peaks in the resistance data presented in Figure 6.2 (a) for the outermost ring of the mesh. The presence of baffles and the impeller can also be observed in Figure 6.2 (b) as the four white sections (note arrows) and the white section in the middle of the interpolated image. The conductivity distribution in the plane (L1) can be observed on the left side.

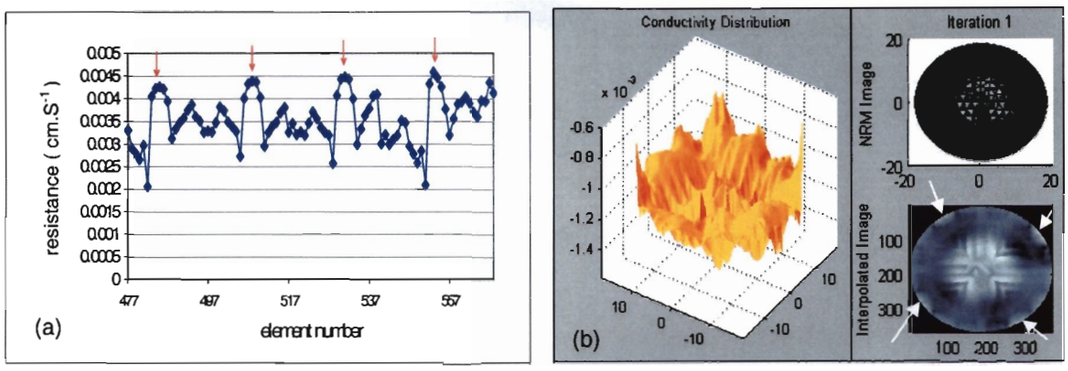


Figure 6.2: Examining resistance data to remove the presence of peaks associated with the 4 non-conducting baffles (a); Matlab™ software (Reconstruction Code III) showing 3D map of conductivity in the lowest plane of electrodes and the Newton-Raphson reconstructed image (1 iteration). The 4 baffles are visible on the outside of the tank wall and the impeller in the centre (in white) (b). Conditions for data collection: Rushton impeller, 547 rpm, 425-600 μm quartzite, 20 % v/v.

The conductivity data were then converted to volume fraction data through the application of Equation 2.13 from Maxwell (1873), which has been successfully applied in solid-liquid environments (Lucas *et al.*, 1999; Nasr-El-Din *et al.*, 1996). All the elements in a ring from the mesh, barring the baffle area, were averaged to produce an average volume fraction for a specific radial position. This process is illustrated in Table 6.1 for the 5 % v/v suspension of the 600 – 850 μm fraction at 236 and 304 rpm using the Rushton impeller.

Table 6.1: Sample Volume Fraction Data for the 5 % v/v suspension of 600 – 850 μm quartzite fraction at 236 and 304 rpm

	speed	236 rpm					304 rpm				
ring	layer	1	2	3	4	ring ave	1	2	3	4	ring ave
1	0.13	0.000	0.000	0.000	0.000	0.000	0.067	0.000	0.000	0.000	0.017
2	0.27	0.068	0.016	0.020	0.109	0.053	0.115	0.025	0.018	0.110	0.067
3	0.37	0.156	0.185	0.179	0.251	0.193	0.175	0.160	0.168	0.255	0.190
4	0.46	0.224	0.260	0.229	0.234	0.237	0.202	0.226	0.220	0.248	0.224
5	0.55	0.231	0.222	0.169	0.119	0.185	0.189	0.202	0.170	0.135	0.174
6	0.63	0.186	0.134	0.083	0.011	0.104	0.154	0.133	0.092	0.030	0.102
7	0.72	0.133	0.068	0.028	0.000	0.057	0.115	0.077	0.039	0.000	0.058
8	0.80	0.081	0.028	0.002	0.000	0.028	0.074	0.040	0.012	0.000	0.031
9	0.86	0.080	0.023	0.000	0.000	0.026	0.075	0.037	0.009	0.000	0.030
10	0.92	0.082	0.032	0.007	0.000	0.030	0.077	0.044	0.015	0.000	0.034
11	0.97	0.061	0.031	0.010	0.000	0.025	0.058	0.035	0.012	0.000	0.026
12	1.00	0.094	0.067	0.030	0.017	0.052	0.087	0.063	0.027	0.020	0.049
	Ave.	0.116	0.089	0.063	0.062		0.116	0.087	0.065	0.067	
	7 ring ave	0.102	0.055	0.023	0.004		0.091	0.061	0.030	0.007	

In Table 6.1 the ring number is presented in the far left column, with the next column indicating the dimensionless radial position (r/R) of the ring. Conductivity data from the 712 element mesh was then averaged for each ring for the specific electrode layer (L1 – 4) and Equation 2.13 was applied to convert this value into a volume

fraction as presented in Table 6.1. The data from r/R = 0.63 to 1.00 was presented graphically to produce the radial concentration profiles, while the data averaged over this radial distance ("7 ring ave" row in Table 6.1) for each electrode layer produced the axial concentration profiles. The complete data set is presented in Appendices Q and R.

6.2.2 Radial Concentration Profiles for the Rushton Impeller

Radial concentration profiles were generated for 5, 10, 15 and 20 % solids loading (by volume) for size fractions of 106 – 212, 425 – 600 and 600 – 850 μm at agitation rates of 236, 304, 353, 460 and 547 rpm. Only the upper and lower speeds (236 and 547 rpm) are presented in this section for comparison purposes. The 10 % volume fraction profiles for the Rushton and pitched blade impellers are presented in Appendix F.

The volume fraction distribution of quartzite at 5 % volume concentration when agitated with a Rushton impeller at 236 rpm is presented in Figure 6.3 (a)-(c) as radial concentration profiles for the three size fractions: 106-212 μm, 425-600 μm and 600-850 μm. The profiles extend from near the impeller zone to the tank wall (70 - 110 mm) and represent each electrode layer (L1-L4), with L1 as the lowest layer. The layer heights are presented as dimensionless heights (z/Z) in Figure 6.3 (a). On each figure the size fraction and the Zwietering critical suspension speed are reported. The Zwietering N_{js} is often used for comparative purposes, although uncertainty has been reported for disc turbines in Table 2.3. More recent values for 's', the Zwietering constant, can be obtained from Armenante and Nagamine (1998). Mixing indices ($\overline{MI}_z, \overline{MI}_r$) are presented for the 5 and 15 % concentrations. The mixing indices are discussed in the examination of homogeneity in Section 6.2.5. Sample calculations of N_{js} and the mixing indices are presented in Appendix G

Comparing the data in Figure 6.3, the effect of increasing particle diameter on particle suspension can be observed by the ERT system with an increasing variation in concentration being observed across the 4 electrode layers. Further, less solids are detected in the upper layer (L4) which is consistent with the increasing N_{js} (as reported on the figure) associated with larger particles. Shamlou and Koutsakos (1989) noted that for a given impeller and tank geometry and at a fixed impeller speed, an increase in particle diameter leads to an increase in the particle terminal velocity and thus a decrease in the homogeneity of the suspension. It is also apparent that the solids concentration in these figures varies with radial position (70-110 mm; r/R = 0.63 to 1). The concentration generally decreases with increasing radius, although a slight increase in concentration was observed at the wall for Figures 6.3 (b) and (c). This increase was associated with the last 5 mm near the wall.

Examining Figure 6.4 (a)-(c), where the same conditions are present except for an increase of solid volume fraction from 0.05 to 0.15, the profiles show a greater variation in concentration across axial position indicating greater axial concentration gradients. This shows that the ERT system is quite capable of detecting increases in solid concentration and the effect of solids loading can be related to the homogeneity of the reactor i.e. the consistency of L1 – L4.

The finer particle (Figure 6.4 (a)) profiles show less variation across axial distance at both 5 and 15 % loading, indicating less pronounced axial gradients than the larger particles (Figure 6.4 (b) and (c)). Thus the axial homogeneity is clearly seen to decrease with increasing particle size with the ERT data. In Figure 6.4 (b) and (c), representing the coarse size distributions, a considerable radial gradient is observed at the bottom of the tank (L1). This was similarly observed by Barresi and Baldi (1987a) who used a wall sampling technique in a 0.390 m diameter vessel (D/T =1/3; H/T =1.19; C/T = 1/3) using radial and axial impellers with a solids volume fraction range of 0.2 to 2 % (size fractions 100-177 μm; 208-250 μm; 417-500 μm, ρ = 2600 $kg.m^{-3}$). Based on their dilute concentrations of solids, significant radial gradients were expected for L1 relative to L2-L4 in Figure 6.3. However, it must be noted that L1 is at z/Z = 0.18 and thus not completely representative of the zone below the impeller, while Barresi and Baldi (1987a) examined concentrations at z/Z = 0.10. With the 15 % solids concentration (Figure 6.4), more solids would be present in this zone aiding radial gradient detection. Barresi and Baldi (1987a) noted that radial homogeneity was good above the impeller on using disk turbines (as in this study), while the particle concentration was found to decrease when approaching the tank wall. Further, they found increasing radial concentration gradients with increasing particle size. This was not found to be always the case in this study and will be discussed with the analysis of homogeneity (Section 6.2.5). However, it must be remembered throughout this study that the results are only concerned with the region of r/R = 0.63 to 1. Furthermore, the wall sampling of Barresi and Baldi (1987a) was conducted 20 mm from the vessel wall and thus the last 4 data points in the radial profiles of this study can only be related to the profile trend of these researchers.

Nasr-El-Din *et al.* (1996) observed radial gradients using a conductivity probe at r/R = 0.3, 0.6 and 0.9 at various heights (0.1 to 0.9 z/H) for mean particle sizes of 255, 410, 500 and 1000 μm for a 0.292 m diameter tank using a solids concentration of 0.1 and 0.3 volume fraction and a Rushton impeller (H/T=1; D/T = 1/3; C/T=0.3) at 440 and 545 rpm. Significant gradients were not observed for the smaller 82 μm particles. They reported the radial solids concentration to increase on approaching the tank wall. This is in contrast with this study, except for slight increases observed for the 425-600 μm fraction (L2-L4 in Figure 6.3 (b); L4 in Figure 6.4 (b); L4 in Figure 6.5 (b)). It must be noted in the study of Nasr-El-Din *et al.* (1996), the closest the reactor was probed to the vessel wall corresponded to a distance of 1.5 cm at r/R =

0.9. Thus again, the last 3 - 4 radial data points in this study cannot be directly compared, neither the data of Nasr-El-Din *et al.* (1996) at r/R = 0.3 and 0.6.

Figures 6.5 and 6.6 represent the radial profiles collected at 5 and 15 % volume concentration at the higher agitation rate of 547 rpm. This agitation rate is greater than N_{js} for all the fractions except the 600-850 μm 15 % loading (Figure 6.6 (c)). Comparison of Figures 6.5 and 6.6 shows the effect of increased loading resulting in greater variation between radial profiles. The relative difference compared to Figures 6.3 and 6.4 is diminished, due to the greater particle suspension through operating above N_{js}. The effect of increased loading is clearly observed in Figure 6.7. A mid agitation rate of 353 rpm and mid size fraction of 425 – 600 μm were examined for each layer for solid loadings of 5 – 20 %. An increase in volume fraction was observed for increasing solids loading at each electrode layer.

The effect of agitation rate can be analysed through comparison of Figure 6.3 with Figure 6.5 and Figure 6.4 with Figure 6.6. The profiles are clearly more consistent at 547 rpm indicating greater axial homogeneity as well as validating the ERT system's ability to detect the effect of changing agitation rate. Further, more solids are detected in the upper regions of the vessel (L3 and L4) at 547 rpm which is consistent with improved suspension on increasing the agitation rate. Across all data, the trend of the radial concentration profiles is constant or decreasing when approaching the tank wall at this higher agitation rate. The effect of agitation rate is clearly observed in Figure 6.8 for the 15 % solids concentration of the 425 – 600 μm fraction. In Figure 6.8 (a) the solids concentration in L1 can be seen to be decreasing with increasing agitation rate in accordance with particle suspension off the tank bottom. In Figure 6.8 (b) and (c), L2 and L3 increase in concentration with increasing agitation rate, although this rate of increase diminishes with increasing speed. There is minimal difference between solids concentration at agitation rates of 460 and 547 rpm. This is in agreement with N_{js} at 515 rpm from the Zwietering correlation. Further, Baldi *et al.* (1981) observed a zone of pseudohomogeneity for z/Z = 0.25 – 0.55 at complete suspension (Section 2.6.1.1). In this study, similar concentrations are observed at L2 and L3 (z/Z = 0.41 and 0.64) in Figure 6.8 at agitation rates of 460 and 547 rpm. The solids concentration at the vessel wall (r/R = 1.00) is constant at each electrode layer for increasing agitation rate. These data cannot be related to previous sampling or conductivity data which are collected away from the vessel wall.

Similar profiles are observed for the 10 % volume fraction profiles in Appendix F. For the 20 % volume fraction profiles presented in Figures 6.13 and 6.14 there appears to be a steeper concentration gradient with the 106-212 μm (at 236 and 547 rpm) and the 425-600 μm (at 547 rpm) fractions showing a rapid decrease in solids concentration in the last 10 mm on approaching the vessel wall.

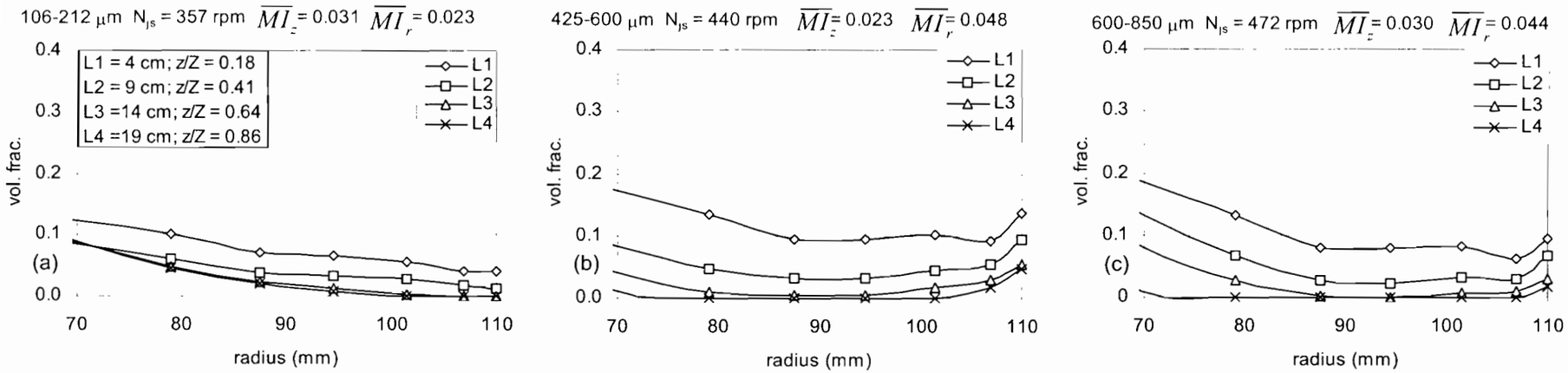


Figure 6.3: Radial concentration profiles for Rushton impeller at 236 rpm 5 % vol., 106-212 μm (a); 425-600 μm (b); 600-850 μm (c).

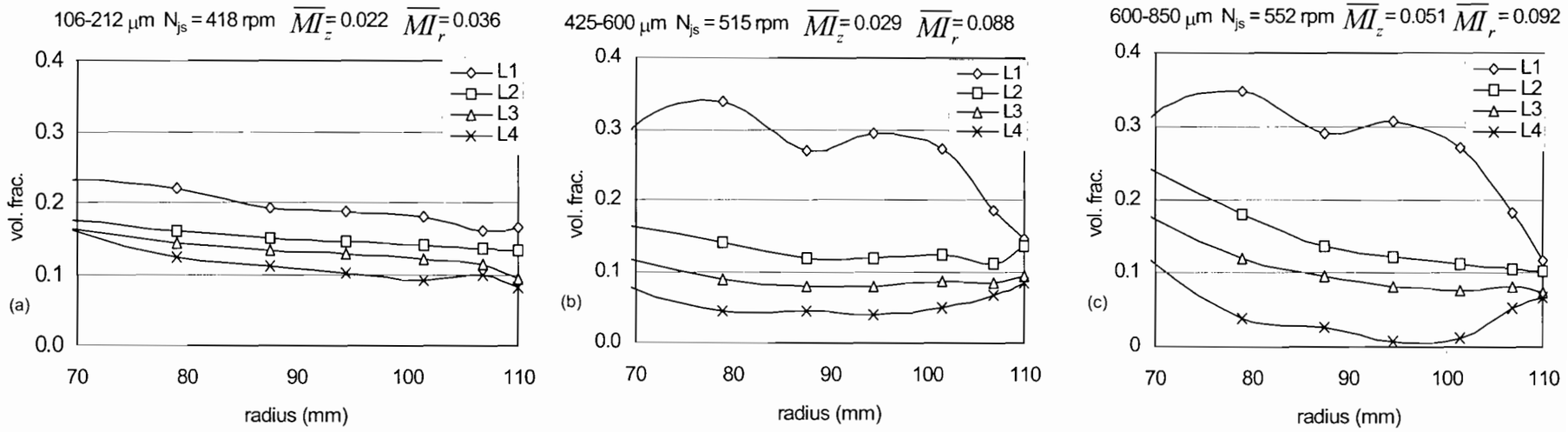


Figure 6.4: Radial concentration profiles for Rushton impeller at 236 rpm 15 % vol., 106-212 μm (a); 425-600 μm (b); 600-850 μm (c).

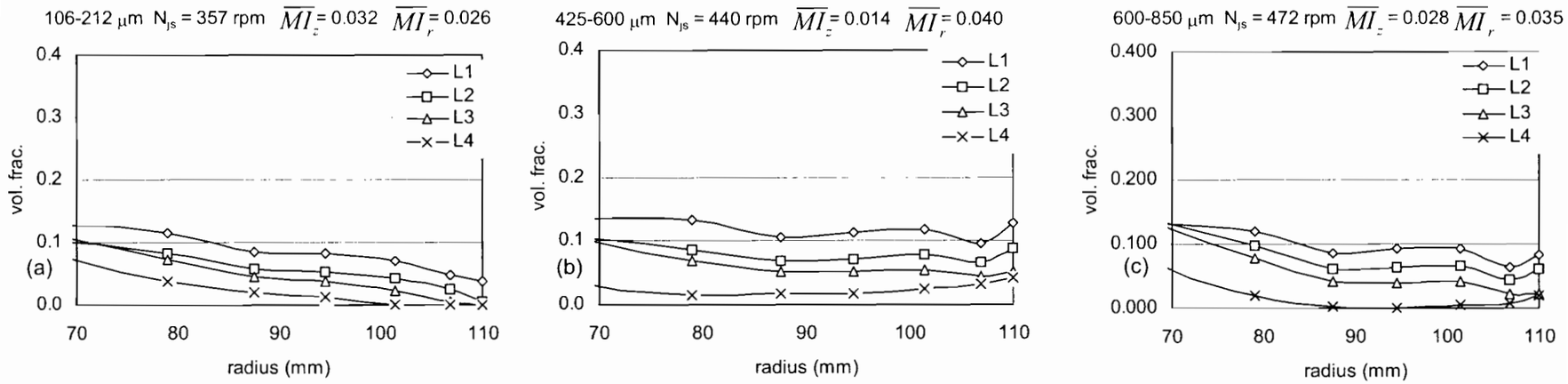


Figure 6.5: Radial concentration profiles for Rushton impeller at 547 rpm 5 % vol., 106-212 μm (a); 425-600 μm (b); 600-850 μm (c).

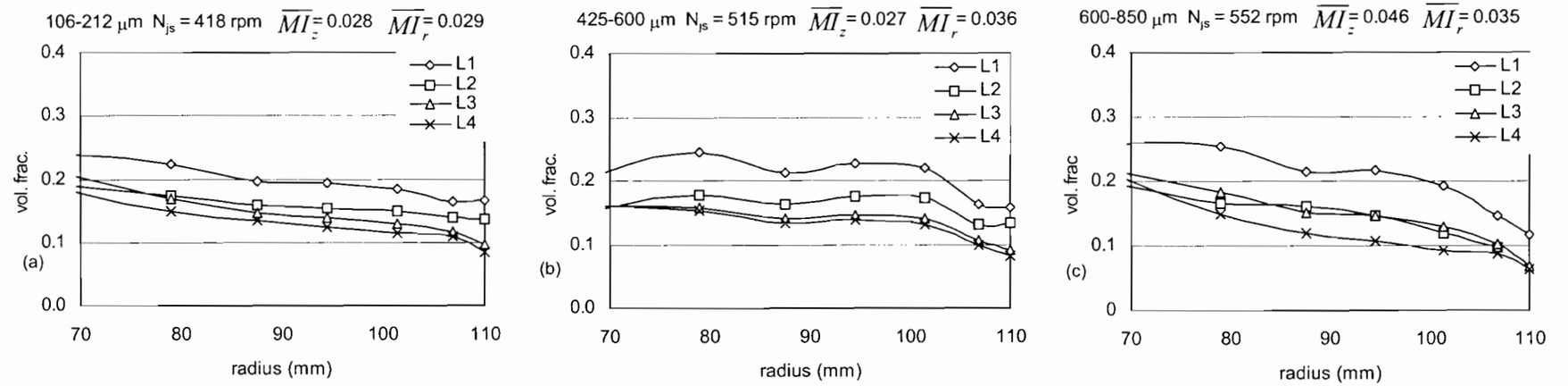


Figure 6.6: Radial concentration profiles for Rushton impeller at 547 rpm 15 % vol., 106-212 μm (a); 425-600 μm (b); 600-850 μm (c).

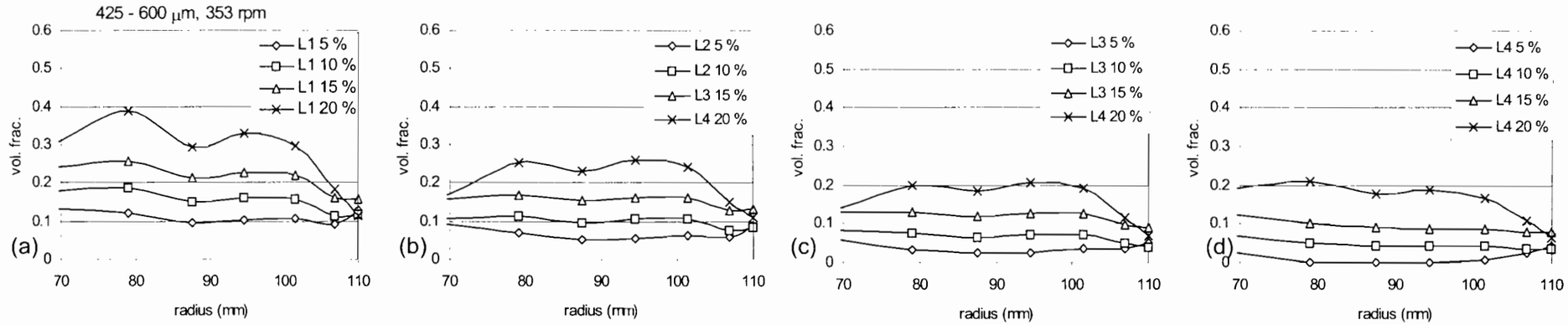


Figure 6.7: The effect of solids loading on radial concentration profiles for the Rushton impeller at 353 rpm for the 425 – 600 μm fraction. L1 (a), L2 (b), L3 (c) and L4 (d).

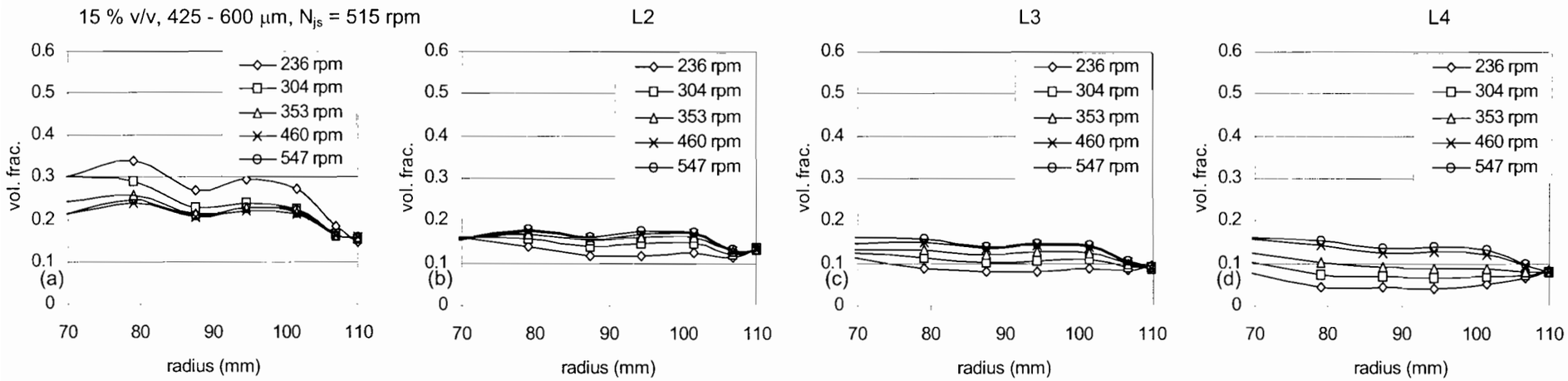


Figure 6.8: The effect of agitation rate on radial concentration profiles for the Rushton impeller at 15 % loading for the 425 – 600 μm fraction. L1 (a), L2 (b), L3 (c) and L4 (d).

6.2.3 Radial Concentration Profiles for the Pitched Blade Impeller

Figures 6.9 and 6.10 represent the radial profiles obtained from the pitched blade impeller (45° pumping downwards) for the three size fractions at 236 rpm for 5 and 15 % solids concentration. The 's' value for Zwietering's N_{js} equation for this impeller (six-blades) was obtained from Armenante and Nagamine (1998) (Appendix G). As observed with the Rushton impeller, the effect of increased particle diameter and particle loading resulted in increased variation between radial concentration profiles.

For the 106-212 μm fraction (Figure 6.9 (a) and Figure 6.10 (a)), the trend in solid concentration with radial position differs from the larger sized particle suspensions. Particle concentration increases quite sharply on approaching the vessel wall. This can be explained by this size fraction's relatively low inertia, thus these particles will tend to follow the fluid circulation flow (Nasr-El-Din *et al.*, 1996). The fluid is pumped down by the pitched blade reaching the corners of the vessel followed by rising up the wall. This is different to the radial impeller where the flow splits into two circulation loops at the wall in the impeller plane. For the larger size fractions (Figure 6.9 (b) and (c); Figure 6.10 (b) and (c)), their inertia is greater than the fluid flow leading to similar profiles observed with the Rushton impeller (Figure 6.3 (b) and (c); Figure 6.4 (b) and (c)). In Figure 6.10 (b) and (c), the radial profile for L1 can be observed to decrease sharply near the impeller zone (70 mm). As this may be a calibration effect from the impeller, the data point at 80 mm should be taken as more representative for these profiles.

The effect of increasing agitation rate to 547 rpm is shown in Figures 6.11 and 6.12. The profiles have greater consistency than that at 236 rpm. The radial profiles at the high agitation rates also generally decrease towards the vessel wall, apart from the 106-212 μm fraction discussed above. In Figure 6.13, the effect of increasing agitation rate is clearly visible on a 15 % suspension of 425 – 600 μm quartzite. Similarly to the Rushton profiles presented in Figure 6.8, L1 concentration decreases with increasing particle suspension (Figure 6.13 (a)). Layers 2 and 3 are also similar at higher agitation rates, while the concentration at L4 showed minimal change with increasing agitation rate and lay below the expected value of 15 % on complete suspension. The pitched blade impeller is therefore less effective than the Rushton impeller in suspending particles to the upper regions of the vessel at the same agitation rate. This can be further observed when examining L4 in Figure 6.14 in which the suspension profiles are compared across impeller types. A constant concentration at the wall (r/R =1.00) is also observed for each electrode layer despite increasing agitation rate.

Limited literature is available on radial profiles using a pitched blade impeller. Barresi and Baldi (1987a) noted (Section 2.6.1) that for axial impellers, gradients along the radius are generally slight, but increase if larger particles are introduced. This is consistent with these results at size fractions of 425 μm and greater. However, a

concentration of particles near the wall was observed for the fine particle profiles (106-212 μm) in this study. Barresi and Baldi (1987a) conducted sampling 20 mm away from the vessel wall, not facilitating determination of these changes. In a CFD study of nickel suspension, Aoyi (2005) sampled at three times the particle settling velocity (nickel particles ρ_p = 8903 kg.m^{-3}, 150-1000 μm, d_{50} = 430 μm, 18 % solids loading (mass), 2.8 % by volume) from seven radial and sixteen axial positions in a round-bottomed stirred tank (H=T) using a Lightnin A315 impeller (D/T=1/3). While this impeller has a different flow pattern to the pitched blade impeller, both are described as axial impellers. Aoyi (2005) observed particle radial concentration increasing towards the vessel wall at N_{js} in the lower (z/Z = 0.15) and upper regions (z/Z = 0.9) of the tank while being more uniform in the middle region (z/Z = 0.5). The last radial sampling point of Aoyi (2005) corresponded to r/R = 0.8, thus there could be a similar trend with the increased concentration of the finer particles (106 -212 μm) near the vessel wall in this study.

Comparing the 425-600 μm and 600-850 μm fractions (Figure 6.11 (b) and (c); Figure 6.12 (b) and (c) with the Rushton profiles (Figures 6.5 and 6.6) suggests greater axial gradients for the pitched blade impeller. This in agreement with the literature as the Rushton impeller is more effective at particle suspension at the same agitation rate, although more energy intensive. This difference is clearly observed in Figure 6.14 for a 15 % concentration of 425 -600 μm quartzite agitated at 353 rpm using both impellers.

The 20 % volume fraction profiles for the pitched blade impeller are represented in Figures 6.15 - 6.16. It can be observed with the 20 % volume concentration for the 106-212 μm fraction (Figure 6.15 (a) and Figure 6.16 (a)) that the profile common to the lesser volume fractions (5-15 %) i.e. concentration increasing on approaching the vessel wall, is not present. In fact, the trend of these pitched blade profiles appear similar to the Rushton profiles for 20 % solids concentration (Figure 6.17 (a) and Figure 6.18 (a)). This suggests that there is a critical solids volume fraction whereupon these fine solids are no longer sharply increasing in concentration on approaching the wall. Thus, both particle diameter and the amount of solids present influence the shape of the radial concentration profile. This profile shape is not necessarily affected by the critical suspension speed, as Figure 6.9 (a) at 236 rpm, which is below N_{js} (447 rpm), has a similar profile to Figure 6.11 (a) at 547 rpm, which is above N_{js}. Similarly for Figures 6.10 (a) and 6.12 (a) there is no correlation between complete suspension and a change in radial profile shape. Thus, there is not only a relation between 'X', the solids loading per unit liquid term in the Zwietering equation, and the critical suspension speed i.e.

$$N_{js} \propto X^{0.13} \tag{2.7}$$

but also a non-linear relationship between 'X' and the radial homogeneity for the pitched blade impeller. This is due to a critical solids concentration radically altering the radial concentration profile.

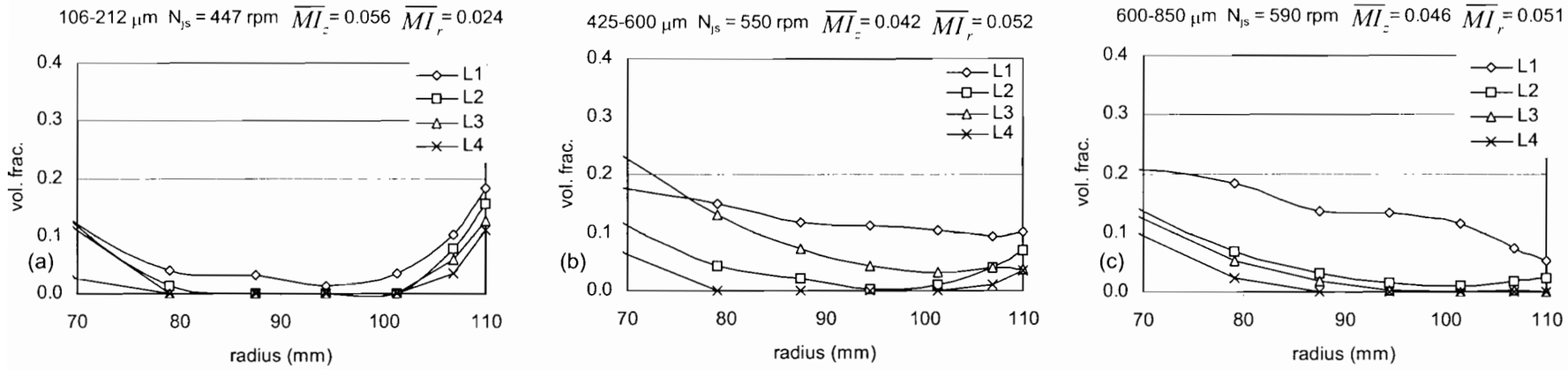


Figure 6.9: Radial concentration profiles for pitched blade impeller at 236 rpm 5 % vol., 106-212 μm (a); 425-600 μm (b); 600-850 μm (c).

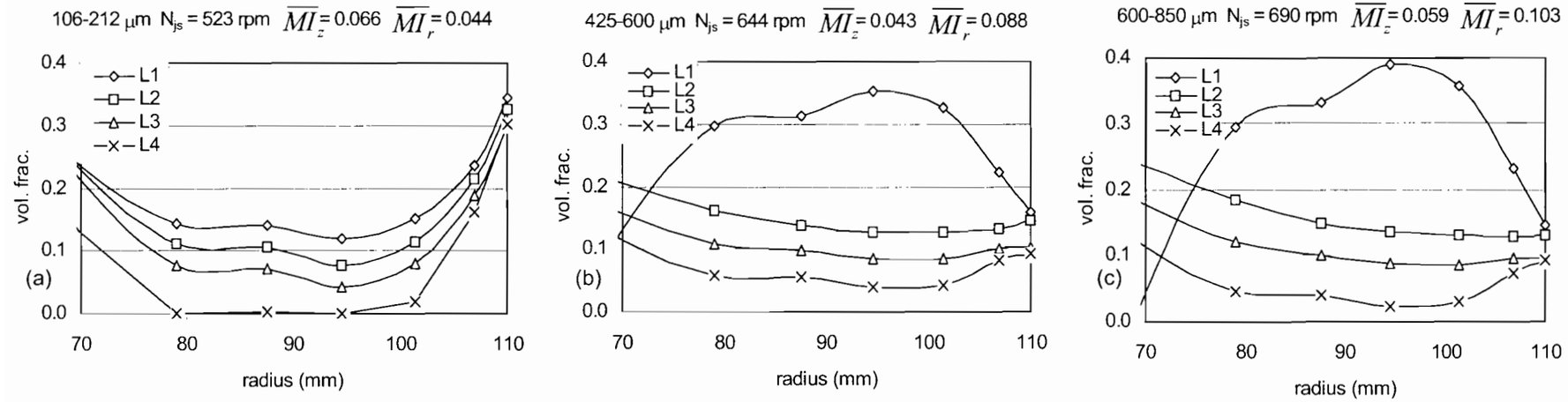


Figure 6.10: Radial concentration profiles for pitched blade impeller at 236 rpm 15 % vol., 106-212 μm (a); 425-600 μm (b); 600-850 μm (c).

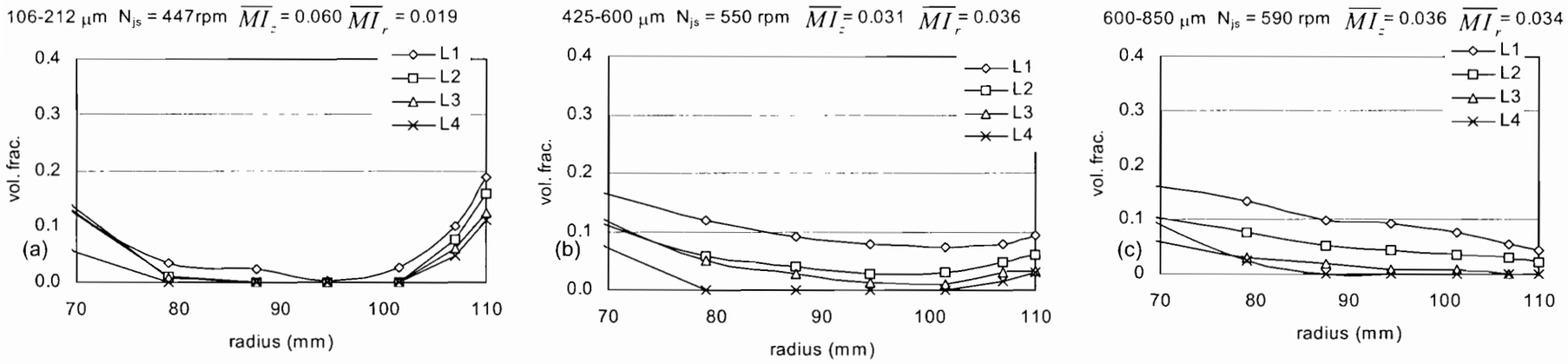


Figure 6.11: Radial concentration profiles for pitched blade impeller at 547 rpm 5 % vol., 106-212 μm (a); 425-600 μm (b); 600-850 μm (c).

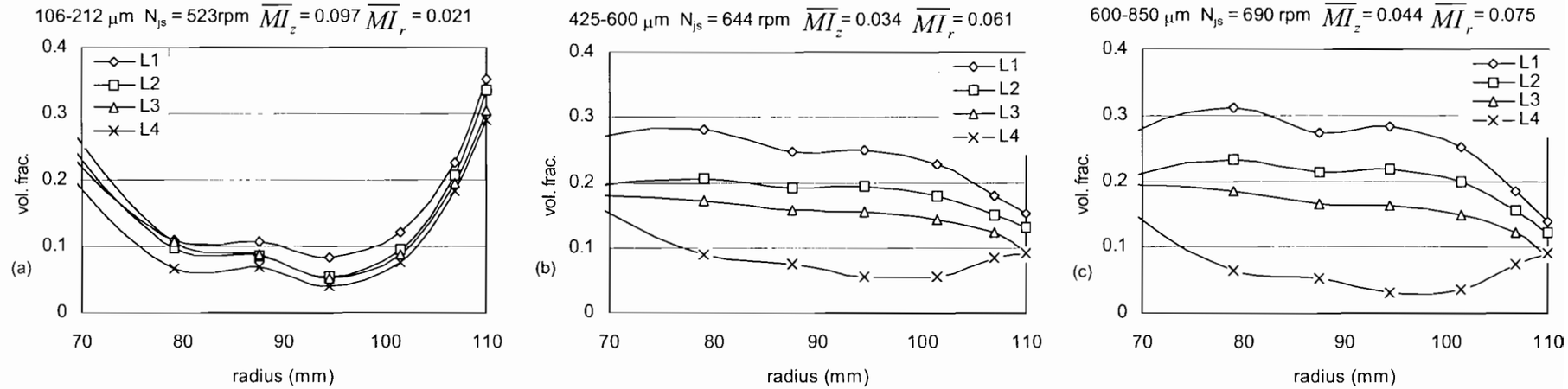


Figure 6.12: Radial concentration profiles for pitched blade impeller at 547 rpm 15 % vol., 106-212 μm (a); 425-600 μm (b); 600-850 μm (c).

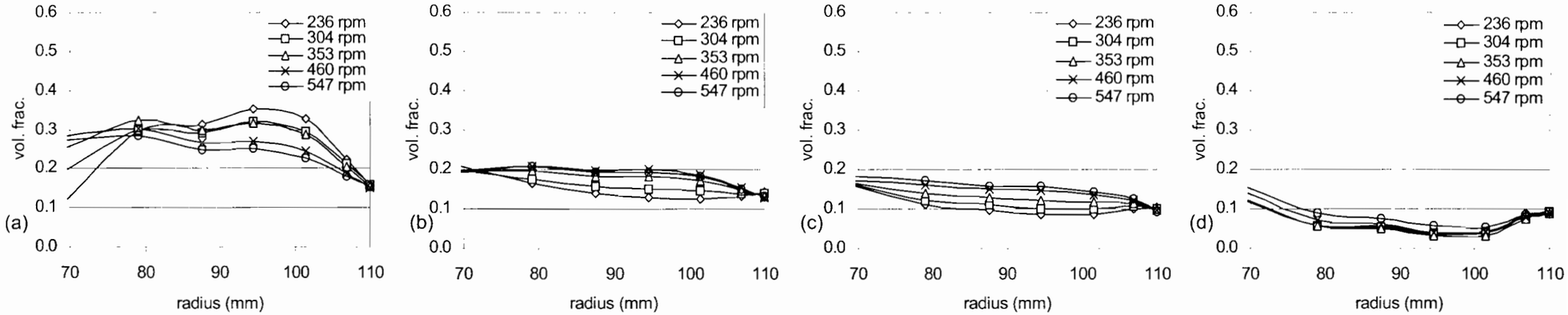


Figure 6.13: The effect of agitation rate on radial concentration profiles for the pitched blade impeller impeller at 15 % loading for the 425 – 600 μm fraction. L1 (a), L2 (b), L3 (c) and L4 (d).

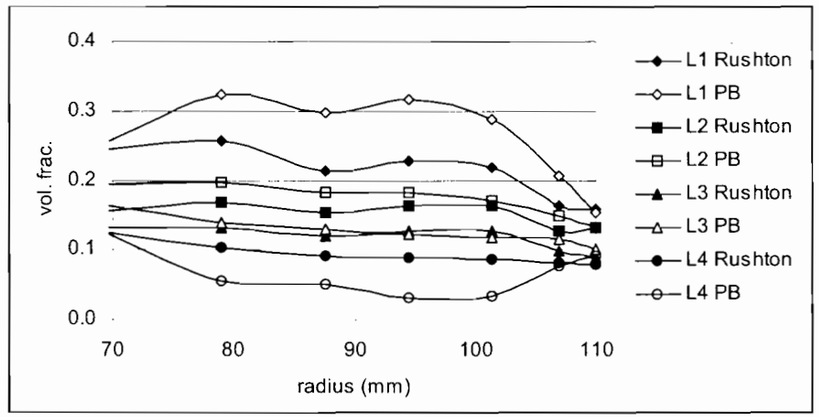


Figure 6.14: The effect of impeller type on particle suspension at the same agitation rate. 15 % suspension of 425 – 600 μm quartzite at 353 rpm with Rushton and pitched blade impellers.

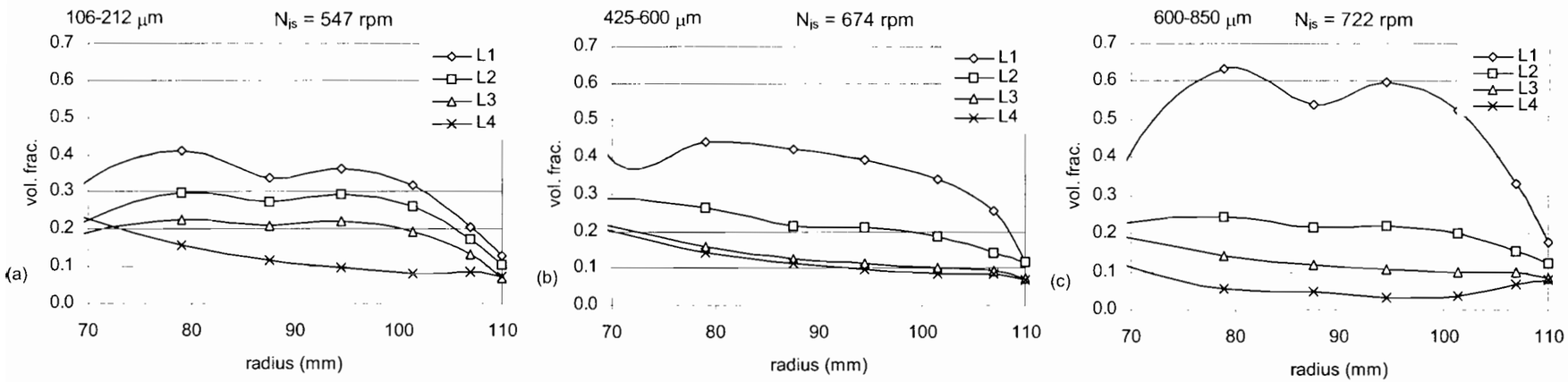


Figure 6.15: Radial concentration profiles for the pitched-blade impeller 20 % vol. at 236 rpm: 106-212 μm (a); 425-600 μm (b); 600-850 μm (c)

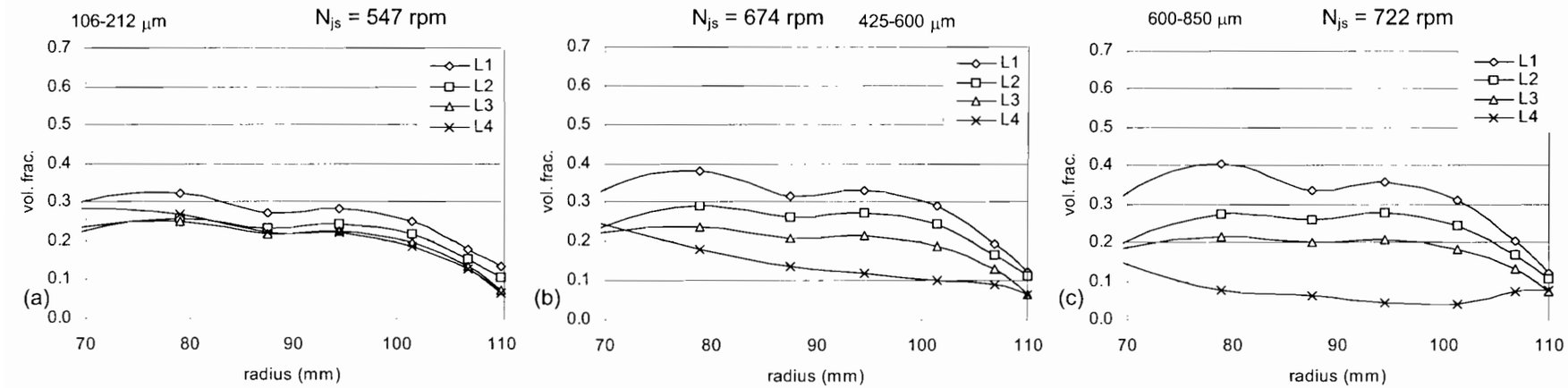


Figure 6.16: Radial concentration profiles for the pitched-blade impeller 20 % vol. at 547 rpm: 106-212 μm (a); 425-600 μm (b); 600-850 μm (c)

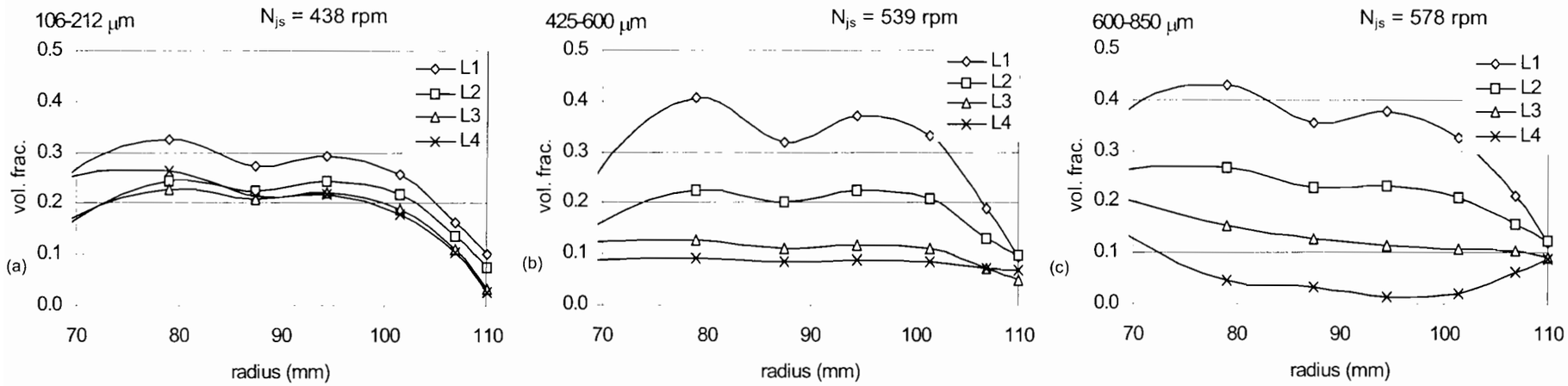


Figure 6.17: Radial concentration profiles for the Rushton impeller 20 % vol. at 236 rpm: 106-212 μm (a); 425-600 μm (b); 600-850 μm (c)

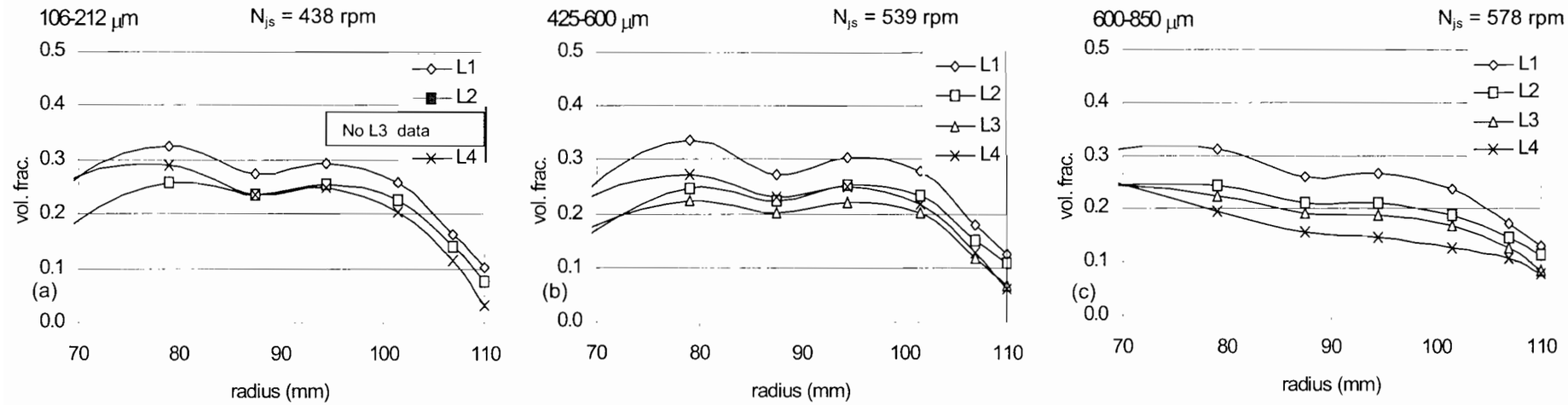


Figure 6.18: Radial concentration profiles for the Rushton impeller 20 % vol. at 547 rpm: 106-212 μm (a); 425-600 μm (b); 600-850 μm (c)

6.2.4 *Axial Concentration Profiles*

The average solids concentration for each layer for the three size fractions and two solids loadings (5 and 15 % vol.) was calculated and related to height (the electrode layer) in Figures 6.19-21. It is clear from these figures that the smallest size fraction generally has a higher concentration than the other fractions in the upper regions of the reactor and a lower concentration at the bottom of the reactor due the lower settling velocity resulting in more ready suspension. At the lower speed, 236 rpm, the axial profile has a curved gradient, while it approaches linearity at higher speed indicating greater axial homogeneity. At 547 rpm and 15 % solids concentration with the Rushton impeller there appears to be minimal difference in axial concentration between the size fractions (Figure 6.20 (b)).

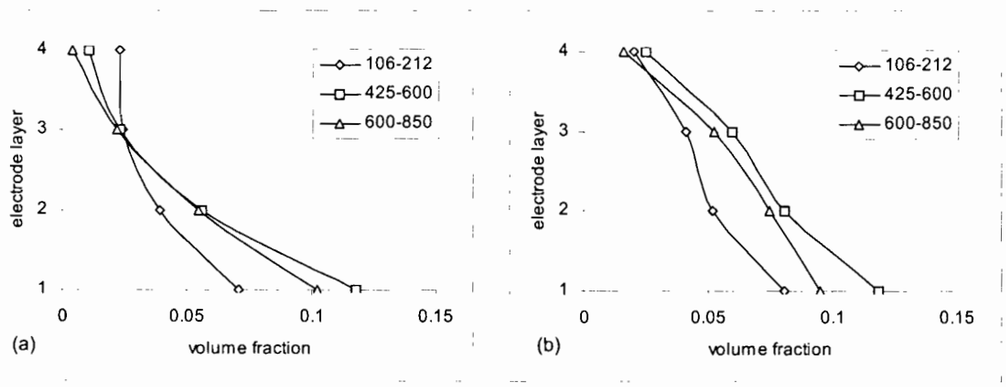


Figure 6.19: Axial concentration profiles for Rushton impeller for 5 % volume fraction at 236 rpm (a) and 547 rpm (b). (z/Z: L1 = 0.18; L2 = 0.41; L3 = 0.64; L4 = 0.86)

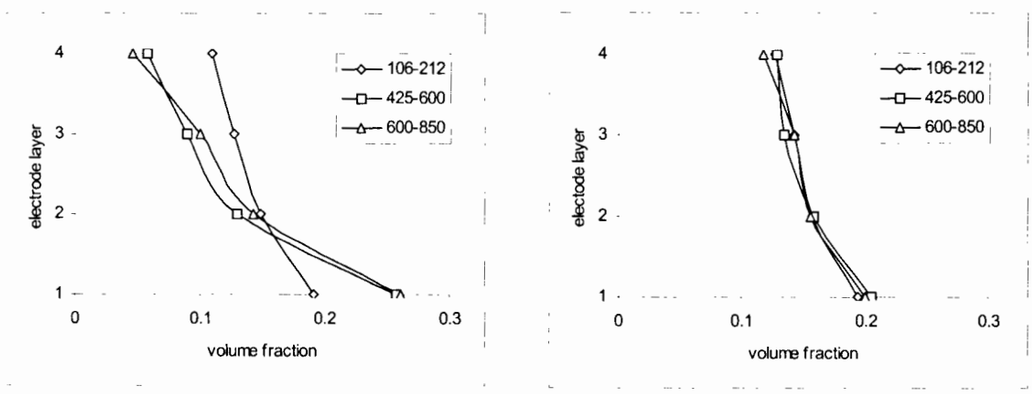


Figure 6.20: Axial concentration profiles for Rushton impeller for 15 % volume fraction at 236 rpm (a) and 547 rpm (b). (z/Z: L1 = 0.18; L2 = 0.41; L3 = 0.64; L4 = 0.86)

The pitched blade impeller does not produce the same degree of homogeneity at the same agitation rate as evidenced by comparing Figure 6.20 (b) to Figure 6.22 (b), i.e. there is a steeper axial gradient in Figure 6.20 (b).

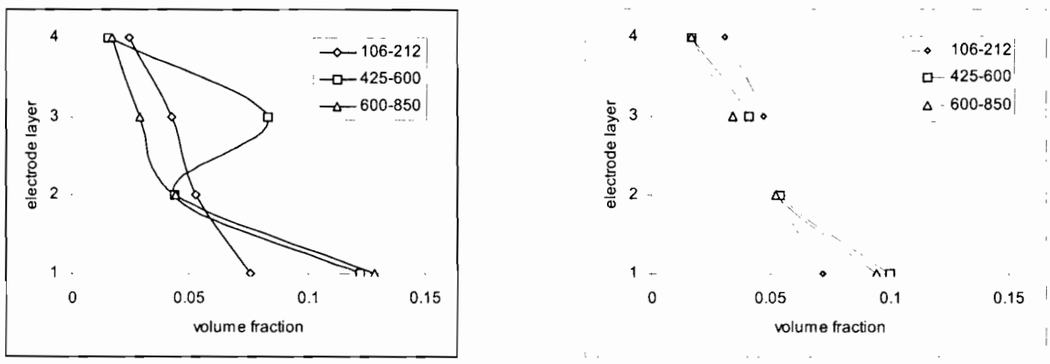


Figure 6.21: Axial concentration profiles for pitched blade impeller for 5 % volume fraction at 236 rpm (a) and 547 rpm (b). (z/Z: L1 = 0.18; L2 = 0.41; L3 = 0.64; L4 = 0.86)

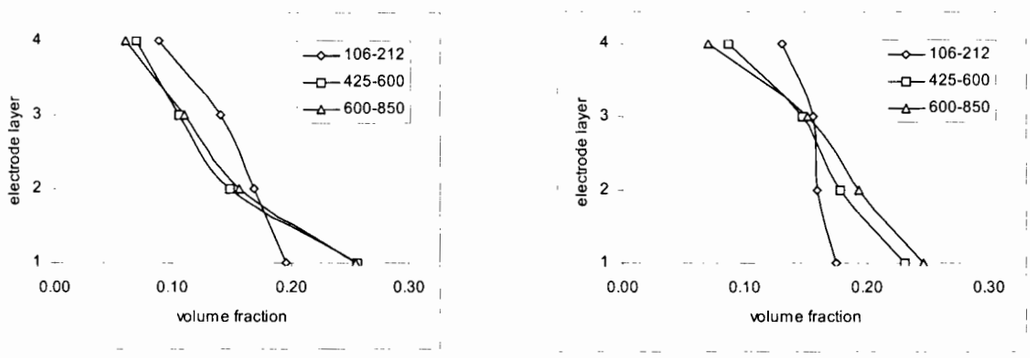


Figure 6.22: Axial concentration profiles for pitched blade impeller for 15 % volume fraction at 236 rpm (a) and 547 rpm (b). (z/Z: L1 = 0.18; L2 = 0.41; L3 = 0.64; L4 = 0.86)

Figure 6.21 (a) for the 425 – 600 μm fraction appears to be anomalous, and this result appears erroneous. The accuracy of electrical resistance tomography is discussed in Section 6.3.

It has generally been observed in the literature that there is an increase in particle concentration in the plane of the impeller (Barresi and Baldi, 1987a; McKee *et al.*, 1995; Nasr-El-Din *et al.,* 1996; Williams *et al.,* 1996). This is reported to be more pronounced with axial flow impellers and at higher agitation rates, which would have greater influence over particle settling velocities. In the data presented in this study, the impeller was approximately in the plane of the second layer of electrodes (L2). Further, it must be noted that the current field across the plane was not completely horizontal, and included axial components; thus some material above and below the impeller regime was detected. Furthermore, these axial profiles are for the

region r/R=0.63 to 1, thus it is not completely representative of all the solids in the horizontal plane. However, similar diagonally shaped axial concentration profiles were produced by Mann *et al.* (2001) using ERT in an 8 electrode layer 2.3 m^3 tank (Rushton turbine, H = T = 1.43 m, D = T/3, C = H/2) charged with 80 kg of polypropylene particles as observed in Figure 2.13.

In Figures 6.23 – 6.25, axial concentration profiles are presented for the three size fraction and two impeller types for the range of speeds tested (236-547 rpm). Increasing homogeneity is observed with increasing speed (the profile becomes more vertical). The Rushton impeller achieved better suspension than the pitched blade impeller for the 425-600 μm and 600-850 μm fractions at the same agitation rate (Figures 6.24 and 6.25). The 106-212 μm fraction appears to have small enough inertia to produce a similar suspension quality from both impellers (Figure 6.23). Williams *et al.* (1996) produced similar vertical profiles in a 30 litre tank with a torospherical base with ERT (4 layers of 16 electrodes) as presented in Figures 2.15, with speeds up to 280 rpm for a pitched blade impeller and 545 rpm for an A310 impeller suspending 150-210 μm quartzite (6.3 vol. %). Beyond these speeds for the respective impellers there was an increase in particle concentration in the plane of the impeller as discussed earlier.

In Figure 6.26, axial profiles are normalised across the solids loading range of 5 – 20 %. The 10 – 20 % concentration profiles appear similar. Higher relative solids concentration is achieved in the upper regions of the vessel with increased solids loading. This is postulated to be caused by particle-particle interaction and is discussed in Section 6.2.7.

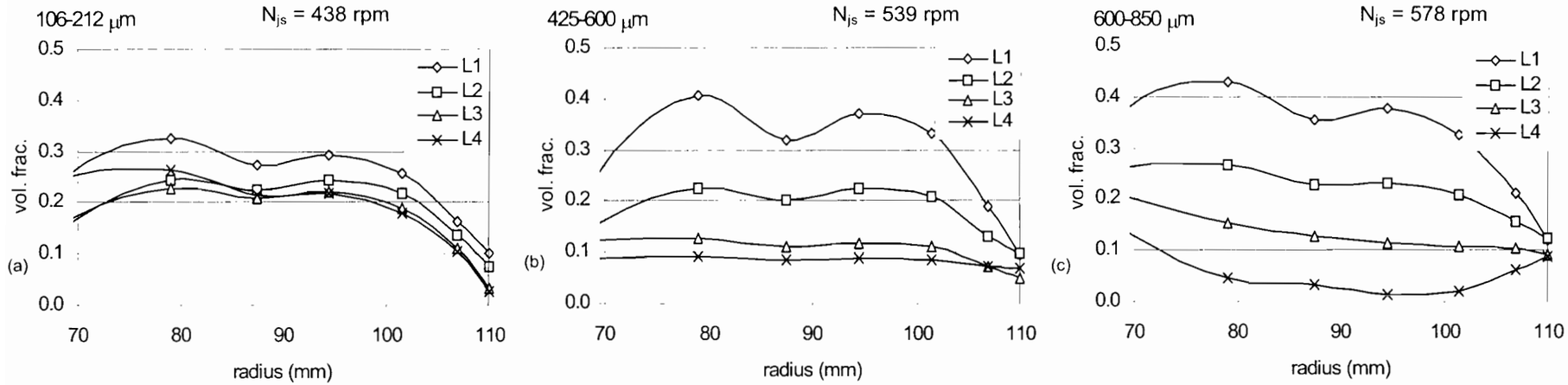


Figure 6.17: Radial concentration profiles for the Rushton impeller 20 % vol. at 236 rpm: 106-212 μm (a); 425-600 μm (b); 600-850 μm (c)

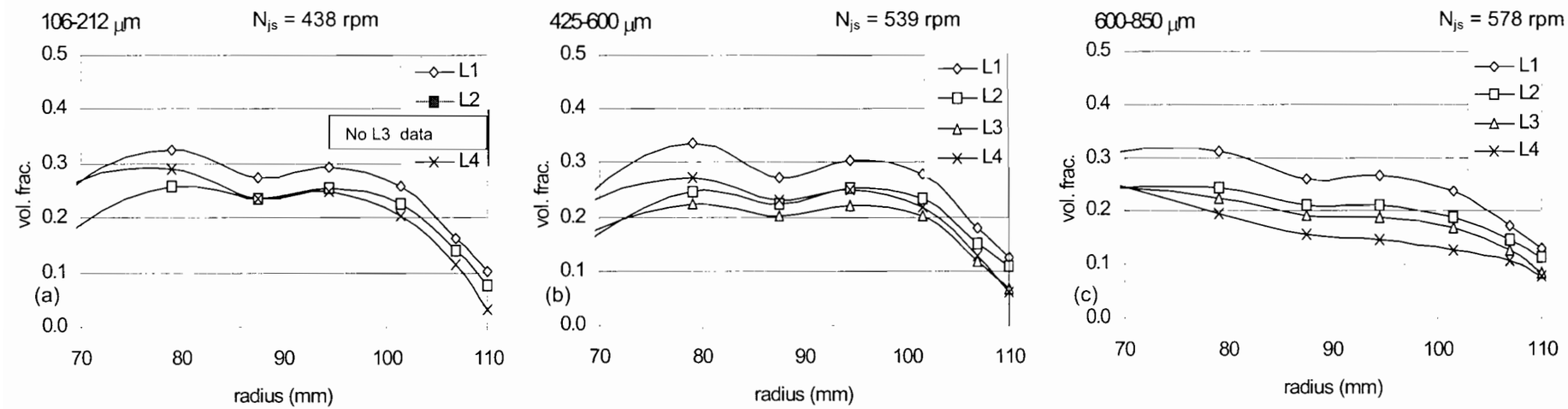


Figure 6.18: Radial concentration profiles for the Rushton impeller 20 % vol. at 547 rpm: 106-212 μm (a); 425-600 μm (b); 600-850 μm (c)

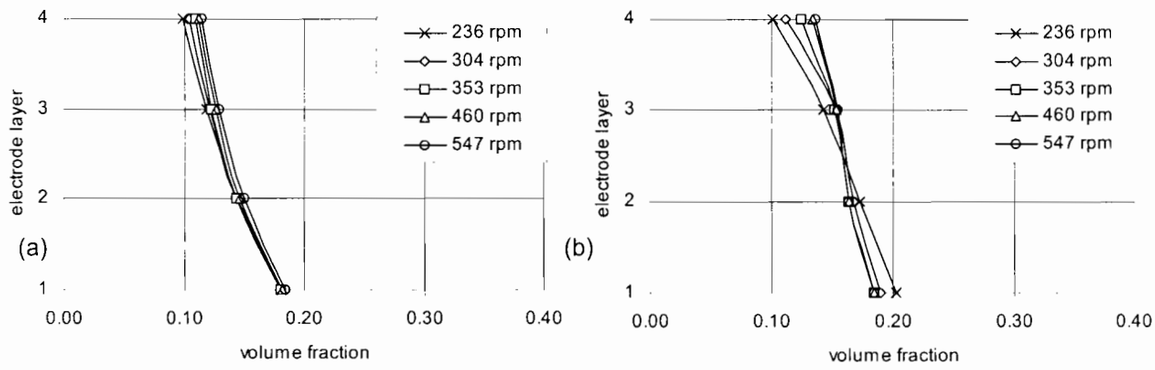


Figure 6.23: Axial concentration profiles for different agitation rates for the 106-212 μm fraction for 15 % solids concentration with the Rushton impeller (a) and the pitched blade impeller (b).

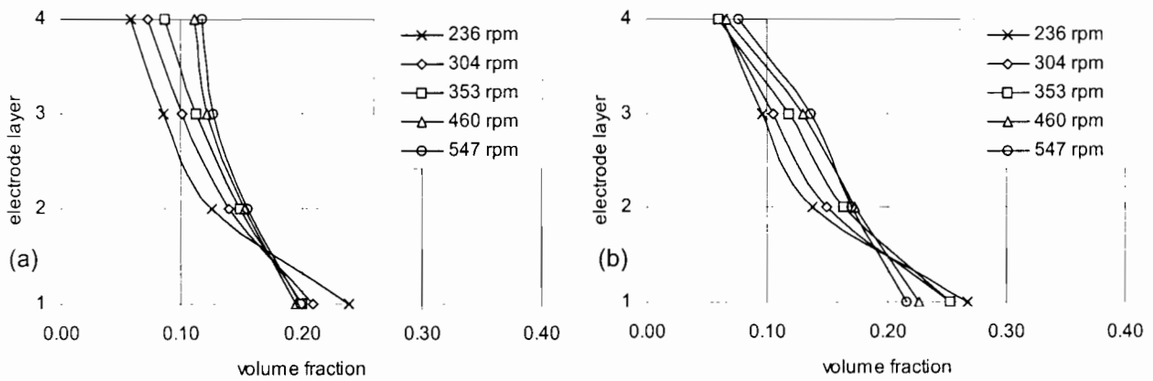


Figure 6.24: Axial concentration profiles for different agitation rates for the 425-600 μm fraction for 15 % solids concentration with the Rushton impeller (a) and the pitched blade impeller (b).

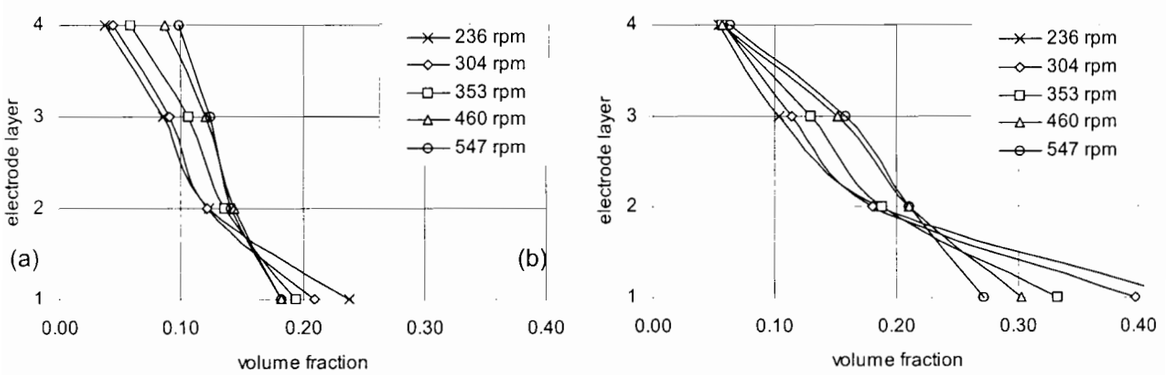


Figure 6.25: Axial concentration profiles for different agitation rates for the 600-850 μm fraction for 15 % solids concentration with the Rushton impeller (a) and the pitched blade impeller (b).

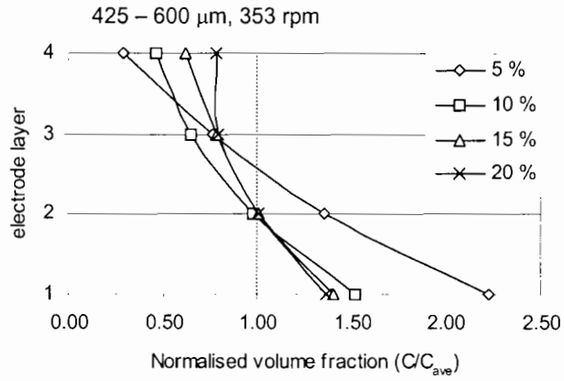


Figure 6.26: The effect of solids loading on normalised axial concentration at 353 rpm for the 425 – 600 μm fraction.

6.2.5 Analysing Reactor Homogeneity

It would aid understanding of mixing performance if the slurry homogeneity could be further quantified allowing analysis and comparison to other systems and operating conditions. Williams *et al.* (1996) defined a mixing index for this purpose:

$$MI_z = \frac{1}{C_m}\left[\frac{1}{n-1}\sum_{k=1}^{n}(C_k - C_m)^2\right]^{1/2} \qquad (2.15)$$

where C_m is the mean solid concentration, C_k, the solid concentration in the k^{th} pixel, and *n* the total number of pixels in the cross-section. This equation thus represents the variation of conductivity in the plane *z* as a standard deviation of concentration. If there is a high MI_Z value, then there is a high variation of solids concentration in the horizontal plane and therefore an indication of a lack of homogeneity. Williams *et al.* (1996) took this further with the concept of an overall mixing number, where the mixing indices for *q* planes in a reactor could be averaged to produce a single mixing number describing the homogeneity of the reactor:

$$\overline{MI} = \frac{1}{q}\sum_{z=1}^{q} MI_z \qquad (6.1)$$

As seen in Figures 6.3-6, a mixing number has been calculated to represent the average standard deviation within the 4 *z* planes. This is the average standard deviation in the radial direction, and has been labelled as $\overline{MI}_z$ (in keeping with Williams *et al.* (1996) coordinate labelling i.e. the *z* represents the plane and not the direction). Comparing the data in Figure 6.3 (a) with (b) and (c), Figure 6.3 (a) has a $\overline{MI}_z$ of 0.031 (or 0.031/0.500*100 = 6.2 % standard deviation in the radial plane),

while (b) and (c) are 0.023 and 0.030 respectively. This means that at 236 rpm the 425 – 600 μm fraction (b) is the most homogenous radially, followed by the 600 – 850 μm fraction (c) and then the 106 – 212 μm fraction (a). This is due to the sloping gradient of the profiles in (a). However, in Figure 6.4, at 547 rpm, the smallest fraction (a) is the most radially homogenous (0.022). In this way comparisons can be made of the operating conditions and how they affect homogeneity. Similarly for the pitched blade profiles (Figures 6.9-12), it can be observed that the 425-600 μm fraction has greater radial homogeneity than the 106-212 μm and 600-850 μm fractions.

While this mixing number is supposed to describe the overall mixing of the system, there is a limitation with this definition. Intuitively, it is known that small size fractions will produce more homogenous mixtures. While the pitched blade produces a steeper radial gradient, it can be observed that there is more consistent spacing between the layer profiles (L1-L4) indicating good axial homogeneity. It is thus proposed in this study that a mixing index be created in order to describe axial homogeneity:

$$MI_r = \frac{1}{C_m}\left[\frac{1}{j-1}\sum_{k=1}^{j}(C_k - C_m)^2\right]^{1/2} \tag{6.2}$$

where *j* is the number of pixels at the same radial position in the vertical direction.

Thus, for a ring in the mesh at a specific radial position, the standard deviation can be calculated in the vertical direction i.e. over all the rings at that radial position in the four planes. The average axial standard deviation can then be calculated by averaging the MI_r over all the radial positions. In this study the outer seven rings of the mesh were used in this calculation. So the axial number can then be defined as:

$$\overline{MI}_r = \frac{1}{s}\sum_{r=0}^{s} MI_r \tag{6.3}$$

where *s* is the number of radial positions in the mesh (seven in this study), which then allows calculation of the average standard deviation of concentration in the radial plane (z direction).

Referring back to Figures 6.3 and 6.4, $\overline{MI}_r$ increases from 0.023 through 0.048 to 0.044 with increasing solids size distribution at 236 rpm and from 0.026 through 0.088 to 0.092 at 547 rpm. This indicates that the suspension of the smallest size fraction of 106-212 μm is axially more homogenous which is in accord with common

sense. Similarly, the 106-212 μm pitched blade profiles can be seen to have far better axial homogeneity than their larger particle counterparts.

It is therefore proposed in this study, that when describing homogeneity for a mixing system that both mixing numbers should be indicated to allow more accurate understanding of the mixing efficiency. These numbers thus describe mixing in two dimensions. Most three dimensional mixing systems can be reduced to two dimensions through examining radial coordinates. These mixing "vectors" can be further reduced to a single number to describe overall homogeneity for the system. This can be achieved through weighting the mixing index according to the area of representation i.e. relating it to the geometry of the system. If these weighted mixing indices are then multiplied, the product effectively represents a 2D mixing area which describes the overall variation in concentration. This calculation procedure can be observed in Appendix G. An overall mixing index is thus postulated as:

$$MI = [\overline{MI}_z * w_r] * [\overline{MI}_r * w_z] \quad (6.4)$$

where MI is the overall mixing index, $\overline{MI}_z$ is the average standard deviation of concentration in the z-plane, w_r is the weighting factor relating to the radial distance that MI_z corresponds to in the reactor, $\overline{MI}_r$ is the average standard deviation of concentration in radial plane (vertical direction), and w_z is the weighting factor according to the vertical distance that MI_r corresponds to in the reactor. For the design of the FEM mesh in this study and according to the spacing of the four electrode layers, the vertical distance of L1 to L4 was greater than the radial distance of the last 7 data points of the mesh. The factor w_r is estimated as 1.00 and w_z equal to 1.88 i.e. w_z is weighted relative to w_r. Each $\overline{MI}_z$, $\overline{MI}_r$ and overall MI is shown in Table 6.2 along with the ratio of the agitation rate to the critical suspension speed (N/N_{js}) for the 5 and 15 % solid volume fractions. These data are graphically represented as in Figures 6.27 and 6.28 to describe reactor homogeneity in terms of the parameters of agitation rate, solids loading and mean particle diameter.

In Figure 6.27 (a) it is clear that at 236 rpm the 15 % solids fraction has a higher overall mixing index than at 5 % solids loading, thereby indicating decreased homogeneity. Furthermore, this difference is accentuated with increasing particle size indicating an exponential relation between particle diameter and reactor homogeneity. For each size fraction in Figure 6.27 (a), there is a decrease in homogeneity with increasing particle size. An increase in agitation rate increases homogeneity as observed in Figure 6.27 (b) as mixing index profiles are lower than those in Figure 6.27 (a). It is interesting to observe in Figure 6.27 (b) that the mixing index for the 425 – 600 μm fraction is slightly lower than the 106 – 212 μm fraction, while the 600 – 850 μm fraction is the same as the 106 – 212 μm fraction. This is

contrary to what is expected, but this can be explained due to the greater horizontal deviation observed in the 106-212 μm fraction concentration profile as seen in Figure 6.5 (a) and Figure 6.6 (a). These profiles tend to have a steeper gradient on approaching the vessel wall.

In Figure 6.28 the mixing index profiles of the pitched blade impeller can be seen to be higher than those of the Rushton impeller (Figure 6.27), indicating decreased overall homogeneity. In Figure 6.28 (b) the influence of a greater agitation rate is observed relative to Figure 6.28 (a), while again the 106 – 212 mm fraction mixing index appears to be greater than expected. However, it must be remembered that there was a sharp increase in concentration near the reactor wall for this size fraction using the pitched blade impeller. This led to an increase in $\overline{MI}_z$ which resulted in the higher than expected overall mixing index, MI.

Table 6.2: Two dimensional mixing indices and the overall mixing index for the specific reactor condition.

			Rushton				Pitched-Blade			
		rpm	MI_z	MI_r	MI	N/N_{js}	MI_z	MI_r	MI	N/N_{js}
5%	106 - 212 μm	236	0.031	0.023	0.0013	0.66	0.056	0.024	0.0025	0.53
		547	0.032	0.026	0.0016	1.53	0.060	0.019	0.0021	1.22
	425 - 600 μm	236	0.023	0.048	0.0021	0.54	0.042	0.052	0.0041	0.43
		547	0.014	0.040	0.0011	1.24	0.031	0.036	0.0021	0.99
	600 - 850 μm	236	0.030	0.044	0.0025	0.50	0.046	0.051	0.0044	0.40
		547	0.025	0.035	0.0016	1.17	0.036	0.034	0.0023	0.93
15%	106 - 212 μm	236	0.022	0.036	0.0015	0.56	0.066	0.044	0.0054	0.45
		547	0.028	0.029	0.0015	1.31	0.097	0.021	0.0038	1.05
	425 - 600 μm	236	0.029	0.088	0.0048	0.46	0.043	0.088	0.0071	0.37
		547	0.027	0.036	0.0018	1.06	0.034	0.061	0.0039	0.85
	600 - 850 μm	236	0.051	0.092	0.0088	0.43	0.059	0.103	0.0114	0.34
		547	0.046	0.035	0.0030	0.99	0.044	0.075	0.0062	0.79

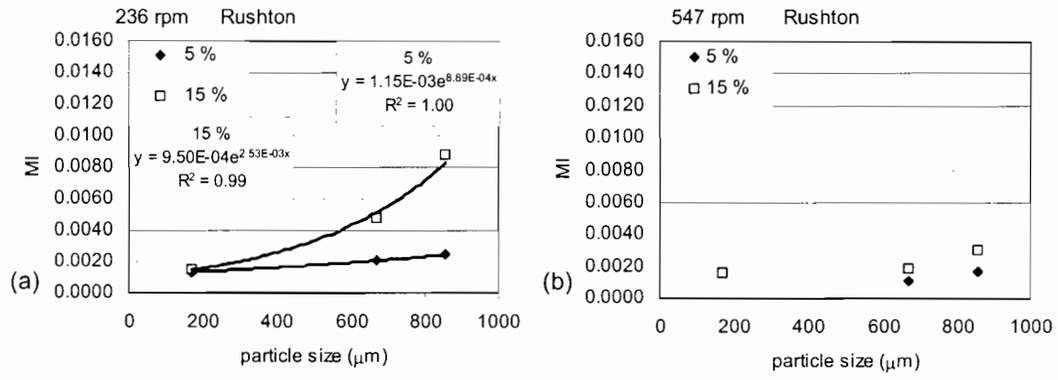


Figure 6.27: The effect of particle size, solids loading and agitation rate on the overall reactor homogeneity using the Rushton impeller. 236 rpm (a), 547 rpm (b).

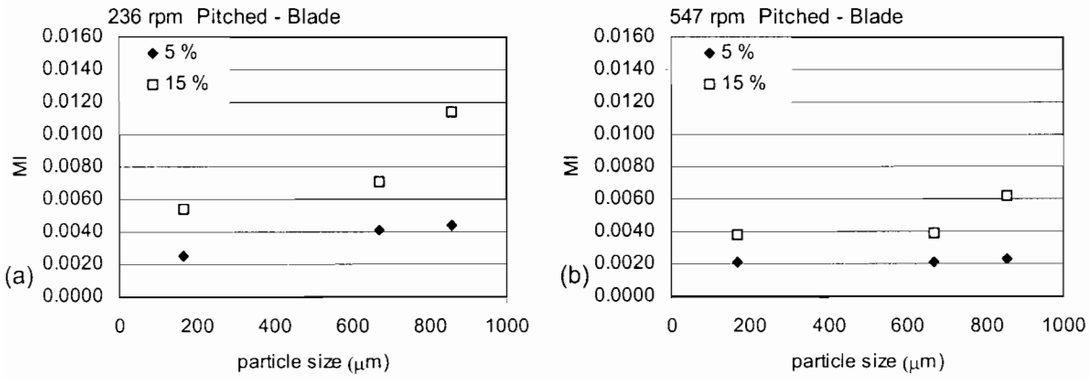


Figure 6.28: The effect of particle size, solids loading and agitation rate on the overall reactor homogeneity using the pitched blade impeller. 236 rpm (a), 547 rpm (b).

In Figure 6.29 (a) and (b), the effect of agitation rate on reactor homogeneity is further explored. Data are presented in Table 6.3. Here it is clearly observed increasing agitation rate increases reactor homogeneity for solid loadings of 5 and 15 % for both impellers. Moreover, there is a good correlation between the flattening out of these profiles at N_{js}, as defined by the Zwietering correlation. This supports this method of describing reactor homogeneity in terms of concentration variation in two dimensions.

Table 6.3: The effect of agitation rate on mixing indices for the 425 – 600 μm fraction

Loading/Impeller	rpm	236	304	353	460	547
	N/N_{js}	0.54	0.69	0.80	1.05	1.24
5%	MI_z	0.023	0.018	0.015	0.014	0.014
Rushton	MI_r	0.048	0.043	0.042	0.040	0.040
	MI	0.0021	0.0015	0.0012	0.0010	0.0010
	N/N_{js}	0.43	0.55	0.64	0.84	0.99
5%	MI_z	0.042	0.033	0.031	0.031	0.031
PB	MI_r	0.052	0.044	0.041	0.037	0.036
	MI	0.0040	0.0028	0.0024	0.0022	0.0021
	N/N_{js}	0.46	0.59	0.69	0.89	1.06
15%	MI_z	0.029	0.023	0.022	0.025	0.027
Rushton	MI_r	0.088	0.067	0.052	0.037	0.036
	MI	0.0048	0.0029	0.0021	0.0017	0.0018
	N/N_{js}	0.37	0.47	0.55	0.71	0.85
15%	MI_z	0.043	0.034	0.035	0.036	0.034
PB	MI_r	0.088	0.080	0.083	0.071	0.061
	MI	0.0071	0.0051	0.0054	0.0048	0.0039

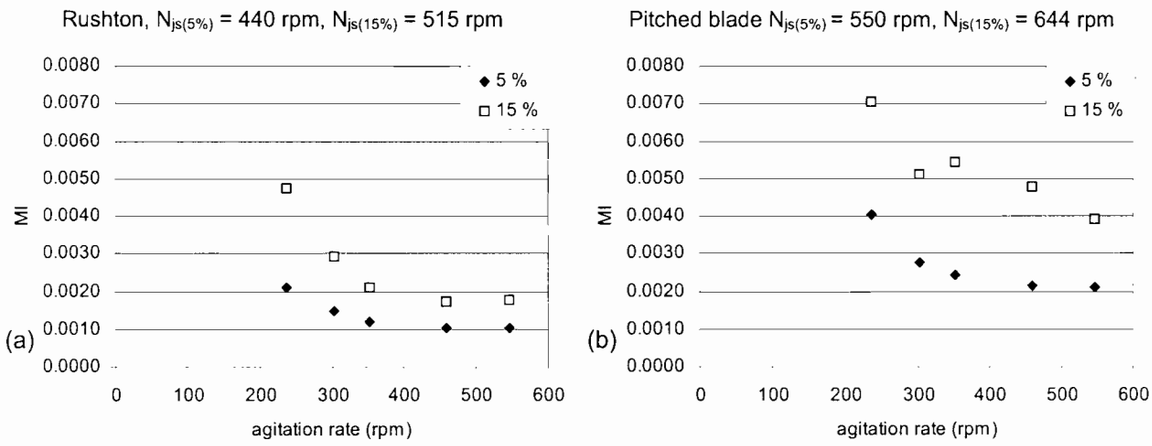


Figure 6.29: The effect of agitation rate on reactor homogeneity for 5 and 15 vol. % suspensions of 425 – 600 μm quartzite using Rushton (a), and pitched blade impellers (b).

In Figure 6.30, the effect of solids loading on reactor homogeneity is further explored for the 425 – 600 μm fraction agitated at 353 rpm. This operating condition represented the mid size fraction at the mid agitation rate. Data are presented in Table 6.4. It is clear an increase in solids loading decreases reactor homogeneity, while a similar trend is observed for both impellers. Furthermore, there appears to be an exponential relationship between solids loading and overall homogeneity.

Table 6.4: The effect of solids loading on mixing indices for the 425 – 600 μm fraction agitated at 353 rpm

Impeller	vol. %	5	10	15	20
Rushton	N/N_{js}	0.80	0.73	0.69	0.66
	MI_z	0.015	0.017	0.022	0.064
	MI_r	0.042	0.047	0.052	0.056
	MI	0.0012	0.0015	0.0021	0.0067
PB	N/N_{js}	0.64	0.58	0.55	0.52
	MI_z	0.031	0.035	0.035	0.071
	MI_r	0.041	0.064	0.083	0.091
	MI	0.0024	0.0042	0.0054	0.0120

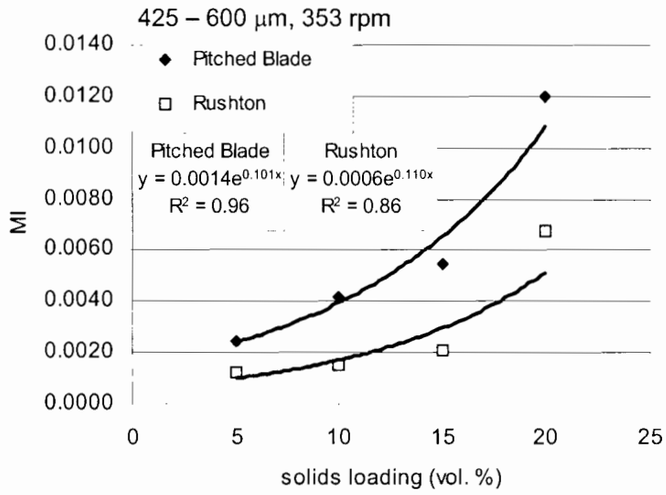


Figure 6.30: The effect of solids loading on reactor homogeneity at constant agitation rate of 353 rpm for 425 – 600 mm quartzite fraction

This mixing concept developed in this study appears to be useful in describing a reactor condition with a single number. Further, this number or overall mixing index can be related to other conditions and the effect of changing parameters on the overall homogeneity can be observed. Thus for a hypothetical online ERT process in an industrial setting, the mixing unit or slurry system could be easily described and monitored.

6.2.6 The Effect of Particle Diameter on Homogeneity

It was observed in the axial concentration profiles (Figures 6.19 – 6.26) that at incomplete suspension (236 rpm), a curved profile was observed, while on approaching complete suspension at 547 rpm a linear profile was present. In examining the effect of particle diameter on homogeneity, a graphical method based on the axial profile is used. In earlier studies, Barresi and Baldi (1987a) developed a suspension model (Section 2.7.3) based on a 'K' parameter:

$$K = \frac{\psi^{\frac{1}{3}} ND}{u_t} \tag{6.5}$$

where ψ is the power number, N the agitation rate, D the impeller diameter and u_t is the terminal settling velocity of the particle. This dimensionless number (similar to a Peclet number) describes the solid distribution in the vessel through accounting for turbulent diffusion and the anistropic turbulent motion. These authors found that the axial concentration profile depended on the *K* number. Increasing *K* increased the

quality of the suspension. Therefore, a stirred tank system at a constant agitation rate, where the addition of solids can be assumed not to affect the bulk fluid viscosity significantly, a change in the terminal velocity of the particle is expected to alter the quality of the suspension. Therefore, increasing the particle diameter is expected to decrease the quality of the suspension.

This principle was examined through focusing on the 5 and 15 % v/v solid suspension data at incomplete suspension (236 rpm) using the Rushton impeller, and the 20 % v/v suspension data at 304 rpm with the pitched blade impeller. The higher agitation rate was used with the pitched blade impeller to operate at a similar N/N_{js} ratio as found for the 15 % suspension agitated by the Rushton turbine. The N/N_{js} ratio ranges are reported on the top of Figure 6.31. To aid visual display, the average concentration for each electrode layer for each size fraction was divided by the average concentration in the top layer (L4). Thus this layer had a relative concentration of 1. An exponential function (ae^{-x}) was then fitted to these normalised data (Figure 6.31). Note that the exponent (x) is not affected by the previous division by the L4 volume fraction.

In Figure 6.31 the suitability of describing suspension quality as an exponential function of axial position is tested. The R^2 terms range from 0.9563 to 0.9991 thus the exponential function adequately describes the axial profile for these conditions. The mean particle diameter for the size fractions (Table 3.2) was then plotted against the exponent (x) (Figure 6.32), and good linear relationships were found ($R^2_{5\%\ Rushton}$ = 0.9824; $R^2_{15\%\ Rushton}$ = 0.9568; $R^2_{20\%\ Pitched\ Blade}$ = 0.9932). This indicates that the particle diameter is directly related to the suspension quality and thereby relates to the work of Barresi and Baldi (1987a).

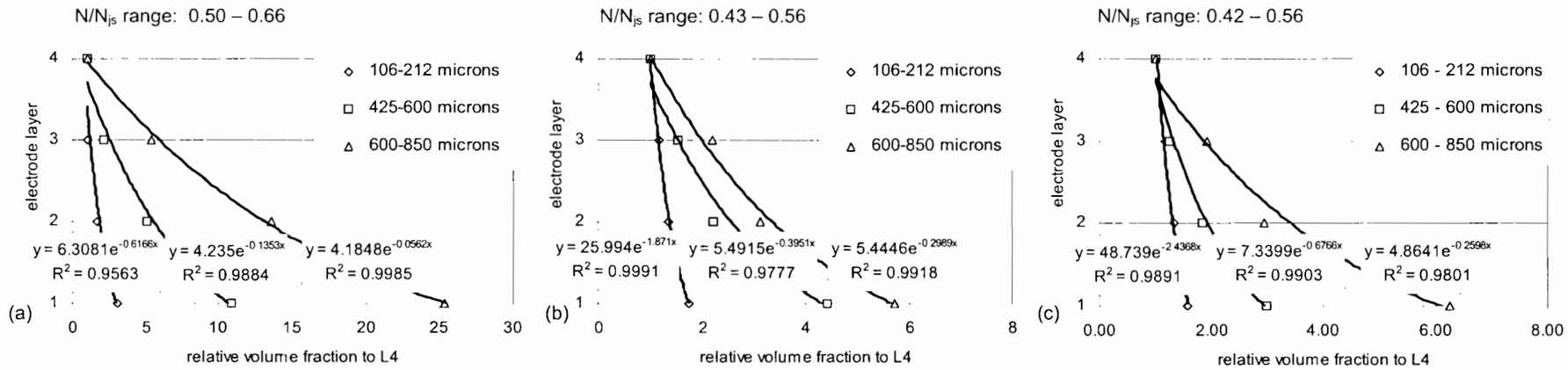


Figure 6.31: Exponential fitting of the axial concentration data for the 5 % solids loading (a) and the 15 % solids loading using a Rushton impeller at 236 rpm (b), and 20 % solids loading (c) at 304 rpm using the pitched blade impeller. Each layer concentration was normalised with respect to L4 fraction to aid visual display.

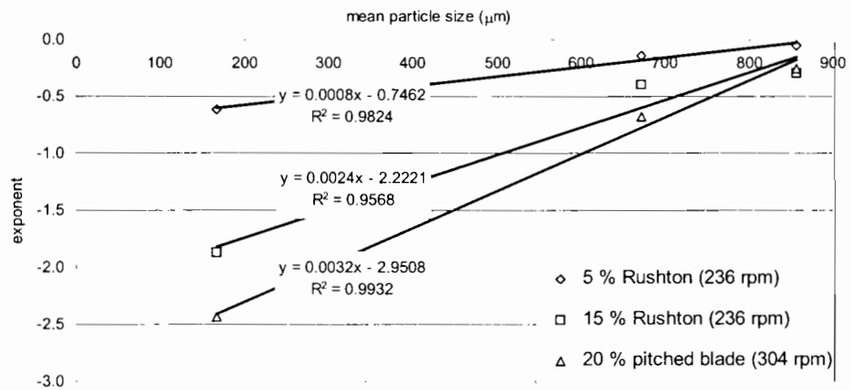


Figure 6.32: The linear relationship between the mean particle diameter and the exponent of the concentration profile (when applying exponential fitting to the axial profile). 5 and 15 vol. % using Rushton impeller at 236 rpm, 20 vol. % with pitched blade at 304 rpm

6.2.7 The Effect of Solids Loading upon Solids Suspension

It can be expected with higher solids loading that there will be a greater absolute presence of particles in the upper regions of the mixing vessel. This can be observed comparing Figure 6.3 with Figure 6.4, Figure 6.5 with Figure 6.6 etc. However, smaller solid fractions i.e. 5 %, produce suspensions of greater axial homogeneity. This can be observed by examining the $\overline{MI}_r$ values for the Rushton and pitched blade impellers in Table 6.2. Similarly, nearly all of the $\overline{MI}_z$ values for radial homogeneity are lower for the 5 % solid fraction than the 15 % fraction. These mixing indices, however, are absolute values and thus should rather be calculated as a percentage of the total solids content. On dividing the $\overline{MI}_z$ value by the total solid volume fraction, lower values are found for the 15 % fraction with respect to their 5 % counterparts, indicating a greater relative axial homogeneity for the former. The Zwietering equation predicts that higher solids loading in a vessel leads to a higher critical suspension speed, thus relatively there should be less solids in the upper region of the vessel at the same speed compared to smaller solid fractions i.e. comparing the amount of solids above the impeller to that of the whole vessel. This is assuming negligible increases in bulk viscosity.

To investigate this using the data from the current study, the $\overline{MI}_r$ values were corrected for solids loading and are compared in Table 6.5. Further, the relative concentration of solids above and below the impeller is examined through plotting the logarithm of volume fraction as a function of axial height for the Rushton impeller in Figures 6.33 and 6.34.

Table 6.5: Relative $\overline{MI}_r$ values for 5 and 15 % solids loading

			Rushton	Pitched-Blade
		rpm	MI_r as a % of solids loading	
5%	106 - 212 μm	236	46	48
		547	52	38
	425 - 600 μm	236	96	104
		547	80	72
	600 - 850 μm	236	88	102
		547	70	68
15%	106 - 212 μm	236	24	29
		547	19	14
	425 - 600 μm	236	59	59
		547	24	41
	600 - 850 μm	236	61	69
		547	23	50

The gradients in Figures 6.33 and 6.34 indicate that there is greater relative solids suspension for increasing solid fraction at 236 and 547 rpm. Gradients and correlation coefficients describing the linear fitting are presented in Table 6.6. Thus, higher solids loading produces greater relative axial homogeneity. Examining the gradients of the least squares fitting in Figure 6.35 suggest that the effect of increased solids concentration upon solids suspension is diminished beyond the range of 15-20 % concentration for the 425 – 600 and 600 – 850 μm fractions. These gradients represent the relative axial homogeneity. No decrease in gradient is observed for the 106 – 212 μm fraction indicating that particle-particle interaction is not approaching a maximum in the range studied (5 – 20 vol. %).

Shamlou and Koutsakos (1989) examined the effect of solids loading on solids hold-up by producing similar plots and found that for less than 4 wt. % solids the distribution of particles in the reactor (d_p = 390 μm, ρ_s = 2900 kg.m^{-3}, D = 10 cm, C = 15 cm, H = 65 cm, T = 22.5 cm, N= 300 rpm) was independent of solids loading. However, for 6 wt. % (2.2 % vol.) solids, which was the upper value of their range of study, it was found that there was greater solids hold-up i.e. the distribution of solids was not independent of the solids fraction. As the total solids concentration in the tank increases, particle-particle interference results, influencing the particle diffusion coefficient and the particle fall velocity in suspension through hindered settling. Shamlou and Koutsakos (1989) explained their results in this manner. Further, this explanation supports the increased hold-up of solids or relative axial homogeneity observed in the 5 - 20 % range when increasing solids concentration in this study.

Furthermore, the particle-particle interaction appears to be independent of agitation rate as observed in Figure 6.35. Moreover, the decreasing effect of solids loading upon relative axial homogeneity observed for the 425 – 600 and 600 – 850 μm fractions at higher concentrations suggests operating above this concentration range would not contribute to solids suspension. Further addition of solids beyond the maximum interaction point of particles would require extra power per unit of solids to achieve further particle homogeneity i.e. there is an operating point where it is inefficient to add more solids, as the positive suspension effects due to particle-particle interaction are at a maximum.

Table 6.6: Data of gradients and linear fitting of log(C) from Figures 6.26 and 6.27

rpm	236						547					
size (μm)	106 - 212		425 - 600		600 - 850		106 - 212		425 - 600		600 - 850	
vol. %	gradient (-)	R^2	gradient (-)	R^2	gradient (-)	R^2	gradient (-)	R^2	gradient (-)	R^2	gradient (-)	R^2
5	5.46	0.91	2.86	1.00	2.06	0.94	5.08	0.96	4.37	0.94	3.51	0.87
10	9.06	0.96	2.76	0.99	3.24	0.99	9.12	0.98	8.83	0.99	11.01	0.96
15	12.39	0.98	4.67	0.98	4.04	0.98	16.26	0.97	13.33	0.92	13.18	0.97
20	14.94	0.64	5.83	0.87	3.94	0.97	22.39	0.55	13.32	0.47	14.92	0.98

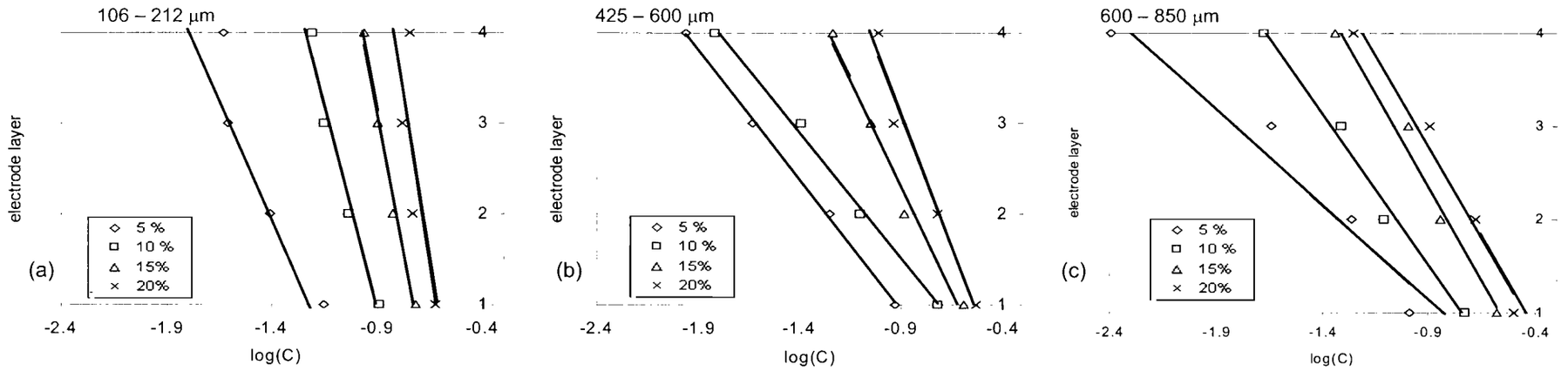


Figure 6.33: The relationship between solids loading and solids hold-up at 236 rpm for the Rushton impeller. 106-212 μm (a); 425-600 μm (b); 600-850 μm (c). *C* is the volume fraction.

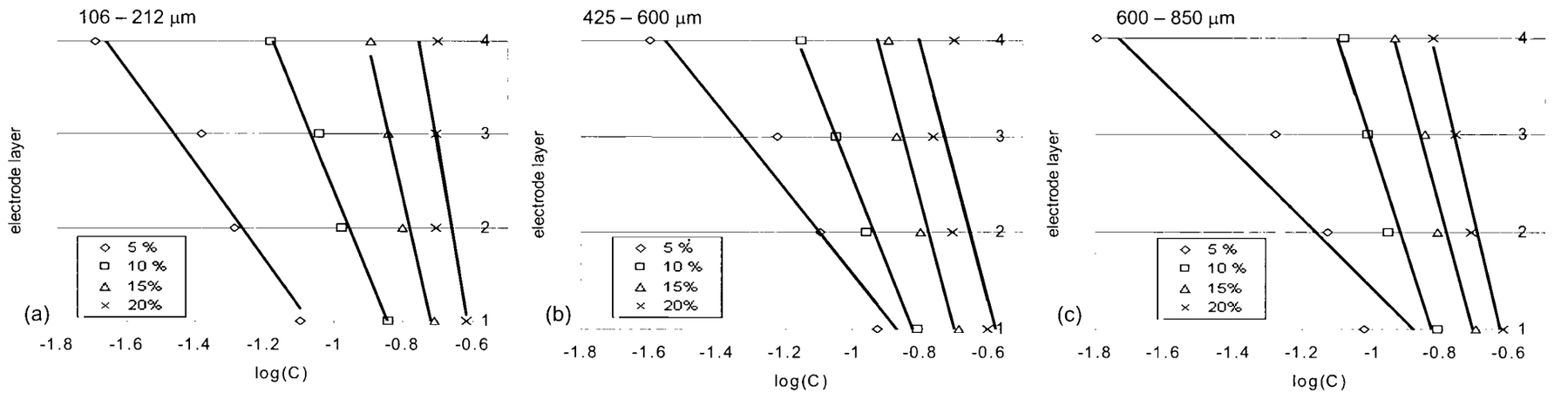


Figure 6.34: The relationship between solids loading and solids hold-up at 547 rpm for the Rushton impeller. 106-212 μm (a); 425-600 μm (b); 600-850 μm (c). *C* is the volume fraction.

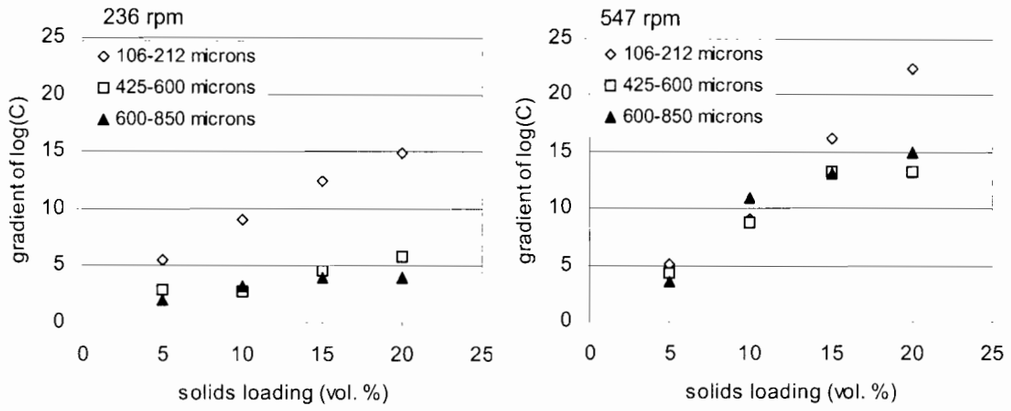


Figure 6.35: The examination of particle-particle interaction at increasing solid loading for the Rushton impeller at 236 rpm (a), and 547 rpm (b)

6.3 The Physical Validation of ERT

ERT was initially explored due to the dearth of other measurement technologies which could provide quantitative data. Further, these other technologies are often tedious in nature when obtaining data from the stirred tank environment. Consequently, there are challenges associated with the validation of ERT. In Section 2.6.1 the limitations of sample withdrawal were discussed, indicating that such data are largely qualitative. The insertion of a conductivity probe has been previously applied to stirred tanks to provide data on suspension concentration (Nasr-El-Din *et al.*, 1996). This has been related to ERT (Lucas *et al.*, 1999) and a greater accuracy has been found than sample withdrawal in establishing solids concentration. These methods for providing validation data are explored in this section for the top two layers of electrodes due to the inaccessibility of probing in the impeller plane and the higher fluctuation of solids concentration below the impeller (Barresi and Baldi (1987a)). Further, an examination of the errors associated with ERT is detailed.

6.3.1 Direct Sample Withdrawal and Gravimetric Analysis

6.3.1.1 Pipette Sampling of the 220 mm ID Tank

A 5 ml pipette tip was cut above the aperture to minimize the hindrance of larger particle sizes being withdrawn with the sample. The average volume of a pure liquid (water) was recorded after 6 withdrawals. The withdrawal velocity was calculated at 31.1 $cm.s^{-1}$ while the terminal settling velocity of an 800 μm particle is 12.7 $cm.s^{-1}$, thus large particles were captured easily (MacTaggart *et al.*, 1993). Sampling from

the surface minimised errors associated with sampling perpendicular to the circulation flow (Nasr-El-Din *et al.*, 1996). Sampling through pipetting was performed in triplicate at the height of the upper two electrode layers and radial distances of 1.00, 3.67, 8.00 and 11.00 cm (r/R = 0.09, 0.33, 0.73, 1.00). At r/R =1, or the vessel wall, the volume fraction of solids was found to fluctuate significantly due to the wall jets. A minimum distance of 20 mm from the wall was suggested by Barresi and Baldi (1987a), hence sampling was performed at 30 mm from the wall (r/R = 0.73). However, extra sampling data was captured for the 5 % concentration of 106 – 212 μm quartzite at 236 rpm in order to provide validation of the trend of the concentration profile approaching the wall. Sampling was performed in this case up to r/R = 0.82.

Thus the ERT data near the vessel wall cannot be validated by this method; however, the trend of the sample profile over the radius 0.09 to 0.73 provides some data for validation. Sample weights were calculated with Equation 3.1 (Section 3.1.10).

Suspension of the 600-850 μm fraction at 15 % solids concentration was sampled at three agitation rates and is presented in Figure 6.36. The ERT data point at r/R =0.63 appears relatively greater than the sample profile. The correlation between ERT data and sampling at r/R =0.72 is good. L3 from the ERT data appears to be a reasonable continuation from the L3 profiles determined from the sample data, while L4 (ERT) appears to be underestimated at the highest speed (547 rpm) relative to the sample data while correlating well with sample data at 236 and 353 rpm. The standard deviation between the samples taken in triplicate ranged between 0.5 and 9 %.

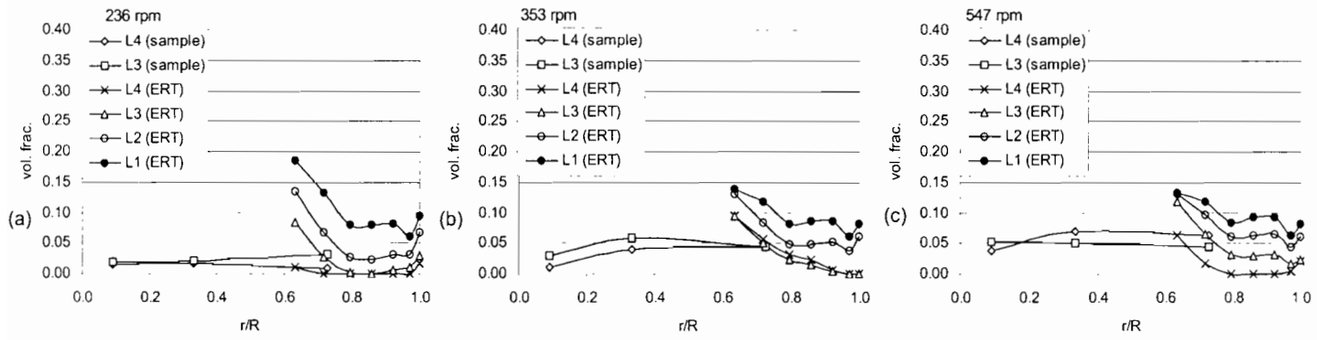


Figure 6.36: 15 % volume concentration of the 600-850 μm fraction representing sample values (L4 and L3) and ERT values (L1-L4). 236 rpm (a); 353 rpm (b); 460 rpm (c).

In Figure 6.37, data are presented for the sampling of the suspension of a 5 % concentration of the 106-212 μm fraction with the results presented for agitation rates of 236 and 353 rpm. The standard deviation between the samples taken in triplicate

ranged between 0.5 and 7 %. Comparing the qualitative sampling results with the ERT results, it is apparent that the first ERT data point at r/R =0.63 appears to be significantly higher than the sampling profile, although there is fair agreement with the second ERT data point with sampled data (r/R =0.72), as reported at 15 % loading. This could attributed to the influence from the impeller calibration at r/R =0.63 for this particle concentration. Extra sampling data was captured at 236 rpm and 5 % loading at r/R = 0.09; 0.33; 0.55; 0.64; 0.73; 0.82. These data indicate a relatively flat profile thus not supporting the higher concentration values for the ERT data at r/R = 0.63. However, the ERT data points closer to the vessel wall are consistent with direct sampling. In Section 2.6.1, MacTaggart *et al.* (1993) argued that a reliable measure of the local solids concentration through sample withdrawal was not possible, while Barresi and Baldi (1987a) found that sample reproducibility was approximately 10 % and that sample accuracy differed approximately 10 – 20 % with the known solids concentration. Nasr-El-Din *et al.* (1996) similarly found errors of up to 20 % with the known solids concentration. Thus only a qualitative comparison is possible with ERT and physical sampling.

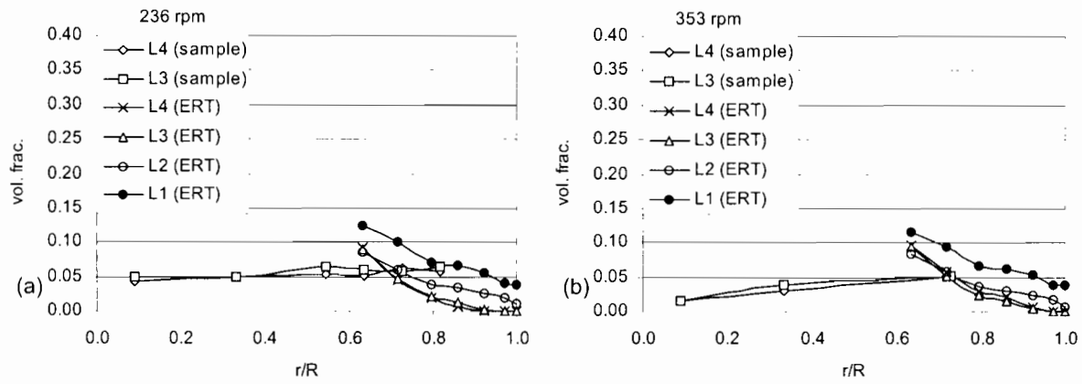


Figure 6.37: 5 % volume concentration of the 106-212 μm fraction representing sample values (L4 and L3) and ERT values (L1-L4). 236 rpm (a); 353 rpm (b).

6.3.1.2 Error Analysis of Pipette Sampling

The standard deviations as a percentage of the mean for the sampling data (Figures 6.36 and 6.37) are presented in Tables 6.7 and 6.8. These were calculated from the sampling in triplicate. The coefficient of variance lay in the range 0.2 to 8.7 %. As expected, standard deviations were generally higher for the higher agitation rates due to increased concentration fluctuations. The representivity of sampling in triplicate from one radial position was determined with the data in Table 6.9. For this data, sampling was performed at L3 at r/R = 0.73 at 304 rpm for 5 % solids concentration (106-212 μm). Four sets of 3 samples were taken with the maximum deviation being 3.11 %, while the deviation across all 12 samples was 1.77 %. Therefore, this sampling method is reproducible. However, it is limited in accuracy by

the withdrawal velocity, the pipette tip shape and alignment with the flow direction as discussed in Section 2.6.1.

Table 6.7: Standard deviations as a percentage of the mean for the sample data collected at 5 % solids loading (106-212 μm)

rpm	r/R	0.09	0.33	0.73
236	L4	1.80	1.00	1.33
	L3	0.83	0.38	0.15
353	L4	0.23	2.48	6.63
	L3	1.47	1.84	4.05

Table 6.8: Standard deviations as a percentage of the mean for the sample data collected at 15 % solids loading (600-850 μm)

rpm	r/R	0.09	0.33	0.73
236	L4	1.58	0.89	0.31
	L3	1.11	1.94	0.82
353	L4	2.05	0.89	3.08
	L3	3.75	1.05	0.87
547	L4	0.54	6.09	8.67
	L3	0.43	3.89	6.64

Table 6.9: Standard deviations and overall deviation (% of mean) of 4 samples taken at 304 rpm for L3 at r/R = 0.73 for 5 % solids concentration (106-212 μm)

r/R	sample no.	% std. dev.
0.73	1	3.11
	2	0.72
	3	0.10
	4	2.02
	overall Std. dev.	1.77

6.3.2 Determination of the Concentration Profile through Conductivity Measurement

6.3.2.1 Conductivity Probing of the 220 mm ID Tank

The conductivity probe described in Section 3.1.7 was inserted into the slurry reactor at the same positions as the direct sampling points. The maximum conductivity of the clear fluid was recorded during agitation allowing volume fraction calculation from the Maxwell relation (See Appendix G).

The conductivity profile for suspension of 5 % quartzite (106-212 μm) at 236 and 353 rpm is given in Figure 6.30. The concentrations determined by the conductivity probe

are slightly lower than the sample values (Figure 6.29). While the ERT data point at r/R = 0.63 again appears to be too high, the rest of the ERT profile appears reasonable. For the 10 % solids concentration (425-600 μm) agitated at 236 rpm, the ERT data point at r/R =0.63 appears reasonable, as shown in Figure 6.31. There is good agreement with L3 and L4 at the higher agitation rate of 353 rpm, shown in Figure 6.31 (b).

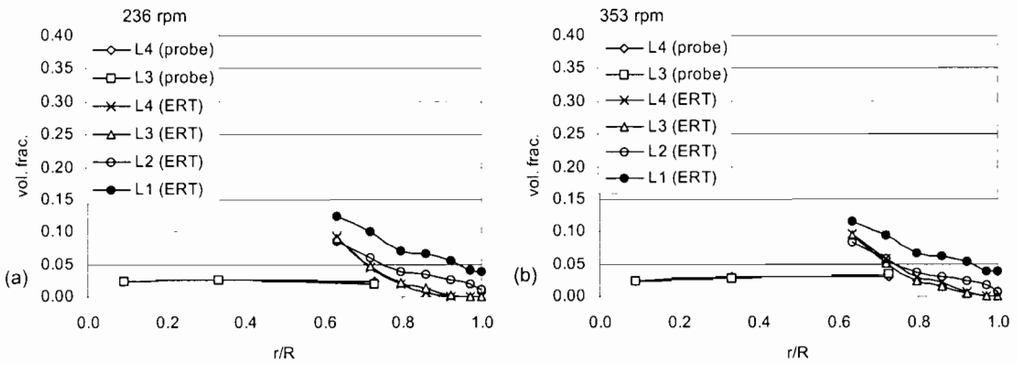


Figure 6.38: 5 % volume concentration of the 106-212 μm fraction representing conductivity probe values (L4 and L3) and ERT values (L1-L4). 236 rpm (a); 353 rpm (b).

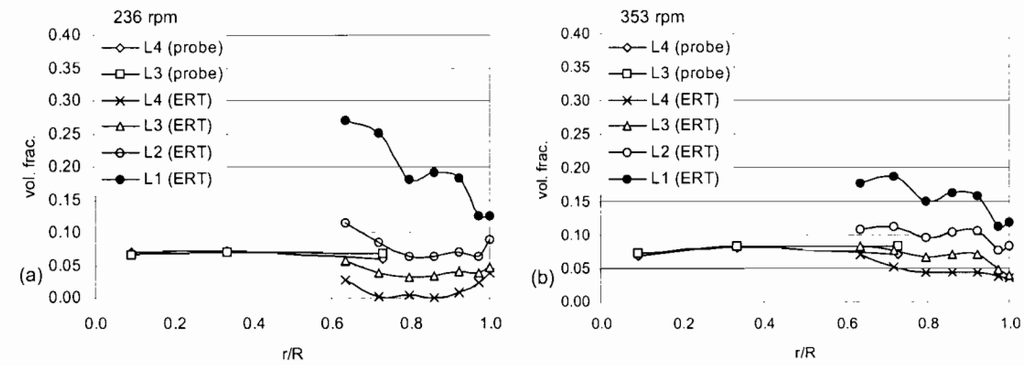


Figure 6.39: 10 % volume concentration of the 425-600 μm fraction representing conductivity probe values (L4 and L3) and ERT values (L1-L4). 236 rpm (a); 353 rpm (b).

As observed with the comparative physical sampling (Figures 6.36 and 6.37), the ERT data at r/R = 0.63 and 0.73 in Figure 6.38 appear higher than the conductivity probe data. However, if an average profile is taken for the ERT data, similar concentrations will result thereby supporting the axial concentration profiles in Section 6.2.4. Nasr-El-Din *et al.* (1996) found very good agreement between conductivity probe data and actual solids concentration in sedimentation vessels and slurry pipelines through application of the Maxwell equation. McKee *et al.* (1995) and

Lucas *et al.* (1999) also used conductivity probe data as representative of solids concentration in ERT studies.

6.3.2.2 Conductivity Probe Error Analysis

Fifteen conductivity readings were taken from each radial position, with each reading being representative of the average conductivity over 5 seconds. In all cases but one, the standard deviation was less than 1 % of the mean (Tables 6.10 and 6.11). It was apparent that there is greater deviation at higher agitation rates.

Table 6.10: Standard deviation of conductivity measurement as a percentage of the mean for the 5 % solids concentration (106-212 μm)

rpm	r/R	0.09	0.33	0.73
236	L4	0.28	0.12	0.25
	L3	0.39	0.50	0.08
353	L4	0.86	0.60	0.68
	L3	0.43	0.46	2.35

Table 6.11: Standard deviation of conductivity measurement as a percentage of the mean for the 10 % solids concentration (425-600 μm)

rpm	r/R	0.09	0.33	0.73
236	L4	0.18	0.39	0.03
	L3	0.18	0.60	0.57
353	L4	0.46	1.45	0.73
	L3	0.63	0.73	0.83

6.3.3 General Error Associated with ERT

As a general estimate, resolution using the 16 electrode system and Newton-Raphson algorithm is limited to approximately 5 % of the vessel diameter (Randall, 2005; Wilkinson, 2005a). This can be influenced by algorithm smoothing factors, FEM mesh coarseness and the design and modeling of the electrodes. In Chapter 7, the error between ERT measurement frames and experiments is examined.

6.4 Conclusions

ERT application to the stirred tank environment was successful with implementation of ERT Hardware I and Reconstruction Code III. The parameters of impeller type, particle size, solids concentration and agitation rate were examined with respect to the radial and axial concentration profiles. In general, the Rushton impeller was found to yield better quality suspensions operating at the same speed as the pitched blade impeller. For the finer particles (106-212 μm) up to 15 % solids concentration, the

radial concentration profiles differed for the pitched blade impeller with respect to the Rushton turbine. With the pitched blade impeller it was hypothesised that the smaller particles followed the circulation flow near the vessel wall resulting in high wall concentrations. In general, particle concentration in the 220 mm vessel decreased or stayed the same on approaching the vessel wall. Suspension quality was quantified through the calculation of the standard deviation of the concentrations in the radial direction to yield a mixing number following on from the work of Williams *et al.* (1996). This concept was extended to calculate the standard deviation of concentration in the vertical plane to provide an overall perspective of the vessel homogeneity. These two mixing indices were combined to form an overall mixing index that described the homogeneity in 2D allowing comparison of reactor states. In this manner the effect of the parameters on particle suspension was quantified. A good correlation was observed between N_{js}, as defined by Zwietering, and a flattening out of the mixing index profile with respect to agitation rate.

As observed in the axial profiles, an increase in agitation rate increases homogeneity, while it was found that particle size is inversely related to the quality of the suspension through the parameter of the particle terminal settling velocity. Increasing the solids content in the vessel, *ceteris paribus*, leads to a decrease in absolute axial homogeneity, but an increase in relative axial homogeneity due to particle-particle interaction. This hindered settling effect approached a maximum at 15 to 20 % solids concentration by volume for the 425 – 600 and 600 – 850 μm fractions.

The data obtained by pipette sampling resulted in trends in solids loading that supported the ERT profiles in general. However, the ERT data point at r/R = 0.63 appeared to be consistently higher than the concentration measured by sampling. Sampling was found to be reproducible, although not necessarily accurate. Sampling uncertainty increased at increasing agitation rate. The data collected using the conductivity probe similarly provided trends that confirmed the ERT profiles, with better agreement obtained for the 10 % suspension of the 425-600 μm fraction compared to the 5 % suspension of the 106-212 μm fraction. The uncertainty using the probe relative to the sampling method decreased, while uncertainty also increased upon increasing agitation rate. It is apparent from these data sets that sampling and conductivity probing cannot validate the solids concentration of the last 2 cm approaching the vessel wall.

ERT has provided valuable information on particle suspension as a function of operating conditions and is supported through similar trends obtained through direct measurement of suspension concentration and conductivity. This knowledge provides further understanding for operating and designing slurry bioreactors.

Chapter 7

Developments in ERT and the Effect of Reactor Scale

7.1 Introduction

A more sophisticated ERT technology became available in the course of this study in the form of ERT Hardware III and Reconstruction Code V. This was developed at UCT and is described in Section 4.8 and 4.9. This system had faster data acquisition rates and more accurate mapping of the reactor geometry and was applied to a small scale ERT reactor. The objectives were two-fold: to apply and evaluate developments in ERT technology to the stirred tank environment and to examine the effects of reactor scale. This small scale reactor had a diameter of 50 mm and was agitated by a Rushton impeller (Section 3.4). Further, this system was geometrically similar to the 220 mm tank. The design of this small reactor was influenced by the limits of the magnet bore width of 63 mm at the Magnetic Resonance Research Centre at the University of Cambridge. This was to allow comparative MRI experiments on the mini-reactor described in Section 3.3 which is presented in Chapter 8. This chapter begins with an initial investigation of phantoms, followed by the application of ERT to the stirred tank environment of the 50 mm reactor with comparison of previous results obtained from the larger vessel. Error between reconstructed measurement frames and experiment reproducibility is examined at the end of the chapter.

7.2 Detecting Physical Phantoms

Figure 7.1 (a) and (b) show the online detection of three conducting (black) and non-conducting (white) physical phantoms in an eight layered 20 cm ID vessel.

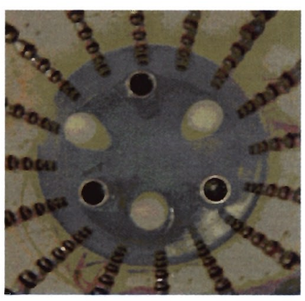
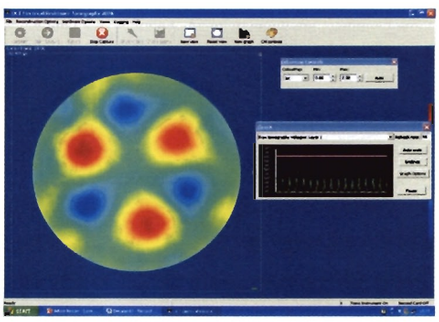
(a)  (b) 

Figure 7.1: Conducting and non-conducting cylinders in a 20 cm ID, 8-layered tank of the University of Manchester (a), and the online image from Reconstruction Code V (b).

These tests were conducted by the Department of Electrical Engineering at the University of Manchester (Randall *et al.*, 2005) and illustrate the system's ability to account for multiple objects of variable conductivity in the tank environment. The calculated conductivity profile from one iteration of the Newton-Raphson algorithm from Reconstruction Code V was compared to the actual object as illustrated in Figure 7.2. In this case it was the non-conducting white cylinder. The conductivity threshold which manipulates the greyscale of the image can be altered to yield higher definition of the object of interest as indicated by the 'upper threshold' and 'lower threshold' in Figure 7.2.

Reconstruction Code V and ERT Hardware III were therefore seen as acceptable in phantom detection and the focus shifted to a comparison with ERT Hardware I and Reconstruction Code III of the suspension of solids in the 220 mm tank.

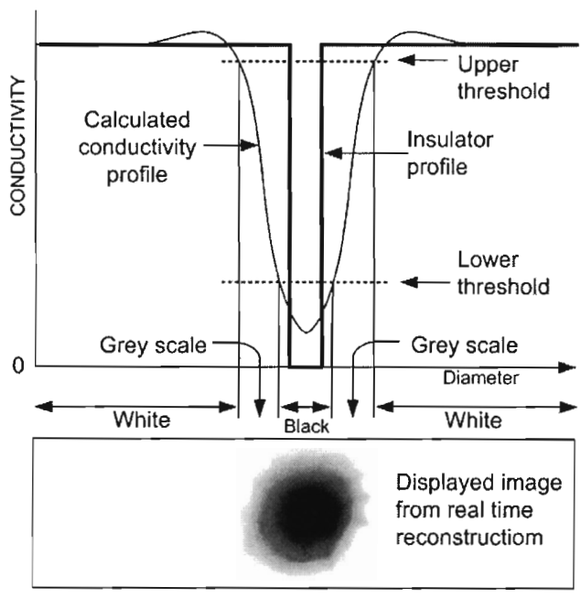


Figure 7.2: Comparison of the calculated conductivity profile with the actual object

7.3 Comparison of Latest ERT system with Initial System

ERT Hardware III and Reconstruction Code V were applied to a 15 % v/v suspension of 600 – 850 μm quartzite at 547 rpm in the 220 mm vessel. The FEM mesh used with this system is given in Appendix J. These profiles were compared to those obtained from Reconstruction Code III and Hardware I and are shown in Figure 7.3. The same $\overline{MI}_r$ values of 0.035 were obtained indicating similar axial homogeneity. The values of $\overline{MI}_z$ were similar at 0.046 and 0.052. However, with the new system profiles, there is a gradual increase in concentration on approaching the vessel wall

in contrast to ERT Hardware I and Reconstruction code III. The latest profiles are expected to have greater accuracy due to more accurate calibration and mapping of the domain.

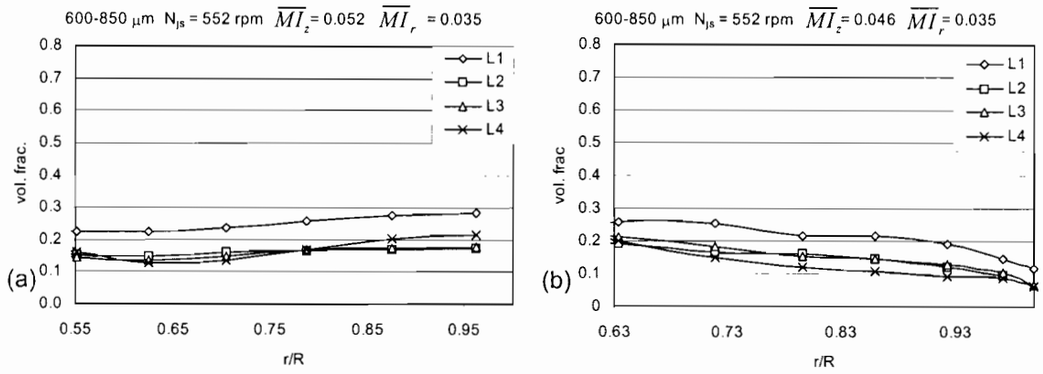


Figure 7.3: Comparison of Reconstruction Code V and ERT Hardware III (a), with Reconstruction Code III and ERT Hardware I (b) at 15 % solids concentration with the 600 – 850 μm quartzite fraction at 547 rpm.

7.4 Quartzite Suspension in the 50 mm ID Perspex Tank

7.4.1 Characterisation of the 50 mm ID Stirred Tank System

ERT experiments with Reconstruction Code V and ERT Hardware III were performed on the mini-CSTR described in Section 3.4 using the 600 - 850 μm fraction of quartzite at concentrations of 5 and 15 % by volume. A new 788 element mesh was created (Appendix H) to account for the different orientation of electrodes with respect to the baffles and the area in the tank cross-section containing baffles. A hole was created in the middle of the mesh to account for the impeller zone. This mesh only produced viable results for the 1 cm near the vessel wall and was thus abandoned. Another mesh of 764 elements was created (Appendix I) with no hole present for the impeller zone. This mesh produced similar profiles to Hardware I and Reconstruction Code III and was used in all experiments for the 50 mm tank. These meshes have irregular elements and thus 12 radial subdivisions were created to calculate the radial profiles as well as to relate to the concentric mesh used in Reconstruction Code III. Information was extracted from a radial distance of 27.5 to 50 mm (r/R = 0.55 to 0.96), providing more information than obtained in the 220 mm tank. The dimensionless radius of 0.96 resulted from averaging radial distances for the outermost radial subdivision. Using this small scale reactor, turbulence conditions similar to those in the 220 mm tank could not be created (Table 7.1). Experiments were based on impeller tip speed as this is often used to quantify shear stress in bioreactors. Specific power was also investigated as this is used in mass

transfer and cell disruption correlations. The power input for these impellers was extracted from the graphical relationship between power number and Reynolds number (Perry *et al.*, 1998). At the high Reynolds numbers tested, presented in Table 7.1, power numbers are similar for the range of agitation rates used. However, a maximum in the N_P-N_{Re} curve is generally observed at N_{js} in the presence of solids (Bohnet and Niesmak, 1980). Thus P/V is expected to increase slightly for all agitation rates tested in the 220 mm tank with the presence of solids, while a slight decrease in P/V for the agitation rates of 2024 and 2407 rpm in the 50 mm tank is expected. Zwietering suspension speeds are presented in Table 7.3. For the purposes of calculation, an approximate power number of 5 is used. This is also the average power number observed by Scholtz-Brown (1998) in a geometrically similar vessel with solids loading of 5 to 20 % with impeller tip speeds of 0.77 to 3.49 $m.s^{-1}$.

Buurman *et al.* (1986) report that transport of a solid particle of diameter between 100 μm and 2 mm requires the size of the eddy to be typically 3 – 5 times larger than the particle. In stirred tanks, largest eddy sizes are determined by the dimensions of the impeller, while the smallest eddy sizes depend on the energy dissipation range, characterised by the Kolmogorov length scale. This length scale was calculated using Equation 7.1 according to Kolmogorov (1941):

$$\eta = \left(\frac{\nu^3}{\varepsilon} \right)^{0.25} \tag{7.1}$$

where η is the eddy length (m), ν is the kinematic viscosity ($m^2.s^{-1}$) and ε is the turbulent power dissipation per mass of liquid ($W.kg^{-1}$). It is presented in Table 7.2.

Thus typically, the inertial sub-range of the turbulence spectrum lies between these two eddy sizes and is responsible for particle lift-off. On operating the 50 mm tank impeller at the same tip speed as the 220 mm tank impeller, the Kolmogorov eddy sizes are smaller (Table 7.2). Therefore, eddy sizes for both tanks are less than 3 – 5 times greater than the smaller particles of the 600 – 850 μm size distribution (Figure 3.12 (c)) ($d_{10} \approx 612$ μm). Furthermore, there is an enhancement of the turbulent energy spectrum with the presence of solids which causes a reduction in the Kolmogorov eddy size (Caulet *et al.*, 1996).

Larger eddies mediate the circulation of the fluid in a tank, while the fluctuating velocity component is proportional to the circulation velocity i.e. the impeller tip speed. Thus, the smaller tank has a fluctuating velocity similar to the 220 mm tank, but the largest eddies are 4.4 times smaller, as they are proportional to the impeller diameter. However, the P/V ratio for the smaller tank is approximately 4.7 times greater than the 220 mm tank at the same tip speed, as indicated in Table 7.1. The upper comparative speed of 2407 rpm could not be produced with the drill press motor; however, the next highest speed of 2024 rpm was achieved in this series of experiments.

Table 7.1: A comparison of Reynolds numbers, tip speeds and approximate power per unit volume for the 220 mm and 50 mm tanks. The required agitation rate of the smaller tank impeller to obtain the same tip speed and Reynolds number as the 220 mm tank is also presented.

	220 mm tank			50 mm tank					
rpm	Re	tip speed ($m.s^{-1}$)	P/V ($W.l^{-1}$)	Re	tip speed ($m.s^{-1}$)	P/V ($W.l^{-1}$)	rpm for same Re as 220 mm tank	rpm for same tip speed	P/V at same tip speed
236	4.76E+04	1.36	0.59	2.46E+03	0.31	0.03	4569	1038	2.77
304	6.13E+04	1.75	1.25	3.17E+03	0.40	0.07	5885	1338	5.92
353	7.12E+04	2.03	1.96	3.68E+03	0.46	0.11	6834	1553	9.27
460	9.28E+04	2.65	4.34	4.79E+03	0.60	0.24	8906	2024	20.51
547	1.10E+05	3.15	7.30	5.70E+03	0.72	0.40	10590	2407	34.49

Table 7.2.: Approximate Kolmogorov eddy sizes for the 220 and 50 mm tanks.

220 mm tank		50 mm tank	
		at same rpm as 220 mm tank	at same tip speed as 220 mm tank
rpm	Kolmogorov length scale of eddy (μm)		
236	36	74	25
304	30	62	20
353	27	55	18
460	22	45	15
547	19	40	13

Table 7.3.: Critical suspension speeds for the 600- 850 μm fraction for the 220 and 50 mm tanks.

vol. frac.	$N_{js\ 220\ mm}$	$N_{js\ 50\ mm}$
5%	473	1665
15%	553	1949

7.4.2 Radial Concentration Profiles for the 50 mm ID Tank

A relatively slow agitation rate of 480 rpm was initially examined with the 5 % concentration. The data in Figure 7.4 clearly show minimal suspension has occurred.

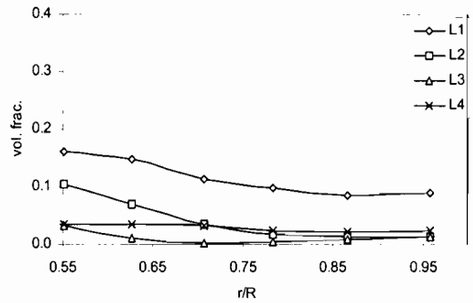


Figure 7.4: Radial concentration profiles for 5 % volume fraction for the 50 mm tank. Rushton impeller, 600-850 μm.

Suspension at tip speeds corresponding to the study in the 220 mm tank were examined for the 5 % concentration (Figure 7.5) using the 50 mm tank. Results collected with the 220 mm tank are presented in Figure 7.6 relating volume fraction in suspension to dimensionless radius. At the high speeds tested in the 50 mm tank, the liquid surface intermittently increased and decreased in height through turbulence and surface aeration. Although the dimensionless heights of the electrode layers are similar for both tanks, the 50 mm tank only has a 2 mm height differential between L4 and the liquid surface thereby leading to greater measurement error at high speeds. Thus, only the two data points of L4 near the vessel wall should be taken as representative. An increased liquid height decreases the resistance for L4 which results in a calculation of decreased solid volume fraction. Surface aeration results in increased resistance and an increase in solid volume fraction. Identical profiles are not to be expected in the 50 and 220 mm tanks as the hydrodynamics are different in the vessels, however it appears that greater homogeneity is achieved in the smaller vessel at the equivalent tip speed e.g. comparing Figure 7.5 (a) with Figure 7.6 (a). This is to be expected considering the higher P/V ratio in the smaller tank, while the larger eddies in the 220 mm tank would not play a significant role in particle lift.

Comparing Figure 7.7 (a) with (c), greater consistency is observed with the increasing agitation rate with the 15 % volume fraction in the 50 mm tank. The radial profiles appear to be slightly increasing in concentration towards the wall for the lowest layer, L1, while slightly decreasing or remaining constant on approaching the wall for the other layers. It is also apparent that the higher P/V ratio in the 50 mm tank produces a more consistent suspension on comparing Figure 7.7 with Figure 7.8.

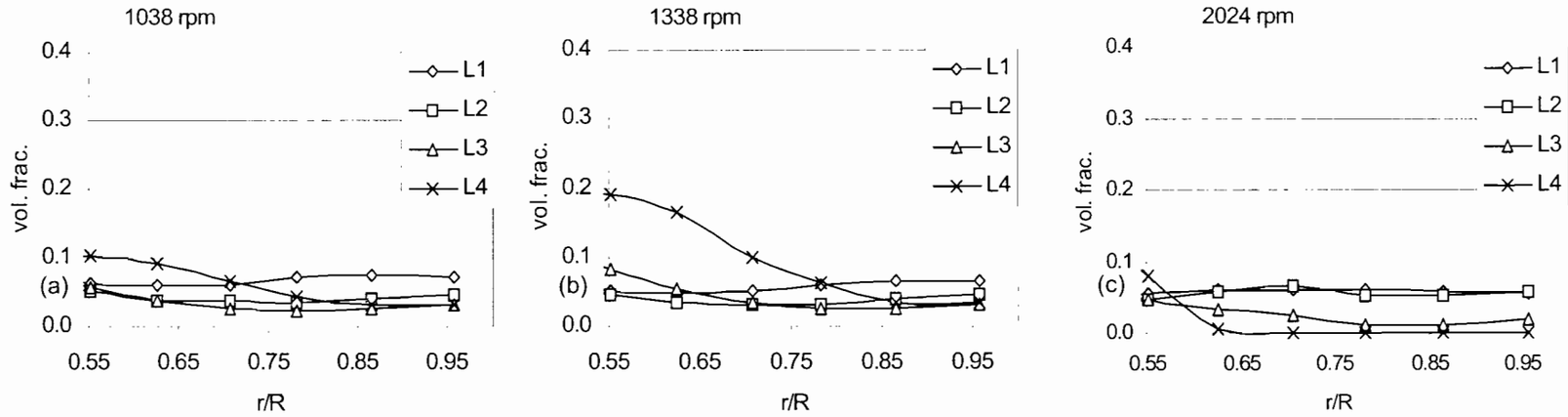


Figure 7.5: Radial concentration profiles for 5 % volume fraction for the 50 mm tank. Rushton impeller, 600 - 850 μm.

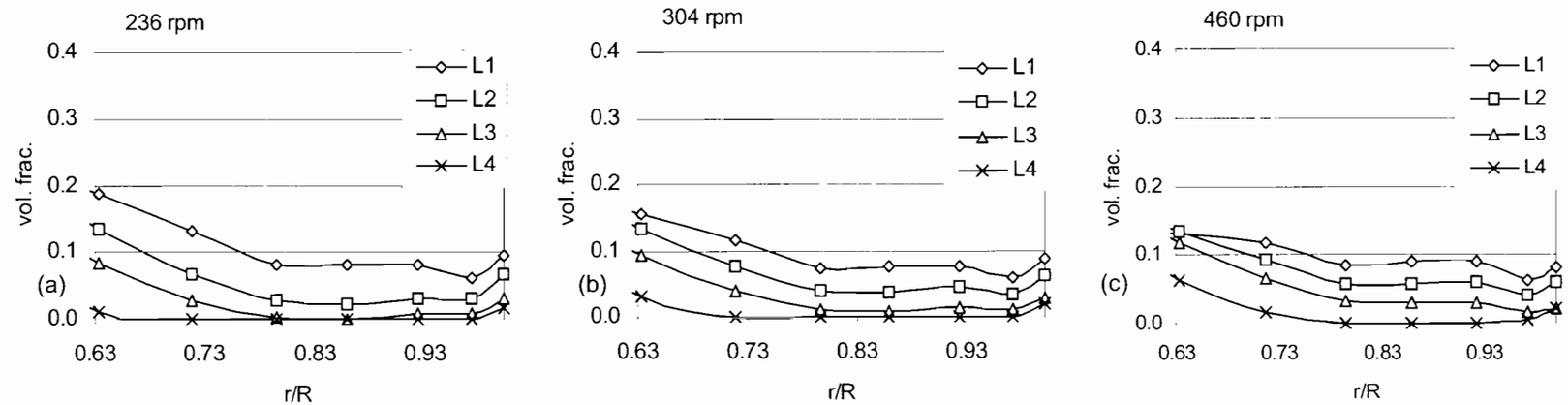


Figure 7.6: Radial concentration profiles for 5 % volume fraction for the 220 mm tank. Rushton impeller, 600 - 850 μm.

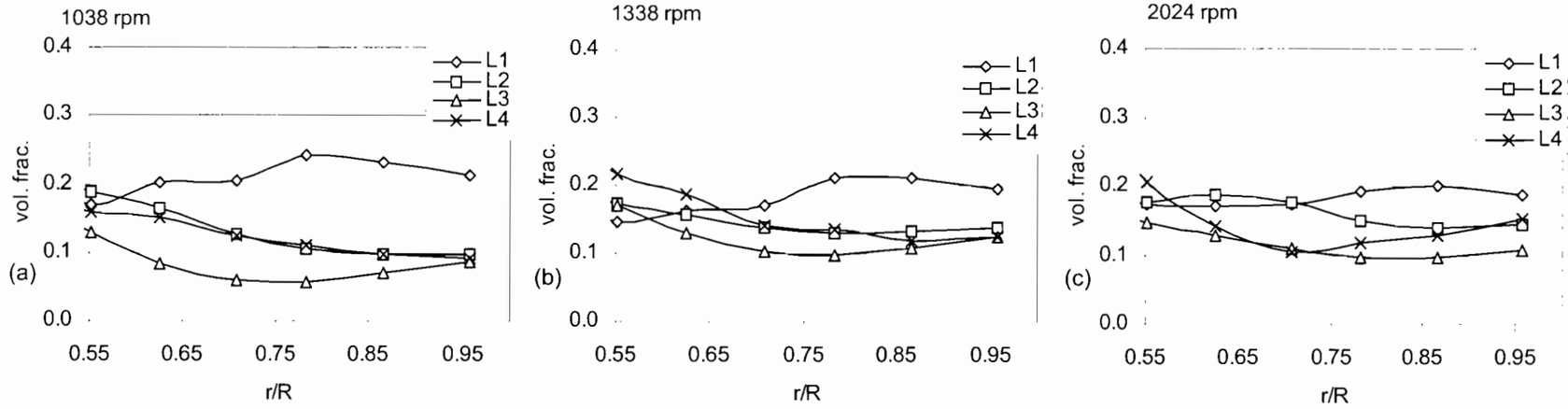


Figure 7.7: Radial concentration profiles for 15 % volume fraction for the 50 mm tank. Rushton impeller, 600 - 850 μm.

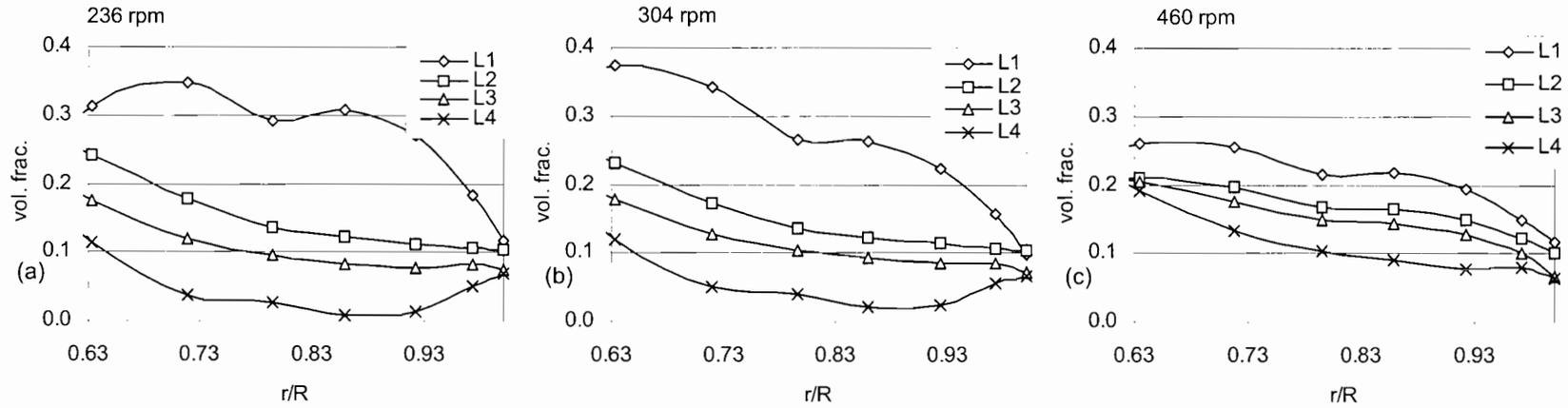


Figure 7.8: Radial concentration profiles for 15 % volume fraction for the 220 mm tank. Rushton impeller, 600 - 850 μm.

Greater consistency was observed in the radial profiles of the 50 mm tank, therefore the effect of specific power and tip speed on the overall mixing index were examined for the 15 % solids loading. These data are presented in Figure 7.9, where it is clear the smaller tank has greater particle homogeneity for the same P/V and tip speed relative to the 220 mm tank. However, data was not available for the 220 mm tank at higher P/V ratios and it is expected that the mixing indices for both tanks would be similar at these higher values. Considering the higher quality of suspension in Figure 7.9 (a) for the smaller tank at the same P/V for the range 0 – 10 $W.l^{-1}$, it is concluded that maintaining P/V in scale-up is not reliable for producing similar suspension quality. It must be noted that overall tank homogeneity in terms of the mixing index defined in Section 6.2.5, and not complete particle suspension, is being analysed here. Further, at the same P/V the impeller in the 50 mm vessel will have a tip speed that is 2.63 times greater than the 220 mm vessel. The scale of eddies in both tanks will also be dissimilar. In Figure 7.9 (b) tank homogeneity is greater for the 50 mm tank at the same tip speed as observed in the radial profiles of Figures 7.5 – 7.8. Lower mixing indices are observed in the 50 mm tank at the same P/V and tip speed despite the higher Reynolds numbers in the 220 mm vessel, as shown in Figure 7.10. Thus Reynolds number is also not a reliable means for scale-up.

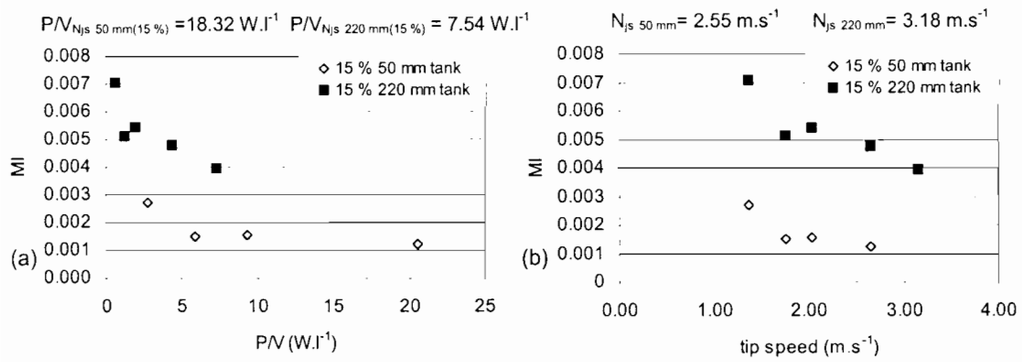


Figure 7.9: The effect of specific power (a) and impeller tip speed (b) on the mixing index for a 15 % suspension of 600 – 850 μm quartzite in the 50 and 220 mm tanks.

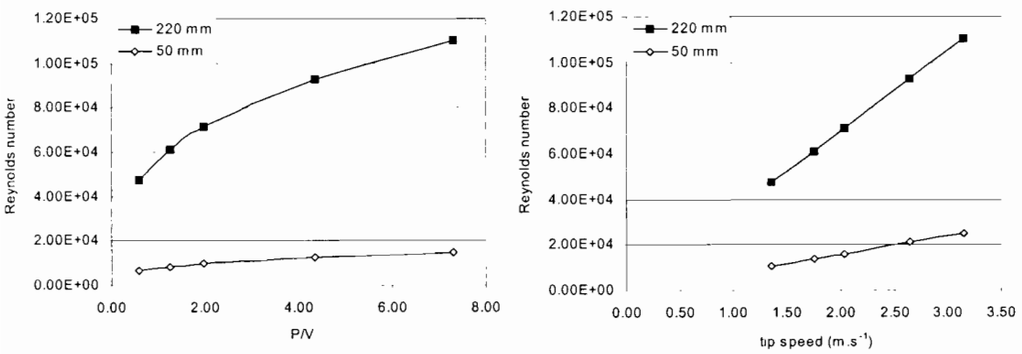


Figure 7.10: Reynolds numbers in the 50 and 220 mm tanks at the same P/V (a), and the same tip speed (b).

The effect of power per unit volume was examined with respect to the concentration of particles detected in the lowest electrode layer, L1. In this manner, the degree of suspension can be monitored as particles should be migrating to higher areas in the stirred tank i.e. L3 and L4, and ideally distribute at the average suspension concentration with increasing power per unit volume. In Figure 7.11, the volume fraction of quartzite in L1 is observed to decrease with increasing P/V for both tanks, while it appears that the volume fraction in L1 is approaching an asymptotic value at the higher P/V ratios. This is in accord with Buurman *et al.* (1986), who noted that absolute homogeneity appears unattainable in practice, and that rather an optimal homogeneity should be achieved. This appears obtainable through monitoring a stirred tank with ERT technology.

Comparing the 5 % solids concentration in both tanks it indicates that the 220 mm tank is approaching an asymptotic concentration at L1 at lower P/V ratios, although there is less homogenisation across L1 to L4. This is postulated to be the effect of the larger eddies in the 220 mm tank which will aid homogenisation, although not necessarily aid particle lift-off. In this manner, optimal suspension concentration is generally attained at lower specific power in larger-scaled vessels. Examining the 15 % solids concentration for both tanks, neither approach the average solids concentration in the agitation rate range studied, while the larger tank approaches the optimal solids concentration at a lower P/V ratio. Although as observed from Figure 7.9, the 220 mm tank is less homogenous across the whole reactor at the same P/V.

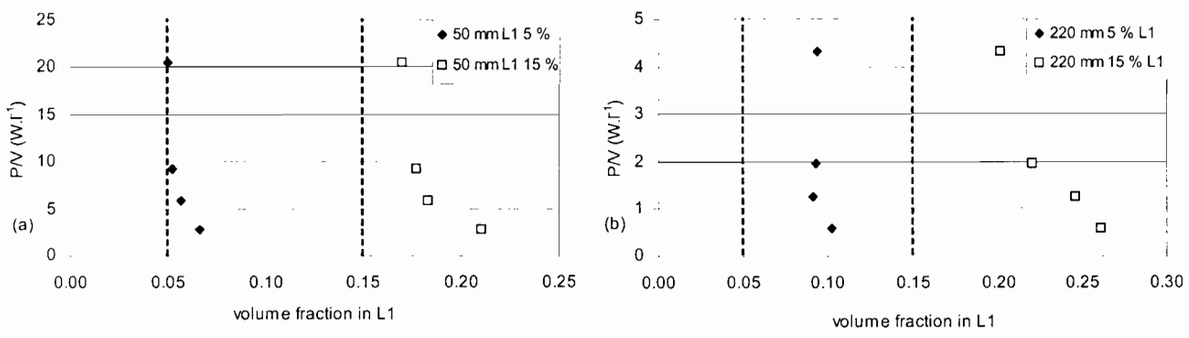


Figure 7.11: Examining the effect of increasing P/V on local particle concentration (L1)

7.4.3 Axial Concentration Profiles for the 50 mm ID Tank

The axial concentration profiles in the 50 and 220 mm tanks are presented as a function of dimensionless height for the 5 and 15 % suspensions in Figure 7.12 and Figure 7.13 respectively. These profiles indicate that the smaller vessel has greater axial homogeneity at the same impeller tip speed, even considering the uncertainty

regarding the top electrode layer (solid data point). Thus for the 50 mm vessel, which is 3.72 times smaller in diameter, the same impeller tip speed leads to greater axial homogeneity although the scale of eddies is smaller.

The mixing index in the vertical plane, MI_r, was calculated for the lower 3 electrode layers for each reactor, as shown in Figure 7.14 (a) and (b) at 5 % and 15 % loading respectively. It is apparent the 50 mm reactor has greater axial homogeneity for both suspension concentrations, while the 5 % suspension shows greater axial homogeneity than the 15 % suspension in both reactors. Similar MI_r values are approached at the highest tip speed shown. This is expected as at the higher impeller tip speed of 2.65 $m.s^{-1}$ both suspensions are close or above N_{js} as reported in Table 7.3. As MI_r values are similar at high tip speeds, the main factor influencing the overall mixing index is radial homogeneity (MI_z). This explains the greater difference in the overall mixing index (MI) observed in Figure 7.9 (b).

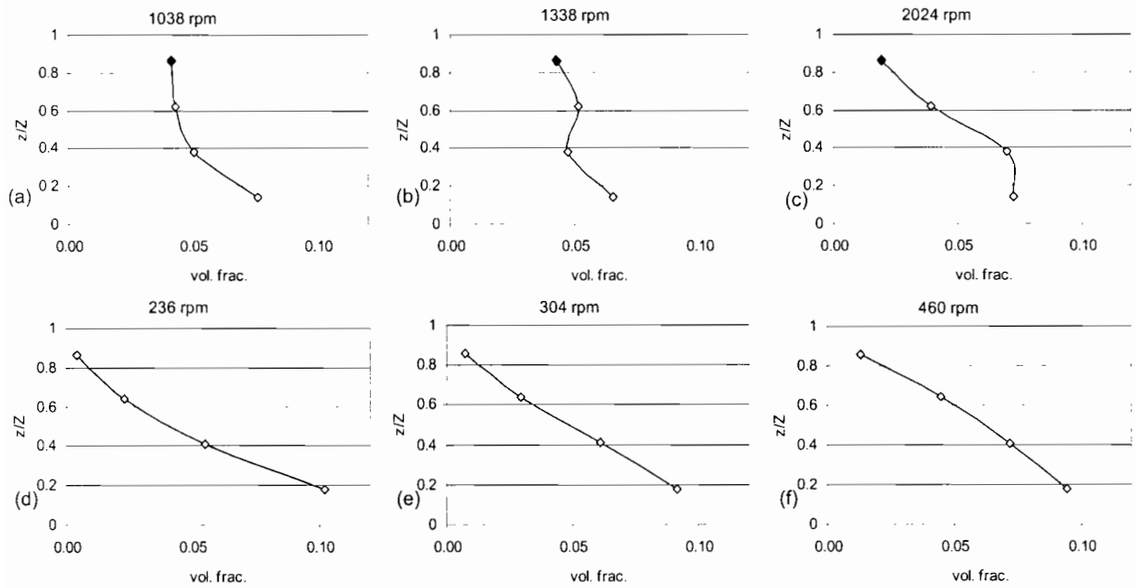


Figure 7.12: Axial concentration profiles for 5 % volume fraction for the 50 mm tank (a-c) and the 220 mm tank (d-f). Rushton impeller, 600-850 μm.

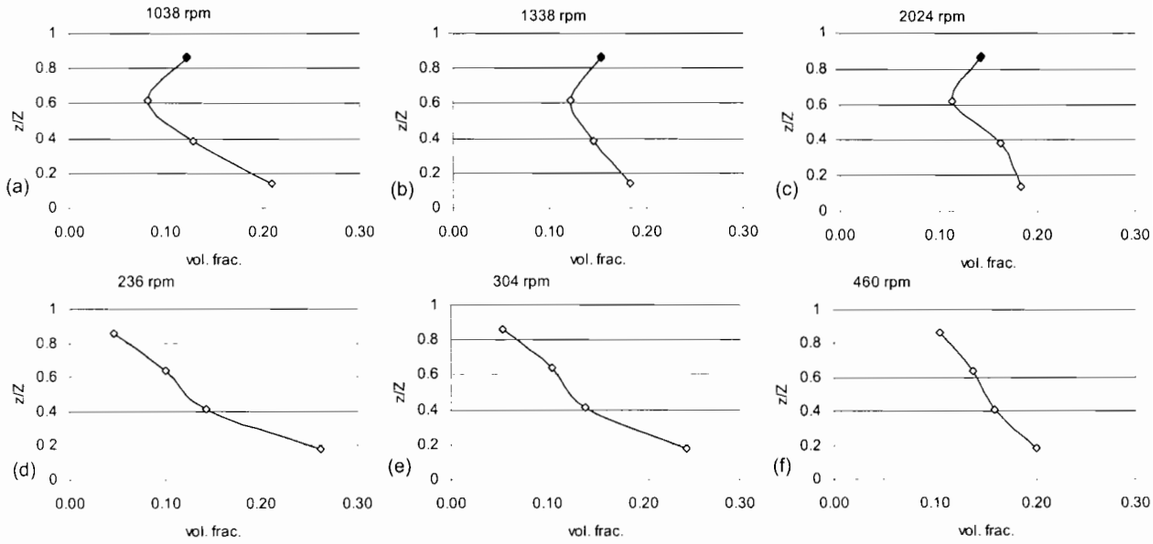


Figure 7.13: Axial concentration profiles for 15 % volume fraction for the 50 mm tank (a-c) and the 220 mm tank (d-f). Rushton impeller, 600-850 μm.

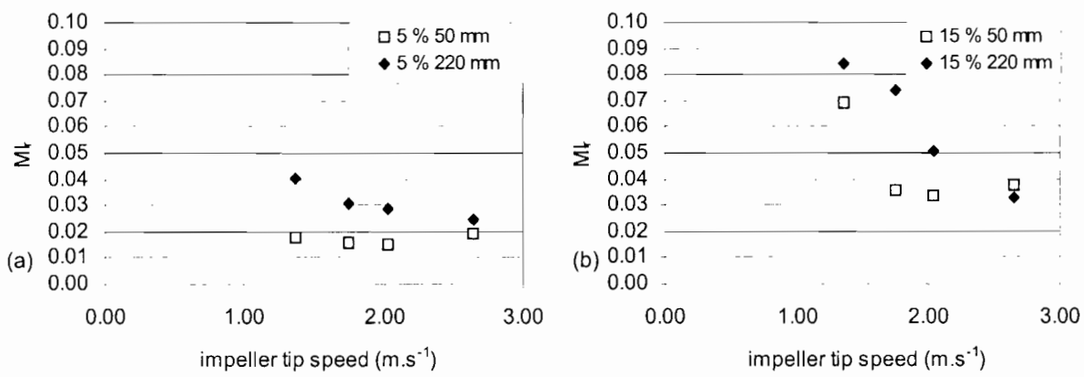


Figure 7.14: The effect of impeller tip speed on $MI_{r(L1-L3)}$ for 5 (a) and 15 % (b) suspensions of 600 – 850 μm quartzite in the 50 and 220 mm reactors

7.5 Error between Reconstructed Frames

The 934 element baffled mesh (Appendix J) was applied to the reconstruction of 15 % quartzite (600-850 μm) at 304 rpm in the 220 mm tank. One hundred and nineteen frames were reconstructed, while averaging 25 frames per recorded frame, thus totalling 2975 frames. The standard deviation as a percentage of the mean is related to the radial position of the element for each electrode layer in Figure 7.15. Uncertainty is expected with movement of particles; this is clearly observed in Figure

7.14 (a), where at 304 rpm (tip speed = 1.75 $m.s^{-1}$) a significant amount of solids remain near the vessel bottom which do not maintain constant position. On comparing L1 with L2 and L3, which appear to be fairly regular, it is apparent that there is greater uncertainty in the position of solids that are not suspended. L4 has greater deviation near the vessel wall which is most likely associated with fluctuations of the liquid surface.

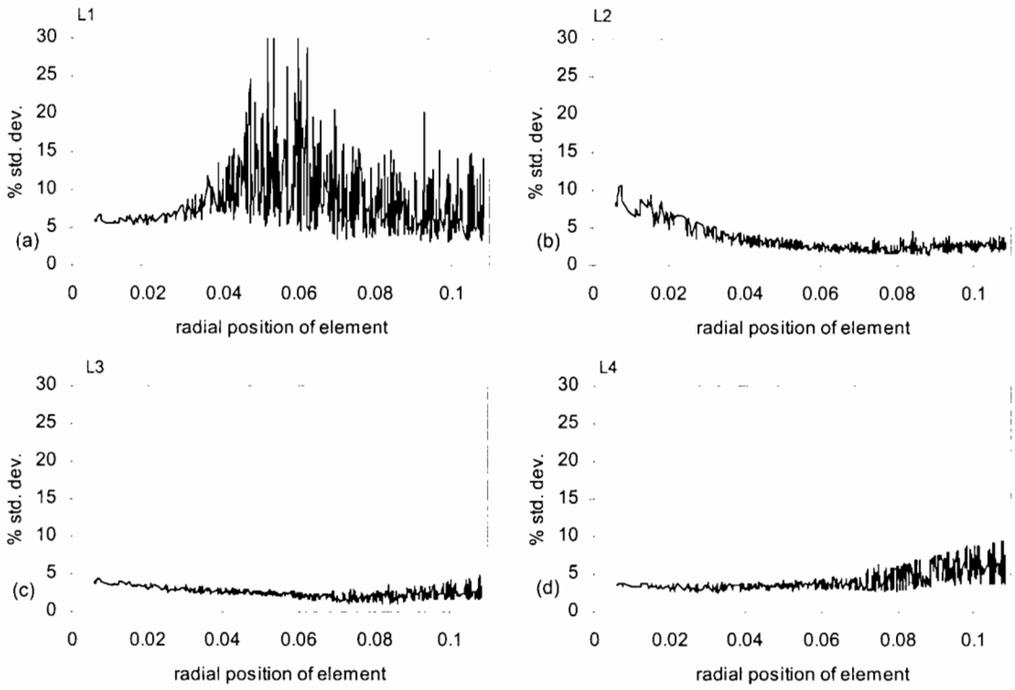


Figure 7.15: The standard deviation with respect to the radial position of the element from reconstructing the 934 element mesh for 119 frames of data. Operating conditions: 15 % volume concentration of the 600-850 μm at 304 rpm. Layers 1 to 4 are presented (a-d).

7.6 Error between ERT Experiments

A subset of experiments were performed in triplicate to examine reproducibility. In Figure 7.16 (a), a 15 % suspension of quartzite (600-850 μm) agitated at 353 rpm in the 220 mm tank is shown. Here the average standard deviation was approximately 10 % of the mean. On agitation of a 15 % suspension of quartzite at 1338 rpm (600-850 μm) in the 50 mm tank, shown in Figure 7.16 (b), the standard deviation was approximately 5 % of the mean. Hydrodynamic conditions differ in these reactors leading to different intensities of concentration fluctuations. It must be noted that the 934 element mesh used for the 220 mm tank equates to 2.5 $elements.cm^{-2}$, while the 762 element mesh used for the 50 mm tank equates to 38.8 $elements.cm^{-2}$. Thus, greater accuracy is expected for the reconstructions using the 50 mm tank, resulting

in a decreased standard deviation. There is also a greater suspension of solids in the 50 mm tank leading to less uncertainty near the tank bottom.

A reproducibility of 5 and 10 % of the mean concentration will result in a 10.3 and 21.0 % error respectively in the overall mixing index.

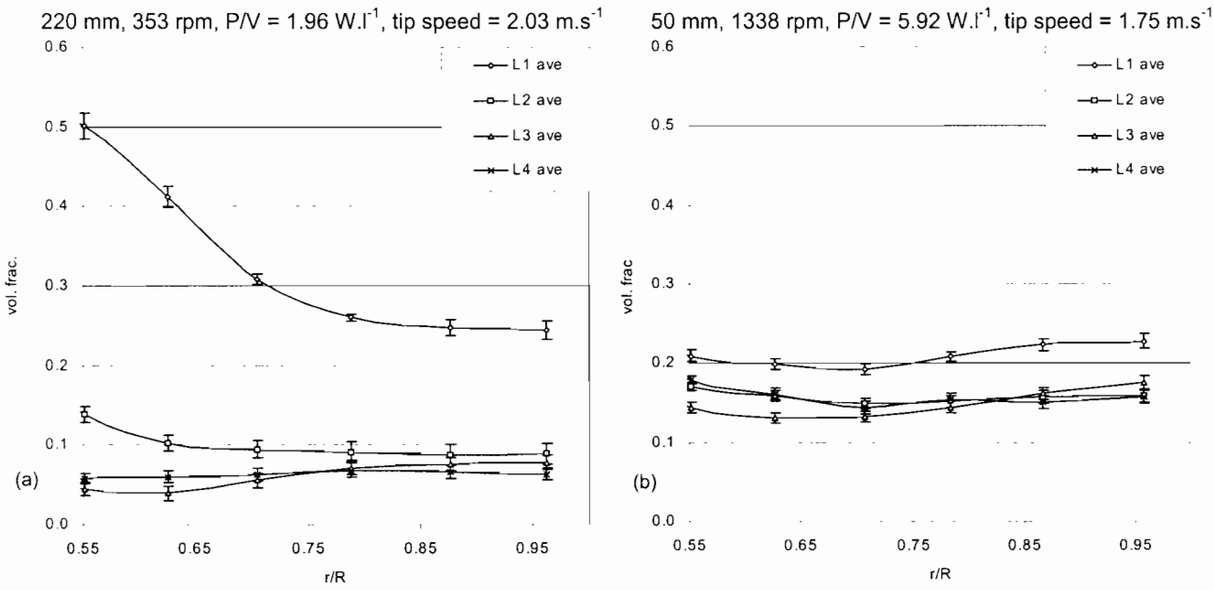


Figure 7.16: Reproducibility of ERT experiments. 15 % quartzite (600-850 μm) at 353 rpm in the 220 mm tank (a) and at 1338 rpm in the 50 mm tank (b).

7.7 Conclusions

Improved measurement technology in the form of Reconstruction Code V and ERT Hardware III successfully detected phantoms. Although differing slightly, the comparative profiles of the 220 mm tank with the old and new technology had similar mixing indices and investigations proceeded to the 50 mm vessel. Using the latest system, more conductivity information from r/R = 0.55 to 1.00 was extracted.

A more consistent suspension at 5 and 15 % solids loading was observed from the radial profiles of the 50 mm tank than the 220 mm tank. This was supported by calculations of the estimated power per unit volume and eddy sizes in the energy dissipation range. It was postulated that the inertial sub-range of the turbulence energy spectrum was responsible for particle suspension in both tanks, while the higher P/V ratios in the smaller vessels led to a more consistent suspension when operating at the same impeller tip speed. Furthermore, at the same P/V, the smaller

vessel achieved a lower mixing index and therefore greater homogeneity. It was postulated that this was due to the different scale of eddies in each vessel. However, the 220 mm vessel approached the optimal suspension concentration in the lower section of the tank (L1) at a lower P/V ratio. This was postulated to be due to the larger eddies present in the 220 mm vessel from the larger impeller. Absolute homogeneity appears to be unattainable as the decreasing concentration in L1 displayed an asymptotic character with increasing P/V. Axial profiles in the 50 mm tank reiterated the greater homogeneity present relative to the 220 mm tank, and this was supported by calculation of mixing indices in the axial plane at the respective impeller tip speeds. At higher impeller tip speeds both vessels had a similar axial mixing index which was postulated to be due to their similar conditions of complete suspension.

The deviation between measurements within 119 measurement frames was greatest for L1 at approximately 5 – 15 % of the mean volume fraction. This was postulated to be related to the movement of solids in this region at sub-suspension agitation rates. Electrode layer 2 and 3 showed deviations of 5 % in the region of interest (r/R = 0.55 – 1.00), while there was a greater uncertainty of approximately 10 % for L4 near the vessel wall. The fluctuating surface level is most likely responsible for this higher deviation. The reconstructed measurements in the 220 mm vessel had a reproducibility of 10 %, while a reproducibility of 5 % was observed in the 50 mm vessel. This increase in reproducibility is postulated to arise from the higher density of elements mapping the 50 mm tank's domain.

ERT has successfully allowed the analysis of scale effects in the suspension of two concentrations of quartzite in the 50 and 220 mm reactors. The concept of mixing indices has provided further support in this endeavour. As a result of this successful application of the latest ERT system to the smaller reactor, comparative experiments are now possible using MRI on the same size vessel.

Chapter 8

Magnetic Resonance Imaging of the Slurry Reactor

8.1 Introduction

Excellent spatial resolution of particle suspension of approximately 1 mm is obtainable through application of MRI to a stirred vessel. In this study, MRI is applied to the stirred tank reactor to exploit the scale of detection and is compared to ERT which exploits the timescale of data collected. This investigation was constrained to a small scale vessel (Section 3.3) due to the size of the magnet. Moreover, the agitation rate was limited to a maximum of 480 rpm due to the type and availability of the overhead stirrer (Figure 3.19 (b)). These experiments provided high resolution axial concentration profiles which provided a further opportunity for confirmation of the ERT data obtained from a similar sized vessel (Section 3.4). This study was undertaken at the Magnetic Resonance Research Centre (MRRC) at Cambridge University on a 200 MHz Bruker magnet, thus basing the resonance on the proton frequency of 199.7 MHz.

Single point imaging techniques were applied in 1D and 3D to ballotini (50 and 100 μm) and nylon particles (500 μm). These experiments allowed the collection of data above and below the impeller which was obstructed while using ERT due to the calibration process. This represents the first study of a baffled stirred tank reported in the literature, although other mixing systems have been examined (Section 2.5.5.6). This study is reported in Section 8.3 to 8.4, with errors associated with MRI being discussed in Section 8.5.

The MRI information further allows the comparison with ERT data obtained near the vessel wall. To this end, ERT experiments were performed under identical conditions and scale to the MRI investigations using the 50 mm ERT vessel (Section 3.4). Comparison of MRI - ERT data is discussed in Section 8.6 to assess the consistency of the data, to highlight preferred areas of use and to draw attention to relative limitations including reproducibility.

8.2 Conversion of MRI Data into Concentration Profiles

Single point imaging techniques were employed to obtain proton signals over the height of the vessel. These 1D (128 pixel) experiments averaged the signal in the radial plane and were 3 minutes in duration (post steady-state was used). Once

Fourier transformed, these data were divided by the data collected from a water only reference condition at the matching agitation rate at the same reactor-probe orientation. These data then represented the water fraction and the particulate fraction could be calculated through subtraction. Where the result did not represent the actual amount of solids present in the vessel, a scaling factor (1.0 to 1.5, average of 1.35) was used to relate the integral of the signal intensity to the correct water fraction. This allowed generation of axial concentration profiles, and this factor would not influence the shape of the profile. 3D MRI experiments (32 x 32 x 32 and 64 x 64 x 64 pixels) of 12 hour duration were also performed and are discussed in Section 8.4.1. Raw 3D signal data were similarly processed as the 1D data. Typical 1D MRI data from the 50 mm reactor containing a water only sample are shown in Figure 8.1. The signal starts at approximately 40 mm up the probe where water in the reactor O-ring and seal is detected. The effect of the Rushton impeller is clearly observed at approximately 60 mm with a decrease in proton signal intensity.

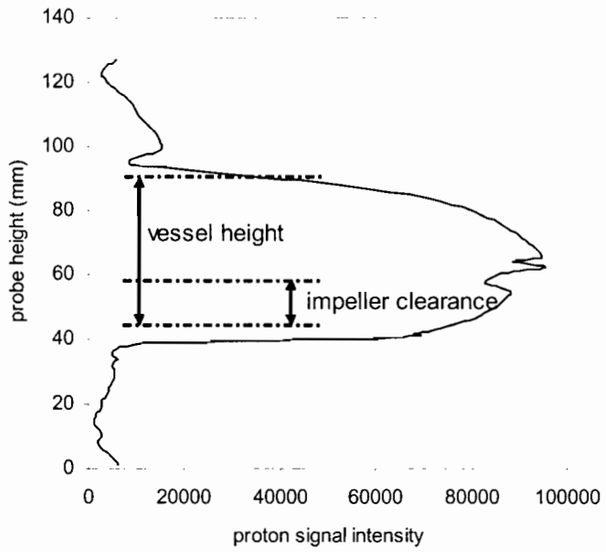


Figure 8.1: Proton signal intensity related to the height of observation within the probe using the 50 mm tank containing water only. The vessel height is observed from approximately 43 to 93 mm.

8.3 1D Examination of Particle Suspension

Suspension was examined at concentrations of 5 and 10 % and 5 - 20 % by volume for the ballotini and nylon particles respectively at agitation rates of 306 to 480 rpm and 186 to 480 rpm respectively using the Rushton impeller.

8.3.1 Suspension of Ballotini

8.3.1.1 Examining the Effects of Particle Size and Solids Loading

The suspension of a 5 and 10 % loading of borosilicate ballotini of 50 μm, and a 5 % loading of 100 μm was studied in the 50 mm tank. Due to the limitations of the custom-built stepper motor (RheoNMR), a maximum agitation rate of 480 rpm was possible. This allowed the examination of incomplete suspension for which there is minimal reporting in the suspension literature.

A clear representation of incomplete suspension is observed in Figure 8.2 for a concentration of 5 % by volume of 100 μm ballotini. The particulate concentration profiles at four agitation rates (306 – 480 rpm) are shown. The amount of material at the vessel bottom is clearly visible at these agitation rates below the critical speed for suspension of 939 rpm (Zwietering N_{js}). At the higher agitation rate (480 rpm) fewer solids are present at the bottom of the vessel (z/Z low), while a more homogenous concentration is present for the rest of the vessel height.

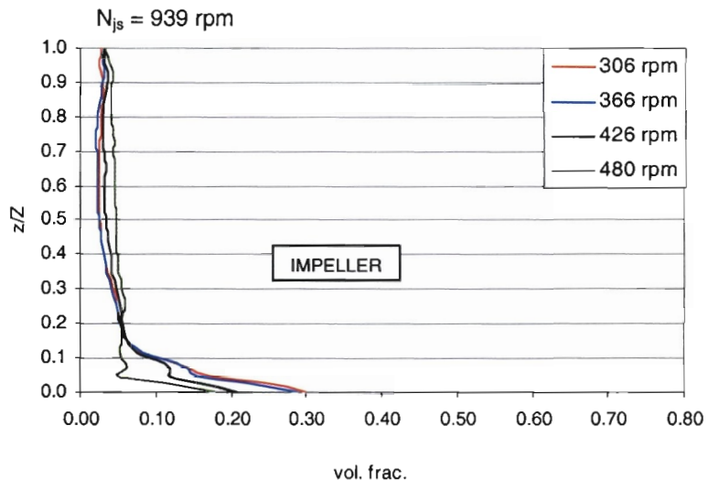


Figure 8.2: Axial concentration profiles generated by MRI for 5 % suspension of 100 μm ballotini for agitation rates 306, 366, 426 and 480 rpm. The Rushton impeller is located at z/Z = 0.33 to 0.43 (i.e. 5 mm blade thickness).

For the 5 and 10 % suspensions of 50 μm ballotini in Figure 8.3 (a) and (b), it is observed that an increase in agitation rate increases particle concentration in the upper regions of the vessel, while decreasing particle concentration at the vessel bottom. Further, the 5 % solids loading of 50 μm ballotini exhibited different suspension behaviour to the 5 % loading of 100 μm ballotini in Figure 8.2. A peak solids concentration is observed in the impeller zone. At the higher volume

concentration of 10 % (Figure 8.3 (b)), the 50 μm ballotini did not exhibit a peak concentration in the impeller plane. It is therefore postulated that the radial and axial forces from the impeller are not sufficient to maintain this increased concentration in the impeller zone. There is thus a critical weight of solids that can be supported just above the impeller plane depending upon the hydrodynamic condition.

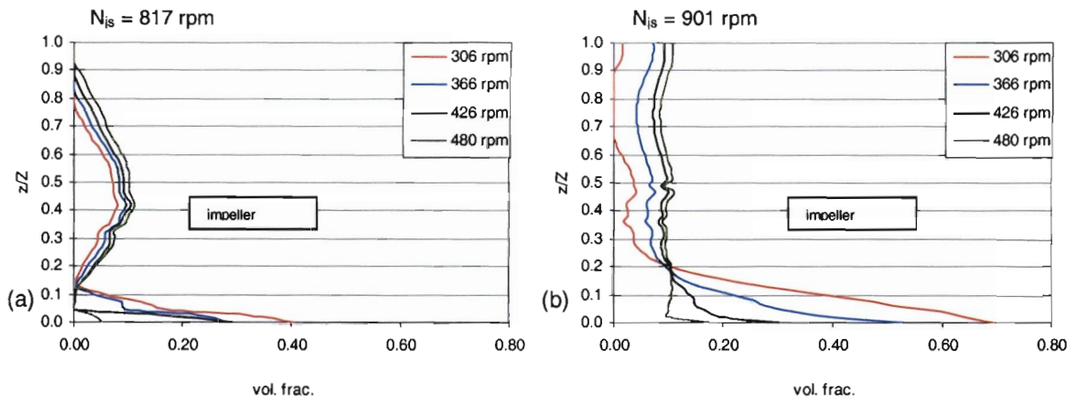


Figure 8.3: Axial concentration profiles generated by MRI for 5 % suspension of 50 μm ballotini (a) and 10 % suspension of 50 μm ballotini (b). The Rushton impeller is located at z/Z = 0.33 to 0.43

This peak concentration in the impeller zone has been observed in previous studies of particle distribution (Shamlou and Koutsakos, 1989; Barresi and Baldi, 1987a; McKee *et al.*, 1995; Nasr-El-Din *et al.*, 1996; Williams *et al.*, 1996). These observations are summarised in Table 8.1. Examining the results of these studies, this peak concentration was only apparent at higher agitation rates (Shamlou and Koutsakos, 1989; McKee *et al.*, 1995; Williams *et al.*, 1996) or with smaller volume fractions (Barresi and Baldi, 1987a; Shamlou and Koutsakos, 1989). Furthermore, Shamlou and Koutsakos (1989) observed this peak concentration closer to the vessel wall i.e. at 0.044T, but not midway between the wall and the impeller shaft at 0.25T (comparing Table 8.1 1(a) with 1(e)). These authors also observed the peak concentration at a lower agitation rate using larger particles (Table 8.1, 1(d)), however, this was with a decreased liquid height and increased impeller clearance. Barresi and Baldi (1987a) also observed a higher peak concentration with larger particles (Table 8.1 2(a)). This was at N_{js}, while a higher peak concentration was observed for axial impellers relative to the Rushton impeller. Nasr-El-Din *et al.* (1996) similarly observed an increase in the peak concentration with an increase in particle size (Table 8.1 4(a)).

Focusing solely on finer particles of 100 – 177 μm, Barresi and Baldi (1987a) observed a decrease in the peak concentration in the impeller zone with increasing agitation rate. However, this was beyond N_{js} and thus further turbulent energy

introduced into the system was spent on particle homogenisation. They further noted with increasing agitation rate that the finer particles increased in concentration in the zone between the impeller and the surface (Table 8.1 2(b)), as in this study. Barresi and Baldi (1987a) noted an increase in the peak concentration with increasing solids concentration (Table 8.1 2(c)). However, this was with dilute solid concentrations ranging from 0.2 to 2.0 % by volume and thus did not exceed the 5 % solids concentration in this study.

Shamlou and Koutsakos (1989) interpreted particle distribution in agitated liquid in terms of a steady-state turbulent diffusion mechanism. The distribution of particles thus results from the balance between the random motion of the fluid and the action of gravity on the particles. However, this does not account for particle-particle interaction and their study concerned low concentrations of solids. With an increased concentration of solids in the impeller zone, an increased downward force is present due to gravity. This could account for the disappearance of a peak concentration in this zone for the 10 % solids concentration of 50 μm ballotini. There is thus a balance of forces in the impeller zone, with larger particles unable to be suspended to the upper regions of the vessel, while only a critical local solids concentration can be held in this region. However, comparison is necessary at complete suspension, as the larger 100 μm ballotini in this study did not exhibit a peak concentration at the same agitation rates. Barresi and Baldi (1987a) noted that the turbulent dispersion coefficient changes significantly along the vessel, while the dispersion of solids is most likely affected by large-scale eddies and macroscopic turbulence. As the 50 mm vessel in this study is operating at the same hydrodynamic conditions, and assuming negligible turbulence enhancement with the presence of particles, the effect of particle concentration has a significant effect on particle distribution. Further, Barresi and Baldi (1987a) confined their study to low concentrations of solids (Table 8.1 2(c)). Moreover, particle drag forces will be increased with increasing solids concentration, and this behaviour in a turbulent field is incompletely understood (Rewatkar *et al.*, 1991), although advances have been made (Brucato *et al.*, 1998). Thus, theoretical models need to be developed which account for the effect of solids loading as opposed to models based on a single particle, as significant changes are observed in the axial concentration profile with increasing solid concentration.

Table 8.1: Observation of a peak solids concentration at the height of the impeller

No.	Description	Tank geometry	Operating Conditions	Solid phase	Technique	Reference
1(a)	Peak solids concentration in impeller zone at 600 rpm	(H = 65 cm) H/T = 3.00 T/D = 2.17 C/H = 0.20 6-bladed Rushton	(No test at 560 rpm) 300 - 600 rpm	ρ_s = 2900 kg.m^{-3} d_p = 390 μm 1 wt %	Laser transmitter at 0.044T	Shamlou and Koutsakos (1989)
1(b)	Peak observed above 560 rpm	(H = 65 cm) H/T = 3.00 T/D = 2.17 C/H = 0.20 6-bladed Rushton	300 - 800 rpm	ρ_s = 2900 kg.m^{-3} d_p = 390 μm 2 wt %	Laser transmitter at 0.044T	Shamlou and Koutsakos (1989)
1(c)	Peak observed above 650 rpm	(H = 65 cm) H/T = 3.00 T/D = 2.17 C/H = 0.20 6-bladed Rushton	300 -700 rpm	ρ_s = 2900 kg.m^{-3} d_p = 390 μm 3 wt %	Laser transmitter at 0.044T	Shamlou and Koutsakos (1989)
1(d)	Peak observed at 500 rpm	(H = 37 cm) H/T = 1.71 T/D = 2.17 C/H = 0.31 6-bladed Rushton	300 -500 rpm	ρ_s = 2900 kg.m^{-3} d_p = 530 μm 1 wt %	Laser transmitter at 0.25T	Shamlou and Koutsakos (1989)
1(e)	No peak observed	(H = 65 cm) H/T = 3.00 T/D = 2.17 C/H = 0.20 6-bladed Rushton	300 -800 rpm	ρ_s = 2900 kg.m^{-3} d_p = 390 μm 1 wt %	Laser transmitter at 0.25T	Shamlou and Koutsakos (1989)
2(a)	Increase in peak solids concentration with increasing particle size	(H = 46 cm) H/T = 1.19 T/D = 3.00 C/H = 0.33 4-bladed pitched blade impeller	N = N_{js}	100 – 177 μm 208 – 250 μm 417 – 500 μm ρ_s = 2600 kg.m^{-3} 0.2 vol. %	wall sampling	Barresi and Baldi (1987a)

Table 8.1: Observation of a peak solids concentration at the height of the impeller continued…

No.	Description	Tank geometry	Operating Conditions	Solid phase	Technique	Reference
2(b)	Decrease in peak concentration with increasing agitation rate	(H = 46 cm) H/T = 1.19 T/D = 3.00 C/H = 0.33 4-bladed pitched blade impeller	0.8 – 1.4 N_{js}	100 – 177 μm 0.5 % kg solid/kg liquid ρ_s = 2600 kg.m^{-3}	wall sampling	Barresi and Baldi (1987a)
2(c)	Increase in peak concentration with increasing solids concentration (dilute range) N = N_{js}	(H = 46 cm) H/T = 1.19 T/D = 3.00 C/H = 0.33 4-bladed pitched blade impeller	N = N_{js}	100 – 177 μm 0.2, 0.6, 2.0 vol. % ρ_s = 2600 kg.m^{-3}	wall sampling	Barresi and Baldi (1987a)
3(a), (b)	Peak observed above 180 rpm	(H = 30.5 cm) H/T = 1 T/D = 3.00 C/H = 0.33 4-bladed pitched blade impeller	180 – 415 rpm	0.063 volume fraction 425 – 500 μm (a) 600 – 710 μm (b) ρ_s = 2650 kg.m^{-3}	cond. probe	McKee *et al.* (1995)
4(a), (b)	Peak observed at r/R = 0.3, 0.6, 0.9 Variation increased with increasing d_p and agitation rate	(H = 29.2 cm) H/T = 1 T/D = 3.00 C/H = 0.30 6-bladed Rushton	545 rpm	0.3 bulk solids concentration d_{50} = 82 μm (a) and 255 μm (b) ρ_s = 2650 kg.m^{-3}	cond. probe	Nasr-El-Din *et al.* (1996)
5(a), (b)	Peak observed above 280 rpm (a), and at 600 rpm (b)	(H = 30.5 cm) H/T = 1 T/D = 3.00 C/H = 0.33 4-bladed pitched blade impeller (a) A310 (b)	200 – 600 rpm	0.063 volume fraction 150 – 210 μm ρ_s = 2650 kg.m^{-3}	ERT (4 electrode layers)	Williams *et al.* (1996)

8.3.1.2 Examining Incomplete Suspension

It is useful to quantify the effect of impeller speed on the degree of solid suspension. Typically this is considered in terms of the critical suspension speed, N_{js}, with the Zwietering (1958) definition being used in this study. In Figure 8.4, the fraction of unsuspended solids is given as a function of agitation rate, normalised with respect to the critical impeller speed. The fraction of unsuspended solids was calculated through examining the point where the axial concentration profile changes sharply rising from the vessel bottom. It is expressed as the ratio of solids below this critical height to all solids present.

On agitation of 50 μm ballotini at a 5 % concentration at 480 rpm, equivalent to 59 % of the Zwietering suspension speed, only 3 % of the total solids remained on the vessel bottom. At the same speed, corresponding to 53 % of N_{js} for the 10 % concentration, the same fraction of particles remained unsuspended. Furthermore, for the 50 μm particles a linear relationship was apparent between the agitation rate and the fraction of unsuspended solids across the range of N/N_{js} of 0.34 to 0.53 and 0.37 to 0.59 corresponding to a suspension of 20 – 94 % and 55 – 97 % for the 10 and 5 % loadings respectively. It is postulated that this linear relationship would not continue with increase in N/N_{js} ratios as complete suspension was approached. This hypothesis is supported by the same fraction of unsuspended solids at 480 rpm for the 5 and 10 % concentrations. However, it must be noted that the agitation rate as a fraction of N_{js} is not necessarily accurate as the smallest vessel examined by Zwietering (1958) in producing the critical suspension correlation was 154 mm in diameter. The gradient of the 10 % line is twice that of the 5 % concentration, indicating that the 10 % volume fraction is relatively easier to suspend.

A non-linear relationship is observed for the suspension of the larger 100 μm particles in Figure 8.4, thus it may be postulated that an increased fluid momentum is required to overcome the increased inertia of the larger particles. These particles have a narrow size distribution, so this is not a factor influencing non-linearity. At 480 rpm, 11 % of the total solids in this size fraction remain on the vessel bottom. The high degree of particle suspension observed at sub-N_{js} agitation rates in Figure 8.4 suggests that incomplete suspension conditions are attractive if operating a stirred tank reactor according to power efficiency.

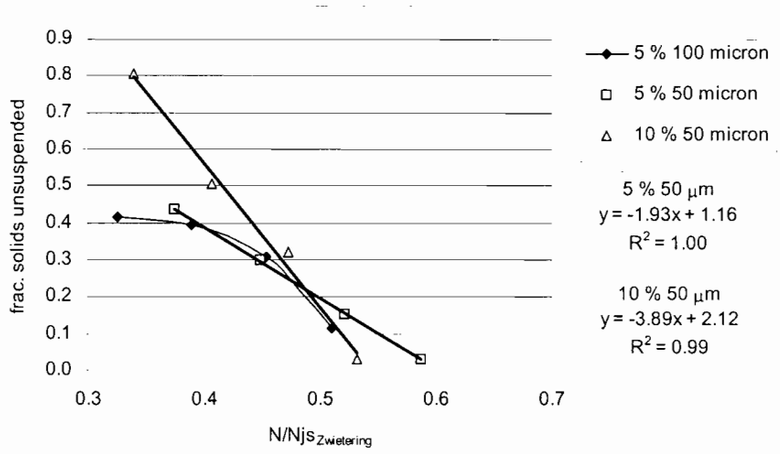


Figure 8.4: The fraction of ballotini (5 % suspension of 100 μm; 5 and 10 % suspension of 50 μm) remaining on the tank bottom with respect to the ratio of the agitation rate to the Zwietering critical suspension speed. Rushton impeller at 306 - 480 rpm

On suspension of a 5 and 10 % concentration of the 50 μm ballotini, there is a linear relationship (Figure 8.5) between the agitation rate and the fraction of solids suspended above the impeller (z/Z =0.43 to 1.00). Above N/N_{js} = 0.45, there is a higher fraction of solids above the impeller for the 10 % concentration than for the 5 % concentration. This is due to the peak solids concentration in the impeller zone for the 5 % concentration (Figure 8.3 (a)). The fraction of the 5 % concentration of 100 μm ballotini that are found above the impeller initially decreases, followed by a linear increasing relation with increasing agitation rate.

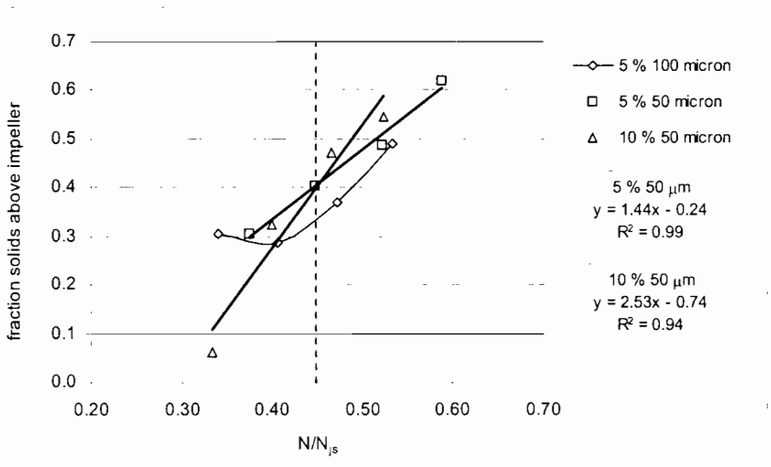


Figure 8.5: The fraction of solids (5 % suspension of 100 μm; 5 and 10 % suspension of 50 μm) above the impeller with respect to the ratio of the agitation rate to the Zwietering critical suspension speed. Rushton impeller at 306 - 480 rpm.

8.3.2 500 μm Nylon Suspensions

The nylon particles had a broad particle size distribution (Figure 3.20 (c)) with a mean size of 513 μm. They were chosen for their low specific gravity (S.G. = 1.13) to enable visualization of complete suspension.

8.3.2.1 Examining Solids Loading

Concentrations of 5 to 20 % by volume were examined at agitation rates of 186 - 480 rpm with 1D MRI (Figure 8.6 (a – d)). The position of the impeller in Figure 8.6 (a-d) correlated with a sudden change in gradient of the axial concentration profile. Compared to the ballotini (S.G. 2.2), greater axial homogeneity is achieved with the nylon particles. The axial profiles for agitation rates of 366 – 480 rpm are very similar; while it appears that the Zwietering correlation overpredicts the critical suspension speed e.g. at 10 % loading, complete suspension is apparent at 426 rpm, rather than 472 rpm. Although the 5 % suspension has the lowest N_{js}, the 15 % suspension displays greater axial homogeneity for agitation rates of 366 rpm and higher. Thus increasing above N_{js} in the case of the 5 % concentration does not necessarily produce greater homogeneity. This has been found in other studies (Shamlou and Koutsakos, 1989) where greater velocity fluctuations induced by the impeller at high speeds beyond N_{js} can reduce overall homogeneity.

The solids distribution of nylon particles was examined at 186 rpm since this sub-suspension speed exhibited the most variation when increasing solids loading. In Figure 8.7, it is shown that, on increasing solids loading, the fraction of solids above the impeller decreased to a minimum at 15 % loading. The reduced dependency of the fraction suspended above the impeller on the impeller speed then occurred despite a decreasing N/N_{js} ratio (secondary y-axis of Figure 8.7). Thus particle-particle effects may have been prevalent in this system. Further, owing to the decreased density of the nylon particle, the height of the bed of nylon particles in the 20 % suspension was close to the impeller at zero agitation. This is expected to influence the fraction of particles suspended above the impeller at 186 rpm.

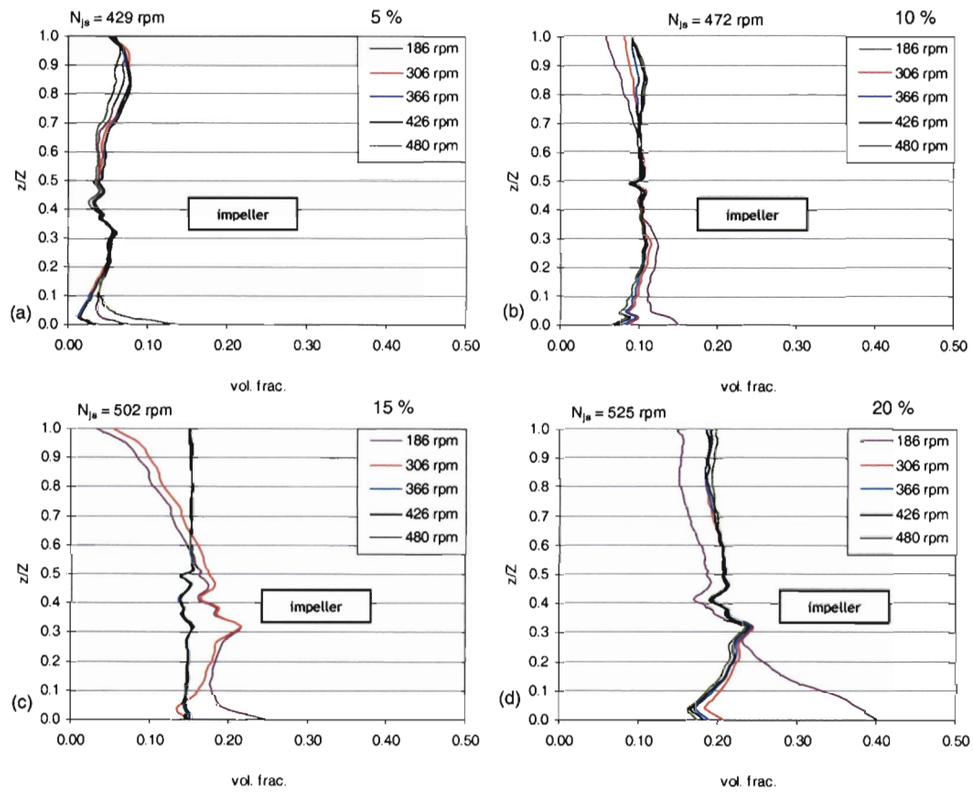


Figure 8.6: Axial concentration profiles of the 500 μm nylon particles at volume concentrations of 5 % (a), 10 % (b), 15 % (c) and 20 % (d). Rushton impeller.

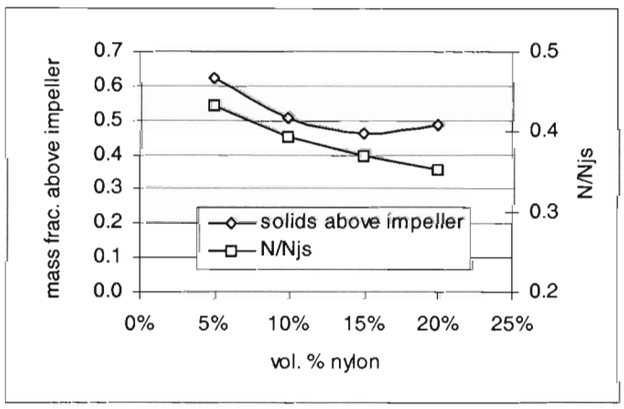


Figure 8.7: The fraction of nylon particles above the Rushton impeller at 186 rpm for 5 – 20 % solids concentration. The agitation rate (186 rpm) is further represented as a fraction of N_{js} with respect to each solid concentration (secondary y-axis).

8.4 3D Examination of Particle Suspension

8.4.1 The 3D Experiment

MRI experiments conducted in 3D (32 x 32 x 32 and 64 x 64 x 64 pixels) were conducted over 12 hour duration and further enabled the analysis of information in the radial direction. Increase in uncertainty near the top of the vessel was found due to geometric fluctuation of the liquid surface and r.f. decay occurring near the top of the coil. The 3D MRI experiments were thus less quantitative than the 1D experiments with regard to axial concentration (Figure 8.8). The calculation procedure using this data can be seen in Appendix L. The raw data was collected in an x-y data format, thus average radial concentration profiles were not possible.

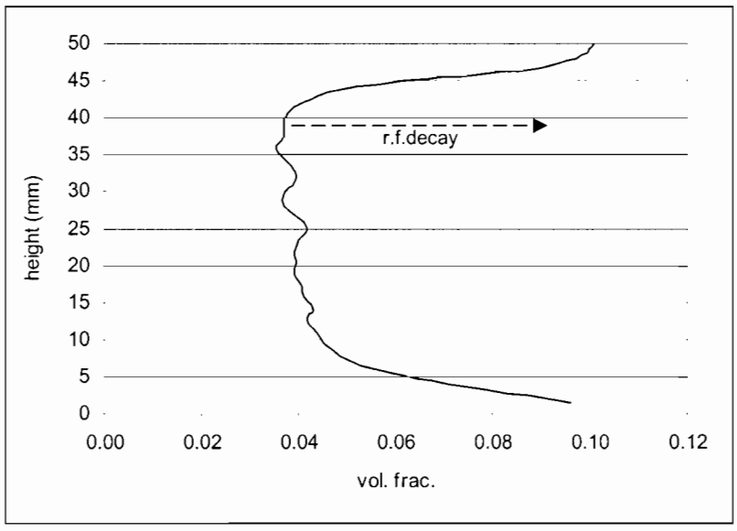


Figure 8.8: Axial concentration profile obtained from 3D data for 5 % suspension of 50 μm ballotini at 480 rpm with Rushton impeller. Above approximately 40 mm (z/Z = 0.80) in height r.f. decay at the top of the probe is apparent.

8.4.2 Radial Concentration Profiles of Ballotini

3D experiments were conducted on 5 and 10 % v/v suspensions of 50 μm ballotini particles. The radial concentration profiles were calculated from the widest strip of data across the reactor diameter (Appendix L), and thus do not represent the entire average radial condition. The strip chosen was representative of average conditions i.e. it was not behind a baffle. At the bottom of the reactor there will be deviation from the average condition as particles are generally concentrated behind the baffles. It has traditionally been very difficult to obtain reliable sampling information near the bottom of the tank (< 5 mm from base). The MRI data, collected here and presented

in Figure 8.9, show that there was a rapid increase in solids concentration on approaching the vessel wall. This is to be expected due to fillet formation from the Rushton impeller. It was observed that at 1.6 mm depth the solids concentration fluctuated considerably. In Figure 8.10, data are presented for the region from the impeller plane (21.9 mm) to a height of 6.3 mm. Significant fluctuations were observed at 6.3 mm (z/Z = 0.13) with solid concentration increasing on approach of the wall. For the heights of 10.9 mm (z/Z = 0.22), 15. 6 mm (z/Z = 0.31) and 21.9 mm (z/Z = 0.44) the profiles showed constant concentrations across the radial plane (0.035 – 0.040 volume fraction), with a small increase occurring near the impeller shaft and at the wall at a 10.9 mm height.

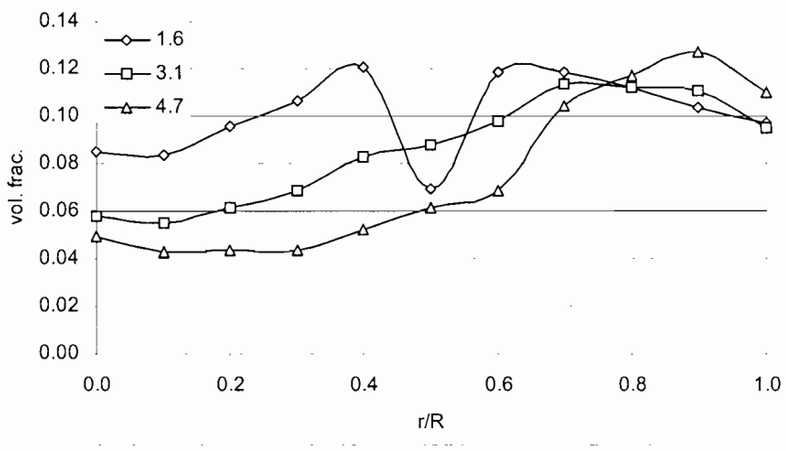


Figure 8.9: Radial concentration profiles for the bottom of the reactor at heights of 1.6 (z/Z = 0.03), 3.1 (z/Z = 0.06) and 4.7 mm (z/Z = 0.05) for the 5 % suspension of 50 μm ballotini agitated by Rushton impeller at 480 rpm.

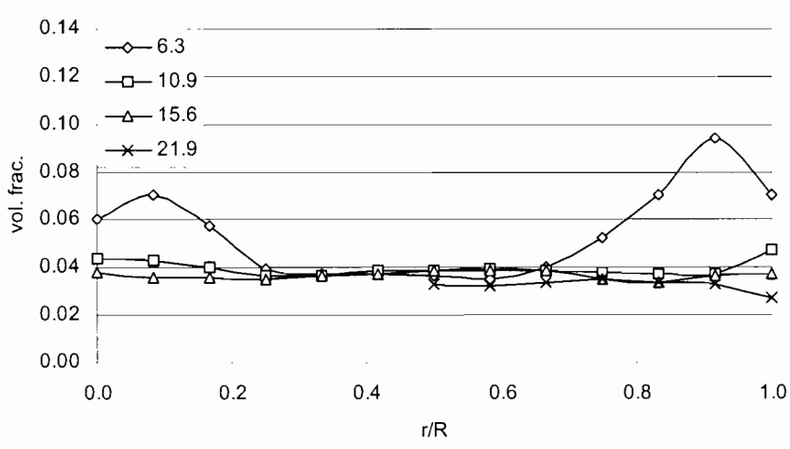


Figure 8.10: Radial concentration profiles for the Rushton impeller region and below at heights of 6.3 (z/Z = 0.13), 10.9 (z/Z = 0.22), 15.6 (z/Z = 0.31) and 21.9 mm (z/Z = 0.44) for the 5 % suspension of 50 μm ballotini at 480 rpm.

In Figure 8.11, it is seen that the profiles collected at a height of 31.3 mm (z/Z = 0.63) and 35.9 mm (z/Z = 0.72) did not vary significantly, although it is apparent that solids concentration decreased slightly near the wall for the 35.9 mm profile. Further, there is a relative decrease near the impeller zone for r/R = 0 to 0.3 for the 26.6 mm height (z/Z = 0.53).

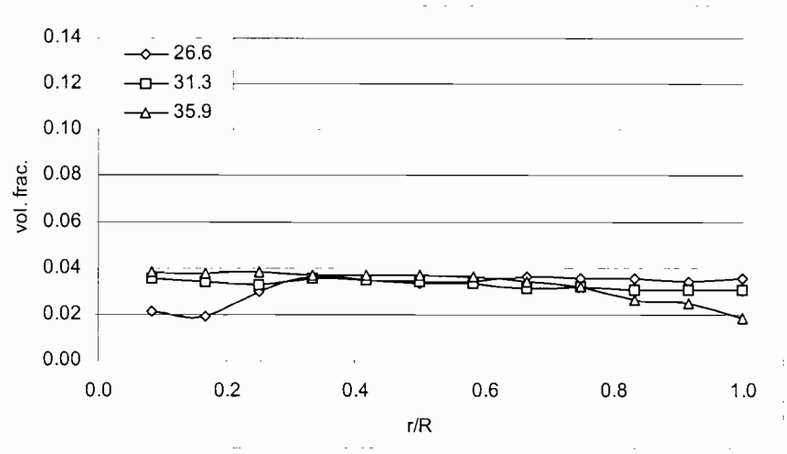


Figure 8.11: Radial concentration profiles above the Rushton impeller at heights of 26.6 (z/Z = 0.53), 31.3 (z/Z = 0.63) and 35.9 mm (z/Z = 0.72) for the 5 % suspension of 50 μm ballotini at 480 rpm.

On studying the 10 % suspension, the axial concentration profile showed that r.f decay initiated from approximately 35 mm (Figure 8.12), thus radial profiles were produced up to this height. In Figure 8.13, it can be observed that the radial concentration profiles at the bottom of the reactor showed significant fluctuation. At a height of 0.9 mm (z/Z = 0.02), the volume fraction varied between 0.00 and 0.11. At heights of 1.8 mm (z/Z = 0.04), 2.7 mm (z/Z = 0.05) and 4.5 mm (z/Z = 0.09), a volume fraction range of approximately 0.04 – 0.10 was observed. These lower profiles showed a raised section in concentration at r/R = 0.2. For this particular strip across the diameter of the tank bottom, concentrations were lower than the average i.e. compared to the concentrations near the tank bottom in Figure 8.12. Further analysis of the tank bottom follows in Section 8.4.3 with a complete view of the reactor cross-section.

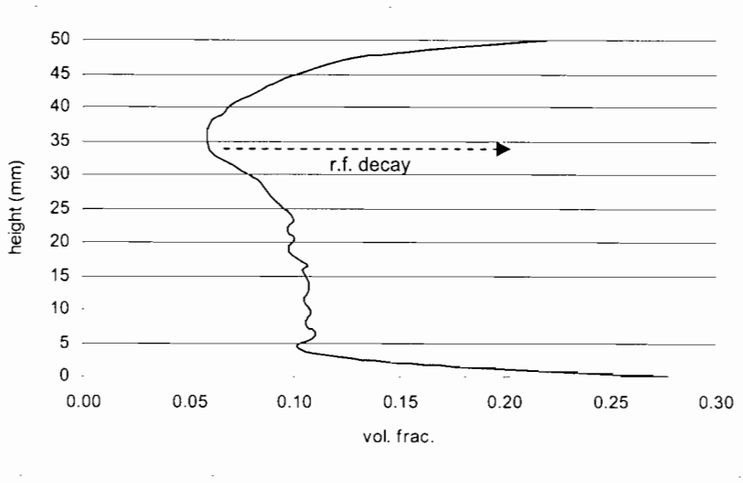


Figure 8.12: Axial concentration profile obtained from 3D data for 10 % suspension of 50 μm ballotini at 480 rpm with Rushton impeller. Above approximately 35 mm (z/Z = 0.70) in height r.f. decay is apparent.

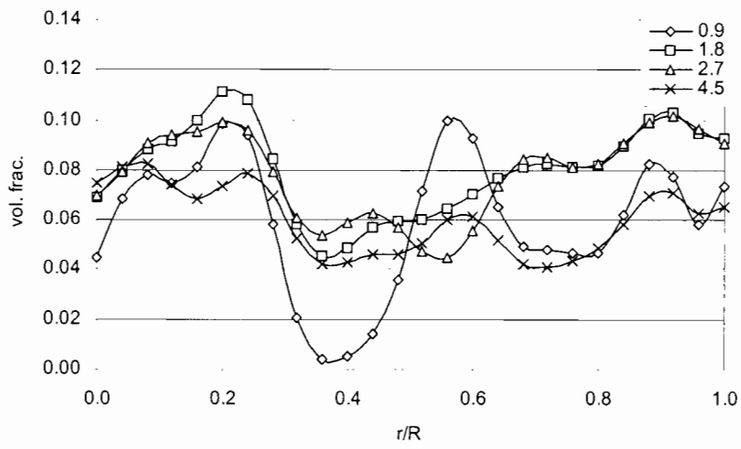


Figure 8.13: Radial concentration profiles for the bottom of the reactor at heights of 0.9 (z/Z = 0.02), 1.8 (z/Z = 0.04), 2.7 (z/Z = 0.05) and 4.5 mm (z/Z = 0.09) for the 10 % suspension of 50 μm ballotini using a Rushton impeller at 480 rpm.

For heights below the impeller at 10.7 to 17.0 mm (z/Z = 0.21 to 0.34), concentration profiles tended to decrease on approaching the vessel wall. At a height of 15.2 mm, which is 1.5 mm below the impeller plane, a high solids concentration of 14 to 17 % was observed for r/R = 0.0 to 0.3. This corresponds to the region directly below the impeller. In the impeller plane at a height of 17.0 mm, the profile tends to be fairly regular from the edge of the impeller to the wall. The data just below (1.5 mm) the impeller is of interest; however, there can be no comparison with previous studies of

stirred tanks. ERT does not provide this resolution, while sampling has not been reported from this region. This increased concentration immediately below the impeller was not observed on analysis of the 5 % v/v suspension using MRI.

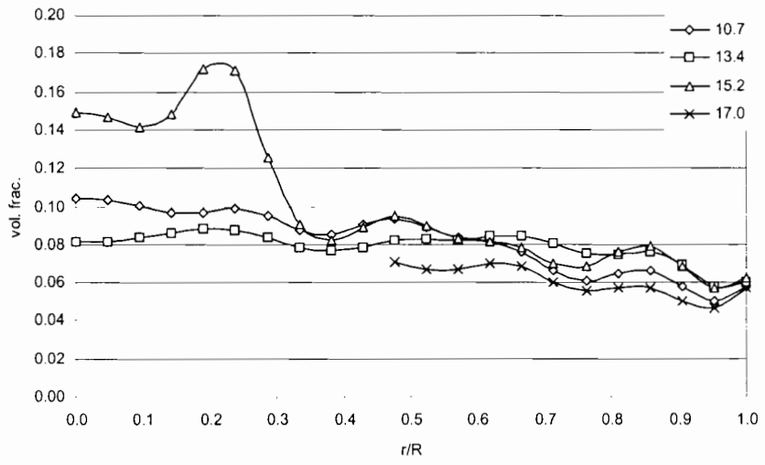


Figure 8.14: Radial concentration profiles for below the Rushton impeller at heights of 10.7 (z/Z = 0.21), 13.4 (z/Z = 0.27), 15.2 (z/Z =0.30) and 17.0 mm (z/Z = 0.34) for the 10 % suspension of 50 μm ballotini at 480 rpm.

An oscillatory pattern was observed above the impeller (Figure 8.15). This behaviour was also apparent in Figure 8.14. This was not observed on analysis of the 5 % suspension concentration. To date, radial profiles have been expected to be more consistent above the Rushton impeller (Barresi and Baldi, 1987a), although these studies used dilute solids concentrations (< 2 vol. %). The sampling method of Barresi and Baldi (1987a) did not produce this degree of resolution as only 3 data points were examined in the radial plane. The profiles at heights of 25.9 mm (z/Z = 0.52), 31. 3 mm (z/Z = 0.63) and 38.4 mm (z/Z = 0.77) all increased slightly in concentration for the last 3.75 mm on approaching the vessel wall (r/R = 0.85 to 1.00) and were in phase with their oscillations.

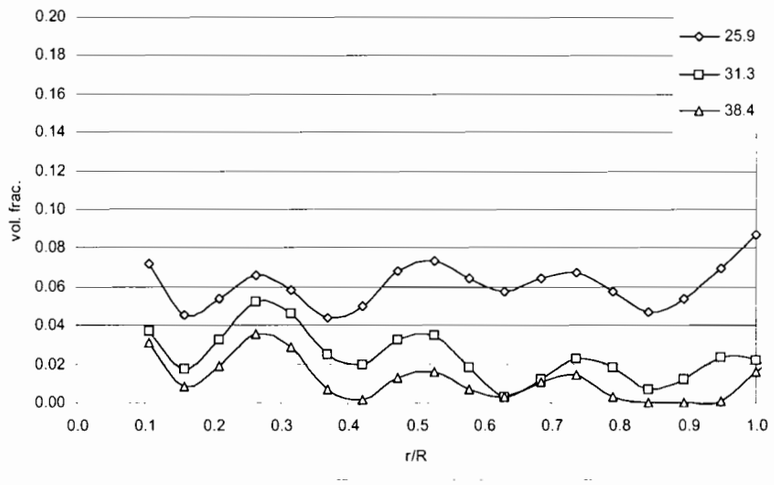


Figure 8.15: Radial concentration profiles above the Rushton impeller at heights of 25.9 (z/Z = 0.52), 31.3 (z/Z = 0.63) and 38.4 mm (z/Z = 0.77) for the 10 % suspension of 50 μm ballotini at 480 rpm.

8.4.3 2D Radial Slices of Incomplete Suspension

The 3D data from the 10 % suspension of 50 μm ballotini experiment is displayed graphically in the form of 2D slices to represent particle distribution at the tank bottom in Figure 8.16 and the detection of the impeller in Figure 8.18. Figure 8.16, in which particles are represented by the darker areas (lower proton signal), is a particularly clear representation of their distribution at incomplete suspension. It provides a clear representation of fillet formation as deduced from Figure 8.9 and 8.13. Such a representation has not been reported in the literature previously. It further refutes the notion of a bed of particles expanding uniformly with increasing suspension. Directly beneath the impeller at the tank center, minimal accumulation of particles was found. A swirl feature then developed ending at each baffle. This data was collected using the 6-bladed Rushton impeller spinning clockwise. However, in Figure 8.16 there were only four swirls. Thus these swirls were independent of the number of blades of the impeller and rather represent the hydrodynamic field associated with the presence of the four baffles. These swirls rose up to a height of 2.8 and 3.7 mm to where the baffle joins the vessel wall, as depicted in Figure 8.16 (c) and (d). This observed pattern should be valuable for the validation of CFD suspension studies. The data presented in Figure 8.13 showing a lower than expected concentration, can thus be explained as the strip examined across the diameter only crossed the tips of the swirl features shown in Figure 8.16. In Figure 8.17, the average x-direction concentration (calculation method in Appendix L) with respect to radius is shown. On

moving outwards from the center of Figure 8.16 (a) and to the right (x-direction) while calculating the y-direction average concentration, two peaks in concentration result. These are observed in Figure 8.17. These patterns were not observed for the 5 % suspension of 50 μm ballotini or for the 10 % suspension of 500 μm nylon particles.

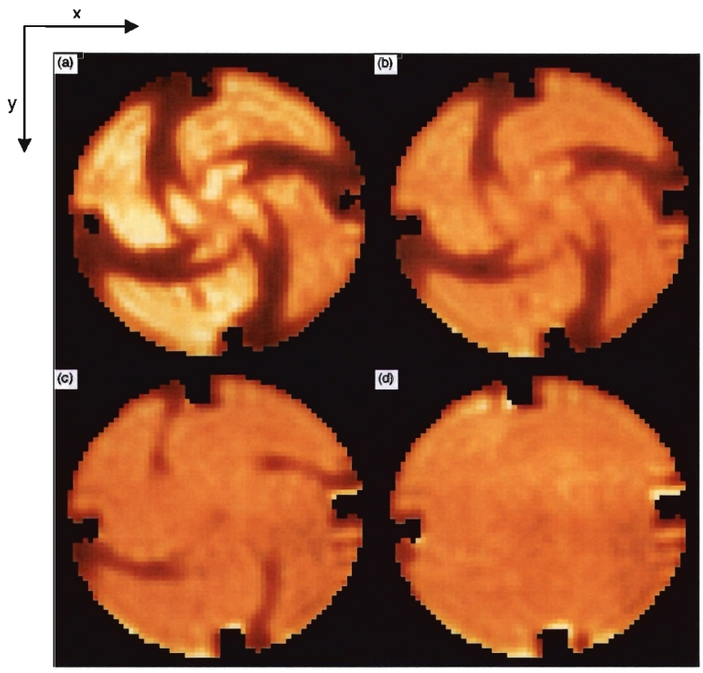


Figure 8.16: 2D slices at the tank bottom for the 10 % v/v 50 μm ballotini particles on agitation with Rushton impeller at 480 rpm at heights of 0.9 mm (a) (z.Z = 0.02), 1.8 mm (b) (z/Z = 0.04), 2.8 mm (c) (z/Z = 0.06) and 3.7 mm (d) (z/Z = 0.07).

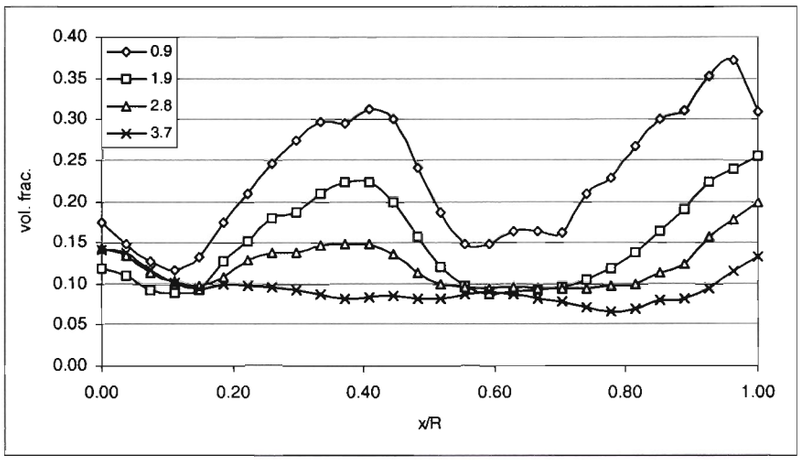


Figure 8.17: The average concentration in the x-direction with respect to the radius of the tank for the 10 % suspension of 50 μm concentration for the heights of 0.9, 1.9, 2.8 and 3.7 mm. z/Z = 0.02 to 0.07.

Faint circular rings are apparent in Figure 8.18 (a) and (b), where data are collected at the impeller zone. These signify the presence of the spinning turbine blades. As rising in height, the base of the impeller becomes apparent before narrowing to the shaft thickness. This can be related to the design of the impeller in Figure 3.18.

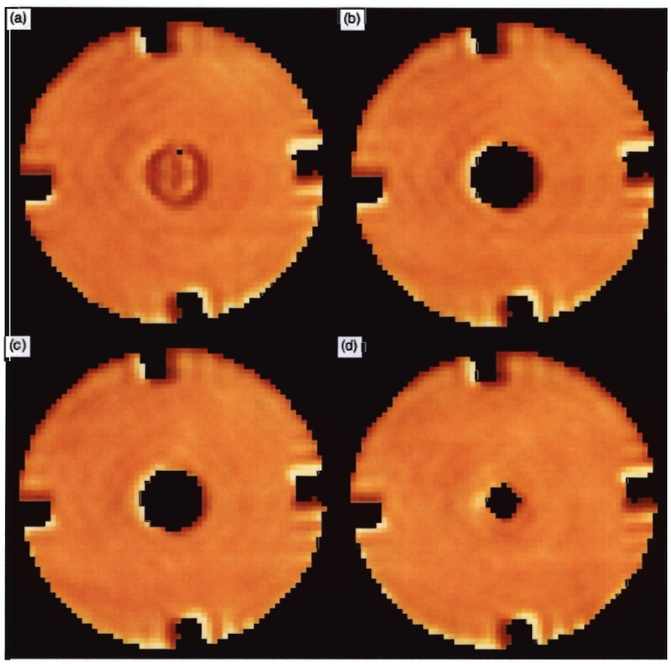


Figure 8.18: 2D slices at the impeller zone for the 10 % v/v suspension of 50 μm ballotini particles agitated by the Rushton impeller at 480 rpm at heights of 16.7 mm (a) (z/Z = 0.33), 17.6 mm (b) (z/Z = 0.35), 18.5 mm (c) (z/Z = 0.37) and 19.4 mm (d) (z/Z = 0.39). Impeller blade width from z/Z = 0.33 to 0.43

8.4.4 Radial Concentration Profiles of 500 μm Nylon particles

A 3D experiment was performed on the 10 % suspension of nylon at 480 rpm. The data was found to be acceptably quantitative (0.11 volume fraction calculated) without implementing mass balance correction. Minimal r.f. decay was experienced and a height of up to 40 mm was examinable (Figure 8.19). This profile showed reduced axial homogeneity compared with the 1D profile. The radial profiles at the bottom of the tank shown in Figure 8.20, have an oscillatory nature as observed previously.

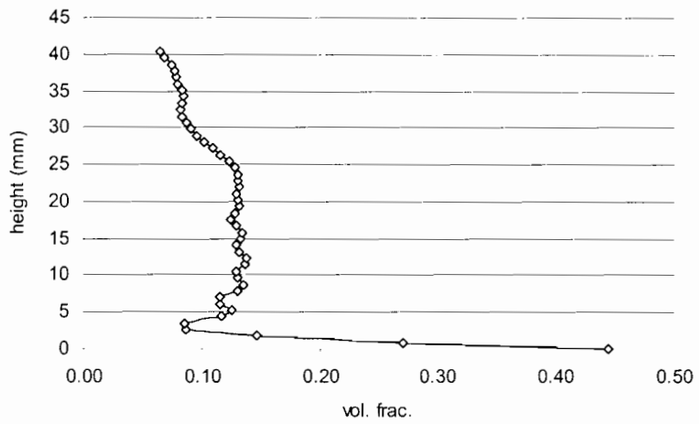


Figure 8.19: Axial concentration of 10 % suspension of 500 μm nylon with Rushton impeller obtained from 3D data. Data was useable up to a height of 40 mm (z/Z = 0.8) and an average volume fraction of 0.11 was calculated for this profile.

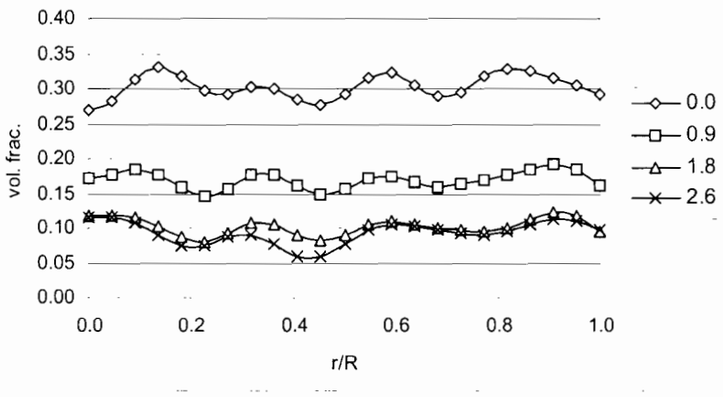


Figure 8.20: Radial concentration profiles for the bottom of the reactor at heights of 0.0, 0.9, 1.8 and 2.6 mm for the 10 % suspension of 500 μm polyamide nylon agitated by Rushton impeller at 480 rpm. z/Z = 0 to 0.05.

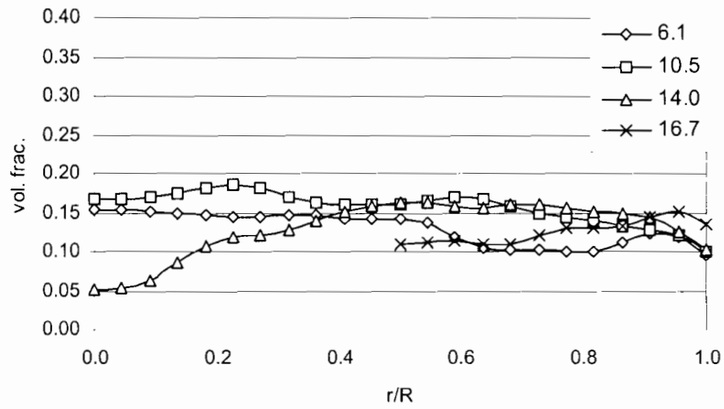


Figure 8.21: Radial concentration profiles below the Rushton impeller at heights of 6.1 (z/Z = 0.12), 10.5 (z/Z = 0.21), 14.0 (z/Z = 0.28) and 16.7 mm (z/Z = 0.33) for the 10 % suspension of 500 μm polyamide nylon at 480 rpm.

Below the impeller at dimensionless heights of 0.12 to 0.33 from the bottom (Figure 8.21), more regular radial profiles were observed apart from at 14.0 mm where a decrease in solids just below the impeller zone was visible. This is in contrast with the 10 % ballotini results shown in Figure 8.14 where an increase in concentration was observed just below the impeller. Above the impeller, the oscillatory radial profile was found again, as shown in Figure 8.22.

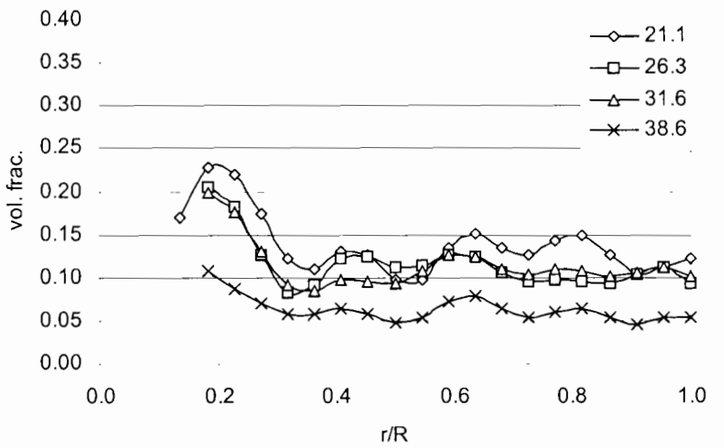


Figure 8.22: Radial concentration profiles above the Rushton impeller at heights of 21.1 (z/Z = 0.42), 26.3 (z/Z = 0.53), 31.6 (z/Z = 0.63) and 38.6 mm (z/Z = 0.77) for the 10 % suspension of 500 μm polyamide nylon at 480 rpm.

8.5 Errors Associated with MRI Experiments

Two types of uncertainty are examined: error while performing an experiment multiple times at a specific agitation rate and specific probe tuning, and error between experiments after having removed the reactor and re-tuned the probe. The 3D experiments could not be performed more than once due to time constraints associated with the research demand for the 4.7 T magnet. Some error resulted in these experiments due to the error associated with the slight drift in tuning over the 12 hour experiment duration. This drift was calculated at approximately ± 0.005 % of the proton frequency.

8.5.1 Error while Maintaining Tuning

Following the tuning of the probe to 199.7 MHz, different agitation rates were implemented. All 1D scans were performed in triplicate. From Figure 8.22, it is apparent that there is good overall reproducibility between experiments. Here the standard deviation for each speed is represented as a percentage of the mean with respect to the reactor height for the 5 % suspension of 100 μm ballotini. Axially, there is uncertainty (0.4 – 1.6 %) at the tank bottom due to the greater fluctuation in solid concentration. Across the heights 5 to 40 mm (z/Z = 0.1 to 0.8), the uncertainty is minimised to 0.1 to 0.4 %. Above 40 mm from the tank bottom (z/Z = 0.8), the r.f. decay increased uncertainty which approached 1.0 to 2.0 %. A scan of water in the absence of a solid fraction yielded minimal standard deviation (average = 0.13 %) across the reactor height with no agitation, as shown in Figure 8.23.

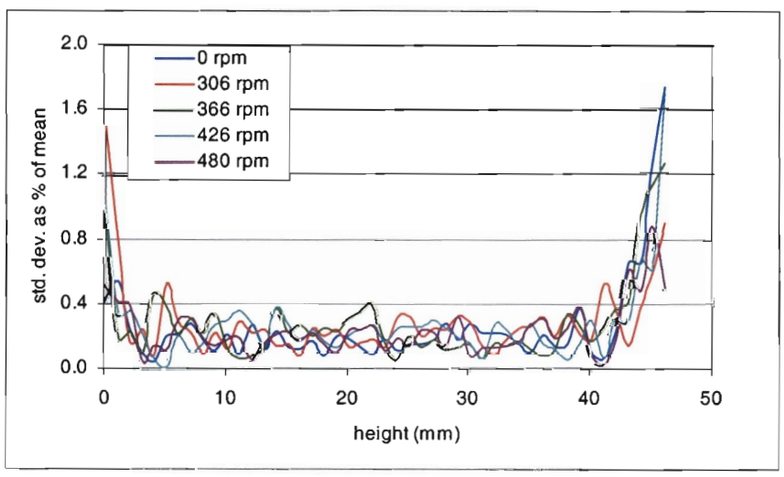


Figure 8.22: Uncertainty with respect to agitation rate and reactor height for 1D scans of the 5 % suspension of 100 μm ballotini.

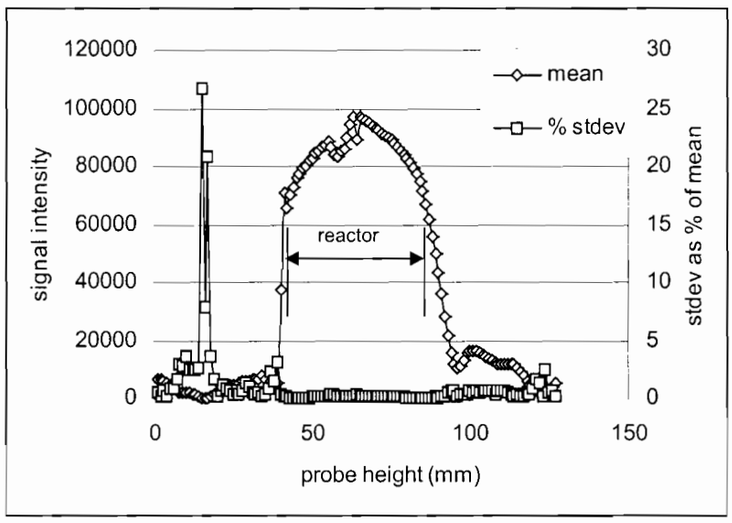


Figure 8.23: Uncertainty with respect to signal intensity across the reactor for water at zero agitation.

8.5.2 Uncertainty between Experiments after Re-tuning

This error was associated with the probe removal and re-tuning. The standard deviation as a percentage of the mean with respect to reactor height is shown in Figure 8.24 for the 10 % suspension of 50 μm ballotini at 480 rpm. This experiment was performed in triplicate. A slight increase in error was observed just below the impeller zone. Further, the error increased above 30 mm (z/Z = 0.60) due to r.f. decay and the change in the liquid surface position.

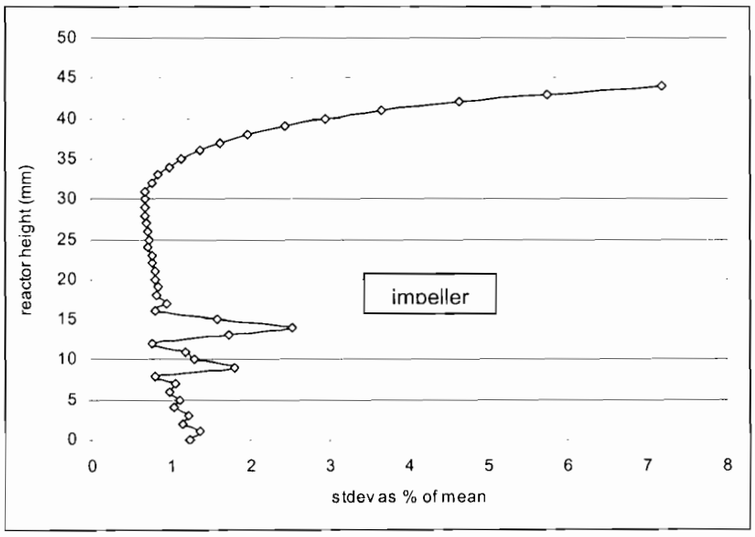


Figure 8.24: Uncertainty with respect to reactor height between re-tuned experiments for the 10 % suspension of 50 μm ballotini agitated by Rushton impeller at 480 rpm.

8.5.3 Resolution

The 1D scans had a resolution of 1 mm, while the 3D 32 x 32 x 32 and 64 x 64 x 64 pixel scans had resolutions of 1.56 and 0.93 mm respectively. However, although the 3D scan (64 x 64 x 64) has higher resolution than the 1D scan, the 1D scan is still recognised as being more accurate in accounting for proton signal intensity (Sederman and Mantle, 2005). Further, MRI has greater resolution than ERT, light scattering methods and direct sample withdrawal.

8.6 Comparisons of MRI with ERT Experiments

8.6.1 Radial Concentration Profiles Determined by ERT and MRI

Radial comparisons of MRI and ERT data were possible for the three 3D experiments, namely the 5 and 10 % suspensions of 50 μm ballotini and the 10 % suspension of nylon particles. In the comparisons of axial data, the ERT (Reconstruction Code V, Hardware IV) profiles were only used to represent information for r/R = 0.55 to 1. The ERT electrodes are 1 cm high and spaced 2 mm apart vertically, with the four electrode layers represented heights z/Z = 0.04 to 0.24 (L1), z/Z = 0.28 to 0.48 (L2), z/Z = 0.52 to 0.72 (L3) and z/Z = 0.76 to 0.96 (L4). Layer 4 is difficult to compare as r.f. decay for the MRI reactor began approximately in the region z/Z = 0.70 to 0.80. Comparative MRI data was averaged for each distance of the electrode height for L1 to L3. Layer 4 was related to the highest data available from the MRI experiments (z/Z = ± 0.76). The ERT data represent the conductivity in the horizontal region between electrodes in a layer as well as conductivity values slightly above and below the electrode layer due to the three dimensional nature of the potential. Conversely, the MRI radial profiles are not average radial data. They represent the widest strip of data across the reactor diameter (see Appendix L), while averaged according to the electrode vertical height for L1 – L3.

The MRI and ERT concentration profiles were consistent within a 20 % variation (Figure 8.25), with the exception of ERT L4. MRI is able to quantify more accurately unsuspended material on the reactor bottom than ERT, therefore the MRI L1 profile was higher than the ERT L1 profile. The MRI L4 profile was taken at a lower height (z/Z = 0.76), and thus the detection of more material is expected. Layers 2 and 3 showed good agreement using both tomographies. A further comparison of radial data is to consider the average radial profile for the whole reactor for both tomographies, as presented in Figure 8.26. Here a similar trend was observed in the radial profile, especially for r/R = 0.75 to 1. It must be noted that the ERT average is only comprised of information for r/R = 0.55 to 1.00.

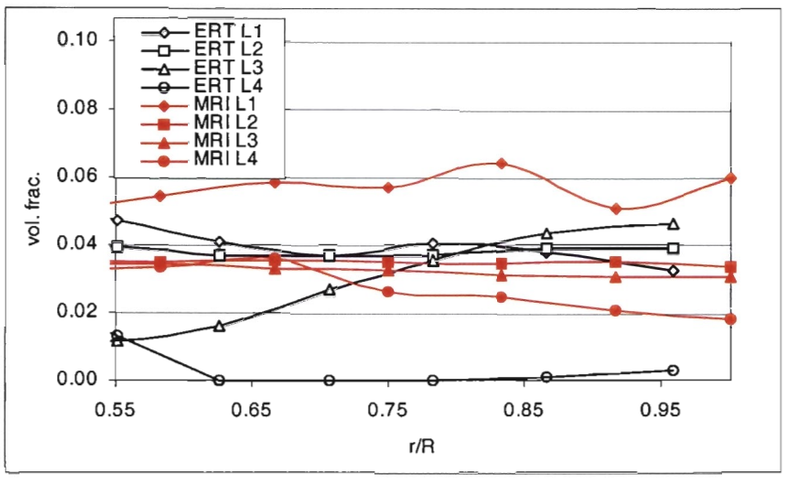


Figure 8.25: Comparison of average radial ERT profiles and location specific MRI profiles at the same heights (L1 – L4). 5 % suspension of 50 μm ballotini agitated by Rushton impeller at 480 rpm.

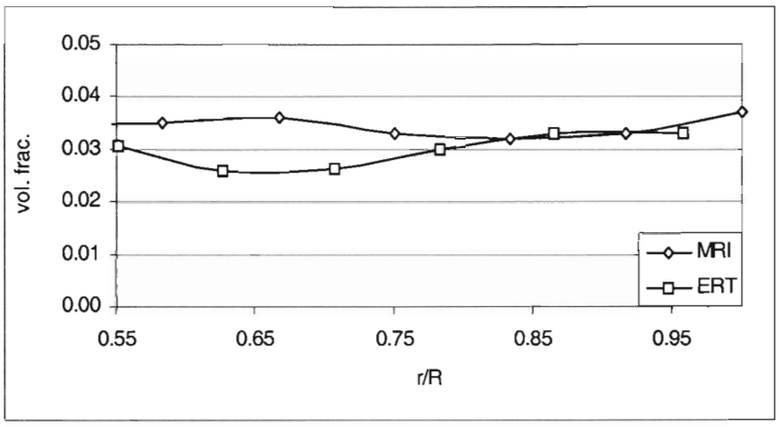


Figure 8.26: A comparison of the average radial profile for the whole reactor for both tomographies. 5 % suspension of 50 μm ballotini at 480 rpm.

Similar data are shown for the 10 % ballotini concentration in Figures 8.27. The outermost data points (r/R = 0.96 to 1.00) of the MRI data show higher wall concentrations. However, it must be noted that this distance is only 2.5 mm from the wall, while the outermost ERT data represents the region r/R = 0.55 to 0.96 as the subdivisions in the mesh were averaged and related to the average radial distance of the subsection. For the average radial profile of the whole reactor there is good agreement (Figure 8.28). The ERT data has greater similarity with the MRI data in this case, which could be related to the higher bed height of the 10 % ballotini

concentration which would be more easily detected by ERT L1. The MRI L4 profile is higher than expected, with possible effects from r.f. decay.

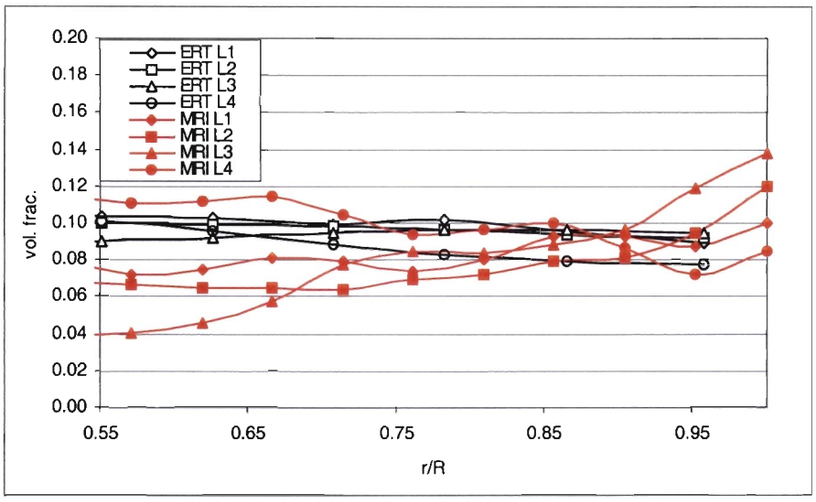


Figure 8.27: Comparison of average radial ERT profiles and location specific MRI profiles at the same heights (L1 – L4). 10 % suspension of 50 μm ballotini agitated at 480 rpm.

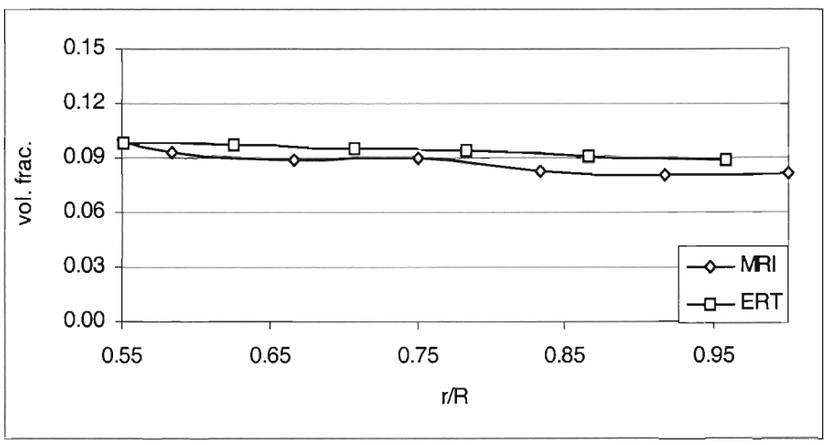


Figure 8.28: A comparison of the average radial profile for the whole reactor for both tomographies. 10 % suspension of 50 μm ballotini agitated by Rushton impeller at 480 rpm.

In general, the MRI data showed agreement within 20 % of the ERT data for the L1 - L3 profiles for the 500 μm nylon particles, as shown in Figure 8.29. The MRI L4 profile did not account for all the material in the upper region due to r.f. decay, and is therefore lower in concentration. The ERT profiles are generally more consistent due

to averaging of all elements in the FEM mesh at the specific radial position. There is excellent agreement between tomographies for the average radial concentration for the whole reactor, as shown in Figure 8.30. This adds support to the ERT data.

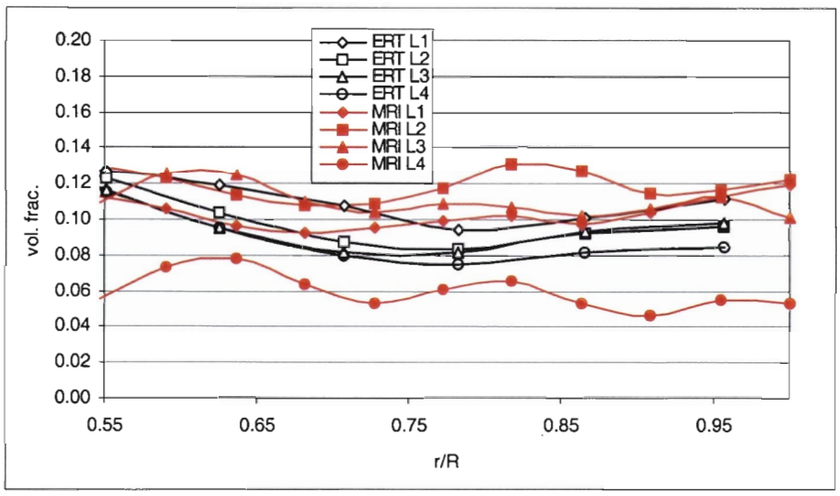


Figure 8.29: Comparison of average radial ERT profiles and location specific MRI profiles at the same heights (L1 – L4). 10 % suspension of 500 μm nylon particles at 480 rpm.

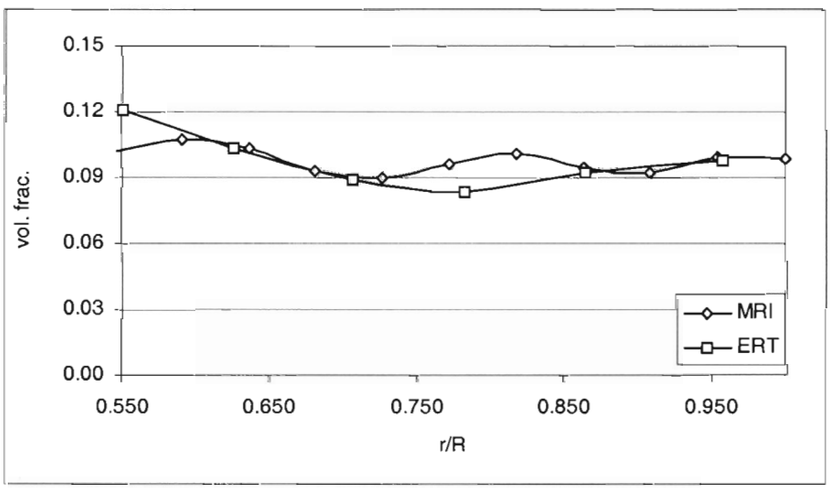


Figure 8.30: A comparison of the average radial profile for the whole reactor for both tomographies. 10 % suspension of 500 μm nylon particles at 480 rpm.

8.6.2 Axial Concentration Profiles of ERT and MRI

Axial concentration profiles were compared from MRI and ERT using data from the 5 and 10 % suspensions of 50 μm ballotini, and the 10 % suspension of nylon agitated at 480 rpm by the Rushton impeller. Identical information could not be related in this endeavour as ERT axial data were comprised of average radial data from r/R = 0.55 to 1.00, while 3D MRI axial data were comprised of the average concentration across the widest strip of the reactor (xy data). Further, the 1D MRI data accounts for information in the complete radial plane. This section compares the ERT axial profiles using data from the four electrode layers, to the 3D and 1D MRI data while taking cognisance of the different nature of these data.

The 3D MRI profile was generated using data from the same widest strip across the tank diameter averaged from r/R = 0.55 to 1 (to match the ERT data) at heights matching the electrode layers. The 1D ERT data represents the complete axial concentration profile as shown in Section 8.3.

For the 5 % suspension of 50 μm ballotini given in Figure 8.31 (a), similar trends were observed in the ERT, 3D MRI and 1D MRI results for L1 to L3, however the concentrations estimated by ERT at L4 are greatly diminished with respect to those estimated by MRI. The ERT results for this layer are most likely inaccurate owing to the surface fluctuation, as discussed in Section 7.5. The MRI 1D should be taken as the best representation of axial concentration as it contains the most information and is more quantitative. Thus it appears the ERT underestimates the amount of material present which is possibly related to the missing information of the 'core' of the vessel. A good agreement is observed between the ERT and MRI 1D for the 10 % suspension of ballotini as shown in Figure 8.31 (b)), while the 3D MRI detects approximately 10 % less material than the ERT and 1D MRI. This is due to the r.f. decay from approximately z/Z = 0.7 and higher. In general, there is good agreement between the 1D MRI concentration profile for the 10 % suspension of nylon and the ERT data, as shown in Figure 8.31 (c). Radio frequency decay is again apparent in the 3D MRI data.

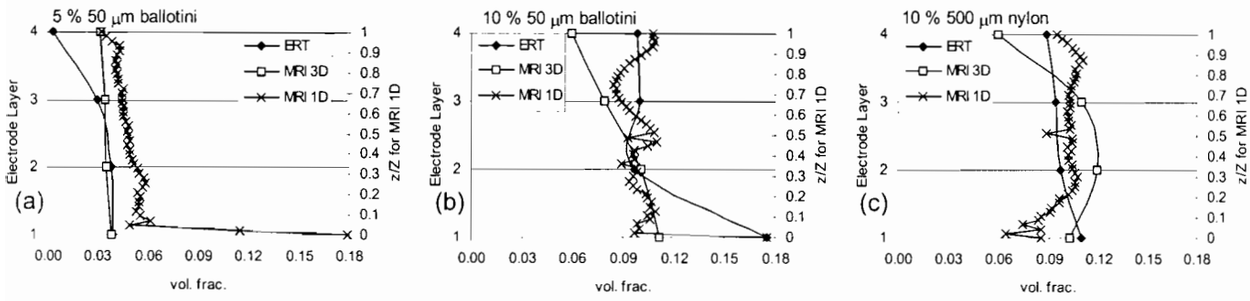


Figure 8.31: Axial concentration profile comparison of tomographies: ERT (averaged data in z plane; average data from r/R = 0.55 to 1 for each electrode layer), MRI 3D (at a specific radial position; average data from r/R = 0.55 to 1 at the equivalent electrode z/Z) and MRI 1D (averaged in z plane; data matching z/Z of electrode layers) for 5 % suspension of 50 μm ballotini (a), 10 % suspension of 50 μm ballotini (b) and 10 % suspension of 500 μm nylon particles (c). All agitated by Rushton impeller at 480 rpm.

8.7 Conclusions

Through quantifying the amount of protons present in the distribution of water in the reactor, the solids concentration could be described accurately in the vessel by MRI in one dimension. This enabled the determination of the amount of particles still unsuspended on the vessel bottom at various agitation rates. This information is essential if considering a reduction in agitation rate for shear sensitive microorganisms and a reduction in particle-cell-particle collisions in the slurry bioreactor. Moreover, the accurate determination of the axial concentration profile with 1D MRI allowed clear visualisation of particle distribution, thus providing information for CFD verification. Further, this is the first reported MRI investigation of a stirred tank.

Linear relationships were found between the agitation rate and the amount of solids unsuspended for the smaller 50 μm ballotini at concentrations of 5 and 10 %. The larger 100 μm ballotini exhibited a non-linear relationship. Linear relationships were similarly found between the fraction of particles above the impeller and the agitation rate for the 5 and 10 % suspensions of 50 μm ballotini. The 5 % suspension of 50 μm ballotini exhibited a peak concentration in the axial plane slightly above the impeller plane. This peak concentration has been reported in the literature at general conditions of high agitation rates and low volume fractions of solids. There thus appears a critical concentration of solids that can be supported by fluid forces in the impeller zone to form a peak concentration. From analysis of this peak concentration it was deduced that the influence of particle concentration and particle interaction need to be considered in theoretical suspension models.

The less dense nylon suspensions showed excellent particle homogeneity. Furthermore, the Zwietering correlation was found to overpredict the critical suspension speed. This is an important observation for the minimising of energy input into the reactor while ensuring appropriate homogeneity. It was postulated at the 20 % volume concentration that particle-particle effects influenced the amount of particles suspended above the impeller.

Less quantitative 3D MRI experiments enabled the generation of radial profiles. These representations were confined to a specific position in the reactor due to the nature of the xy MRI data. At a millimeter resolution, it was found that homogeneity was generally good directly above and below the impeller, while solids concentration fluctuated near the reactor base. This is in accordance with sampling data from stirred tanks (Barresi and Baldi, 1987a). For the 10 % suspension of 50 μm ballotini and the 10 % suspension of 500 μm nylon particles, an oscillating behaviour was observed in the radial profiles above and below the Rushton impeller. ERT cannot be used to verify the oscillation due to the nature of its resolution and broad electric field lines i.e. above and below the excited electrode. Sampling in literature has normally been achieved with three or four data points in the radial plane, again not facilitating observation of such fluctuations.

2D radial slices of the 3D data enabled clear depiction of incomplete suspension for the 10 % suspension of 50 μm ballotini; yielding a pattern clearly affected by the tank hydrodynamics as opposed to a generic particle bed expansion. This interesting particle pattern had not been reported previously in the literature.

The ERT and MRI radial profile comparison showed a general similarity, with the average ERT profiles being more consistent due to a greater amount of data being represented from a single axial position. However, the average radial profile for the reactor illustrated good similarity between tomographic methods. Axial profiles were also compared with greater similarity being observed between the more quantitative 1D MRI and ERT than the 3D MRI data. Finally, the similarity in radial and axial profile trends from the MRI data support ERT Reconstruction Code V and Hardware IV.

Chapter 9

The Distribution of Air and Microorganisms in Stirred Tanks

9.1 Introduction

Microbial submerged culture processes in stirred tank reactors often include a gaseous phase. An additional solid phase or immiscible liquid phase may also be present. The gaseous phase is required either to supply oxygen to microorganisms in aerobic processes or to provide a carbon source in the form of carbon dioxide in autotrophic processes. Supply of these compounds is frequently limited due to gas-liquid mass transfer limitations, hence gas dispersion is of interest. Moreover, the theoretical understanding of three phase mixing is still in early stages (Frijlink *et al.*, 1990; Micale *et al.*, 2000; Rewatkar *et al.*, 1991). ERT is difficult to apply to three phase suspensions, as both gas bubbles and solid phases are non-conducting. Differentiation between conducting species has not been reported in the ERT literature, nor attempted in this study. In this investigation, dispersion of air has been considered in a two – phase system.

The presence of a gaseous phase reduces the power of the agitator (Barigou and Greaves, 1992; Oldshue, 1983). This influences the suspension of particles, as well as the heat transfer coefficient (Kim and Kang, 1997). ERT has been successfully applied to air-water systems in horizontal pipes (Ma *et al.*, 2001) and aerated stirred tanks with variable liquid viscosity (Wang *et al.*, 2000). Although visualisation has been achieved, there has been no previous attempt to quantify the volume fraction of air in stirred tanks through ERT and relate it to the hold-up. This has, however, been previously performed on bubble columns by Fransolet *et al.* (2005) who related ERT results to partial pressure probe data.

Here, ERT (Reconstruction Code V, ERT Hardware IV) was applied to two phase air-water mixtures to examine the efficacy of the technology on a gaseous phase, and to increase understanding of gaseous phase distribution in stirred tanks. This investigation began qualitatively with application of the LBP algorithm on an industrial scaled vessel, followed by further experimentation on the sparging of the 220 mm ID tank with the latest ERT system. The phenomenon of surface aeration at higher agitation rates was also investigated.

Another component of slurry bioreactors is naturally the microorganism. Microorganisms have not been previously examined with ERT; thus this was attempted in the 220 mm and 50 mm ID reactors using a saline solution – yeast

system. Complementary MRI experiments were performed on the 50 mm reactor to examine similarity. Lastly, a closer representation of the slurry bioreactor was attempted through ERT and MRI application on a nylon – yeast system, thereby investigating a different, yet pertinent, three phase system.

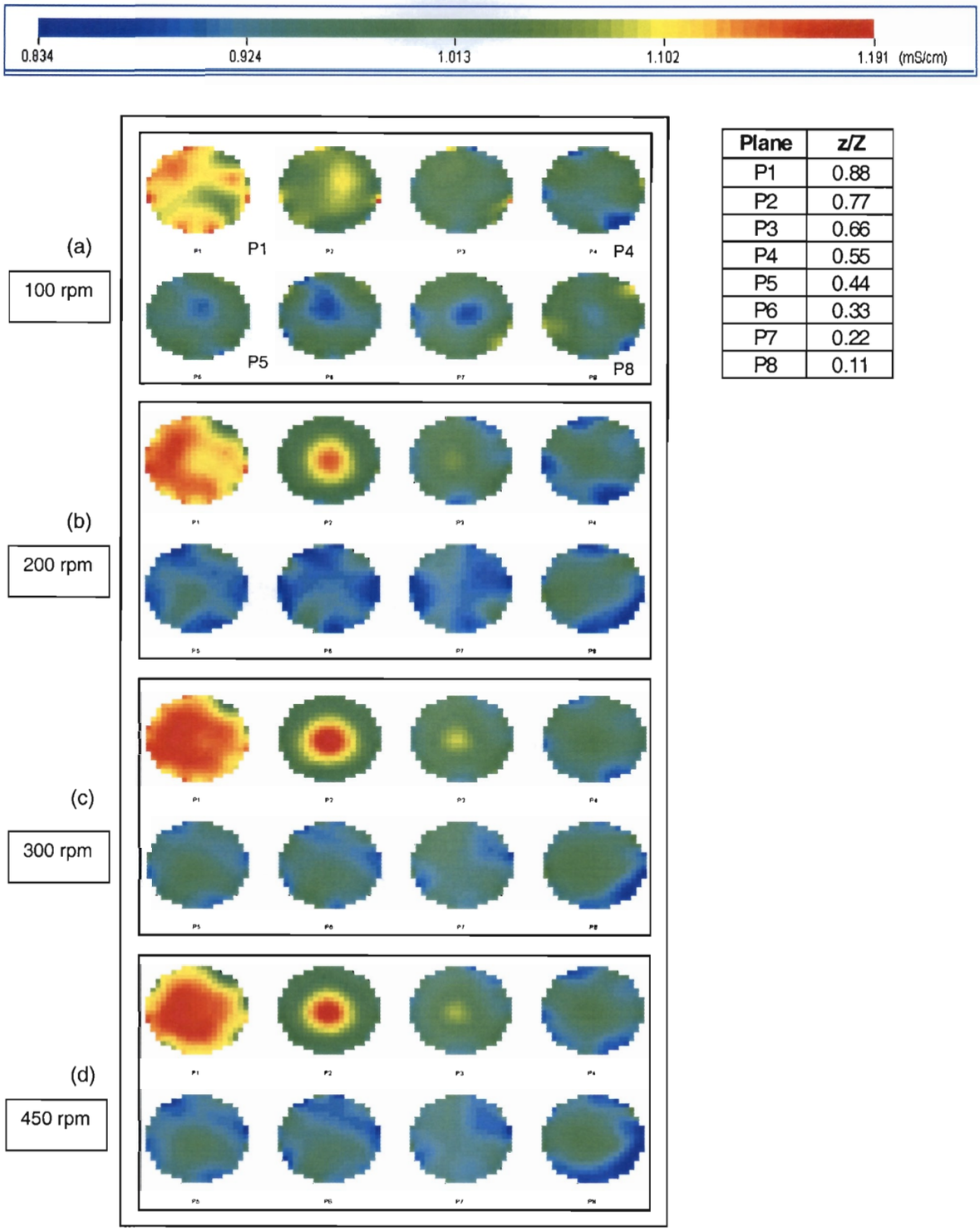
9.2 The Examination of a Gaseous Phase in Stirred Tanks

9.2.1 Detection of Air in the Pilot-Scale Tank

The LBP algorithm (Reconstruction Code IV) was applied to ERT data obtained using ERT Hardware II on the 0.61 m diameter tank described in Section 3.5 at the University of Manchester. Air was sparged at 0.5 vvm at agitation rates ranging from 100 to 450 rpm with the gas foil impeller (D = T/2; H = 2T). Tomograms are shown for agitation rates 100, 200, 300 and 450 rpm in Figures 9.1 (a) – (d) with electrode layers numbered in accordance with the software from top to bottom (P1 – P8). These LBP tomograms from the ITS software are more qualitative (Sections 2.7.4.4.1 and 4.7) than Reconstruction Code V. Data from the top three layers needs to be disregarded due to surface fluctuation. However, the behaviour of sparged air with increasing agitation rate is observed clearly in the remaining electrode layers.

In Figure 9.1 (a), it is apparent at this low agitation rate that the air is rising up the center of the vessel as indicated by the blue zone in Planes 5 – 8 (Plane 1 below the surface). The rising air is more dispersed at Plane 4, while Planes 1 - 3 show an increase in conductivity relative to their calibration conditions. The surface level rose with the introduction of the air thus providing a greater conductive area relative to the initial condition, hence the yellow and red colour. On increasing the agitation rate, shown through Figures 9.1 (b) – (d), the air is displaced towards the vessel wall through the motion of the gas foil. Figures 9.1 (c) and (d) do not show the same amount of dark blue colour in Planes 5 – 8 as Figure 9.1 (b), as the rising air is broken into smaller bubbles with more even distribution in the reactor plane.

Barigou and Greaves (1992) and Alves *et al.* (2002) observed that bubble sizes at the impeller plane near the wall were greater than those in the bulk fluid due to coalescence of the upward rising bubbles with the bubbles moving downwards from the impeller stream. This is observed in Figure 9.2 where the tomograms for the electrode layer beneath the impeller plane (P7) are stacked together with agitation rate increasing from left to right (100 – 450 rpm). At lower agitation rates, a light blue colour is visible in the middle of the tomogram of P7 signifying air rising up the centre of the tank. As agitation is increased, air is dispersed to the vessel wall and coalescence occurs, resulting in the darker blue colour signifying lower conductivity. Correlations predicting the critical impeller speed at which gas dispersion takes place



Plane	z/Z
P1	0.88
P2	0.77
P3	0.66
P4	0.55
P5	0.44
P6	0.33
P7	0.22
P8	0.11

Figure 9.1: Air sparged at 0.5 vvm into the 8 electrode layer, 2.3 m^3 tank fitted with a gasfoil impeller and operated at increasing agitation rates of 100 rpm (a), 200 rpm (b), 300 rpm (c), 450 rpm (d). P1 is below the liquid surface (top electrode layer) and the impeller is at z/Z = 0.30. Dimensionless heights of the 8 planes are given.

have been proposed (Nagata, 1975; Van Direndonck *et al.*, 1968; Westerterp *et al.*, 1963). ERT can detect this transition thereby aiding dispersion modelling, as observed in Figure 9.2.

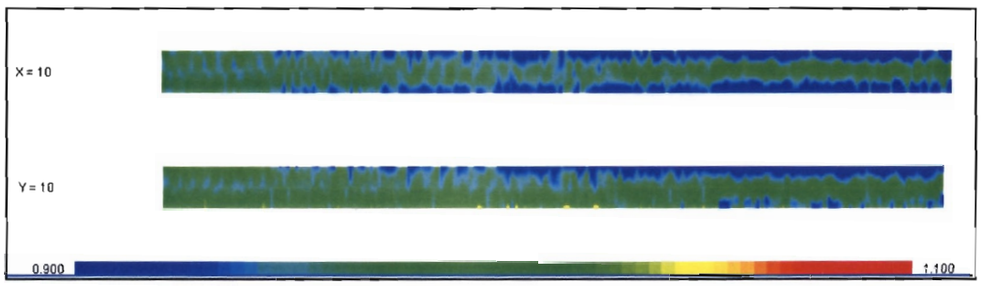


Figure 9.2: Tomograms stacked for x and y positions midway in the vessel (x = y = 10; grid = 20 x 20 pixels) with increasing agitation rate from left to right, 100 – 450 rpm. The vertical cross section represents P7 (electrode layer beneath impeller plane).

In Figure 9.3, the average resistance is related to the agitation rate for Planes 4 to 8. Resistance increases due to the increase in gas hold-up in each electrode layer, while a maximum resistance is apparent at 400 rpm. It is postulated that this maximum is due to a combination of sparged air and air introduced from the surface, while further surface aeration reduces the effectiveness of the impeller at 450 rpm, thereby resulting in a decreased local hold-up.

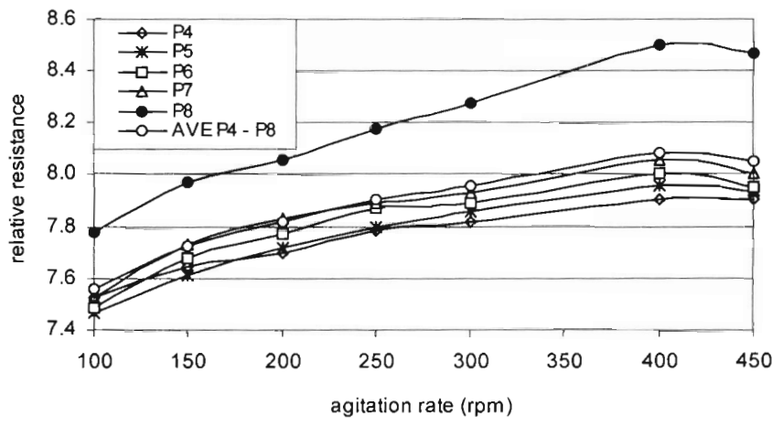


Figure 9.3: The general increase in resistance (presence of air) in the electrode layer with increasing agitation rate. P1 is at the top of the reactor with P8 in the impeller plane. Gasfoil impeller, 0.5 vvm.

9.2.2 Examining Hold-up in the 220 mm ID Tank

As the distribution of air with increasing agitation rate was successfully monitored qualitatively, a quantitative analysis was performed on the 220 mm reactor using ERT Hardware III and Reconstruction Code V. Air was sparged at 0.5 and 1.0 vvm at agitation rates of 236, 353 and 547 rpm using the Rushton impeller with simultaneous observation of the liquid height of the reactor. The pipe sparger described in Section 3.1.4 was situated at the tank bottom. Results are presented for electrode layers L1 – L3 (Figures 9.4 and 9.5) along with the average volume fraction of air calculated from the observed hold-up (Appendix M). Similar to the study in the pilot-scale tank (Section 9.2.1), the uppermost electrode layer (L4) results were distorted due to the change in the conducting area available on the surface level rising.

In Figure 9.4 the radial concentration profiles of air at 0.5 vvm are presented. At agitation rates of 236 and 353 rpm, the calculated average hold-up is higher than that indicated by the ERT profiles. There is better agreement at 547 rpm. In Figure 9.5 it is apparent from the ERT profiles that at 1.0 vvm greater amounts of air are detected relative to the 0.5 vvm aeration rate. Thus, it is possible with ERT to estimate local hold-up values in a stirred tank reactor.

On comparing the average volume fraction of air determined for L1 – L3 from the ERT data (r/R = 0.55 – 1.00) for the three agitation rates with the average volume fraction from measurement of liquid height, a linear relationship is apparent (Figure 9.6). If the gas phase were homogeneously distributed across the reactor, a gradient of unity is expected for the parity line. However, both the impeller zone (r/R = 0.00 to 0.55) and the surface zone (z/Z >0.72) are excluded from the ERT analysis. For an air flow rate of 0.5 vvm, less air is detected than observed for speeds less than 547 rpm, while at 547 rpm identical amounts are detected (0.076 volume fraction). At 1.0 vvm, slightly more air is detected with ERT at 353 rpm (0.053 compared to 0.049), however, at 547 rpm considerably more is detected (0.091 compared to 0.076). Therefore, in general, more air is being detected with ERT than observed at the higher aeration rate. This can be seen with the 1.0 vvm trendline having a slightly lower gradient than the 0.5 vvm trendline. These differences are postulated to arise from the different areas of detection; the ERT measurement area is from r/R = 0.55 to 1.00 and thus does not account for increased or decreased amounts of air rising through the tank centre at different aeration and agitation rates. At lower agitation rates, more air will be rising through the centre of the tank leading to decreased detection in the region between the impeller and vessel wall. Surface aeration will also contribute to gas hold-up and this analysis was limited to the planes L1 – L3.

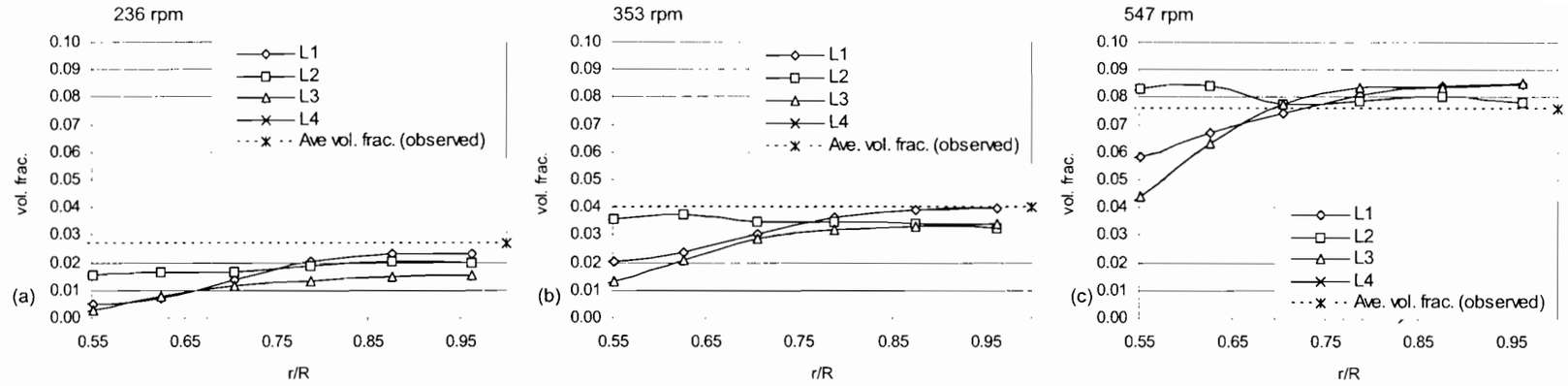


Figure 9.4: The volume fraction of air in the reactor at 0.5 vvm at increasing agitation rates using the Rushton impeller for r/R = 0.55 to 1.00. The calculated average volume fraction of air from the observed hold-up is represented by the dashed line.

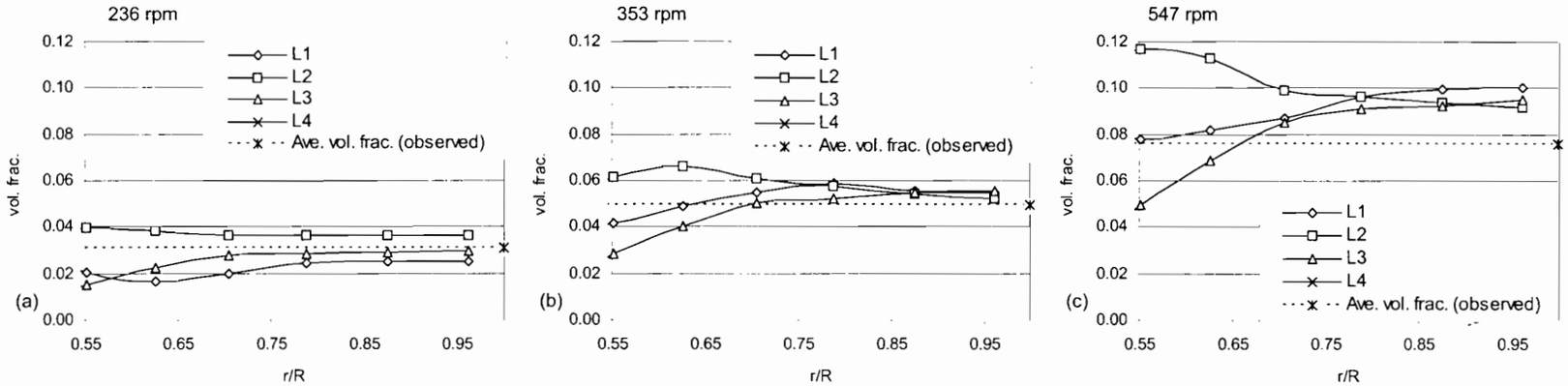


Figure 9.5: The volume fraction of air in the reactor at 1.0 vvm at increasing agitation rates using the Rushton impeller for r/R = 0.55 to 1.00. The calculated average volume fraction of air from the observed hold-up is represented by the dashed line.

The observed maxima in the presence of air detected in the pilot scale tank at 400 rpm was not present in the agitation rate range (236 - 547 rpm) studied in the 220 mm tank. The intensity of turbulence quantified as Reynolds number and the range of tip speeds are greater in the larger tank (Table 9.1). Thus the bubble size and gassed power can not be assumed similar. Further, the gasfoil impeller is more efficient than the Rushton impeller at gas dispersion.

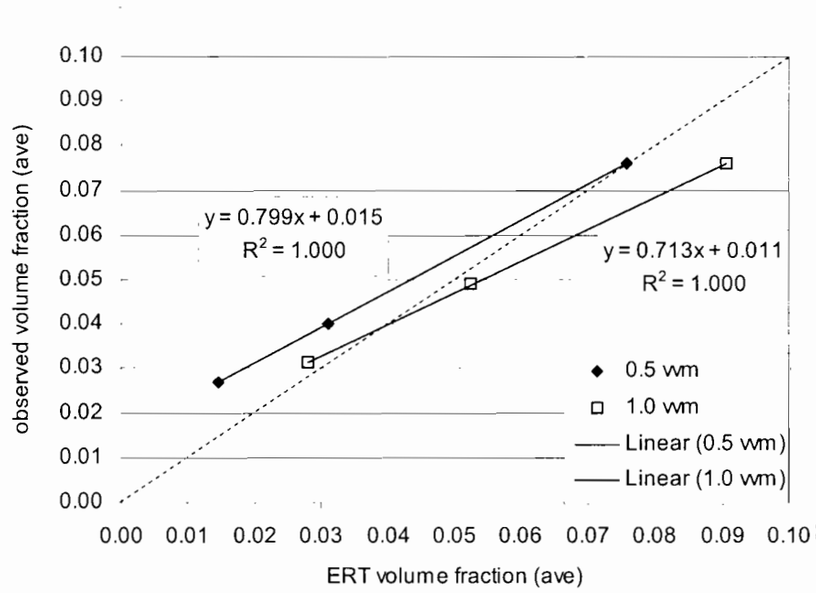


Figure 9.6: The relationship between the observed volume fraction of air and that estimated by ERT. The three points for each sparging condition represent the agitation rates of 236, 353 and 547 rpm using the Rushton impeller

Table 9.1: Reynolds numbers and tip speeds for the 0.68 m and 0.22 m diameter tanks

680 mm tank			220 mm tank		
speed (rpm)	N_{Re}	tip speed ($m.s^{-1}$)	speed (rpm)	N_{Re}	tip speed ($m.s^{-1}$)
100	1.55E+05	1.60	236	4.76E+04	1.36
150	2.32E+05	2.39	304	6.13E+04	1.75
200	3.10E+05	3.19	353	7.12E+04	2.03
250	3.87E+05	3.99	460	9.28E+04	2.65
300	4.65E+05	4.79	547	1.10E+05	3.15
400	6.19E+05	6.38			
450	6.97E+05	7.18			

In Section 2.3.1.2, Barigou and Greaves (1992) observed that, at constant agitation rate, the effect of increasing the air rate led to an increase in bubble size and coalescence. It is apparent from Figure 9.6 that the Maxwell equation, which assumes a spherical non-conductor, has good application to gaseous systems. However, it is likely with increasing coalescence due to higher aeration rates that the sphericity of the larger bubbles is decreased, with a concomitant decrease in the

accuracy of the Maxwell equation. This could contribute further to the differences in detection of air between the 0.5 and 1.0 vvm aeration rates.

Veera *et al.* (2001) argued that in order to design large scale aerated tanks, the local volume fraction is needed to quantify overall mass transfer performance (Section 2.3.1.3). This is possible with ERT.

9.2.3 Surface Aeration in the 220 mm ID Tank

Surface aeration effects are more important for small scale bioreactors or for vessels with H/D ratios close to unity (Ho and Oldshue, 1987). Further, for broths containing biomass, the cells' adsorption to the liquid free surface limits the surface aeration (Galaction *et al.*, 2004). Oxygen mass transfer studies of surface aeration have been performed (Chisti and Jauregui-Haza, 2002; Galaction *et al.*, 2004; Zieverink *et al.*, 2006) and more recently monitoring of surface aeration by conductivity probing has been reported (Sun *et al.*, 2006). Quantifying the aeration rate in the upper regions of the reactor is complicated by the random behaviour of vortices observed visually at the liquid surface with increasing impeller speed (Sun *et al.*, 2006). These authors further report that no constitutive equation for local surface aeration rate is available in the open literature. However, ERT is suited to examining surface aeration through the capturing and averaging of multiple data frames.

In this section, ERT was used to quantify surface aeration in an air-water system in the 220 mm tank and relate it to the previous submerged aeration data. Examination focused on electrode layers L1 - L3 corresponding to z/Z from 0.04 to 0.72 and the outer annulus of the reactor corresponding to r/R = 0.55 to 1.00 at agitation rates from 236 – 547 rpm. Hence, the effect of surface aeration was considered across the impeller region. The surface level fluctuated too severely for analysis of L4. Calibration was performed at 236 rpm, the lowest speed examined in the 220 mm ID tank. Few bubbles were visible above the impeller. This amount of entrained air was assumed to be negligible as the observed increase in liquid height was negligible.

As the agitation speed was increased, lower conductivities were recorded corresponding to a greater presence of air. These data are shown in Figure 9.7. The lowest entrainment of air was observed in L1. This is to be expected because the air originated from the surface. In the outer region corresponding to r/R = 0.7 to 1.0, the volume fraction of air at L3 is greater than L1 and L2, indicating a greater presence of air bubbles near the vessel wall higher up in the vessel.

Figure 9.8 illustrates that a linear relationship is found between the agitation rate and the average volume fraction of air entrained in the region from L1 to L3 for r/R = 0.55 to 1.00. Thus the visually observed random nature of surface aeration is directly

proportional to the agitation rate. Layer 4, however, would most likely contain a higher volume fraction of air than L1 - L3, but it is reasonable to assume that the relationship between the volume fraction of air for L1 – L3 and the agitation rate was similar to that of L4 and the agitation rate. Further, in the region of L1 – L3 gas-liquid mass transfer is greater than at L4. Sun *et al.* (2006) reported higher volume fractions of air near the surface using a conductivity probe and numerical simulation in an air-water system agitated by a Rushton impeller (H=T;D/T=2; impeller at T/3 below surface). Above the impeller, higher hold-ups were observed near the tank centre and near the vessel wall. Near the tank bottom, hold-up exhibited a flat radial profile. In this study, an increase in hold-up can be observed above the impeller on approaching the vessel wall in L3 for agitation rates of 460 and 547 rpm.

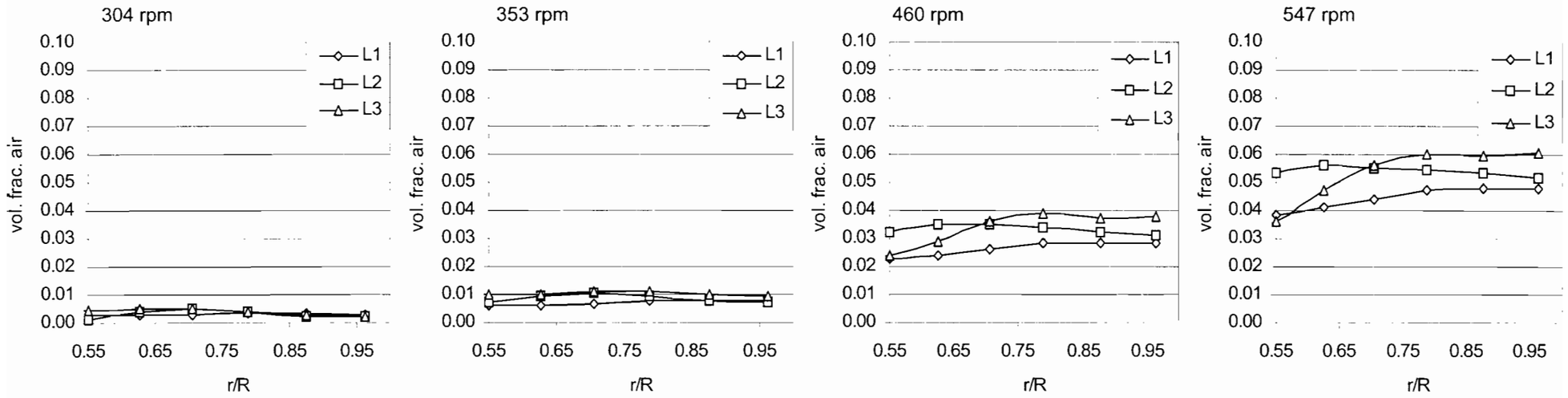


Figure 9.7: The volume fraction of air entrained for electrode layers L1 - L3 at agitation rates of 304 - 547 rpm with Rushton impeller

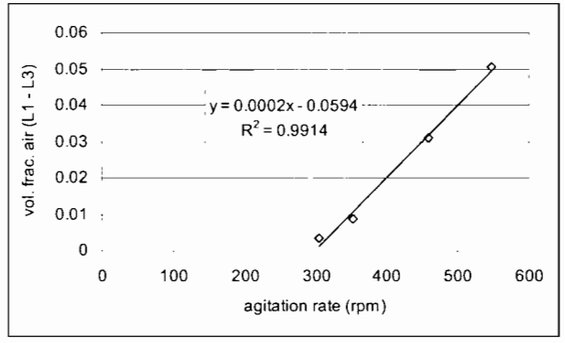


Figure 9.8: The average amount of entrained air for L1 – L3 with respect to agitation rate. Rushton impeller, data: r/R = 0.55 to 1.00.

Comparing the concentration of air entrained during surface aeration determined by ERT ($ERT_{0.0\ vvm}$) to that detected by ERT and calculated from visual observation during sparging at 0.5 and 1.0 vvm (Table 9.2), it is seen that the volume fraction of air entrained from the surface is significant at higher agitation rates. At 547 rpm, the air present in the reactor due to surface aeration (0.051 volume fraction) is equivalent to that present due to sparging at 0.5 vvm at 460 rpm. However, this does not necessarily mean that the contribution to k_La would be equivalent, as there would be greater air bubble - impeller collisions with the location of the sparger below the impeller. Further, the bubbles introduced from the sparger are smaller than those entrained from surface aeration, thereby aiding mass transfer.

Zieverink *et al.* (2006) reported that the mass transfer in bench-scale stirred tanks due to surface aeration was much lower compared to submerged aeration mass transfer at higher aeration rates. Chisti and Jauregui-Haza (2002) found that surface aeration provided a 1.5 to 11.6 % contribution to total oxygen transfer in a hydrofoil-agitated airlift bioreactor on agitation at 110 – 260 rpm (H = 2.46 m; T = 0.76 m; D = 0.32 m; V = 1.10 m^3). These authors further observed an exponential relation between k_La from surface aeration and the agitation rate. Therefore, although the increase in hold-up is linear with increasing agitation rate as observed with ERT, this relationship does not apply to the mass transfer coefficient. Further analysis of bubble size distribution is necessary to expand our understanding of this phenomenon.

Galaction *et al.* (2004) found k_La to be two orders of magnitude lower with surface aeration than submerged aeration in a dual-impeller bioreactor (H/D = 2.15; D/T = 0.36; Rushton turbines; V = 4 litres). These authors found that using a superficial air velocity of 8.36×10^{-4} $m.s^{-1}$, the contribution of surface aeration to k_La in broths of *P. shermanii* was 0.06 to 0.09 %; *S. cerevisiae*, 0.08 to 0.19 %; *P. chrysogenum* mycelial aggregates, 0.01 to 0.25 % and *P. chrysogenum* free mycelia, 0.01 to 0.25 %. It was found that the biomass reduced oxygen solubility and blocked the liquid surface from surface aeration. However, Chisti and Jauregui-Haza (2002) suggested that surface aeration can contribute more significantly (i.e. > 11.6 %) to total mass transfer in shallow reactors such as those used in animal cell cultures.

Table 9.2: Volume fraction of air detected from surface aeration related to that during sparging (L1 – L3)

Agitation rate (rpm)	304	353	460	547
$ERT_{0.0\ vvm}$	0.0033	0.0086	0.0311	0.0505
$ERT_{0.5\ vvm}$	0.0219	0.0311	0.0501	0.0759
$Observed_{0.5\ vvm}$	0.0313	0.0402	0.0581	0.0760
$ERT_{1.0\ vvm}$	0.0408	0.0526	0.0713	0.0907
$Observed_{1.0\ vvm}$	0.0447	0.0491	0.0626	0.0760

Comparing the concentration of air entrained during surface aeration determined by ERT ($ERT_{0.0\ vvm}$) to that detected by ERT and calculated from visual observation during sparging at 0.5 and 1.0 vvm (Table 9.2), it is seen that the volume fraction of air entrained from the surface is significant at higher agitation rates. At 547 rpm, the air present in the reactor due to surface aeration (0.051 volume fraction) is equivalent to that present due to sparging at 0.5 vvm at 460 rpm. However, this does not necessarily mean that the contribution to k_La would be equivalent, as there would be greater air bubble - impeller collisions with the location of the sparger below the impeller. Further, the bubbles introduced from the sparger are smaller than those entrained from surface aeration, thereby aiding mass transfer.

Zieverink *et al.* (2006) reported that the mass transfer in bench-scale stirred tanks due to surface aeration was much lower compared to submerged aeration mass transfer at higher aeration rates. Chisti and Jauregui-Haza (2002) found that surface aeration provided a 1.5 to 11.6 % contribution to total oxygen transfer in a hydrofoil-agitated airlift bioreactor on agitation at 110 – 260 rpm (H = 2.46 m; T = 0.76 m; D = 0.32 m; V = 1.10 m^3). These authors further observed an exponential relation between k_La from surface aeration and the agitation rate. Therefore, although the increase in hold-up is linear with increasing agitation rate as observed with ERT, this relationship does not apply to the mass transfer coefficient. Further analysis of bubble size distribution is necessary to expand our understanding of this phenomenon.

Galaction *et al.* (2004) found k_La to be two orders of magnitude lower with surface aeration than submerged aeration in a dual-impeller bioreactor (H/D = 2.15; D/T = 0.36; Rushton turbines; V = 4 litres). These authors found that using a superficial air velocity of 8.36×10^{-4} $m.s^{-1}$, the contribution of surface aeration to k_La in broths of *P. shermanii* was 0.06 to 0.09 %; *S. cerevisiae*, 0.08 to 0.19 %; *P. chrysogenum* mycelial aggregates, 0.01 to 0.25 % and *P. chrysogenum* free mycelia, 0.01 to 0.25 %. It was found that the biomass reduced oxygen solubility and blocked the liquid surface from surface aeration. However, Chisti and Jauregui-Haza (2002) suggested that surface aeration can contribute more significantly (i.e. > 11.6 %) to total mass transfer in shallow reactors such as those used in animal cell cultures.

Table 9.2: Volume fraction of air detected from surface aeration related to that during sparging (L1 – L3)

Agitation rate (rpm)	304	353	460	547
$ERT_{0.0\ vvm}$	0.0033	0.0086	0.0311	0.0505
$ERT_{0.5\ vvm}$	0.0219	0.0311	0.0501	0.0759
$Observed_{0.5\ vvm}$	0.0313	0.0402	0.0581	0.0760
$ERT_{1.0\ vvm}$	0.0408	0.0526	0.0713	0.0907
$Observed_{1.0\ vvm}$	0.0447	0.0491	0.0626	0.0760

9.3 The Examination of Microorganisms in Stirred Tanks

Saccharomyces cerevisiae, Bakers' yeast, was chosen as the model organism for study in the slurry reactor. The focus of the study was on its detection. Yeast cells are approximately 5 μm in diameter and mostly comprised of water (± 70 %). Under normal conditions the cell membrane conductivity is many orders smaller that that of the external medium (Pavlin *et al.*, 2002). Pavlin *et al.* (2002) showed that Maxwell's equation can be successfully applied to explain conductivity measurements in cell suspensions. Their study approximated cells as spheres using FEMs, and further established that rod shaped cells should be modeled on their real dimensions. However, yeast cells are ovoid in shape and it is a fair approximation to model yeast cells used in this study as spheres, as shown in Figure 9.9.

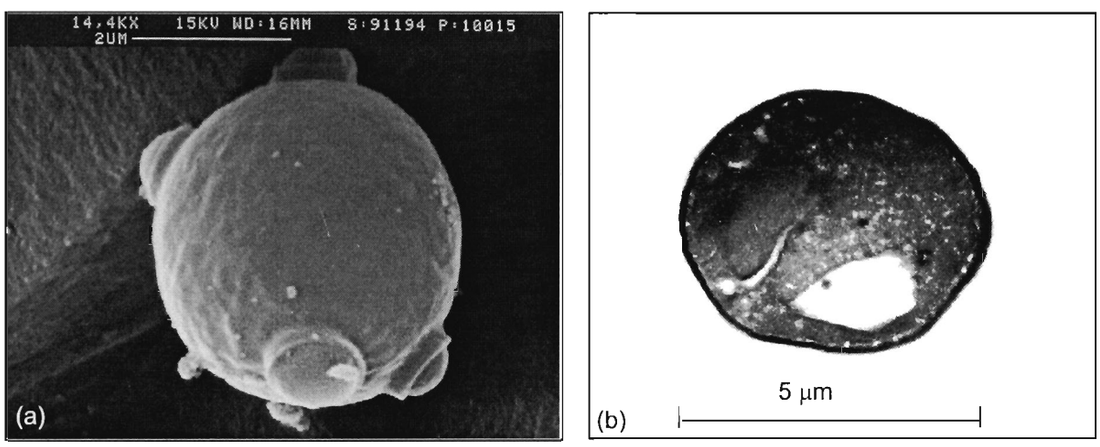


Figure 9.9: Micrograph of budding *Saccharomyces cerevisiae*. (a) Scanning electron micrograph at 14400x magnification (Scholtz-Brown, 1998). (b) Transmission electron micrograph (Bangaru, 2004). Scale is given in picture.

The initial examination of yeast was carried out in the 220 mm ID vessel with ERT Hardware III and Reconstruction Code V using the Rushton turbine at 236 rpm. Further studies were conducted in the 50 mm ID vessel, using both ERT and MRI analysis, agitated at 480 rpm and 186 to 480 rpm respectively.

9.3.1 ERT Detection of Yeast in the 220 mm ID Vessel

A 5 % volume fraction of yeast was added to the reactor and sufficiently mixed before applying ERT. The yeast was detected by ERT (Figure 9.10) in the 220 mm ID vessel using Reconstruction Code V and ERT Hardware III with an average volume fraction calculated at 0.55 (10 % error). These results were generated using an agitation rate of 236 rpm in order to minimise influence from surface aeration. It appeared that from the impeller zone to halfway to the vessel wall (r/R = 0.55 to 0.70) there was a slight

axial gradient with concentration decreasing with height as expected with a solid particle. However, from r/R = 0.80 to 1.00 the Layer 3 and 4 volume fractions were higher; indicating a greater presence of yeast cells within 2 cm of the vessel wall above the impeller. The axial concentration profile (Figure 9.11) exhibited good homogeneity apart from the impeller region where there was a decrease in concentration.

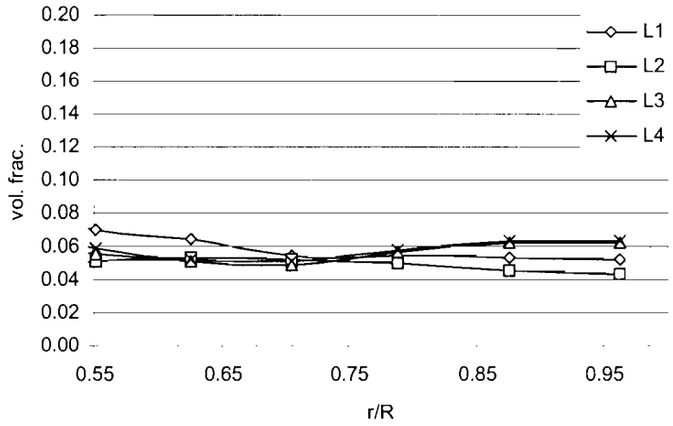


Figure 9.10: Radial concentration profile of 5 % yeast at 236 rpm in the 220 mm ID tank using the Rushton impeller. Average yeast volume fraction detected is 0.55.

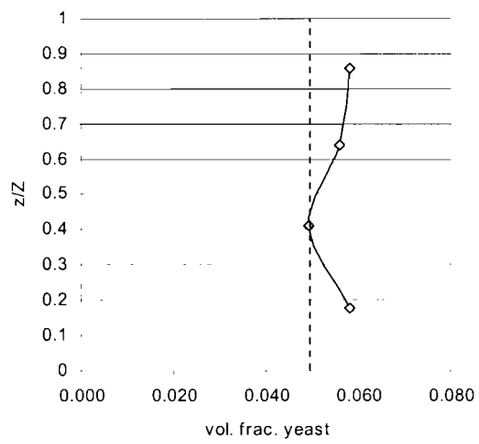


Figure 9.11: Axial concentration profile of 5 % yeast at 236 rpm in the 220 mm ID tank using the Rushton impeller. (r/R = 0.55 to 1.00)

9.3.2 ERT and 1D MRI Yeast Detection with the 50 mm ID Vessel

ERT (Reconstruction Code V, Hardware III) was applied to study the suspension of a 5 and 11 vol. % concentration of yeast in the 50 mm vessel at 480 rpm. The radial gradients determined are presented in Figure 9.12. An average volume fraction of

0.064 (28 % error) and 0.081 (26 % error) were detected respectively. ERT therefore over and underpredicted the amount of yeast present. Qualitative detection was achieved, but a calibration process would be needed for direct quantification. Examining the radial concentration profiles of the 11 vol. % yeast data in Figure 9.12 (b), the yeast concentration measured at L4 is lower than that at L3 for r/R = 0.55 to 1.00. This is in contrast to suspension of the 5 % yeast concentration where the yeast concentration at L4 was equivalent to our higher than that in L1 to L3. Further, the 5 % concentration had a more consistent suspension, as shown in Figure 9.12 (a).

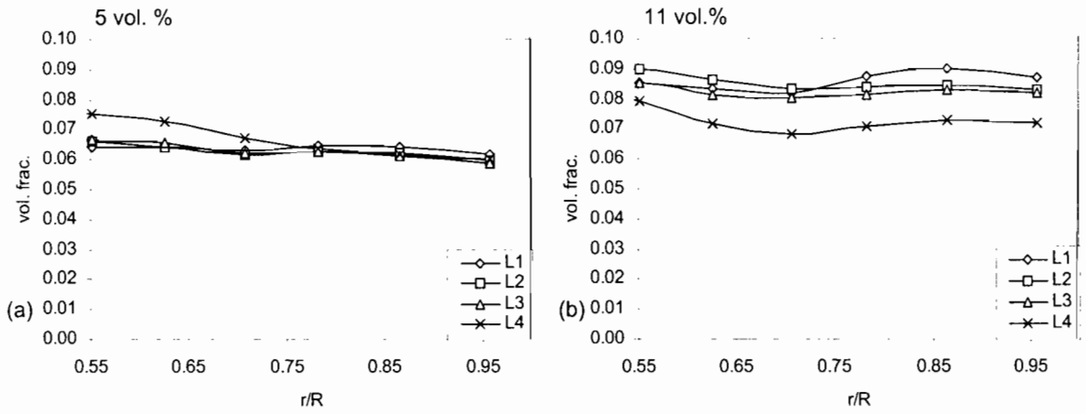


Figure 9.12: ERT radial concentration profiles for 5 and 11 vol. % yeast agitated at 480 rpm with the Rushton impeller in the 50 mm reactor. Average volume fraction detected is 0.064 and 0.081 respectively.

Complementary 1D MRI experiments were performed. These data were corrected by a mass balance process such that the proton signal integral accounted for the actual amount of water present. These data are presented in Figure 9.13 for 5 and 11 % yeast concentrations along with the ERT axial profiles. Radio frequency decay was apparent above a dimensionless height of 0.80. MRI axial profiles were therefore analysed below this height.

The 1D MRI profiles indicate the agitated yeast suspension is not homogeneous. A sharp deviation in the MRI axial profile is observed above the impeller (z/Z = 0.47) at all agitation rates. Similar peaks and troughs in concentration are observed below the impeller for both concentrations. In Figure 9.13 (a), representing the 5 % yeast concentration, an increase in agitation rate resulted in a decrease in yeast concentration above the impeller. This was in contrast to the 11 % concentration shown in Figure 9.13 (c), where yeast concentration increased above the impeller upon increase in agitation rate. Furthermore, although the minimum agitation rate is greater than the critical suspension speed (N_{js} = 135 rpm for 11 vol. %), as calculated

using the Zwietering correlation, the concentration of yeast on the tank bottom is greater than that in the bulk of the tank at both concentrations.

The ERT axial concentration profiles shown in Figure 9.13 (b) and (d) indicate good homogeneity, although resolution is limited using four electrode layers. Moreover, the ERT measurement process from each electrode accounts for changes in conductivity above and below the electrode, leading to smoother profiles. Possible concentration of yeast on the tank bottom could not be determined as this region lay below the lowest plane detected by the ERT system. Furthermore, if MRI data were averaged for the equivalent areas of detection for each electrode of the ERT system, an axial profile indicating good homogeneity and good resemblance to the ERT data would result. It must be reiterated that ERT yeast calibration was not quantitative, therefore greater uncertainty can be expected.

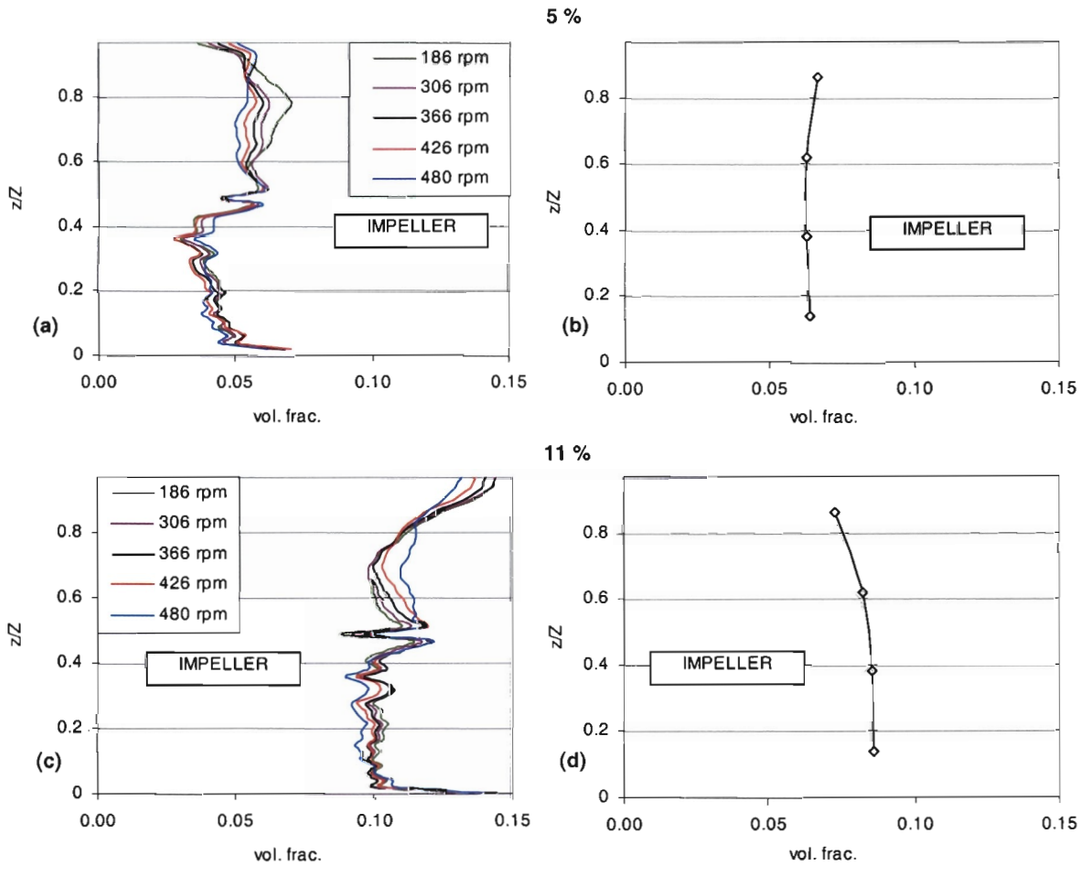


Figure 9.13: Axial concentration profiles for 5 % yeast at 186 – 480 rpm produced from MRI data (a); ERT axial concentration profile for 5 % yeast at 480 rpm, data from r/R = 0.55 – 1.00 (b); Axial concentration profiles for 11 % yeast at 186 – 480 rpm produced from MRI data (c); ERT axial concentration profile for 11 % yeast at 480 rpm, data from r/R = 0.55 – 1.00 (d). Rushton impeller at 0.33 to 0.43.

On comparing the axial profiles of yeast to the axial profiles of the suspension of nylon particles of similar density (Figure 8.6), the sharp deviation in concentration is also present at z/Z = 0.47. Moreover, similar decreases and increases in particle concentration above the impeller with increasing agitation rate are observed for the 5 and 10 % nylon suspensions respectively (Figure 8.6 (a) and (b)). Therefore, yeast does exhibit similar suspension behaviour as a solid particle.

The difference in suspension behaviour of the two yeast concentrations is further observed in Figure 9.14. Here, a normalised average concentration is shown for the agitation rate range (186 – 480 rpm) for both concentrations. A higher normalised concentration is apparent above the impeller for the 11 % yeast concentration.

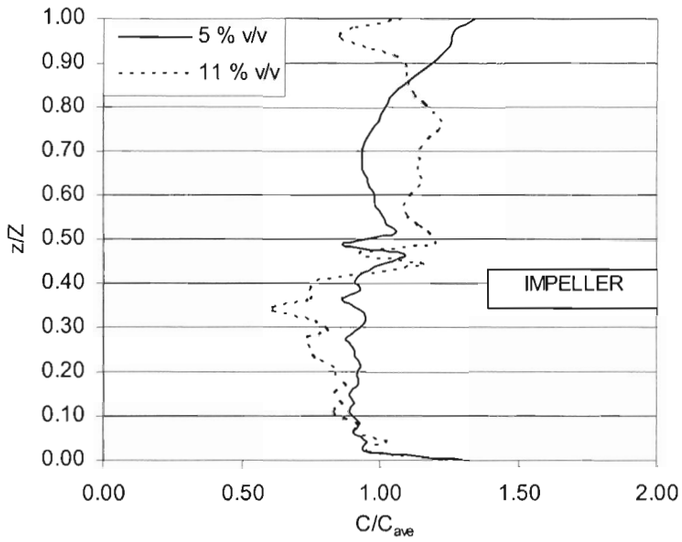


Figure 9.14: Normalised average concentration for the agitation rate range of 186 to 480 rpm for the 5 and 11 % yeast concentrations. Rushton impeller

On initial examination of these results it was postulated that T_1 contrast effects influence behaviour (Sederman and Mantle, 2005). With these effects protons would possibly return faster to the original state (spin – lattice) due to the close proximity of the water molecules to the yeast cell. Thus a higher proton signal would result, leading to the calculation of a decrease in particle concentration. However, this hypothesis is not applicable to the 11 vol. % yeast results. Further, the potential of the velocity to influence the measured proton signal and thereby the microbial concentration profiles was considered. However, the proton signal for the yeast is divided by a pure water phase signal at the same velocity, thus eliminating these effects. Furthermore, if velocity effects were significant, both yeast concentrations would be affected similarly at the same agitation rate. As this is not observed, this potential interference may be ignored.

Yeast is a microscopic particle (~5 μm) compared to the size of particles typically observed in suspension studies (50 – 2000 μm). Further, it is only slightly denser than water (S.G = 1.05). Thus, the concentration patterns are greatly influenced by the change in hydrodynamics with increasing agitation rate. In addition, these small particles increase the fluid viscosity leading to a dampening of turbulence. It is unexpected that agitation rate does affect axial concentration for microorganisms in a reactor. In biological reactors e.g. fermentation processes, complete cellular homogeneity has always been assumed. The axial inhomogeneity observed, even above the calculated N_{js}, implies that different consumption rates of the substrate and product production rates occur in different locations of the reactor. Therefore, these rates are not only dependent on the cell's physiological condition associated with the degree of shear stress, or the presence of oxygen, carbon source or other nutrients, but also on the microbial biomass present in the particular reactor location.

9.3.3 Examination of Nylon-Yeast Mixtures with ERT and 1D MRI in the 50 mm ID Vessel

A slurry bioreactor was simulated as a mixture of nylon particles and yeast in the 50 mm vessel. Differentiation between non-conducting species was not possible with ERT, although the analysis of concentration profiles still yields information about mixing behaviour. Complementary MRI experiments were similarly performed. Resolving two non-conducting phases with ERT may be possible in future studies through analysis of the magnitude of their respective permittivities (Wilkinson, 2005a).

The ERT radial profiles of a mixture of 10 % nylon particles and 5 % yeast exhibit a similar trend to 10 % nylon particles suspended in isolation in layers L1 – L3 (Figure 9.15 (a) and (c)); although displaced by a volume fraction of 0.05 in accordance with the yeast addition. The volume fraction in L4 in Figure 9.15 (a) appears to be considerably lower than L1 – L3. This suggests a lower contribution of yeast in this layer or a change in distribution of nylon mediated by the presence of yeast. This same behaviour is not observed in the MRI 1D axial profile (Figure 9.16 (a)). MRI average radial profiles (Figure 9.15 (b)) were generated using the method described in Appendix L from 3D MRI data. These lie in a similar range to the ERT profiles (Figure 9.15 (a)). Radio frequency decay was observed from approximately z/Z = 0.62 (Appendix N), thus L4 is not shown.

On comparing the MRI 1D axial profiles shown in Figure 9.16 (a) and (b), it is apparent that the presence of the yeast in addition to the nylon decreased axial homogeneity, and exaggerated trends observed in the sample containing nylon only. This is further apparent in Figure 9.17 (a) where 5 % yeast, 10 % nylon and their combination are shown agitated at 480 rpm. This is postulated to be a viscosity

effect. The 15 % pure nylon axial profile (Figure 9.17 (b)) is more homogenous than Figure 9.16 (a) at 366 to 480 rpm, indicating that an equivalent volume fraction which contains a greater amount of smaller particles i.e. the 5 μm yeast cells, results in the homogeneity being adversely affected at the same agitation rate. Further rheology effects are possible from yeast such as the cell surface hydrophobicity and charge.

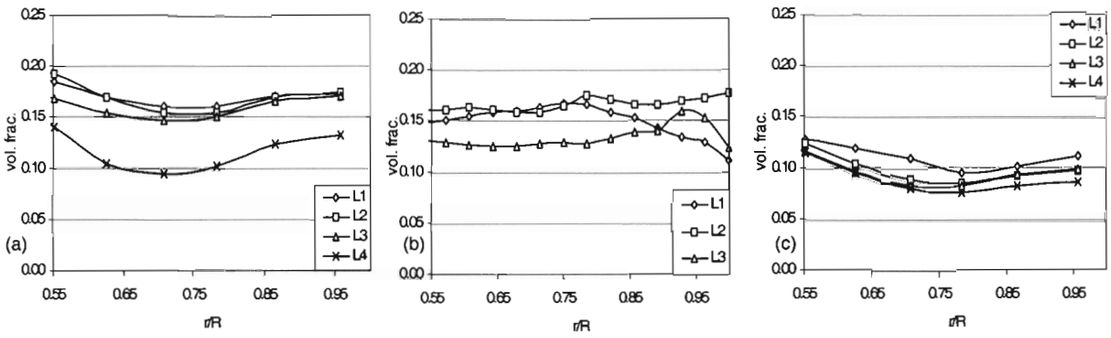


Figure 9.15: Radial profiles of suspensions of 10 % nylon particles with 5 % yeast generated by ERT (a) and MRI (b), and radial profiles of 10 % nylon suspension from ERT (c) in the 50 mm ID vessel agitated at 480 rpm with Rushton turbine.

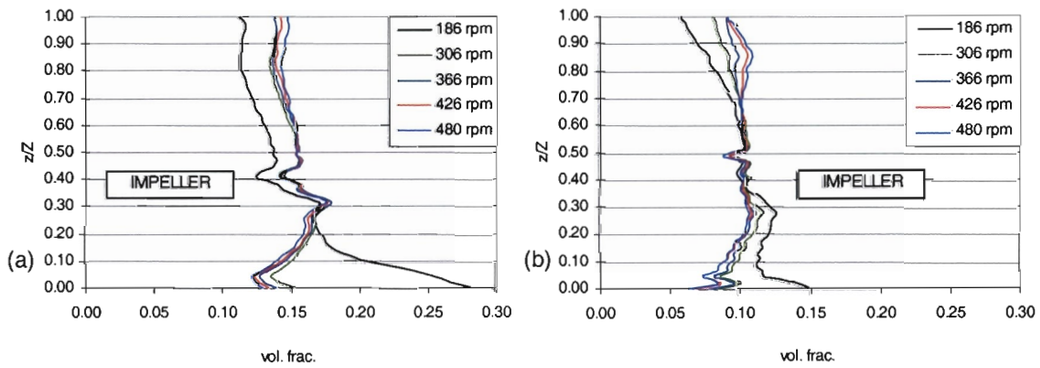


Figure 9.16: MRI 1D axial concentration profiles for 10 % nylon particles and 5 % yeast (a) and 10 % nylon particles (b) agitated at 186 – 460 rpm with Rushton turbine.

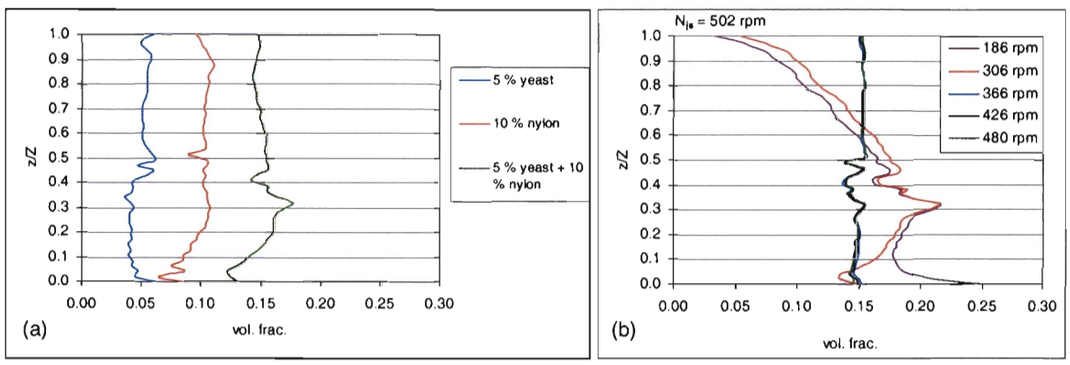


Figure 9.17: 5 % yeast, 10 % nylon and their combination agitated at 480 rpm (a); 15 % nylon agitated at 186 to 480 rpm (b). Rushton turbine.

9.4 Conclusions

The qualitative (Reconstruction Code IV, Hardware II) and quantitative (Reconstruction Code V, Hardware IV) examination of aerated reactor processes was achieved through application of ERT. The distribution of air bubbles, whether originating from a sparger or the surface level, was measured and allowed further comparison with visual observation. Surface aeration, which is complex in nature, was found to be directly proportional to the agitation rate, while significant volume fractions of air were entrained at higher agitation rates.

The model microorganism, *Saccharomyces cerevisiae*, was detected with ERT and MRI. Slight concentration gradients were unexpectedly observed with both ERT and MRI. The MRI provided greater resolution. These concentration gradients were influenced by agitation rate despite the latter being above N_{js}. These concentration gradients influence the consumption of substrate and thus affect the product yield according to the location in the reactor. A higher concentration of yeast behaved differently in the reactor, with the 11 % concentration increasing in quantity above the impeller with increasing agitation rate. This was in contrast to the 5 % concentration. Similar behaviour was observed with the 5 and 10 % nylon suspensions thus confirming the particle nature of yeast.

Inert particle – biomass mixtures were explored to simulate a slurry bioreactor. Radial concentration profiles exhibited similar trends to solid particles only, while accounting for the biomass volume fraction. Deviations of the axial concentration profile with the addition of yeast differed from that attained on addition of the same fraction of inert particles. This is postulated to result from the increased viscosity of the suspension owing to the altered particle size distribution and surface properties of yeast.

10.2 The Effect of Hydrodynamic Forces on the Microbial Phase

Hydrodynamic forces are created as fluctuating velocity components change rapidly with time or position. These can give rise to shear stresses which may damage biological cells (Croughan *et al.*, 1987). Short-term forces can arise through the motion of turbulent eddies; thus these are examined in Section 10.2.1.

10.2.1 The Effect of Fluctuating Velocity Components

The turbulent energy spectrum is a description of the manner in which energy is transferred from the impeller in the form of large eddies to smaller eddies. The eddy scale at which the eddy Reynolds number, as quantified in Section 7.4, is unity is termed the Kolmogorov microscale (Kolmogorov, 1941). Viscous effects increase in strength when the eddy Reynolds number becomes less than unity, resulting in increased heat dissipation. Kolmogorov eddy sizes were calculated in Table 7.2 using a power input approximated in the absence of particulates. The smallest eddy size calculated at an agitation rate of 547 rpm for the 220 mm tank was 19 μm. On maintaining the same tip speed for the 50 mm tank, an eddy size of 13 μm resulted. As approximate power was estimated neglecting the influence of particles, the actual eddy sizes are expected to be smaller. However, this effect is negligible as increasing the power number from 5 to 10 results in a decrease in eddy size from 19 to 16 μm for the 220 mm tank and 13 to 11 μm for the 50 mm tank respectively. More significant is the influence of particles on fluid turbulence. Caulet *et al.* (1996) found this effect to be negligible below a solids volume fraction of 2 %. Between 2 and 10 % loading, the particles created small-scale turbulence from wakes produced from their velocity relative to the bulk fluid motion. This results in increased energy transfer thus revising the turbulent energy spectrum and reducing the Kolmogorov eddy size. At solid volume fractions greater than 20 to 30 %, the flow mechanism changed from fluid-particle interactions to particle-particle interactions (Caulet *et al.*, 1996) with viscous effects dominating. This decreases the particle relative velocity and the overall energy transfer resulting in larger eddies than predicted by Equation 7.1. In Section 6.2.7, particle-particle effects were observed in the 220 mm tank in the concentration range of 15 to 20 %, thus for this study the enhanced turbulence is postulated to be effective at a concentration range of 5 to 15 %.

When eddies are larger than the average diameter of the abiotic particulates or biological cells, entrainment tends to occur which reduces the net forces on their surface. Eddies smaller than the suspended solids or cells are dissipated on their surface (Croughan *et al.*, 1987), and thus more likely to cause cell disruption. As yeast cells are 5 μm in diameter, it is anticipated that eddy sizes do not decrease below this size under typical operating conditions, even considering the enhanced turbulence in the presence of solids. At the maximum agitation rate of 547 rpm in the

220 mm tank, the eddy size was 19 μm. Thus a fourfold decrease in eddy size would be required to approach the yeast particle size. This requires a 220-fold increase in turbulent energy dissipation. This enhancement does not seem likely through the increased energy transfer due to the presence of particles. Thus, for the 220 and 50 mm reactors at the agitation rates tested in this study, Kolmogorov eddies are not expected to be responsible for cell disruption.

10.2.2 The Effect of Time-Averaged Velocity Components

Quantifying the effect of time-averaged velocity components on biological cells has been achieved with respect to the average and maximum time-averaged shear rates and shear stresses (Nagata, 1975; Oldshue, 1983; Radež *et al.*, 1991; Wichterle *et al.*, 1984; Wichterle *et al.*, 1985; Wichterle *et al.*, 1988). In stirred tanks, most of the energy is dissipated in the impeller zone (Illing, 1996; Illing and Harrison, 1999), thus the majority of biological cell disruption is expected to occur in this region (Scholtz-Brown, 1998). Shear stresses and shear rates are presented in Table 10.1 where the relative difference in magnitude in forces can be observed between the vessels. Shear rates in the bulk flow are proportional to tip speed and less than the impeller zone shear rates. These shear rates and stresses are calculated for a liquid phase only. These are not applicable to a slurry reactor in which these forces have not yet been quantified. However, enhanced turbulence due to the presence of particles is postulated to slightly increase shear rates and shear stresses.

Table 10.1: Time-averaged velocity effects in a liquid phase CSTR based on similar tip speed of the 220 mm vessel (236 – 547 rpm; 1.36 – 3.15 m.s^{-1})

Shear rate/shear stress	Eq.	Location	220 mm	152 mm *	50 mm
shear rate (γ) (s^{-1})	10.1	bulk flow	45 - 105	67 - 156	199 - 461
shear rate ($\gamma_{max\ Rushton}$) (s^{-1})	10.2	impeller zone	$5.41x10^3$ - $1.91x10^4$	$6.59x10^3$ - $2.33x10^4$	$1.13x10^4$ - $4.00x10^4$
shear stress ($\tau_{max\ Rushton}$) (Pa)	10.3	vessel base and walls	0.87 - 1.33	0.68 - 1.03	0.42 - 0.63
shear stress ($\tau_{max\ PB}$) (Pa)	10.4	vessel base and walls	0.70 - 1.07	0.59 - 0.90	~

* reactor of Scholtz-Brown (1998)

$\gamma = KN$ K = 11.5 Rushton turbine (Radež *et al.*, 1991) (10.1)

$$\gamma_{max} = N(1+5.3\beta)^{\frac{1}{\beta}} N_{Re}^{\frac{1}{(1+\beta)}}$$ β = 1 for Newtonian fluids (Wichterle *et al.*, 1984) (10.2)

$$\tau_{max} = \frac{16(\rho\mu)^{0.5} N^{0.5} D^3}{T^2}$$ Rushton turbine (Wichterle *et al.*, 1985) (10.3)

$$\tau_{max} = \frac{10(\rho\mu)^{0.5} N^{0.5} D^3}{(D+C)^2}$$ Pitched blade (Wichterle *et al.*, 1988) (10.4)

These values indicate that, at the same tip speed, higher shear rates are experienced in smaller vessels in the impeller zone and in the bulk fluid, while higher shear stresses are experienced at the vessel base and walls for larger vessels. In the study of Scholtz-Brown (1998) using the smaller scale 152 mm reactor at agitation

rates of 200 to 900 rpm (tip speeds of 0.77 to 3.49 $m.s^{-1}$) in the absence of aeration, negligible disruption of *Saccharomyces cerevisiae* occurred in the absence of particles. Since significant cell disruption was observed with the presence of solid particles, particle-cell-particle interactions have been proposed as the dominant cause of cell disruption (Scholtz-Brown, 1998).

10.3 Solid-Cell Interactions in the Slurry Bioreactor

10.3.1 Modelling of Cell Disruption

Scholtz-Brown (1998) examined yeast disruption at varying power input with variable solids concentration across the range 5 to 40 vol. % using a Rushton turbine and pitched-blade impeller. One size fraction of 600 to 850 μm of quartzite was used throughout her study. Through analysing soluble protein release from *Saccharomyces cerevisiae* as a function of time, a first order expression was used to model the data:

$$R = R_i\,(1 - e^{-kt}) \qquad (10.5)$$

where R is the soluble protein released at time t (mg protein/g cell),
R_i is the maximum soluble protein released and
k is the first order disruption rate constant (s^{-1}).

Typical data are shown in Figure 10.1 for yeast at 5 % quartzite loading agitated at 749 rpm with the Rushton impeller.

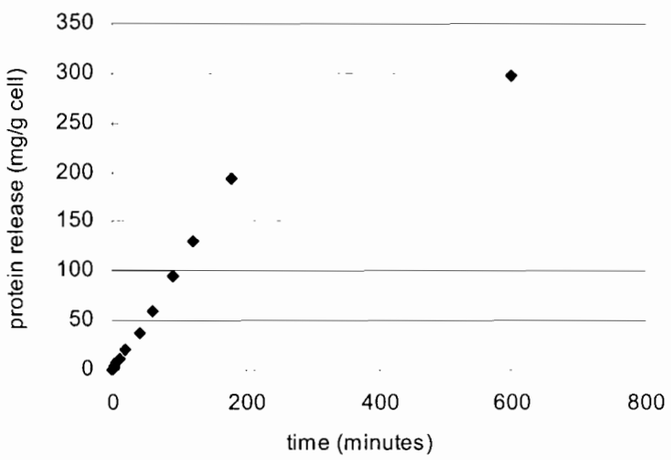


Figure 10.1: Soluble protein released as a function of time for a 5 % solids loading of 600 – 850 μm quartzite agitated at 749 rpm with the Rushton impeller. Cell dry weight of 54.3 $g.l^{-1}$, R_i = 321 $mg.g^{-1}$ (Data from Scholtz-Brown (1998))

Scholtz-Brown (1998) determined the point of complete solids suspension through examining the maximum in the power number – Reynolds number curve using the Rushton impeller. Power measurements were taken using a load cell. Protein release was modelled in the region of complete suspension of solids assuming homogenous suspension. The disruption rate constant was modelled as a function of power per unit volume and the degree of solids loading to yield:

$$k = 7.11 \times 10^{-5} (P/V)^{0.56} \Phi^{1.64} \qquad (10.6)$$

where Φ is the solids volume fraction. Equation 10.6 had a coefficient of variance of 4.7 % with the measured *k* values.

10.3.2 Localised Cell Disruption in the Slurry Bioreactor

As radial and axial particle distribution has been established in the stirred tank experiments using ERT and MRI, the local disruption rate constant can be estimated as '*k*' is a function of solids volume fraction. However, this local disruption rate constant is an approximation due to the assumption of a constant P/V throughout the reactor. Turbulent energy dissipation rates have been reported to be from 13 to 25 times greater in the impeller zone than the average dissipation rate in the reactor (Illing, 1996; Illing and Harrison, 1999). Therefore, the disruption rate constant is expected to be $(13 \text{ to } 25)^{0.56}$ or 4.2 to 6.1 times greater in this zone assuming a homogenous particulate concentration. For the purposes of an approximation of cell disruption in the reactor, the disruption rate is therefore estimated as 5 times greater in this zone.

10.3.2.1 Hypothetical Cell Disruption in the 220 mm Reactor

Examining the ERT axial concentration profiles determined in the 220 mm tank (Section 6.2.4) for the size fraction of 600 – 850 μm, as used by Scholtz-Brown (1998), axial profiles of the disruption rate constant '*k*' can be determined by applying Equation 10.6. These profiles are presented in Figure 10.2 using data from the Rushton impeller while accounting for increased turbulence at L2 through multiplying by a factor of 5. The profile of the disruption rate constant resembles the particle concentration profile, with variation being exaggerated through the exponent of 1.64 to which the volume fraction is raised and the higher energy dissipation in the impeller zone. Thus, it can be reasoned that a significant amount of cell disruption occurs in the impeller zone. In Figure 10.2 (a) it is observed that upon increase of the agitation rate the disruption rate increases for a 5 % solids loading. Increased solids loading results in a higher disruption rate constant, as shown in Figure 10.2 (b). It is postulated that minimal cell disruption occurs in the upper regions of the vessel, as

Chapter 10

The Slurry Bioreactor

10.1 Introduction

The slurry bioreactor is a complex, dynamic environment. Microorganisms experience stress and shear caused by the hydrodynamics within the reactor, while collisions occur between cells, solid particles, air bubbles and the reactor's internal geometry. The presence of spatial temperature variations as well as concentration gradients of solutes and particulates can influence growth. Both liquid-liquid and gas-liquid mass transfer coefficients are influenced by the intensity of agitation and the presence of solid particles and cells. If cell growth is desired, particularly via attachment to, or association with a particle, these factors may come into conflict. Therefore, understanding of these key factors and the intensity of their variation within the reactor is critical.

In this chapter, the information that has been obtained through tomographic methods is brought together with the literature to yield further insight into this dynamic environment. Particular attention is given to the influence of solid particles. The effect of particulates on cell growth has been examined by Lamaignere (2002) for yeast, and Nemati and Harrison (2000), Nemati *et al.* (2000), Harrison *et al.* (2003b) and Raja (2005) in mineral bioleaching systems, while its disruptive mechanism has been previously examined and modelled by Croughan *et al.* (1987, 1988) for immobilised animal cells and Scholtz-Brown (1998) for yeast. The latter work was performed on a yeast suspension using a geometrically similar vessel (T = 152 mm) to the vessels in this study (T = 220 mm and 50 mm), with both Rushton and pitched blade impellers. Thus, particle distribution information provided in this study is related to data collected by Scholtz-Brown and to the previous modelling of yeast disruption through cell-particle interaction. Firstly, the interaction between cells and fluid eddies from time-fluctuating and time-average velocity components is examined. Thereafter, particulate-yeast interaction is considered. This is followed by discussion of the parameters of heat transfer, the oxygen mass transfer coefficient and the influence of a microbial phase on the slurry bioreactor. The role of this chapter is to use the new knowledge gained on the distribution of phases and to examine their potential application to biological studies in the slurry bioreactor. Through this analysis, recommendations are made with respect to the key focus areas of the extension studies of the slurry bioreactor proposed. This chapter is therefore largely a thought experiment which can inform the direction of future work.

seen by the disruption rate constant at L4 or z/Z = 0.86. Scholtz-Brown (1998) found that for incomplete suspension, Equation 10.6 provided a poor prediction of the rate constant where an average volume fraction was used. This was postulated to be due to a decrease in particulate-yeast collisions occurring due to a decrease in suspended solids. However, it was further postulated that unsuspended solids would partake in a grinding motion resulting in attrition of the yeast on the tank bottom, thus contributing to cell disruption.

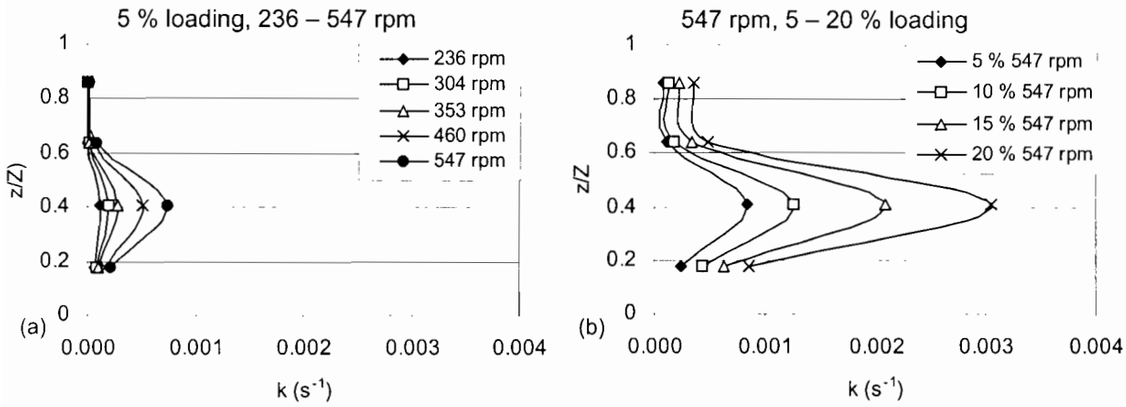


Figure 10.2: The local cell disruption rate constant for the 5 % volume fraction agitated at 236 to 547 rpm (assuming ERT accounts for suspended solids) (a), and the local disruption rate constant for 5 to 20 % volume fraction agitated at 547 rpm (b). Both with Rushton impeller and 600 – 850 μm quartzite fraction

In this examination of the axial variation in the disruption rate constant, the radial distribution of solids has been assumed constant. However, the degree to which the disruption rate could potentially vary can be given by the mixing indices in the horizontal plane, $\overline{MI}_z$. This index represents the standard deviation of solids volume fraction. Thus raising these values to the power of 1.64 yields the effective variation in the disruption rate assuming the energy dissipation rates are similar in the horizontal plane. Applying this reasoning to the mixing indices in Table 6.2 results in a standard deviation in the disruption rate constant of 73 to 105 % and 47 to 58 % in the radial direction for the 5 and 15 % solid concentrations respectively (calculation in Appendix O). This indicates greater radial variation in k for lower solid concentrations. Although rates were not established for the pitched blade impeller, it can be postulated that a similar power relationship of volume fraction would be present. Thus in some cases there would be higher disruption rates near the vessel wall with the pitched blade turbine, particularly for the 106 – 212 μm fraction.

10.3.2.2 Hypothetical Cell Disruption in the 50 mm Reactor

Operating at the same tip speed as the 220 mm reactor, the 50 mm reactor has increased radial and axial particle homogeneity, therefore a decreased variation in k with the 600 – 850 μm fraction is expected. Increasing the agitation rate decreases the overall mixing index in the 220 mm reactor, however, again greater cell disruption is postulated to occur in the impeller zone due the higher localised energy dissipation rate.

Harrison *et al.* (2003b) found a rapid decrease in the cell disruption rate for smaller particle diameters (Section 2.5.2), while Nemati *et al.* (2000) found improved leaching performance through the increased interfacial area. Examining the MRI 1D data for the 5 % concentration of 50 μm ballotini (Section 8.2.1), there is an increase in solids concentration in the impeller plane, thus significant cell disruption is postulated to occur in this region due to a higher presence of solids and the higher specific power input. The Zwietering equation overpredicts the critical suspension speed for the 50 mm vessel, but it is clear from the MRI data that unsuspended solids can be quantified allowing potentially more accurate modelling of the hypothetical cell disruption rate. It can also be postulated that operating the Rushton impeller with fine particles at sub-critical speeds may achieve significant suspension and thus cell disruption. When there is a decreased density difference between fluid and particle, as in the 500 μm nylon particles, axial homogeneity is excellent. This, however, comes at the cost of decreased energy transfer between cell and solid if the objective is to disrupt cells or extract proteins.

In the study of Scholtz-Brown (1998) it was postulated that a grinding mechanism was active in the bottom of the tank in which unsuspended solids interact with cells in an expanded bed. However, examining the 2D slices obtained from the 3D MRI examination of a 10 % concentration of 50 μm ballotini (Section 8.3.2) at conditions of incomplete suspension, it is clear that the unsuspended solids do not form an expanded bed of particles in which grinding action occurs. This is apparent from the four swirls of solids deposited on the tank bottom that maintain their position over the 12 hour experiment. Analysis of cell disruption on incomplete suspension therefore requires a combined 3D analysis of energy dissipation rate and particle distribution. This study has only provided data on particle distribution to date.

10.3.2.3 The Influence of Local Cell Concentration on Cell Disruption

In Section 9.5.2, ERT and MRI were applied to microbial populations of 5 and 11 vol. % with apparently successful detection. From the axial concentration profiles it is

observed that local cell concentration is a function of impeller speed, reactor height and total cell loading. Thus, both a difference in local solids concentration in the reactor and in the local cell concentration result. This affects the solid-cell-solid collision frequency accordingly. In Figure 9.12, for example, a cell concentration of 0.070 volume fraction is observed at z/Z = 0.79 at 186 rpm in the 50 mm vessel, while a cell concentration of 0.055 is observed at the same height at 480 rpm. As the frequency of solid-cell collisions is a function of both the concentration of cells and particulates and of the velocity profile, it cannot be assumed that the collision frequency is proportionally lower at the lower agitation rate.

10.4 Heat Transfer in the Slurry Bioreactor

Depending upon the solids concentration, turbulence increases in the reactor due to the effect of wakes produced by particle relative velocities (Caulet *et al.*, 1996). Thus in the solids concentration range of 2 to 10 % by volume an increase in the heat transfer coefficient should be expected. Above 20 % by volume, particle-particle interaction dominates the fluid behaviour (Caulet *et al.*, 1996) increasing the viscosity, while Kim and Kang noted that heat transfer decreased with increasing viscosity for three-phase fluidised beds (Section 2.2.5). Particle-particle interaction was observed in this study in the range of 5 to 20 % by volume (Section 6.2.7). In Section 2.2.5 it was reported that heat transfer coefficients for suspensions in a jacketed tank decreased gradually with increased solid concentration (Kawase and Moo-Young, 1989). Furthermore, Wichterle (1994) suggested that there was a complex distribution of heat transfer coefficients on the vessel wall (Section 2.2.1). This structure will be further affected by the variation of solids concentration near the vessel wall. It is further postulated that the effect of turbulence enhancement through particles is not constant throughout the reactor; it is influenced by the position of the agitator and the axial concentration profile, analogous to the cell disruption constant. Steiff and Weinspach (1982), as cited by Kim and Kang (1989), noted controversy regarding the effect of particles on the heat transfer coefficient with the relative increase or decrease depending upon the impeller speed. This may result due to the changes in the axial concentration profile of particles.

Increasing the concentration of the microbial phase increases the yield stress and increases the viscosity, thereby decreasing the heat transfer coefficient. However, at conditions of high turbulence the effect of the plastic viscosity is more significant in decreasing the heat transfer coefficient (Kawase and Moo-Young, 1989). In Section 9.5.2, depending upon the concentration of *Saccharomyces cerevisiae*, an increase or decrease in cell concentration was observed above the impeller with increasing agitation rate using MRI. Thus, this is expected accordingly to result in a minor decrease or increase in the heat transfer coefficient above the impeller.

In Section 9.2, sparging at 0.5 vvm was examined qualitatively using ERT in the 2.3 m^3 vessel. At low agitation rates the air bubbles rose through the centre of the tank, while increased agitation produced higher concentrations of gas near the vessel wall. At low agitation rates air flow behaviour is similar to a bubble column, where an increase in the heat transfer coefficient has been observed due to an increase in turbulence (Lin and Wang, 2001). Thus, this should hold true for the stirred tank at low agitation rates. Similarly, it was observed by Prakash *et al.* (2001) in a bubble column that heat transfer coefficients obtained in an air-water-yeast system were higher in the central region of the column, but lower at the wall. This increase in the centre region was attributed to larger bubbles that pass through the centre of the column. Barigou and Greaves (1992) observed that increasing the air rate at constant agitation rate led to an increase in bubble size and coalescence, thus under conditions of low agitation rates this is postulated to increase the heat transfer coefficient in the centre of the tank. In Section 2.2.4, it was reported that the heat transfer either stays constant or increases beyond a critical agitation rate. This may be due to the changing distribution and size of bubbles near the vessel wall at high agitation rates as observed with ERT.

Surface aeration is significant at higher agitation rates as observed from the ERT data (Section 9.4). Visually, it appears that there is an increase in turbulence with surface aeration, with ERT showing higher bubble concentration near the surface of the tank. Wichterle (1994) noted that heat transfer experiments are often performed at very high agitation rates, where similarity assumptions across reactor scale are no longer valid due to the disturbances of surface aeration. He noted that a decrease in density of the agitated media in the impeller zone due to gas hold-up from surface aeration, would result in a decrease in power output and pumping capacity of the impeller. This was postulated to lead to a decrease in heat transfer. This indicates that the loss in pumping capacity of the impeller is potentially more significant than increased turbulence due to the presence of a gaseous phase.

10.5 The Oxygen Mass Transfer Coefficient in the Slurry Bioreactor

It has been reported that the concentration of solids affects the oxygen mass transfer coefficient (Section 2.3.1.5). Mills *et al.* (1987) found a decrease in k_La while increasing glass bead (66 μm) concentration, while van Weerts *et al.* (1995) found decreases of up to 65 % in k_La with a 40 % volume concentration of solids (66 μm quartzite). However, Mills *et al.* (1987) observed no changes on k_La using up to 10 % volume fraction of glass beads, while Derksen *et al.* (2000) observed a decrease of about 40 % in k_La for a 15 % vol. quartzite slurry (d_{50} = 13 μm). Thus, it is postulated that above a critical quartzite volume fraction, the k_La is negatively affected. Hence,

the local k_La values in the reactor are postulated to be influenced by the shape of the axial and radial solids concentration profiles. Focusing on the axial concentration profile, it is thus postulated that local k_La values will be lower near the bottom of the tank where there is generally higher concentrations of solids. Higher k_La values are then expected in the high energy dissipation zone of the impeller, and above the impeller due to a decrease in the concentration of solids. As there will be a higher concentration of a nutrient in the bottom of the tank if the solid particle is a nutrient, the postulated decrease in k_La is deleterious to the maximum growth rate in this region. Derksen *et al.* (2000), however, observed a 50 % increase in k_La with a 12.7 % volume pyrite slurry (d_{50} = 14 μm). Thus physico-chemical factors come into play depending upon the nature of the particle. With pyrite, the above reasoning is reversed and higher k_La values will be present in the bottom half of the tank promoting cell growth. The oxygen mass transfer coefficient is positively correlated with agitation rate through P/V (Derksen *et al.*, 2000), although this relationship was only found at higher agitation rates in the presence of carbon particles and electrolytes (Kluytmans *et al.*, 2003). Kluytmans *et al.* (2003), however, observed no dependency of k_La on carbon particle concentration, thus reiterating the specific physico-chemical nature of the particle in agitated slurries.

10.6 The Microbial Phase in the Slurry Bioreactor

Viscosity increases with increase in cell concentration through volume fraction (Cilliers and Harrison, 1998; Radež *et al.*, 1991), leading to increased coalescence of bubbles (Pandit and Joshi, 1983) and decreased turbulence. This results in a decrease in the mass transfer coefficient (Oldshue, 1983) and decreased particle suspension (Zwietering, 1958). However, effective viscosity can reduce during operation of a filamentous fungal system through fragmentation of mycelia (Radež *et al.*, 1991). Examining the yeast MRI results (Section 9.3), increasing the concentration of the microbial phase (11 % v/v) appears to result in increasing microbial concentrations above the impeller with increasing agitation, while a decreasing microbial concentration is observed above the impeller for increasing agitation rate with the 5 % v/v yeast concentration. Similar behaviour was observed with nylon particles. It is thus postulated that cells act as a solid particle in suspension. Cells also affect rheology as observed through the addition of a 5 % yeast concentration to a 10 % concentration of 500 μm nylon particles (Section 9.3.3). This increased viscosity and exaggerated the axial suspension profile relative to a suspension of nylon particles in the absence of yeast. Further, local variations in biomass concentration impact upon utilisation rates of media components and localised cell growth and cell disruption in mineral systems.

10.7 Conclusions

The application of tomography to the stirred tank environment yielded information that increases the understanding of parameters that affect cell behaviour in the slurry bioreactor. Hydrodynamic effects from velocity fluctuations were quantified. It can be concluded that owing to eddy size, cell disruption does not relate directly from fluid forces. The study of Scholtz-Brown (1998) illustrated that solid-cell-solid collisions are the dominant mechanism inhibiting cell growth. Hence, the distribution of solids in the reactor is of particular significance. The distribution of solids was related to the cell disruption rate constant which was previously modelled by Scholtz-Brown on a geometrically similar vessel. In combination with analysis of localised energy dissipation rates, this provides insight on regions providing the major contribution to cell disruption in a slurry bioreactor. Further, it has identified key variables monitored through ERT and MRI to aid the design of larger scale processes. ERT and MRI information obtained on solids, air and cell distribution were then related to previous studies of heat and oxygen transfer and the effect on rheology. This provided new postulations and increased insight into the multifactorial interaction of parameters affecting the slurry bioreactor. This is valuable for further studies on this reactor environment.

Chapter 11

Conclusions and Recommendations

This study has been concerned with the analysis of dynamic two phase systems to understand phase distribution and to thereby increase understanding of system parameters which affect heat, mass and momentum transfer. The dominant technology used to examine phase distribution has been tomography, in the form of electrical resistance tomography (ERT) and magnetic resonance imaging (MRI). The principal system has been the slurry bioreactor. This system contains solid particles, a liquid and microbial phase in an agitated environment. Additional gaseous and immiscible liquid phases may also be present. This system was simplified through separate examination of the distribution of an inert solid phase, a gaseous phase and a microbial phase. The results from this investigation find application in microbial cell disruption, cell growth using particulates or immiscible fluids, immobilised cell suspensions, minerals bioleaching and general biological and mineral processes in stirred tank reactors. Further knowledge generated centres on the development and application of tomography to two phase systems. The major findings from this study follow, including a summary of key contributions to knowledge. Recommendations for the application of this knowledge and areas for further research are given.

11.1 Summary and Conclusions of the Study

It was necessary to provide a background of the slurry bioreactor environment to examine key parameters of influence and to investigate how previous phase distribution had been quantified. This was achieved in the literature review. It was further revealed the non-invasive technologies of ERT and MRI had potential to examine this environment.

The prototype ERT hardware and software was available at the start of this study. Physical phantoms were successfully examined in the tank environment before resolving more complex swirling suspensions in an industrial pipeline. The proficiency of this initial ERT technology was thus validated. This allowed the investigation into the suspension of particles in the more complex stirred tank environment.

The study of the 220 mm stirred tank slurry environment considered 3 size fractions of particulates at 4 solid loadings, agitated by a Rushton or pitched blade impeller at 5 agitation rates. This reactor was a scaled-up version of that used by Scholtz-Brown (1998) in a study of microbial cell disruption. ERT allowed the generation of radial

and axial concentration profiles for this environment. This information gained from ERT was used to analyse reactor homogeneity, thereby expanding upon the concept of a critical suspension speed of particles used in suspension studies. These concepts included mixing indices, the relation of particle diameter to the axial concentration profile and particle-particle effects at higher solid loadings. The Rushton impeller resulted in increased particle suspension relative to the pitched blade impeller at the same agitation rate. However, for the smallest particle size fraction of 106 – 212 μm at loadings of 5 – 15 % by volume, the pitched blade impeller increased particle concentration closer to the vessel wall. It was thus postulated that finer particles are influenced by the circulation flow pattern of the impeller. The ERT radial concentration profiles were related to those generated from pipette sampling and conductivity probing in the 220 mm tank. In general, these profiles were supported by these methods of physical validation. However, due to the nature of the calibration process, ERT information was available only from the boundary of the zone swept by the impeller to the vessel wall.

A more sophisticated ERT system became available during the course of this study as an output of concomitant research carried out in the chemical and electrical engineering departments at the University of Cape Town. This increased information and allowed more accurate mapping of the reactor domain. This system was successfully tested on a small-scale 50 mm reactor, thereby allowing a comparative suspension study with the 220 mm vessel. Impeller tip speed was used as the common variable, with the smaller vessel exhibiting greater particle suspension due to the higher power input per unit volume. It was further demonstrated that absolute particle homogeneity is infeasible through analysis of the trends of power input relative to local particle concentration.

MRI was successfully applied to the 50 mm reactor stirred tank slurry and is the first study of its kind. Excellent resolution was obtained in one dimension allowing a clear representation of axial concentration profiles of borosilicate ballotini and polyamide nylon particles. From this information, the amount of particles unsuspended, or suspended in the upper regions of the tank, was established. The Zwietering correlation was found to overpredict the critical suspension speed for the 50 mm vessel. Operating below the critical suspension speed was thus found to be an efficient operating condition considering the high degree of particle suspension observed. When microbial growth is desired, this would decrease the energy dissipation rate required, the particle-cell collisions and shear stress, thereby minimising cell damage. A peak solids concentration in the impeller zone was observed for a 5 % loading of ballotini agitated at 306 to 480 rpm. This was related to literature observations where it was postulated that the peak occurs due to a balance of forces in the impeller zone. Further, the effects of particle-particle interactions and solids loading need to be accounted for in theoretical suspension models. 3D MRI

allowed the generation of radial concentration profiles that bore similarity to comparative ERT experiments. In general, good radial homogeneity was observed above and below the impeller, with increased concentration fluctuations near the reactor base. For the 10 % suspension of 50 μm ballotini and the 10 % suspension of 500 μm nylon particles an oscillating radial concentration profile was observed, although this exhibited good average radial homogeneity. This can not be supported by ERT nor available literature due to their lack of spatial resolution. 2D slices of the 10 % suspension of 50 μm ballotini agitation at 480 rpm in the 50 mm reactor allowed a clear representation of incomplete suspension. Four swirls of increased particle concentration were observed on the tank bottom and corresponded to the position of the four baffles. It is thus clear that there is not a uniform expanded bed of particles with increasing agitation rate on incomplete suspension. These data further provide information for CFD code validation. In general, the similarity of the ERT and MRI radial and axial concentration profiles provide support for the accuracy of the more recently developed ERT system.

The distribution of sparged air was examined qualitatively in a large scale 609 mm tank and quantitatively in the 220 mm tank. ERT monitored the changing distribution of air with increasing agitation rate. This was related to the observed gas hold-up, where slightly more air was detected using ERT than observed at higher aeration rates. This was postulated to be due to the non-sphericity of bubbles upon increased coalescence, leading to inaccuracies with the Maxwell equation. Such an analysis with relation to hold-up has not been reported previously in the ERT stirred tank literature. Surface aeration was examined in the 220 mm tank. The amount of air entrained at agitation rates above 460 rpm was significant. This entrainment was found to be directly proportional to the agitation rate. Literature reports that surface aeration contribution to the oxygen mass transfer coefficient is, at most, approximately 10 %. It increases exponentially with agitation rate and is significantly reduced with the presence of a microbial phase. Clearly these differences relate to bubble size and energy dissipation. They provide a basis for refining the optimisation of mass transfer in stirred tank reactors. Previous ERT examinations of surface aeration have not been reported in the literature.

Similarly, the detection of microorganisms with ERT has not been reported to date. *Saccharomyces cerevisiae*, Bakers' yeast, was the model microbe and radial and axial profiles for the 220 and 50 mm reactors were successfully generated using ERT. However, ERT calibration of a microbial phase concentration requires further study. Complementary MRI experiments were performed which exhibited greater resolution. Unexpectedly, microbial concentration is not homogenous in the axial plane and varies with agitation rate. Similar axial concentration behaviour was observed relative to the suspension of nylon particles which are of similar density, illustrating the particle-like behaviour of the yeast. The variation of cell concentration

in the slurry bioreactor has implications for both cell disruption and cell growth through the consumption of substrate and product formation.

A slurry bioreactor was simulated as a mixture of nylon particles and yeast. Radial concentration profiles exhibited similar trends to solid particle only mixtures; however, there was an exacerbation in the deviations of the axial concentration profile with the addition of yeast. This was postulated to result from the increased viscosity of the mixture.

The implications of tomographic data obtained were explored with respect to our understanding of the slurry bioreactor environment. Hydrodynamic shear and stress were quantified for the reactor sizes. However, the dominant cell disruptive mechanism is solid-cell-solid collision. This was investigated in relation to the model of Scholtz-Brown (1998). Theoretical local cell disruption rate constants were established in the 220 mm reactor with the highest rate constants present in the impeller zone. Extrapolations of parameter interaction were then discussed with reference to the heat and mass transfer coefficient, and the microbial phase present in a slurry bioreactor.

11.2 Contribution to Knowledge

Based on the study concluded, the following can be highlighted as key contributions to knowledge achieved:

- Swirling slurry flow was visualised in 3D dimensions using ERT with variation in structure related to slurry concentration and superficial velocity. Further, the deposition of particles was monitored along the slurry pipeline.
- The application of ERT to slurry systems has been supported through examining direct sample withdrawal and conductivity probing in the stirred tank reactor.
- It is apparent that further developments in ERT hardware and software are supported through increased information obtained from two – phase environments.
- A novel comparison between tomographies of ERT and MRI regarding microbial and slurry environments was achieved. This allowed comparison of spatial and temporal resolution and provided support for ERT data.
- Concepts of reactor homogeneity were expanded to account for particle distribution in two dimensions. An overall mixing index was then determined which allows ease of comparison with variable operating conditions and different mixing systems.

- Further knowledge regarding radial and axial particle concentration as a function of operating variable in stirred tanks was generated. This can provide further information for CFD and suspension modelling studies.
- Through examining the incomplete suspension of quartzite and ballotini, the findings indicate adequate particle distribution is achieved below N_{js}. This has advantages for the minimisation of cell damage and power usage in slurry bioreactor operation.
- The first application of MRI to a stirred tank reactor was reported. High resolution concentration profiles were obtained. A swirl pattern of solids was detected on the tank bottom at incomplete suspension. This is contrary to the idea of an expanded bed of particles with increasing agitation rate.
- ERT can detect air and quantify gas hold-up due to sparging and quantify the amount of air entrained due to surface aeration. Surface aeration contributes substantially to gas hold-up at high agitation rates and increases linearly as a function of agitation rate.
- ERT and MRI can detect biological cells. The inhomogeneity of these stirred suspensions was further detected. Cells have similar suspension behaviour to low density solid particles. The implications of their inhomogeneity are variable substrate utilisation and the frequency of particle-cell-particle collisions.
- Through relating a previous cell disruption model to particle distribution information, it was found the majority of microbial cell disruption occurs in the impeller region when a Rushton impeller is used in a slurry bioreactor.

11.3 Recommendations

Recommendations are made from this study regarding operating conditions and design of the slurry bioreactor. Suggestions for further areas of research are included.

- The axial concentration profile of solids should be the design basis when considering cell disruption or cell growth in large scale slurry bioreactors. ERT can be used on pilot scale vessels to establish the desired axial concentration profile. This can provide an adequate semi-empirical approach before theoretical models increase in accuracy.
- It is not necessary to operate above N_{js}. A high degree of suspension can be achieved at lower agitation rates. This has advantages when cell growth is desired and power is to be minimised. Local suspension concentration approaches an asymptote below N_{js}, while complete homogeneity is not feasibly attained.

- Overall reactor homogeneity should be expressed with reference to radial and axial particle concentration. The mixing index defined in this study can be used for this purpose.
- Surface aeration should be considered in its effect upon gas hold-up and its slight effect upon k_La, as well as the decreased power of the agitator leading to possible decreases in overall mixing and heat transfer.

Further research should examine the observed microbial concentration gradients in the stirred tank. Microbial kinetics should be examined to investigate if they change significantly according to reactor location. Obtaining complete 3D ERT information of the reactor through 3D tomography code and current injection will improve data analysis and understanding. This will be further aided through increasing the number of layers of electrodes for ERT. Complementary CFD studies for the 50 mm reactor should be related to the MRI and ERT information to gain confirmation of the tank hydrodynamics. Information on the energy dissipation rate in three dimensions can also be related to information on three dimensional particle distribution to allow more detailed analysis of localised cell disruption in the slurry bioreactor.

References

1. Akse, H., Beek, W. J., van Berkel, F. C., A. A., de Graauw, J., (1967). The local heat transfer at the wall of a large vessel agitated by turbine impellers, *Chem Eng. Sci.* **22**, 135
2. Alpher E., Ozturk S. (1986). The effect of activated carbon loading on oxygen absorption into aqueous sodium sulphide solutions in a slurry reactor, *Chem. Eng. J.* **32**, 127-130
3. Alpher E., Wichtendahl B., Deckwer W. D. (1980). Gas absorption mechanism in catalytic slurry reactors, *Chem. Eng. Sci.* **35**, 217-222
4. Altobelli S. A., Caprihan A., Fukushima E., Jeong E. –K., Nakagawa M. (1992). NSF-DOE Workshop on Flow of Particulate and Fluids, Gaithersburg, MD
5. Alves S. S., Maia C. I., Vasconcelos J. M. T (2004). Gas-Liquid mass transfer coefficient in stirred tanks interpreted through bubble contamination kinetics, *Chem. Eng. and Proc.* **43**, 823-830
6. Alves S. S., Maia C. I., Vasconcelos J. M., Serralheiro (2002). Bubble size in aerated stirred tanks, *Chem. Eng. J.* **89**, 109-117
7. Amundson N. R. (1988). *Frontiers in Chemical Engineering: Research Needs and Opportunities*, National Research Council, National Academy Press, Washington D.C.
8. Arjunwadkar S. J., Sarvanan K., Kulkarni P. R., Pandit A. B. (1998). Gas-liquid mass transfer in dual impeller bioreactor, *Biochem. Eng. Journ.* **1**, 99-106
9. Armenante P. M., Nagamine E. U. (1998). Effect of low off-bottom impeller clearance on the minimum agitation speed for complete suspension of solids in stirred tanks, *Chem. Eng. Sci.* **53**, 1757-1775
10. Askew, W. S., Beckman, R. B., (1965*).* Heat and mass transfer in an agitated vessel, *Ind. Eng. Chem. Process Des. Dev.* **4**, 311
11. Bailey A. D., Hansford G. S. (1993). Factors affecting biooxidation of sulphide minerals at high concentrations of solids: a review, *Biotech. Bioeng.* **42**, 1164-1174
12. Baker, C. G. J., Armstrong, E. R., Bergougnou, M. A. (1978). Heat transfer in three-phase fluidised beds, *Powder Technology* **21**, 195-206
13. Balakrishna, M., Murthy, M. (1980). Heat transfer studies in agitated vessels, *Chem. Eng. Sci.* **35**, 1486-1494
14. Baldi G., Conti R. (1978). Continuous removal of a solid from stirred tanks, *International Symposium on Mixing*, Mons. 21-24 Feb., Paper B5
15. Baldi G., Conti R., Alaria E. (1978). Complete suspension of particles in mechanically agitated vessels, *Chem. Eng. Sci* **33**, 21-25
16. Baldi G., Conti R., Gianetto A. (1981). Concentration profiles for solids suspended in a continuous agitated reactor, *AIChE J.* **27**, 1017-1020
17. Bangaru, B. (2004). A detailed investigation of microbial cell disruption by hydrodynamic cavitation for selective product release. PhD thesis, Department of Chemical Engineering, University of Cape Town
18. Barber D. C., Brown B. H., Freston I. L. (1983). Imaging spatial distributions of resistivity using applied potential tomography, *Electronic Letters* **19**, 993-995
19. Barigou M. (1987). PhD thesis, University of Bath as cited by Barigou and Greaves (1992)
20. Barigou M., Greaves M. (1992). Bubble size distributions in a mechanically agitated gas-liquid contactor, *Chem. Eng. Sci.* **47**, 2009-2025
21. Barker J. J., Treybal R. E. (1960). Mass transfer coefficient for solids suspended in agitated liquids, *AIChE J.* **6**, 289-295
22. Barnes E. C., Wilson D. I., Johns M. L. (2006). Velocity profiling inside a ram extruder using magnetic resonance (MR) techniques, *Chem. Eng. Sci.* **61**, 1353-1363
23. Barresi A., Baldi G. (1987a). Solid dispersion in an agitated vessel, *Chem. Eng. Sci.* **42**, 2949-2956
24. Barresi A., Baldi G. (1987b). Solid dispersion in an agitated vessel: effect of particle shape and density, *Chem. Eng. Sci.* **42**, 2969-2972

25. Beck M. S., Dyakowski T., Williams R. A. (1998). Process tomography- the state of the art, *Trans. Inst. Meas. Contr. (London)* **20**, 163-177
26. Beenackers A. A. C. M., van Swaaij W. P. M. (1993). Mass transfer in gas-liquid slurry reactors, *Chem. Eng. Sci.* **35**, 3109-3139
27. Beuling E. E., van Dusschoten D., Lens P., van den Heuvel J. C., Van As H., Ottengraf S. P. P. (1998), Characterisation of the diffusive properties of biofilms using pulsed field gradient nuclear magnetic resonance, *Biotech. Bioeng.* **60**, 283
28. Binley A., Shaw B., Siobhan H-P. (1996). Flow pathways in porous media: electrical resistance tomography and dye staining image verification, *Meas. Sci. Tech.* **7**, 384-390
29. Bittorf K. J., Kresta S. M. (2003). Prediction of cloud height for solid suspensions in stirred tanks, *Trans. IChemE* **81** Part A, May
30. Bohnet M., Niesmak G. (1980). Distribution of solids in stirred suspensions. *German Chemical Engineering* **3**, 57-65
31. Bolton G. T., Hooper C. W., Mann R., Stitt E. H. (2004). Flow distribution and velocity measurement in a radial flow fixed bed reactor using electrical resistance tomography, *Chem. Eng. Sci.* **59**, 1989-1997
32. Boogerd F. C., Van Alphen M. M. Q., Van Anrooij W. J., De Bruyn J. C., Bos P., Kuenen J. G. (1989). The role of growth and maintenance in the oxidation of pyrite in batch culture by a moderately thermophilic, facultative chemolithoautotroph, in: Salley J., McCready G. L., Wichlacz P. L. (Eds.), *Biohydromet., Proc. Int. Symp.,* CANMET, 735-761
33. Boon M., Heijnen J. J. (1998). Gas-liquid mass transfer phenomena in bio-oxidation experiments of sulphate minerals: a critical review of literature data, *Hydromet.* **48**, 187-294
34. Boone K. G., Holder D. S. (1995). Design considerations and performance of a prototype system for imaging neuronal depolarisation in the brain using 'direct current' electrical resistance tomography, *Physiol. Meas.* **16**, 87-98
35. Bourne J. R., Sharma R. N. (1974). Suspension characteristics of solid particles in propeller-agitated tanks, in *First European Conference on Mixing and Centrifugal Separation*, BHRA, Cambridge, U.K., 3-25
36. Bourne, J. R., Buerli, M., Regenass, W. (1981). Heat transfer and power measurements in stirred tanks using heat flow calorimetry, *Chem. Eng. Sci.* **36**, 347-351
37. Bourne, J. R., Dossenbach, O., Post, T. (1984). Local and average mass and heat transfer generated by Pfaudler-type impellers, *Instn Chem. Engrs Symp. Ser.* **89**, 177
38. Breckon W. R. (1990). Image reconstruction in electrical impedance tomography, PhD thesis, School of Computing and Mathematical Sciences, Oxford Polytechnic
39. Breckon W. R., Pidcock M. K. (1987). Mathematical aspects of impedance imaging, *Clin. Phys. Physiol. Meas.* **8** (Suppl. A), 77-84
40. Breucker C., Steiff A., Weinspach P. M. (1988). Interactions between stirrer, sparger and baffles concerning different mixing problems, *Proc. 6th Eur. Conf. Mixing* BHRA, Cranfield, 399
41. Brian P. L. T., Hales H. B., Sherwood T. K. (1969). Transport of heat and mass between liquids and spherical particles in an agitated tank, *AICHe J.* **15**, 727-733
42. Brown B. H. (2001). Medical impedance tomography and process impedance tomography: a brief review, *Meas. Sci. Tech.* **12**, 991-996
43. Brucato, A., Grisafi, F., Montante, G. (1998). Particle drag coefficients in turbulent fluids, *Chem. Eng. Sci.*, **53**, 3295–3314
44. Bujalski W., Takenaka K., Paolini S., Jahoda M., Paglianti A., Takahashi K., Nienow A. W., Etchells A. W. (1999). Suspension and liquid homogenisation in high solids concentration stirred chemical reactors, *Trans. IChemE* **77** (Part A), 241-247
45. Burnett D. S. (1987). *Finite element analysis, from concepts to applications*, Addison-Wesley, Reading
46. Calderbank P. H. (1958). Physical rate processes in industrial fermentation, Part 1: The interfacial area in gas-liquid contacting with mechanical agitation, *Trans. Inst. Chem. Engrs. (London)* **36**, 443

47. Calderbank P. H., Moo-Young M. B. (1961). The continuous phase heat and mass-transfer properties of dispersions, *Chem. Eng. Sci.* **16**, 39-54
48. Callaghan P. T. (1993). *Principles of Nuclear Magnetic Resonance Microscopy*, Oxford University Press, Oxford
49. Caulet P. J. C., van der Lans R. G. J. M., Luyben K. C. A. M. (1996). Hydrodynamical interactions between particles and liquid flows in biochemical applications, *Chem. Eng. J.* **62**, 193-206
50. Chang S. K., Kang Y., Kim S. D. (1986). Mass transfer in two- and three-phase fluidised beds, *J. Chem. Eng. Japan* **19**, 524-530
51. Chapman M., Nienow A., Cooke M., Middleton J. (1983). Particle-gas-liquid mixing in stirred vessels: Part III, Three-phase mixing, *Chem. Eng. Res. Des.* **61**, 167-181
52. Chapman M., Nienow A., Middleton J. (1981). Particle suspension in a gas sparged Rushton turbine agitated vessel, *Trans. IChemE* **59**, 134-137
53. Chapman, F.S., Dallenbach, H., Holland, F. A. (1964). Heat transfer in baffled agitated tanks, *Trans. Instn Chem. Engrs* **42**, 398-406
54. Cheney M., Isaacson D., Newell J. C., Simske S., Goble J. (1990). Noser: an algorithm for solving the inverse conductivity problem, *Int. J. Imag. Sys. Tech.* **2**, 66-75
55. Chilton, T. H., Drew, T. B., Jebens, R. H., (1944). Heat Transfer coefficients in agitated vessels, *Ind. Eng. Chem.* **36**, 510
56. Chisti Y., Jauregui-Haza U. J. (2002). Oxygen transfer and mixing in mechanically agitated airlift bioreactors, *Biochemical Engineering Journal* **10**, 143-153
57. Chiu, T.-M and Ziegler, E. N. (1983). Heat transfer in three-phase fluidised beds, *AIChE J.* **29**, 677-685
58. Chudacek M. W. (1985). Solid suspension behaviour in profiled-bottom and flat-bottom mixing tanks, *Chem. Eng. Sci.* **40**, 385-392
59. Cilliers J. J., Harrison S. T. L. (1998). Yeast separation using small diameter hydrocyclones. In Williams, R.A. (ed.) Innovation in physical separation technologies, Richard Mozley Memorial Volume, pp. 121-132. London: Institution of Mining and Metallurgy.
60. Cilliers J. J., Xie W., Neethling S. J., Randall E. W., Wilkinson A. J. (2001). Electrical resistance tomography using a bi-directional current pulse technique, *Meas. Sci. Tech.* **12**, 997-1001
61. Conti R., Nienow A. W. (1979). Particle abrasion at high solids concentration in stirred vessels II, *Chem. Eng. Sci.* **35**, 543-547
62. Conti R., Sicardi S., Specchia V. (1981). Effect of the stirrer clearance on suspension in agitated vessels, *Chem. Eng. J.* **22**, 247-249
63. Cook R. D., Malkus D. S., Plesha M. E., Witt R. J. (2002). *Concepts and applications of finite element analysis*, 4th Edition, USA, John Wiley and Sons
64. Croughan M. S., Hamel J. F. P., Wang D. I. C. (1987). Hydrodynamic effects on animal cells grown in microcarrier cultures. *Biotech. Bioeng.* **29**, 130-141
65. Croughan M. S., Hamel J. F. P., Wang D. I. C. (1988). Effects of microcarrier concentration in animal cell culture, *Biotech. Bioeng.* **32**, 975-982
66. Danckwerts P. V. (1951). Significance of liquid-film coefficients in gas absorption, *Ind. and Eng. Chem.* **43**, 1460-1467
67. De Maerteleire E. (1978). Heat transfer in turbine agitated gas liquid dispersions, *Proc. Int. Symp. Mix*. XC-07-35
68. Deans S. R. (1983). *The Radon Transform and Some of Its Applications*, as cited by York (2001)
69. Demmink J. F., Mehra A., Beenackers A. A. C. M. (1998). Gas absorption in the presence of particles showing interfacial affinity: case of fine sulphur precipitates, *Chem. Eng. Sci* **53**, 2885-2902
70. Derksen J. J., Buist K., van Weert G., Reuter M. A. (2000). Oxygen transfer in agitated silica and pyrite slurries, *Min. Eng.* **13**, 25-36
71. Desplanches H., Essayem F., Chevalier J. L., Bruxelmane M., Delvosalle C. (1988). Hydrodynamics and heat transfer in agitated, aerated, Newtonian and highly viscous liquids, in the transitional flow regime, *Proc. Eur. Conf. Mix.* **6**, 479

72. Dickin F., Wang M. (1996). Electrical resistance tomography for process applications, *Meas. Sci. Tech.* **7**, 247-260
73. Ditl P., Rieger F. (1984). Congress CHISA, Prague *cited by* Rieger and Ditl (1994)
74. Dunlap, I. R. and Rushton, J. H. (1953). *Chem. Eng. Prog. Symp. Ser.* **49**, 137
75. Edney H. G. S, Edwards M. F. (1976). Heat transfer to non-Newtonian and aerated fluids in stirred tanks, *Trans. Inst. Chem. Eng.* **54**, 160
76. Einenkel W. D., Mersmann A. (1977). Erforderliche Drekzaken zum Suspendieren ia Riihrnerben. *Verfahrenstechnik* **11**, 90-94
77. Einstein A. (1906). Eine neue Bestimmung der Molekuldimensionen, *Ann. Phys.* **19**, 289-306
78. Elkins C. J., Markl M., Iyengar A., Wicker R., Eaton J. K. (2004). Full-field velocity and temperature measurements using magnetic resonance imaging in turbulent complex internal flows, *Int. J. Heat and Fluid Flow* **25**, 702-710
79. Fajner D., Magelli F., Nocentini M., Pasquali G. (1985). Solids concentration profiles in a mechanically stirred and staged column slurry reactor, *Chem. Eng. Res. Des.* **63**, 235-240
80. Fan L. S., Yamashita T.,Jean R. (1987). Solids mixing and segregation in a gas liquid solid fluidised bed, *Chem. Eng. Sci.* **42**, 17-25
81. Fangary Y. S., Williams R. A., Neil W. A., Bond J., Faulks I. (1998). Application of electrical resistance tomography to detect deposition in hydraulic conveying systems, *Powder Tech.* **95**, 61-66
82. Fennel P. S., Davidson J. F., Dennis J. S., Gladden L. F., Hayhurst A. N., Mantle M. D., Müller C. R., Rees A. C., Scott S. A., Sederman A. J. (2005). A study of the mixing of solids in gas-fluidised beds, using ultra-fast MRI, *Chem. Eng. Sci.* **60**, 2085-2088
83. Fischer, J. Broring, S., Lubbert, A. (1992). Gas phase properties in stirred tank bioreactors, *Chem. Eng. Tech.* **15**, 390
84. Fransolet E., Crine M., L'Homme G., Toye D., Marchot P. (2002). Electrical resistance tomography sensor simulations: comparison with experiments, *Meas. Sci. Tech.* **13**, 1239-1247
85. Fransolet E., Crine M., Marchot P., Toye D. (2005). Analysis of gas hold-up in bubble columns with non-Newtonian fluid using electrical resistance tomography and dynamic gas disengagement technique, *Chem. Eng. Sci.* **60**, 6118-6123
86. Freeman R. (1988). *A handbook of nuclear magnetic resonance*, Longman Scientific and Technical, Essex, England
87. Frijlink J., Bakker A., Smith J. (1990). Suspension of solid particles with gassed impellers, *Chem. Eng. Sci.* **45**, 1703-1718
88. Frijlink J., Kalijn M., Smith J. M. (1984). Suspension of solids with aerated pitched blade turbines, *Fluid Mixing II*, The Institution of Chemical Engineers Symposium Series **89**, 49
89. Galaction A. –I., Cascaval D., Oniscu C., Turnea M. (2004). Prediction of oxygen mass transfer coefficients in stirred bioreactors for bacteria, yeasts and fungus broths, *Biochem. Eng. J.* **20**, 85-94
90. Garcia-Ochoa F., Gomez E. (1998). Mass transfer coefficient in stirred tank reactors for xanthum gum solutions, *Biochem. Eng. J.* **1**, 1-10
91. Garcia-Ochoa F., Gomez E. (2004). Theoretical prediction of gas-liquid mass transfer coefficient, specific area and hold up in sparged stirred tanks, *Chem. Eng. Sci.* **59**, 2489-2501
92. George P. L. (1991). *Automatic mesh generation: application to the finite element methods*, Masson, John Wiley and Sons Ltd.
93. Gladden L. F. (1995). Industrial applications of nuclear magnetic resonance, *Chem. Eng. J.* **56**, 149-158
94. Gladden L. F. (2003). Magnetic resonance: ongoing and future role in chemical engineering research, *AIChE J.* **49**, 2-8
95. Gladden L. F., Buckley C., Chow P. S., Davidson J. F., Mantle M. D., Sederman A. J. (2004). 'Looking into' chemical products and processes, *Curr. A, Phys.* **4**, 93-97

96. Gladden L. F., Lim M. H. M., Mantle M. D., Sederman A. J., Stitt E. H. (2003). MRI visualisation of two-phase flow in structured supports and trickle-bed reactors, *Cat. Today* **79-80**, 203-210
97. Gogate P. R., Beenackers A., Pandit A. B. (2000). Multiple-impeller systems with a special emphasis on bioreactors: a critical review, *Biochem. Eng. J.* **6**, 109-144
98. Gray D. J. (1987). Impeller clearance effect on off-bottom particle suspension in agitated vessels, *Chem. Eng. Comm.* **61**, 151-158
99. Hagedorn, D., Salamon, J. J. (1967). Batch heat transfer coeffients for pseudoplastic fluids in agitated vessels, *IEC Proc. Des. Dev.* **6**, 469
100. Harriot P. (1962). Mass transfer to particles: Part I. Suspended in agitated tanks. Part II. Suspended in a pipeline, *AIChE J.* **8**, 93-102
101. Harrison S. T. L., Sissing A., Raja S. and Nemati M. (2003a). Identifying and quantifying biological responses of *Sulfolobus* to high pulp densities in the slurry bioleach reactor. *Proceedings of IMPC* (ed. Lorenzen L., Bradshaw D. J., Aldrich C., Eksteen J. J., Wright M., Thom E.) **3**, 1344-1354
102. Harrison S. T. L., Sissing A., Raja S., Pearce S. J. A., Nemati M. (2003b). Solids loading in the bioleach slurry reactor: mechanisms through which particulate parameters influence slurry bioreactor performance, *International Biohydrometallurgy Symposium*, Sept. 15 – 19, Hellas, Athens, 359-376
103. Havelkova D. (1987), Dissertation CVUT FSI, Praha, cited by Rieger and Ditl (1994)
104. Hayashi K., Kawashima K., Kose K., Inouye T. (1988). *Journ. Phys. D-Appl. Phys.* **21**, 1037, *as cited by* Mantle and Sederman (2003)
105. Hicks M. T., Myers K. J., Bakker A. (1997). Cloud height in solids suspension agitation, *Chem. Eng. Comm.* **160**, 137-155
106. Higbie R. (1935). The rate of absorbtion of a pure gas into a still liquid during short periods of exposure, *Trans. AIChE* **31**, 365-389
107. Hirkeskorn F. S., Miller S. A. (1953). Agitation of viscous solid-liquid suspensions, *Chem. Eng. Prog.* **49**, 459-470
108. Ho C. S., Oldshue J. Y. (eds) (1987). Biotechnology Processes Scale-up and Mixing, AIChE, pp. 128 as cited by A. –I. Galaction *et al.* (2004)
109. http://www.itoms.com (retrieved 15 February 2006).
110. http://eidors3d.sourceforge.net/news.shtml (retrieved 15 February 2006).
111. Hua P., Woo E. J. (1990). *Reconstruction algorithms- electrical impedance tomography*, (Editor: J. G. Webster), The Adam Hilger Series on Biomedical Engineering, Bristol: IOP Pubilshing Ltd. pp. 97-136
112. Ibrahim S., Nienow A. W. (1999). Comparing impeller performance for solid-suspension in the transitional flow regime with Newtonian fluids, *Trans. IChemE* **77** Part A, Nov., 721-727
113. Illing, S. (1996). An investigation of the effect of hydrodynamic stress on the growth, morphology and metabolism of microorganisms, PhD thesis, Department of Chemical Engineering, University of Cape Town
114. Illing S., Harrison S. T. L. (1999). The kinetics and mechanism of Corynebacterium glutamicum aggregate breakup in bioreactors, *Chem. Eng. Sci.* **54**, 441-454
115. Johns M. L., Gladden L. F. (2003). Magnetic resonance studies of dissolving particulate solids, *Mag. Res. Imag.* **21**, 395-396
116. Johns M. L., Sederman A. J., Bramley A. S., Alexander P., Gladden F. (2000). Local transitions in flow phenomena through packed beds identified by MRI, *AIChE J.* **46**, 2151
117. Kai, W., Shengyao, Yu (1989). Heat transfer and power consumption of non-Newtonian fluids in agitated vessels, *Chem. Eng. Sci.* **44**, 33-40
118. Kaminoyama M., Taguchi S., Misumi R., Nishi K. (2005). Monitoring stability of reaction and dispersion states in a suspension polymerisation reactor using electrical resistance tomography measurements, *Chem. Eng. Sci.* **60**, 5513 – 5518

119. Kang Y., Suh I. S., Kim S. D. (1985). Heat transfer characteristics of three phase fluidised beds, *Chem. Engng Commun*. **34** , 1-13
120. Kawase, Y., Moo-Young, M. (1989). Heat transfer in bioreactors with dense suspension broths, *Chem. Eng. Journ*. **41**, 17-26
121. Kemna A., Vanderborght J., Kulessa B., Vereecken H. (2002). Imaging and characterisation of subsurface solute transport using electrical resistance tomography (ERT) and equivalent transport models, *Journal of Hydrology* **267**, 125-146
122. Kim S. D., Laurent A. (1991). The state of knowledge on heat transfer in three-phase fluidised beds, *International Chemical Engineering* **31**, 284-302
123. Kim, S. D., Kang, Y. (1997). Heat and mass transfer in three-phase fluidised-bed reactors-an overview, *Chem. Eng. Sci*. **52**, 3639-3660
124. Kluytmans J. H. J., van Wachem B. G. M., Kuster B. F. M., Schouten J. C. (2003). Mass transfer in sparged and stirred reactors: influence of carbon particles and electrolyte, *Chem. Eng. Sci*. **58**, 4719-4728
125. Kneule F. (1956). Die Prüfung von Ruhren durch Löslichkeitsbeistimmung, *Chem. - Ing. –Tech*. **28**, 221
126. Kolar V. (1961). Suspending solid particles in liquids by means of mechanical agitation, *Colln. Czech. Chem. Comm.* **26**, 601-627
127. Kolehmainen V., Vauhkonen M., Karkalainen P. A., Kaipo J. P. (1997). Assessment of errors in static electrical impedance tomography, *Physiol. Meas*. **18**, 289-303
128. Kolmogorov A. N. (1941). The local structure of turbulence in incompressible viscous fluid for very large Reynolds numbers. *CR. Acad. Sci. USSR* **30**, 299-303
129. Kotre C. J. (1989). A sensitivity coefficient method for the reconstruction of electrical impedance tomograms, *Clin. Phys. Physiol. Meas.* **10**, 275 - 281
130. Koutsakos E. (1988). PhD thesis, University College of London, as cited by Shamlou and Koutsakos (1989)
131. Kralj, F., Sinčić, D. (1983). Hold-up and mass transfer in a two- and three-phase stirred tank reactor, *Chem. Eng. Sci* **39**, 604-607
132. Kraume, M. (1992). Mixing times in stirred suspensions, *Chem. Eng. Tech*. **15**, 313-318
133. Krishna R., de Swart J. W. A., Ellenberger J., Martina G. B., Maretto C. (1997). Gas holdup in slurry bubble columns: effect of column diameter and slurry concentrations, *AIChE Journal* **43**, 311
134. Kunas K. T., Papoutsakis E.T. (1990). Damage mechanisms of suspended animal cells in agitated bioreactors with and without bubble entrainment, *Biotech. Bioeng.* **36**, 476-483.
135. Kung D. M., Harriott P. (1987). Heat transfer to concentrated suspensions in agitated systems, *Ind. Eng. Chem. Res*., **26**, 1654
136. Kupčik, F. (1965). Heat transfer on the wall and bottom of an agitated vessel (in Czech), *Chem. Průmysl* **15**, 465
137. Lamaignere V (2002). Effects of hydrodynamic stress on growing *Saccharomyces cerevisiae* in a slurry reactor. MSc dissertation in Chemical Engineering, University of Cape Town.
138. Lee Y., McCarthy M. J., McCarthy K. L. (2001). Extent of mixing in a two-component batch system measured using MRI, *J. Food Eng*. **50**, 167-174
139. Leighton D., Acrivos A. (1986). Viscous resuspension, *Chem. Eng. Sci*. **41**, 1377-1384
140. Levenberg K. (1944). A method for the solution of certain problems in least squares, *SIAM J. Numer. Anal*. **16**, 588 – 604
141. Lewis D. A., Field R. W., Xavier A. M., Edwards D. (1982). Heat transfer in bubble columns, Transactions of the Institution of Chemical Engineers **60**, 40 – 47
142. Li H., Prakash A. (2000). Influence of slurry concentrations on bubble population and their rise velocities in a three-phase slurry bubble column, *Powder Technology* **113**, 158

143. Lilly M. D., Ison A., Ayazi Shamlou P. (1992). The influence of the physical environment in fermenters on antibiotic production by micro-organisms. In *Harnessing biotechnology for the 21st century, Proc. Ninth International Biotechnology Symposium*, 219-222.
144. Lim M. H. M., Sederman A. J., Gladden L. F., Stitt E. H. (2004). New insights to trickle and pulse flow hydrodynamics in trickle-bed reactors using MRI, *Chem. Eng. Sci.* **59**, 5403-5410
145. Lin T., Wang S. (2001). Effects of macroscopic hydrodynamics on heat transfer in bubble columns, *Chem. Eng. Sci.* **56**, 1143-1149
146. Logan D. L. (2002). *A first course in the finite element method*, 3rd Edition, USA, Brooks/Cole Thomson Learning
147. Long T. (2006). M.Sc. thesis on ERT reconstruction (in progress), Department of Electrical Engineering, University of Cape Town
148. Lucas G. P., Cory J., Waterfall R. C. (2000). A six electrode probe for measuring solids velocity and volume fraction profiles in solids-water flows, *Meas. Sci. Technol.* **11**, 1498-1509
149. Lucas G. P., Cory J., Waterfall R. C., Loh W. W., Dickin F. J. (1999). Measurement of the solids volume fraction and velocity distributions in solid-liquid flows using dual-plane electrical resistance tomography, *Flow Measurement and Instrumentation* **10**, 249-258
150. Ma Y., Zheng Z., Xu L., Liu X., Wu Y. (2001). Application of electrical resistance tomography system to monitor gas/liquid two-phase flow in a horizontal pipe, *Flow* Measurement and Instrumentation **12**, 259-265
151. Machon V., Fort I., Skrivanek J. (1982). Local solids distribution in the space of a stirred vessel, in *4th European Conference on Mixing*, Netherlands, 289-302
152. MacTaggart R. S., Nasr-El-Din H. A., Masliyah J. H. (1993). Sample withdrawal from a slurry mixing tank, *Chem. Eng. Sci* **48**, 921-931
153. Magiliotou M., Chen Y.-M., Fan L.-S. (1988). Bed-immersed object heat transfer in a three-phase fluidised bed, *AIChE Journal* **34**, 1043-1047
154. Man K. L., Edwards M. F., Poley G. T. (1984). A study of local heat transfer coefficients in agitated vessels, *Instn Chem. Engrs Symp. Ser.* **89**, 193
155. Mann R., Dickin F. J., Wang M., Dyakowski T., Williams R. A., Edwards R. B., Forrest A. E., Holden P. J. (1997a). Application of electrical resistance tomography to interrogate mixing processes at plant scale, *Chem. Eng. Sci.* **52**, 2087-2097
156. Mann R., Pillai S. K., El-Hamouz A. M., Ying P., Togatorop A., Edwards R. B. (1995). Computational fluid mixing for stirred vessels: progress from seeing to believing, *Chem. Eng. J. and Biochem. Eng. J.* **59**, 39-50
157. Mann R., Stanley S., Vlaev D., Wabo E. (2001). Augmented-reality visualization of fluid mixing in stirred chemical reactors using electrical resistance tomography, *J. Electronic Imaging* **10**, 620-629
158. Mann R., Williams R. A., Dyakowski T., Dickin F. J., Edwards R. B. (1997b). Development of mixing models using electrical resistance tomography, *Chem. Eng. Sci.* **52**, 2073-2085
159. Mantle M. D., Sederman A. J. (2003). Dynamic MRI in chemical process and reaction engineering, *Prog. in Nuc. Mag. Res. Spec.* **43**, 3-60
160. Marquardt D. W. (1963). An algorithm for the least-square estimation of non-linear parameters, *J. Appl. Math.* **11**, 431-441
161. Maxwell J. C. (1873). *Treatise on electricity and magnetism*, U.K. Oxford University Press.
162. McCarthy K. L., Kerr W. L. (1998). Rheological characterisation of a model suspension during pipe flow using MRI, *J. Food Eng.* **37**, 11-23
163. McKee S. L., Williams R. A., Boxman A. (1995). Development of solid-liquid mixing models using tomographic techniques, *Chem. Eng. J.* **56**, 101-107

164. Mersmann A., Werner F., Maurer S., Bartosch K. (1998). Theoretical prediction of the minimum stirrer speed in mechanically agitated suspensions, *Chem. Eng. and Proc.* **37**, 503-510
165. Metzner, A. B., Otto, R. E. (1957). Agitation of non-Newtonian fluids, *AIChE J.* **3** , 3
166. Micale G., Carrara V., Grisafi F., Brucato A. (2000). Solids suspension in three-phase tanks, *Trans. IChemE* **78** Part A, April, 319-326
167. Michaels, J. D., Mallik, A. K., Papoutsakis, E. T. (1996). Sparging and agitation-induced injury of cultured animal cells: do cell-to-bubble interactions in the bulk liquid injure cells?, *Biotech. Bioeng.* **51**, 399-409
168. Miles N. (2002). Personal communication
169. Mills B. D., Bar R., Kirwan D. J. (1987). Effects of solids on oxygen transfer in agitated three-phase systems, *AIChE J.* **33**, 1542-1549
170. Miyahara T., Lee M-S., Takahasi T. (1993). Mass transfer characteristics of a three-phase fluidised bed containing low density and/or small particles, *Int. Chem. Eng.* **33**, 680-686
171. Molerus O., Latzel W. (1987). Suspension of solid particles in agitated vessels-1. Archimedes Numbers ≤40, *Chem. Eng. Sci.* **42**, 1423
172. Molinari M., Cox S. J., Blott B. H., Daniell G. J. (2001b). Adaptive mesh refinement techniques for electrical impedance tomography, *Physiol. Meas.* **22**, 91- 96
173. Molinari M., Fangohr H., Generowicz J., Cox S. J. (2001a). Finite element optimisations for efficient non-linear electrical tomography reconstruction, *2nd World Congress on Industrial Process Tomography*, Hannover, Germany, , 406-417
174. Morooka S., Kusakabe K., Kato Y. (1980). Mass transfer coefficient at the wall of a rectangular fluidised bed for liquid-solid and gas-liquid-solid systems, *Int. Chem. Eng.* **20**, 433-438
175. Moser K. W., Raguin L. G., Georgiadis J. G. (2003). Synchronized EPI phase contrast velocimetry in a mixing reactor, *Mag. Res. Imag.* **21**, 127-133
176. Muller F. L., Davidson J. F. (1992). *Chem. Eng Sci* **47**, 3525, as cited by Arjunwadkar *et al.* (1998)
177. Murugesan T. (2001). Critical impeller speed for solid suspension in mechanically agitated contactors, *J. Chem. Eng. Jap.* **34**, 423-429
178. Musil L., Vlk J. (1978). Suspending solid particles in an agitated conical-bottom tank, *Chem. Eng. Sci.* **33**, 1123
179. Musil L., Vlk J., Jirondkora H. (1984). Suspending solid particles in an agitated tank with axial-type impellers, *Chem. Eng. Sci.* **39**, 621-628
180. Nagata S. (1975). Mixing Principles and Applications, Kodansha Ltd., Chapters 2, 4, 6, 8
181. Naidoo T. (2002). *Signal and Image Processing for Electrical Resistance Tomography*, M.Sc. thesis, Department of Electrical Engineering, University of Cape Town
182. Narayanan S., Bhatia V. K., Guha D. K., Rao M. N. (1969). Suspension of solids by mechanical agitation, *Chem. Eng. Sci.* **24**, 223
183. Nasr-El-Din H. (1987). Comments on scaling-up rules for solids suspension in stirred vessels, *Chem. Eng. Sci.* **42**, 2986
184. Nasr-El-Din H. (1989). Sampling from slurry pipelines, in *Wastewater Treatment Technology* (Edited by P. N. Cheremisinoff), Gulf, Houston. Vol. 3, Chap. 14.
185. Nasr-El-Din H., MacTaggart R., Masliyah J. (1996). Local solids concentration in a slurry mixing tank, *Chem. Eng. Sci.* **51**, 1209-1220
186. Nasr-El-Din H., Shook C. A., Esmail M. N (1984). Isokinetic probe sampling from slurry pipelines, *Can. Journ. Chem. Eng.* **62**, 179-185
187. Nasr-El-Din H.,Shook C. A., Esmail M. N. (1985). Wall sampling in slurry systems, *Can. Journ. Chem. Eng.* **63**, 746-753
188. Nemati M., Harrison S. T. L. (2000). Effect of solid loading on thermophilic bioleaching of sulphide minerals, *Journal of Chemical Technology and Biotechnology* **75**, 526-532

189. Nemati M., Lowenadler J., Harrison S. T. L. (2000). Particle effects in bioleaching of pyrite by acidophilic thermophile *Sulfolobus metallicus*, *Appl. Microbiol. Biotech.* **53**, 173 – 179
190. Ni X., Gao S., Cumming R. H., Pritchard D. W. (1995). A comparative study of mass transfer in yeast for a batch pulsed baffled bioreactor and a stirred tank fermenter, *Chem. Eng. Sci*. **50**, 2127-2136
191. Nienow A. (1968). Suspension of solid particles in turbine agitated baffled vessels, *Chem. Eng. Sci.* **23**, 1453-1459
192. Nienow A. W. (1969). Dissolution mass transfer in a turbine agitated vessel, *Can. J. Chem. Eng*. **47**, 248-258
193. Nienow A. W. (1975). Agitated vessel particle-liquid mass transfer: a comparison between theories and data, *Chem. Eng. J*. **9**, 153-161
194. Nienow A. W. (1985). The suspension of solid particles, in *Mixing in the Process Industries* (Edited by N. Harnby, M. F. Edwards and A. W. Nienow). Butterworths, London
195. Nienow A. W. (1997). The mixer as a reactor – liquid/solid systems, in *Mixing in the Process Industries*, 2nd edition, (Editors, N. Harnby, M. F. Edwards and A. W. Nienow), Butterworth Heinemann, London, Chapter 17 pp. 394-411
196. Nienow A. W., Conti R. (1978). Particle abrasion at high solids concentration in stirred vessels, *Chem. Eng. Sci*. **33**, 1077-1086
197. Nienow A. W., Lilly M. D. (1979). Power draw by multiple impellers in sparged agitated vessels, *Biotech. Bioeng.* **21**, 2341-2345
198. Nienow A., Konno M., Bujalski W. (1986). Studies on three-phase mixing: a review and recent results, *Chem. Eng. Res. Des.* **64**, 35-42
199. Nienow A., Miles D. (1978). The effect of impeller/tank configurations on fluid-particle mass transfer, *Chem. Eng. J.* **15**, 13-24
200. Nott K. P., Paterson-Beedle M., Macaskie L. E., Hall L. D. (2000). Visualisation of metal deposition in biofilm reactors by three-dimensional magnetic resonance imaging, *Biotech. Lett*. **23**, 1749
201. Oguz H., Brehm A., Deckwer W. D. (1987). Gas/Liquid mass transfer in sparged agitated slurries, *Chem. Eng. Sci.* **42**, 1815-1822
202. Ohiaeri I. N. (1981). PhD thesis, University of Bradford, as cited by Shamlou and Koutsakos (1989)
203. Oldshue J. Y. (1983), Fluid Mixing Technology, McGraw-Hill Publications Co., New York, Chapters 5, 11-14
204. Oldshue, J. Y. and Gretton, A. T. (1954). Helical coil heat transfer in mixing vessels, *Chem. Eng. Prog.* **50**, 615-621
205. Pandit A. B, Joshi J. B. (1983). Mixing in mechanically agitated gas-liquid contactors, bubble columns and modified bubble columns, *Chem. Eng. Sci.* **38**, 1189-1215
206. Pavlin M., Slivnik T., Miklavčič D. (2002). Effective conductivity of cell suspensions, *IEEE Transactions on Biomedical Engineering* **49**, 77-80
207. Pepper D. W., Heinrich J. C. (1992). *The finite element method: basic concepts and applications*, Series in Computational and Physical Processes in Mechanics and Thermal Sciences, USA, Tailor and Francis
208. Perry R. H., Green D. W., Maloney J. O. (1998). Perry's Chemical Engineers' Handbook, 7th ed., McGraw-Hill, Chapter 18.
209. Pinheiro P. A. T., Loh W. W., Dickin F. J. (1997). Smoothness-constrained inversion for two-dimensional electrical resistance tomography, *Meas. Sci. Tech*. **8**, 293-302
210. Pollard R., Topiwala H. H. (1976). Heat transfer in mechanically agitated vessels, *Biotech. Bioeng.* **18**, 1517
211. Polydorides, N. (2002). Personal communication

212. Polydorides, N., and Lionheart, W. (2002). A MATLAB toolkit for three dimensional Electrical Impedance Tomography: A contribution to the EIDORS project, *Meas. Sci. Tech*. **13**, 1871-1893
213. Potgieter T.P. (2002). Optimisation of lysine production using biomass retention by microfiltration, PhD dissertation, University of Cape Town.
214. Prakash A., Margaritis A., Li H., Bergougnou M. A. (2001). Hydrodynamics and local heat transfer measurements in a bubble column with suspension of yeast, *Biochemical Engineering Journal* **9**, 155-163
215. Radež, I., Hudcova, V., Koloini, T. (1991). Heat transfer in aerated and non-aerated mycelial fermentation systems in stirred tank reactors, *Chem. Eng. Journ*. **46**, 83-91
216. Raja S. (2005). The effect of particulate-induced hydrodynamic stress on the bioleaching of chalcopyrite by a *Sulfolobus*-like culture, PhD dissertation, University of Cape Town
217. Randall E. W. R (2005). Personal communication
218. Randall, E., Wilkinson, A., Cilliers, J., Xie, W., Neethling, S. (2001). Current pulse technique for Electrical Resistance Tomography Measurements, *2nd World Congress on Industrial Process Tomography*, Hannover, Germany, 29-31st August, 493-501
219. Rao K. B., Murthy P. S. (1973). Heat transfer in mechanically agitated gas liquid system, *Ind. Eng. Chem. Process. Des. Dev*. **12**, 190
220. Rao R., Mondy L., Sun A., Altobelli S. (2002). *Int. J. Numer. Meth. Fluids*. **39**, 465
221. Rao S. S. (1999). *The finite element method in engineering*, 3rd Edition, Boston, Butterworth-Heinemann
222. Regan D. L., Dunhill P., Lilly M. D. (1974). *Biotech. Bioeng.* **16**, 333
223. Rewatkar V. B., Raghav Rao K. S. M. S., Joshi J. B. (1991). Critical impeller speed for solid suspension in mechanically agitated three phase reactors I: Experimental part, *Ind. Eng. Chem. Res*. **30**, 1770-1779
224. Rieger F., Ditl P. (1994). Suspension of solid particles, *Chem. Eng. Sci*. **49**, 2219-2227
225. Rieger F., Ditl P., Novák V. (1980). Research Report No. 218-11/80, CVUT FSI, Praha, cited by Rieger and Ditl (1994).
226. Rieger F., Novák V., Ditl P. (1982). Mixing of concentrated bauxite suspensions, *Proc. of the 19th Conf. OSCHI*, Sachticky, 71 (in Czech).
227. Rushton J. H. (1965). The continuous removal of mixed phases from a mixing tank, *AIChE Ind. Chem. Eng. Symp*. **10**, 3
228. Scholtz N J, Pandit A B and Harrison S T L (1997). Effect of solids suspension on microbial cell disruption. In *Bioreactor & Bioprocess Fluid Dynamics*, (ed. A W Nienow), pp. 199 - 215.
229. Scholtz-Brown,N. (1998). The effects of non-biological particulates on microbial cell disruption in a slurry bioreactor, PhD dissertation, University of Cape Town.
230. Schumpe A., Deckwer W. D., Nigam K. D. P. (1989). Gas-Liquid mass transfer in three-phase fluidised beds with viscous pseudoplastics liquids, *Can. J. Chem. Eng*. **67**, 873-877
231. Sederman A. J., Johns M. L, Alexander P., Gladden F. (1998). Structure-flow correlations in packed beds, *Chem. Eng. Sci*. **53**, 2117
232. Sederman A. J., Mantle M. D. (2005). Personal communication.
233. Sederman A. J., Mantle M. D., Buckley C., Gladden L. F. (2004). MRI technique for measurement of velocity vectors, acceleration, and autocorrelation functions in turbulent flow, *Journ. Mag. Res*. **166**, 182-189
234. Shah Y. T. (1979). *Gas-Liquid-Solid Reactor Design*, McGraw-Hill, New York
235. Shamlou P. A. (1993). Suspension of particles in liquids in stirred vessels, in *Processing of Solid-Liquid Suspensions*, (Editor P. A. Shamlou), Butterworth Heinemann, London) Chapter 10, pp. 273-286
236. Shamlou P. A., Koutsakos E. (1986). Solids suspension in mechanically agitated systems, in *Proceedings of the International Conference on Mechanical Agitation,* Toulouse, France, 3-9 – 3-16

237. Shamlou P. A., Koutsakos E. (1989). Solids suspension and distribution in liquids under turbulent agitation, *Chem. Eng. Sci.* **44**, 529-542
238. Sharma R. N., Shaikh A. A. (2003). Solids suspension in stirred tanks with pitched blade turbines, *Chem. Eng. Sci.* **58**, 2123-2140
239. Sieder, E. N. and Tate, G. E. (1936). Heat transfer and pressure drop of liquids in tubes, *Ind. Eng. Chem.* **28**, 1429 – 1436
240. Simske S. J. (1987). An adaptive current determination and a one-step reconstruction technique for a current tomography system, MSc. Thesis, Rensselaer Polytechnic Institute
241. Sissing A. and Harrison S. T. L. (2003). Thermophilic mineral bioleaching performance: a compromise between maximising mineral loading and maximising microbial growth and activity, *SAIMM Journal*, March 2003, 1-4.
242. Slater L., Binley A., Versteeg R., Cassiani G., Birken R., Sandberg S. (2002). A 3D ERT study of solute transport in a large experimental tank, *J. Appl. Geophys.* **49**, 211-229
243. Smith J. M. (1990). Industrial needs for mixing research, *Trans. Inst. Chem. Engrs.* **68**, 3-6
244. Smith, J. J., Lilly, M. D., Fox, R. I. (1990). The effect of agitation on the morphology and penicillin production of *Pencillium chrysogenum*, *Biotech. Bioeng.* **29**, 1011-1023.
245. Sommier N., Porion P., Evesque P., Leclerc B., Tchoreloff P,. Couarraze G. (2001). Magnetic resonance imaging investigation of the mixing-segregation process in a pharmaceutical blender, *Int. J. Pharmaceutics* **222**, 243-258
246. Steiff A., Weinspach P. M. (1978). Heat transfer in stirred and unstirred gas liquid reactors, *Ger. Chem. Eng.* **1**, 150
247. Steiff A., Weinspach P. M. (1982). *Ger. Chem. Eng.* **5**, 342, as cited by Kawase and Moo-Young (1989)
248. Stevenson R., Harrison S. T. L., Miles N., Cilliers J. (2006). Examination of swirling flow using electrical resistance tomography, *Powder Technology* **162**, 157-165
249. Strek, F. (1963). Heat transfer in liquid mixers, study of a turbine agitator with six flat blades, *International Chemical Engineering* **3**, 533
250. Strek, F. (1971). Mieszanie a Mieszalnik,. *Vyd. Nauk. Tech.*, Warsaw
251. Subbarao D., Taneja V. K. (1979). Three phase suspension in agitated vessels, *Proc. 3rd Eur. Conf. Mixing* **1**, 229
252. Sun H., Mao Z-S., Yu G. (2006). Experimental and numerical study of gas hold-up in surface aerated stirred tanks. *Chem. Eng Sci.* **61**, 4098 - 4110
253. Sun L., Hall L. D. (2001). An experimental solution of the Graetz problem in Heat Exchangers, *Int. Comm. Heat and Mass Trans.* **28**, 461
254. Tallerek U., Albert K., Bayer E., Guiochon G. (1996). Measurement of transverse and axial apparent dispersion coefficients in packed beds, *AIChE J.* **42**, 3041
255. Tapp H. S., Williams R. A. (2000). Status and application of microelectrical resistance tomography, *Chem. Eng. J.* **77**, 119-125
256. Toma, M. K., Ruklisha, M. P., Vanags, J. J., Zeltina, M. O., Leite, M. P., Galinina, N. I., Viesturs, U. E., Tengerdy, R. P. (1991). Inhibition of microbial growth and metabolism by excess turbulence, *Biotech. Bioeng.* **38**, 552-556.
257. Torma, A.E., Walden, C.C., Duncan D.W., Branion R.M.R. (1972). The effect of carbon dioxide and particle surface area on the microbiological leaching of a zinc sulphide concentrate, *Biotech. Bioeng.* **14**, 777
258. Uhl, V. W. and Gray J. B. (1966). *Mixing, Theory and Practice*, Vol. 1, Academic, New York
259. Ujhidy A., Németh J., Szépvölgyi J. (2003). Fluid flow in tubes with helical elements, *Chem. Eng. and Proc.* **42**, 1-7
260. Valk J., MacLean C., Algra P. R. (1985). *Basic principles of nuclear magnetic resonance imaging*, Elsevier, Amsterdam

261. Van Direndonck L. L., Fortuin J. M. H., Vanderboss D. (1968). Proc. 4th European Symp. Chemical Reaction Engineering, supplement to *Chem. Eng. Sci.* pp. 205, Pergamon Press, Oxford
262. Van Weert G., van der Werff D., Derksen J. J. (1995). Transfer of O_2 from air to mineral slurries in a Rushton turbine agitated tank, *Min. Eng.* **8**, 1109-1124
263. Vauhkonen M. (1997). Electrical impedance tomography and prior information, PhD thesis, Department of Applied Physics, University of Kuopio
264. Vauhkonen P. J., Vauhkonen M., Kaipio J. P. (2000). Errors due to the truncation of the computational domain in static three-dimensional electrical impedance tomography, *Phys. Meas.* **21**, 125-135
265. Vavasis S. (1996). Stable finite elements for problems with wild coefficients, *SIAM J. Numer. Anal.* **33**, 890 - 916
266. Veera U. P., Patwardhan A. W., Joshi J. B. (2001). Measurement of gas hold-up profiles in stirred tank reactors by gamma ray attenuation technique, *Trans IChemE* **79** (Part A), 684
267. Voit H., Mersmann A. (1986). General statement for the minimum stirrer speed during suspension, *Ger. Chem. Eng.* **9**, 101
268. Wang M., Dickin F. J., Williams R. A. (1995). Group-node technique as a means of handling large electrode surface, *Physio. Meas.* **16** (Su, 3A), 219-226
269. Wang M., Dorward A., Vlaev D., Mann R. (2000). Measurements of gas-liquid mixing in a stirred vessel using electrical resistance tomography (ERT), Chem. Eng. J. **77**, 93-98
270. Webster J. G. (1990). *Electrical Impedance Imaging*, The Adam Hilger Series on Biomedical Engineering, edited by J. G. Webster, Adam Hilger, New York
271. Westerterp K. R. (1963). *Chem. Eng. Sci.* **18**, 157
272. Whitman W. G. (1923). Preliminary experimental confirmation of the two-film theory of gas-absorption, *Chem. and Metalurg. Eng.* **29**, 146-148
273. Wichterle K. (1988). Conditions for suspension of solids in agitated vessels, *Chem. Eng. Sci.* **43**, 467
274. Wichterle K., Kadlec M., Zak L., Mitschka P. (1984). Shear rates on turbine impeller blades. *Chem. Eng. Commun.* **26**, 25-32
275. Wichterle K., Mitschka P., Hajek J., Zak L. (1988). Shear stress on the walls of vessels with axial impellers. *Chem. Eng. Res. Des.* **66**, 102-106
276. Wichterle, K. (1994). Heat transfer in agitated vessels, *Chem. Eng. Sci.* **49**, 1480-1483
277. Wichterle, K. Žák, L., Mitschka, P. (1985). Shear stress on the walls of agitated tanks, *Chem. Eng. Commun.* **32**, 153
278. Wilkinson A. J. (2005). Personal communication
279. Wilkinson A. J., Randall E. W., Cilliers J. J., Durrett D., Naidoo T., Long T. (2005). A 1000 frames/second ERT Data Capture System with Real Time Visualization, *IEEE J.* **5**, 300
280. Wilkinson A. J., Randall E. W., Long T. M., Collins A. (2006). The design of an ERT system for 3D data acquisition and a quantitative evaluation of performance. *Measurement Science and Technology* **17**, 2088-2096
281. Williams R. A. (2003). The impact of fundamental research on minerals processing operations of the future, *Proceedings XXII International Mineral Processing Congress*, 2- 13, Cape Town, South Africa, 29 Sept. – 3 Oct.
282. Williams R. A., Jia X., McKee S. L. (1996). Development of slurry mixing models using resistance tomography, *Powder Tech.* **87**, 21-27
283. Wood R. J. K., Jones T. F. (2003). Investigations of sand-water induce erosive wear of AISI 304L stainless steel pipes by pilot-scale and laboratory-scale testing, *Wear* **255**, 206-218
284. Wood R. J. K., Jones T. F., Miles N. J., Ganeshalingam J. (2001). Upstream swirl-induction for reduction of erosion damage from slurries in pipeline bends, *Wear* **250**, 770 -778

285. Xie W. (2002). Measurement and prediction of coalescence in flowing foams, PhD thesis, Department of Chemical Engineering, UMIST (now University of Manchester)
286. Yasunishi A., Fukuma M., Muroyama K. (1988). Wall-to-liquid mass transfer in packed fluidised beds with gas-liquid co-current upflow, *J. Chem. Eng. Japan* **21**, 522-528
287. York T. (2001). Status of electrical resistance tomography in industrial applications, *J. Electronic Imaging* **10**, 608-619
288. Yorkey T. J. (1986). Comparing reconstruction algorithms for electrical impedance tomography, PhD thesis, Department of Electrical and Computational Engineering, University of Wisconsin, as cited by Randall *et al.* (2001).
289. Zaharadník J., Mann R., Fialová M., Vlaev D., Vlaev S. D., Lossev V., Seichter P. (2001). A network-of-zones analysis of mixing and mass transfer in three industrial bioreactors, *Chem. Eng. Sci.* **56**, 485-492
290. Zehner P. (1986). Fluiddynamik beim Suspendieren im Rührbehälter, *Chem. Ing. Tech.* **58**, 830-831
291. Zehner P., Tebel K. H. (1984). Hydrodynamik beim Suspendieren in Rührbehälter, *Mischvorgänge*, Freising, as cited by Rieger and Ditl (1994)
292. Zienkiewicz O. C., Taylor R. L. (2000). *The finite element method. Volume 1: The Basis*, 5th Edition, Oxford, Butterworth-Heinemann
293. Zieverink M. M. P., Kreutzer M. T., Kapteijn F., Moulijn J. A. (2006). Gas-liquid mass transfer in bench-scale stirred tanks – fluid properties and critical impeller speed for gas induction. Report by Delft University of Technology, Reactor and Catalysis Engineering, Julianalaan 136, 2628 BL Delft, Netherlands
294. Zuidervaart E., Reuter M. A., Heerema R. H., Van Der Lans R. G. J. M., Derksen J. J. (2000). Effect of dissolved metal sulphates on gas-liquid oxygen transfer in agitated quartz and pyrite slurries, *Minerals Engineering* **13**, 1555-1564
295. Zwietering T. (1958). Suspending of solid particles in liquid by agitators, *Chem. Eng. Sci.* **8**, 244-253

APPENDICES

APPENDIX A	104-point ERT measurement sequence	A1
APPENDIX B	Matlab™ EIDORS code for 3D ERT	A2
APPENDIX C	Matlab™ code to average frames in ERT data set	A3
APPENDIX D	Matlab™ code to transpose data set	A4
APPENDIX E	Matlab™ code to interpolate between tomograms	A5
APPENDIX F	Radial concentration profiles for 10 % vol. fraction	A8
APPENDIX G	Sample calculation for N_{js}, Maxwell Eq. and Mixing Indices	A9
APPENDIX H	ERT impeller mesh (50 mm)	A11
APPENDIX I	ERT baffled mesh (50 mm)	A12
APPENDIX J	ERT baffled mesh (220 mm)	A13
APPENDIX K	Extended 182 point ERT measurement sequence	A14
APPENDIX L	Calculation procedure for 3D MRI data	A15
APPENDIX M	Calculation of air hold-up	A16
APPENDIX N	Yeast and Nylon axial concentration profile	A17
APPENDIX O	Calculation of the radial variation in disruption rate	A18

RAW DATA

APPENDIX P1-3	ERT 220 mm: 3 size fractions, 5 – 20 %, 5 speeds, Rushton
APPENDIX Q1-3	ERT 220 mm: 3 size fractions, 5 – 20 %, 5 speeds, pitched blade
APPENDIX R	Pipette sampling and conductivity probe data
APPENDIX S	ERT 50 mm: Suspension of 600 – 850 μm quartzite
APPENDIX T	ERT 50 mm: Ballotini and nylon suspension, MRI axial comparison
APPENDIX U1-4	MRI 50 mm: Axial and radial data for ballotini and nylon suspension
APPENDIX V	ERT 220 mm: Air data, and pilot scale data (609 mm tank)
APPENDIX W	Yeast and yeast/nylon ERT and MRI data (220 mm, 50 mm)

APPENDIX A

Initial measurement sequence for Hardware I

Table A1: Electrode excitation and measuring sequence for 16 electrode system containing 104 unique measurements (Barber *et al.*, 1983).

Excitation Pairs		Measured Pairs (via input Multiplexer)													Number of pairs
		1	2	3	4	5	6	7	8	9	10	11	12	13	
1	16	2-3	3-4	4-5	5-6	6-7	7-8	8-9	9-10	10-11	11-12	12-13	13-14	14-15	13
2	1	3-4	4-5	5-6	6-7	7-8	8-9	9-10	10-11	11-12	12-13	13-14	14-15	15-16	13
3	2	4-5	5-6	6-7	7-8	8-9	9-10	10-11	11-12	12-13	13-14	14-15	15-16		12
4	3	5-6	6-7	7-8	8-9	9-10	10-11	11-12	12-13	13-14	14-15	15-16			11
5	4	6-7	7-8	8-9	9-10	10-11	11-12	12-13	13-14	14-15	15-16				10
6	5	7-8	8-9	9-10	10-11	11-12	12-13	13-14	14-15	15-16					9
7	6	8-9	9-10	10-11	11-12	12-13	13-14	14-15	15-16						8
8	7	9-10	10-11	11-12	12-13	13-14	14-15	15-16							7
9	8	10-11	11-12	12-13	13-14	14-15	15-16								6
10	9	11-12	12-13	13-14	14-15	15-16									5
11	10	12-13	13-14	14-15	15-16										4
12	11	13-14	14-15	15-16											3
13	12	14-15	15-16												2
14	13	15-16													1
															104

APPENDIX B

EIDORS code to apply slicer_plot.m function

```
% 3D reconstruction with Eidors software
%  Ryan Stevenson

load nick.mat

A=input('load data file of empty tank: ','s');

q=load(A);

B=input('load data file of object in tank: ','s');
 r =load(B);

L=iso_f_smooth(simp,1);

lambda = input('What relaxation factor will you use: ');


% The solution matrix


      solution = ((J'*J)+lambda*(L'*L))\J'*(r-q);

            max_h=max(vtx(:,3))
           min_h=(vtx(:,3));
            minheight=min(min_h);
             display(minheight)

      % slicer plot

       load edges.mat
         h=input('Height of desired solution: ');

  [fc]=slicer_plot(h,solution,vtx,simp,fc);
```

These functions were obtained from the EIDORS website and used in the above code:

slicer_plot.m
db23d.m
solution_ext.m
jacobian_3d_comp.m
jacobian_3d.m
iso_s_smooth.m
iso_f_smooth.m
edges.mat
delfix.m

Nick.mat (2 x 8 electrode layer model coherent with *ERT system I* created separately by Nick Polydorides for this experiment)

APPENDIX C

A function file was created for averaging the data sets prior to reconstruction

```
function [v_raw] = LoadDataFrame(infilename, outfilename)

 % Open the file
fid = fopen(infilename, 'rb');

if fid == -1
      errordlg('File not found','ERROR')
      return;
end

no_of_layers = fread(fid, 1, 'uint32');
frame_size = fread(fid, 1, 'uint32');
frame_no = fread(fid, 1, 'uint32');

v_raw = [];
while feof(fid)==0
    v_raw = [v_raw; fread(fid, frame_size*no_of_layers, 'float64')'];
    frame_no = fread(fid, 1, 'uint32');
end

v_raw = mean(v_raw);
fclose(fid);

% Open the file
fid = fopen(outfilename, 'wb');

if fid == -1
      errordlg('File not found','ERROR')
      return;
end

fwrite(fid, no_of_layers, 'uint32');
fwrite(fid, frame_size, 'uint32');

frame_no = 1;
fwrite(fid, frame_no, 'uint32');
fwrite(fid, v_raw, 'float64');
frame_no = 2;
fwrite(fid, frame_no, 'uint32');
fwrite(fid, v_raw, 'float64');
frame_no = 3;
fwrite(fid, frame_no, 'uint32');
fwrite(fid, v_raw, 'float64');
frame_no = 4;
fwrite(fid, frame_no, 'uint32');
fwrite(fid, v_raw, 'float64');
fclose(fid);
```

On Matlab™ command line:

e.g. avedataframe = LoadDataFrame('C:\UCT Tomography\345 rpm 4 layer 5 % ballotini.tom', 'temp');

APPENDIX D

A function file was created for transposing the .csv file to allow examination in Excel

```
[filename path] = uigetfile({'*.csv','CSV files'},'Select Input CSV File');
if filename ~= 0
    M = csvread([path filename]);
    [p d] = size(M);

    fprintf('Transposing...');
    M = M';

    [filename path] = uiputfile({'*.csv', 'CSV files'}, 'Specify Output CSV
File');
    if filename ~= 0
        csvwrite([path filename], M);
    end
end
```

APPENDIX E

Program displaying four tomograms and interpolating into a 3D surface

```
 % 3D reconstruction from 2D slices

R=input('load first data file: ','s');                    % load first array

f=load(R);

   x=f(:,1);
   y=f(:,2);
   v=f(:,3);

    xx=min(x):(max(x)-min(x))/100:max(x);
    yy=min(y):(max(y)-min(y))/100:max(y);

  [XX1,YY1]=meshgrid(xx,yy);

    VV1=griddata(x,y,v,XX1,YY1);

    figure(1)

    surf(XX1,YY1,VV1);
    shading interp
    colorbar



Q=input('load second data file: ','s');          % load 2nd array

g=load(Q);

   a=g(:,1);
   b=g(:,2);
   c=g(:,3);

    aa=min(a):(max(a)-min(a))/100:max(a);
    bb=min(b):(max(b)-min(b))/100:max(b);

  [XX2,YY2]=meshgrid(aa,bb);

    VV2=griddata(a,b,c,XX2,YY2);

    figure(2)

    surf(XX2,YY2,VV2);
    shading interp
    colorbar



   T=input('load third data file: ','s');           % load 3rd array
```

```
h=load(T);

   d=h(:,1);
   e=h(:,2);
   f=h(:,3);

    dd=min(d):(max(d)-min(d))/100:max(d);
    ee=min(e):(max(e)-min(e))/100:max(e);

  [XX3,YY3]=meshgrid(dd,ee);

    VV3=griddata(d,e,f,XX3,YY3);

    figure(3)

    surf(XX3,YY3,VV3);
    shading interp
    colorbar


U=input('load fourth data file: ','s');          % load 4th array

j=load(U);

   g=j(:,1);
   h=j(:,2);
   i=j(:,3);

    gg=min(g):(max(g)-min(g))/100:max(g);
    hh=min(h):(max(h)-min(h))/100:max(h);

  [XX4,YY4]=meshgrid(gg,hh);

    VV4=griddata(g,h,i,XX4,YY4);

    figure(4)

    surf(XX4,YY4,VV4);
    shading interp
    colorbar

 ZZ1=ones(101)*0;
 ZZ2=ones(101)*2/3;
 ZZ3=ones(101)*4/3;
 ZZ4=ones(101)*2;

 ZZ=zeros(101,101,4);
 XX=zeros(101,101,4);
 YY=zeros(101,101,4);
 VV=zeros(101,101,4);

 ZZ(:,:,1)=ZZ1;
 XX(:,:,1)=XX1;
 YY(:,:,1)=YY1;
 VV(:,:,1)=VV1;

 ZZ(:,:,2)=ZZ2;
```

```
XX(:,:,2)=XX2;
YY(:,:,2)=YY2;
VV(:,:,2)=VV2;

ZZ(:,:,3)=ZZ3;
XX(:,:,3)=XX3;
YY(:,:,3)=YY3;
VV(:,:,3)=VV3;

ZZ(:,:,4)=ZZ4;
XX(:,:,4)=XX4;
YY(:,:,4)=YY4;
VV(:,:,4)=VV4;

Znew=zeros(101,101,101);
Xnew=zeros(101,101,101);
Ynew=zeros(101,101,101);

for N = 1:101,
   ZN=ones(101)*2*(N-1)/(101-1);
   XN=XX1;
   YN=YY1;

   Znew(:,:,N)=ZN;
   Xnew(:,:,N)=XN;
   Ynew(:,:,N)=YN;
 end

 Vnew=interp3(XX,YY,ZZ,VV,Xnew,Ynew,Znew);  %Matlab interpolation function

 q=input('Choose a surface threshold value: ');

 figure(5)
 clf
  isosurface(Xnew,Ynew,Znew,Vnew,q);
    light
```

APPENDIX F

Radial Concentration Profiles for 10 % volume fraction (Rushton)

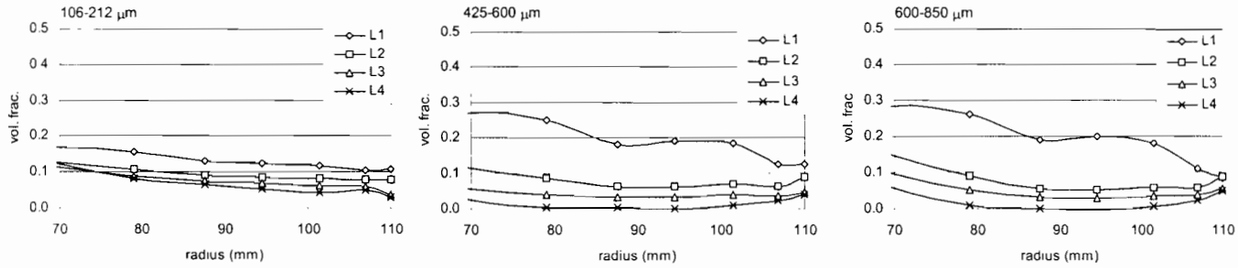


Figure F1: Radial concentration profiles for 10 % solids volume fraction at 236 rpm

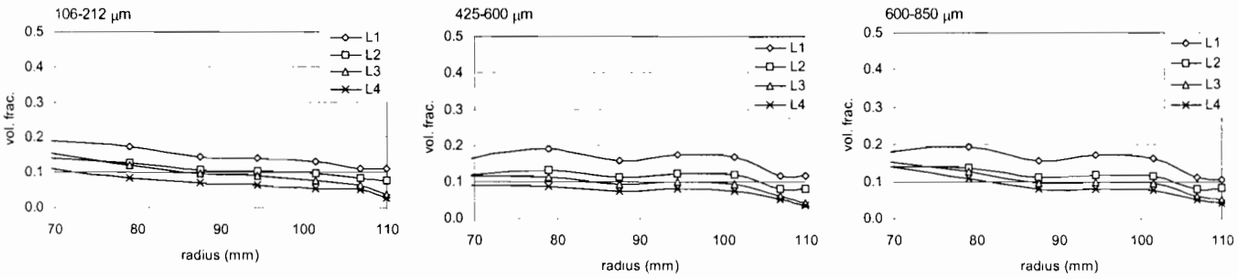


Figure F2: Radial concentration profiles for 10 % solids volume fraction at 547 rpm

Radial Concentration Profiles for 10 % volume fraction (Pitched Blade)

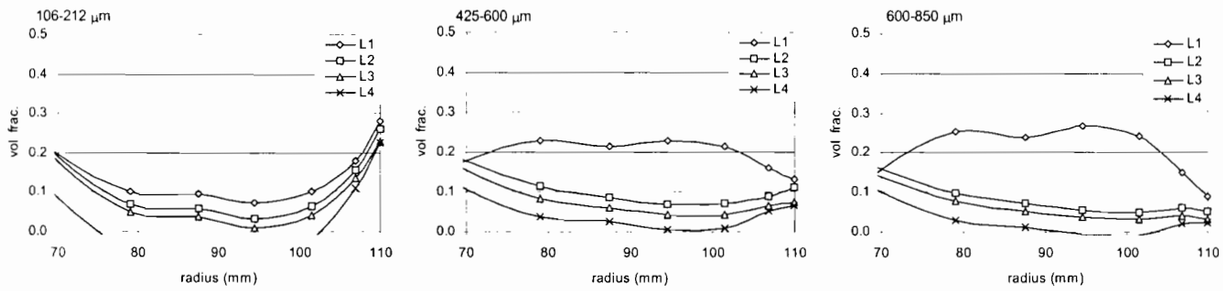


Figure F3: Radial concentration profiles for 10 % solids volume fraction at 236 rpm

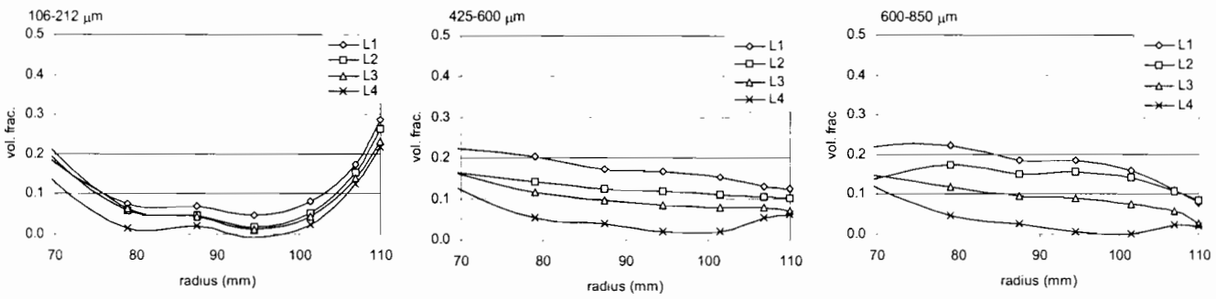


Figure F4: Radial concentration profiles for 10 % solids volume fraction at 547 rpm

APPENDIX G

Sample Calculations for N_{js}, Maxwell Eq. and Mixing Index

Critical Suspension Speed

The Zwietering equation for critical suspension speed:

$$N_{js} = s_1 \nu^{0.1} \left(\frac{g\Delta\rho}{\rho_L} \right)^{0.45} d_p^{0.2} X^{0.13} D^{-0.85} \qquad (2.27)$$

e.g. The N_{js} of 600- 850 μm silica, 15 % vol., Rushton impeller ?

for the 6-bladed Rushton s_1 is 4 (Zwietering, 1958)
the kinematic viscosity, ν is μ/ρ = 0.001 kg.m^{-1}.s^{-1}/1000 kg.m^{-3}
the gravitational constant is 9.81 m.s^{-2}
$\Delta\rho$ is the difference between solid and liquid densities = 2650 – 1000 = 1650 kg.m^{-3}
ρ_L is the liquid density = 1000 kg.m^{-3}
d_p is the particle diameter, the mean diameter was used = 857 μm

X is the amount of solids per liquid as a mass percent = f*V*ρ_S / ((1-f)*V*ρ_L)*100
Where f is the volume fraction, ρ_S is the particle density and V is the reactor volume
= (0.15)*8.363*(2650/1000) / ((1-0.15)*8.363*(1000/1000))*100 % = 47.8 %

D is the stirrer length = 0.11 m

Inserting all of these values into Equation 2.27 results in a N_{js} of 552 rpm

The '*s*' constant for the pitched blade impeller was obtained from Armenante and Nagamine (1998) and is equal to 5.

The Maxwell Equation

From equation 2.13:

$$\alpha = \frac{2\sigma_w - 2\sigma_m}{\sigma_m + 2\sigma_w}$$

where α is the local solids volume fraction, σ_m is the measured conductivity and σ_w is the conductivity of the continuous water, or pure liquid phase.

E.g. Measured conductivity = 400 μS.cm^{-1}, liquid phase conductivity (prior to solid addition, or a clear section of the slurry) = 460 μS.cm^{-1}.

Inserting values into Equation 2.13 yields a solid volume fraction of 0.091 or 9.1 %

Mixing Indices

$\overline{MI}_z$ is the average standard deviation of the volume fractions in the radial direction of the reactor for the four electrode layers. $\overline{MI}_r$ is the average standard deviation of the volume fractions in the axial direction of the reactor for the four electrode layers.

The overall mixing index is given by: MI = $\overline{MI}_z$*1.000*$\overline{MI}_r$*1.875

e.g. Mixing Index of 5 % 106-212 μm silica with Rushton impeller at 236 rpm

Radial position

Electrode layers

Std. dev of vol. fractions in the axial direction (i.e. row data) **(A)**

mm	1	2	3	4	STDEV	
70	0.123	0.086	0.089	0.091	0.017	
79	0.101	0.061	0.047	0.045	0.026	
88	0.071	0.039	0.021	0.019	0.024	
95	0.066	0.033	0.013	0.007	0.027	
101	0.056	0.027	0.002	0.000	0.026	
107	0.041	0.019	0.000	0.000	0.019	
110	0.039	0.011	0.000	0.000	0.019	
					0.023	MI_r
STDEV	0.0310	0.0260	0.0329	0.0342	0.031	MI_z

Average of these **(A)** std. deviations = $\overline{MI}_r$

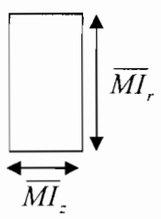
Std. deviations of vol. fraction data in the radial direction (i.e. column data) **(B)**

Average of these **(B)** std. deviations = $\overline{MI}_z$

Calculation of Weighting Factors

The weights were calculated to relate the geometry of the vessel to the mixing indices ($\overline{MI}_z$, $\overline{MI}_r$) and s

The four electrode layers from L1 to L4 correspond to a vertical distance of 15 cm, thus $\overline{MI}_r$ will be related to this distance. The seven radial data points relate to 4 cm on either side of the tank. Since a 2D approach to homogeneity is being considered both sides of the tank are considered, thus $\overline{MI}_z$ is for 8 cm in the radial direction. Weighting these distances, leaves a factor of 15/8 or 1.875 for $\overline{MI}_r$ due to this mixing index accounting for a greater distance. Multiplying these mixing indices and the corresponding weights thus corresponds to a 2D area of homogeneity and the overall mixing index of 0.0013.



APPENDIX H

Converting conductivities into radial profiles for impeller mesh

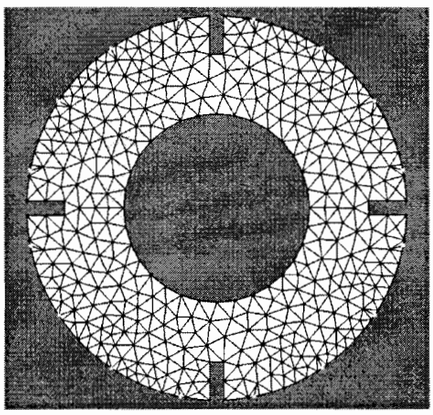


Figure H1: Irregular mesh (788 elements) to accommodate D/2 impeller. Radial subdivisions extends from r/R = 0.6 to 1.00

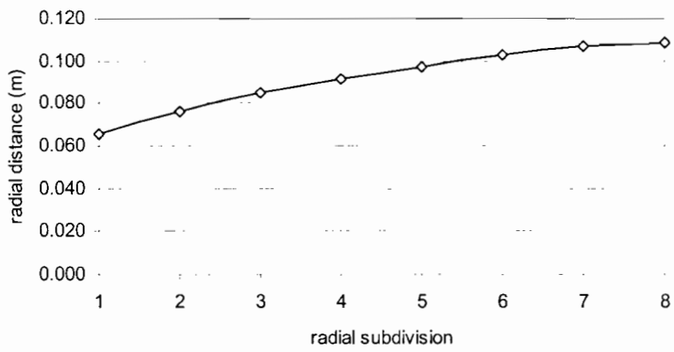


Figure H2: The 8 radial subdivisions for the above mesh. Note that subdivisions decrease in radial distance to account for the smaller elements at the mesh perimeter.

Note: All the conductivities present in each subdivision were averaged and then converted to a volume fraction using the Maxwell equation.

APPENDIX I

Converting conductivities into radial profiles for baffled mesh (50 mm tank)

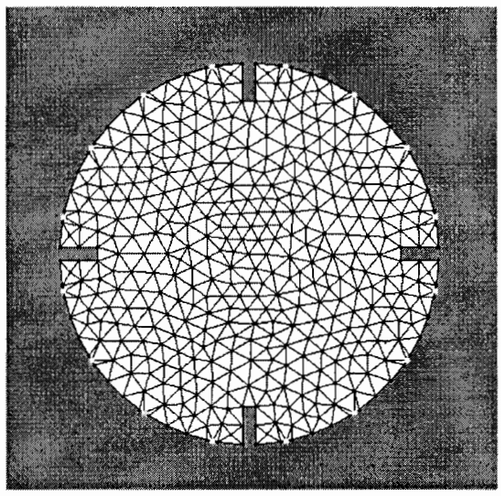


Figure J1: Irregular mesh (764 elements) only accommodating the baffles for the 50 mm ID tank. Radial subdivisions extend from 0.0054 to 0.05 m. Information was analysed from r/R = 0.55 to 1.00.

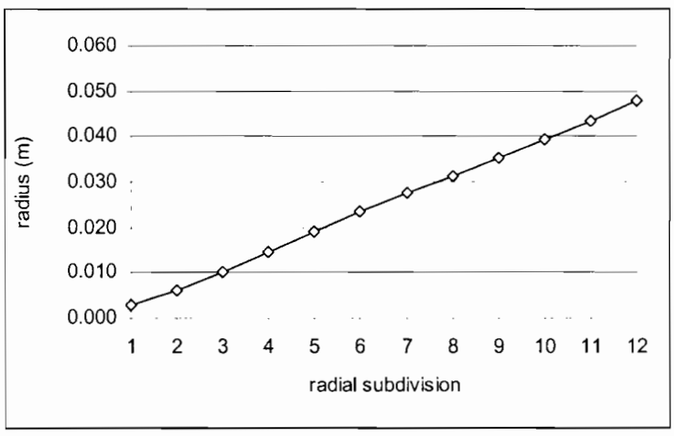


Figure J2: The 12 radial subdivisions for the above mesh. There was not much difference between the sizes of the elements in this mesh thus subdivisions are nearly equal.

Note: All the conductivities present in each subdivision were averaged and then converted to a volume fraction using the Maxwell equation.

APPENDIX J

Converting conductivities into radial profiles for baffled mesh (220 mm tank)

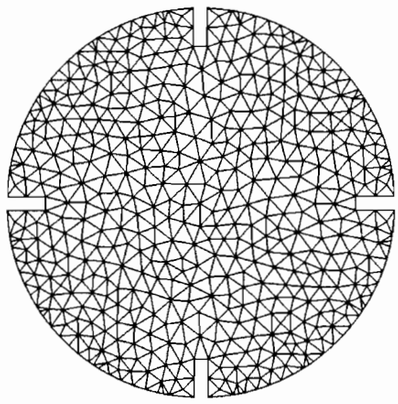


Figure I1: Irregular mesh (934 elements) only accommodating the baffles. Radial subdivisions extend from 0.007 to 0.110 m. Information was analysed from r/R = 0.55 to 1.

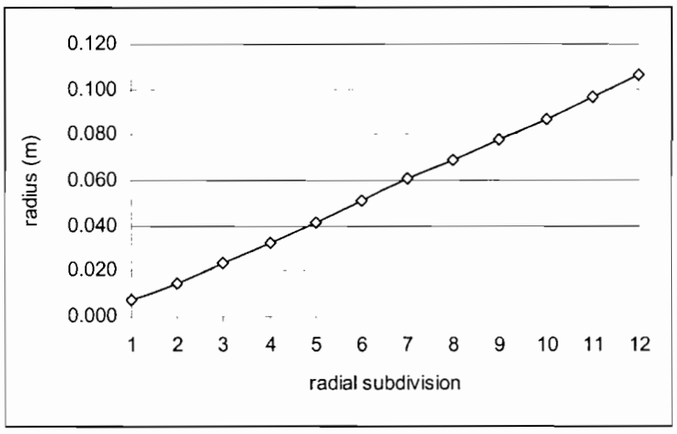


Figure I2: The 12 radial subdivisions for the above mesh. There was not much difference between the sizes of the elements in this mesh thus subdivisions are nearly equal.

Note: All the conductivities present in each subdivision were averaged and then converted to a volume fraction using the Maxwell equation.

APPENDIX K

Extended 182 point measurement sequence (Hardware I)

Table K1: Electrode excitation and measuring sequence for 16 electrode system containing 182 measurements.

Excitation Pairs		Measured Pairs (via input Multiplexer)													Number of pairs
		1	2	3	4	5	6	7	8	9	10	11	12	13	
1	16	2-3	3-4	4-5	5-6	6-7	7-8	8-9	9-10	10-11	11-12	12-13	13-14	14-15	13
2	1	3-4	4-5	5-6	6-7	7-8	8-9	9-10	10-11	11-12	12-13	13-14	14-15	15-16	26
3	2	4-5	5-6	6-7	7-8	8-9	9-10	10-11	11-12	12-13	13-14	14-15	15-16	16-1	39
4	3	5-6	6-7	7-8	8-9	9-10	10-11	11-12	12-13	13-14	14-15	15-16	16-1	**1-2**	52
5	4	6-7	7-8	8-9	9-10	10-11	11-12	12-13	13-14	14-15	15-16	16-1	**1-2**	2-3	65
6	5	7-8	8-9	9-10	10-11	11-12	12-13	13-14	14-15	15-16	16-1	**1-2**	2-3	3-4	78
7	6	8-9	9-10	10-11	11-12	12-13	13-14	14-15	15-16	16-1	**1-2**	2-3	3-4	4-5	91
8	7	9-10	10-11	11-12	12-13	13-14	14-15	15-16	16-1	**1-2**	2-3	3-4	4-5	5-6	104
9	8	10-11	11-12	12-13	13-14	14-15	15-16	16-1	**1-2**	2-3	3-4	4-5	5-6	6-7	117
10	9	11-12	12-13	13-14	14-15	15-16	16-1	**1-2**	2-3	3-4	4-5	5-6	6-7	7-8	130
11	10	12-13	13-14	14-15	15-16	16-1	**1-2**	2-3	3-4	4-5	5-6	6-7	7-8	8-9	143
12	11	13-14	14-15	15-16	16-1	**1-2**	2-3	3-4	4-5	5-6	6-7	7-8	8-9	9-10	156
13	12	14-15	15-16	16-1	**1-2**	2-3	3-4	4-5	5-6	6-7	7-8	8-9	9-10	10-11	169
14	13	15-16	16-1	**1-2**	2-3	3-4	4-5	5-6	6-7	7-8	8-9	9-10	10-11	11-12	182

APPENDIX L

Calculation procedure for 3D MRI data

A radial profile is obtained from taking information across the widest point (Figure L1 (a)), thus it is not the average radial concentration, but radial symmetry is assumed. This point was not behind or in front of a baffle. The average x-direction concentration was obtained through averaging the values in each column (Figure L1 (b)). The axial concentration profile was obtained through averaging all the column values (Figure L1 (c)) to yield an average concentration for each z. The 5 % suspension of 50 μm ballotini 3D experiment had a 32 x 32 x 32 grid, while the rest of the 3D experiments had a 64 x 64 x 64 grid.

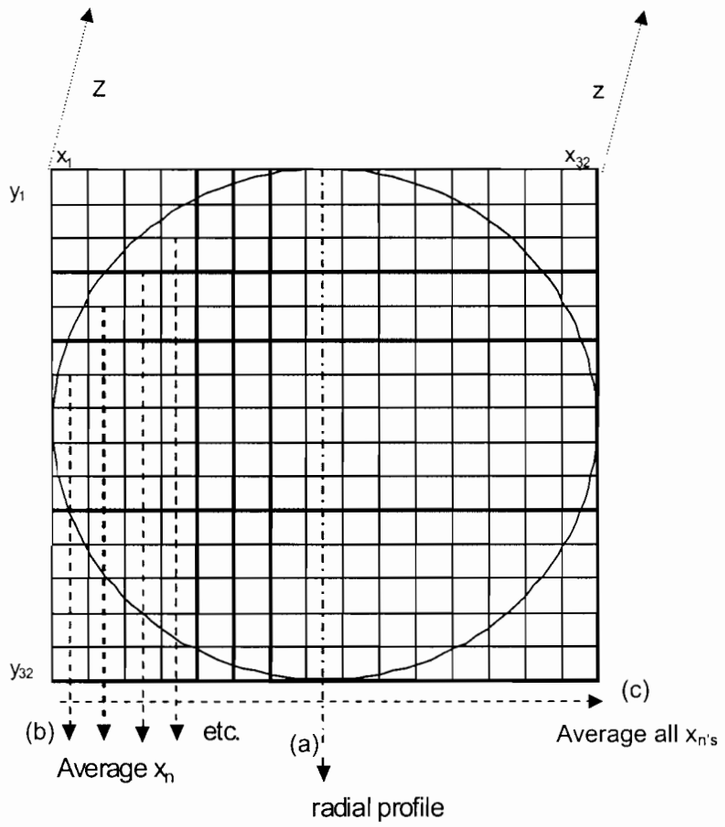


Figure L1: 3D MRI calculation procedure

APPENDIX M

Calculation of the average volume fraction of air from the observed holdup

220 mm ID tank

cross sec. area **tank vol.** 8363 ml

	tank	380.133	cm^2
less	shaft	0.317	cm^2
	baffles	6.160	cm^2
		373.656	cm^2

	height in cm (holdup)		holdup volume		0.5 vvm	1.0 vvm
rpm	*0.5 vvm*	*1.0 vvm*	*0.5 vvm (ml)*	*1.0 vvm (ml)*	vol frac	vol frac
236	0.6	0.7	224	262	0.027	0.031
304	0.7	1.0	262	374	0.031	0.045
353	0.9	1.1	336	411	0.040	0.049
460	1.3	1.4	486	523	0.058	0.063
547	1.7	1.7	635	635	0.076	0.076

APPENDIX N

The examination of yeast and nylon

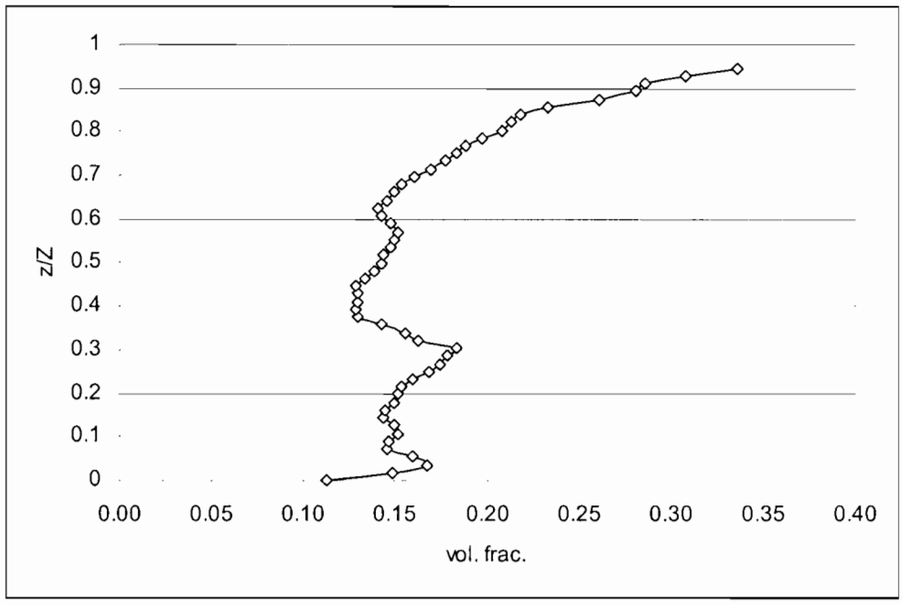


Figure N1: Axial concentration profile of 10 % nylon and 5 % yeast generated from 3D MRI data.

APPENDIX O

Calculation of the radial variation in disruption rate for the 600 – 850 μm fraction

Table O1: Calculation of radial variation in k with the Rushton impeller

Volume fraction	0.0500	0.1500
Average MI_z for 236 and 547 rpm	0.0275	0.0485
lower limit volume fraction	0.0225	0.1015
upper limit volume fraction	0.0775	0.1985
% variation in k (lower limit)	73.01	47.30
% variation in k (upper limit)	105.18	58.32

$$\text{Percent variation} = \frac{(\text{volume fraction}^{1.64} \text{ less upper/lower limit}^{1.64})}{(\text{volume fraction}^{1.64})} \times 100$$

APPENDIX P1

Hardware I, Reconstruction Code III, 220 mm vessel
Volume fractions for the 106 -212 μm size fraction with the Rushton impeller

5 %	236 rpm				
r/R	1	2	3	4	Average
0.63	0 123	0.086	0.089	0.091	0 097
0.72	0 101	0 061	0.047	0.045	0.064
0.80	0 071	0 039	0.021	0.019	0 038
0 86	0 066	0.033	0.013	0 007	0 030
0.92	0.056	0.027	0 002	0.000	0.021
0 97	0 041	0 019	0 000	0 000	0.015
1.00	0.039	0.011	0 000	0.000	0.013
Average	0.071	0.039	0 025	0 023	

5 %	304 rpm				
r/R	1	2	3	4	Average
0.63	0 117	0.083	0.091	0 097	0 097
0 72	0.096	0.058	0 049	0 052	0 064
0.80	0 067	0.037	0.023	0.025	0 038
0.86	0 063	0 031	0.014	0.014	0 031
0.92	0 054	0 025	0 003	0 000	0 020
0 97	0 039	0.017	0 000	0 000	0 014
1.00	0 038	0 008	0 000	0.000	0.012
Average	0.068	0 037	0 026	0.027	

5 %	353 rpm				
r/R	1	2	3	4	Average
0 63	0.115	0.083	0.094	0.095	0 097
0 72	0.094	0.057	0.051	0.057	0 065
0 80	0.067	0 036	0 024	0 031	0 039
0.86	0.063	0 030	0.015	0 022	0 033
0.92	0.054	0 024	0 004	0 007	0.022
0.97	0.039	0 016	0 000	0 000	0.014
1.00	0 038	0.007	0 000	0.000	0 011
Average	0.067	0.036	0.027	0.030	

5 %	460 rpm				
r/R	1	2	3	4	Average
0.63	0 121	0.093	0 101	0 083	0.100
0.72	0 105	0.070	0 062	0 048	0 071
0.80	0.076	0.047	0 034	0 026	0 046
0 86	0.073	0.041	0 026	0 018	0 040
0 92	0.062	0 033	0 013	0.004	0.028
0 97	0.043	0.020	0 000	0 000	0.016
1.00	0 037	0 006	0.000	0.000	0 011
Average	0.074	0 044	0 034	0 025	

5 %	547 rpm				
r/R	1	2	3	4	Average
0 63	0 127	0 100	0 106	0.071	0.101
0 72	0 115	0 082	0.073	0.038	0.077
0 80	0 085	0 057	0 044	0 020	0.052
0.86	0 083	0.053	0.038	0 013	0 047
0.92	0 071	0.042	0.023	0 000	0 034
0.97	0 046	0 024	0.004	0 000	0 019
1.00	0.037	0 006	0.000	0 000	0 011
Average	0.081	0.052	0 041	0 020	

10 %	236 rpm				
r/R	1	2	3	4	Average
0 63	0.170	0.127	0.114	0 123	0 134
0.72	0 154	0 106	0 087	0.081	0 107
0.80	0.129	0 090	0.074	0.064	0 089
0 86	0.125	0.085	0.068	0.052	0.082
0.92	0.118	0.081	0.061	0.042	0.075
0 97	0.103	0.078	0.057	0.047	0.071
1.00	0.109	0.078	0.037	0.028	0.063
Average	0.130	0.092	0.071	0.062	

10 %	304 rpm				
r/R	1	2	3	4	Average
0.63	0 170	0.131	0.126	0.128	0.139
0.72	0.153	0.108	0.095	0.089	0 111
0.80	0.128	0.091	0.077	0.071	0 092
0.86	0.124	0.085	0.070	0.060	0.085
0.92	0.117	0.082	0.062	0.050	0.078
0.97	0.103	0.078	0.058	0.051	0.072
1.00	0.109	0.078	0.038	0.028	0.063
Average	0 129	0.093	0.075	0.068	

10 %	353 rpm				
r/R	1	2	3	4	Average
0 63	0.172	0.132	0.135	0 130	0 142
0.72	0.153	0.109	0.100	0.093	0 114
0 80	0.127	0 092	0.079	0.074	0 093
0.86	0.123	0.086	0.071	0 064	0.086
0.92	0.117	0.082	0.063	0 053	0 079
0.97	0.103	0.079	0.058	0.052	0.073
1.00	0.109	0.079	0 039	0.029	0.064
Average	0 129	0 094	0 078	0.071	

10 %	460 rpm				
r/R	1	2	3	4	Average
0.63	0.178	0.138	0.144	0.124	0.146
0.72	0.162	0.118	0 110	0.095	0.121
0.80	0.135	0.100	0.087	0 079	0 100
0.86	0.131	0.095	0.080	0.072	0.095
0.92	0 123	0.090	0.070	0.060	0.086
0.97	0.106	0.082	0.061	0.055	0.076
1.00	0 109	0.079	0.038	0.029	0.064
Average	0 135	0.100	0 084	0 073	

10 %	547 rpm				
r/R	1	2	3	4	Average
0.63	0 190	0.142	0 153	0.111	0.149
0.72	0 175	0.127	0 121	0.083	0.126
0.80	0.144	0.108	0 096	0.071	0.105
0.86	0.141	0.104	0 089	0.064	0 100
0.92	0.132	0.097	0.078	0.053	0 090
0.97	0.110	0.085	0.064	0.052	0.078
1.00	0.111	0.077	0.038	0.027	0.063
Average	0.143	0.106	0.091	0 066	

15 %	236 rpm				
r/R	1	2	3	4	Average
0 63	0.233	0.174	0.162	0.160	0.182
0.72	0.219	0.162	0.143	0.123	0.162
0 80	0.192	0.150	0.133	0.112	0.146
0 86	0.189	0.146	0.128	0.100	0.141
0.92	0.181	0.142	0.120	0.091	0 134
0 97	0 161	0.135	0.114	0.099	0 127
1.00	0.166	0.134	0.094	0.082	0.119
Average	0 191	0.149	0.128	0 110	

15 %	304 rpm				
r/R	1	2	3	4	Average
0 63	0.229	0 177	0.177	0.171	0.188
0.72	0 216	0 164	0.151	0.133	0 166
0 80	0.190	0.151	0 136	0.119	0.149
0 86	0.187	0.146	0.130	0.107	0 142
0 92	0.179	0.142	0.121	0.097	0 135
0.97	0.161	0.135	0 114	0 102	0 128
1.00	0.166	0.135	0.095	0.083	0 120
Average	0 190	0 150	0.132	0 116	

15 %	353 rpm				
r/R	1	2	3	4	Average
0.63	0 232	0.182	0.187	0.180	0 195
0.72	0.215	0.165	0.156	0 143	0 170
0.80	0.189	0.151	0.138	0 126	0 151
0.86	0 186	0.146	0.131	0 115	0 144
0 92	0.178	0.142	0 122	0 105	0 137
0 97	0.160	0 135	0.115	0 105	0 129
1 00	0.167	0 135	0.096	0.086	0 121
Average	0.190	0 151	0 135	0 123	

15 %	460 rpm				
r/R	1	2	3	4	Average
0.63	0.234	0.185	0.197	0.173	0.197
0.72	0 218	0 170	0 164	0 142	0 174
0 80	0.191	0 155	0.143	0 129	0 154
0 86	0.188	0 150	0 135	0 120	0 148
0.92	0.180	0 145	0 126	0 109	0 140
0.97	0.161	0.137	0 116	0 107	0 130
1.00	0 166	0.135	0 096	0 085	0 121
Average	0 191	0 154	0.140	0 124	

15 %	547 rpm				
r/R	1	2	3	4	Average
0 63	0.238	0 189	0 203	0 179	0 202
0.72	0.223	0.175	0 170	0 149	0.179
0.80	0.196	0.159	0 147	0 133	0.159
0.86	0.193	0.155	0 140	0 125	0.153
0.92	0 184	0 150	0 130	0 113	0.144
0.97	0 163	0 139	0 118	0 109	0 132
1 00	0 166	0 136	0.096	0 084	0.120
Average	0 195	0 157	0 143	0.127	

20 %	236 rpm				
r/R	1	2	3	4	Average
0.63	0.264	0.165	0 171	0 253	0.213
0 72	0 325	0.242	0 227	0 263	0 265
0 80	0.273	0.225	0 206	0 214	0.230
0.86	0.291	0 244	0 221	0 217	0.243
0.92	0 256	0 217	0 189	0.178	0 210
0 97	0 162	0 135	0 109	0 103	0.127
1.00	0 102	0 075	0 033	0 027	0.059
Average	0.239	0 186	0.165	0.179	

20 %	304 rpm				
r/R	1	2	3	4	Average
0 63	0 257	0 172	0.185	0.264	0 219
0 72	0 320	0.246	0.235	0.276	0 269
0 80	0 270	0 227	0.210	0.224	0.233
0 86	0.289	0.246	0.224	0.229	0 247
0 92	0.255	0 218	0.191	0.189	0 213
0 97	0.162	0.136	0 110	0.108	0 129
1 00	0 102	0 076	0 035	0 029	0 060
Average	0.237	0.189	0 170	0.188	

20 %	353 rpm				
r/R	1	2	3	4	Average
0 63	0 258	0.176	0 192	0 271	0 224
0 72	0 318	0.248	0 239	0 283	0 272
0.80	0.269	0 227	0.211	0 230	0.234
0.86	0.287	0 246	0.225	0 236	0 249
0 92	0.253	0.218	0.192	0 196	0 215
0.97	0.161	0.136	0 111	0 112	0 130
1.00	0 103	0 076	0.036	0 031	0 062
Average	0 236	0.190	0.172	0 194	

20 %	460 rpm				
r/R	1	2	3	4	Average
0.63	0.260	0.180	0 200	0 268	0.227
0.72	0.321	0.254	0.247	0 288	0 277
0.80	0.271	0.232	0.217	0 235	0.239
0.86	0 290	0.251	0 231	0 244	0.254
0.92	0.256	0.222	0 197	0 203	0 219
0.97	0.162	0.138	0 113	0 115	0.132
1 00	0 102	0 077	0 036	0 031	0.062
Average	0.237	0 193	0.177	0.198	

20 %	547 rpm				
r/R	1	2	3	4	Average
0 63	0.266	0 185	0 185	0 268	0 226
0.72	0.326	0 259	0 259	0 290	0 284
0.80	0 274	0 236	0.236	0 237	0 246
0 86	0 293	0 255	0 255	0 247	0 263
0.92	0.258	0.226	0 226	0 205	0.228
0.97	0.163	0 139	0 139	0.116	0.139
1 00	0 102	0.077	0.077	0.031	0 072
Average	0 240	0.197	0 197	0 199	

APPENDIX P2

Hardware I, Reconstruction Code III, 220 mm vessel
Volume fractions for the 425 -600 μm size fraction with the Rushton impeller

5 %	236 rpm				
r/R	1	2	3	4	Average
0.63	0.174	0.084	0.041	0.012	0.078
0.72	0.134	0.048	0.010	0.000	0.048
0.80	0.094	0.033	0.006	0.000	0.033
0.86	0.094	0.031	0.004	0.000	0.032
0.92	0.101	0.045	0.017	0.000	0.041
0.97	0.091	0.054	0.030	0.016	0.048
1.00	0.135	0.096	0.055	0.047	0.083
Average	0.118	0.056	0.023	0.011	

5 %	304 rpm				
r/R	1	2	3	4	Average
0.63	0.086	0.048	0.020	0.075	0.057
0.72	0.058	0.021	0.000	0.047	0.031
0.80	0.043	0.016	0.000	0.035	0.023
0.86	0.043	0.015	0.000	0.034	0.023
0.92	0.054	0.026	0.000	0.045	0.032
0.97	0.057	0.034	0.020	0.050	0.040
1.00	0.091	0.053	0.046	0.080	0.068
Average	0.062	0.030	0.012	0.052	

5 %	353 rpm				
r/R	1	2	3	4	Average
0.63	0.133	0.090	0.060	0.026	0.077
0.72	0.121	0.068	0.034	0.000	0.056
0.80	0.096	0.053	0.026	0.000	0.044
0.86	0.101	0.054	0.026	0.000	0.045
0.92	0.108	0.063	0.035	0.008	0.053
0.97	0.092	0.060	0.036	0.024	0.053
1.00	0.128	0.089	0.050	0.044	0.078
Average	0.111	0.068	0.038	0.015	

5 %	460 rpm				
r/R	1	2	3	4	Average
0.63	0.132	0.095	0.080	0.030	0.084
0.72	0.125	0.077	0.052	0.008	0.066
0.80	0.100	0.061	0.038	0.010	0.052
0.86	0.107	0.063	0.038	0.009	0.054
0.92	0.112	0.071	0.044	0.019	0.061
0.97	0.094	0.063	0.040	0.029	0.057
1.00	0.127	0.088	0.050	0.044	0.077
Average	0.114	0.074	0.049	0.021	

5 %	547 rpm				
r/R	1	2	3	4	Average
0.63	0.135	0.103	0.097	0.029	0.091
0.72	0.132	0.087	0.069	0.014	0.075
0.80	0.107	0.069	0.051	0.016	0.061
0.86	0.114	0.072	0.051	0.017	0.064
0.92	0.118	0.078	0.055	0.025	0.069
0.97	0.097	0.066	0.045	0.032	0.060
1.00	0.127	0.088	0.051	0.043	0.077
Average	0.119	0.080	0.060	0.025	

10 %	236 rpm				
r/R	1	2	3	4	Average
0.63	0.271	0.115	0.057	0.028	0.118
0.72	0.251	0.086	0.038	0.003	0.094
0.80	0.181	0.064	0.032	0.003	0.070
0.86	0.192	0.064	0.033	0.000	0.072
0.92	0.183	0.070	0.040	0.009	0.076
0.97	0.125	0.063	0.038	0.023	0.062
1.00	0.126	0.090	0.046	0.038	0.075
Average	0.190	0.079	0.041	0.015	

10 %	304 rpm				
r/R	1	2	3	4	Average
0.63	0.076	0.111	0.069	0.048	0.076
0.72	0.088	0.102	0.060	0.026	0.069
0.80	0.081	0.083	0.052	0.022	0.060
0.86	0.089	0.088	0.056	0.020	0.063
0.92	0.085	0.091	0.059	0.025	0.065
0.97	0.056	0.071	0.044	0.029	0.050
1.00	0.040	0.084	0.042	0.037	0.051
Average	0.073	0.090	0.055	0.030	

10 %	353 rpm				
r/R	1	2	3	4	Average
0.63	0.178	0.108	0.083	0.070	0.110
0.72	0.187	0.113	0.077	0.052	0.107
0.80	0.150	0.096	0.066	0.043	0.089
0.86	0.163	0.105	0.071	0.043	0.095
0.92	0.158	0.105	0.071	0.044	0.094
0.97	0.112	0.076	0.049	0.037	0.069
1.00	0.118	0.083	0.041	0.036	0.069
Average	0.152	0.098	0.065	0.046	

10 %	460 rpm				
r/R	1	2	3	4	Average
0.63	0.160	0.111	0.101	0.084	0.114
0.72	0.184	0.123	0.098	0.080	0.121
0.80	0.152	0.106	0.083	0.069	0.103
0.86	0.167	0.117	0.089	0.074	0.112
0.92	0.162	0.115	0.086	0.070	0.108
0.97	0.113	0.080	0.056	0.048	0.074
1.00	0.116	0.080	0.042	0.034	0.068
Average	0.151	0.105	0.079	0.065	

10 %	547 rpm				
r/R	1	2	3	4	Average
0.63	0.165	0.119	0.117	0.091	0.123
0.72	0.191	0.132	0.114	0.087	0.131
0.80	0.158	0.113	0.094	0.075	0.110
0.86	0.174	0.123	0.101	0.080	0.120
0.92	0.168	0.121	0.096	0.076	0.115
0.97	0.116	0.082	0.060	0.050	0.077
1.00	0.116	0.081	0.043	0.034	0.069
Average	0.155	0.110	0.089	0.071	

15 %	236 rpm				
r/R	1	2	3	4	Average
0.63	0.300	0.163	0.115	0.077	0.164
0.72	0.338	0.140	0.089	0.046	0.153
0.80	0.268	0.118	0.080	0.045	0.128
0.86	0.293	0.119	0.079	0.040	0.133
0.92	0.273	0.124	0.086	0.050	0.133
0.97	0.185	0.112	0.083	0.066	0.111
1.00	0.147	0.136	0.094	0.084	0.115
Average	0.258	0.130	0.090	0.058	

15 %	304 rpm				
r/R	1	2	3	4	Average
0.63	0.301	0.160	0.123	0.101	0.171
0.72	0.291	0.157	0.112	0.075	0.159
0.80	0.228	0.139	0.103	0.069	0.135
0.86	0.240	0.145	0.106	0.066	0.139
0.92	0.226	0.146	0.108	0.070	0.138
0.97	0.164	0.121	0.092	0.073	0.113
1.00	0.154	0.135	0.091	0.080	0.115
Average	0.229	0.143	0.105	0.076	

15 %	353 rpm				
r/R	1	2	3	4	Average
0.63	0.243	0.156	0.132	0.125	0.164
0.72	0.257	0.169	0.132	0.102	0.165
0.80	0.214	0.153	0.121	0.091	0.144
0.86	0.228	0.163	0.127	0.088	0.151
0.92	0.219	0.162	0.126	0.087	0.149
0.97	0.162	0.127	0.099	0.080	0.117
1.00	0.158	0.133	0.089	0.079	0.115
Average	0.211	0.152	0.118	0.093	

15 %	460 rpm				
r/R	1	2	3	4	Average
0.63	0.214	0.155	0.147	0.157	0.168
0.72	0.239	0.174	0.148	0.143	0.176
0.80	0.206	0.159	0.134	0.125	0.156
0.86	0.221	0.170	0.141	0.127	0.165
0.92	0.214	0.168	0.137	0.120	0.160
0.97	0.161	0.130	0.104	0.095	0.122
1.00	0.159	0.131	0.089	0.080	0.115
Average	0.202	0.155	0.129	0.121	

15 %	547 rpm				
r/R	1	2	3	4	Average
0.63	0.214	0.159	0.159	0.160	0.173
0.72	0.245	0.179	0.158	0.152	0.183
0.80	0.211	0.163	0.140	0.134	0.162
0.86	0.228	0.175	0.147	0.138	0.172
0.92	0.220	0.172	0.142	0.130	0.166
0.97	0.163	0.132	0.106	0.100	0.125
1.00	0.159	0.132	0.091	0.081	0.116
Average	0.206	0.159	0.135	0.128	

20 %	236 rpm				
r/R	1	2	3	4	Average
0.63	0.278	0.173	0.140	0.103	0.173
0.72	0.417	0.239	0.141	0.107	0.226
0.80	0.330	0.215	0.124	0.099	0.192
0.86	0.382	0.238	0.131	0.103	0.213
0.92	0.342	0.222	0.125	0.101	0.198
0.97	0.202	0.144	0.087	0.085	0.130
1.00	0.108	0.113	0.065	0.084	0.093
Average	0.294	0.192	0.116	0.097	

20 %	304 rpm				
r/R	1	2	3	4	Average
0.63	0.289	0.185	0.124	0.141	0.185
0.72	0.409	0.231	0.161	0.157	0.239
0.80	0.319	0.203	0.152	0.139	0.203
0.86	0.366	0.222	0.168	0.145	0.225
0.92	0.328	0.208	0.157	0.134	0.207
0.97	0.197	0.138	0.102	0.097	0.134
1.00	0.109	0.114	0.068	0.077	0.092
Average	0.288	0.186	0.133	0.127	

20 %	353 rpm				
r/R	1	2	3	4	Average
0.63	0.307	0.167	0.142	0.193	0.202
0.72	0.388	0.251	0.198	0.209	0.262
0.80	0.292	0.230	0.186	0.178	0.221
0.86	0.329	0.258	0.207	0.186	0.245
0.92	0.296	0.240	0.190	0.165	0.223
0.97	0.184	0.151	0.115	0.107	0.139
1.00	0.112	0.110	0.067	0.066	0.089
Average	0.273	0.201	0.158	0.158	

20 %	460 rpm				
r/R	1	2	3	4	Average
0.63	0.256	0.166	0.167	0.236	0.206
0.72	0.337	0.244	0.216	0.263	0.265
0.80	0.270	0.223	0.196	0.220	0.227
0.86	0.304	0.250	0.216	0.234	0.251
0.92	0.278	0.233	0.197	0.205	0.228
0.97	0.178	0.148	0.118	0.121	0.141
1.00	0.123	0.110	0.067	0.061	0.090
Average	0.249	0.196	0.168	0.191	

20 %	547 rpm				
r/R	1	2	3	4	Average
0.63	0.254	0.166	0.178	0.234	0.208
0.72	0.338	0.245	0.225	0.273	0.270
0.80	0.272	0.225	0.201	0.231	0.232
0.86	0.306	0.252	0.221	0.250	0.257
0.92	0.280	0.235	0.201	0.219	0.234
0.97	0.179	0.149	0.120	0.128	0.144
1.00	0.124	0.110	0.067	0.061	0.090
Average	0.250	0.198	0.173	0.199	

APPENDIX P3

Hardware I, Reconstruction Code III, 220 mm vessel
Volume fractions for the 600 - 850 μm size fraction with the Rushton impeller

5 %	236 rpm				
r/R	1	2	3	4	Average
0.63	0.186	0.134	0.083	0.011	0.104
0.72	0.133	0.068	0.028	0.000	0.057
0.80	0.081	0.028	0.002	0.000	0.028
0.86	0.080	0.023	0.000	0.000	0.026
0.92	0.082	0.032	0.007	0.000	0.030
0.97	0.061	0.031	0.010	0.000	0.025
1.00	0.094	0.067	0.030	0.017	0.052
Average	0.102	0.055	0.023	0.004	

5 %	304 rpm				
r/R	1	2	3	4	Average
0.63	0.154	0.133	0.092	0.030	0.102
0.72	0.115	0.077	0.039	0.000	0.058
0.80	0.074	0.040	0.012	0.000	0.031
0.86	0.075	0.037	0.009	0.000	0.030
0.92	0.077	0.044	0.015	0.000	0.034
0.97	0.058	0.035	0.012	0.000	0.026
1.00	0.087	0.063	0.027	0.020	0.049
Average	0.091	0.061	0.030	0.007	

5 %	353 rpm				
r/R	1	2	3	4	Average
0.63	0.139	0.130	0.102	0.047	0.105
0.72	0.117	0.084	0.051	0.000	0.063
0.80	0.081	0.048	0.021	0.000	0.038
0.86	0.086	0.048	0.018	0.000	0.038
0.92	0.087	0.052	0.022	0.000	0.040
0.97	0.061	0.038	0.014	0.000	0.028
1.00	0.082	0.061	0.024	0.021	0.047
Average	0.093	0.066	0.036	0.010	

5 %	460 rpm				
r/R	1	2	3	4	Average
0.63	0.132	0.132	0.117	0.063	0.111
0.72	0.117	0.093	0.066	0.016	0.073
0.80	0.084	0.057	0.032	0.000	0.043
0.86	0.091	0.058	0.029	0.000	0.044
0.92	0.091	0.061	0.031	0.000	0.046
0.97	0.062	0.041	0.017	0.004	0.031
1.00	0.082	0.061	0.022	0.022	0.047
Average	0.094	0.072	0.045	0.015	

5 %	547 rpm				
r/R	1	2	3	4	Average
0.63	0.133	0.131	0.126	0.061	0.113
0.72	0.119	0.097	0.077	0.019	0.078
0.80	0.085	0.062	0.042	0.001	0.047
0.86	0.092	0.064	0.040	0.000	0.049
0.92	0.092	0.066	0.040	0.005	0.051
0.97	0.063	0.044	0.021	0.006	0.034
1.00	0.082	0.060	0.023	0.020	0.046
Average	0.095	0.075	0.053	0.016	

10 %	236 rpm				
r/R	1	2	3	4	Average
0.63	0.283	0.148	0.098	0.058	0.147
0.72	0.260	0.090	0.052	0.011	0.103
0.80	0.190	0.056	0.033	0.001	0.070
0.86	0.200	0.050	0.029	0.000	0.070
0.92	0.179	0.057	0.037	0.006	0.070
0.97	0.111	0.057	0.038	0.024	0.057
1.00	0.084	0.088	0.054	0.048	0.068
Average	0.187	0.078	0.049	0.021	

10 %	304 rpm				
r/R	1	2	3	4	Average
0.63	0.258	0.138	0.107	0.076	0.145
0.72	0.228	0.105	0.071	0.032	0.109
0.80	0.167	0.077	0.050	0.018	0.078
0.86	0.173	0.077	0.048	0.013	0.078
0.92	0.161	0.081	0.053	0.020	0.079
0.97	0.108	0.066	0.044	0.029	0.062
1.00	0.103	0.084	0.051	0.045	0.071
Average	0.171	0.090	0.061	0.033	

10 %	353 rpm				
r/R	1	2	3	4	Average
0.63	0.207	0.143	0.127	0.109	0.147
0.72	0.200	0.119	0.095	0.066	0.120
0.80	0.155	0.091	0.069	0.044	0.090
0.86	0.165	0.093	0.070	0.039	0.092
0.92	0.155	0.094	0.070	0.041	0.090
0.97	0.105	0.071	0.050	0.037	0.066
1.00	0.101	0.082	0.049	0.044	0.069
Average	0.156	0.099	0.076	0.054	

10 %	460 rpm				
r/R	1	2	3	4	Average
0.63	0.173	0.133	0.138	0.140	0.146
0.72	0.185	0.130	0.114	0.106	0.134
0.80	0.152	0.106	0.087	0.078	0.105
0.86	0.165	0.112	0.090	0.077	0.111
0.92	0.157	0.111	0.087	0.073	0.107
0.97	0.106	0.078	0.058	0.051	0.073
1.00	0.102	0.083	0.049	0.044	0.070
Average	0.149	0.108	0.089	0.081	

10 %	547 rpm				
r/R	1	2	3	4	Average
0.63	0.180	0.141	0.153	0.140	0.154
0.72	0.194	0.136	0.128	0.108	0.141
0.80	0.157	0.110	0.097	0.080	0.111
0.86	0.171	0.117	0.100	0.081	0.117
0.92	0.163	0.115	0.095	0.076	0.112
0.97	0.110	0.080	0.062	0.052	0.076
1.00	0.106	0.082	0.050	0.043	0.070
Average	0.154	0.112	0.098	0.083	

15 %	236 rpm				
r/R	1	2	3	4	Average
0.63	0.313	0.240	0.176	0.114	0.211
0.72	0.348	0.179	0.120	0.038	0.171
0.80	0.291	0.136	0.095	0.028	0.137
0.86	0.306	0.122	0.082	0.008	0.130
0.92	0.271	0.112	0.076	0.012	0.118
0.97	0.182	0.106	0.081	0.052	0.105
1.00	0.117	0.103	0.074	0.068	0.091
Average	0.261	0.143	0.101	0.046	

15 %	304 rpm				
r/R	1	2	3	4	Average
0.63	0.229	0.177	0.120	0.225	0.188
0.72	0.172	0.127	0.050	0.172	0.130
0.80	0.134	0.103	0.038	0.135	0.103
0.86	0.122	0.092	0.021	0.124	0.090
0.92	0.113	0.084	0.023	0.111	0.083
0.97	0.106	0.084	0.056	0.101	0.087
1.00	0.103	0.071	0.067	0.085	0.082
Average	0.140	0.106	0.054	0.136	

15 %	353 rpm				
r/R	1	2	3	4	Average
0.63	0.314	0.219	0.186	0.144	0.216
0.72	0.292	0.189	0.152	0.079	0.178
0.80	0.234	0.157	0.127	0.063	0.145
0.86	0.232	0.150	0.120	0.046	0.137
0.92	0.204	0.136	0.108	0.042	0.122
0.97	0.151	0.115	0.093	0.063	0.105
1.00	0.114	0.099	0.068	0.061	0.085
Average	0.220	0.152	0.122	0.071	

15 %	460 rpm				
r/R	1	2	3	4	Average
0.63	0.260	0.210	0.204	0.190	0.216
0.72	0.255	0.196	0.176	0.132	0.190
0.80	0.215	0.168	0.147	0.104	0.159
0.86	0.216	0.165	0.142	0.089	0.153
0.92	0.194	0.149	0.126	0.078	0.137
0.97	0.147	0.121	0.101	0.079	0.112
1.00	0.118	0.099	0.067	0.062	0.087
Average	0.201	0.158	0.138	0.105	

15 %	547 rpm				
r/R	1	2	3	4	Average
0.63	0.257	0.209	0.213	0.202	0.220
0.72	0.254	0.193	0.184	0.148	0.195
0.80	0.215	0.165	0.152	0.119	0.163
0.86	0.216	0.161	0.147	0.107	0.158
0.92	0.194	0.146	0.130	0.093	0.141
0.97	0.147	0.119	0.103	0.087	0.114
1.00	0.118	0.098	0.069	0.064	0.087
Average	0.200	0.156	0.143	0.117	

20 %	236 rpm				
r/R	1	2	3	4	Average
0.63	0.384	0.262	0.200	0.131	0.244
0.72	0.427	0.265	0.152	0.047	0.223
0.80	0.354	0.228	0.125	0.034	0.185
0.86	0.375	0.231	0.115	0.012	0.183
0.92	0.326	0.208	0.107	0.018	0.165
0.97	0.209	0.155	0.103	0.063	0.133
1.00	0.120	0.122	0.092	0.086	0.105
Average	0.314	0.210	0.128	0.056	

20 %	304 rpm				
r/R	1	2	3	4	Average
0.63	0.403	0.280	0.196	0.153	0.258
0.72	0.405	0.243	0.169	0.075	0.223
0.80	0.322	0.196	0.146	0.058	0.181
0.86	0.333	0.188	0.141	0.038	0.175
0.92	0.288	0.170	0.129	0.039	0.156
0.97	0.193	0.139	0.112	0.071	0.128
1.00	0.116	0.118	0.088	0.084	0.101
Average	0.294	0.191	0.140	0.074	

20 %	353 rpm				
r/R	1	2	3	4	Average
0.63	0.415	0.268	0.214	0.168	0.266
0.72	0.404	0.243	0.192	0.100	0.235
0.80	0.316	0.202	0.165	0.081	0.191
0.86	0.325	0.196	0.161	0.063	0.186
0.92	0.281	0.177	0.144	0.058	0.165
0.97	0.191	0.140	0.117	0.079	0.132
1.00	0.119	0.114	0.084	0.078	0.099
Average	0.293	0.192	0.154	0.089	

20 %	460 rpm				
r/R	1	2	3	4	Average
0.63	0.319	0.246	0.242	0.235	0.261
0.72	0.320	0.246	0.226	0.178	0.243
0.80	0.267	0.214	0.193	0.143	0.204
0.86	0.272	0.215	0.191	0.129	0.202
0.92	0.242	0.194	0.169	0.111	0.179
0.97	0.176	0.148	0.127	0.101	0.138
1.00	0.131	0.114	0.083	0.075	0.101
Average	0.247	0.197	0.176	0.139	

20 %	547 rpm				
r/R	1	2	3	4	Average
0.63	0.311	0.245	0.244	0.245	0.261
0.72	0.311	0.242	0.224	0.194	0.243
0.80	0.260	0.210	0.190	0.157	0.204
0.86	0.265	0.210	0.188	0.146	0.202
0.92	0.236	0.189	0.167	0.126	0.180
0.97	0.173	0.146	0.127	0.109	0.139
1.00	0.130	0.115	0.084	0.078	0.102
Average	0.241	0.194	0.175	0.151	

APPENDIX Q1

Hardware I, Reconstruction Code III, 220 mm vessel
Volume fractions for the 106 -212 μm size fraction with the pitched blade impeller

5 %	236 rpm				
r/R	1	2	3	4	Average
0 63	0 125	0 122	0.112	0 026	0 096
0 72	0.041	0.013	0.000	0.000	0 014
0.80	0.032	0.000	0.000	0.000	0 008
0 86	0.012	0.000	0.000	0 000	0 003
0 92	0.035	0.001	0.000	0 000	0.009
0.97	0.102	0.078	0 058	0.035	0.068
1.00	0 182	0 155	0.126	0 110	0.143
Average	0.076	0 053	0 042	0.025	

5 %	304 rpm				
r/R	1	2	3	4	Average
0 63	0.130	0 232	0 121	0 038	0 130
0.72	0.036	0 094	0.000	0 000	0 032
0 80	0 024	0 046	0.000	0 000	0 017
0 86	0.002	0 013	0.000	0 000	0 004
0 92	0 027	0 031	0.000	0 000	0 014
0.97	0 099	0.100	0 058	0 039	0 074
1 00	0.187	0 186	0 126	0.112	0.153
Average	0 072	0.100	0 044	0 027	

5 %	353 rpm				
r/R	1	2	3	4	Average
0.63	0.128	0.124	0 130	0 046	0 107
0.72	0.036	0 010	0.005	0 000	0.013
0.80	0.025	0.000	0 000	0 000	0.006
0.86	0.004	0 000	0.000	0 000	0 001
0.92	0.028	0 000	0.000	0 000	0 007
0 97	0 100	0.076	0.060	0.041	0 069
1 00	0.187	0.157	0 125	0 110	0.145
Average	0 073	0.053	0 046	0.028	

5 %	460 rpm				
r/R	1	2	3	4	Average
0.63	0 128	0.125	0 133	0 050	0.109
0.72	0 037	0 012	0 007	0 000	0 014
0 80	0 025	0 000	0 000	0 000	0 006
0 86	0 004	0 000	0 000	0 000	0 001
0 92	0 029	0 000	0 000	0 000	0 007
0.97	0 100	0 077	0 060	0 044	0 070
1.00	0 187	0 158	0 124	0 111	0 145
Average	0 073	0 053	0 046	0 029	

5 %	547 rpm				
r/R	1	2	3	4	Average
0.63	0 128	0 126	0 136	0 057	0.112
0 72	0 035	0 012	0 009	0 000	0 014
0 80	0 024	0 000	0 000	0 000	0 006
0 86	0 003	0 000	0 000	0 000	0 001
0 92	0 027	0 000	0 000	0 000	0 007
0 97	0 100	0 077	0 060	0 047	0 071
1 00	0 187	0.159	0 124	0.111	0.145
Average	0 072	0.053	0.047	0.031	

10 %	236 rpm				
r/R	1	2	3	4	Average
0.63	0.199	0.193	0.182	0.090	0 166
0.72	0.102	0.069	0 048	0.000	0.055
0.80	0.094	0.059	0.038	0.000	0 048
0 86	0.071	0 031	0.008	0.000	0 028
0 92	0.100	0.064	0.041	0.000	0.051
0.97	0 180	0.157	0.136	0.109	0.146
1.00	0.281	0.261	0.227	0.225	0.249
Average	0.147	0.119	0.097	0.061	

10 %	304 rpm				
r/R	1	2	3	4	Average
0.63	0 187	0.192	0.197	0 105	0 170
0.72	0 083	0.065	0.056	0.000	0 051
0.80	0.077	0.054	0.041	0.000	0.043
0.86	0.053	0.026	0.009	0 000	0.022
0 92	0.085	0.060	0.041	0 002	0.047
0 97	0.175	0.156	0.137	0.116	0.146
1.00	0.285	0 263	0.230	0.221	0.250
Average	0.135	0.116	0.101	0 063	

10 %	353 rpm				
r/R	1	2	3	4	Average
0.63	0 184	0.190	0 202	0.112	0 172
0 72	0.079	0.060	0.059	0 000	0 050
0.80	0.073	0.049	0.042	0 000	0.041
0 86	0.049	0.020	0.010	0 000	0.020
0.92	0.082	0 055	0.041	0.007	0.046
0.97	0.174	0 154	0.137	0 118	0.146
1.00	0.286	0.264	0.230	0.220	0.250
Average	0.133	0.113	0.103	0 065	

10 %	460 rpm				
r/R	1	2	3	4	Average
0.63	0.183	0.190	0.205	0.121	0 175
0.72	0.077	0.060	0.062	0 001	0.050
0.80	0.071	0.049	0.043	0.008	0.043
0.86	0.047	0.019	0.011	0.000	0.019
0.92	0.081	0.055	0.042	0 015	0.048
0.97	0.173	0.154	0.137	0.122	0.147
1.00	0.286	0.264	0.230	0.219	0.250
Average	0.131	0.113	0.104	0.069	

10 %	547 rpm				
r/R	1	2	3	4	Average
0 63	0.181	0 190	0.208	0.134	0.178
0.72	0.075	0 059	0.063	0.016	0.053
0.80	0.070	0 047	0.044	0.020	0.045
0.86	0.046	0 017	0.011	0.000	0 019
0.92	0.080	0.053	0.042	0.024	0.050
0.97	0.173	0.153	0.138	0.126	0.147
1.00	0.287	0.264	0.231	0.218	0.250
Average	0.130	0.112	0 105	0 077	

15 %	236 rpm				
r/R	1	2	3	4	Average
0 63	0.238	0.232	0.218	0.132	0.205
0.72	0.142	0.110	0.078	0.000	0 083
0.80	0.140	0.105	0.073	0.002	0 080
0.86	0.118	0.078	0.042	0.000	0 059
0.92	0.150	0 114	0.080	0 019	0 091
0.97	0.236	0.214	0.189	0.161	0.200
1.00	0 343	0.326	0 300	0 303	0 318
Average	0 195	0 168	0 140	0.088	

15 %	304 rpm				
r/R	1	2	3	4	Average
0.63	0.227	0 234	0 244	0.152	0 214
0.72	0.120	0.101	0 101	0.018	0 085
0.80	0.119	0 093	0.088	0.029	0 082
0.86	0.094	0 064	0.055	0.000	0 053
0.92	0 131	0.103	0 091	0 042	0.092
0 97	0 229	0.210	0.194	0 170	0.201
1 00	0 349	0 331	0 301	0 295	0.319
Average	0 181	0 162	0.153	0 101	

15 %	353 rpm				
r/R	1	2	3	4	Average
0.63	0.223	0.235	0.252	0.171	0.220
0.72	0.111	0.097	0 102	0.042	0.088
0.80	0.110	0.088	0.085	0.050	0.083
0.86	0.085	0.057	0.052	0.019	0.053
0.92	0.123	0.098	0.088	0.059	0 092
0.97	0 226	0 208	0 194	0 178	0 201
1.00	0 352	0.334	0 304	0.294	0 321
Average	0.176	0 160	0 154	0 116	

15 %	460 rpm				
r/R	1	2	3	4	Average
0.63	0.223	0 237	0.256	0.186	0.226
0.72	0 110	0 097	0 106	0.061	0.094
0.80	0 108	0 087	0 087	0.065	0.087
0.86	0 083	0.056	0.053	0.035	0.057
0 92	0.121	0 097	0.089	0.073	0.095
0 97	0.225	0 208	0.194	0.183	0.203
1 00	0 352	0 335	0.305	0.290	0.321
Average	0.175	0 159	0.156	0.128	

15 %	547 rpm				
r/R	1	2	3	4	Average
0.63	0.223	0.237	0.259	0.190	0.227
0.72	0.110	0 097	0.107	0.066	0.095
0 80	0 108	0 086	0.088	0.069	0.088
0.86	0.083	0.055	0.053	0.039	0.058
0.92	0.121	0 096	0.089	0.076	0.096
0.97	0.225	0 208	0 194	0 184	0.203
1 00	0 353	0 335	0.305	0 289	0 321
Average	0.175	0.159	0.157	0.131	

20 %	236 rpm				
r/R	1	2	3	4	Average
0.63	0 328	0 222	0.187	0.229	0.241
0.72	0 409	0.298	0.224	0.155	0.271
0.80	0 336	0.274	0.209	0.116	0 234
0.86	0 361	0.293	0 220	0 096	0.243
0 92	0 316	0.260	0.193	0.081	0 212
0.97	0 206	0.172	0.131	0.084	0 148
1.00	0 128	0.106	0 068	0.071	0 093
Average	0 298	0 232	0 176	0.119	

20 %	304 rpm				
r/R	1	2	3	4	Average
0.63	0 302	0.216	0.220	0 258	0 249
0 72	0.336	0.270	0 250	0.220	0 269
0 80	0.284	0 247	0.224	0.178	0 233
0.86	0 295	0 261	0 233	0 167	0.239
0 92	0 261	0.233	0 203	0 140	0 209
0.97	0.182	0.161	0 135	0 108	0 147
1.00	0 132	0 106	0 070	0 064	0 093
Average	0 256	0 213	0 191	0.162	

20 %	353 rpm				
r/R	1	2	3	4	Average
0.63	0.291	0.216	0 229	0 268	0 251
0 72	0 321	0 261	0.249	0 242	0 268
0.80	0.273	0.238	0 220	0 198	0 232
0.86	0 284	0.250	0 227	0 190	0.238
0 92	0 253	0 223	0 198	0.159	0 208
0.97	0.179	0.156	0 133	0 116	0.146
1.00	0.134	0 105	0 071	0 064	0.094
Average	0 248	0 207	0 190	0.177	

20 %	460 rpm				
r/R	1	2	3	4	Average
0.63	0 300	0.220	0.236	0.277	0 258
0.72	0 328	0.263	0.252	0 256	0.275
0.80	0 278	0 239	0 220	0 210	0.237
0.86	0 289	0 250	0 227	0 204	0 242
0 92	0.257	0.223	0 197	0.171	0.212
0.97	0.182	0 156	0 133	0 122	0.148
1.00	0 135	0 106	0 071	0.065	0.094
Average	0.253	0.208	0.191	0.186	

20 %	547 rpm				
r/R	1	2	3	4	Average
0.63	0 300	0 223	0.237	0 283	0.261
0 72	0 322	0 258	0 251	0.269	0.275
0.80	0.272	0 232	0.219	0.222	0.236
0.86	0 282	0 241	0 225	0 220	0.242
0 92	0 251	0 216	0 196	0.185	0.212
0.97	0.179	0.154	0 133	0.128	0.148
1.00	0 135	0 107	0.072	0.066	0 095
Average	0 249	0 205	0 190	0.196	

APPENDIX Q2

Hardware I, Reconstruction Code III, 220 mm vessel
Volume fractions for the 425 - 600 μm size fraction with the pitched blade impeller

5 %	236 rpm				
r/R	1	2	3	4	Average
0.63	0.177	0.114	0.231	0.064	0.147
0.72	0.150	0.043	0.130	0.000	0.081
0.80	0.119	0.022	0.071	0.000	0.053
0.86	0.113	0.004	0.043	0.000	0.040
0.92	0.105	0.010	0.031	0.000	0.036
0.97	0.093	0.041	0.041	0.011	0.046
1.00	0.100	0.069	0.037	0.034	0.060
Average	0.122	0.043	0.083	0.015	

5 %	304 rpm				
r/R	1	2	3	4	Average
0.63	0.177	0.114	0.114	0.067	0.118
0.72	0.142	0.048	0.038	0.000	0.057
0.80	0.109	0.027	0.016	0.000	0.038
0.86	0.101	0.010	0.000	0.000	0.028
0.92	0.094	0.014	0.000	0.000	0.027
0.97	0.087	0.042	0.027	0.011	0.042
1.00	0.097	0.065	0.038	0.034	0.058
Average	0.115	0.046	0.033	0.016	

5 %	353 rpm				
r/R	1	2	3	4	Average
0.63	0.176	0.110	0.111	0.066	0.116
0.72	0.137	0.054	0.042	0.000	0.058
0.80	0.104	0.035	0.021	0.000	0.040
0.86	0.094	0.020	0.005	0.000	0.030
0.92	0.087	0.022	0.006	0.000	0.029
0.97	0.083	0.044	0.030	0.012	0.042
1.00	0.094	0.058	0.036	0.033	0.055
Average	0.111	0.049	0.036	0.016	

5 %	460 rpm				
r/R	1	2	3	4	Average
0.63	0.167	0.111	0.119	0.068	0.116
0.72	0.125	0.060	0.050	0.000	0.059
0.80	0.094	0.042	0.027	0.000	0.041
0.86	0.084	0.028	0.011	0.000	0.031
0.92	0.078	0.028	0.010	0.000	0.029
0.97	0.080	0.046	0.031	0.011	0.042
1.00	0.094	0.056	0.034	0.031	0.054
Average	0.103	0.053	0.040	0.016	

5 %	547 rpm				
r/R	1	2	3	4	Average
0.63	0.165	0.111	0.120	0.073	0.117
0.72	0.120	0.059	0.051	0.000	0.058
0.80	0.090	0.041	0.028	0.000	0.040
0.86	0.079	0.028	0.012	0.000	0.030
0.92	0.075	0.029	0.011	0.000	0.029
0.97	0.078	0.048	0.031	0.015	0.043
1.00	0.094	0.062	0.034	0.031	0.055
Average	0.100	0.054	0.041	0.017	

10 %	236 rpm				
r/R	1	2	3	4	Average
0.63	0.177	0.181	0.157	0.107	0.156
0.72	0.228	0.115	0.083	0.036	0.116
0.80	0.215	0.086	0.060	0.027	0.097
0.86	0.230	0.069	0.043	0.007	0.087
0.92	0.213	0.070	0.044	0.010	0.084
0.97	0.160	0.089	0.067	0.050	0.091
1.00	0.131	0.113	0.075	0.067	0.097
Average	0.193	0.103	0.076	0.043	

10 %	304 rpm				
r/R	1	2	3	4	Average
0.63	0.211	0.174	0.156	0.111	0.163
0.72	0.238	0.126	0.090	0.037	0.123
0.80	0.214	0.101	0.068	0.026	0.102
0.86	0.223	0.088	0.052	0.006	0.092
0.92	0.205	0.086	0.052	0.009	0.088
0.97	0.153	0.095	0.070	0.050	0.092
1.00	0.125	0.109	0.074	0.066	0.094
Average	0.195	0.111	0.080	0.044	

10 %	353 rpm				
r/R	1	2	3	4	Average
0.63	0.233	0.170	0.154	0.110	0.167
0.72	0.241	0.137	0.098	0.036	0.128
0.80	0.208	0.116	0.078	0.025	0.107
0.86	0.211	0.106	0.065	0.004	0.097
0.92	0.193	0.101	0.063	0.007	0.091
0.97	0.147	0.101	0.074	0.049	0.093
1.00	0.123	0.105	0.072	0.065	0.091
Average	0.194	0.119	0.086	0.042	

10 %	460 rpm				
r/R	1	2	3	4	Average
0.63	0.233	0.167	0.159	0.124	0.171
0.72	0.218	0.145	0.112	0.049	0.131
0.80	0.184	0.126	0.092	0.034	0.109
0.86	0.180	0.119	0.081	0.012	0.098
0.92	0.164	0.112	0.075	0.013	0.091
0.97	0.135	0.106	0.079	0.051	0.093
1.00	0.123	0.104	0.069	0.064	0.090
Average	0.177	0.126	0.095	0.050	

10 %	547 rpm				
r/R	1	2	3	4	Average
0.63	0.224	0.163	0.162	0.123	0.168
0.72	0.204	0.142	0.117	0.054	0.129
0.80	0.172	0.124	0.096	0.040	0.108
0.86	0.167	0.118	0.085	0.020	0.097
0.92	0.153	0.111	0.079	0.019	0.090
0.97	0.131	0.105	0.080	0.053	0.092
1.00	0.124	0.103	0.069	0.061	0.089
Average	0.168	0.123	0.098	0.053	

15 %	236 rpm				
r/R	1	2	3	4	Average
0.63	0.124	0.206	0.158	0.117	0.151
0.72	0.296	0.163	0.110	0.058	0.157
0.80	0.313	0.139	0.097	0.056	0.151
0.86	0.353	0.128	0.085	0.039	0.151
0.92	0.326	0.126	0.085	0.042	0.145
0.97	0.223	0.131	0.101	0.081	0.134
1.00	0.158	0.144	0.102	0.093	0.124
Average	0.256	0.148	0.105	0.069	

15 %	304 rpm				
r/R	1	2	3	4	Average
0.63	0.197	0.198	0.160	0.121	0.169
0.72	0.299	0.176	0.122	0.058	0.164
0.80	0.292	0.157	0.111	0.054	0.154
0.86	0.318	0.152	0.102	0.035	0.152
0.92	0.294	0.146	0.098	0.039	0.144
0.97	0.211	0.139	0.106	0.080	0.134
1.00	0.159	0.139	0.100	0.094	0.123
Average	0.253	0.158	0.114	0.069	

15 %	353 rpm				
r/R	1	2	3	4	Average
0.63	0.256	0.194	0.163	0.123	0.184
0.72	0.323	0.197	0.139	0.056	0.179
0.80	0.296	0.182	0.129	0.051	0.165
0.86	0.316	0.182	0.123	0.031	0.163
0.92	0.288	0.171	0.117	0.034	0.153
0.97	0.206	0.147	0.115	0.077	0.136
1.00	0.154	0.133	0.100	0.091	0.119
Average	0.263	0.172	0.127	0.066	

15 %	460 rpm				
r/R	1	2	3	4	Average
0.63	0.283	0.192	0.171	0.138	0.196
0.72	0.303	0.208	0.159	0.071	0.185
0.80	0.266	0.196	0.149	0.062	0.168
0.86	0.270	0.199	0.146	0.041	0.164
0.92	0.243	0.186	0.136	0.041	0.152
0.97	0.186	0.153	0.122	0.080	0.135
1.00	0.149	0.129	0.096	0.091	0.116
Average	0.243	0.181	0.140	0.075	

15 %	547 rpm				
r/R	1	2	3	4	Average
0.63	0.271	0.196	0.180	0.155	0.201
0.72	0.282	0.206	0.171	0.089	0.187
0.80	0.248	0.191	0.158	0.076	0.168
0.86	0.250	0.193	0.156	0.057	0.164
0.92	0.228	0.180	0.144	0.055	0.152
0.97	0.180	0.151	0.124	0.086	0.135
1.00	0.154	0.131	0.094	0.092	0.118
Average	0.231	0.178	0.147	0.087	

20 %	236 rpm				
r/R	1	2	3	4	Average
0.63	0.400	0.285	0.215	0.201	0.275
0.72	0.442	0.262	0.160	0.142	0.251
0.80	0.421	0.213	0.126	0.112	0.218
0.86	0.393	0.209	0.114	0.097	0.203
0.92	0.338	0.187	0.102	0.084	0.178
0.97	0.254	0.143	0.094	0.085	0.144
1.00	0.118	0.116	0.074	0.068	0.094
Average	0.338	0.202	0.126	0.113	

20 %	304 rpm				
r/R	1	2	3	4	Average
0.63	0.390	0.262	0.205	0.203	0.265
0.72	0.432	0.262	0.176	0.140	0.253
0.80	0.411	0.222	0.148	0.109	0.223
0.86	0.383	0.223	0.142	0.093	0.210
0.92	0.328	0.200	0.126	0.080	0.184
0.97	0.244	0.147	0.104	0.083	0.145
1.00	0.128	0.112	0.073	0.067	0.095
Average	0.331	0.204	0.139	0.111	

20 %	353 rpm				
r/R	1	2	3	4	Average
0.63	0.090	0.243	0.213	0.205	0.188
0.72	0.382	0.280	0.199	0.136	0.249
0.80	0.401	0.249	0.171	0.103	0.231
0.86	0.373	0.259	0.169	0.085	0.222
0.92	0.318	0.231	0.149	0.073	0.193
0.97	0.234	0.160	0.113	0.080	0.147
1.00	0.148	0.110	0.071	0.067	0.099
Average	0.278	0.219	0.155	0.107	

20 %	460 rpm				
r/R	1	2	3	4	Average
0.63	0.349	0.236	0.214	0.223	0.255
0.72	0.420	0.301	0.222	0.153	0.274
0.80	0.339	0.272	0.197	0.115	0.231
0.86	0.362	0.288	0.200	0.097	0.237
0.92	0.313	0.255	0.175	0.082	0.206
0.97	0.202	0.172	0.122	0.084	0.145
1.00	0.115	0.111	0.065	0.066	0.089
Average	0.300	0.233	0.171	0.117	

20 %	547 rpm				
r/R	1	2	3	4	Average
0.63	0.330	0.236	0.221	0.243	0.258
0.72	0.381	0.290	0.237	0.179	0.272
0.80	0.314	0.261	0.210	0.137	0.231
0.86	0.331	0.275	0.215	0.120	0.235
0.92	0.289	0.244	0.188	0.100	0.205
0.97	0.194	0.167	0.128	0.090	0.145
1.00	0.122	0.110	0.066	0.063	0.090
Average	0.280	0.226	0.181	0.133	

APPENDIX Q3

Hardware I, Reconstruction Code III, 220 mm vessel
Volume fractions for the 600 - 850 μm size fraction with the pitched blade impeller

5 %	236 rpm				
r/R	1	2	3	4	Average
0 63	0.207	0.137	0 125	0 096	0 142
0.72	0 184	0 069	0 052	0 022	0 082
0.80	0 135	0 032	0 018	0.000	0.046
0 86	0 134	0 017	0 002	0 000	0 038
0 92	0 115	0 012	0.000	0 000	0 032
0 97	0 073	0 019	0 003	0 000	0 024
1.00	0 051	0 023	0.000	0 000	0 019
Average	0 129	0 044	0 029	0 017	

5 %	304 rpm				
r/R	1	2	3	4	Average
0.63	0 202	0 120	0 110	0 088	0 130
0.72	0 173	0 061	0 045	0 017	0 074
0.80	0 125	0 029	0 015	0.000	0 042
0 86	0 121	0 015	0.000	0.000	0 034
0 92	0 102	0 010	0.000	0.000	0 028
0 97	0.066	0 017	0 002	0.000	0 021
1.00	0 047	0 018	0.000	0.000	0 016
Average	0 119	0 039	0 024	0 015	

5 %	353 rpm				
r/R	1	2	3	4	Average
0 63	0 184	0 109	0 104	0 080	0 119
0 72	0 163	0 066	0 046	0 010	0 071
0 80	0 120	0 039	0 018	0 000	0 044
0 86	0 116	0 028	0 005	0 000	0 037
0 92	0 098	0 022	0 000	0 000	0 030
0 97	0 064	0 024	0 004	0 000	0 023
1.00	0 046	0 025	0 000	0 000	0 018
Average	0 113	0 045	0 025	0 013	

5 %	460 rpm				
r/R	1	2	3	4	Average
0.63	0 173	0 108	0 110	0 090	0 120
0 72	0 143	0 075	0 058	0 020	0 074
0.80	0 103	0 050	0 030	0 000	0 046
0 86	0 097	0 042	0 018	0 000	0 039
0 92	0 081	0 034	0 009	0 000	0 031
0 97	0 057	0 029	0 009	0 000	0 024
1.00	0 045	0 022	0 000	0 000	0 017
Average	0 100	0 052	0 033	0 016	

5 %	547 rpm				
r/R	1	2	3	4	Average
0 63	0 160	0 102	0 113	0 093	0 117
0.72	0 135	0 075	0 060	0 024	0 073
0.80	0 098	0 052	0 031	0 000	0 045
0.86	0 093	0 045	0 018	0 000	0 039
0.92	0 077	0 037	0 009	0 000	0 031
0 97	0 055	0 030	0 008	0 000	0 023
1 00	0 043	0 023	0.000	0 000	0.016
Average	0 094	0 052	0 034	0 017	

10 %	236 rpm				
r/R	1	2	3	4	Average
0.63	0.152	0 162	0.142	0 103	0 140
0.72	0.254	0.099	0.079	0 029	0.115
0.80	0.238	0.071	0.051	0 012	0.093
0.86	0.267	0.056	0.036	0.000	0.090
0 92	0.240	0.050	0.030	0 000	0.080
0.97	0.151	0.059	0.039	0.021	0.068
1.00	0.089	0.053	0.033	0 024	0.050
Average	0.199	0 078	0 058	0 027	

10 %	304 rpm				
r/R	1	2	3	4	Average
0.63	0.182	0 160	0.140	0.103	0.146
0.72	0.264	0 104	0.084	0.031	0 121
0.80	0.238	0.078	0.058	0.013	0.097
0.86	0.263	0.064	0.044	0.000	0.093
0.92	0.236	0.057	0.037	0.000	0.082
0.97	0.148	0.062	0.042	0.021	0.068
1.00	0.089	0.050	0.030	0.023	0.048
Average	0.203	0.082	0.062	0.027	

10 %	353 rpm				
r/R	1	2	3	4	Average
0 63	0.208	0.191	0.138	0.104	0.160
0 72	0 263	0 174	0.096	0.031	0 141
0.80	0.229	0.158	0.073	0.013	0.118
0.86	0 247	0 143	0.063	0.000	0.113
0.92	0.218	0.127	0.053	0.000	0.099
0.97	0 136	0 114	0.049	0.020	0.080
1.00	0.082	0 107	0 030	0.022	0.060
Average	0.198	0 145	0 072	0.027	

10 %	460 rpm				
r/R	1	2	3	4	Average
0 63	0.226	0.131	0 138	0.112	0.152
0.72	0 242	0.181	0 113	0.037	0.143
0.80	0.201	0.150	0 091	0.017	0.115
0.86	0.205	0.155	0.084	0.000	0.111
0.92	0.176	0.137	0.071	0.000	0.096
0.97	0.117	0.103	0.055	0.021	0.074
1.00	0 074	0.077	0.026	0.022	0.050
Average	0 177	0 133	0 083	0.030	

10 %	547 rpm				
r/R	1	2	3	4	Average
0.63	0.220	0 139	0.146	0.117	0.156
0.72	0.224	0.174	0.120	0.046	0.141
0.80	0.184	0.151	0.096	0 025	0.114
0 86	0.185	0 156	0.090	0.006	0.109
0.92	0.160	0.140	0.076	0.001	0.094
0 97	0 111	0.106	0.057	0.024	0.074
1.00	0.077	0.084	0.026	0.020	0.052
Average	0 166	0 136	0.087	0.034	

15 %	236 rpm				
r/R	1	2	3	4	Average
0.63	0.034	0.235	0.179	0 117	0 141
0 72	0 295	0.183	0.121	0 045	0 161
0.80	0.332	0.148	0.101	0 041	0 155
0.86	0.390	0.136	0.087	0 022	0 159
0.92	0 357	0 131	0.085	0 029	0 150
0.97	0.232	0 127	0.097	0 072	0 132
1.00	0.147	0 132	0.096	0 093	0 117
Average	0.255	0 156	0 109	0 060	

15 %	304 rpm				
r/R	1	2	3	4	Average
0.63	0.103	0.230	0.181	0.124	0.159
0.72	0.288	0.190	0.135	0.052	0.166
0.80	0.309	0.157	0.116	0.045	0.157
0.86	0.353	0.148	0.105	0.027	0.158
0.92	0.326	0 140	0.099	0.032	0 149
0 97	0 220	0 130	0.103	0.073	0 132
1.00	0 151	0 129	0 094	0 093	0 117
Average	0 250	0 161	0 119	0 064	

15 %	353 rpm				
r/R	1	2	3	4	Average
0.63	0.187	0 217	0 184	0.123	0 178
0.72	0.311	0.209	0 150	0 047	0.179
0.80	0.304	0.185	0 131	0 041	0.165
0.86	0.336	0.183	0.123	0 021	0 166
0.92	0.308	0.170	0 115	0 028	0.155
0 97	0.213	0 143	0 109	0 071	0 134
1 00	0 149	0 126	0 091	0 092	0 115
Average	0 258	0 176	0 129	0 061	

15 %	460 rpm				
r/R	1	2	3	4	Average
0.63	0 282	0.207	0.192	0 135	0 204
0.72	0 331	0.233	0 175	0 055	0.198
0.80	0.292	0.215	0.157	0 044	0.177
0.86	0.304	0.220	0.153	0 024	0.175
0.92	0 270	0.201	0.139	0 029	0.160
0.97	0 191	0.155	0 118	0 071	0 134
1.00	0 135	0.122	0 086	0 092	0 109
Average	0 258	0.193	0 146	0 064	

15 %	547 rpm				
r/R	1	2	3	4	Average
0.63	0.279	0 210	0.194	0.143	0.206
0.72	0.311	0.232	0 183	0.065	0.198
0.80	0.274	0 214	0.165	0.052	0.176
0.86	0.282	0 218	0 163	0.032	0 174
0.92	0.252	0.200	0 148	0 035	0.159
0.97	0.185	0 155	0.121	0 074	0 134
1.00	0.138	0.122	0.086	0.091	0.110
Average	0.246	0.193	0.152	0.070	

20 %	236 rpm				
r/R	1	2	3	4	Average
0 63	0.399	0.226	0.188	0.116	0.232
0.72	0.633	0 244	0 142	0 053	0.268
0.80	0 540	0.217	0 118	0 048	0.231
0.86	0 599	0 221	0 107	0.032	0 240
0.92	0.523	0.201	0 098	0.034	0.214
0 97	0.329	0.153	0 097	0 069	0.162
1 00	0.176	0.121	0.082	0.080	0.114
Average	0.457	0 198	0 119	0.062	

20 %	304 rpm				
r/R	1	2	3	4	Average
0 63	0 363	0 236	0 181	0 123	0 226
0.72	0 576	0 245	0 154	0 061	0.259
0 80	0 491	0 214	0 134	0 054	0.223
0 86	0 545	0 216	0 127	0 038	0 231
0.92	0.476	0 195	0 116	0 039	0.206
0.97	0.299	0 148	0.104	0.071	0.155
1.00	0 160	0 116	0.079	0.079	0.108
Average	0 416	0 196	0 128	0 066	

20 %	353 rpm				
r/R	1	2	3	4	Average
0 63	0.302	0 222	0 175	0 126	0.206
0 72	0 480	0 250	0 171	0 060	0 240
0 80	0 409	0 225	0 157	0.051	0.211
0 86	0.454	0 231	0 157	0 033	0.219
0 92	0.397	0 208	0.141	0.035	0.195
0 97	0.249	0 153	0 114	0 069	0 146
1 00	0 139	0 113	0 078	0 079	0 102
Average	0.347	0 200	0 142	0.065	

20 %	460 rpm				
r/R	1	2	3	4	Average
0 63	0.275	0.202	0.186	0 137	0.200
0 72	0 436	0.273	0 205	0.066	0 245
0.80	0.372	0.258	0.190	0.054	0.219
0 86	0 413	0.274	0 195	0 035	0.229
0 92	0.361	0 245	0.173	0.035	0.203
0 97	0 227	0.169	0.127	0 068	0.148
1.00	0 126	0.110	0 075	0 077	0 097
Average	0 316	0.219	0.165	0 068	

20 %	547 rpm				
r/R	1	2	3	4	Average
0 63	0.326	0.199	0 185	0 147	0 214
0.72	0.404	0.274	0 214	0 078	0.242
0.80	0 337	0 260	0 200	0.063	0.215
0 86	0 358	0.276	0 208	0 044	0.221
0 92	0.311	0.245	0 184	0 042	0.195
0 97	0.205	0.168	0.130	0.071	0 144
1.00	0 122	0 107	0 072	0 076	0.094
Average	0.295	0 218	0.170	0.074	

APPENDIX R

Pipette Sampling Data

		5 % v/v 106 - 212 mm, Rushton					
		r/R					
rpm	Layer	0.09	0.33	0.55	0.64	0.73	0.82
236	L4	0.044	0.050	0.0530	0.0520	0.062	0.0584
	L3	0.050	0.049	0.0644	0.0602	0.058	0.0651
304	L4	0.008	0.059			0.058	
	L3	0.020	0.029			0.058	
353	L4	0.015	0.031			0.052	
	L3	0.015	0.037			0.052	

		15 % v/v 600 - 850 µm, Rushton		
		r/R		
rpm	Layer	0.09	0.33	0.73
236	L4	0.014	0.017	0.009
	L3	0.020	0.020	0.032
304	L4	0.022	0.026	0.016
	L3	0.029	0.031	0.039
353	L4	0.012	0.039	0.045
	L3	0.030	0.060	0.044
460	L4	0.037	0.070	0.063
	L3	0.052	0.051	0.045
547	L4	0.029	0.070	0.050
	L3	0.052	0.026	0.063

12 samples from L3

5 % v/v, 106 - 212 µm, Rushton	
L3, 304 rpm	5.563
	5.342
	5.235
	5.364
	5.418
	5.439
	5.478
	5.488
	5.487
	5.406
	5.292
	5.510
Mean	5.419
Std dev	0.096
% dev.	1.772

Conductivity Probe Data

		5 % v/v 106 - 212 µm, Rushton		
		r/R		
rpm	Layer	0.09	0.33	0.73
236	L4	0.023	0.026	0.023
	L3	0.024	0.026	0.019
304	L4	0.025	0.029	0.030
	L3	0.027	0.031	0.029
353	L4	0.024	0.031	0.030
	L3	0.023	0.028	0.034

		10 % v/v 425 - 600 µm, Rushton		
		r/R		
rpm	Layer	0.09	0.33	0.73
236	L4	0.070	0.072	0.059
	L3	0.066	0.071	0.068
304	L4	0.068	0.076	0.073
	L3	0.070	0.076	0.079
353	L4	0.069	0.081	0.072
	L3	0.074	0.084	0.084

APPENDIX S

ERT Data for the 50 and 220 mm tanks

600 - 850 μm sand suspension at 15 % concentration in the 220 mm vessel at 547 rpm

	Layer			
r/R	1	2	3	4
0.551	0.225	0.153	0.143	0.161
0.626	0.223	0.150	0.135	0.128
0.705	0.236	0.160	0.150	0.133
0.788	0.260	0.164	0.170	0.167
0.876	0.275	0.168	0.175	0.201
0.962	0.283	0.172	0.177	0.215

600 - 850 μm sand suspension at 5 % concentration in the 50 mm vessel

480 rpm	Layer			
r/R	1	2	3	4
0.551	0.162	0.103	0.032	0.036
0.626	0.149	0.069	0.011	0.034
0.707	0.113	0.035	0.003	0.032
0.783	0.097	0.018	0.004	0.025
0.866	0.084	0.012	0.009	0.023
0.958	0.089	0.013	0.013	0.025
Average	0.116	0.042	0.012	0.029

1038 rpm	Layer			
r/R	1	2	3	4
0.551	0.064	0.050	0.058	0.103
0.626	0.059	0.039	0.038	0.092
0.707	0.060	0.036	0.027	0.065
0.783	0.071	0.035	0.022	0.044
0.866	0.074	0.041	0.025	0.032
0.958	0.072	0.047	0.032	0.032
Average	0.067	0.041	0.034	0.061

1338 rpm	Layer			
r/R	1	2	3	4
0.551	0.052	0.046	0.082	0.191
0.626	0.049	0.034	0.055	0.164
0.707	0.050	0.032	0.035	0.099
0.783	0.060	0.032	0.026	0.063
0.866	0.064	0.038	0.025	0.033
0.958	0.064	0.045	0.033	0.035
Average	0.057	0.038	0.043	0.097

2024 rpm	Layer			
r/R	1	2	3	4
0.551	0.048	0.039	0.039	0.073
0.626	0.052	0.050	0.026	0.000
0.707	0.053	0.058	0.017	0.000
0.783	0.052	0.045	0.004	0.000
0.866	0.051	0.044	0.004	0.000
0.958	0.047	0.051	0.013	0.000
Average	0.051	0.048	0.017	0.012

600 - 850 μm sand suspension at 15 % concentration in the 50 mm vessel

1038 rpm	Layer			
r/R	1	2	3	4
0.551	0.170	0.187	0.130	0.160
0.626	0.201	0.164	0.082	0.150
0.707	0.204	0.126	0.058	0.124
0.783	0.243	0.105	0.057	0.111
0.866	0.230	0.096	0.071	0.096
0.958	0.212	0.096	0.085	0.093
Average	0.210	0.129	0.081	0.122

1338 rpm	Layer			
r/R	1	2	3	4
0.551	0.147	0.173	0.171	0.217
0.626	0.163	0.158	0.130	0.185
0.707	0.171	0.139	0.104	0.139
0.783	0.210	0.130	0.098	0.134
0.866	0.212	0.132	0.108	0.119
0.958	0.193	0.137	0.123	0.125
Average	0.183	0.145	0.122	0.153

2024 rpm	Layer			
r/R	1	2	3	4
0.551	0.160	0.161	0.133	0.209
0.626	0.159	0.172	0.114	0.143
0.707	0.160	0.162	0.096	0.106
0.783	0.178	0.136	0.082	0.119
0.866	0.186	0.126	0.082	0.129
0.958	0.173	0.129	0.093	0.155
Average	0.169	0.148	0.100	0.144

APPENDIX T

ERT radial data for ballotini and nylon

5 % 50 μm ballotini				
480 rpm	Layer			
r/R	1	2	3	4
0.551	0.050	0.042	0.014	0.016
0.626	0.044	0.040	0.019	0.000
0.707	0.040	0.040	0.030	0.000
0.783	0.043	0.040	0.038	0.000
0.866	0.041	0.042	0.046	0.004
0.958	0.035	0.042	0.049	0.006
Average	0.042	0.041	0.033	0.004

10 % 50 μm ballotini				
480 rpm	Layer			
r/R	1	2	3	4
0.551	0.104	0.100	0.090	0.101
0.626	0.103	0.099	0.092	0.095
0.707	0.099	0.098	0.094	0.089
0.783	0.101	0.097	0.096	0.083
0.866	0.096	0.094	0.096	0.079
0.958	0.090	0.092	0.095	0.077
Average	0.099	0.097	0.094	0.087

10 % 500 μm nylon				
480 rpm	Layer			
r/R	1	2	3	4
0.551	0.127	0.123	0.116	0.115
0.626	0.119	0.104	0.095	0.095
0.707	0.108	0.088	0.082	0.080
0.783	0.094	0.084	0.082	0.075
0.866	0.101	0.092	0.094	0.082
0.958	0.111	0.096	0.098	0.085
Average	0.110	0.098	0.094	0.089

ERT and MRI comparative axial profile data

5 % 50 μm ballotini			
Layer	ERT	3D MRI	1D MRI
1	0.042	0.039	0.055
2	0.041	0.035	0.051
3	0.033	0.035	0.045
4	0.004	0.031	0.041

10 % 50 μm ballotini			
Layer	ERT	3D MRI	1D MRI
1	0.099	0.083	0.108
2	0.097	0.077	0.097
3	0.094	0.079	0.094
4	0.087	0.060	0.096

10 % 500 μm nylon			
Layer	ERT	3D MRI	1D MRI
1	0.110	0.103	0.094
2	0.098	0.119	0.102
3	0.094	0.110	0.103
4	0.089	0.060	0.110

APPENDIX U1

1D MRI data of ballotini suspension in the 50 mm tank

	volume fractions for 5 % 100 μm ballotini				volume fractions for 5 % 50 μm ballotini			
	rpm				rpm			
r/R	306	366	426	480	306	366	426	480
0.000	0.300	0.288	0.207	0.179	0.406	0.288	0.292	0.052
0.023	0.248	0.223	0.160	0.115	0.321	0.228	0.161	0.034
0.047	0.175	0.156	0.119	0.049	0.171	0.095	0.000	0.000
0.070	0.144	0.141	0.119	0.061	0.126	0.088	0.004	0.000
0.093	0.111	0.112	0.101	0.056	0.072	0.050	0.001	0.000
0.116	0.079	0.081	0.076	0.053	0.021	0.011	0.005	0.003
0.140	0.064	0.065	0.065	0.055	0.006	0.006	0.014	0.014
0.163	0.058	0.058	0.059	0.054	0.009	0.015	0.024	0.027
0.186	0.057	0.054	0.058	0.056	0.014	0.021	0.032	0.035
0.209	0.052	0.051	0.055	0.054	0.020	0.029	0.040	0.046
0.233	0.051	0.050	0.055	0.057	0.028	0.038	0.049	0.055
0.256	0.048	0.048	0.053	0.058	0.035	0.047	0.057	0.065
0.279	0.047	0.044	0.051	0.058	0.042	0.055	0.065	0.073
0.302	0.044	0.042	0.048	0.055	0.045	0.059	0.067	0.076
0.326	0.042	0.039	0.046	0.054	0.048	0.060	0.066	0.075
0.349	0.037	0.035	0.042	0.051	0.066	0.080	0.085	0.096
0.372	0.034	0.034	0.040	0.051	0.071	0.084	0.090	0.099
0.395	0.032	0.032	0.040	0.049	0.077	0.092	0.098	0.108
0.419	0.030	0.030	0.038	0.049	0.082	0.096	0.104	0.114
0.442	0.028	0.028	0.036	0.048	0.075	0.089	0.096	0.108
0.465	0.027	0.027	0.037	0.049	0.074	0.085	0.093	0.104
0.488	0.026	0.026	0.035	0.048	0.073	0.085	0.092	0.103
0.512	0.026	0.024	0.033	0.047	0.072	0.084	0.091	0.103
0.535	0.025	0.024	0.033	0.048	0.069	0.082	0.090	0.102
0.558	0.025	0.023	0.032	0.047	0.065	0.078	0.086	0.098
0.581	0.025	0.023	0.031	0.046	0.058	0.072	0.080	0.094
0.605	0.025	0.023	0.031	0.045	0.052	0.066	0.075	0.088
0.628	0.025	0.022	0.032	0.045	0.044	0.057	0.066	0.081
0.651	0.025	0.024	0.033	0.045	0.035	0.049	0.060	0.074
0.674	0.026	0.024	0.032	0.045	0.028	0.041	0.052	0.066
0.698	0.025	0.022	0.032	0.044	0.021	0.034	0.046	0.061
0.721	0.026	0.022	0.031	0.045	0.015	0.030	0.043	0.058
0.744	0.027	0.021	0.030	0.042	0.009	0.024	0.038	0.052
0.767	0.028	0.022	0.030	0.042	0.003	0.019	0.031	0.048
0.791	0.028	0.022	0.030	0.041	0.000	0.011	0.024	0.040
0.814	0.028	0.023	0.030	0.040	0.000	0.002	0.016	0.032
0.837	0.029	0.025	0.031	0.041	0.000	0.000	0.010	0.026
0.860	0.030	0.027	0.032	0.041	0.000	0.000	0.005	0.021
0.884	0.030	0.028	0.033	0.041	0.000	0.000	0.000	0.015
0.907	0.030	0.030	0.037	0.043	0.000	0.000	0.000	0.006
0.930	0.029	0.033	0.037	0.043	0.000	0.000	0.000	0.000
0.953	0.026	0.029	0.033	0.039	0.000	0.000	0.000	0.000
0.977	0.027	0.030	0.031	0.036	0.000	0.000	0.000	0.000
1.000	0.027	0.033	0.033	0.032	0.000	0.000	0.000	0.000

	volume fractions for 10 % 50 μm ballotini			
	rpm			
r/R	306	366	426	480
0.00	0.693	0.528	0.303	0.175
0.02	0.643	0.398	0.195	0.097
0.04	0.597	0.323	0.170	0.100
0.06	0.511	0.276	0.150	0.099
0.09	0.435	0.246	0.146	0.106
0.11	0.356	0.202	0.135	0.105
0.13	0.282	0.161	0.126	0.109
0.15	0.219	0.131	0.111	0.106
0.17	0.167	0.113	0.106	0.107
0.19	0.122	0.099	0.101	0.105
0.21	0.090	0.090	0.100	0.104
0.23	0.066	0.080	0.093	0.099
0.26	0.050	0.073	0.089	0.097
0.28	0.040	0.068	0.086	0.094
0.30	0.037	0.068	0.089	0.096
0.32	0.037	0.070	0.091	0.098
0.34	0.032	0.067	0.089	0.098
0.36	0.019	0.057	0.081	0.089
0.38	0.027	0.064	0.089	0.097
0.40	0.026	0.062	0.086	0.096
0.43	0.025	0.062	0.087	0.097
0.447	0.035	0.070	0.095	0.105
0.47	0.041	0.075	0.101	0.110
0.49	0.037	0.064	0.087	0.093
0.51	0.037	0.072	0.098	0.108
0.53	0.032	0.068	0.095	0.106
0.55	0.028	0.066	0.093	0.104
0.57	0.022	0.061	0.089	0.101
0.60	0.015	0.058	0.086	0.098
0.62	0.009	0.053	0.082	0.094
0.64	0.005	0.050	0.079	0.092
0.66	0.000	0.047	0.077	0.089
0.68	0.000	0.045	0.075	0.088
0.70	0.000	0.044	0.073	0.086
0.72	0.000	0.043	0.072	0.086
0.74	0.000	0.042	0.071	0.085
0.77	0.000	0.043	0.072	0.086
0.79	0.000	0.044	0.073	0.087
0.81	0.000	0.046	0.074	0.089
0.83	0.000	0.049	0.076	0.091
0.85	0.000	0.053	0.080	0.094
0.87	0.000	0.056	0.082	0.097
0.89	0.001	0.061	0.086	0.101
0.91	0.006	0.065	0.089	0.104
0.94	0.012	0.070	0.093	0.108
0.96	0.015	0.072	0.093	0.109
0.98	0.016	0.072	0.092	0.108
1.00	0.015	0.072	0.092	0.108

APPENDIX U2

1D MRI data of nylon suspension in the 50 mm tank

	volume fractions for 5 % 500 μm nylon					volume fractions for 10 % 500 μm nylon					volume fractions for 15 % 500 μm nylon					volume fractions for 20 % 500 μm nylon				
	rpm					rpm					rpm					rpm				
r/R	186	306	366	426	480	186	306	366	426	480	186	306	366	426	480	186	306	366	426	480
0.00	0.077	0 038	0.032	0.034	0.139	0 198	0 118	0.112	0.094	0 085	0.249	0.148	0 152	0 149	0.146	0.4022	0 2059	0.1886	0 1815	0.1740
0.02	0.043	0.016	0.014	0.015	0.078	0 150	0.086	0.079	0.068	0.065	0 213	0 135	0 149	0 147	0.146	0.3885	0.1910	0.1773	0.1710	0.1656
0 04	0.037	0.016	0.015	0 016	0.058	0 140	0.101	0.097	0.088	0.086	0.191	0 134	0 145	0.143	0 142	0.3745	0.1837	0.1713	0 1665	0.1631
0 06	0.036	0.021	0.020	0 021	0.046	0.116	0.087	0.083	0.075	0 075	0 182	0.147	0 147	0 145	0 144	0 3611	0 1927	0.1820	0 1775	0.1745
0.09	0.039	0 027	0.026	0.027	0.043	0.116	0 096	0.091	0.084	0.084	0.180	0.158	0.148	0.146	0.145	0 3415	0 2002	0.1913	0 1867	0.1834
0.11	0.038	0 028	0.029	0.029	0.039	0.112	0.095	0.092	0 085	0.085	0.178	0.163	0.148	0.147	0.145	0.3197	0.2056	0.1983	0.1943	0.1895
0.13	0.041	0.033	0.034	0.034	0.041	0 114	0.101	0.097	0 092	0.091	0 177	0.168	0.149	0.148	0 146	0.2983	0 2106	0.2041	0.2012	0.1978
0.15	0.042	0.036	0.037	0 037	0.043	0.112	0.100	0.097	0.092	0.092	0 180	0.171	0.150	0.149	0 147	0.2825	0.2167	0.2112	0 2091	0.2045
0.17	0.046	0.041	0.042	0 042	0.047	0 116	0.104	0.100	0.097	0.096	0 180	0 173	0 149	0.148	0 147	0.2689	0.2192	0.2144	0.2130	0 2077
0.19	0.049	0.045	0.045	0.045	0.050	0.115	0.104	0.100	0.097	0.097	0 184	0.178	0.150	0.149	0.148	0.2593	0.2234	0.2195	0.2175	0 2137
0.21	0.052	0.049	0.049	0.049	0.054	0.119	0.109	0.104	0.103	0.102	0.185	0.180	0.150	0.149	0.149	0.2493	0.2273	0.2231	0.2205	0.2158
0.23	0.052	0.050	0.050	0.049	0.054	0.121	0.111	0.107	0.105	0.104	0 189	0.183	0.150	0.149	0.149	0.2421	0.2282	0.2240	0.2202	0.2158
0.26	0.053	0.051	0.051	0.050	0.055	0.122	0.112	0.108	0.106	0.106	0 191	0.184	0.148	0.147	0.147	0.2333	0.2267	0.2235	0.2192	0.2152
0.28	0.052	0.051	0 051	0.050	0.055	0.123	0.113	0.109	0.107	0 106	0.196	0 190	0.149	0.148	0 149	0.2311	0 2313	0 2278	0 2230	0.2198
0.30	0.054	0.055	0.055	0.053	0 058	0.125	0.116	0.112	0.109	0 108	0.208	0.204	0.152	0.151	0 152	0.2357	0.2391	0.2363	0 2309	0.2279
0 32	0 058	0.060	0.060	0.056	0.062	0.122	0 113	0.108	0.107	0 106	0.216	0.216	0.154	0.154	0 156	0.2358	0 2439	0.2429	0 2386	0.2368
0.34	0.052	0.054	0.054	0.052	0 054	0.118	0 108	0.105	0.106	0.104	0.196	0.196	0.146	0.146	0.148	0 2108	0.2241	0.2243	0.2212	0.2193
0 36	0.040	0 043	0.044	0.041	0.040	0.114	0.108	0 106	0 107	0.105	0.182	0.184	0.141	0 141	0 143	0 1961	0 2122	0.2142	0 2110	0.2088
0.38	0.044	0 046	0.047	0.044	0.042	0 107	0.105	0.103	0 103	0.102	0.184	0 188	0.143	0 144	0.146	0 1919	0.2107	0 2130	0.2107	0 2095
0.40	0.034	0.037	0.037	0.036	0.029	0 104	0.104	0.102	0 103	0.102	0.163	0.167	0 137	0 138	0 140	0 1709	0.1934	0 1964	0 1939	0 1910
0.43	0 031	0 034	0 035	0 033	0.026	0.102	0.107	0.105	0.104	0.104	0 162	0.166	0 139	0 141	0 142	0 1731	0.1951	0 1978	0 1953	0 1931
0.447	0.038	0 041	0 042	0.040	0.034	0.099	0 105	0.104	0.102	0 101	0.174	0.180	0.148	0.150	0 150	0.1868	0 2092	0.2110	0 2090	0.2086
0.47	0.042	0.045	0 046	0.044	0.039	0.102	0 108	0.107	0.106	0.105	0 174	0 183	0 152	0.154	0 154	0.1907	0 2131	0.2141	0 2117	0.2111
0.49	0.034	0.038	0.039	0.038	0.033	0.103	0.108	0 107	0.106	0.104	0 164	0.176	0 138	0.140	0 139	0.1862	0.2099	0.2087	0.2057	0.2077
0 51	0.040	0 043	0.045	0.043	0.036	0.089	0.094	0.094	0.093	0.089	0 164	0 175	0 154	0.155	0.156	0 1878	0.2099	0.2111	0 2084	0.2079
0.53	0.039	0.042	0.045	0 043	0.036	0.102	0 107	0 106	0.105	0.103	0 159	0.170	0.154	0.155	0.155	0.1840	0.2086	0.2092	0 2076	0.2068
0.55	0 040	0 043	0 046	0.045	0 038	0.102	0 108	0 106	0.106	0 104	0 157	0.169	0 153	0 155	0.155	0.1844	0 2087	0.2098	0 2078	0 2082
0.57	0.040	0 043	0 046	0.046	0.037	0.102	0.106	0 104	0.104	0 102	0.152	0.165	0.152	0 153	0 153	0 1811	0 2068	0.2082	0 2068	0 2073
0 60	0.040	0 043	0 047	0.047	0.037	0.101	0 106	0 104	0.104	0 102	0 149	0 162	0.152	0 153	0 152	0 1795	0 2056	0.2077	0 2074	0 2068
0.62	0 038	0 043	0.046	0.046	0 035	0.099	0.105	0.103	0.103	0 102	0 143	0.157	0.151	0 152	0 152	0 1753	0 2016	0.2036	0 2050	0 2043
0.64	0 039	0 044	0 048	0 048	0.036	0.100	0 105	0.104	0 104	0.103	0 139	0.153	0 153	0.153	0 152	0 1730	0.2006	0.2026	0 2034	0 2040
0.66	0.040	0.045	0.049	0.049	0.035	0.098	0 103	0.103	0 104	0.103	0.133	0.147	0 153	0 154	0 153	0 1686	0.1977	0.1998	0 1999	0 2012
0.68	0.044	0 050	0.053	0 053	0.038	0.098	0 102	0.102	0.103	0.103	0 130	0.143	0 154	0 154	0 153	0 1663	0.1954	0 1975	0 1986	0 2020
0.70	0 049	0 055	0.058	0 059	0.043	0.096	0.101	0.101	0 102	0.102	0.127	0 140	0.153	0 154	0.152	0.1638	0 1931	0 1960	0 1972	0.2005
0.72	0.054	0.060	0.063	0.064	0.047	0.094	0.100	0.101	0.103	0.103	0.127	0.138	0 153	0.154	0.152	0 1615	0 1909	0 1935	0 1963	0.1981
0.74	0.056	0 063	0.065	0.066	0 048	0 091	0.098	0.100	0.102	0 104	0 122	0 134	0 153	0.153	0 152	0 1580	0.1879	0 1909	0 1944	0 1963
0.77	0 059	0.067	0 068	0.070	0.051	0 089	0.097	0.099	0.103	0 105	0 115	0.126	0 154	0 154	0 153	0.1567	0 1876	0.1890	0 1926	0 1958
0 79	0 062	0 070	0 071	0 073	0.053	0 087	0.096	0.099	0.103	0 106	0 109	0 120	0.155	0 155	0 154	0.1543	0 1860	0 1868	0 1901	0 1941
0.81	0.065	0.074	0.075	0.076	0.057	0 085	0.094	0.098	0.103	0.107	0 103	0 115	0.155	0.154	0 154	0.1521	0 1846	0.1857	0 1886	0 1929
0 83	0.069	0.077	0.077	0.078	0 058	0.081	0.093	0.096	0 103	0 106	0 099	0 112	0 154	0 154	0 154	0 1513	0 1840	0 1851	0 1868	0 1925
0.85	0.070	0.079	0.077	0.079	0.060	0.079	0.093	0.098	0 105	0.108	0 098	0.110	0 153	0.153	0.154	0 1522	0 1847	0 1849	0 1879	0 1933
0.87	0.070	0.078	0.076	0.077	0.060	0.078	0.093	0.101	0 107	0.111	0 092	0.106	0 152	0.152	0 153	0 1529	0.1857	0 1858	0 1890	0 1950
0.89	0.069	0 077	0 073	0.075	0.060	0.075	0.091	0 099	0.106	0.109	0.086	0 101	0.152	0 153	0 154	0.1535	0.1862	0.1868	0.1887	0 1961
0.91	0.070	0 077	0.072	0 073	0.062	0.071	0.088	0.096	0.103	0.106	0.080	0.096	0.153	0 153	0 154	0.1544	0.1874	0.1878	0 1897	0.1961
0.94	0.072	0.077	0 071	0 073	0.065	0.068	0.086	0.095	0.101	0.104	0 074	0 091	0.153	0.154	0.155	0.1558	0 1893	0.1890	0 1913	0.1979
0 96	0.070	0.072	0 066	0.068	0 065	0 065	0.084	0.093	0.098	0.101	0.063	0.080	0.151	0 152	0 154	0.1565	0.1909	0.1896	0 1934	0.1994
0.98	0.063	0 064	0.058	0.060	0.062	0 062	0.084	0.092	0 096	0.099	0 049	0.067	0.149	0 150	0.153	0 1559	0.1896	0.1886	0 1930	0.1983
1.00	0.059	0.058	0.051	0.054	0.059	0.061	0 083	0.092	0 094	0 095	0 032	0.053	0 150	0 151	0 152	0.1494	0.1872	0.1860	0.1920	0 1980

APPENDIX U3

3D radial MRI data of particle suspension in the 50 mm tank

5 % 50 μm ballotini at 480 rpm

	z (mm)				z (mm)						
r/R	1.6	3.1	4.7	r/R	6.3	10.9	15.6	21.9	26.6	31.3	35.9
0.00	0.085	0.058	0.049	0.00	0.060	0.044	0.038			0.036	
0.10	0.084	0.055	0.043	0.08	0.070	0.043	0.036		0.038	0.035	0.038
0.20	0.095	0.062	0.043	0.17	0.057	0.040	0.036		0.039	0.034	0.037
0.30	0.106	0.069	0.044	0.25	0.039	0.037	0.035		0.040	0.033	0.038
0.40	0.121	0.083	0.052	0.33	0.037	0.037	0.037		0.042	0.035	0.037
0.50	0.069	0.088	0.062	0.42	0.038	0.039	0.038		0.041	0.035	0.037
0.60	0.119	0.098	0.068	0.50	0.037	0.039	0.038	0.033	0.039	0.034	0.037
0.70	0.119	0.114	0.104	0.58	0.036	0.039	0.039	0.032	0.039	0.034	0.036
0.80	0.112	0.112	0.117	0.67	0.040	0.039	0.039	0.034	0.039	0.031	0.034
0.90	0.104	0.110	0.127	0.75	0.052	0.038	0.035	0.035	0.037	0.032	0.032
1.00	0.097	0.095	0.110	0.83	0.070	0.037	0.034	0.034	0.037	0.031	0.026
				0.92	0.094	0.037	0.037	0.033	0.039	0.031	0.025
				1.00	0.070	0.047	0.037	0.028	0.038	0.030	0.018

10 % 50 μm ballotini at 480 rpm

	z (mm)				z (mm)							
r/R	0.9	1.8	2.7	4.5	r/R	10.7	13.4	15.2	17.0	25.9	31.3	38.4
0.00	0.045	0.069	0.070	0.075	0.00	0.104	0.081	0.149				
0.04	0.069	0.080	0.079	0.081	0.05	0.104	0.082	0.147				
0.08	0.078	0.088	0.091	0.082	0.10	0.101	0.083	0.141		0.072	0.037	0.031
0.12	0.075	0.092	0.094	0.074	0.14	0.097	0.086	0.149		0.046	0.018	0.008
0.16	0.081	0.100	0.095	0.068	0.19	0.097	0.088	0.172		0.054	0.033	0.019
0.20	0.099	0.111	0.099	0.073	0.24	0.099	0.087	0.171		0.066	0.052	0.036
0.24	0.094	0.108	0.096	0.079	0.29	0.095	0.083	0.125		0.059	0.046	0.028
0.28	0.058	0.084	0.079	0.070	0.33	0.088	0.079	0.090		0.044	0.025	0.007
0.32	0.021	0.058	0.061	0.053	0.38	0.085	0.076	0.082		0.050	0.020	0.002
0.36	0.004	0.045	0.054	0.042	0.43	0.090	0.078	0.089		0.068	0.033	0.013
0.40	0.005	0.049	0.059	0.043	0.48	0.093	0.082	0.095	0.071	0.074	0.035	0.016
0.44	0.014	0.057	0.063	0.046	0.52	0.089	0.083	0.090	0.067	0.064	0.018	0.007
0.48	0.036	0.060	0.057	0.046	0.57	0.084	0.082	0.083	0 067	0.057	0.003	0.003
0.52	0.072	0.060	0.047	0.051	0.62	0.081	0.084	0.082	0.070	0.064	0.012	0.011
0.56	0.100	0.064	0.045	0.060	0.67	0.076	0.085	0.078	0.068	0.067	0.023	0.014
0.60	0.093	0.071	0.056	0.062	0.71	0.066	0.080	0.070	0.060	0.057	0.018	0.003
0.64	0.065	0.077	0.074	0.052	0.76	0.061	0.075	0.068	0.055	0.047	0.007	0.000
0.68	0.049	0.081	0.084	0.042	0.81	0.065	0.075	0.076	0.057	0.054	0.012	0.000
0.72	0.048	0.083	0.085	0.041	0.86	0.066	0.076	0.079	0.057	0.070	0.023	0.001
0.76	0.047	0.081	0.081	0.044	0.90	0.058	0.069	0.069	0.050	0.087	0.022	0.016
0.80	0.047	0.082	0.083	0.048	0.95	0.050	0.058	0.057	0.046		0.009	0.029
0.84	0.062	0.090	0.091	0.058	1.00	0.058	0.060	0.062	0.057			
0.88	0.082	0.101	0.099	0.069								
0.92	0.078	0.103	0.102	0.071								
0.96	0.058	0.095	0.097	0.063								
1.00	0.073	0.093	0.091	0.065								

The x-direction concentration for the 10 % 50 μm ballotini at 480 rpm

	z (mm)			
x/R	0.93	1.85	2.78	3.70
0.00	0.175	0.119	0.143	0.142
0.04	0.149	0.111	0.134	0.137
0.07	0.128	0.093	0.114	0.116
0.11	0.117	0.089	0.103	0.102
0.15	0.132	0.092	0.098	0.095
0.19	0.175	0.128	0.109	0.100
0.22	0.209	0.152	0.130	0.097
0.26	0.246	0 180	0.138	0.096
0.30	0.274	0.187	0 139	0.092
0.33	0.296	0.210	0.147	0.088
0.37	0.295	0.223	0.148	0.082
0.41	0.313	0.223	0.148	0.083
0.44	0.301	0.199	0.136	0.085
0.48	0.241	0.157	0.114	0.082
0.52	0.187	0.120	0.099	0.083
0.56	0.148	0.098	0.096	0.088
0.59	0.148	0.088	0.095	0.090
0.63	0.164	0.091	0.097	0.088
0.67	0.165	0.093	0.095	0.082
0.70	0.162	0.097	0.094	0.078
0.74	0.209	0.104	0.095	0.072
0.78	0.228	0.119	0.098	0.067
0.81	0.267	0.139	0.100	0.070
0.85	0.300	0.165	0.113	0.080
0.89	0.311	0.190	0.125	0.082
0.93	0.353	0.224	0.158	0.095
0.96	0.372	0.239	0.178	0.115
1.00	0.309	0.256	0.199	0.132

APPENDIX U4

10 % suspension of 500 μm nylon at 480 rpm

	z (mm)											
r/R	0.0	0.9	1.8	2.6	6.1	10.5	14.0	16.7	21.1	26.3	31.6	38.6
0	0.270	0.171	0.117	0.115	0.155	0.168	0.052					
0.05	0.283	0.177	0.118	0.115	0.154	0.168	0.053					
0.09	0.314	0.184	0.115	0.107	0.152	0.169	0.064					
0.14	0.330	0.178	0.102	0.089	0.149	0.173	0.086		0.169			
0.18	0.318	0.160	0.086	0.075	0.146	0.181	0.107		0.227	0.206	0.199	0.107
0.23	0.298	0.147	0.080	0.075	0.144	0.186	0.117		0.219	0.183	0.176	0.087
0.27	0.293	0.158	0.091	0.086	0.145	0.181	0.121	0.546	0.175	0.126	0.130	0.071
0.32	0.302	0.178	0.107	0.089	0.148	0.170	0.128	0.241	0.122	0.083	0.090	0.059
0.36	0.300	0.178	0.105	0.076	0.146	0.163	0.139	0.209	0.110	0.092	0.086	0.058
0.41	0.283	0.160	0.090	0.060	0.142	0.161	0.150	0.168	0.131	0.121	0.098	0.063
0.45	0.278	0.148	0.081	0.060	0.142	0.161	0.159	0.129	0.126	0.125	0.096	0.058
0.50	0.291	0.157	0.090	0.078	0.143	0.161	0.163	0.110	0.096	0.112	0.092	0.048
0.55	0.315	0.172	0.105	0.097	0.136	0.166	0.162	0.112	0.098	0.114	0.108	0.055
0.59	0.322	0.175	0.111	0.106	0.119	0.170	0.158	0.114	0.135	0.127	0.126	0.073
0.64	0.306	0.166	0.106	0.104	0.105	0.167	0.157	0.109	0.152	0.125	0.125	0.078
0.68	0.289	0.160	0.100	0.097	0.101	0.157	0.160	0.110	0.136	0.106	0.110	0.063
0.73	0.296	0.164	0.096	0.091	0.103	0.148	0.161	0.121	0.126	0.095	0.104	0.053
0.77	0.317	0.170	0.094	0.090	0.101	0.143	0.156	0.129	0.144	0.097	0.109	0.060
0.82	0.328	0.176	0.099	0.095	0.100	0.139	0.152	0.130	0.150	0.096	0.107	0.065
0.86	0.326	0.185	0.113	0.105	0.111	0.133	0.150	0.133	0.127	0.094	0.102	0.053
0.91	0.316	0.192	0.124	0.112	0.124	0.129	0.143	0.145	0.104	0.103	0.106	0.046
0.95	0.305	0.184	0.117	0.110	0.118	0.121	0.126	0.150	0.112	0.112	0.113	0.055
1.00	0.291	0.161	0.095	0.098	0.096	0.099	0.103	0.135	0.123	0.094	0.101	0.053

Radial MRI data at electrode postions for 5 % 50 μm ballotini

	z/Z			
r/R	0.14	0.38	0.62	0.86
0.50	0.037	0.035	0.034	0.034
0.58	0.039	0.034	0.034	0.033
0.67	0.042	0.035	0.031	0.036
0.75	0.040	0.034	0.032	0.026
0.83	0.037	0.035	0.031	0.025
0.92	0.047	0.034	0.031	0.021
1.00	0.063	0.036	0.030	0.018

Radial MRI data at electrode postions for 10 % 500 μm nylon

	z/Z			
r/R	0.14	0.38	0.62	0.86
0.545	0.164	0.119	0.108	0.055
0.591	0.153	0.148	0.126	0.073
0.636	0.140	0.155	0.125	0.078
0.682	0.132	0.134	0.110	0.063
0.727	0.130	0.122	0.104	0.053
0.773	0.130	0.138	0.109	0.060
0.818	0.133	0.149	0.107	0.065
0.864	0.139	0.133	0.102	0.053
0.909	0.143	0.113	0.106	0.046
0.955	0.136	0.107	0.113	0.055
1.000	0.116	0.104	0.101	0.053

Radial MRI data at electrode postions for 10 % 50 μm ballotini

	z/Z			
r/R	0.14	0.38	0.62	0.86
0.52	0.089	0.068	0.034	0.115
0.57	0.049	0.067	0.038	0.111
0.62	0.041	0.065	0.029	0.112
0.67	0.043	0.064	0.030	0.115
0.71	0.055	0.064	0.046	0.105
0.76	0.064	0.069	0.052	0.094
0.81	0.068	0.072	0.032	0.097
0.86	0.074	0.079	0.019	0.100
0.90	0.083	0.081	0.046	0.086
0.95	0.087	0.095	0.100	0.072
1.00	0.087	0.120	0.102	0.085

APPENDIX V

ERT data for air

LBP relative resistance data for sparging in pilot scale tank

	Plane Number							
rpm	1	2	3	4	5	6	7	8
100	8.78	7.75	7.53	7.53	7.46	7.49	7.53	7.78
150	8.59	7.78	7.61	7.65	7.61	7.68	7.73	7.97
200	8.46	7.78	7.64	7.70	7.72	7.77	7.83	8.06
250	8.37	7.78	7.67	7.78	7.80	7.87	7.89	8.17
300	8.27	7.78	7.70	7.82	7.86	7.89	7.93	8.28
400	8.17	7.79	7.76	7.90	7.95	8.00	8.06	8.50
450	8.15	7.77	7.75	7.90	7.94	7.95	8.00	8.47

ERT data of air at 0.5 vvm while agitated

rpm	236			353			547		
r/R	L1	L2	L3	L1	L2	L3	L1	L2	L3
0.551	0.005	0.015	0.003	0.020	0.035	0.013	0.058	0.083	0.044
0.626	0.007	0.016	0.008	0.024	0.037	0.021	0.067	0.084	0.063
0.705	0.014	0.016	0.012	0.030	0.035	0.029	0.074	0.078	0.077
0.788	0.020	0.019	0.013	0.036	0.034	0.032	0.081	0.079	0.083
0.876	0.023	0.020	0.015	0.039	0.034	0.033	0.084	0.080	0.083
0.962	0.023	0.020	0.015	0.039	0.033	0.034	0.085	0.078	0.085

ERT data of air at 1.0 vvm while agitated

rpm	236			353			547		
r/R	L1	L2	L3	L1	L2	L3	L1	L2	L3
0.551	0.021	0.040	0.015	0.042	0.061	0.028	0.078	0.116	0.049
0.626	0.016	0.038	0.023	0.049	0.066	0.040	0.082	0.112	0.069
0.705	0.020	0.036	0.028	0.055	0.060	0.050	0.087	0.099	0.085
0.788	0.024	0.036	0.028	0.059	0.057	0.052	0.096	0.096	0.091
0.876	0.025	0.037	0.029	0.055	0.054	0.054	0.099	0.094	0.092
0.962	0.025	0.036	0.029	0.055	0.052	0.056	0.101	0.092	0.095

ERT surface aeration data

rpm	304			353			460			547		
r/R	L1	L2	L3	L1	L2	L3	L1	L2	L3	L1	L2	L3
0.551	0.0026	0.0011	0.0046	0.0059	0.0072	0.0098	0.023	0.032	0.024	0.038	0.053	0.036
0.626	0.0026	0.0038	0.0049	0.0060	0.0097	0.0100	0.024	0.035	0.029	0.041	0.056	0.047
0.705	0.0029	0.0049	0.0048	0.0068	0.0105	0.0109	0.026	0.035	0.036	0.044	0.055	0.056
0.788	0.0032	0.0038	0.0039	0.0076	0.0093	0.0111	0.028	0.034	0.039	0.047	0.054	0.060
0.876	0.0031	0.0024	0.0029	0.0077	0.0077	0.0097	0.028	0.032	0.037	0.048	0.053	0.059
0.962	0.0030	0.0020	0.0025	0.0076	0.0073	0.0095	0.028	0.031	0.038	0.048	0.052	0.060

APPENDIX W

Yeast Data

ERT Data

ERT 5 % v/v yeast at 236 rpm in 220 mm tank

r/R	L1	L2	L3	L4
0.551	0.071	0.052	0.056	0.060
0.626	0.065	0.055	0.052	0 053
0.705	0 055	0.053	0.050	0.052
0.788	0 055	0.050	0.057	0.059
0.876	0.054	0.046	0.063	0.064
0.962	0.053	0.044	0.063	0.065
average	0 059	0.050	0.057	0.059

ERT 5 % v/v yeast at 480 rpm in 50 mm tank

r/R	L1	L2	L3	L4
0.551	0.064	0.066	0.067	0.075
0.626	0.064	0.064	0.066	0.073
0.707	0.063	0.062	0.062	0.067
0.783	0 065	0.063	0.063	0.064
0.866	0.064	0.062	0.061	0.062
0.958	0 062	0.060	0.058	0.060
average	0 064	0.063	0.063	0 067

ERT 11 % v/v yeast at 480 rpm in 50 mm tank

r/R	L1	L2	L3	L4
0.551	0.085	0.090	0.085	0 079
0.626	0.083	0.086	0.082	0 072
0.707	0.082	0.083	0.080	0.068
0.783	0.087	0.084	0.081	0.071
0.866	0.090	0.084	0.083	0.073
0.958	0.087	0.083	0 082	0.072
average	0.086	0.085	0.082	0.072

ERT 5 % yeast + 10 % nylon at 480 rpm in 50 mm tank

r/R	L1	L2	L3	L4
0.551	0.185	0.193	0 169	0 140
0.626	0.170	0.169	0 154	0 105
0.707	0.160	0.155	0 146	0 095
0.783	0.161	0.154	0.151	0 103
0.866	0.171	0.169	0.166	0.124
0.958	0.174	0.175	0.171	0.133
average	0.170	0.169	0.160	0.117

MRI Data

Axial data for 5 % yeast at 480 rpm in 50 mm vessel

	rpm				
z/Z	186	306	366	426	480
0.00	0 066	0.064	0.068	0.071	0.062
0.02	0.046	0.047	0.051	0.052	0.045
0.04	0.050	0.050	0.054	0.054	0.048
0.06	0.044	0.045	0.048	0.047	0.042
0.08	0.046	0.046	0.048	0.047	0.043
0.10	0.043	0.043	0.044	0.041	0.038
0.12	0.045	0.045	0.045	0.042	0.040
0.14	0.044	0.043	0.043	0.040	0.039
0.16	0.046	0.046	0.044	0.042	0.042
0.18	0.044	0.044	0.042	0.039	0.041
0.20	0.044	0.043	0.041	0.038	0.041
0.22	0.041	0.040	0.037	0.035	0.039
0.24	0.040	0.038	0.036	0.034	0.039
0.26	0.038	0.037	0.035	0.034	0.040
0.28	0 042	0.041	0.038	0.038	0.044
0.30	0.038	0.038	0.034	0.034	0.041
0.32	0.030	0.031	0.028	0.028	0.035
0.34	0.036	0.038	0.035	0.035	0.042
0.36	0.035	0.038	0.036	0.036	0.042
0.38	0 036	0.039	0.037	0.037	0.043
0.40	0 048	0 051	0.049	0.049	0.053
0.42	0 057	0.059	0.057	0.057	0.060
0.44	0 047	0.046	0.045	0.045	0.047
0.46	0.058	0.061	0.060	0.060	0.061
0.48	0.058	0.061	0.059	0 059	0.060
0.50	0.056	0.059	0.057	0.057	0.057
0.52	0.055	0.057	0.055	0.054	0.053
0.54	0.056	0.057	0 054	0.053	0 051
0.56	0 058	0.058	0.055	0.054	0.051
0.58	0.061	0.060	0.057	0 055	0.051
0.60	0.063	0.061	0 058	0.055	0.052
0.62	0.063	0.060	0.057	0.054	0.051
0 64	0.064	0 060	0 057	0.054	0.051
0.66	0.065	0.060	0.057	0.054	0.050
0.68	0.067	0.061	0 058	0.055	0.052
0.70	0.070	0.063	0.060	0.057	0.054
0.72	0.070	0.063	0.060	0.058	0.055
0.74	0 068	0.061	0.059	0.057	0.055
0.76	0.066	0.059	0.057	0.056	0.055
0.78	0.062	0.056	0.055	0.054	0.055
0.80	0 060	0.054	0.054	0 054	0.055
0.82	0 057	0.053	0.054	0.055	0.056
0.84	0 055	0.052	0.054	0.056	0.058
0.86	0 050	0.050	0.052	0.055	0.058
0.88	0.041	0.044	0.047	0.051	0.054
0.90	0 035	0.039	0.043	0.047	0.050
0.92	0 036	0.041	0.047	0.051	0.052
0.94	0.044	0.050	0.057	0.062	0.061
0.96	0.042	0.052	0.061	0.068	0.066
0.98	0 031	0.045	0.056	0.065	0.062
1.00	0.030	0 043	0.055	0.065	0.059

Axial data for 11 % yeast at 480 rpm in 50 mm vessel

	rpm				
z/Z	186	306	366	426	480
0.00	0.144	0.144	0.140	0.142	0.142
0.02	0.103	0.103	0.100	0.103	0.108
0.04	0.105	0.104	0.102	0.104	0.108
0.06	0.100	0.099	0.097	0 099	0.101
0 09	0.104	0.103	0.101	0.102	0.101
0.11	0.100	0.099	0.097	0.098	0.096
0.13	0.102	0.101	0.100	0.100	0.096
0.15	0.101	0.099	0.098	0.098	0.094
0.17	0.104	0.102	0.101	0.101	0.096
0.19	0.104	0.102	0.101	0.099	0.096
0.21	0.106	0.104	0.103	0.101	0.098
0.23	0.103	0.101	0.100	0.098	0.096
0.26	0.103	0.101	0.100	0.097	0.094
0.28	0.100	0.098	0.097	0.094	0.092
0.30	0.105	0.103	0.103	0.099	0 096
0.32	0.107	0.107	0.106	0.103	0.098
0.34	0.104	0.104	0.104	0.101	0 096
0.36	0.095	0.096	0.097	0.094	0.090
0.38	0.102	0.103	0.105	0 102	0.099
0.40	0.098	0.100	0.102	0 101	0.098
0 43	0.100	0.102	0 105	0 105	0 104
0.447	0.108	0.111	0 114	0.114	0.114
0.47	0.115	0.117	0 121	0.121	0.122
0 49	0.088	0.092	0 096	0 098	0.100
0 51	0.110	0.113	0.117	0 120	0.119
0.53	0.106	0.109	0.113	0 117	0.115
0.55	0.104	0.107	0.111	0 115	0.116
0 57	0.101	0.104	0.108	0.112	0.115
0 60	0.101	0.103	0.107	0.112	0 115
0.62	0.100	0.101	0.104	0 109	0.114
0.64	0.100	0.101	0.104	0 108	0.113
0.66	0.098	0.099	0.101	0 105	0 110
0 68	0.099	0.099	0 101	0.104	0 110
0.70	0.099	0.099	0.100	0.104	0.111
0.72	0.101	0.101	0.102	0.105	0.113
0.74	0.104	0 103	0.104	0.106	0.114
0.77	0.108	0 107	0.107	0.108	0.115
0.79	0.111	0.110	0.109	0.109	0.115
0.81	0 114	0.113	0.112	0.111	0.116
0.83	0.118	0.116	0.115	0.113	0.115
0.85	0.122	0.121	0.119	0.117	0.118
0.87	0.127	0.126	0.124	0.121	0.121
0.89	0.133	0.132	0.130	0.126	0.124
0.91	0.139	0.138	0.135	0.131	0.127
0.94	0.143	0.142	0.139	0.135	0.130
0.96	0.144	0.143	0.139	0.136	0.131
0.98	0.145	0.145	0.141	0.138	0.133
1.00	0.153	0.153	0.148	0.145	0 141

Axial data for 5 % yeast + 10 % nylon at 480 rpm in 50 mm vessel

	rpm				
z/Z	186	306	366	426	480
0.00	0.282	0.153	0.140	0.135	0.131
0.02	0.267	0.141	0.132	0.128	0.125
0.04	0.253	0.136	0.127	0.124	0.122
0.06	0.238	0.143	0.135	0.132	0.130
0.09	0.219	0.148	0.143	0.139	0.137
0.11	0.200	0.152	0.148	0.145	0.141
0.13	0.186	0.155	0.152	0.150	0.148
0.15	0.180	0.160	0.157	0.156	0.153
0.17	0.175	0.162	0.160	0.159	0.155
0.19	0.173	0.165	0.163	0.162	0.159
0.21	0.170	0.168	0.166	0.164	0.161
0.23	0 169	0.168	0.166	0.164	0.161
0.26	0.166	0.167	0 166	0.163	0.161
0.28	0 167	0.171	0 169	0.167	0.164
0.30	0 170	0.177	0.176	0.172	0.170
0.32	0 171	0.180	0 181	0.178	0.176
0.34	0 154	0.166	0.167	0.165	0.163
0.36	0 144	0.156	0 159	0 157	0.155
0.38	0 141	0.155	0.158	0.157	0.156
0.40	0.125	0.142	0.146	0.145	0 142
0.43	0 127	0.143	0.147	0.146	0 144
0.447	0 137	0.154	0.157	0.156	0 155
0 47	0 139	0.157	0.159	0.158	0.157
0 49	0.137	0.155	0.155	0.154	0.155
0.51	0.138	0 155	0.157	0.156	0.155
0.53	0 135	0.154	0 156	0.155	0.154
0.55	0 135	0.154	0 156	0.155	0.155
0.57	0 133	0.152	0 155	0.155	0.155
0.60	0 132	0.151	0 154	0.155	0.154
0.62	0 129	0.148	0.151	0.153	0 152
0.64	0.128	0.147	0 150	0.152	0.152
0.66	0 124	0.145	0 148	0.150	0.150
0.68	0 123	0.144	0.146	0.149	0.151
0.70	0.122	0.143	0 145	0.147	0.150
0.72	0 120	0.141	0.144	0.147	0.148
0.74	0.118	0.138	0.142	0.145	0.146
0.77	0 117	0.138	0.140	0.144	0.146
0.79	0.115	0.137	0 139	0.142	0.145
0.81	0.113	0.136	0.139	0.141	0 144
0.83	0.113	0.135	0.138	0.139	0.144
0.85	0.113	0.136	0.138	0.140	0.144
0.87	0.114	0.137	0.138	0.141	0.146
0.89	0.114	0.137	0 139	0.141	0.147
0.91	0.114	0.138	0.139	0.142	0.147
0.94	0 115	0.140	0.140	0.143	0.148
0.96	0.117	0.141	0.140	0.144	0.149
0.98	0.116	0.140	0.139	0.144	0.149
1.00	0.111	0.138	0.138	0.143	0.148

Radial data 5 % yeast +10 % nylon at 480 rpm in 50 mm vessel

r/R	L1	L2	L3	L4
1.00	0 110	0.178	0.124	0.210
0.96	0.129	0.172	0.153	0.204
0.93	0.134	0.170	0.159	0.214
0.89	0.143	0.166	0.141	0.211
0.86	0.153	0.165	0.139	0.215
0.82	0.159	0.171	0.133	0.206
0.79	0 166	0.175	0.128	0.208
0.75	0 167	0.165	0.128	0.206
0.71	0.163	0.158	0.127	0.202
0.68	0.160	0.158	0.125	0.204
0.64	0.158	0 161	0.125	0.210
0.61	0 155	0.163	0.126	0.216
0.57	0.150	0.160	0 129	0.224
0.54	0.148	0.160	0.132	0.233